Signal Theory and Communications Department

Ph.D. Thesis

Automatic Detection of Signals by Using Artificial Intelligence Techniques

Author:

Raúl Vicen Bueno

Supervisors:

Prof. Manuel Rosa Zurera

Assoc. Prof. María Pilar Jarabo Amores

2011

Time waits for none ...

... fortunately, *Cristina*, *Víctor* and *Diego*
have known how to wait for this moment.

For this and other reasons,
this work is dedicated to them.

Acknowledgements

I would like to thank my supervisors, Ph.D. *Manuel Rosa Zurera* and Ph.D *María Pilar Jarabo Amores*, their advices and support during the research and the writing of this Ph.D. thesis.

I would also like to thank Ph.D. *José Carlos Nieto Borge* his advices during the research. Moreover, I want to thank him the access to the WaMoS II marine radar scans (real-live database) used in the thesis. These radar scans were obtained at the FINO 1 German research platform (North Sea, Germany) and provided by the Federal Marine and Hydrographic Agency of Germany (Bundesamt für Seeschifffahrt und Hydrographie, BSH) and OceanWaveS GmbH, Germany. Without these radar scans, I could not check the magnitude of the contributions made in this thesis and the utility of them for the marine radar community.

Finally, I would like to thank all the students that have been working with me in topics close to the one presented in this thesis for making me think in a different way. Even when their research topics were sometimes really far from the topic of the thesis, they have made me think about the way of dealing with research:

"*Research is worthless when no applicability*
is found for people and society."

Raúl Vicen, 2011

Resumen

La detección automática de señales (blancos) en interferencia aditiva (clutter más ruido) es un problema no resuelto hoy en día. Muchos y diversos esquemas de detección son propuestos constantemente en revistas especializadas sobre temas de investigación radar y de procesado de señal. Esos esquemas son adaptados normalmente a la casuística del problema, es decir, a los blancos y al tipo de clutter presentes en esos experimentos. Es por ello que la tesis presentada a continuación busca proponer un esquema de detección que trabaje con altas prestaciones en distintos entornos.

En esta tesis se pretende resolver dos tipos de problemas: uno centrado en la detección de blancos radar de tipo Swerling 0 en presencia de clutter sintético modelado con una distribución Weibull y ruido blanco Gaussiano; y otro centrado en la detección de barcos en movimiento a partir de imágenes radar provenientes de un radar marino comercial. Se ha comprobado que los datos reales están estadísticamente relacionados con los datos sintéticos simulados, lo cual permitirá proponer un único esquema de detección que trabaje en ambos casos.

Teniendo en cuenta los problemas de detección planteados, se asumen varias premisas. Las imágenes radar generadas en entornos simulados tienen en cuenta una correlación temporal entre celdas consecutivas de la imagen y una distribución espacial constante de los parámetros estadísticos del clutter dentro de una misma imagen, pero variable de una imagen a otra. Dentro de este entorno simulado, se asumen distintos tamaños y formas de blanco. Estos entornos han sido simulados mediante el uso de los parámetros estadísticos del clutter descritos en la literatura. Comparando dichos entornos, se observa una gran disparidad en sus parámetros estadísticos, haciendo más difícil aún si cabe la tarea de proponer un detector radar que trabaje correctamente y con altas prestaciones en distintos entornos radar.

Para resolver los problemas de detección planteados, se han considerado detectores radar utilizados habitualmente en la literatura. Así, se ha seleccionado como detector de referencia para el caso de trabajar con datos procedente de un radar coherente el detector de blanco conocido a priori (TSKAP: *target sequence known a priori*). Detectores basados en técnicas CFAR (*constant false alarm rate*) han sido elegidos para el caso de trabajar con datos procedentes de un radar incoherente. Por otro lado, se ha estudiado el uso de técnicas de inteligencia artificial (IA) para crear detectores que resuelvan los dos problemas de detección planteados. De las posibles técnicas de IA existentes en la literatura, se han elegido dos tipos de redes neuronales artificiales (RNAs):

el perceptron multicapa (MLP: *Multilayer perceptron*) y las RNAs basadas en funciones de base radial (RBFNs: *Radial basis function networks*). Mediante este tipo de técnicas, se proponen nuevas estrategias de detección para los casos coherente e incoherente. Aparte de la contribución en el uso de técnicas de IA en temas de detección radar, se presenta otra contribución importante: el uso de nuevos modos de selección de celdas de una imagen para la mejora de las prestaciones del detector radar propuesto. Estos modos están basados en esquemas de selección con retardo (en una o dos dimensiones), dentro de los cuales se pueden elegir más celdas para poder realizar una mejor estimación de los parámetros del clutter que rodea al blanco. Además, el uso de estos modos de selección en dos dimensiones en detectores CFAR también puede ser considerado contribución ya que antes no se habían presentado resultados para los modos aquí propuestos.

Los experimentos desarrollados consideran entornos simulados de mar, mar helado y tierra para el diseño y test de los detectores coherentes tomados como referencia y los basados en IA. En estos experimentos, se estudió la influencia de los siguientes parámetros durante el diseño de los detectores bajo estudio: las propiedades del clutter presente en las imágenes de los conjuntos de diseño (para entrenar RNAs y establecer el umbral de detección); los modos de selección; el número de celdas seleccionadas; así como el número de neuronas ocultas en las RNAs. A partir de estos estudios, se obtienen los valores de dichos parámetros, de tal forma que se obtienen altas prestaciones, mientras que se mantiene un coste computacional moderado en el detector propuesto. Una vez diseñados los detectores, éstos se testean utilizando un conjunto de datos de test no utilizado previamente. Este conjunto de test está compuesto por imágenes radar con distintas propiedades estadísticas para simular lo que ocurre en entornos reales. Las prestaciones observadas para este conjunto son ligeramente inferiores a los obtenidas en la etapa de diseño. Además, se observa que las prestaciones del detector para las distintas imágenes radar del conjunto, es decir, para distintos condiciones de clutter, presentan pequeñas variaciones. Esto nos indica un alto grado de robustez en los detectores cuando las condiciones de clutter cambian con el tiempo. Teniendo en cuenta estas pequeñas variaciones de las prestaciones del detector, podemos inferir que las mismas prestaciones presentadas aquí se pueden obtener cuando el detector diseñado procese nuevas imágenes radar en el futuro.

Por otro lado, se han realizado estudios similares para el caso de detectores incoherentes en entornos simulados de mar, mar helado y tierra. De estos estudios, destacamos las diferencias que existen entre los resultados obtenidos por los detectores coherentes e incoherentes en entornos simulados de clutter de mar. La primera diferencia que se observa es que las prestaciones del detector incoherente son ligeramente menores que las obtenidas por el coherente, aspecto que era de esperar porque sólo considera la información de amplitud. La segunda diferencia observada es la alta reducción de coste computacional que se obtiene, siendo esto debido a que en estos detectores se utiliza menos información a la entrada. Los resultados obtenidos para los entornos simulados de mar helado y tierra no han sido incorporados en la memoria de la tesis porque tanto las prestaciones como el coste computacional obtenidos son similares a los obtenidos para el caso de entornos marinos.

Finalmente, se han diseñado y testeado detectores incoherentes para trabajar con imágenes provenientes de un radar marino comercial situado en la plataforma de investigación alemana FINO-1, la cual se encuentra localizada en el mar del Norte (Alemania). Antes de proceder con el diseño de estos detectores, se comprobó que las medidas de clutter contenidas en las imágenes radar seguían una distribución Weibull, tal y como se asumió en el entorno simulado

de mar. Acto seguido a esta comprobación, se procedió con el ajuste de los parámetros de cada uno de los detectores bajo estudio (CFAR y basados en técnicas de IA) para obtener las mejores prestaciones posibles, así como un coste computacional moderado. Una vez diseñados los detectores, se procedió a testearlos, llegando a las mismas conclusiones a las que se llegó para el caso sintético: alta robustez frente a cambios en las condiciones de diseño y baja pérdida de prestaciones cuando se procesan nuevas imágenes radar. También se muestra cual es el coste computacional de la configuración seleccionada en los casos de detectores incoherentes basados en MLPs y RBFNs, así como la velocidad de computo necesaria para poder procesar imágenes radar en tiempo real. A partir de estos resultados, se llega a la conclusión final de que como las unidades de procesado disponibles en el mercado permiten trabajar a las velocidades que necesita el sistema, el procesado en tiempo real está garantizado.

A partir del análisis de las prestaciones obtenidas para los distintos casos de estudio abordados en la tesis, se llega a la siguiente conclusión general: los detectores basados en técnicas de IA mejoran las prestaciones obtenidas por los detectores de referencia seleccionados de la literatura en todos los casos de estudio presentados. Ésta conclusión se obtiene para radares que trabajan a distintas frecuencias, con distintas resoluciones y con receptores diferentes (coherentes e incoherentes). Además, esta conclusión también es independiente del entorno radar bajo estudio (mar, mar helado y tierra).

Abstract

The automatic detection of signals (targets) in additive interference (clutter and noise) is not a problem completely solved nowadays. Many different approaches are reported every year in the specialized literature depending on the targets to be detected and the kind of interference present in the environment where the sensor is working. In this way, a detection approach that is able to work in different environments is searched in this thesis.

This thesis tries to solve two detection problems: the detection of moving Swerling 0 targets in synthetic Weibull-distributed clutter and white Gaussian noise; and the detection of moving vessels in marine radar environments. A relationship between these two problems is found in the thesis, allowing to propose a unique detection scheme that works in both cases.

According to the detection problems to be solved in the thesis, some premises are set. Synthetic radar scans are generated in simulated environments having: time-correlation between consecutive cells; and constant clutter properties (skewness parameter) inside a scan, but variable scan-to-scan. Targets of different sizes and shapes are included in the synthetic radar scans. Different radar environments have been considered in the thesis by using the statistical parameters of sea, sea-ice and ground clutters reported in the literature. From these environments, it is observed that the clutter statistics are different each other, making the problem of proposing a detector scheme able to work with high performance in different environments more complicated.

For solving the detection problems this thesis deals with, Artificial Intelligence (AI) based detectors are proposed, and compared with commonly used detectors selected from the literature. The coherent detector set as reference is the *target sequence known a priori* (TSKAP) detector. The incoherent detector set as reference is based on *constant false alarm rate* (CFAR) techniques. From AI techniques, two feed-forward artificial neural networks (ANNs) strategies are selected: the multilayer perceptrons (MLPs) and the radial basis function ANNs (RBF-ANNs, also referred as RBFNs). By using these AI techniques, coherent and incoherent approaches are proposed. An additional contribution is made in the thesis by proposing new modes of selecting the cells to be processed. Thus, not only the commonly used non-delayed selection modes are used, but also additional delayed selection modes are studied. These proposed modes are based on 2-dimension selection templates, instead of the 1-dimension templates commonly used in CFAR detectors.

Experiments considering the reference and AI-based coherent detectors have been carried out in simulated sea, sea-ice and ground environments. In these experiments, the influence of the

following parameters in the design stage of the detectors is studied: the clutter properties of the data sets used to design the detectors (for training the MLPs and RBFNs, and for setting the detection threshold); the selection modes; the number of selected cells; and the number of hidden neurons in AI-based detectors. From these studies, the values for obtaining the highest performance, while maintaining a low computational cost, are selected. Once the reference and AI-based detectors are designed, they are tested using a set of radar scans never processed before (test data set). This data set is composed of radar scans with different clutter conditions (simulating real environments). The performance obtained for this data set is slightly lower than the one achieved in the design stage. Moreover, the performances achieved for each particular radar scan of the test data set, i.e. for different clutter conditions, present low variations, denoting high robustness of the detector against changes in clutter conditions. According to these low performance variations, we can infer the performance achieved by the detectors when processing new radar scans in the future with similar clutter properties as the ones used here.

Similar studies have been made when using reference and AI-based incoherent detectors in synthetic sea, sea-ice and ground environments. From the analysis of incoherent detectors in synthetic sea clutter, we focus on the differences observed with respect to coherent detectors in synthetic sea clutter. First, a low performance decrease is observed, being expected because the incoherent detectors only process the amplitude of the cells. And second, a high computational cost decrease is observed in AI-based incoherent detectors because less information is used at their inputs. The results obtained when designing and testing incoherent detectors in synthetic sea-ice and ground environments are not reported in the thesis because similar performance losses and computational cost decreases as the ones presented above are obtained.

Finally, incoherent detectors have been designed and tested when processing radar scans obtained by a standard marine radar. This marine radar was sited in the FINO-1 German research platform (North Sea, Germany). It has been statistically checked that the measurements of the clutter fit the Weibull distribution. In this way, CFAR and AI-based detectors were designed by tuning their parameters in order to obtain the highest performance, while maintaining a reasonable computational cost. Once designed, they were tested obtaining similar conclusions as for the synthetic case: high robustness against clutter condition changes and low performance loss when processing new radar scans. The computational costs of the proposed configurations of MLP and RBFN-based incoherent detectors are reported. The processing speed needed to process radar scans in real-time is also reported. And since commercial processing units can fulfill this processing speed, the proposed AI-based detector can process marine radar scans in real-time.

From the analysis of the performance obtained in the different cases of study, this thesis finishes with the following conclusion: the proposed AI-based detectors outperform the reference detectors in all the cases of study presented in the thesis. This conclusion is obtained when processing radar scans from radars working at different frequencies, with different resolutions and with different receivers (coherent and incoherent). Moreover, this conclusion is independent of the radar environment under study (sea, sea-ice and ground).

INDEX

Part I

Preliminary Study: Motivation, Radar Data and Reference Detectors

CHAPTER 1

Motivation, State of the Art, Objectives and Structure of the Thesis

This chapter presents the motivation of the thesis, which can be synthesized as: "*the automatic detection of desired signals in presence of interference*", which drives the study of the state of the art about this topic. This study let us find some commonly used detectors, which are taken as reference in our studies. Moreover, from this study, several objectives are set before starting to solve this problem. Finally, according to these objectives, the structure of the thesis is presented to explain how the detectors are designed and validated.

1.1 Motivation of the Thesis

The automatic detection of desired signals (targets) in presence of interference signals (clutter and noise) is a difficult task, especially when the interference is strong. Moreover, depending on the target and clutter statistics, finding the analytical expressions that characterize the detectors is very difficult and sometimes not possible. In these situations, numerical approximations are used and suboptimum detectors, in the Neyman-Pearson[1] sense, are considered. Therefore, it motivates us to search a detection scheme that approximates this detector. The Neyman-Pearson detector can be implemented by comparing the likelihood ratio $\Lambda(\mathbf{z}[n])$ for a given observation vector, $\mathbf{z}[n]$, with a detection threshold (THR) fixed taking into account the P_{fa} requirements, as stated in Eq. (1.1) [Neyman1933, VanTrees1997]. In this expression, $f(\mathbf{z}[n]|H_1)$ and $f(\mathbf{z}[n]|H_0)$ are the likelihood functions under the alternative (H_1) and null (H_0) hypothesis, respectively.

$$\Lambda(\mathbf{z}[n]) = \frac{f(\mathbf{z}[n]|H_1)}{f(\mathbf{z}[n]|H_0)} \underset{H_0}{\overset{H_1}{\gtrless}} \text{THR}(P_{\text{fa}}) \tag{1.1}$$

After analyzing the Neyman-Pearson detection theory, the basic detection scheme used in the thesis is presented in Fig. 1.1. $F(\mathbf{z}[n])$ represents the function approximated by the signal processing technique under consideration.

Among other signal processing techniques, some artificial intelligent (AI) techniques, such as artificial neural networks (ANNs), have been satisfactorily used for detecting different kind of tar-

[1] The Neyman-Pearson detector maximizes the probability of detection (P_{d}), while maintaining the probability of false alarm (P_{fa}) below or equal to a given value [Neyman1933].

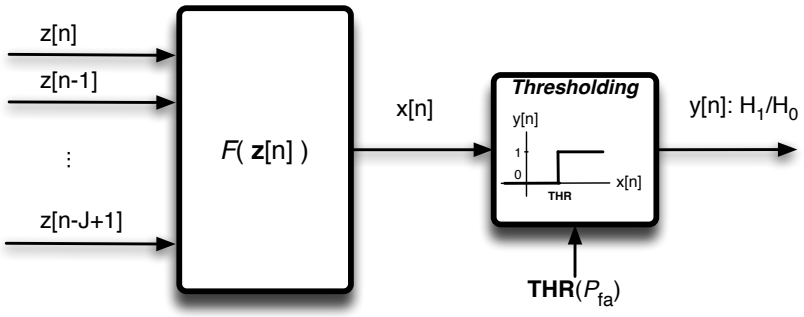

Figure 1.1: Basic scheme of the proposed detector to approximate the Neyman-Pearson detector

get models in synthetic noise [Jarabo2004, Andina1996, Andina1995a]. Moreover, in [Jarabo2009] and [Jarabo2005] the approximation of the Neyman-Pearson detector by learning machines trained with supervised learning machines, such as ANNs, was described for these detection problems. Considering these studies, this Ph.D. thesis studies the application of these AI techniques to design detectors that are able to detect targets in presence of clutter and noise.

The environments where the proposed detectors try to detect the targets are scanned by coherent or incoherent remote sensing systems. For the research carried out in this thesis, real-live measurements are available from an incoherent system. Unfortunately coherent measurements are not available. Some target and clutter models commonly used in the literature are considered in the thesis for coherent measurements.

Coherent systems give information about the environment by the in-phase and quadrature components, or, by the magnitude and phase components. One example of the measurements contained in a scan done by a coherent radar are depicted in Fig. 1.2, where the clutter conditions are very strong. The radar configuration and environment are the ones used in modeling the measurements of ground clutter (see Sect. 2.3.5). Observing this scan, the following questions could come to our mind: Is there any target in the scan (environment)? How many targets are there? Where are they? etc.

Incoherent systems give only the information about the magnitude of the measurements. One example of the real-live measurements done by a incoherent marine radar is depicted in the scan of Fig. 1.3, where the environment is not so severe as in the previous coherent scan. The radar configuration and environment are presented in Sect. 2.4. Observing this scan, the same questions as in the coherent measurements could rise up again.

It is important to note that although the applications considered in the thesis are particularized for radar (*radio detection and ranging*) systems, the proposals presented in this thesis try to be as general as possible to be applied in other systems where similar problems are found. For instance, as a Weibull distribution is used to model the clutter in our case of study, the proposed detectors could be extrapolated and used in problems like: detection of trends in extreme temperatures modeled by the Weibull distribution [Jandhyala1999]; detection of watermarks in image processing [Cheng2003, Barni2003, Oostveen2000]; detection of outliers in Weibull-distributed problems [Fung1985]; and detection of frailties in lifetime data [Caroni2004].

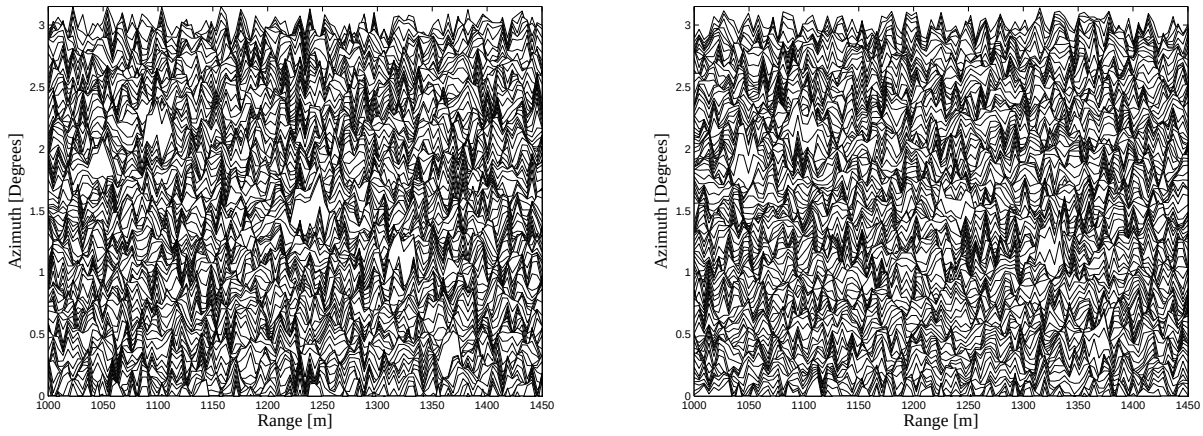

(a) In-Phase component

(b) Quadrature component

Figure 1.2: Example of a synthetic scan obtained with a coherent measurement (radar) system.

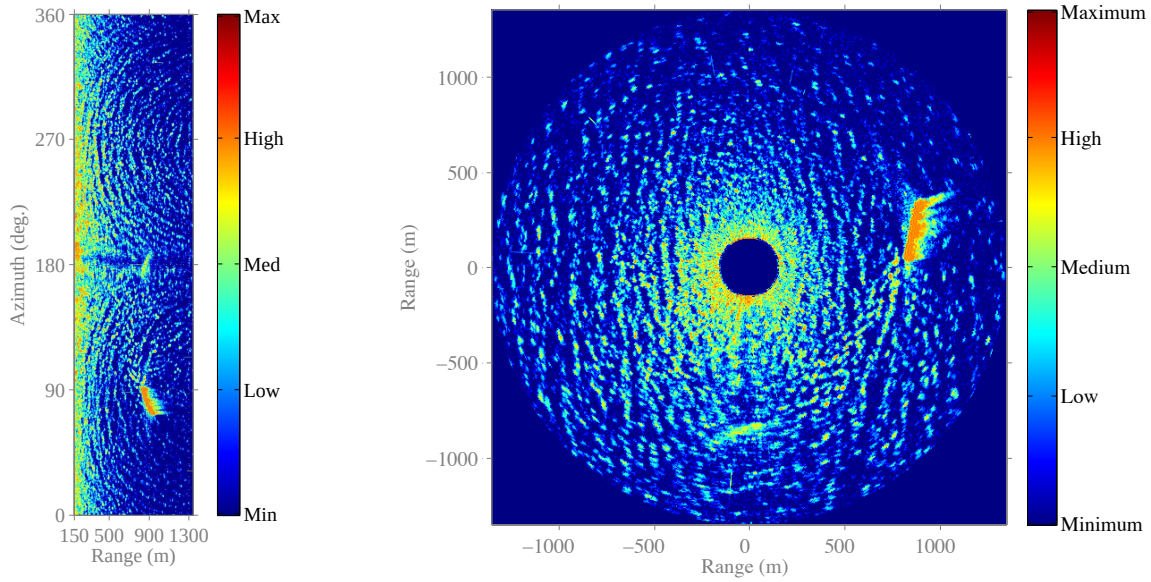

(a) Cartesian plot of polar data

(b) Cartesian plot of range data

Figure 1.3: Example of a scan obtained with an incoherent marine radar.

1.2 State of the art

As discussed in the previous section, the main motivation of the thesis is the search of a detection scheme able to work correctly with both coherent and incoherent data. Because real-live coherent data are not available, a study of the models and parameters that are used to synthesize these data is done first. After that, a study of the detection schemes that could be used in our case of study is done. From this last study, several coherent and incoherent detection schemes are selected as reference in our studies. Moreover, several opportunities are found where new

contributions in this field can be made.

1.2.1 From measurements to synthetic clutter models

The measurement systems considered in this thesis can work in different environments. For that reason, and taking into account that having access to real-live data is sometimes difficult, accurate clutter models are needed. A study of several clutter models considered in the literature is done according to sea, sea-ice and ground clutter conditions, which will be used in the section concerning to the experimental results of this thesis.

Sea clutter

From the beginning of the 1970's decade, several studies have been done about the statistical properties of sea clutter. Trunk et al. studied in [Trunk1970, Trunk1972] the statistics of sea clutter measurements, finding non-Gaussian and non-Rayleigh properties. They proposed the use of models based on the log-normal distribution. In the same decade, Jakeman and Pusey [Jakeman1976] proposed a model for non-Rayleigh sea echo measurements. In this study, log-normal and K distributions were successfully used to model the sea surface radar cross section (RCS), where spatial and temporal correlations were considered. In the 1980's, non-Gaussian clutter models in the frequency domain were proposed in [Baker1985], where K-distributed clutter models were successfully used. The same statistical distribution was used by Watts in [Watts1985, Watts1987a, Watts1987b]. The first two works were focused on sea clutter modeling by compound K distribution models, whereas the third one presented the spatial correlation of the K-distributed sea clutter. On the other hand, Farina et al. proposed in [Farina1986b] the use of log-normal clutter models. A different clutter model was used in [Lewinski1983], where the RCS measurements from the sea clutter were modeled by a Weibull distribution. This model was successfully used, not only for sea clutter, but also for other kinds of clutters, as presented Sekine in [Sekine1990]. These works changed the way of modeling the clutter, both for sea clutter and other kinds of clutter, as discussed in the following subsections.

From the 1990's decade, several research works were published about sea clutter modeling. In this way, Haykin et al. presented in [Haykin1997, Haykin2002] that the dynamic of sea clutter is mainly non-linear. As Haykin noted, due to this non-linear dynamic, non-linear signal processing is needed to reduce the level of clutter and to achieve high performance detectors in clutter-governed environments. This author also proposed in [Haykin1997] that non-linear clutter dynamics can be modeled by the chaos theory. In parallel, this work also proposed the use of K and Weibull distributions to model sea clutter.

Other studies were done about sea clutter modeling of real-live data using:

- Log-normal distribution [Farina1998, Billingsley1999, Gini2000] and [Greco2004].
- K and generalized K distributions [Farina1998, Billingsley1999, Gini2000, Greco2004] and [Ward2006].
- Weibull distribution [Billingsley1999, Gini2000, Greco2004] and [Ward2006]. These studies were compared with the results obtained with the previous distributions, denoting that the Weibull distribution fitted better the real-live data under consideration.

- Log-Weibull distribution [Sayama2001]. In this study, Weibull, log-Weibull and K distributions were used to model sea and other kinds of clutter. In this case, the Weibull and log-Weibull distributions fitted better their measurements.

Sea-ice clutter

RCS is greater for sea-ice than for sea waves. It is known that the RCS of sea clutter mainly depends on sea state, while the RCS of sea-ice mainly depends on type (young or multiyear ice) and thickness of sea-ice. In general, sea-ice includes fast ice and pack ice. Fast ice is defined as stationary ice near the coast, while pack ice is a moving ice. Pack ice collides together and hummocks are formed, which grow from a height of a few meters to ten meters.

Radar returns from sea-ice depend not only on volumetric structure, but also on surface roughness, dielectric constant, age, thickness, development history and temperature of the ice [Golden1998, Sekine1990]. Moreover, the dynamics of sea-ice clutter is purely non-linear, as Haykin noted in [Haykin1997, Haykin2002], where Weibull and K distributions were considered as valid models. The same distribution was successfully used for the same purpose by Sayama et al. in [Sayama2001, Sayama2002, Sayama2004, Sayama2005], where log-normal and log-Weibull distributions were also used to approximate the statistical behavior of sea-ice clutter. From the previous works we can conclude that the distribution that best fit the radar measurements is the Weibull one.

Ground/Land clutter

The RCS of ground clutter, also referred as land clutter, has been described in the literature for many types of terrain. This RCS is obtained with radars of different frequencies (L and X bands) and at different grazing angles (angle between the mean horizontal at the scene and the incoming radar illuminator). The considered analytical models predict many of the observed trends in data as a function of range, antenna height, terrain roughness and wavelength.

The interest of modeling this kind of clutter starts practically in the 1980's with the work of Barton [Barton1985], where non-Gaussian and non-Rayleigh clutter models were used. Nevertheless, Schleher [Schleher1976] previously proposed the use of Rayleigh and non-Rayleigh distributions. Both works have a common factor: the authors used the Weibull distribution to model different types of ground clutter and terrains. Schleher's work is very important because the skewness parameter of the Weibull distribution was given for several kinds of terrain (rocky mountains, wooded hills, forest, cultivated land) and sea states. On the other hand, Rayleigh and Gaussian distributions were used to model ground clutter measured by different radar systems, as discussed in [Billingsley1999, Billingsley2002] and [Diani1996, Billingsley2002, Conte2005], respectively. These and other studies denoted that better models can be obtained using different statistical distributions, such as:

- Log-normal distribution [Billingsley1999, Billingsley2002].
- K and generalized K distributions [Sujuan1996, Billingsley1999, Sayama2001, Billingsley2002] and [Davidson2004] to model the measured data. In [Lombardo1999a], K-distributed models were used to model the power spectral density (PSD) of the clutter. On the other hand, in [Oliver1985, Marier1995], correlated K-distributed models were considered.

- Weibull distribution [Sekine1990, Billingsley1999, Sayama2001, Billingsley2002] and [Davidson2004]. These works demonstrate that this model fits better the real-live data than the previous ones.

Conclusions about the clutter models

From the results presented in the research works studied above for different kinds of clutter, a general conclusion is extracted: The models that best fit the clutter measurements are generally based on the K and Weibull distributions. For that reason, the Weibull distribution is selected to model different kind of clutters considered in this thesis.

1.2.2 Automatic target detection in clutter

Radar signal detection in clutter is a very complex task, which is generally performed by statistical methods. In this way, if the probability density functions (*pdf*s) of the target and clutter signals are known, optimum detectors can be obtained [VanTrees1997, Skolnik2001, Richards2005, Skolnik2008]. In real-live data, the statistical properties of the target and clutter signals can vary in time and are not usually known, making the use of optimum detectors unfeasible. Suboptimum detectors can be obtained instead. For these kind of detectors, parametric and non-parametric techniques can be used. Parametric techniques suppose that the target and clutter *pdf* models are known and their statistical parameters can be estimated. On the other hand, non-parametric techniques do not suppose that the signal *pdf*s follow a given statistical distribution model.

Depending on the different techniques used to automate the process of detection, several kinds of detectors can be found. Most of them are presented in the following subsections. As noted below, several detectors could be grouped in two or more kinds of detectors, but they are mainly classified in one of them because of its relevancy.

Clutter reduction techniques in detection systems

Different clutter reduction techniques can be used to improve the performance of radar detectors. They usually depend on the clutter model. Only the most relevant ones are analyzed below.

Considering clutter environments following a log-normal distribution, Farina et al. presented in [Farina1986b] two processor architectures. The first one, used in current practice, was composed of a linear transversal filter (for clutter attenuation and target enhancement) cascaded with a quadratic envelope detector and a comparison with a suitable threshold. The second processor differed from the previous one in the clutter cancellation filter. In this case, a non-linear homomorphic filter was used to obtain a higher clutter suppression. On the other hand, Almarshad et al. presented in [Almarshad2008] two novel algorithms for automatic censoring of radar interfering targets in different log-normal clutter environments. These algorithms consisted in removing the corrupted reference cells (censoring) before detection. Both steps were performed dynamically by using a suitable set of ranked cells to estimate the unknown background level and set the adaptive thresholds accordingly. The proposed detectors, neither require any prior information about the clutter parameters, nor require the number of interfering targets.

Concerning the detection of targets embedded in compound-Gaussian clutter, Conte and De Maio [Conte2004] proposed clutter mitigation techniques. These techniques were used on adap-

tive detection schemes for ensuring constant false alarm rate (CFAR). Thus, the threshold could be set independently of the clutter distribution as well as its covariance, even if the environment is highly heterogeneous. Clutter reduction was done by a decision rule based on a recursive clutter covariance matrix estimator.

Focusing on Weibull-distributed clutter environments, Farina et al. presented in [Farina1987a, Farina1987b] optimum and suboptimum radar processors to detect a priori known target signals in this kind of clutter. The processors were based on two non-linear estimators of the clutter samples in the two alternative hypotheses (H_0 and H_1). These processors were suitable even in challenging environments including spiky clutter and/or spiky target (e.g. stealth). Because of the relevance of the suboptimum coherent detector presented in these works, it is taken as reference in the thesis to validate the proposed coherent detectors.

Finally, it is important to emphasize the work of Farina et al. [Farina1997], where the application of different (linear and non-linear) clutter cancellation techniques in coherent radar detectors were analyzed. From the results, they concluded that non-linear techniques improved the capability of detecting targets with Doppler frequencies close to the clutter mean Doppler frequency, compared to linear techniques. This conclusion is very useful in the thesis because it indicates that non-linear signal processing techniques are better to obtain high performance detectors under non-Gaussian-distributed clutter.

Detectors using frequency domain information

Frequency domain techniques are successfully used in radar detection because of the relative movement (Doppler effect) between target and clutter. Some examples are the classical approaches moving target indicator (MTI) and moving target detector (MTD) [Skolnik2001]. Next, some works where clutter environments are close to the ones considered in the thesis are analyzed.

An adaptive radar detection algorithm for the detection of small pieces of ice floating in an open sea environment was presented in [Battacharya1992]. The detection was carried out in the time-frequency domain, which eliminated the limitations of standard Doppler processing. The detection scheme used an MLP as pattern classifier, where the final decision was done.

The detection of incoherent pulse trains in compound-Gaussian disturbance with known spectral density was discussed in [Conte1999]. This work proposed three alternative processors, where only one of them (based on the fast Fourier transform, FFT) was implementable in real clutter and target situations. Although this processor was suboptimum, it works properly even in the presence of very spiky clutter. This processor was independent of the clutter amplitude *pdf*, what involves CFAR independently of the clutter distribution.

Orthogonal frequency division multiplexing (OFDM) techniques were considered in [Sen2009], where the problem of detecting a moving target in clutter environments was considered. The broadband OFDM signal provided frequency diversity to improve the performance of the system.

Detectors based on statistical signal processing

Statistical signal processing techniques have been widely used during the last decades for radar detection purposes. They are commonly based on: generalized likelihood ratio (GLR) or likelihood ratio (LR) tests; Neyman-Pearson tests; or covariance matrix estimations.

The detection of targets in presence of coherent and incoherent K-distributed clutter was discussed in several works, as presented below. In [Aluffi1992], the detection of a priori known Swerling zero targets embedded in coherent clutter was done by using a LR test. In [Conte1991], the detection of signals with unknown parameters in correlated noise was considered by using the Neyman-Pearson strategy. In [Conte1994], two schemes for detecting targets in clutter were compared: one implementing the GLR test, and the other using a discrete realization of the Neyman-Pearson detector. The results showed that both strategies yield equivalent performance, but the GLR test was simpler in its structure and offered some additional advantages, both at the design and analysis stages. In [Farina1995], the optimum strategy to detect a priori known targets in coherent clutter was presented, which was based on the LR test. But these optimum approaches are not realistic because it is necessary to know the target before detecting it. Because of that, suboptimum approaches are used. In this way, a suboptimum approach for detecting known signals in coherent K-distributed and Gaussian-distributed clutter sources was presented in [Gini1995] and [Gini1997b] by using the LR test. The resulting detection strategy was linear-quadratic, clutter distribution free (guaranteeing CFAR behavior) and achieved performances similar to the optimum case. Continuing with the previous problem, an approximation to the optimum detector was determined in [Gini1997a] by thresholding an appropriate LR test in an interference environment with unknown correlation. In [Lombardo1996], another approach to the optimum radar detection of targets embedded in K-distributed clutter with partially correlated texture was studied. Parallel and sequential implementations of the approaches to the optimum detector were given. These detectors were interpreted as the conditional estimate of the Gaussian LR of the speckle averaged over the correlated texture distribution. On this basis, a suboptimum detection scheme was derived, replacing the conditional mean estimation by a maximum a posteriori estimate.

Different detection schemes were proposed when other clutter conditions are considered. Rajesh and Prabhu presented in [Rajesh1999] the detection of targets embedded in Weibull clutter. This problem was addressed using modified sample matrix inversion (MSMI) and GLR techniques and adaptive filtering and CFAR control. Although the GLR algorithm is robust for non-Gaussian interference, the MSMI algorithm was quite sensitive and gave rise to false alarms. To deal with non-Gaussian interference, such as Weibull clutter, the Gaussianing-whitening approach was adopted since MSMI and GLR are optimized for Gaussian interference. On the other hand, radar detection in Weibull clutter was examined from a statistical detection viewpoint in [Schleher1976]. Weibull clutter parameters were determined and related to measured values of land and sea clutter. Optimum performance in Weibull clutter was determined and practical receivers that approach this performance were identified. The receiver performances in Rayleigh, log-normal and Weibull clutter were also evaluated and compared.

Finally, other statistical signal processing techniques can be used. Thus, for the clutter reduction-based detectors presented in [Conte2004], a covariance matrix estimation was used for maintaining CFAR behavior independently of the clutter parameters. Farina and Russo presented in [Farina1986a] the theory of estimator-correlator receiver to the case of a Gaussian-distributed time-correlated target embedded in clutter and thermal noise. Two equivalent detection schemes were obtained: a batch detector and a recursive detector. The problem of covariance matrix estimation for adaptive radar detection in heavly-tailed correlated clutter with unknown statistics was also dealt with in [Gini2002]. This work presented an approximation to the maximum

likelihood estimator.

CFAR detectors

These techniques can be considered as a part of the previous one, but they are explained in a separate section because of their relevance in target detection. The purpose of these techniques is to maintain a constant false alarm rate by an automatic adaptation of the detection threshold according to the clutter power and characteristics. This threshold adaptation is necessary because the statistical parameters of the clutter distribution are not usually known and may be non-stationary. CFAR techniques are commonly used with incoherent measurements. Some of the commonly used CFAR detectors/processors are presented below.

Cell Averaging (CA) CFAR detectors. CA-CFAR detectors are commonly used in the literature as basic reference for comparison purposes. Some modifications of this kind of detector are proposed in the literature, being: Greatest Of (GO) CFAR detector, also known as GOCA-CFAR; and Smallest Of (SO) CFAR detector, also known as SOCA-CFAR.

Starting with the analysis of CA-CFAR detectors, Watts et al. [Watts1990] and Sciotti et al. [Sciotti2001] presented several methods and analytical approximations for the performance of these detectors. In these works, the detection of fluctuating targets in real-live sea clutter (K-distributed) from maritime surveillance radars was presented.

Continuing with the analysis of CA, GOCA and SOCA-CFAR detectors, an analytical study of their performances is found in [Gandhi1988]. In this work, multiple environments with one or several interfering Swerling I targets in heterogeneous Gaussian-distributed clutter were considered. El Mashade presented in [Mashade1998b, Mashade2000, Mashade2002] a similar study of these detectors but considering homogeneous and correlated clutter. The targets considered in these studies were modeled by Rayleigh and Chi-square distributions, including moderately fluctuating targets between Swerling I and II models [Swerling1997]. Finally, the application of these detectors was also presented in [Davidson2004] where land clutter was considered.

The application of CA-CFAR detectors when Weibull-distributed clutter is present was considered in [Anastassopoulos1995, DeMiguel1998, Liu2003]. The basic principles of the CA-CFAR detection scheme are set in [DeMiguel1998]. Moreover, in this work, analytical expressions that relate the P_{fa} with the detection threshold are set for Weibull clutter. This work and detector are taken as basic reference in the thesis.

Maximum Likelihood (ML) CFAR detectors. ML-CFAR detectors outperform CA-CFAR detectors by doing more accurate estimations of the clutter parameters to set better the detection threshold.

The application of ML-CFAR detectors when Weibull-distributed clutter is studied in several works [Ravid1992, Anastassopoulos1995, Mezache2007, Mezache2008]. The first one [Ravid1992] is the most relevant one because it sets the principles of the ML-CFAR detector when uniform clutter and multi-target situations are considered. Its principles are based on the estimation of the shape and scale parameters of the Weibull-distributed clutter to automatically adapt the detection threshold. For that reason, this work is taken as reference in the studies of the thesis

when incoherent radar data are used. The other works use the ML-CFAR detectors as reference for proposing new and improved detection schemes in Weibull clutter.

Ordered Statistics (OS) CFAR detectors. OS-CFAR detectors are usually considered to alleviate the problems of CA-CFAR detectors. These detectors set the decision threshold by processing magnitude-ordered observations within finite moving windows.

Analytical expressions of OS-CFAR detectors were derived in [Gandhi1988], demonstrating that these detectors outperform the CA-CFAR ones. The analysis of the OS-CFAR detector and a comparison with CA-CFAR detectors was presented in [Armstrong1991] when correlated, fluctuating and Rayleigh-distributed targets in K-distributed sea clutter are considered.

OS-CFAR detectors has also been successfully applied when Weibull-distributed clutter is considered [Levanon1990, Anastassopoulos1995, Liu2003, Mezache2008, Zaimbashi2008]. From these works, the first one [Levanon1990] is the most important one because it sets the basic principles of these kind of detectors. For this reason, it will be considered as a reference in the thesis. The other works make use of the OS-CFAR detector as a reference to validate their proposed detectors.

OS-CFAR detectors may resolve multi-target situations quite well. They lack effectiveness in preventing excessive false alarms during clutter power transitions.

Even though OS-CFAR detectors allow to achieve high detection performances, several authors proposed modifications and/or combinations of them to outperform their performances. Thus, El Mashade proposed in [Mashade1998b, Mashade1998a] modified OS-CFAR detectors for detecting fluctuating targets in homogeneous clutter. These detectors are the Mean Level OS (MLOS), the Greatest Of OS (GOOS) and the Smallest Of OS (SOOS) CFAR detectors. On the other hand, different combinations of conventional and modified OS-CFAR detectors were proposed in [Zaimbashi2006, Zaimbashi2008] for detecting moderately fluctuating targets in homogeneous Weibull-distributed sea and land clutters. Other combinations were also presented in [Liu2003, Mezache2008], outperforming again the performance of conventional OS-CFAR detectors.

Finally, it is important to note that another modified OS-CFAR detector, known as the trimmed mean (TM) CFAR detector was presented in [Gandhi1988]. This detector implements a trimmed averaging after ordering. By judiciously trimming the ordered samples, the TM-CFAR detector outperforms the OS-CFAR detector.

Other CFAR detectors. Other CFAR techniques can be found in the literature, such as excision (EX) or censored (CE) CFAR detectors.

El Mashade presented in [Mashade1997, Mashade2001] how EX-CFAR detectors, also known as Excision Cell Averaging (EXCA) CFAR detectors, can be implemented. Their performances were reported when detecting multiple targets (moderately fluctuating targets) in homogeneous and heterogeneous clutter. when homogeneous and heterogenous clutter and multitarget (moderately fluctuating targets) situations were reported. His first work [Mashade1997] presented not only the EX-CFAR detector, but also a set of modified EX-CFAR detectors, being: Mean Level EX (MLEX), Greatest Of EX (GOEX) and Smallest Of EX (SOEX) CFAR detectors. These modified detectors outperformed the EX-CFAR detector under these target and clutter conditions.

EX-CFAR detectors were also studied by Erfanian and Tabataba [Erfanian2008] when Swerling I targets in homogeneous and heterogenous K-distributed sea environments are considered. They made a new proposal by combining an excision processor and a switching-CFAR detector. The results shown that EX-CFAR and the proposed detectors outperform CA-CFAR detectors.

After the analysis of the previous works, it can be concluded that EX-CFAR detectors usually outperform the performance of CA and OS-CFAR detectors. This performance improvement is achieved because it removes strong samples exceeding the excision threshold from the reference window prior to calculate the detection threshold. The EX-CFAR detector is usually used in radar systems to control the increase of false alarms that occurs in non-stationary clutter environments. On the other hand, the GOEX operation is included to control false alarms at clutter edges and the SOEX operation is proposed to resolve closely spaced targets.

Other CFAR techniques, such as the one based on censoring can be used. An automatic CE-CFAR detector processing multitarget situations and using incoherent pulse integration was proposed in [Farrouki2007]. The proposed detection scheme was based on an optimal selection of the appropriate censored mean level according to the actual background environment.

Finally, other not commonly used CFAR detectors are presented in the literature. In this way, a clutter map (CMAP) CFAR detector was proposed in [Hamadouche2000] when Weibull-distributed clutter is present, its shape parameter is known and the fluctuating target is assumed as Swerling I model [Swerling1997]. Closed-form expressions for the P_{d} and P_{fa} in terms of shape and scale parameters are determined and the performance of the system is investigated and analyzed. On the other hand, CFAR in non-homogeneous Weibull-distributed clutter was studied in [Gandhi1995]. In this study, the difficulty of estimating the two parameters of Weibull distributions to calculate the appropriate decision threshold was discussed. For this purpose, a log-t detector is commonly used.

Detectors based on artificial intelligence (AI)

From an empirical perspective, the application of supervised learning machines to approximate the Neyman-Pearson detector has already been studied for detecting signals in noise. In previous works dealing with the design of ANN-based detectors, two possible solutions have been proposed to vary the P_{fa}, once the ANN has been trained: varying the detection threshold [Andina1995b, Andina1995c, Burian1999, Jarabo2009], or the bias of the output neuron [Ramamurti1993, Gandhi1997]. In [Munro1996] a two-output ANN with outputs in (0,1) was used, comparing the subtraction of both outputs to a threshold. This approach is equivalent to using an ANN with only one output and desired outputs [-1, 1] [Ruck1990]. More recently, RBF-ANNs have also been applied to approximate the Neyman-Pearson detector [Casasent2003a, Casasent2003b, Jarabo2003].

In [Jarabo2005], the possibility of approximating the Neyman-Pearson detector using adaptive systems, such as ANNs, trained in a supervised manner was studied. In this work, the case where the likelihood functions are unknown is considered. This is very similar to the case where the statistical parameters of the likelihood functions are unknown, as occur in our case of study and in real-live situations. For these reasons, ANNs are considered in the problem of detecting targets in clutter in this thesis.

The above-mentioned works presented how AI techniques are able to approximate the Neyman-

Pearson detector when background noise is present. Now, lets study the application of these techniques to the detection of signals in clutter and noise. In this case, non-parametric techniques are usually used because parametric models of clutter and target returns are generally unavailable. So, AI techniques, and exactly ANNs, provide an attractive approach to perform non-parametric identification. Next, several examples of radar target detection in clutter are given, where different kind of ANNs are used.

Focusing on the use of MLPs, we can find the work presented by Battacharya and Haykin in [Battacharya1992], where an adaptive radar detection algorithm for detecting small pieces of ice floating in an open sea environment was presented. The detection was carried out in the time-frequency domain, reducing the limitations of standard Doppler processing. This detection scheme used an MLP as a pattern classifier. Cheikh and Faozi presented in [Cheikh2004] an MLP-based radar detector working in a K-distributed environment. The use of MLPs was justified against conventional statistical methods because they work faster and generalize better than the statistical methods. It is due to statistical methods are optimal only for one type of clutter distribution. The results showed that the MLP architecture outperformed the classical CA-CFAR detector. A different radar detector scheme was presented in [Haykin1994] for detecting a radar target signal buried in strong clutter. This scheme was based on the application of the Wigner-Ville decomposition (WVD) followed by a principal component analysis and by an MLP binary classifier. This work noted the superior performance of the new detection strategy compared to conventional CFAR processors.

Focusing on the use of RBF-ANNs, we can find the work of Cheikh and Faozi presented in [Cheikh2006]. The authors presented a radar detector based on RBF-ANNs, which was compared with the MLP-based detector presented in [Cheikh2004] and with CA-CFAR detectors. This comparison emphasizes the performance improvement achieved by both ANN-based detectors with respect to CFAR detectors. A different way of using RBF-ANNs in a radar detector was presented in [Xie2003]. In this case, RBF-ANNs were used to model and predict clutter to mitigate it and enhance the target signal, improving the detection performance.

Detectors based on other techniques

Other signal processing techniques can be used in radar detection, which cannot be directly classified in any of the previous kinds of detectors. Some of them are presented below.

Considering the dwell time as a parameter of a radar detector, two interesting works can be found in the literature [Nohara1994, McDonald2005]. In [Nohara1994], X-band radar measurements were analyzed to determine the characteristics of clutter and growler (small pieces of glacial ice) returns that could lead to their separability. The authors report on the performance of two coherent, medium and long dwell-time, detectors. In [McDonald2005], the difficulty of detecting small maritime surface targets from sea clutter in radar backscattered signals was presented. Incoherent integration, coherent integration, the Kelly detector and the adaptive linear-quadratic detector were considered. Target detectability was improved by combining the results of a single dwell across multiple scans. Analysis of high-range-resolution coherent X-band data of small boats revealed that fast scan rates (short dwell times) improved target detection.

The use of asymptotically optimum detectors (AODs) was presented in [Lombardo1999b, Lombardo1998]. In [Lombardo1999b], the use of a multiband case of the AOD was compared

to a multiband GLR test linear-quadratic detector when coherent radar target detection in compound-Gaussian clutter background was considered. In [Lombardo1998], the non-CFAR characteristic of the AOD was discussed when K-distributed clutter is present and the target Doppler frequency is varied. Moreover, the AOD presented another problem because it assumes a knowledge of the local clutter power in the cell under test (CUT). A practical scheme was obtained by replacing the known local power value by its estimate, named locally adaptive-AOD (LA-AOD). These detectors shown a CFAR behavior, but yielded strong detection losses in the same Doppler frequency region where the original AOD operated effectively with CFAR. Finally, a combined AOD was proposed, which used the benefits of both AOD and LA-AOD structures. Its detection performance was fully characterized as the clutter spikiness and correlation vary.

Multiple-Input Multiple-Output (MIMO) techniques have been recently used in radar detection. Two examples of its application can be found in [Sheikhi2006, Sheikhi2008]. In [Sheikhi2006], the problem of target detection using coherent data was considered for MIMO radars. This work presented how a GLR test was successfully used in two adaptive decision schemes for clutter with unknown statistics. In [Sheikhi2008], the problem of adaptive target detection using coherent data in the presence of non-homogeneous clutter (different clutter statistics in receivers) was considered for MIMO radars. For clutter with unknown statistics, three adaptive decision rules have been developed using the GLR test. The results show the superiority of the MIMO radars with temporal coherent processing over conventional phased arrays in the presence of clutter.

The different kinds of detectors presented here are not considered in the studies of the thesis because of their high computational cost.

Conclusions about the detectors under study

Since the studies done in thesis consider both coherent and incoherent data, the detection techniques commonly used in the literature for each case are selected. For incoherent systems, both simulated and real-live data are available. Then, the incoherent detectors taken as reference are studied with both kinds of data. On the other hand, synthetic data are only available for coherent systems. Consequently, the coherent detector taken as reference can only be studied with synthetic data.

Considering the detection of signals in clutter and noise by using coherent data, the coherent detector presented in [Farina1987a, Farina1987b] is selected, as discussed in Sect. 1.2.2. This detector is based on reducing the level of clutter previous to apply a detection threshold fixed according to a desired P_{fa}.

Considering the detection of signals in clutter and noise by using incoherent data, several commonly used incoherent detectors have been selected. These detectors are based on CFAR techniques, being: CA-CFAR [DeMiguel1998], ML-CFAR [Ravid1992] and OS-CFAR [Levanon1990].

Finally, it is demonstrated in the literature that ANNs are able to approximate the Neyman-Pearson detector when the unique interference is the noise. Moreover, they are satisfactorily used for detecting signals in clutter with a distribution different of the Weibull one (the one considered in the thesis). Because of these properties, ANNs are considered as candidates to outperform the different detectors taken as reference.

1.3 Objectives of the Thesis

According to the main motivation of the thesis, and after the analysis of the state of the art about the detection of targets in clutter, the following objective is set as principal in the thesis:

> "*To propose high performance detection schemes working in different environments, outperforming commonly used detectors and having real-time applicability.*"

The main objective can be divided in four particular objectives, being:

- Particular objective 1: *To propose detection schemes that work in sea, sea-ice and ground clutter conditions, presenting high performance.*
- Particular objective 2: *To propose detection schemes that outperform detectors commonly used in the literature, regardless of the kind of system (coherent or incoherent) that is making the measurements.*
- Particular objective 3: *To propose detection schemes that maintain the performance obtained in a design stage when processing new data in a test stage.*
- Particular objective 4: *To propose detection schemes with low computational cost to process the data in real-time.*

1.4 Structure of the Thesis

Once a preliminary analysis of the main topic of the thesis is done and its objectives are established, the thesis has been structured in this way:

- The first part of the thesis, in which this chapter is included, presents the coherent and incoherent measurement systems considered in the experiments. Moreover, an analysis of the clutter data obtained from them is done, especially for the way the synthetic clutter is generated. Finally, the coherent and incoherent detectors taken as reference are presented.
- The second part contains the description of the proposed detectors, from where the main contributions of the thesis are obtained. At the beginning of this part, the general scheme of the proposed AI-based detector is explained. Moreover, the different ways of selecting the data to be processed by the detector and the way to estimate the detector performance are discussed. Afterwards, the particular details of design of the MLP-based and RBFN-based detectors are given.
- The third part of the thesis presents the main results obtained during the research. This part starts with an statistical analysis of the databases used for the coherent and incoherent experiments in order to be sure that the performance achieved is statistically correct and highly accurate. After that, the design and test of coherent detectors in sea, sea-ice and ground clutter is presented. Finally, the design and test of incoherent detectors in synthetic and real-live sea clutter data are presented.
- The last part of the thesis summarizes the main conclusions obtained from the research. The main contributions as well as some future research lines are also presented.

CHAPTER 2

Coherent and Incoherent Measurement Systems: Radar Data

The performance of a detector embedded in coherent or incoherent radar systems can be estimated by using real-live and/or synthetic radar data. To use real-live radar data is not often possible because data are not always available. In addition, it is not sometimes the most appropriate option because the available radar environmental conditions do not cover all the possibilities where the system can work. In these situations, the use of signal modeling is needed.

In this chapter, two radar systems are presented. The first one is a coherent radar system, which is described in Sect. 2.1. Since real-live data are not available for this kind of systems, signal models are used, being described in Sect. 2.2. These models allow us generating synthetic radar data to simulate different radar environments (sea, ground, etc.), being described in Sect. 2.3. The second radar system is incoherent, being described in Sect. 2.4. The real-live data obtained by this incoherent radar are presented in Sect. 2.5.

2.1 Coherent radar system model

The system model considered in this thesis for coherent measurements is a coherent monopulse radar working at a given frequency, f_c, of a given band (L, X, etc.). This model is composed of a monopulse transmitter and a coherent receiver. The information of the *in-phase* and *quadrature* components of the received echo signals is available. The general scheme of the radar model is depicted in Fig. 2.1, where an amplifier and a matched filter is included in the intermediate frequency (IF) stage. The antenna of the radar is rotating (scanning) at a certain speed (ω_a) and pointing to different directions of the environment (A_i, $i = 1, 2 \dots K_a$) in the horizontal plane (azimuthal observation). The azimuthal sampling period (ΔA) is determined by the antenna rotation speed and the pulse repetition frequency (PRF) as

$$\Delta A = A_i - A_{i-1} = \frac{6\,\omega_a}{\mathrm{PRF}}\,. \tag{2.1}$$

The constant 6 comes from the division of $\frac{360^\circ}{\mathrm{rad}}$ and $\frac{60\,\mathrm{s}}{\mathrm{min}}$ to convert ω_a from (rev/min) to (°/s) and to achieve the azimuthal sampling period in degrees (°).

For a given azimuthal direction, A_i, the radar transmits an electromagnetic pulse of a certain duration (pulse width), τ (s), which is scattered by the object/s (desired or not desired) present

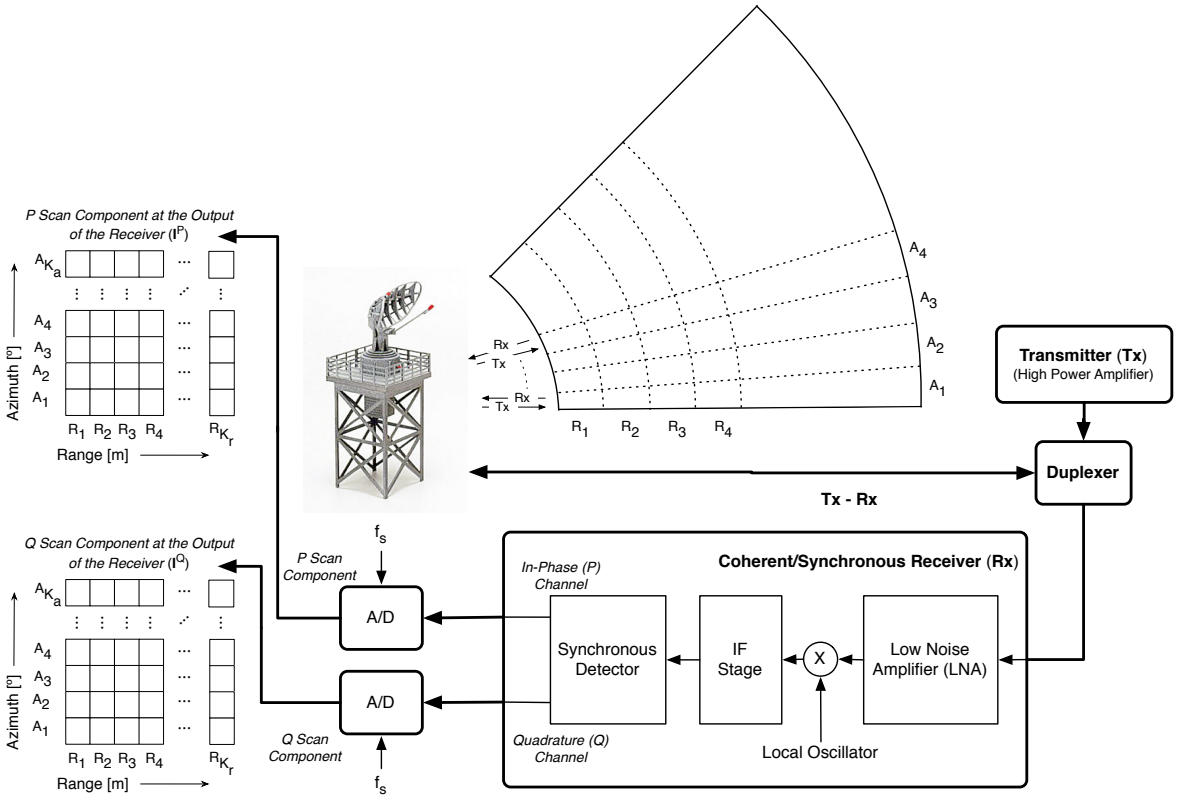

Figure 2.1: Coherent radar system model

in this direction. Due to the way of working of pulsed radars, the maximum non-ambiguous range ($R_{\max}$) is given by Eq. (2.2), which depends on the propagation speed of the electromagnetic waves in the air ($c = 3 \times 10^8$m/s) and the inverse of the PRF (time between the transmission of two consecutive pulses). This value will delimitate the range coverage of the radars under study, i.e. the range coverage is limited by this time constraint instead of received power sensibility and/or noise constraints. On the other hand, the minimum distance of the range coverage ($R_{\min}$) is given by Eq. (2.3), which depends on c (m/s) and τ (s).

$$R_{\max} = \frac{c}{2 \times PRF} \tag{2.2}$$

$$R_{\min} = \frac{c \cdot \tau}{2} \tag{2.3}$$

The range coverage of each scan ($[R_{K_r} - R_1]$) is always between these range limits, i.e. $R_{K_r} < R_{\max}$ and $R_1 > R_{\min}$. The range coverage is divided in K_r bins or cells: R_j, $j = 1, 2 \ldots K_r$. Considering no pulse compression, the range resolution (ΔR) depends on c (m/s) and τ (s), as

$$\Delta R = R_j - R_{j-1} = \frac{c \cdot \tau}{2}\,. \tag{2.4}$$

Finally, and since the radar works at grazing incidence, the grazing angle is related to the ratio between the antenna height (h_{a}) and the distance range cell-radar site (R_j). In this way,

the maximum and minimum grazing angles are given in Eq. (2.5) for the minimum and maximum cell distances, respectively, as

$$[\theta_{\mathrm{g,max}}\,,\,\theta_{\mathrm{g,min}}] = \left[\tan^{-1}\left(\frac{h_{\mathrm{a}}}{R_1}\right)\,,\,\tan^{-1}\left(\frac{h_{\mathrm{a}}}{R_{N_{\mathrm{r}}}}\right)\right]\,. \tag{2.5}$$

According to this way of exploring the radar environment and the way the received information is divided, a scan matrix ($\mathbf{I}$) is obtained in each radar scan. Each element ($I_{r,c}$) of the obtained scan matrix contains a complex value ($I^{\mathrm{P}}_{r,c} + j \cdot I^{\mathrm{Q}}_{r,c}$), where r and c are indexes that denote the r-th row and c-th column of the matrix, which are related to the r-th azimuthal and c-th range cell indexes, respectively.

On the other hand, and according to the problem formulation presented in Sect. 3.1, the signal in each cell can be composed of the following contributions:

$$z[n] = s[n] + c[n] + g[n] \quad \text{, when target is present} \tag{2.6}$$

$$z[n] = c[n] + g[n] \quad \text{, when target is absent} \tag{2.7}$$

where $s[n]$, $c[n]$ and $g[n]$ are the target, clutter and noise signals, respectively.

During this thesis, real-live data from coherent systems were not available. Therefore, synthetic models are used for $s[n]$, $c[n]$ and $g[n]$, which are described below. In the following section, several procedures and hints are given in order to implement the generators of random sequences, especially for the case of clutter signals.

2.2 Generating synthetic radar data: Coherent target and interference models

2.2.1 Coherent target models

In microwave frequencies, e.g. in X-band ($[8, 12]$ GHz), the wavelength of the transmitted signal ($[3.75, 2.5]$ cm) is usually smaller than the object dimensions. Depending on the variation of the RCS with the frequency and angle of observation, several target models are used in the literature. A commonly used model is the non-fluctuating one. It is called Swerling 0 or V in the literature [Swerling1997]. In this model, the received echoes are considered to have a RCS independent of the frequency and angle of observation of the object. On the other hand, more complex objects (ships, aircrafts, terrain or sea surface) depends on the frequency and angle of illumination. These objects can be modeled as a combination of multiple scatterers, where the received echo is the sum of the echoes from these scatterers. Because of that, the RCS must be modeled as a random variable. As a conclusion, both non-fluctuating and fluctuating [Skolnik2001] (Gaussian or Swerling I-IV [Swerling1997]) models are considered in the literature. In this thesis, a non-fluctuating target model is used because it approximates correctly the target data available in the real-live data available and they are widely accepted in the radar detection community.

As mentioned above, the target signal ($s[k]$) is modeled with a Swerling 0 model, where the amplitude of the echoes is constant cell to cell, as well as scan to scan. On the contrary, the phase of the echoes is constant cell to cell but uniformly distributed in the range $[0, 2\pi)$ scan

to scan. Considering that A is the constant amplitude and θ is the phase of a given target, the signal of the moving target is given by

$$s[k] = Ae^{j\theta}e^{j\frac{2\pi k f_{\mathrm{dt}}}{\mathrm{PRF}}},\ k = 1, 2 \ldots K\,, \tag{2.8}$$

where the target occupies K range cells ($K < K_{\mathrm{a}}$). Its movement is denoted by its Doppler frequency (f_{dt}).

2.2.2 Coherent clutter model

This section presents the mathematical procedure to obtain a complex-valued sequence obtained with a coherent radar. This sequence has: a Weibull probability density function (*pdf*) for the amplitude, a uniform *pdf* for the phase and an autocorrelation function (ACF) selected at will. The model used for the experiments is a suitable generalization of the coherent Gaussian sequence generator usually used to model echo sequences from target and interference. In the following subsections, the statistical properties of Weibull-distributed sequences are discussed, as well as the Weibull sequence generator used in the thesis and its limitations and constraints.

Introduction to coherent Weibull clutter sequences

As concluded from the analysis of the state of the art about clutter modeling given in Sect. 1.2.1, the Weibull clutter model has received much attention in the last decades. It is because it represents the clutter observed by radar systems more accurately than other models, especially for high-resolution radars and radars operating at low grazing angles. It is worth noting that the Rayleigh distribution, which was very used in the past for other kind of radar systems, is a special case of the Weibull distribution family.

Szajnowski in [Szajnowski1977] and Marier in [Marier1995] discussed methods for generating Weibull sequences with a desired ACF and specific Weibull parameters for modeling different kind of clutters. These schemes were restricted to the generation of real-valued correlated samples from incoherent radars. On the other hand, Farina et al. [Farina1987b] proposed a coherent Weibull model. Although they dealt with a complex-valued process (coherent model), they only considered the case in which the ACF is real, i.e. when the spectral density of the process is symmetrical with respect to the origin (in-phase and quadrature components are uncorrelated). However, for many practical radar applications, this symmetry may not be guaranteed. In this case, it is useful to consider the case where the ACF is not real. In this way, Li and Yu extended Farina's model to the complex-valued ACF case in [Li1989]. The model and generation scheme proposed by Li and Yu is also considered an extension of Liu and Munson's scheme [Liu1982] for real to complex processes. For those reasons, this complex-valued model is considered in this thesis and summarized in the following subsections.

Complex-valued Weibull random variable

Consider a complex-valued Weibull random variable (r.v.) given by

$$w = u + jv\,, \tag{2.9}$$

where u and v are the real (in-phase) and imaginary (quadrature) components of the Weibull random variable, respectively.

The complex-valued r.v., w, is obtained by two real-valued r.v.'s as

$$w = |w| \cdot e^{j\phi}\,, \tag{2.10}$$

where its amplitude ($|w|$) is a real-valued Weibull r.v., given by Eq. (2.11), and its phase (ϕ) is a real-valued r.v. uniformly distributed in $[0, 2\pi)$. Both r.v.'s are independent, what involves that $p(|w|, \phi) = p(|w|)p(\phi)$.

$$p(|w|) = ab^{-a}|w|^{a-1}e^{-\left(\frac{|w|}{b}\right)^a} \tag{2.11}$$

The joint *pdf* of (u, v) has been found to be [Farina1987b]

$$p(u,v) = \frac{1}{2}\frac{a}{2\pi\sigma^2}\left(u^2+v^2\right)^{\frac{a}{2}-1} e^{\left[-\frac{1}{2\sigma^2}\left(u^2+v^2\right)^{\frac{a}{2}}\right]}\,, \tag{2.12}$$

where a is the *skewness* parameter of the Weibull variable, and σ^2 is the variance of the random process, being related to the power of w.

On the other hand, the scale parameter of the Weibull process, b, is related to a and σ [Schleher1980] by

$$b = \left(2\sigma^2\right)^{\frac{1}{a}}\,. \tag{2.13}$$

Finally, the mean-squared value (power) of w is related to the Weibull process parameters, a and b, as

$$E\{|w|^2\} = E\{|u^2+v^2|\} = \frac{2b^2}{a}\Gamma\left(\frac{2}{a}\right)\,, \tag{2.14}$$

where $\Gamma()$ is the *Gamma* function.

According to Eq. (2.14), if a desired power of a Weibull r.v. is needed, the scale parameter of the distribution can be obtained for a given skewness parameter, and vice versa. The variance of the random process can be obtained by using Eq. (2.13) to achieve the joint *pdf* of (u,v) by Eq. (2.12).

Special cases of the skewness parameter can be considered. In this way, when $a = 2$, the *pdf* of $p(u, v)$ is Gaussian-distributed and its corresponding amplitude ($|w|$) is Rayleigh-distributed. In this case, the Weibull case is a suitable generalization of the Gaussian case. On the other hand, when $a = 1$, an exponential *pdf* of the amplitude is obtained. A set of drawings representing $p(u)$ versus u and $p(|w|)$ versus $|w|$ for several values of the skewness parameter are presented in Fig. 2.2. The considered mean-squared value is always 30 dB ($10log_{10}\left(E\{|w|^2\}\right) = 30\,\text{dB}$). As can be observed, the lower the skewness parameter, the greater the tails of the Weibull distribution.

Complex-valued Weibull sequence generator

Generation of Weibull-distributed clutter sequences with a desired ACF, covariance matrix and power can be achieved by a cascade of two operations, as shown in Fig. 2.3. The first one consists of a *Correlator Filter*, which is used to correlate coherent white Gaussian sequences (CWGSs) to obtain coherent correlated Gaussian sequences (CCGSs) with a desired ACF. The second operation, called *NonLinear MemoryLess Transformation* (NLMLT), is used to obtain

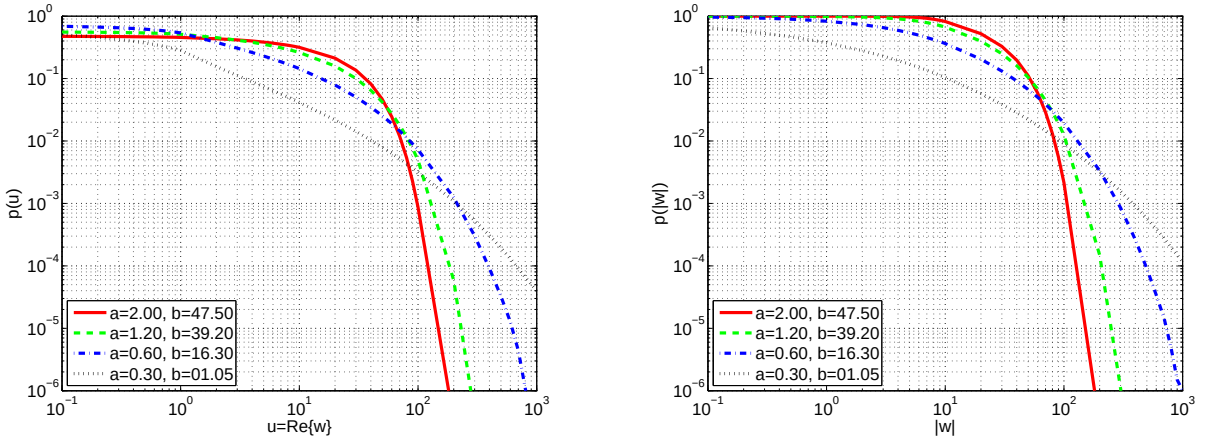

(a) *pdf* of the in-phase component (b) *pdf* of the amplitude

Figure 2.2: *pdf* of the in-phase component (u) and amplitude ($|w|$) of coherent Weibull r.v.'s with mean-square values of 30 dB and different skewness parameters

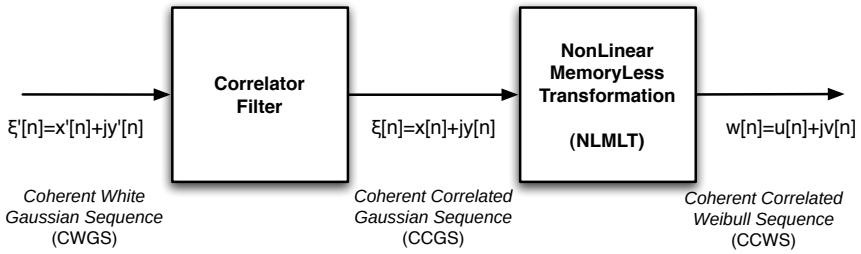

Figure 2.3: Generator of coherent correlated Weibull sequences

coherent correlated Weibull sequences (CCWSs) with a specified covariance matrix and power from CCGSs. Both operations are analyzed in depth below.

Correlator filter. The aim of this block is to obtain a CCGS with a desired covariance matrix (related to the ACF) from a zero mean and unity power CWGS. The covariance matrix of the CCGS is determined in the NLMLT design, being explained in the following subsection.

Suppose we have a zero mean and unity power CWGS

$$\xi'[n] = x'[n] + jy'[n]\,, \tag{2.15}$$

where n denotes the n-th index of each sequence and x' and y' are two independent real-valued Gaussian sequences with zero mean and $\frac{1}{\sqrt{2}}$ variance each.

For transforming the CWGS into the desired CCGS, the coefficients of the *Correlator filter* must be obtained. This linear filter makes the following transformation:

$$\xi = \mathbf{U}^{*}\mathbf{L}^{\frac{1}{2}}\xi'\,, \tag{2.16}$$

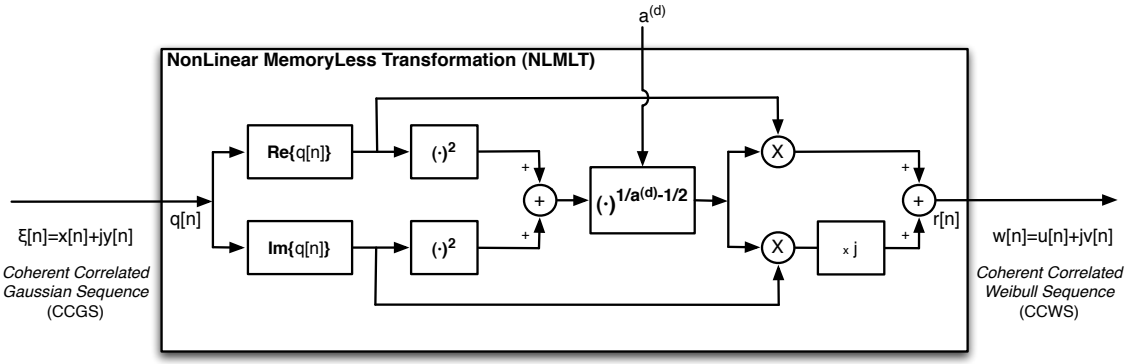

Figure 2.4: Nonlinear memoryless transformation (NLMLT)

where $\mathbf{U}$ and $\mathbf{L}$ are the matrixes with the eigenvectors and eigenvalues [Friedberg1999] of the covariance matrix of the desired CCGS ($\mathbf{M}_{\mathrm{cG}}$), respectively. The size of both matrixes is NxN, being N the length of the sequences ξ and ξ' (column vectors).

NonLinear MemoryLess Transformation. This transformation modifies the *pdf* of a Gaussian random process into a Weibull one. In this way, the NLMLT can be used to obtain a CCWS with a desired covariance matrix ($\mathbf{M}_{\mathrm{cW}}$) from a CCGS with a given covariance matrix ($\mathbf{M}_{\mathrm{cG}}$).

The *pdf* transformation is obtained by a modified box-cox transformation [Kay1988] as

$$r[n] = q[n] \cdot |q[n]|^{\frac{2}{a}-1}\,, \tag{2.17}$$

where $q[n] = \xi[n]$ and $r[n] = w[n]$ are the input and output sequences of the NLMLT, respectively, and $||$ denotes modulus. Note that the NLMLT depends on the skewness parameter of the Weibull random process. Since the sequences are complex-valued, $q[n]$ can be expressed by its real ($\mathrm{Re}\{\cdot\}$) and imaginary ($\mathrm{Im}\{\cdot\}$) parts. In this way, Eq. (2.17) can be rewritten as

$$\begin{aligned} r[n] = \mathrm{Re}\{q[n]\} \cdot [(\mathrm{Re}\{q[n]\})^2 + (\mathrm{Im}\{q[n]\})^2]^{\frac{1}{a}-\frac{1}{2}} \\ + j\mathrm{Im}\{q[n]\} \cdot [(\mathrm{Re}\{q[n]\})^2 + (\mathrm{Im}\{q[n]\})^2]^{\frac{1}{a}-\frac{1}{2}}\,. \end{aligned} \tag{2.18}$$

A block diagram of the NLMLT can be obtained from Eq. (2.18), as shown in Fig. 2.4. This figure considers $a^{(\mathrm{d})}$ because it is used as designing parameter in the TSKAP detector (see Sect. 3.3.1). In the current section, $a = a^{(\mathrm{d})}$ for describing the NMLT and its properties.

On the other hand, a covariance matrix transformation is also done by the NLMLT, being discussed below. In [Aloisio1994], it is demonstrated that the ACF of a Weibull process (R_{cW}), and consequently its covariance matrix ($\mathbf{M}_{\mathrm{cW}}$), depends on: its power (P_{cW}), its one-lag correlation coefficient (ρ_{cW}), its Doppler frequency (f_{cW}) and the PRF. Eq. (2.19) presents R_{cW} for a Weibull process having Gaussian ACF, which is considered in the thesis.

$$R_{\mathrm{cW}}[k] = P_{\mathrm{cW}} \rho_{\mathrm{cW}}^{|k|^2} e^{j\frac{2\pi k f_{\mathrm{cW}}}{\mathrm{PRF}}} \tag{2.19}$$

The covariance matrix corresponding to the CCWS ($\mathbf{M}_{\mathrm{cW}}$) is given by Eq. (2.20) when N samples are considered. The covariance matrix of the CCGS ($\mathbf{M}_{\mathrm{cG}}$) follows the same structure

as $\mathbf{M}_{\mathrm{cW}}$ but considering its own ACF ($R_{\mathrm{cG}}[k]$).

$$\mathbf{M}_{\mathrm{cW}} = \begin{pmatrix} R_{\mathrm{cW}}[0] & R_{\mathrm{cW}}[1] & \dots & R_{\mathrm{cW}}[N-1] \\ R^*_{\mathrm{cW}}[1] & R_{\mathrm{cW}}[0] & \dots & R_{\mathrm{cW}}[N-2] \\ \vdots & \vdots & \vdots & \vdots \\ R^*_{\mathrm{cW}}[N-1] & R^*_{\mathrm{cW}}[N-2] & \dots & R_{\mathrm{cW}}[0] \end{pmatrix} \tag{2.20}$$

The way to obtain the ACF of the Gaussian process ($R_{\mathrm{cG}}[k]$), from which the ACF of the Weibull process ($R_{\mathrm{cW}}[k]$) is going to be obtained is explained in the next subsection. In this subsection the ACF properties and constraints are discussed.

Other ACFs could be used in the model, maintaining the covariance mapping between the Weibull and Gaussian processes. As an example, an exponential ACF could be established by

$$R_{\mathrm{cW}}[k] = P_{\mathrm{cW}} \rho_{\mathrm{cW}}^{|k|} e^{j \frac{2\pi k f_{\mathrm{cW}}}{\mathrm{PRF}}} . \tag{2.21}$$

There are several relationships between the parameters that define the ACF in the Weibull domain (NLMLT output) and those that define the ACF in the Gaussian domain (NLMLT input), being:

- The power of the CCWS (P_{cW}) is given by Eq. (2.14), which only depends on the skewness and scale parameters of the Weibull r.v. The power of the CCGS (P_{cG}) is also related to the same parameters, but in a different way:

$$P_{\mathrm{cG}} = b^a \tag{2.22}$$

- The Doppler frequency of the CCGS (f_{cG}) is equal to the Doppler frequency of the CCWS (f_{cW}):

$$f_{\mathrm{cG}} = f_{\mathrm{cW}} \tag{2.23}$$

- The relationship between the one-lag correlation coefficient of the CCWS (ρ_{cW}) and the equivalent of the CCGS (ρ_{cG}) is given by

$$\rho_{\mathrm{cW}} = \frac{\rho_{\mathrm{cG}} a}{a\Gamma(\frac{2}{a})} \left(1 - \rho_{\mathrm{cG}}^2\right)^{\frac{2}{a}+1} \Gamma^2 \left(\frac{1}{a} + \frac{3}{2}\right) F\left(\frac{1}{a} + \frac{3}{2}; \frac{1}{a} + \frac{3}{2}; 2; \rho_{\mathrm{cG}}^2\right) , \tag{2.24}$$

  where $F(A; B; C; D)$ is the *Gauss Hypergeometric* function [Bailey1935], which converges for $|D| < 1$.

Analyzing the relationships given above, several aspects can be observed for $a = 2$. First, $\rho_{\mathrm{cW}} = \rho_{\mathrm{cG}}$ as observed in Eq. (2.24). And second, the power of both sequences, given by Eq. (2.14) and (2.22), are equal. It happens because the input and output sequences of the NLMLT are equal, as can be observed from the analysis of the transformation given in Eq. (2.17).

Coherent Weibull sequence ACF properties

The relationship between the ACFs of the Gaussian (input) and Weibull (output) sequences in the NLMLT was presented in [Farina1987b], demonstrating that the ACF depends on the one-lag correlation coefficient. But, what does it happen if the ACFs present a different relationship and its calculus is more complicated? Li and Yu described in [Li1989] how this relationship can be generalized to a complex-valued case, where different relationships exist and more sophisticated calculus must be done, as discussed below. This generalized approach is very useful when the relationship between the Gaussian and Weibull ACFs is programmed for running in a computer.

ACF Mapping. Let's consider the general case, where the ACFs of the NLMLT input and output sequences are complex-valued. In this case, the ACF of a coherent Weibull sequence ($w[n] = u[n] + jv[n]$) can be expressed by its real and imaginary parts as follows:

$$\begin{aligned} R_w[k] =& E\{w[n]w^*[n+k]\} = E\{(u[n] + jv[n])(u[n+k] - jv[n+k])\} \\ =& (Ruu[k] + Rvv[k]) + j(Rvu[k] - Ruv[k]) \end{aligned} \tag{2.25}$$

where $R_{uu}[k] = E\{u[n]u[n+k]\}$, $R_{uv}[k] = E\{u[n]v[n+k]\}$, $R_{vu}[k] = E\{v[n]u[n+k]\}$ and $R_{vv}[k] = E\{v[n]v[n+k]\}$, which are real-valued sequences. Suppose that $w[n]$ is a wide-sense stationary narrowband process. Then, the following properties are fulfilled [Papoulis1984]:

$$\begin{aligned} R_{uu}[k] =& R_{vv}[k] \\ R_{uv}[k] =& -R_{vu}[k] \end{aligned} \tag{2.26}$$

In this way, Eq. (2.25) can be simplified to

$$R_w[k] = 2(R_{uu}[k] - jR_{uv}[k])\,. \tag{2.27}$$

The normalized ACF, indicated by lower case characters, is defined by

$$r_w[k] = \frac{R_w[k]}{R_w[0]} = r_{uu}[k] - jr_{uv}[k]\,, \tag{2.28}$$

where the real and imaginary parts of the normalized Weibull sequence ACF are given by Eq. (2.29) and (2.30), respectively.

$$r_{uu}[k] = \frac{R_{uu}[k]}{\frac{1}{2}R_w[0]} \tag{2.29}$$

$$r_{uv}[k] = \frac{R_{uv}[k]}{\frac{1}{2}R_w[0]} \tag{2.30}$$

Applying the same principles as above to the input Gaussian process, ξ ($\xi[n] = x[n] + jy[n]$), we can obtain its normalized ACF sequence as:

$$r_\xi[k] = r_{xx}[k] - jr_{xy}[k]\,, \tag{2.31}$$

where its real and imaginary parts are given by $r_{xx}[k]$ and $r_{xy}[k]$, respectively.

Next, the relationships between $\{R_{xx}[k], R_{xy}[k]\}$ and $\{R_{uu}[k], R_{uv}[k]\}$, or their normalized versions, i.e. between $\{r_{xx}[k], r_{xy}[k]\}$ and $\{r_{uu}[k], r_{uv}[k]\}$, is derived.

According to the instantaneous nonlinear transformation given in Eq. (2.17), $R_{uu}[k]$ and $R_{uv}[k]$ can be expressed in terms of the input r.v.'s $x[n]$ and $y[n]$. After some operations on $R_{uu}[k]$ and $R_{uv}[k]$, which can be found in [Li1989], the following expressions are obtained:

$$\begin{aligned} R_{uu}[k] =& 2^{\frac{2}{a}-1}\sigma^{\frac{4}{a}} r_{xx}[k](1-r_{xx}^2[k]-r_{xy}^2[k])^{\frac{2}{a}+1} \\ & \cdot \Gamma^2\left(\frac{1}{a}+\frac{3}{2}\right) F\left(\frac{1}{a}+\frac{3}{2},\frac{1}{a}+\frac{3}{2};2;r_{xx}^2[k]+r_{xy}^2[k]\right), \end{aligned} \tag{2.32}$$

$$\begin{aligned} R_{uv}[k] =& 2^{\frac{2}{a}-1}\sigma^{\frac{4}{a}} r_{xy}[k](1-r_{xx}^2[k]-r_{xy}^2[k])^{\frac{2}{a}+1} \\ & \cdot \Gamma^2\left(\frac{1}{a}+\frac{3}{2}\right) F\left(\frac{1}{a}+\frac{3}{2},\frac{1}{a}+\frac{3}{2};2;r_{xx}^2[k]+r_{xy}^2[k]\right). \end{aligned} \tag{2.33}$$

A direct map between $\{R_{uu}[k], R_{uv}[k]\}$ and $\{r_{xx}[k], r_{xy}[k]\}$ is not usually done. Instead of that, a mapping between $\{r_{uu}[k], r_{uv}[k]\}$ and $\{r_{xx}[k], r_{xy}[k]\}$ is used, for which $R_w[0]$ is needed. $R_w[0]$ can be obtained by knowing that:

$$R_{uu}[0] = E\{u[n]u[n]\} = E\{x^2[n](x^2[n]+y^2[n])^{\frac{2}{a}-1}\}, \tag{2.34}$$

and after some manipulations [Li1989], $R_w[0]$ can be obtained from the following relationship

$$R_{uu}[0] = \frac{1}{2}R_w[0] = \frac{(2\sigma^2)^{\frac{2}{a}}}{a}\Gamma\left(\frac{2}{a}\right). \tag{2.35}$$

In this way, the normalized components of the ACF of a Weibull sequence can be obtained from the normalized components of the ACF of a Gaussian sequence as:

$$\begin{aligned} r_{uu}[k] = \frac{R_{uu}[k]}{R_{uu}[0]} =& \frac{a r_{xx}[k]}{2\Gamma\left(\frac{2}{a}\right)}(1-r_{xx}^2[k]-r_{xy}^2[k])^{\frac{2}{a}+1} \\ & \cdot \Gamma^2\left(\frac{1}{a}+\frac{3}{2}\right) F\left(\frac{1}{a}+\frac{3}{2},\frac{1}{a}+\frac{3}{2};2;r_{xx}^2[k]+r_{xy}^2[k]\right), \end{aligned} \tag{2.36}$$

$$\begin{aligned} r_{uv}[k] = \frac{R_{uv}[k]}{R_{uu}[0]} =& \frac{a r_{xy}[k]}{2\Gamma\left(\frac{2}{a}\right)}(1-r_{xx}^2[k]-r_{xy}^2[k])^{\frac{2}{a}+1} \\ & \cdot \Gamma^2\left(\frac{1}{a}+\frac{3}{2}\right) F\left(\frac{1}{a}+\frac{3}{2},\frac{1}{a}+\frac{3}{2};2;r_{xx}^2[k]+r_{xy}^2[k]\right). \end{aligned} \tag{2.37}$$

As a check, when $a = 2$, the Weibull process becomes Gaussian.

Finally, it should be pointed out that there is a convergence condition when deriving Eq. (2.32)-(2.33) and (2.36)-(2.37). This constraint is given by

$$r_{xx}^2[k] + r_{xy}^2[k] < 1 \tag{2.38}$$

and is known as the unit circle condition.

The ACF of the narrowband process generally meets this requirement because it is a property of the ACF [Li1989]; i.e.

$$|r_\xi[k]| = \sqrt{r_{xx}^2[k]+r_{xy}^2[k]} \leq 1. \tag{2.39}$$

Moreover, for a non-periodical process, generally

$$r_{xx}^2[k] + r_{xy}^2[k] < 1, \quad |k| > 0\,. \tag{2.40}$$

Therefore, the convergence condition is naturally satisfied by the ACF of this narrowband process.

Applying the same principles to the ACF of the narrowband Weibull process, we obtain:

$$r_{uu}^2[k] + r_{uv}^2[k] \leq 1, \quad |k| > 0\,. \tag{2.41}$$

As a conclusion, this last constraint implies that when the covariance matrix of the Weibull sequence ($\mathbf{M}_{\mathrm{cW}}$) is specified, and consequently the ACF of the Weibull process ($r_{uu}[k]$ and $r_{uv}[k]$) cannot be arbitrarily chosen. In this way, the point $(r_{uu}[\cdot], r_{uv}[\cdot])$, which is related to the point $(r_{xx}[\cdot], r_{xy}[\cdot])$ that fulfills Eq. (2.40), must be inside the unit circle on the r_{uu}-r_{uv} plane. Thus, Eq. (2.41) is the constraint for the sequence $r_w[k]$. Moreover, there is another constraint on $r_w[k]$: the non-negative definite property.

Solving the Nonlinear Equation for the ACF Mapping. To simplify the procedure of solving the two nonlinear equations given in (2.36) and (2.37) for the two unknowns $r_{xx}[k]$ and $r_{xy}[k]$, we make use of the following relation:

$$\mu[k] = \frac{R_{uv}[k]}{R_{uu}[k]} = \frac{r_{uv}[k]}{r_{uu}[k]} = \frac{r_{xy}[k]}{r_{xx}[k]} \tag{2.42}$$

It means that the nonlinear transformation of Eq. (2.17) does not change the ratio between the real and imaginary parts of the ACF. This fact is used to convert the problem of solving two unknowns for two nonlinear equations into the problem of solving one unknown for one nonlinear equation.

In this way, obtaining $r_{xy}[k]$ from Eq. (2.42) as

$$r_{xy}[k] = \mu[k] r_{xx}[k]\,, \tag{2.43}$$

and substituting Eq. (2.43) into Eq. (2.36), we obtain:

$$\begin{aligned} r_{uu}[k] =& \frac{a r_{xx}[k]}{2\Gamma\left(\frac{2}{a}\right)} \left(1 - (1+\mu^2[k]) r_{xx}^2[k]\right)^{\frac{2}{a}+1} \\ & \cdot \Gamma^2\left(\frac{1}{a}+\frac{3}{2}\right) F\left(\frac{1}{a}+\frac{3}{2}, \frac{1}{a}+\frac{3}{2}; 2; (1+\mu^2[k]) r_{xx}^2[k]\right)\,. \end{aligned} \tag{2.44}$$

Therefore, for a given μ, instead of two equations, just only one nonlinear equation must be solved to obtain $r_{xx}[\cdot]$ and $r_{xy}[\cdot]$ from $r_{uu}[\cdot]$ and $r_{uv}[\cdot]$. Conventional methods could be used to solve Eq. (2.44), e.g. iterative or recursive algorithms. A detailed analysis of these expressions can be found in [Li1989]. When the Weibull parameter a deviates from 2, it is observed that: the nonlinearity increases, the effect of varying μ reports large r_{uu} values, and $r_{uu}[\cdot] < r_{xx}[\cdot]$.

As discussed in the *Constraints and Limitations on ACFs* paragraph, the solution of the nonlinear Eq. (2.36) and (2.37) should be inside the unit circle in the r_{xx}-r_{xy} plane. It involves that the solution cannot exist outside this area, in which case the compatibility problem arises, which is analyzed below.

Compatibility Problem. Considering the Weibull and Gaussian processes, the unit circle constraints given in Eq. (2.41) and (2.40) can be rewritten, respectively, as

$$r_{uu}^2[k]\left(1+\mu^2[k]\right) \leq 1, \quad r_{uu}[k] \neq 0\,. \tag{2.45}$$

$$r_{xx}^2[k]\left(1+\mu^2[k]\right) \leq 1, \quad r_{xx}[k] \neq 0 \tag{2.46}$$

From the results given in [Li1989], it is known that usually

$$r_{xx}[k] \geq r_{uu}[k]\,. \tag{2.47}$$

But for some $r_w[k]$, or $r_{uu}[k]$ and $\mu[k]$, it is possible that the corresponding $r_{xx}[k]$ does not fulfill Eq. (2.46), i.e.

$$r_{xx}^2[k]\left(1+\mu^2[k]\right) > 1\,. \tag{2.48}$$

It means that there is no solution to Eq. (2.36) and (2.37) in the unit circle of the r_{xx}-r_{xy} plane. Therefore, for that case of $r_w[k]$, we cannot find the corresponding $r_\xi[k]$ being valid, although $r_w[k]$ itself is within the unit circle of the r_{uu}-r_{uv} plane. Consequently, we cannot use this method to generate such a process.

As a conclusion, the condition that guarantees the existence of feasible $r_\xi[k]$ is given by Eq. (2.48) or

$$|\mu^2[k]| \leq \sqrt{\frac{1}{r_{xx}^2[k]} - 1}\,. \tag{2.49}$$

2.2.3 Coherent noise model

Additive white Gaussian noise (AWGN) is usually present in radar systems. This kind of noise is characterized by a uniform-distributed spectral density (expressed as watts per hertz of bandwidth) and a Gaussian-distributed amplitude. The model does not take into account the phenomena of fading, frequency selectivity, interference, nonlinearity or dispersion in the propagation channel. However, it produces simple mathematical models, which are useful for gaining insight into the underlying behavior of a system before other phenomena are considered.

Wide-band Gaussian noise has many natural sources. For instance, it comes from the thermal vibrations of atoms in antennas (usually referred as thermal noise), shot noise, black body radiation from the earth and other warm objects, or from celestial sources such as the sun.

The way of modeling additive coherent white Gaussian noise is based on the assumption that each component of the coherent noise signal has also white spectral density and a Gaussian-distributed amplitude, but with the half power of the coherent white Gaussian noise. In this way, the coherent sequence that characterize the coherent white Gaussian noise is

$$g[n] = g_{\mathrm{P}}[n] + g_{\mathrm{Q}}[n] \tag{2.50}$$

where $g_{\mathrm{P}}[n]$ and $g_{\mathrm{Q}}[n]$ are the in phase and quadrature components of the coherent noise, respectively. In the thesis, the AWGN is taken as unity power noise. Then, each component of this coherent signal has a half unity power.

2.3 Coherent synthetic radar data

In order to design the coherent detection schemes used and proposed in the thesis, synthetic data have been generated. The way to synthesize radar scans from coherent signal models is presented first, to continue with the generation of target and clutter data. Three different environments are considered: sea, sea-ice and ground. For each environment, both the technical characteristics of the considered radar system and the parameters of the clutter model are presented.

2.3.1 Generation and properties of synthetic radar scans

Considering that the radar is rotating, two kind of fluctuations can be identified in the radar scans, which affect to the stationarity of the clutter [Sekine1990]:

- *Temporal fluctuation*: when the clutter statistical properties change scan-to-scan for the same radar scan cell.
- *Spatial fluctuation*: when the clutter statistical properties change for radar scan cells collected for the same range bin but for different pointing directions (azimuth angles) in the same radar scan.

In the case of study of the thesis, only temporal fluctuations are considered, as done in [Sekine1990].

From the point of view of the spatial correlation in the radar scans, the criterion established in [Mashade2002b] is taken into consideration for generating the synthetic radar scans. This criterion considers uncorrelated samples from range cell to range cell in a range sweep, and correlated samples from two consecutive pointing directions within the same range bin. Following this criterion, the procedure for synthetically generate radar scans is presented. For this purpose, suppose that a scan of size K_{a}xK_{r} is needed, where K_{a} is the number of azimuth bins and K_{r} is the number of range bins. Then, K_{r} vectors of K_{a} samples are generated according to the spatial correlation of the scans. The parameters that control this spatial correlation in the scan model are the one-lag correlation coefficients of the clutter (ρ_{c}) and target (ρ_{t}).

According to this procedure of generating radar scans, the vectors corresponding to the target and interference (clutter and noise) echoes are independently generated, to finally be added (additive interference). The target signal is characterized by fixed amplitude (A) and phase (θ) values for each of the K samples that compose it (Swerling 0 model), as presented in Sect. 2.2.1, where $K << K_{\mathrm{a}}$ and $K << K_{\mathrm{r}}$. The clutter signal is modeled as a coherent correlated complex-valued Weibull sequence, as discussed in Sect. 2.2.2. The noise signal is modeled as a coherent white Gaussian complex-valued process of unity power, as presented in Sect. 2.2.3.

Taking into account that the noise signal considered in the studies is of unity power ($P_{\mathrm{g}} = 1$ W), the following power relationships are considered in our studies:

$$\begin{aligned}
\text{Signal-to-noise ratio:} \quad & \mathrm{SNR\,(dB)} = \; 10 \cdot \log_{10}\left(\frac{P_{\mathrm{t}}}{P_{\mathrm{g}}}\right) = 10 \cdot \log_{10}\left(A^2\right) \\
\text{Clutter-to-noise ratio:} \quad & \mathrm{CNR\,(dB)} = \; 10 \cdot \log_{10}\left(\frac{P_{\mathrm{c}}}{P_{\mathrm{g}}}\right) = 10 \cdot \log_{10}\left(P_{\mathrm{c}}\right) \\
\text{Signal-to-clutter ratio:} \quad & \mathrm{SCR\,(dB)} = \; 10 \cdot \log_{10}\left(\frac{P_{\mathrm{t}}}{P_{\mathrm{c}}}\right) = 10 \cdot \log_{10}\left(\frac{A^2}{P_{\mathrm{c}}}\right)
\end{aligned} \tag{2.51}$$

Table 2.1: Parameters of the target model considered in the experiments

Target type		Swerling 0
Target Doppler frequency	f_{dt}	$0.2 \times \mathrm{PRF}$
One-lag target corr. coef.	ρ_{t}	1.0
Signal-to-noise ratio	SNR	40.0 dB
Signal-to-clutter ratio	SCR	10.0 dB

Sect. 2.2.1-2.2.3 describe how the target, clutter and noise signals can be generated. On the other hand, Sect. 2.3.2 presents the characteristics of the target data and Sect. 2.3.3-2.3.5 present the characteristics of the different kinds of Weibull-distributed clutters considered in the thesis.

2.3.2 Target data

The target conditions used in the different radar environments considered in the studies are presented here. The general characteristics of the targets are summarized in table 2.1, although they can be particularized in each particular case under study (sea clutter, sea-ice clutter, etc.).

As observed in table 2.1, the selected target model is the simplest one of the Swerling's models [Swerling1997, Skolnik2001], i.e. the Swerling 0 model, also known as Swerling V. This target model corresponds to target echoes completely correlated ($\rho_{\mathrm{t}} = 1$) for adjacent cells in a scan and for the same range-azimuth cells from scan to scan. This kind of target is selected because it is commonly used by the radar community to model simple and well-defined targets. Moreover, it is selected because it allows to make easy analyses of the performance improvement achieved by the proposed detector against reference detectors. On the other hand, since the objective of the thesis is the detection of targets in movement, its Doppler frequency is not null ($f_{\mathrm{dt}} \neq 0\mathrm{Hz}$). Moreover, considering a CNR = 30 dB, the target power could vary with respect to the average noise and clutter powers, being indicated by the SNR and SCR parameters, respectively.

Finally, it is important to note that when introducing the target data in the synthetic radar scans, the effect of the illumination of the radar antenna is considered. In other words, since a target cell is illuminated several times by the radar antenna, even when the antenna is not directly pointing it, the retrieved information from the cells adjacent to this one will also contain information of the target, even when physically there is no target in these cells. This effect is considered when generating the simulated scenarios.

2.3.3 Sea clutter data

Sea clutter is different from ground/land clutter because of its statistical properties. In this case, the sea state rather than the type of surface conditions these statistical properties. At the time of measurement, there is only one sea state. Therefore, sea clutter is more homogeneous than ground/land clutter, especially for low-resolution radars. It involves that no spatial distribution is usually observed in radar scans. On the other hand, the RCS of sea waves is smaller than that of ground terrain, especially for Rocky mountains. It increases with grazing angle, radar

Table 2.2: Transmission, reception and coverage characteristics of the radar system used for the modeling of sea clutter measurements

Freq. band and radar freq.	Band: f_c	K_a: 34.86 GHz
Radar pulse width	τ	30.0 ns
Pulse repetition frequency	PRF	4000 Hz
Antenna rotation speed	ω_a	20.0 rev/min
Antenna horizontal beamwidth	θ_h	0.25°
Antenna vertical beamwidth	θ_v	5.0°
Polarization		HH
Grazing angles	$[\theta_{g,max}, \theta_{g,min}]$	$[2.58°, 0.25°]$
Sampling frequency	f_s	33.3 MHz
Coding of the I and Q data	format	8-bit unsigned int.
Azimuthal characteristics:		
Coverage	$[A_1, A_{K_a}]$	$[0.00°, 7.68°]$
Sampling period	$\Delta A = A_i - A_{i-1}$	0.03°
Range characteristics:		
Coverage	$[R_1, R_{K_r}]$	$[200.0\,\text{m}, 2120.0\,\text{m}]$
Resolution	$\Delta R = R_j - R_{j-1}$	4.5 m

Table 2.3: Radar environmental conditions in sea clutter

Clutter model		Weibull
Clutter Doppler frequency	f_{dc}	$0.03 \times \text{PRF} = 120$ Hz
One-lag clutter corr. coef.	ρ_c	0.99
Clutter-to-noise ratio	CNR	30.0 dB
Skewness/shape parameter	a	$\sim \text{N}(4.46, 0.12)$
Scale parameter	b	$\sim \text{N}(33.57, 0.01)$

frequency and sea state. As the sea state increases with the wind speed, a wind speed increase provokes greater tails in the statistical distribution of the clutter. It denotes that lower values of the skewness parameter of the Weibull-distributed clutter are achieved, being more deviated from the Rayleigh distribution (particular case of the Weibull distribution for $a = 2.0$). This effect is clearly noted when X-band radars are used. But when millimeter wave radars are used (increasing the radar frequency), the skewness parameter tends to be greater than $a = 2.0$, deviating again from the Rayleigh distribution. Moreover, the RCS of sea clutter is greater for vertical than horizontal polarization and is maximum with up-wind, minimum with down-wind

and of intermediate value for cross-wind. In addition, there are often some spikes accompanied by noise-like sea clutter. Since the correlation time of the sea clutter is rated from several ms to several tens of ms, noise-like is only in the sense of single sweep or in the range direction.

One way to reduce the strength of sea clutter is to decrease the cell resolution established in the radar. However, as the cell resolution decreases below 75 m (pulse width $< 0.5\,\mu s$), it is observed that the clutter RCS peaks are approximately constant in time. The only effect observed when decreasing the cell resolution is the decrease of the period between clutter peaks.

The parameters of the radar model used to synthetically generate data from sea measurements are extracted from the work of Sayama and Sekine described in [Sayama2005]. The radar used in Sayama and Sekine's work was sited at the Yokosuka port in Kanagawa, Japan. Even when X-band marine radars are usually used to measure sea clutter, as presented in [Schleher1976, Sekine1990], the measurements of sea clutter were made by a millimeter wave radar in this case. The technical and coverage characteristics of this radar are summarized in table 2.2, which are considered in the model of radar used in this thesis. The sea clutter measurements were made from the Tokyo bay [Sayama2005]. The radar environmental conditions were conditioned by sea states from 2 to 4, moving clutter and highly correlated clutter. The Weibull-distributed sea clutter parameters reported by Sayama and Sekine in [Sayama2005] are summarized in table 2.3, which are used for modeling sea clutter in this thesis. The skewness parameter of the Weibull-distributed sea clutter follows a normal distribution with mean $\mu_a = 4.46$ and variance $\sigma_a^2 = 0.12$ ($\sim \mathrm{N}(4.46, 0.12)$). Since the CNR is constant, the scale parameter of this clutter also follows a normal distribution with mean $\mu_b = 33.57$ and variance $\sigma_b^2 = 0.01$ ($\sim \mathrm{N}(33.57, 0.01)$). Apart of following the normal distribution, Sayama and Sekine also observed that maximum and minimum values were observed for the skewness ($[a_{\min}, a_{\max}]$) and scale ($[b_{\min}, b_{\max}]$) parameters of the Weibull-distributed clutter, being: $[4.11, 5.17]$ and $[33.55, 33.59]$, respectively.

2.3.4 Sea-Ice clutter data

The RCS of sea-ice is much greater than that of sea waves. The RCS of sea clutter mainly depends on the sea state. Whereas the RCS of sea-ice depends on much more parameters, such as: type (young or multiyear ice), thickness, volumetric structure, surface roughness, dielectric constant, age, development history and temperature of the sea-ice. Sea-ice includes fast ice and pack ice. Fast ice is defined as stationary ice near the coast, while pack ice is a moving ice. Segments of pack ice collide together and hummocks are formed, which grow from a height of a few meters to ten meters.

The formation of sea-ice is complex and depends on the brine content of the sea surface water, temperature, vertical salinity profile, and depth of the water. For forming sea-ice, seawater must be cooled to temperatures some degrees below the freezing point of fresh water, because of its salinity. Needle-like fragile ice, containing spherical ice crystals, is formed when seawater is cooled below its freezing temperature. When these crystals are rapidly cooled and close together, a uniform sheet of ice is created, known as young ice. In its first year, ice can grow to a thickness of more than one meter. During this year, it is classified as thin (< 30 cm) or thick (> 30 cm) first-year ice. The ice surface melts during summer and refreezes during winter, and the thickness also increases further over the years. Ice that has undergone several melt-and-refreeze cycles and has a thickness of more than 2 m is called multiyear ice. The salinity of young ice is much higher

Table 2.4: Transmission, reception and coverage characteristics of the radar system used for the modeling of sea-ice clutter measurements

Freq. band and radar freq.	Band: f_c	X: 9.5 GHz
Radar pulse width	τ	40.0 ns
Pulse repetition frequency	PRF	1680 Hz
Antenna rotation speed	ω_a	28 rev/min
Antenna horizontal beamwidth	θ_h	1.2°
Antenna vertical beamwidth	θ_v	Not Available
Polarization		Not Available
Grazing angles	$[\theta_{g,max}, \theta_{g,min}]$	$[0.53°, 0.24°]$
Sampling frequency	f_s	25.0 MHz
Coding of the I and Q data	format	8-bit unsigned int.
Azimuthal characteristics:		
Coverage	$[A_1, A_{K_a}]$	$[22.0°, 47.0°]$
Sampling period	$\Delta A = A_i - A_{i-1}$	0.1°
Range characteristics:		
Coverage	$[R_1, R_{K_r}]$	[1320.0 m, 2856.0 m]
Resolution	$\Delta R = R_j - R_{j-1}$	6.0 m

Table 2.5: Radar environmental conditions in sea-ice clutter

Clutter model		Weibull
Clutter Doppler frequency	f_{dc}	$0.01 \times \text{PRF} = 16.8$ Hz
One-lag clutter corr. coef.	ρ_c	0.95
Clutter-to-noise ratio	CNR	30.0 dB
Skewness/shape parameter	a	$\sim \text{N}(1.20, 0.14)$
Scale parameter	b	$\sim \text{N}(20.80, 8.24)$

than that of first-year ice, and the salinity of first-year ice is much higher than that of multiyear ice. Therefore, the RCS of multiyear ice is greater than that of fresh-water (lake) ice, and the RCS of first-year ice is greater than that of multiyear ice.

The technical and coverage characteristics of the radar model used to synthetically generate sea-ice clutter are obtained from the works presented in [Sekine1990] and [Ogawa1987]. The radar used in these works was sited at the city of Mombetsu (Hokkaido), Japan. The technical and coverage characteristics of this radar are summarized in table 2.4, which are considered in the model of radar used in this thesis. The sea-ice clutter measurements reported in both works

were made in the sea of Okhost by a coherent X-band radar. The radar measurements were made at midnight. The weather conditions were clear and the wind velocity was 3.7 m/s. The direction of wind was southwest and the temperature was $-9.3°$ C. The radar environmental conditions were also conditioned by the movement of the sea-ice clutter and its moderate-highly correlated ($\rho_c = 0.95$) behavior. The Weibull-distributed sea-ice clutter parameters reported in [Sekine1990] and [Ogawa1987] are summarized in table 2.5, which are used for modeling sea-ice clutter in this thesis. As observed for sea clutter, the skewness and scale parameters of the Weibull-distributed sea-ice clutter reported in these two works follow normal distributions with means $\mu_a = 1.20$ and $\mu_b = 20.80$, and variances $\sigma_a^2 = 0.14$ and $\sigma_b^2 = 8.24$, respectively. The observed skewness and scale parameters were in the following limits: $a \in [0.50, 1.65]$ and $b \in [6.45, 30.02]$.

2.3.5 Ground clutter data

Ground clutter is different from sea clutter because there are more different types of terrain/land (cultivated land, rocky mountains, etc.) than sea states. Different values of the skewness parameter can be used to model these types of terrain by the Weibull distribution. This variability of values does not allow to model ground clutter with a Rayleigh distribution.

The parameters of the radar model used to synthetically generate data from ground measurements are extracted from the work of Sekine and Mao presented in [Sekine1990]. The radar used in Sekine and Mao's work was sited at the at Kagoshima prefecture, Japan. The radar model considered in these ground clutter studies was an L-band long-range air-route surveillance radar (ARSR), being a low-resolution coherent monopulse radar system. The observed area was on the Ohsumi peninsula across the big bay of Kagoshima. There was no obstacle between the radar and the observed area. Consequently no shadowing effects were present. The technical and coverage characteristics of this radar are summarized in table 2.6, which are considered in the model of radar used in this thesis. In Sekine and Mao's work, ground clutter from cultivated land was measured, demonstrating that the measurements fit a Weibull distribution. The measurements were made at midnight, weather conditions were clear and wind velocity was $\in [1, 5]$ m/s from east to west. The radar environmental conditions were also conditioned by a quite ground clutter and its moderately correlated ($\rho_c = 0.90$) behavior. The Weibull-distributed ground clutter parameters reported by Sekine and Mao in [Sekine1990] are summarized in table 2.7, which are used for modeling ground clutter in this thesis. As also observed for sea and sea-ice clutter, both the skewness and scale parameters of the Weibull-distributed ground clutter reported in Sekine and Mao's work follow normal distributions with means $\mu_a = 1.76$ and $\mu_b = 30.30$, and variances $\sigma_a^2 = 0.03$ and $\sigma_b^2 = 0.81$, respectively. The observed skewness and scale parameters were in the following limits: $a \in [1.50, 2.00]$ and $b \in [28.98, 31.62]$.

2.4 Incoherent marine radar system

The measuring and monitoring marine radar system used to obtain the real-live electromagnetic backscatter measurements used in this thesis is described here. This measuring and monitoring system is located at the FINO 1 (Forschungsplattformen in Nord-und Ostsee) German research platform, as presented in Fig. 2.5. This platform is located in Borkum Riff, 45 km North of Borkum Island. The system is composed of an X-band radar and an analog-to-digital converter,

Table 2.6: Transmission, reception and coverage characteristics of the radar system used for the modeling of ground clutter measurements

Freq. band and radar freq.	Band: f_c	L: 1.33 GHz
Radar pulse width	τ	446 ns
Pulse repetition frequency	PRF	500 Hz
Antenna rotation speed	ω_a	8.33 rev/min
Antenna horizontal beamwidth	θ_h	1.2°
Antenna vertical beamwidth	θ_v	3.2°
Polarization		HH
Grazing angles	$[\theta_{g,max}, \theta_{g,min}]$	$[0.20°, 0.16°]$
Sampling frequency	f_s	2.25 MHz
Coding of the I and Q data	format	10-bit signed int.
Azimuthal characteristics:		
Coverage	$[A_1, A_{K_a}]$	$[90.6°, 113.4°]$
Sampling Period	$\Delta A = A_i - A_{i-1}$	0.1°
Range characteristics:		
Coverage	$[R_1, R_{K_r}]$	[14040 m, 17060 m]
Resolution	$\Delta R = R_j - R_{j-1}$	67 m

Table 2.7: Radar environmental conditions in ground clutter

Clutter model		Weibull
Clutter Doppler frequency	f_{dc}	$0 \times \text{PRF} = 0$ Hz
One-lag clutter corr. coef.	ρ_c	0.90
Clutter-to-noise ratio	CNR	30.0 dB
Skewness/shape parameter	a	$\sim \text{N}(1.76, 0.03)$
Scale parameter	b	$\sim \text{N}(30.30, 0.81)$

the Wave Monitoring System II (WaMoS II), to acquire and digitize the measurements from the North Sea, and a personal computer to process these measurements. The antenna of the system is 20 m over the mean sea level, so maximum and minimum grazing angles of 0.13° and 0.01° are obtained for the minimum (150 m) and maximum (2152 m) coverage distance ranges. Due to its great versatility, this system can be tuned with different configurations. In the studies presented in this thesis, two different configurations are used: one where the system is configured for high range coverage and low range resolution; and the other one where the system is configured for low range coverage and high range resolution. The technical parameters of the used configurations

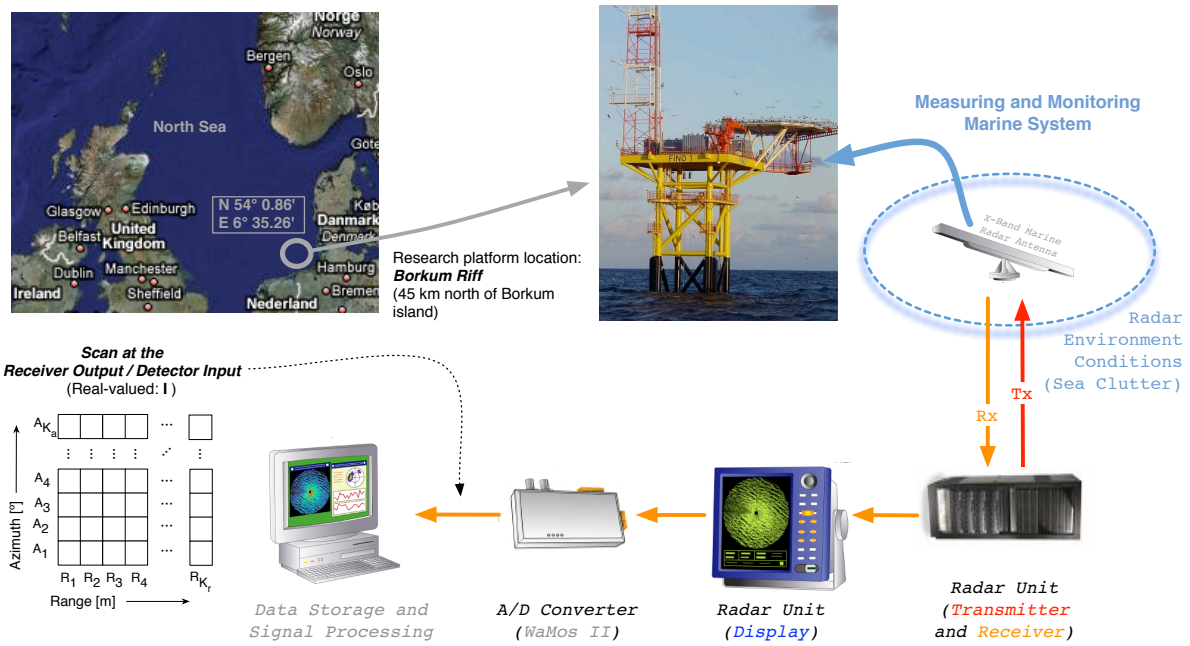

Figure 2.5: Incoherent marine radar system

are summarized in table 2.8.

As noted from its configuration, this measurement system is based on a standard marine X-band radar, that, among other properties, incorporates a logarithmic amplifier and has no frequency agility. Once the measurements are acquired and plotted in the radar unit display, its analog video signal is digitized by the WaMoS II [OceanWaves, Nieto2005] Analog-to-Digital (A/D) converter. The WaMoS II was originally developed at the German GKSS Research Center Geesthacht. Under the measurement system configurations given in table 2.8, the system acquires a temporal sequence of 32 consecutive radar images every 80 s. The image spatial resolution depends on the azimuthal and range resolutions of the measurement system. The intensity of each radar image cell is coded without sign and 8 bits, what sets a cell dynamic range of $[0-255]$. Finally, the digitized images are processed by a standard computer to perform the desired ending radar application by software. In our case of study, the radar application the thesis is focused on is the automatic detection of ships in sea clutter. Note that, since the radar raw data from the WaMoS II system are used, no signal preprocessing (e.g. rain filter, image intensity amplification, etc.) is done before the proposed detection scheme is applied.

2.5 Incoherent real-live marine radar data

The database selected for the experiments is composed of 12 different radar data image sequences obtained by the incoherent radar measurement system presented in the previous section. All these sequences are different each other in order to cover: different types of ships (see Sect. 2.5.1); and different sea states (see Sect. 2.5.2). Moreover, one half of these sequences represents a radar environment where a target (ship) is present in sea clutter, and the other half represents situations

Table 2.8: Transmission, reception and coverage characteristics of the incoherent marine radar system configured for high range coverage and low range resolution

Radar configuration		Low-resolution	High-resolution
Freq. band and radar freq.	Band: f_c	X: 9.5 GHz	
Radar pulse width	τ	50.0 ns	31.0 ns
Pulse repetition frequency	PRF	500 Hz	750 Hz
Antenna rotation speed	ω_a	23 rev/min	42 rev/min
Antenna horizontal beamwidth	θ_h	Not Available	
Antenna vertical beamwidth	θ_v	Not Available	
Polarization		HH	
Elevation angle	θ_e	Not Available	
Sampling Frequency	f_s	20.0 MHz	32.25 MHz
Coding of the data	format	8-bit unsigned int.	
Azimuthal characteristics:			
Coverage	$[A_1, A_{K_a}]$	$[0°, 360°]$	
Sampling period	ΔA	0.28°	0.34°
Range characteristics:			
Coverage	$[R_1, R_{K_r}]$	[240.0 m, 2152.5 m]	[150.0 m, 1344.5 m]
Resolution	ΔR	7.5 m	4.7 m

where no target is present.

2.5.1 Target data

The available real-live radar data include different types of ships, having maximum lengths and widths of 350 and 35 m, respectively. The types of ships available in database of real-live radars scans are:

- *Cruise ships* with a length of 350 m and a width of 35 m. These vessels where observed using the low-resolution configuration of the radar ($\Delta R = 7.5$ m). In this way, sizes from 47 to 5 cells are observed.

- *Ferries* with a length of 200 m and a width of 28 m. These vessels where observed using the low-resolution configuration of the radar ($\Delta R = 7.5$ m). In this way, sizes from 27 to 4 cells are observed.

- *Container ships* with a length of 200 m and a width of 32 m. These vessels where observed using the high-resolution configuration of the radar ($\Delta R = 4.7$ m). In this way, sizes from 43 to 7 cells are observed.

- *General cargo ships* with a length of 120 m and a width of 18 m. These vessels where observed using the high-resolution configuration of the radar ($\Delta R = 4.7\,\mathrm{m}$). In this way, sizes from 26 to 4 cells are observed.

2.5.2 Sea clutter data

Sea clutter usually depends on sea state. In oceanography, a sea state is defined as the general condition of the free surface on a large body of water -with respect to wind waves and swell- at a certain location and moment. A sea state is characterized by statistics, including the significant wave height (H_s), period, and power spectrum. The sea state varies over time, as the wind or swell conditions change. The large number of variables involved in sea states cannot be quickly and easily summarized. Simpler scales are used to give a sea state approximate but with a concise description of their conditions.

Different sea states are available in the data obtained by the marine radar. Exactly, for the studies done in this thesis, sea states 1-5 of the World Meteorological Organization (WMO) [WMO] are considered. The main properties of these sea states are:

- *Sea state 1*: with $H_\mathrm{s} \in [0 - 0.10]\,\mathrm{m}$ and a low (short or average) character of the sea swell. It is also known as *calm* (rippled) *sea*.
- *Sea state 2*: with $H_\mathrm{s} \in [0.10 - 0.50]\,\mathrm{m}$ and a low (long) character of the sea swell. It is also known as *smooth* (wavelets) *sea*.
- *Sea state 3*: with $H_\mathrm{s} \in [0.50 - 1.25]\,\mathrm{m}$ and a moderate (short) character of the sea swell. It is also known as *slight sea*.
- *Sea state 4*: with $H_\mathrm{s} \in [1.25 - 2.50]\,\mathrm{m}$ and a moderate (average) character of the sea swell. It is also known as *moderate sea*.
- *Sea state 5*: with $H_\mathrm{s} \in [2.50 - 4.00]\,\mathrm{m}$ and a moderate (long) character of the sea swell. It is also known as *rough sea*.

CHAPTER 3

Automatic Detection of Signals in Clutter and Noise

This chapter presents, first, the basic principles of detecting signals in clutter and noise in Sect. 3.1.1, to continue with the formulation of optimum and suboptimum detectors in the Neyman-Pearson sense Sect. 3.1.2. Two different cases of study are analyzed: one considering Gaussian-distributed interference, and another considering non-Gaussian-distributed interference. When Gaussian-distributed interference is considered, optimum detection schemes are analyzed in Sect. 3.2. Suboptimum detection schemes are also considered in order to fulfill several limitations that can exist in real-live situations when implementing these detectors. Both optimum and suboptimum approaches are presented when working with coherent and incoherent data. When non-Gaussian-distributed interference is considered, optimum and suboptimum approaches are also studied in Sect. 3.3. Due to the difficulty of obtaining closed form expressions for the optimum detector when Weibull-distributed clutter is considered, especially when this clutter is correlated, suboptimum detectors become the most relevant approaches. Finally, suboptimum detection approaches are selected from the literature and shown in Sect. 3.3.1 and 3.3.2 for the cases of working with coherent and incoherent radar data, respectively. These suboptimum approaches will be taken as reference detectors in the thesis.

3.1 Principles of detecting signals in clutter and noise

In this section, the problem formulation used during this chapter is set. Thereafter, the Neyman-Pearson detector is presented. Optimum and suboptimum approaches are introduced in Sect. 3.2 and 3.3.

3.1.1 Problem formulation: Detection of signals in clutter

The problem of detecting signals (radar targets) in presence of interference (clutter and noise) can be formulated as a binary hypothesis test. In this test, the detector has to discern between two hypotheses: target is absent (null hypothesis: H_0) or target is present (alternative hypothesis: H_1). This decision is made from an observation vector obtained by the radar receiver. Two examples of radar receivers were given in Fig. 2.1 and 2.5 for the cases of coherent and incoherent

systems, respectively. In both cases, the received signal is composed of a noisy component due to the radiation of external sources received by the antenna and the thermal noise internally generated in the electronic devices of the receiver chain. Apart of this noise, the presence of clutter (energy reflected by non-desired targets) makes the decision even more difficult.

The basic parameters used to evaluate the detection capabilities of a detector are the probabilities of detection (P_{d}) and false alarm (P_{fa}). The P_{d} is defined as the probability of deciding that target is present when the received signal is coming from a target. The P_{fa} is defined as the probability of deciding that target is present when the received signal is not coming from a target, i.e. comes from clutter and noise.

Although the formulation presented below was partially introduced in Eq. (2.6) and (2.7) for the case of coherent data, it is reproduced here for convenience but from a general point of view, where coherent or incoherent data can be indistinctly used. To mathematically formulate the detection problem, consider $z[n]$ being the radar echo received at the time instant nT_s, where T_s is the sampling period of the receiver. This radar echo is composed of different components depending on the hypothesis, i.e.

$$\text{Hypothesis } H_1: \quad z[n] = s[n] + c[n] + g[n] \tag{3.1}$$

$$\text{Hypothesis } H_0: \quad z[n] = c[n] + g[n] \tag{3.2}$$

where $s[n]$, $c[n]$ and $g[n]$ are the target, clutter and noise components/signals at this time, respectively. These signals are taken at the output of the coherent ($z[n]$ is complex-valued) or incoherent ($z[n]$ is real-valued) receivers.

The above-presented expressions correspond to the signal received at a given time instant. The performance of the detector can be improved if multiple observations are used to make the decision. In this way, a set of N samples is incorporated in a vector to make the decision, which are summarized in Eq. (3.3)-(3.6).

$$\mathbf{z}[n] = \left[\, z[n-(N-1)] \;\; z[n-(N-2)] \;\; \ldots \;\; z[n] \,\right]^{\mathrm{T}}, \tag{3.3}$$

$$\mathbf{s}[n] = \left[\, s[n-(N-1)] \;\; s[n-(N-2)] \;\; \ldots \;\; z[n] \,\right]^{\mathrm{T}}, \tag{3.4}$$

$$\mathbf{c}[n] = \left[\, c[n-(N-1)] \;\; c[n-(N-2)] \;\; \ldots \;\; c[n] \,\right]^{\mathrm{T}}, \tag{3.5}$$

$$\mathbf{g}[n] = \left[\, g[n-(N-1)] \;\; g[n-(N-2)] \;\; \ldots \;\; g[n] \,\right]^{\mathrm{T}}, \tag{3.6}$$

From this observation vector of N samples, and as discussed in the motivation of the thesis (see Sect. 1.1 and Fig. 1.1), a decision rule must be implemented to make the decision:

$$F(\mathbf{z}[n]) \underset{H_0}{\overset{H_1}{\gtrless}} \mathrm{THR}(P_{\mathrm{fa}}), \tag{3.7}$$

where the decision threshold, THR, is set according to achieve a desired P_{fa}.

Different ways of defining the discriminant function implemented by the processor of the detector, $F()$, have been used in the literature. The most important and relevant ones for this thesis are reproduced in the following sections and subsections attending to different criteria.

3.1.2 The Neyman-Pearson Detector: Optimum and Suboptimum Approaches

In radar systems, the most suitable criterion used for detection purposes is the Neyman-Pearson detector. This detector maximizes the P_{d} while maintaining the P_{fa} lower or equal to a specified value [Neyman1933].

To formulate the Neyman-Pearson detector when the N received radar echoes in $\mathbf{z}[n]$ are processed, consider $f(\mathbf{z}[n]|H_1)$ and $f(\mathbf{z}[n]|H_0)$ as the probability density functions (fdp's) of $\mathbf{z}[n]$ under the hypotheses H_1 and H_0, respectively. A realization of the Neyman-Pearson detector ($F(\mathbf{z}[n])$ in Eq. (3.7)) is based on the comparison of the likelihood ratio, $\mathrm{LR}[n]$, with a threshold previously established for fulfilling the established P_{fa} criterion (ratio test detector):

$$\mathrm{LR}(\mathbf{z}[n]) = \frac{f(\mathbf{z}[n]|H_1)}{f(\mathbf{z}[n]|H_0)} \underset{H_0}{\overset{H_1}{\gtrless}} \mathrm{THR}(P_{\mathrm{fa}})\,. \tag{3.8}$$

When the numerator and denominator of the LR follow Gaussian distributions, the Neyman-Pearson detector can be implemented by a bank of linear filters followed by a quadratic-law envelope detector [Aloisio1994]. When both the target and interference signals of Eq. (3.1) and (3.2) present known pdf's and their statistical parameters (mean and standard deviation) are known, these approaches are referred as *optimum detectors*.

When Gaussian models are not suitable for approximating the target and clutter signals, as the problem this thesis deals with, the joint pdf of the process H_1 may not have a closed solution. In this case, the characterization of the joint pdf of the observation vectors is usually done using the pdf of their samples (coherent data) or amplitudes (incoherent data) and their covariance matrixes. In these cases, *suboptimum approaches* are applied basing on approximations or estimations of the pdf and covariance matrixes.

Finally, it is important to note that the statistics of the target and/or interference models usually change in time and are sometimes unknown. In these cases, suboptimum approaches are used. The computational cost of many suboptimal solutions proposed in the literature is very high, and even their performances are poorer than the theoretical optimum detector. But, they are considered because they can find a solution for these detection problems.

3.2 Detection of Signals in Gaussian-distributed Interference

This section presents different solutions to solve the problem of detecting signals in Gaussian-distributed interference. The approaches presented when processing coherent data are based on recursive or batch modes of working. Both approaches are presented for the optimum and suboptimum cases of study. Other approaches are selected from the literature for the case of processing incoherent data to formulate the optimum and suboptimum detection schemes.

3.2.1 Coherent Detection: Optimum Approaches

Optimum approaches assume that both the properties of the statistical processes that model the target and interference signals, as well as their statistical parameters are known through the time. Assuming this knowledge in time, different optimum approaches can be formulated. In this section, two optimum approaches for detecting signals in Gaussian interference are presented. These approaches process a set of N received radar echoes (current time instant and $N-1$ previous instants) in a recursive or a batch mode.

Optimum Coherent Detection: Recursive Approach

The optimum detector, in the Neyman-Pearson sense [Neyman1933, VanTrees1997], for solving the problem of detecting signals in Gaussian interference from a set of N radar echoes ($\mathbf{z}[n]$) can be formulated by thresholding the LR of Eq. (3.8) using a detection threshold attending to P_{fa} constraints. Alternatively, this detector can also be obtained by thresholding the log-likelihood ratio (LLR) [Farina1986a], i.e.:

$$\text{LLR}[n] = \log\left(\frac{f(\mathbf{z}[n]|H_1)}{f(\mathbf{z}[n]|H_0)}\right) \underset{H_0}{\overset{H_1}{\gtrless}} \text{THR'}(P_{\text{fa}})\,. \tag{3.9}$$

where log() denotes natural logarithm and $\text{THR'}(P_{\text{fa}}) = \log(\text{THR}(P_{\text{fa}}))$.

Applying the Bayes theorem [Papoulis1984] to Eq. (3.9), a recursive equation is achieved:

$$\text{LLR}[n] = \log\left(\frac{f(z[n]|\mathbf{z}[n-1], H_1)}{f(z[n]|\mathbf{z}[n-1], H_0)}\right) + \text{LLR}[n-1]\,, \tag{3.10}$$

which shows that the LLR can be calculated from the evaluation of the pdf's of the received signal under both hypothesis in the current time instant conditioned to the N-1 samples previously received, and the LLR for the previous instant.

Considering that the radar echo is composed of target, clutter and noise under hypothesis H_1 and of clutter and noise under hypothesis H_0, as set Eq. (3.1) and (3.2), the LLR given in (3.9) is equivalent to

$$\text{LLR}[n] = \log\left(\frac{f(\mathbf{s}[n] + \mathbf{c}[n] + \mathbf{g}[n])}{f(\mathbf{c}[n] + \mathbf{g}[n])}\right)\,, \tag{3.11}$$

which can be calculated as the difference of two LLRs, one for detecting the target plus clutter in noise (LLR_{s+c+g}) and the other for detecting clutter in noise (LLR_{c+g}), as:

$$\text{LLR}[n] = \log\left(\frac{f(\mathbf{s}[n] + \mathbf{c}[n] + \mathbf{g}[n])}{f(\mathbf{g}[n])}\right) - \log\left(\frac{f(\mathbf{c}[n] + \mathbf{g}[n])}{f(\mathbf{g}[n])}\right)\,. \tag{3.12}$$

Then, Eq. (3.11) can be summarized as

$$\text{LLR}[n] = \text{LLR}_{s+c+g}[n] - \text{LLR}_{c+g}[n]\,. \tag{3.13}$$

First, let's start with the calculus of the LLR concerning to the detection of target and clutter in noise. As introduced in Eq. (3.11) and (3.13), this partial LLR is given by

$$\text{LLR}_{s+c+g}[n] = \log\left(\frac{f(\mathbf{s}[n] + \mathbf{c}[n] + \mathbf{g}[n])}{f(\mathbf{g}[n])}\right)\,, \tag{3.14}$$

which can be rewritten by the recursive approach of the LLR given in (3.10), obtaining:

$$\text{LLR}_{s+c+g}[n] = \log\left(\frac{f(s[n] + c[n] + g[n]|\mathbf{s}[n-1] + \mathbf{c}[n-1] + \mathbf{g}[n-1])}{f(g[n]|\mathbf{g}[n-1])}\right) + \text{LLR}_{s+c+g}[n-1]\,. \tag{3.15}$$

Since $s[n] + c[n]$ is a Gaussian process, $f(s[n] + c[n] + g[n]|\mathbf{s}[n-1] + \mathbf{c}[n-1] + \mathbf{g}[n-1])$ is also Gaussian, having a mean of $\mu_1[n]$ and a variance of $\sigma_1^2[n]$. Moreover, since the noise is also Gaussian-distributed with zero mean and constant variance σ_g^2, the LLR follows [Farina1986a]:

$$\text{LLR}_{s+c+g}[n] = \frac{|z[n]|^2}{\sigma_g^2} - \frac{(z[n] - \mu_1[n])(z[n] - \mu_1[n])^*}{\sigma_1^2[n]} + \log\left(\frac{\sigma_g^2}{\sigma_1^2[n]}\right) + \text{LLR}_{s+c+g}[n-1]\,, \tag{3.16}$$

Considering $u_1[n]$ the difference between the received radar echo ($z[n]$) and the mean of the received signal under hypothesis H_1, i.e.

$$u_1[n] = z[n] - \mu_1[n]\,, \tag{3.17}$$

the LLR corresponding to the detection of target and clutter in noise is finally given by

$$\mathrm{LLR}_{s+c+g}[n] = \frac{|z[n]|^2}{\sigma_g^2} - \frac{u_1[n]u_1^*[n]}{\sigma_1^2[n]} + \log\left(\frac{\sigma_g^2}{\sigma_1^2[n]}\right) + \mathrm{LLR}_{s+c+g}[n-1]\,. \tag{3.18}$$

Following with a similar procedure for the calculus of the LLR corresponding to the detection of clutter in noise, this LLR is given by

$$\mathrm{LLR}_{c+g}[n] = \log\left(\frac{f(\mathbf{c}[n]+\mathbf{g}[n])}{f(\mathbf{g}[n])}\right)\,, \tag{3.19}$$

which can be rewritten by the recursive relationship for the LLR given in (3.10) to obtain

$$\mathrm{LLR}_{c+g}[n] = \log\left(\frac{f(c[n]+g[n]|\mathbf{c}[n-1]+\mathbf{g}[n-1])}{f(g[n]|\mathbf{g}[n-1])}\right) + \mathrm{LLR}_{c+g}[n-1]\,. \tag{3.20}$$

Since $c[n]$ is a Gaussian process, $f(c[n]+g[n]|\mathbf{c}[n-1]+\mathbf{g}[n-1])$ is also Gaussian, having a mean of $\mu_0[n]$ and a variance of $\sigma_0^2[n]$. Moreover, since the noise is also Gaussian-distributed with zero mean and constant variance σ_g^2, the LLR follows [Farina1986a]:

$$\mathrm{LLR}_{c+g}[n] = \frac{|z[n]|^2}{\sigma_g^2} - \frac{(z[n]-\mu_0[n])(z[n]-\mu_0[n])^*}{\sigma_0^2[n]} + \log\left(\frac{\sigma_g^2}{\sigma_0^2[n]}\right) + \mathrm{LLR}_{c+g}[n-1]\,, \tag{3.21}$$

Considering $u_0[n]$ the difference between the received radar echo ($z[n]$) and the mean of the received signal under hypothesis H_0, i.e.

$$u_0[n] = z[n] - \mu_0[n]\,. \tag{3.22}$$

the LLR corresponding to the detection of clutter and noise is finally given by

$$\mathrm{LLR}_{c+g}[n] = \frac{|z[n]|^2}{\sigma_g^2} - \frac{u_0[n]u_0^*[n]}{\sigma_0^2[n]} + \log\left(\frac{\sigma_g^2}{\sigma_0^2[n]}\right) + \mathrm{LLR}_{c+g}[n-1]\,. \tag{3.23}$$

Once both LLRs are achieved for the Gaussian-distributed case of study, the next objective is to obtain an explicit mathematical expression for the log-likelihood ratio, as denoted in Eq. (3.9) and (3.13). Since $f(\mathbf{z}[n]|H_1)$ and $f(\mathbf{z}[n]|H_0)$ are Gaussian processes, the conditional probabilities $f(z[n]|\mathbf{z}[n-1], H_1)$ and $f(z[n]|\mathbf{z}[n-1], H_0)$ are also Gaussian, having pairs mean-variance of μ_1-σ_1^2 and μ_0-σ_0^2, respectively. Therefore, combining Eq. (3.18) and (3.23) in Eq. (3.13), the LLR becomes:

$$\mathrm{LLR}[n] = -\frac{|u_1[n]|^2}{\sigma_1^2[n]} + \frac{|u_0[n]|^2}{\sigma_0^2[n]} + \log\left(\frac{\sigma_0^2[n]}{\sigma_1^2[n]}\right) + \mathrm{LLR}[n-1]\,. \tag{3.24}$$

Considering that

$$v[n] = -\frac{|u_1[n]|^2}{\sigma_1^2[n]} + \frac{|u_0[n]|^2}{\sigma_0^2[n]} + \log\left(\frac{\sigma_0^2[n]}{\sigma_1^2[n]}\right)\,, \tag{3.25}$$

the LLR can be summarized as

$$\mathrm{LLR}[n] = v[n] + \mathrm{LLR}[n-1]\,. \tag{3.26}$$

Another way of calculating the LLR can be done by adding the current value of $v[n]$ and their $N-1$ previous evaluations, i.e.

$$\mathrm{LLR}[n] = v[n] + \ldots + v[n-(N-1)] = \sum_{k=0}^{N-1} v[n-k]\,, \tag{3.27}$$

In this way, the use of Eq. (3.25)-(3.26) is recommended because more accurate estimations can be done. But, due to a set of N radar echoes are used to make the decision, the approach given in Eq. (3.27) is recommended.

Optimum Coherent Detection: Batch Approach

The theory of Gaussian signal detection in Gaussian interference is widely addressed in the literature, as shown in the review of the state of the art presented in Sect. 1.2.2. Next, the formulation of a batch detector for solving the detection problem formulated in Sect. 3.1.1 is given. This detector was proposed in [Aloisio1994] as a particular approach for detecting zero-mean Gaussian signals in Gaussian interference and in [Farina1986a] as a general approach for detecting Gaussian-distributed signals in correlated Gaussian interference.

The difference of this approach with respect to the one based on the recursive approach presented above lies in the way the radar echoes are processed. Whereas in the recursive approach the decision is made according to the evaluation of a cumulative result of the LLR, in the batch approach the evaluation of the LLR is made according to a set of N received radar echoes. In [Schweppe1965] it is demonstrated how the recursive and batch approaches are equivalent in terms of performance.

In the batch approach detector presented below, the matrix notation considered in Eq. (3.3)-(3.6) is used. Therefore, this detector makes decisions considering observation vectors of length N. Moreover, this detector assumes stationary and zero-mean processes. In this way, the covariance matrixes ($\mathbf{M}$) of the processes involved in the formulated detection problem, i.e. the target ($\mathbf{s}$), clutter ($\mathbf{c}$) and noise ($\mathbf{g}$) signals, are Toeplitz, which fulfill that $M_{jj} = \max\{\mathbf{M}\}$, $j = 1, 2 \ldots N$.

The statistical process that models the target is assumed to be Gaussian-distributed, having the following covariance matrix:

$$\mathbf{M}_\mathrm{s} = P_\mathrm{s}\mathbf{B}\,. \tag{3.28}$$

Since $\mathbf{M}_\mathrm{s}$ is Toeplitz, the matrix $\mathbf{B}$ is also Toeplitz, having the main diagonal elements equal to the unity, and P_s represents the mean square value (power) of the process.

The interference is assumed to be the sum of: colored clutter with covariance matrix $\mathbf{M}_\mathrm{c}$ and power P_c, and white Gaussian noise with power P_g. Hence, its covariance matrix can be written as:

$$\mathbf{M}_\mathrm{i} = \mathbf{M}_\mathrm{c} + P_\mathrm{g}\mathbf{I} = P_\mathrm{c}\mathbf{C} + P_\mathrm{g}\mathbf{I} \tag{3.29}$$

where $\mathbf{C}$ is Toeplitz with $C_{jj} = 1$, $j = 1, 2 \ldots N$, $\mathbf{I}$ is the identity matrix and the ratio $P_\mathrm{c}/P_\mathrm{g}$ is the clutter-to-noise ratio expressed in natural units (cnr).

Considering the covariance matrixes of the target and interference signals, and assuming that these processes are Gaussian-distributed, the pdf's of the observation vector, $\mathbf{z}[n]$, for the true (H_1) and alternative (H_0) hypotheses are [Aloisio1994]:

$$f(\mathbf{z}[n]|H_1) = \frac{1}{\pi|\mathbf{M}_\mathrm{s}+\mathbf{M}_\mathrm{i}|} e^{-\mathbf{z}[n]^\mathrm{T}(\mathbf{M}_\mathrm{s}+\mathbf{M}_\mathrm{i})^{-1}\mathbf{z}^*[n]}\,, \tag{3.30}$$

$$f(\mathbf{z}[n]|H_0) = \frac{1}{\pi|\mathbf{M}_\mathrm{i}|} e^{-\mathbf{z}[n]^\mathrm{T}(\mathbf{M}_\mathrm{i})^{-1}\mathbf{z}^*[n]}\,, \tag{3.31}$$

respectively, where $|\mathbf{M}|$ represents the determinant of the matrix $\mathbf{M}$, the super-index $^\mathrm{T}$ denotes vector transposition, the super-index * denotes complex-conjugate of the elements of the vector and $(\mathbf{M})^{-1}$ denotes matrix inversion.

Once these pdf's are obtained for this detection problem, and applying the Neyman-Pearson criterion presented in Sect. 3.1.2, exactly calculating the likelihood ratio of Eq. (3.8), the following LR is obtained:

$$\mathrm{LR}(\mathbf{z}[n]) = \frac{|\mathbf{M}_\mathrm{i}|}{|\mathbf{M}_\mathrm{s}+\mathbf{M}_\mathrm{i}|} e^{\mathbf{z}[n]^\mathrm{T}\left((\mathbf{M}_\mathrm{i})^{-1}-(\mathbf{M}_\mathrm{s}+\mathbf{M}_\mathrm{i})^{-1}\right)\mathbf{z}^*[n]} \tag{3.32}$$

Applying the natural logarithm to this LR, the following LLR is obtained:

$$\mathrm{LLR}(\mathbf{z}[n]) = \log\left(\frac{|\mathbf{M}_\mathrm{i}|}{|\mathbf{M}_\mathrm{s}+\mathbf{M}_\mathrm{i}|}\right) + \mathbf{z}[n]^\mathrm{T}\left((\mathbf{M}_\mathrm{i})^{-1} - (\mathbf{M}_\mathrm{s}+\mathbf{M}_\mathrm{i})^{-1}\right)\mathbf{z}^*[n]\,, \tag{3.33}$$

which can be summarized as

$$\mathrm{LLR}(\mathbf{z}[n]) = \mathbf{z}[n]^\mathrm{T}\,\mathbf{Q}\,\mathbf{z}^*[n] + k\,, \tag{3.34}$$

where k is an immaterial constant mainly dependent on the powers of the processes and $\mathbf{Q} = (\mathbf{M}_\mathrm{i})^{-1} - (\mathbf{M}_\mathrm{s}+\mathbf{M}_\mathrm{i})^{-1}$. Therefore, the decision should be made taking into account the quadratic dependence of the LLR on $\mathbf{z}[n]$, i.e.

$$\mathrm{LLR}(\mathbf{z}[n]) = \mathbf{z}[n]^\mathrm{T}\,\mathbf{Q}\,\mathbf{z}^*[n] \underset{H_0}{\overset{H_1}{\gtrless}} \mathrm{THR}(P_\mathrm{fa})\,. \tag{3.35}$$

The non-linear (quadratic) processor expressed in Eq. (3.35) for implementing the batch approach detector is optimum according to the Neyman-Pearson criterion. This processor requires the computation of the quadratic form:

$$q = \mathbf{z}[n]^\mathrm{T}\,\mathbf{Q}\,\mathbf{z}^*[n]\,, \tag{3.36}$$

involving that q is real because $\mathbf{Q}$ is Hemitian.

Closed form expressions for the P_fa and P_d for the above presented optimum detector can be obtained for this detector. These expressions are given in [Aloisio1994] for a particular approach for detecting zero-mean Gaussian signals in Gaussian interference and in [Farina1986a] for a general approach for detecting Gaussian-distributed signals in correlated Gaussian interference.

3.2.2 Coherent Detection: Suboptimum Approaches

The optimum approaches presented in Sect. 3.2.1 assume that both Gaussian properties of the processes and their statistical properties are known. Nevertheless, in real-live situations, Gaussian properties can be maintained, but the statistical properties usually vary in time. In these cases, suboptimum approaches have been proposed. Following with the structure of Sect. 3.2.1, recursive and batch approaches are presented.

Suboptimum Coherent Detection: Recursive Approach

The calculus of the LLR given in Eq. (3.26) or (3.27), requires the knowledge of the mean and variance of the current radar echo conditioned to the previous echoes (see Eq. (3.25)): $\mu_1[n]$ and $\sigma_1^2[n]$ for LLR_{s+c+g}; and $\mu_0[n]$ and $\sigma_0^2[n]$ for LLR_{c+g}.

Consider that the estimates of these mean and variance values are given by: $\hat{z}_1[n|n-1]$ and $P_1[n|n-1]$ under H_1 conditions; and $\hat{z}_0[n|n-1]$ and $P_0[n|n-1]$ under H_0 conditions. In this way, the residue under hypothesis H_1 of Eq. (3.17), i.e. the difference between the received radar echo ($z[n]$) and its estimate under hypothesis H_1 ($\hat{z}_1[n]$), is now given by its estimate:

$$u_1[n|n-1] = z[n] - \hat{z}_1[n|n-1]\,. \tag{3.37}$$

Therefore, considering Eq. (3.37) and substituting $\mu_1[n]$ and $\sigma_1^2[n]$ by their estimates ($\hat{z}_1[n|n-1]$ and $P_1[n|n-1]$, respectively) in Eq. (3.18), the LLR corresponding to the detection of target and clutter in noise is obtained by

$$\Lambda_{s+c+g}[n] = \frac{|z[n]|^2}{\sigma_g^2} - \frac{u_1[n|n-1]u_1^*[n|n-1]}{P_1[n|n-1]} + \log\left(\frac{\sigma_g^2}{P_1[n|n-1]}\right) + \Lambda_{s+c+g}[n-1]\,. \tag{3.38}$$

Applying the same principles as previously, but for the case of detecting clutter in noise and substituting $\mu_0[n]$ and $\sigma_0^2[n]$ in Eq. (3.18) by their estimates, i.e. $\hat{z}_0[n|n-1]$ and $P_0[n|n-1]$, respectively, and considering that the residue under hypothesis H_0 of Eq. (3.22) is now given by its estimate:

$$u_0[n|n-1] = z[n] - \hat{z}_0[n|n-1]\,. \tag{3.39}$$

the LLR corresponding to the detection of clutter in noise is obtained by

$$\text{LLR}_{c+g}[n] = \frac{|z[n]|^2}{\sigma_g^2} - \frac{u_0[n|n-1]u_0^*[n|n-1]}{P_0[n|n-1]} + \log\left(\frac{\sigma_g^2}{P_0[n|n-1]}\right) + \text{LLR}_{c+g}[n-1]\,. \tag{3.40}$$

For the case of having Gaussian processes, both $f(\mathbf{z}[n]|H_1)$ and $f(\mathbf{z}[n]|H_0)$, and $f(z[n]|\mathbf{z}[n-1], H_1)$ and $f(z[n]|\mathbf{z}[n-1], H_0)$, are Gaussian-distributed as $\text{N}(\mu_1|\sigma_1^2)$ and $\text{N}(\mu_0|\sigma_0^2)$. Under these conditions, $\hat{z}_1$, P_1, $\hat{z}_0$ and P_0 can be evaluated by means of two linear Kalman filters [Farina1987a].

Once the way of obtaining a suitable estimate of the statistical parameters of the processes is set and once both partial LLRs are approximated for the Gaussian-distributed case of study, the overall $\text{LLR}[n]$ is obtained by combining Eq. (3.38) and (3.40) in Eq. (3.13), resulting:

$$\text{LLR}[n] = -\frac{|u_1[n|n-1]|^2}{P_1[n|n-1]} + \frac{|u_0[n|n-1]|^2}{P_0[n|n-1]} + \log\left(\frac{P_0[n|n-1]}{P_1[n|n-1]}\right) + \text{LLR}[n-1]\,. \tag{3.41}$$

On the other hand, considering that in this case

$$v[n] = -\frac{|u_1[n|n-1]|^2}{P_1[n|n-1]} + \frac{|u_0[n|n-1]|^2}{P_0[n|n-1]} + \log\left(\frac{P_0[n|n-1]}{P_1[n|n-1]}\right)\,, \tag{3.42}$$

the LLR can be calculated as in Eq. (3.27) for a set of N observations.

A detection scheme implementing the detector obtained above [Farina1987a] is shown in Fig. 3.1. This scheme considers that the integration is done over the last N observation vectors, i.e. from $v[n]$ to $v[n-(N-1)]$. In this detection scheme, the received radar echo, $z[n]$, is processed

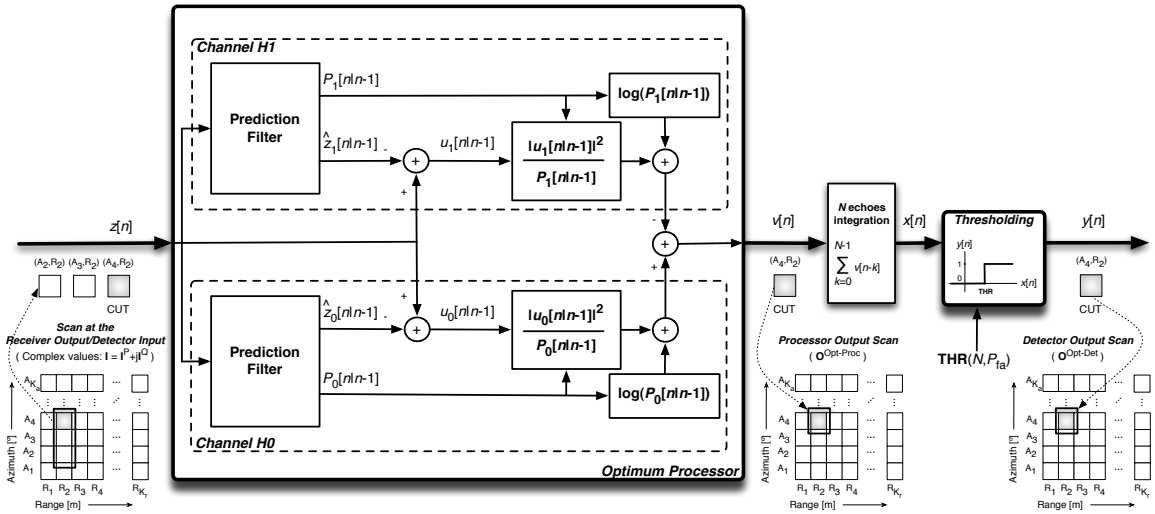

Figure 3.1: Optimum radar detector for target and/or clutter having any type of pdf and ACF

through two linear Kalman filters (prediction filters). The upper filter (Channel H_1) is matched to the case of detecting target and clutter in noise, whereas the bottom filter (Channel H_0) is built according to the case of detecting clutter in noise. By taking the difference between the two estimates ($\hat{z}_1[n|n-1]$ and $\hat{z}_0[n|n-1]$) and the incoming echo, $z[n]$, the residuals ($u_1[n|n-1]$ and $u_0[n|n-1]$) of the estimates are obtained. The variance of the previous estimates ($P_1[n|n-1]$ and $P_0[n|n-1]$) are also obtained from these filters. The detection is made by integrating (over N observations) the difference between the two normalized quadratic residuals and the natural logarithm of the variances. Note that the processor operates on the correlated radar echo $z[n]$ by providing two sequences, $u_1[n|n-1]$ and $u_0[n|n-1]$, one of which is white Gaussian noise. In other words, the Kalman filters act as whitening filters and the decision is made according to which of these two estimates is Gaussian-distributed, i.e. corresponds to the correct hypothesis under test. Finally, a threshold is applied in the integrated output to decide whether a target is present ($y[n] = 1$) or not ($y[n] = 0$). This threshold depends on the desired P_{fa}, as set in Eq. (3.7).

Suboptimum Coherent Detection: Batch Approach

The batch approach of the optimum processor for detecting signals in Gaussian interference is only possible if the covariance matrixes and the statistical parameters of the processes are known, as set Sect. 3.2.1. But, when the statistics of the target and interference signals change in time, i.e. their covariance matrixes change in time, even when the pdf's of the processes don't vary in time, the optimum approach is not suitable. Then, and since these covariance matrixes must be estimated, suboptimum approaches are needed.

Let's consider the estimate of the covariance matrix corresponding to the interference signal. Since the clutter-to-noise ratio is usually much greater than the unity, i.e. $P_{\text{c}} >> P_{\text{g}}$, the covariance matrix of the interference given in Eq. (3.29) can be approximated by $\mathbf{M}_{\text{i}} \sim \mathbf{M}_{\text{c}}$ with low error. Then, for making the estimate of the covariance matrix of the clutter, let's consider

we have a set of M independent observations of the N-dimensional random vector $\mathbf{c}[n]$ ($N \times 1$ column-vector as indicated in Eq. (3.5)), being given in the matrix $\mathbf{C} = [\,\mathbf{c}[1]\,\mathbf{c}[2]\,\ldots\,\mathbf{c}[M]\,]$ with a size of $N \times M$. An unbiased estimator for the estimate of this covariance matrix is [Hayes1996]:

$$\hat{\mathbf{M}}_{\mathrm{c}} = \frac{1}{M-1}\sum_{i=1}^{M}(\mathbf{c}[i]-\bar{\mu})^{*}(\mathbf{c}[i]-\bar{\mu})^{\mathrm{T}}\,, \tag{3.43}$$

where T denotes transposition, the * indicates complex-conjugation of the vector/matrix elements and $\bar{\mu}$ is the sample mean vector. This sample mean is estimated by:

$$\bar{\mu} = [\,\mu_1\ \ldots\ \mu_N\,]^{\mathrm{T}} = \frac{1}{M}\left[\sum_{j=1}^{M} C_{1,j}\ \ \ldots\ \ \sum_{j=1}^{M} C_{N,j}\right]^{\mathrm{T}}. \tag{3.44}$$

On the other hand, the covariance matrix of the target ($\mathbf{M}_{\mathrm{s}}$) is difficult to estimate. This difficulty is found out in the problem of separating the target and interference source signals, which are added, and because the target is not always present to be illuminated by the radar. In these cases, a target model is usually assumed, including an assumption of the covariance matrix of the target signal.

Finally, since the covariance matrix of the interference is estimated, it is not free of error. As a consequence, the matrix $\mathbf{Q} = (\mathbf{M}_{\mathrm{i}})^{-1} - (\mathbf{M}_{\mathrm{s}} + \mathbf{M}_{\mathrm{i}})^{-1}$ might be not Hermitian, involving that LLR in Eq. (3.35) or q in Eq. (3.36) are not real-valued. In this case, the magnitudes of LLR and q are considered to make the final decision (target is present: H_1; or target is absent: H_0).

3.2.3 Incoherent Detection: Optimum Approach

The optimum detection of signals in Gaussian interference was presented in Sect. 3.2.1 for the case of having data coming from coherent radars. In this section, the optimum detection problem supposing that the data are provided by incoherent radars is discussed.

As done for the case of study of the optimum coherent detector by using a recursive approach (see Sect. 3.2.1), the LLR is expressed as the difference of two LLRs (see Eq. (3.12) and (3.13)): one designed for detecting target plus clutter in noise (alternative hypothesis: H_1), and the other for detecting clutter in noise (null hypothesis: H_0). For this case of study, the target ($\mathbf{s}[n]$) is supposed to have a constant magnitude and a variable phase (depending of the Doppler due to its movement) for each element of the observation vector $\mathbf{z}[n]$ under hypothesis H_1, i.e. a Swerling 0 model with Doppler effect is assumed. The clutter ($\mathbf{c}[n]$) and noise ($\mathbf{g}[n]$) signals are supposed to be Gaussian-distributed with zero mean and variances σ_{c}^2 and σ_{g}^2, respectively. Under these assumptions, the signals under both hypotheses follow the following distributions: a Gaussian distribution with mean A and variance $\sigma_1^2 = \sigma_{\mathrm{c}}^2 + \sigma_{\mathrm{g}}^2$ under H_1, and a Gaussian distribution with zero mean and variance $\sigma_0^2 = \sigma_{\mathrm{c}}^2 + \sigma_{\mathrm{g}}^2$ under H_0. Note that under both hypotheses, the same variance is present, i.e. $\sigma_0^2 = \sigma_1^2$. With these data the optimum detector can be formulated for this problem.

Another way of formulating in the literature the optimum detector considering incoherent Gaussian-distributed interference is by using an envelope detector followed by an integrator of N pulses [Eaves1987]. In this section, the joint of envelope detector and integrator is denoted as envelope detector for simplicity, unless the opposite is indicated.

For formulating the envelope detector, let's consider the observation vector given in Eq. (3.3) containing N coherent radar echoes. Two envelope detectors are commonly used in the literature. The first one is the linear-law envelope detector, being its output computed as:

$$x[n] = \sum_{i=1}^{N} \sqrt{(\mathrm{Re}\{z_i[n]\})^2 + (\mathrm{Im}\{z_i[n]\})^2}\,. \tag{3.45}$$

The second one is the quadratic-law envelope detector, being its output:

$$x[n] = \sum_{i=1}^{N} (\mathrm{Re}\{z_i[n]\})^2 + (\mathrm{Im}\{z_i[n]\})^2\,. \tag{3.46}$$

The optimum detector is formulated next only for the case of using the quadratic-law envelope detector of Eq. (3.45). In order to implement the Neyman-Pearson detector, as indicated in Eq. (3.8), the pdf's at the output of the integrator must be calculated for both H_0 and H_1 hypotheses. The output of this envelope detector under observation vectors belonging to H_0 and H_1 follow non-centered chi-square distributions with $2N$ degrees of freedom, being [Eaves1987]:

$$f(x[n]|H_0) = \frac{1}{\sigma_0^{2N}\Gamma(N)}\, x^{N-1}\, e^{-\frac{x}{\sigma_0^2}}\,, \tag{3.47}$$

$$f(x[n]|H_1) = \frac{1}{\sigma_0^2}\left(\frac{x}{NA^2}\right)^{\frac{N-1}{2}} e^{-\frac{x+NA^2}{\sigma_0^2}}\, \mathrm{I}_{N-1}\left(\frac{2\sqrt{xNA^2}}{\sigma_0^2}\right)\,, \tag{3.48}$$

where N is the number of pulses in the integration, $\Gamma()$ is the Gamma function and I_{N-1} is the modified Bessel function with $N-1$ degrees of freedom.

Once the likelihood functions are known at the output of the quadratic-law envelope detector at a given time instant n ($x[n]$), the optimum detector in the Neyman-Pearson sense given by the likelihood ratio ($\mathrm{LR}(x[n])$) is computed, resulting:

$$\mathrm{LR}(x[n]) = e^{-\frac{NA^2}{\sigma_0^2}} (xNA^2)^{-\frac{N-1}{2}} \mathrm{I}_{N-1}\left(\frac{2\sqrt{xNA^2}}{\sigma_0^2}\right) \underset{H_0}{\overset{H_1}{\gtrless}} \mathrm{THR}(P_{\mathrm{fa}}) \tag{3.49}$$

where the decision target present/target absent is made by using the threshold, THR, set for a desired P_{fa}.

Closed forms of the P_{fa} and P_{d} expressions depending on THR can be obtained for this detector under these target and interference conditions. These expressions can be found in [Eaves1987]. Considering that the interference power is normalized to the unity, i.e. $\sigma_0 = 1$, the threshold, T, can be obtained for a desired P_{fa} from Eq. (3.50) [Eaves1987].

$$P_{\mathrm{fa}} = e^{-T} \sum_{m=0}^{N-1} \frac{T^m}{m!} \tag{3.50}$$

But, if the interference power is not the unity, the threshold to be applied is denormalized, being:

$$\mathrm{THR}(P_{\mathrm{fa}}) = \sigma_0^2\, T(P_{\mathrm{fa}}) \tag{3.51}$$

3.2.4 Incoherent Detection: Suboptimum Approaches

Optimum approaches for detecting signals in Gaussian interference can be formulated when both the pdf's of the statistical processes under hypotheses H_0 and H_1, and the statistical parameters of the target and interference signals remain constant in time. But, when these conditions are not fulfilled, suboptimum approaches are needed. In this case, a suboptimum approach commonly used in the literature is presented below.

For formulating the suboptimum approach described in this section, let's consider the same detection problem as formulated for the optimum incoherent detector described in Sect. 3.2.3. For this approach, let's assume that the statistical distributions of the likelihood functions at the output of the quadratic-law envelope detector given in Eq. (3.47) and (3.48) under both hypotheses don't vary in time. But, let's assume that the statistical parameters of the target (A: mean value of the Swerling 0 target model) and interference (variances σ_c^2 and σ_g^2) signals vary in time. In this way, and assuming that the clutter-to-noise ratio is much greater than the unity ($\sigma_c^2 >> \sigma_g^2$), the variance of the interference could be estimated from a set of M observation vectors under H_0 ($\hat{\sigma}_0^2$). On the other hand, once knowing the variance of the interference, the mean value of the target signal could also be estimated ($\hat{A}$). Therefore, once these parameters are estimated, the likelihood functions of Eq. (3.47) and (3.48) can be evaluated and the LR of Eq. (3.49) can be estimated for the observation vector under evaluation. In this way, the detector can decide whether target information is present or not in the observation vector at the output of the envelope detector. It is important to note that since the parameters of the likelihood functions are estimated, an error exists in this estimate. This error tends to decrease with the number of integrated pulses and the number of observation vectors used for the estimate. As a consequence of this error, the performance of this suboptimum detector will be always lower than for the optimum one.

The suboptimum approach presented above can be used to detect Swerling 0 target signals in correlated Gaussian-distributed interference. Other suboptimum approaches considered in the literature are the ones based on the incoherent MTI (moving target indicator). But, the approaches most commonly used in the literature are the ones based on CFAR techniques. These approaches try to adapt the threshold set in Eq. (3.51) according to: a fixed value of T set for a desired P_{fa} and the estimate of the variance of the clutter power. This approach is conditioned to the case of having a clutter-to-noise ratio greater than the unity, where $\sigma_c^2 >> \sigma_g^2$, and consequently $\sigma_0^2 \sim \sigma_c^2$ [Skolnik2008]. A block diagram of a general CFAR approach is summarized in Fig. 3.2. In this case, and to follow the nomenclature commonly used in the literature, the observation vector $\mathbf{z}[n]$ obtained at a given time instant n, i.e. $\mathbf{z}[n]$, is defined in a different way as in (3.3), being:

$$\mathbf{z}[n] = \left[z[n - \tfrac{N-1}{2}] \ \ldots \ z[n] \ \ldots \ z[n + \tfrac{N+1}{2}] \right] , \tag{3.52}$$

where N must be an odd value. Then, this new observation vector is the one used in the envelope detector (with an N-pulse integrator) defined in Eq. (3.45)-(3.46) to obtain each sample that is used in the CFAR detector of Fig. 3.2. Finally, it is important to note that the estimate of the clutter statistical parameters is done according to the information contained in the lead and lag windows (cells adjacent to the cell under test (CUT)) but removing some cells corresponding to the guard cells (the ones closest to the CUT).

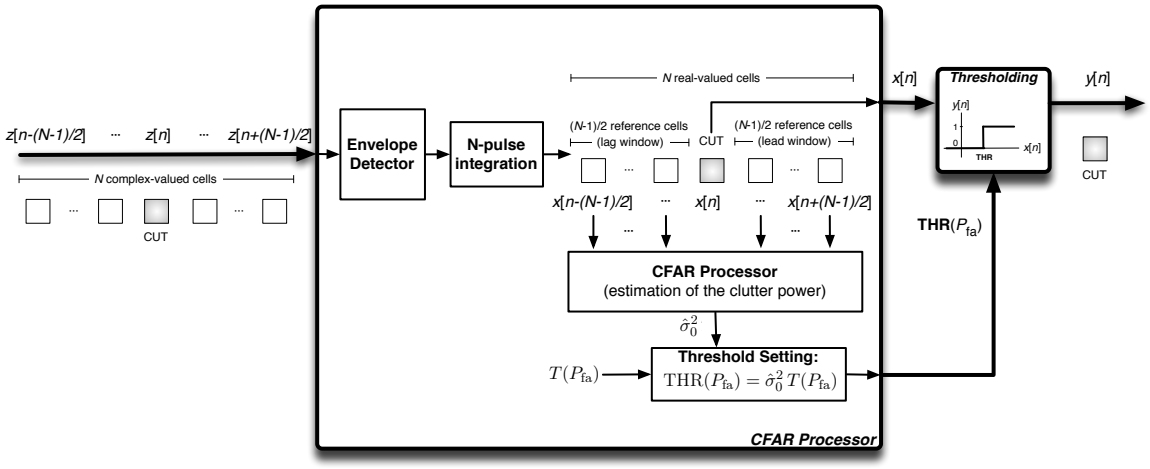

Figure 3.2: Suboptimum approach for detecting signals in Gaussian interference based on a CFAR detector scheme

3.3 Detection of Signals in Non-Gaussian-distributed Interference

Unfortunately, Gaussian-distributed processes are not so common in real-live situations. In this case, other interference models are needed, as the ones discussed in Sect. 1.2.1 for the clutter. In this thesis, the Weibull distribution has been selected to model the radar clutter. In this way, the likelihood functions $f(\mathbf{z}[n]|\mathrm{H}_i)$, with $i = 0, 1$, to be used in the Neyman-Pearson detector of Eq. (3.8), are no longer Gaussian-distributed. Thus, an explicit mathematical expression for the Neyman-Pearson detector is difficult to obtain in general. Therefore, it is very difficult to obtain an analytical expression that relates the threshold to be applied for maintaining a certain P_{fa}. In consequence, suboptimum approaches are need to solve this detection problem.

Next, coherent and incoherent approaches for detecting Swerling 0 target signals in Weibull-distributed clutter and white Gaussian noise are presented. Both approaches are selected as reference detectors in the thesis because they are commonly used in the literature as basic references. In Sect. 3.3.1, the suboptimum coherent approach is presented. In Sect. 3.3.2, three different incoherent CFAR detectors are considered.

3.3.1 Suboptimum Coherent Detection of Signals in Weibull-distributed Interference: The TSKAP Detector

According to the difficulty of finding analytical expressions for the Neyman-Pearson detector under Weibull-distributed coherent clutter conditions, the detection problem can be restated in a more convenient way, which allows to obtain suboptimal solutions. In this way, let's consider the relationship given in Eq. (3.2) under H_0 and express $c[n]$ as the sum of the best estimation ($\hat{c}[n]$) plus a white Gaussian unpredictable residual ($\tilde{c}[n]$) [Farina1986a]:

$$z[n] = \hat{c}[n] + \tilde{c}[n] + g[n]\,. \tag{3.53}$$

Considering that $u_0[n]$ is a white Gaussian signal obtained from the sum of $\tilde{c}[n]$ and $g[n]$, the received radar echo can be expressed as

$$z[n] = \hat{c}[n] + u_0[n]\,. \tag{3.54}$$

Applying the same procedure to Eq. (3.1) under H_1, the received signal can be reformulated as

$$z[n] = (\widehat{s[n] + c[n]}) + u_1[n]\,, \tag{3.55}$$

where $u_1[n]$ is a white Gaussian signal composed of the sum of $(\widetilde{s[n] + c[n]})$ and $g[n]$.

In other words, the original detection problem of Eq. (3.1) and (3.2) has been restated as the problem of recognizing two signals $(\widehat{s[n] + c[n]})$ and $\hat{c}[n]$ (also indicated with $\hat{z}_1$ and $\hat{z}_0$, respectively) embedded in white Gaussian noises u_1 and u_0, respectively. Fig. 3.1 illustrated this approach when Gaussian interference is considered. But, for a non-Gaussian distributed case, the novelty of the approach is the non-linear nature of the two parallel non-linear estimators. These estimators can be regarded as a means to obtain a zero-mean white Gaussian sequence through the channel corresponding to the currently occurring hypothesis.

This suboptimum recursive approach presents four major problems:

- The first is due to the difficulty of finding explicit (analytical) expressions for the two recursive non-linear filters.
- The second problem refers to the inability of evaluating the corresponding detection performance of the conceived processor. The general case to proceed is to derive suboptimal non-linear estimators and to assess detection performance by means of Monte Carlo simulation techniques.
- The third problem refers to the on-line evaluation of the non-linear filter parameters by means of adaptive procedures. It involves high computational cost.
- And the last problem concerns to the threshold setting, which depends on the parameters of the processor and on the signal and clutter sources.

In this section, the processor proposed in [Farina1987b] for detecting a target signal known a priori (Swerling 0) embedded in coherent Weibull clutter and white Gaussian noise (WGN) is presented. The major problem to tackle is the derivation of the two non-linear filters of Fig. 3.1, as mentioned above.

As presented in [Farina1987b], this detector can be implemented for our case of study as the block diagram of Fig. 3.3, which depends on two important parameters: the signal to detect ($s[n]$) and the skewness parameter of the Weibull distribution in the design stage ($a^{(\mathrm{d})}$). The received echo, $z[n]$, is processed in the detector through two non-linear prediction filters. The upper filter is matched to the condition that the signal to detect is the sum of the target plus clutter in noise (channel H_1), while the lower filter is built under the condition that the signal to detect is just the clutter source in noise (channel H_0). Channel H_1 differs from channel H_0 in the presence of the target sequence $s[n]$, which is supposed to be *known a priori*. This sequence is first subtracted from the incoming radar echo $z[n]$. Then, the estimation of the disturbance $c[n]$ can be performed as in the channel H_0, and hence summed again to the non-linear prediction

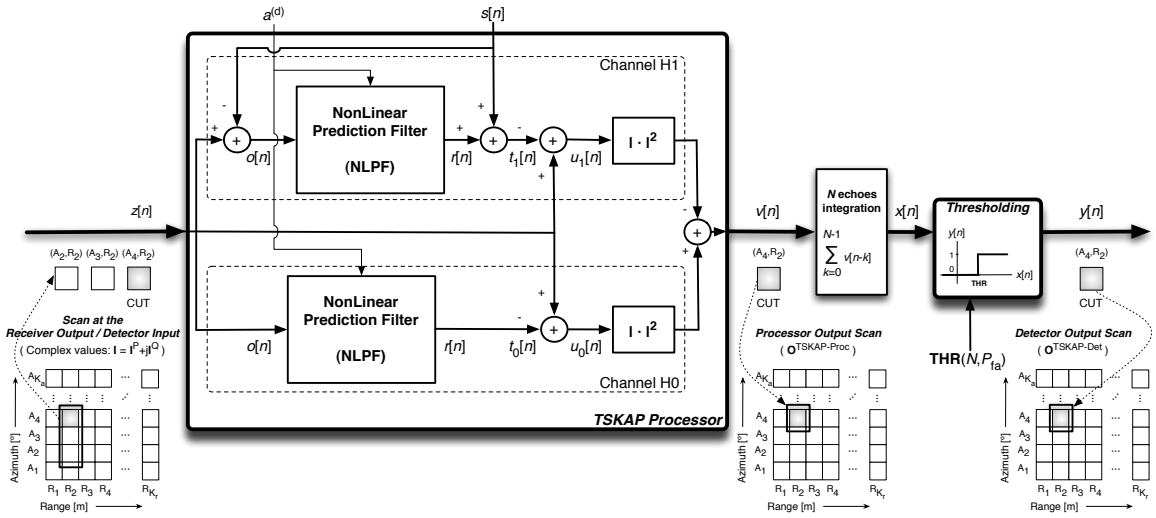

Figure 3.3: *Target sequence known a priori* (TSKAP) detector

filter output. By making the difference of the two estimates obtained from the incoming echo $z[n]$ ($\hat{z}_1[n|n-1]$ and $\hat{z}_0[n|n-1]$), two estimate residuals ($u_1[n|n-1]$ and $u_0[n|n-1]$) are obtained. To ascertain which of the two residuals is a zero-mean WGN sequence and to perform detection, the difference of its squares ($|u_0[n|n-1]|^2 - |u_1[n|n-1]|^2$) is integrated along the last N received echoes [1]. The result is compared with a threshold established to obtain the desired P_{fa}, where the final decision is made: target is present (H_1) or absent (H_0).

The issue, which remains to be solved, is the derivation of the non-linear prediction filters in the two alternative hypotheses. A good, even though suboptimal, solution is represented as the cascade of the inverse of the non-linear memoryless transformation (NLMLT^{-1}), a linear prediction filter (LPF) and a NLMT. Assuming that the cnr is much greater than unity (cnr $>>$ 1 or CNR $>>$ 0 dB), the inverse of the NLMLT transforms the Weibull clutter in a Gaussian random variable. Thereafter, the LPF operates on the Gaussian-distributed disturbance. Finally, the NLMLT obtains the predicted disturbance in the Weibull domain. This approach is followed in the NLPFs of Fig. 3.3, illustrating its internal structure in Fig. 3.4. The LPF and the inverse of the NLMLT are explained below. The NLMLT was explained in Sect. 2.2.2 because it was necessary to explain the scheme used to model the Weibull clutter sequences.

Inverse of the non-linear memoryless transformation (NLMLT)

The NLMLT (see section 2.2.2) transforms a Gaussian-distributed signal into a Weibull-distributed one, while the inverse of the NLMLT (NLMLT^{-1}) makes the opposite transformation. This inverse transformation modifies the pdf of the random process from Weibull to Gaussian and the temporal properties of the sequences, i.e. their autocorrelation functions. Thus, the NLMLT^{-1}

[1] Note that to perform the afore-mentioned difference, the two quadratic forms, $|u_0[n|n-1]|^2$ and $|u_1[n|n-1]|^2$, should be divided by their corresponding variances P_0 and P_1, respectively, as shown in Fig. 3.1. Being the target sequence known a priori, it follows that P_0 is equal to P_1 and hence the residual normalization can be avoided, with the corresponding saving of the variance computation.

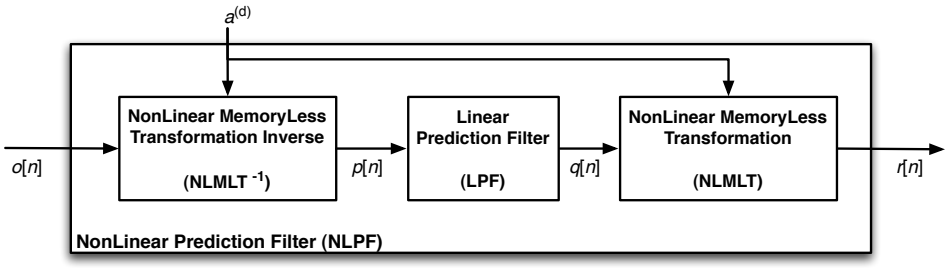

Figure 3.4: Nonlinear prediction filter (NLPF) structure

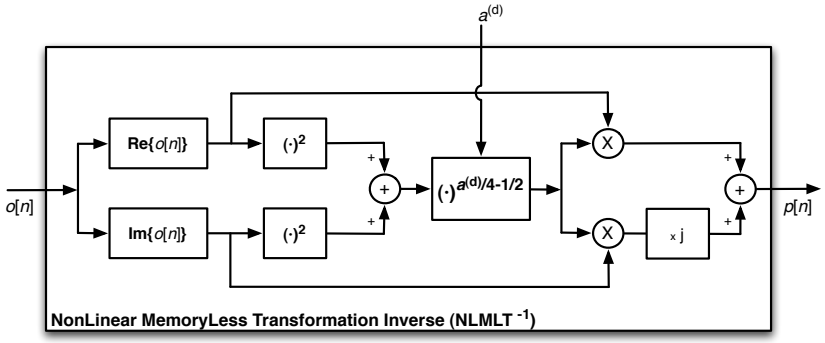

Figure 3.5: Inverse of the non-linear memoryless transformation (NLMLT^{-1})

can be achieved according to a box-cox transformation [Kay1988], as follows:

$$p[n] = o[n] \cdot |o[n]|^{\frac{a^{(\mathrm{d})}}{2}-1} \tag{3.56}$$

where $o[n]$ and $p[n]$ are the input (Weibull-distributed) and output (Gaussian-distributed) sequences of the NLMLT^{-1}, respectively, $|o[n]|$ is the modulus of the NLMLT^{-1} input sequence and $a^{(\mathrm{d})}$ is the skewness parameter of the Weibull random process. As the sequences represent to coherent random distributions, the input sequence $o[n]$ can be expressed by its real (Re$\{\cdot\}$) and imaginary (Im$\{\cdot\}$) parts. Thus, Eq. (3.56) can be rewritten as

$$p[n] = \left[\mathrm{Re}\left\{o[n]\right\} + j\mathrm{Im}\left\{o[n]\right\}\right] \cdot \left(|o[n]|^2\right)^{\frac{a^{(\mathrm{d})}}{4}-\frac{1}{2}} . \tag{3.57}$$

Finally, if the squared modulus of the input sequence is expressed by its real and imaginary parts, Eq. (3.57) can be rewritten as

$$\begin{aligned} p[n] =& \mathrm{Re}\left\{o[n]\right\} \cdot \left[(\mathrm{Re}\{o[n]\})^2 + (\mathrm{Im}\{o[n]\})^2\right]^{\frac{a^{(\mathrm{d})}}{4}-\frac{1}{2}} \\ &+ j\mathrm{Im}\left\{o[n]\right\} \cdot \left[(\mathrm{Re}\{o[n]\})^2 + (\mathrm{Im}\{o[n]\})^2\right]^{\frac{a^{(\mathrm{d})}}{4}-\frac{1}{2}} . \end{aligned} \tag{3.58}$$

Analyzing Eq. (3.58), the block diagram of the NLMLT^{-1} shown in Fig. 3.5 is obtained. It depends on the skewness parameter of the Weibull distribution in the design stage ($a^{(\mathrm{d})}$).

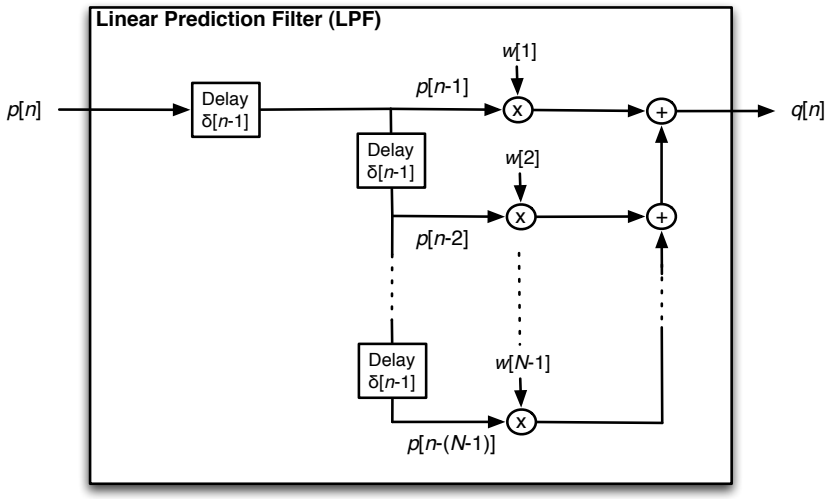

Figure 3.6: Linear prediction filter

Linear Prediction Filter

Consider an input signal, $p[n]$, which can come from target and interference (clutter and noise) sources or only from interference sources. The linear filtering that composes the processor is designed following the linear filtering theory established in [Makhoul1975].

From a general perspective, the linear prediction of the n-th sample of a random process p can be achieved by a linear combination of the previous samples $p[n-k]$ and the input ($u[n]$) of an hypothetical system from which $p[n]$ is obtained. This prediction is summarized in Eq. (3.59), where $w[n]$, $b[n]$ and the gain G are the parameters of the hypothesized system.

$$\hat{p}[n] = \sum_{l=1}^{N-1} w[l]p[n-l] + G\sum_{k=0}^{s-1} b[k]u[n-k] \tag{3.59}$$

With noise-free observations, approximation that can be done when cnr >> 1 (CNR >> 0 dB), linear prediction is concerned with the estimation of the desired signal with the minimum mean square error. Fig. 3.6 shows the flow chart of the finite impulse response (FIR) linear prediction filter used in this approximation. Note that since an FIR filter is considered, G and $b[n]$ are null in Eq. (3.59). In this case, the desired output of the LPF will be $q[n] = \hat{p}[n]$, where a linear combination of the $N-1$ previous samples of the input signal is applied. Therefore, the LPF coefficients can be achieved when the desired output signal of the Wiener filter ($q[n]$) is equal to the current sample of the filter input, i.e., $q[n] = p[n]$. In the case of study of the thesis, the FIR linear predictor of order $N-1$ is computed as

$$\hat{p}[n] = w[0]p[n] + \sum_{l=1}^{N-1} w[l]p[n-l] \tag{3.60}$$

where $w[n]$ are the coefficients of the LPF, being stored in the row vector $\mathbf{w}$. Independently of the LPF order, its first coefficient is null ($w[0] = 0$) because the objective is to predict the current input at the n-th instant from the $N-1$ previous ones [Hayes1996]. Assuming this criterion,

there is not any dependence between the output at the current time instant (n-th time instant) and the input at the same time instant.

Using a matrix notation, Eq. (3.60) can be rewritten as:

$$q[n] = \mathbf{w} \cdot \mathbf{p}\,, \tag{3.61}$$

where $\mathbf{p}$ is a column vector containing the input samples from $p[n-1]$ to $p[n-(N-1)]$ and $\mathbf{w}$ is a row vector containing the weights of the FIR linear filter ($\mathbf{w} = w[1] \dots w[N-1]$). As the linear predictor may be cast into a Wiener filtering problem when $q[n] = p[n]$ (see Appendix B), to set up the Wiener-Hopf equations, it is only needed the evaluation of the cross-correlation between $q[n]$ and $p[n]$. Since

$$r_{qp}[n] = \mathrm{E}\left\{q[k]p^*[k-1-n]\right\} = \mathrm{E}\left\{p[k]p^*[k-1-n]\right\} = r_p[n+1]\,, \tag{3.62}$$

and the autocorrelation sequence is conjugate symmetric, i.e. $r_p[n] = r_p^*[-n]$, the Wiener-Hopf equations for the optimum linear predictor are

$$\begin{pmatrix} r_p[0] & r_p^*[1] & r_p^*[2] & \dots & r_p^*[N-2] \\ r_p[1] & r_p[0] & r_p^*[1] & \dots & r_p^*[N-3] \\ r_p[2] & r_p[1] & r_p[0] & \dots & r_p^*[N-4] \\ \vdots & \vdots & \vdots & & \vdots \\ r_p[N-2] & r_p[N-3] & r_p[N-4] & \dots & r_p[0] \end{pmatrix} \begin{pmatrix} w[1] \\ w[2] \\ w[3] \\ \vdots \\ w[N-1] \end{pmatrix} = \begin{pmatrix} r_p[1] \\ r_p[2] \\ r_p[3] \\ \vdots \\ r_p[N-1] \end{pmatrix}, \tag{3.63}$$

where the minimum mean-square error of the estimation ($\hat{p}[n]$) is

$$\epsilon_{min} = r_p[0] - \sum_{l=1}^{N-1} w[l] r_p^*[l]\,. \tag{3.64}$$

The equations system given by (3.63) can be rewritten in matrix notation as

$$\mathbf{R}_p \mathbf{w} = \mathbf{r}_{z^{+1}} \tag{3.65}$$

where $\mathbf{R}_p$ is an $[(N-1) \times (N-1)]$ Hermitian Toeplitz matrix of autocorrelations of $p[n]$ and $\mathbf{r}_{z^{+1}}$ is a column vector storing the $N-1$ autocorrelations of $p[n]$. Thus, the coefficients of the LPF can be obtained as

$$\mathbf{w} = \mathbf{R}_p^{-1} \mathbf{r}_{p^{+1}}\,. \tag{3.66}$$

The vector $\mathbf{w}$ will contain the LPF coefficients $w[1], w[2], \cdots, w[N-1]$, so all the coefficients of the LPF are given by

$$\begin{pmatrix} w[0] \\ \mathbf{w} \end{pmatrix} = \begin{pmatrix} w[0] \\ w[1] \\ w[2] \\ \vdots \\ w[N-1] \end{pmatrix} = \begin{pmatrix} 0 \\ w[1] \\ w[2] \\ \vdots \\ w[N-1] \end{pmatrix}. \tag{3.67}$$

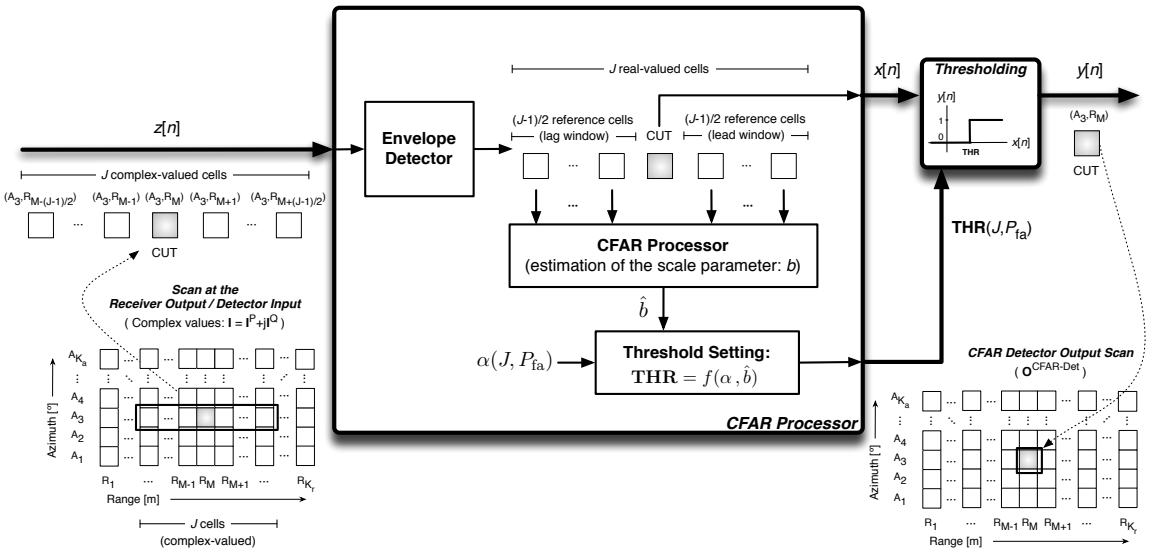

Figure 3.7: CFAR detector scheme

3.3.2 Suboptimum Incoherent Detection of Signals in Weibull-distributed Interference: CFAR Detectors

As occurred with the coherent detection problem, when the pdf's of the incoherent processes under the null and alternative hypotheses are not known, suboptimum approaches are used to approximate to the Neyman-Pearson detector. The commonly used suboptimum approaches when using incoherent data are based on CFAR techniques [Skolnik2001].

The general scheme of a parametric CFAR detector when considering incoherent Weibull clutter is depicted in Fig. 3.7. A linear envelope detector is used. In this case, the output of the envelope detector for each cell is

$$x_i[n] = \sqrt{z_{i,P}^2[n] + z_{i,Q}^2[n]}\,, \quad , i = 1, 2 \ldots N \tag{3.68}$$

where $z_{i,P}[n] = \mathrm{Re}\{z[n]\}$ and $z_Q[n] = \mathrm{Im}\{z[n]\}$. Once the observation vector at the output of the envelope detector ($\mathbf{x}[n]$) is obtained, the decision of whether a target is present or not in a CUT is made considering an adaptive threshold. This threshold is automatically adapted according to the information contained in the cells of the observation vector surrounding the CUT. Note that the cells concerning to the guard region (guard cells) are rejected for making this estimation. Depending on the kind of CFAR detector, this threshold is adapted following different criteria. The different ways of working of the CFAR detectors taken as reference in the thesis are explained below.

Before presenting the particularities of each CFAR detector, the nomenclature to be used in the formulations is set. Consider the general case, where an observation vector containing complex-valued cells is processed. In Fig. 3.7, the J cells that compose the observation vector are selected from a coherent radar scan ($\mathbf{I}$) by using an horizontal mode (range direction). For

this example, the observation vector (complex-valued in the general case) is:

$$\begin{aligned}\mathbf{z}[n] &= \left[I_{(A_3,R_{M-\frac{J-1}{2}})} \quad \dots \quad I_{(A_3,R_M)} \quad \dots \quad I_{(A_3,R_{M+\frac{J-1}{2}})} \right]^{\mathrm{T}} \\ &= \left[\quad z_1[n] \quad \dots \quad z_{\frac{J+1}{2}}[n] \quad \dots \quad z_J[n] \quad \right]^{\mathrm{T}} . \end{aligned} \tag{3.69}$$

At the output of the envelope detector, the following vector is obtained:

$$\mathbf{x}[n] = \left[\quad x_1[n] \quad \dots \quad x_{\frac{J+1}{2}}[n] \quad \dots \quad x_J[n] \quad \right]^{\mathrm{T}} . \tag{3.70}$$

Assuming that Weibull-distributed clutter is present, the power of the clutter is estimated in order to adapt the detection threshold (THR) [DeMiguel1998, Ravid1992, Levanon1990]. This power estimation is done by using the CUT adjacent cells, but removing the ones included in the guard region. From the analysis of Weibull-distributed sequences presented in Sect. 2.2.2, it was observed that its power is related to its scale parameter (b), as set in Eq. (2.14), considering that its skewness parameter is known. In consequence, this parameter must be estimated ($\hat{b}$) and taken into account for the adaptation of the threshold. This estimation is done each time a new observation vector is available. Finally, this threshold is adapted according to $\hat{b}$ and to a constant (α). This constant usually depends on the number of selected cells (J) and the desired P_{fa}, i.e. $\alpha = f(J, P_{\mathrm{fa}})$, and it is set in the design stage of each detector. Depending on the CFAR detector, two main differences can be found. First, the scale parameter is estimated in a different way. And second, the expression that relates α and $\hat{b}$ with THR can change. Both aspects are presented below for the CFAR detectors taken as reference in the thesis.

CA-CFAR detector

Considering the cell averaging approach, which is explained in depth in [DeMiguel1998] for the case of detecting multiple target signals in presence of Weibull-distributed clutter, the CA-CFAR detector is implemented. This detector is able to work properly in multi-target environments and when homogeneous and heterogeneous clutter is observed. Moreover, due to its reduced computational cost for being implemented, it has been widely spread in the radar community. The signal processing applied in the CA-CFAR processor is:

- The estimation of the scale parameter is done by:

$$\hat{b}[n] = \frac{1}{J-G} \sum_{k=1}^{J} x_k[n] \,, \; k \neq k_{\mathrm{CUT}} = \frac{J+1}{2} \,, \tag{3.71}$$

  and k is out of the guard region.

  Note that only $(J-1)-(G-1) = J-G$ cells are considered in this expression, being J the number of available cells (the CUT and the $J-1$ surrounding cells) and G the number of cells contained in the guard region (the CUT and the $G-1$ surrounding cells).

- The adaptation of the detection threshold is done by:

$$\mathrm{THR}[n] = \alpha \, \hat{b}[n] \,, \tag{3.72}$$

  where the constant α is fixed in the design stage for a given P_{fa}.

ML-CFAR detector

The estimation of the clutter power made by the CA-CFAR processor is not always as accurate as possible. In this way, the estimate of the clutter power can be improved considering an approach based on the maximum likelihood estimation. This approach is explained in depth in [Ravid1992] for the case of detecting multiple target signals (fluctuating and non-fluctuating) in presence of Weibull-distributed clutter. This approach is called ML-CFAR detector. The way this detector processes the observation vector for making an estimated of the clutter power is:

- The estimation of the scale parameter is done by:

$$\hat{b}[n] = \left(\frac{1}{J-G} \sum_{k=1}^{J} x_k^{a^{(\mathrm{d})}}[n] \right)^{\frac{1}{a^{(\mathrm{d})}}}, \; k \neq k_{\mathrm{CUT}} = \frac{J+1}{2}, \tag{3.73}$$

  and k is out of the guard region.

  As occurred for the CA-CFAR detector, only $J-G$ cells are considered in this expression.

- The adaptation of the detection threshold is done by:

$$\mathrm{THR}[n] = \alpha^{\frac{1}{a^{(\mathrm{d})}}} \hat{b}[n], \tag{3.74}$$

  where the skewness parameter of the Weibull-distributed clutter must be known, which is established in the design stage ($a^{(\mathrm{d})}$). Again, the constant α is fixed in the design stage for a given P_{fa}.

As observed, the computational cost of this approach is greater than the one needed for implementing the CA-CFAR detector, but being compensated by the performance improvement achieved.

OS-CFAR detector

It is known that the CA-CFAR detector presents some problems of detection when close targets are observed in a multi-target environment or when clutter conditions changes for adjacent regions in the scan. Under these situations, the CA-CFAR detector usually present an increase of false alarm, being reduced its performance considerably. For reducing this performance lost, order statistics techniques are used in CFAR detectors. One of the proposed CFAR detectors proposed in the literature is the OS-CFAR detector. It is known that this detector is able to work maintaining a high performance in multitarget-environments and with homogeneous and heterogeneous Weibull-distributed clutter conditions [Levanon1990]. This detector is completely different to the CA-CFAR detector in terms of the applied signal processing. But, it follows a similar philosophy of working with the ML-CFAR detector in terms of threshold adaptation. The signal processing applied in the OS-CFAR processor is divided in three steps:

- First: sort in ascending order the $J-G$ reference cells contained in the observation vector that are not the CUT and are out of the guard region:

$$\mathbf{x}^{\mathrm{sort}}[n] = \mathrm{sort}(\mathbf{x}[n]): \; x_1^{\mathrm{sort}}[n] \leq \ldots \leq x_k^{\mathrm{sort}}[n] \leq \ldots \leq x_{J-G}^{\mathrm{sort}}[n]. \tag{3.75}$$

Table 3.1: Estimation of the scale parameter and threshold adaptation in CFAR detectors.

CFAR detector	*Scale Parameter Estimate*	*Threshold*
CA-CFAR	$\hat{b}[n] = \frac{1}{J-G}\sum_{k=1}^{J} x_k[n],\ \ k \neq k_{\text{CUT}}$	$\text{THR}[n] = \alpha\,\hat{b}[n],$
	and k is out of the guard region.	α depends on P_{fa}.
ML-CFAR	$\hat{b}[n] = \left(\frac{1}{J-G}\sum_{k=1}^{J} x_k^{a^{(\text{d})}}[n]\right)^{\frac{1}{a^{(\text{d})}}},\ \ k \neq k_{\text{CUT}}$	$\text{THR}[n] = \alpha^{\frac{1}{a^{(\text{d})}}}\,\hat{b}[n],$
	and k is out of the guard region.	α depends on P_{fa}.
OS-CFAR	$\hat{b}[n] = x_k^{\text{sort}}[\text{n}]$	$\text{THR}[n] = \alpha^{\frac{1}{a^{(\text{d})}}}\,\hat{b}[n],$
	$x_1^{\text{sort}}[n] \leq \cdots \leq x_k^{\text{sort}}[n] \leq \ \ldots\ \leq x_{J-G}^{\text{sort}}[\text{n}]$	α depends on P_{fa}.

- Second: estimate of the scale parameter by selecting the k-th element of the sorted observation vector, i.e.

$$\hat{b}[n] = x_k^{\text{sort}}[n]\,. \tag{3.76}$$

  The value of k mainly depends on the target conditions present in the environment. This value will be empirically studied in the thesis.

- And third, adapt the detection threshold by:

$$\text{THR}[n] = \alpha^{\frac{1}{a^{(\text{d})}}}\,\hat{b}[n]\,, \tag{3.77}$$

  where the skewness parameter of the Weibull-distributed clutter must be known, which is established in the design stage ($a^{(\text{d})}$). As occurred for the previous CFAR approaches, the constant α is fixed in the design stage for a given P_{fa}.

Summary of CFAR detectors

Finally, once the detection threshold is adapted according to the environmental conditions surrounding the CUT, the final decision (H_1: target is present; H_0: target is absent) is made:

$$y[n] = \left(x_{\frac{J+1}{2}}[n] \underset{H_0}{\overset{H_1}{\gtrless}} \text{THR}(P_{\text{fa}})[n]\right)\,, \tag{3.78}$$

being this decision assigned to the corresponding cell in the detector output scan:

$$O_{(A_3,R_M)}^{\text{CFAR-Det}} = y[n] \tag{3.79}$$

For ending this section, the different ways of estimating the scale parameter and adapting the threshold done by each CFAR detector scheme are summarized in Table 3.1.

Part II

Automatic Detection based on Artificial Intelligence (AI)

CHAPTER 4

Detection Scheme based on Artificial Intelligence

4.1 Coherent and incoherent detection schemes based on AI

Two different approaches to detect targets in Weibull-distributed clutter are proposed in Chap. 5 and 6. These approaches are based on the scheme presented in Fig. 4.1. Both complex-valued and real-valued scans/matrixes obtained with coherent and incoherent measurement systems, respectively (see Chap. 2: Fig. 2.1 and 2.5) can be processed by this scheme. To decide whether a cell under test (CUT) at the n-th instant contains information from a target or not, an observation vector ($\mathbf{z}[n]$) is extracted from the received radar scan ($\mathbf{I}$). The nomenclature set in Eq. (3.3) when using a batch processor is considered in the proposed detection scheme. This nomenclature (columns vectors) is also commonly used in ANNs literature, as presented in Chap. 5 and 6. The obtaining of an observation vector from a radar scan is summarized in Fig. 4.1. For the example shown in this figure, an observation vector containing $N = 3$ cells (CUT: $z[n]$; and $N - 1 = 2$ previous cells: $z[n-k], k = 1, \ldots, N-1$) is selected, being:

$$\begin{aligned} \mathbf{z}[n] &= [z[n-2] \quad z[n-1] \quad z[n] \quad]^{\mathrm{T}} \\ &= \left[I_{(A_{L-2},R_M)} \; I_{(A_{L-1},R_M)} \; I_{(A_L,R_M)}\right]^{\mathrm{T}} \\ &= [z_1[n] \quad z_2[n] \quad z_3[n] \quad]^{\mathrm{T}} \,, \end{aligned} \tag{4.1}$$

where the super-index T denotes vector transposition. This kind of modes are called *non-delayed selection modes* in the thesis because the decision is taken only considering the current and previous cells, not depending on posterior (future) cells. Other selection modes are considered in the thesis, which will be presented in next sections.

Considering this observation vector, the output of the processor of the proposed detection scheme is obtained as:

$$x[n] = f_{\mathrm{proc}}(\mathbf{z}[n]) \,, \tag{4.2}$$

where $f_{\mathrm{proc}}(\cdot)$ represents the function implemented by the AI technique, which is discussed in Chap. 5 and 6. This real-valued output is stored in the corresponding cell of the processor output scan, being in this example:

$$O^{\mathrm{Proc}}_{(A_L,R_M)} = x[n] \,. \tag{4.3}$$

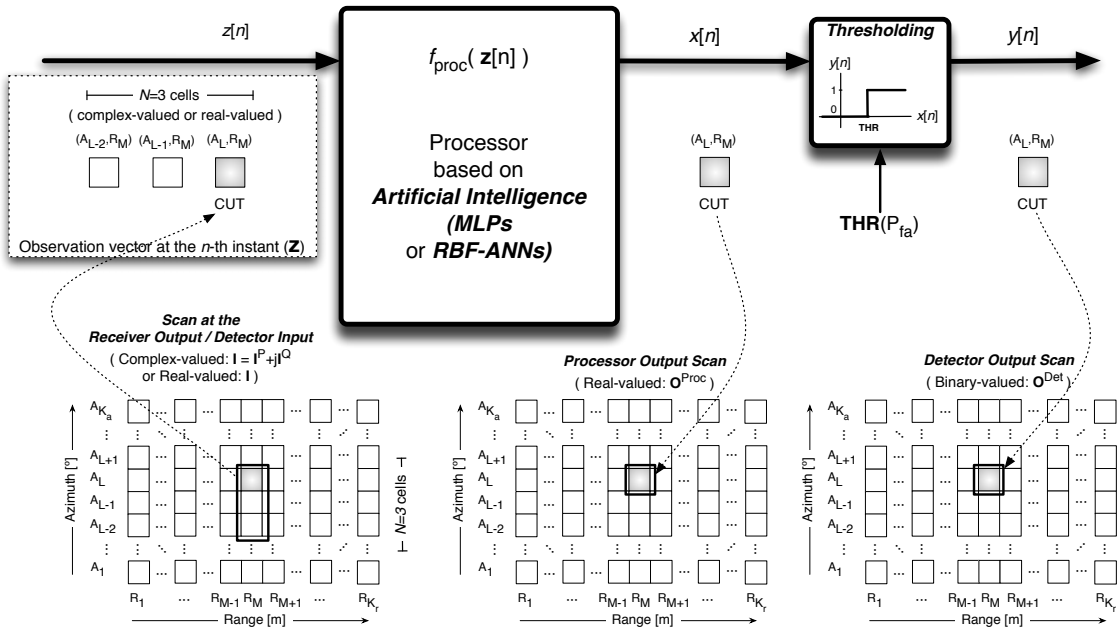

Figure 4.1: Proposed detection scheme based on AI techniques when non-delay selection modes are used

Finally, the processor output is compared with a threshold (THR), deciding whether the CUT contains information of the target ($y[n] = 1$) or not ($y[n] = 0$) by:

$$y[n] = \begin{cases} 1 & , \text{if } x[n] \geq \text{THR}, \\ 0 & , \text{if } x[n] < \text{THR}, \end{cases} \tag{4.4}$$

and storing this value in the corresponding cell of the detector output scan, being in this example:

$$O^{\text{Det}}_{(A_L,R_M)} = y[n]. \tag{4.5}$$

As previously mentioned, the observation vector selected from the radar scan presented in Eq. (4.1) corresponds to a non-delay selection mode. Other selection modes are discussed in the next section. As an example, Fig. 4.2 presents the proposed detection scheme working with a selection mode depending on future cells. In this case, the observation vector is formed of J cells and stored as a column vector:

$$\begin{aligned} \mathbf{z}[n] &= \left[z[n - \tfrac{J-1}{2}] \quad \dots \quad z[n] \quad \dots \quad z[n + \tfrac{J-1}{2}] \quad \right]^{\text{T}} \\ &= \left[I_{(A_L,R_{M-\frac{J-1}{2}})} \cdots I_{(A_L,R_M)} \cdots I_{(A_L,R_{M+\frac{J-1}{2}})} \right]^{\text{T}} \\ &= \left[z_1[n] \quad \dots \quad z_{\frac{J+1}{2}}[n] \dots \quad z_J[n] \quad \right]^{\text{T}}, \end{aligned} \tag{4.6}$$

where the CUT in placed in the cell (A_L, R_M) and in the middle of $\mathbf{z}[n]$, involving that J must be an odd number. The signal processing carried out the detection scheme is the same as the indicated in Eq. (4.2)-(4.5). As observed in Eq. (4.6), the system is non-causal because it depends

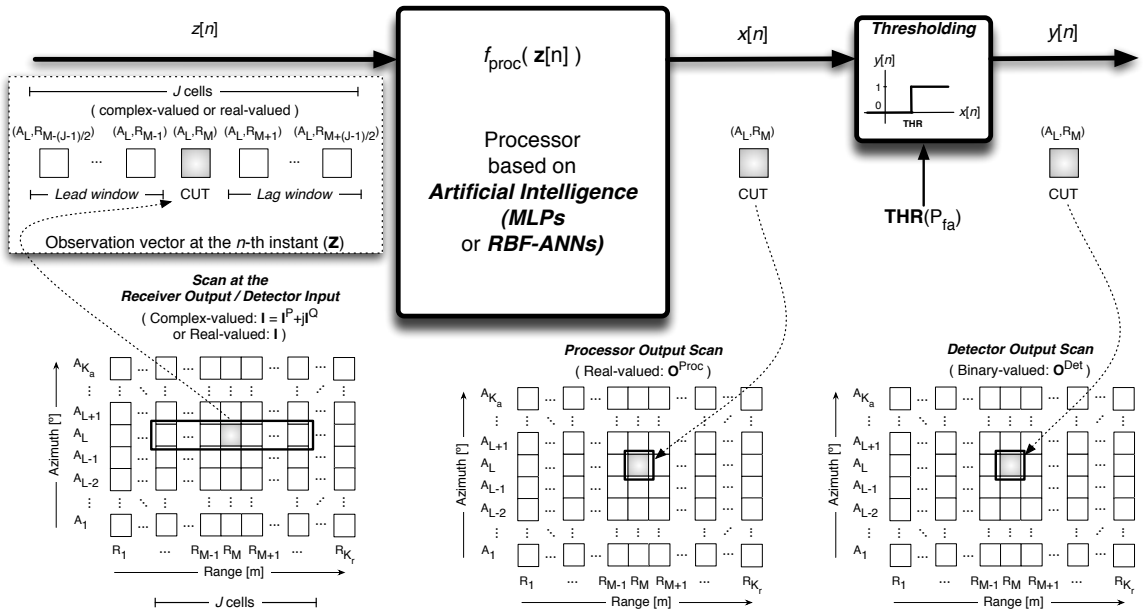

Figure 4.2: Proposed detection scheme based on AI techniques when 1-D and 2-D (delayed) selection modes are used

on future cells, but it can be converted into a casual one applying, in this case, a delay of $\frac{J-1}{2}$ cells. The time delay depends on the selection mode, as discussed in the next section. This delay is the reason why this kind of modes are called *delayed selection modes* in this thesis.

As observed in Fig. 4.1 and 4.2, J cells are integrated in the proposed detection scheme to make the final decision. This kind of integration is similar to the one used in the CFAR detectors presented in Sect. 3.3.2 (see Fig. 3.7). This kind of integration is commonly known as *incoherent integration*. On the other hand, the integration used in the proposed scheme is different to the one used in the TSKAP detector taken as reference in the thesis (see Fig 3.3 of Sect. 3.3.1), that is known as *coherent integration*.

Finally, after observing the proposed detection scheme working with different selection modes, the following questions should be answered to correctly design the proposed detection scheme:

- How must the scheme select the data from the received scan? Fig. 4.1 and 4.2 present two different modes of selecting data considering or not delay in the selection. These and other selection modes are discussed in Sect. 4.2.

- Which is the detection threshold that must be applied in the scheme to achieve a desired P_{fa}? The way this threshold is set is discussed in Sect. 4.3.

- How can the performance of the detectors can be evaluated? The ways to evaluate their performances are presented in Sect. 4.4.

- Finally, observing a real-live radar scan, as the one plotted in Fig. 1.3 (page 5), a problem is observed. The rate between cells under the true (target is present) and alternative (target is absent) hypothesis is unbalanced in favor of the alternative hypothesis. Therefore, since the

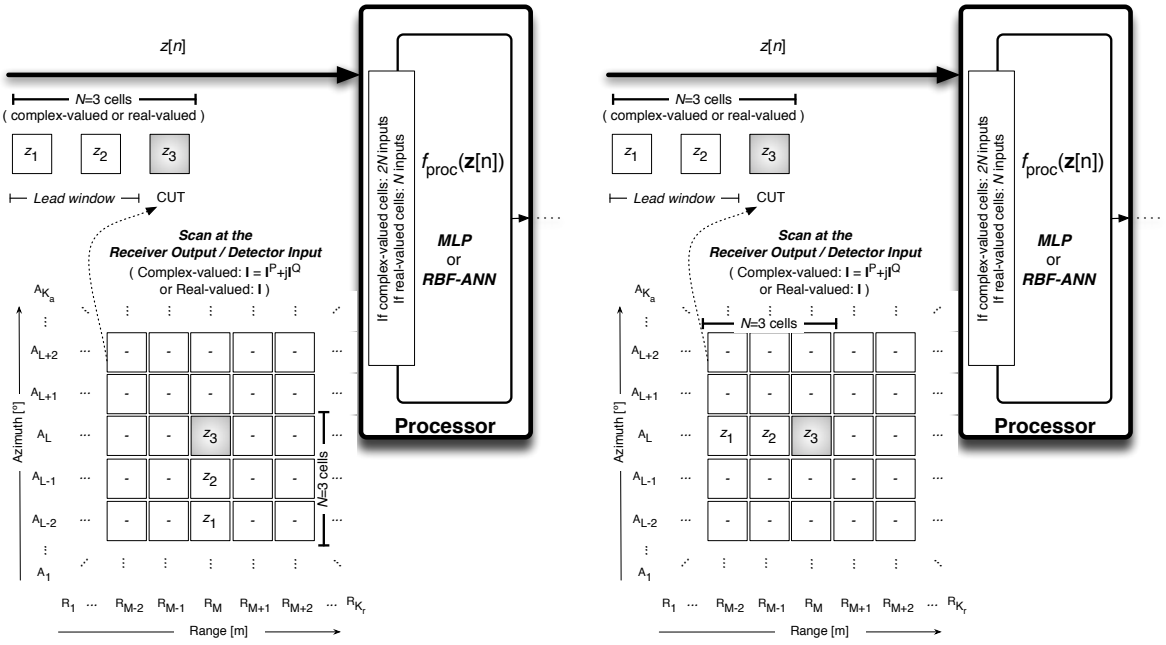

(a) Azimuthal Selection Mode

(b) Range Selection Mode

Figure 4.3: Non-Delayed selection modes considering $N = 3$ cells in the general proposed detection scheme

AI-based techniques used in the processor of the detection scheme are based on supervised learning machines, this unbalance can provoke trainings that take long time and present poor performances. How can this problem be solved? Sect. 4.5 presents a method for selecting the most relevant zones of the scan to be used during the design (train) stage of the processors that compose the detectors.

4.2 Modes of selecting data from radar scans

The way to select the data from radar scans is usually referred in the literature as "sliding window" or "selection mode" [Nathanson1999]. In this thesis, the term "selection mode" is used.

Different selection modes are considered in the literature. Non-delayed selection modes, as discussed in Sect. 4.2.1, are commonly used. As an example, moving target indicators (MTIs) and moving target detectors (MTDs) work using selection modes as in Fig. 4.1 and CFAR detectors work as in Fig. 4.2. Other selection modes not commonly used in the literature are considered in the thesis. Their applicability to radar detection is possible [Nathanson1999], being it the main reason why they are investigated in this thesis. In this sense, delayed 1 dimensional (1-D) and 2 dimensional (2-D) selection modes are considered in the design of the proposed detector. Both selection modes are discussed in Sect. 4.2.2 and 4.2.3, respectively.

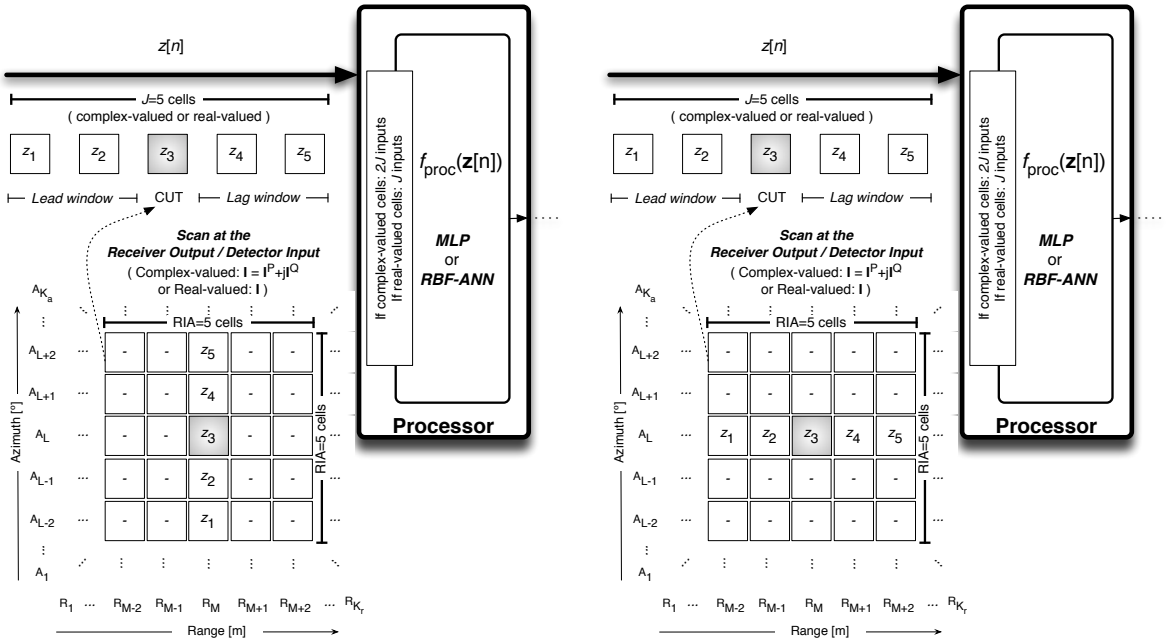

(a) Vertical (V) Selection Mode ($J = 5$ cells)

(b) Horizontal (H) Selection Mode ($J = 5$ cells)

Figure 4.4: Delayed 1-D selection modes considering RIA = 5 cells in the general proposed detection scheme

4.2.1 Non-delayed (ND) selection modes

Coherent detection schemes, as the one taken as reference in this thesis, i.e. the TSKAP detector (see Sect. 3.3.1), usually use the azimuthal orientation to select the CUT and the previous cells from a radar scan [Farina1987a, Farina1987b]. Non-coherent detection techniques, such as MTIs, also use this kind of modes after applying the envelope detector and filtering. Among others, this selection mode will be investigated in the detection scheme proposed in this thesis. An example of how the azimuthal selection mode is applied in the proposed detection scheme is depicted in Fig. 4.3a for a selection of $N = 3$ cells. As observed, the CUT and the two previous cells are obtained from the same range bin but for different range sweeps, i.e. pointing (azimuthal) directions.

Although the range selection mode is not commonly used in detectors based on coherent clutter reduction filters, as in the TSKAP detector, it is usually used in CFAR detectors. In consequence, this mode is also considered in the proposed detection scheme in this thesis. In this case, the CUT and the $N - 1$ previous cells are selected from consecutive range bins in a range sweep, i.e. for the same pointing (azimuthal) direction. Because of the way of generating the synthetic radar scans in the thesis (see Sect. 2.3.1), in this case, the detector performance is studied when no correlation between consecutive cells is supposed. An example of how this selection mode is applied in the proposed scheme is depicted in Fig. 4.3b for $N = 3$ cells.

4.2.2 Delayed 1-D selection modes

Incoherent detection schemes, as the ones taken as reference in this thesis, i.e. the CFAR detectors (see Sect. 3.3.2), usually consider a range orientation to select the CUT and its previous (lead window) and posterior (lag window) cells from a radar scan [Rholing1987, Hammoudi2004, Mashade2008]. In this case, the cells are selected considering consecutive range bins in a range sweep, i.e. for the same azimuthal direction. This mode is called horizontal (H) selection mode in the thesis. An example of how it is applied in the proposed detection scheme is depicted in Fig. 4.4b, where $J = 5$ cells are selected considering that the CUT is placed in the position (A_L, R_M).

On the other hand, the application of a selection mode in a vertical way could be considered in the proposed detection scheme. In this case, the cells are selected for the same range bin and consecutive azimuthal directions of consecutive range sweeps. This mode is called vertical (V) selection mode in the thesis. Similar to the H selection mode, an example of how it is applied in the proposed detection scheme is depicted in Fig. 4.4a, where $J = 5$ cells are also selected.

As observed, J is always an odd number in both H and V selection modes. It is due to the CUT must be in the middle of the observation vector, $\mathbf{z}[n]$, because a symmetrical selection of the surrounding data is considered. Moreover, J is equal to a variable called range of integrated area (RIA) in both modes, i.e.

$$\begin{aligned} J^{\mathrm{H}} &= \mathrm{RIA}\,, \\ J^{\mathrm{V}} &= \mathrm{RIA}\,. \end{aligned} \tag{4.7}$$

The term RIA is considered in this thesis as a parameter of study in the proposed detector scheme. It is explained with more detail in the next section, where 2-D selection modes are explained.

Finally, it is important to analyze the time delay applied in these selection modes to make the system causal. Depending on the selection mode, two different kind of delays are applied:

- If an H selection mode is considered, the delay is related to the time between consecutive range cells from the same range sweep. In this case, this time is related to the duration of the transmitted pulse (pulse width: τ), i.e.

$$t_{\mathrm{d}}^{\mathrm{Ran}} = \tau\,. \tag{4.8}$$

  This time is inversely proportional to the bandwidth of the transmitted pulse. Therefore, for an H selection mode using RIA cells, where $\frac{\mathrm{RIA}-1}{2}$ cells form the lag window (future cells), the time delay is

$$t_{\mathrm{d}}^{\mathrm{H}} = \tfrac{\mathrm{RIA}-1}{2} \cdot t_{\mathrm{d}}^{\mathrm{Ran}} = \tfrac{\mathrm{RIA}-1}{2} \cdot \tau\,. \tag{4.9}$$

- If a V selection mode is considered, the delay is related to the time elapsed between two consecutive range cells from different range sweeps (different azimuthal directions) in the same range bin. In this case, the time delay from one cell to the next one is related to the pulse repetition period, i.e. the inverse of the PRF:

$$t_{\mathrm{d}}^{\mathrm{Az}} = \tfrac{1}{\mathrm{PRF}}\,. \tag{4.10}$$

So, for a V selection mode using RIA cells, where $\frac{\text{RIA}-1}{2}$ cells form the lag window (future cells), the time delay is

$$t_{\text{d}}^{\text{V}} = \frac{\text{RIA}-1}{2} \cdot t_{\text{d}}^{\text{Az}} = \frac{\text{RIA}-1}{2} \cdot \frac{1}{\text{PRF}} \,. \tag{4.11}$$

4.2.3 Delayed 2-D selection modes

Not only 1-D (azimuthal/vertical or range/horizontal) selection modes can be considered for selecting the data from a radar scan, but also a combination of them could be used. In [Nathanson1999], [Dimitrijevic2001] and [Magaz2008], the use of 2-D selection modes were considered for radar detection purposes. For this reason, they are investigated in this thesis.

Before presenting the different 2-D selection modes considered in the thesis, it is important to define what the term RIA involves. This term denotes the length (number of cells) of a side of a squared zone centered in the CUT. In this squared zone, a maximum of RIA $\times$ RIA cells can be selected to be processed by the proposed detection scheme.

Fig. 4.5 shows the way the different delayed 2-D selection modes extract the cells from a scan for a given CUT placed in the position (A_L, R_M). Depending on the 2-D selection mode, the number of selected cells (J), or detection scheme inputs, is related to the RIA in the following way:

1. For the plus-shape (P) selection mode, which can be considered as a combination of H and V selection modes at the same time, this relationship is given by

$$J^{\text{P}} = 2 \times \text{RIA} - 1 \,. \tag{4.12}$$

2. For the cross-shape (X) selection mode, this relationship is given by

$$J^{\text{X}} = 2 \times \text{RIA} - 1 \,, \tag{4.13}$$

being the same as the one given in Eq. (4.12) for the P selection mode.

3. For the rhombus (R) selection mode, this relationship is given by [Gray2003]

$$J^{\text{R}} = (\text{RIA} - 1) \times \left(\tfrac{\text{RIA}-1}{2} + 1\right) + 1 \,, \tag{4.14}$$

being this mode related to the Von Neumann neighborhood used in computer science.

4. For the square (S) selection mode, this relationship is given by [Gray2003]

$$J^{\text{S}} = \text{RIA} \times \text{RIA} \,, \tag{4.15}$$

being this mode related to the Moore neighborhood used in computer science. In this case, all the cells of the squared zone are selected.

The delay time that must be applied when these selection modes are used depends on both the range and azimuthal delay times given in Eq. (4.8) and (4.10), respectively. Depending on the selection mode, the following delay times (t_{d}) must be applied to make the system causal:

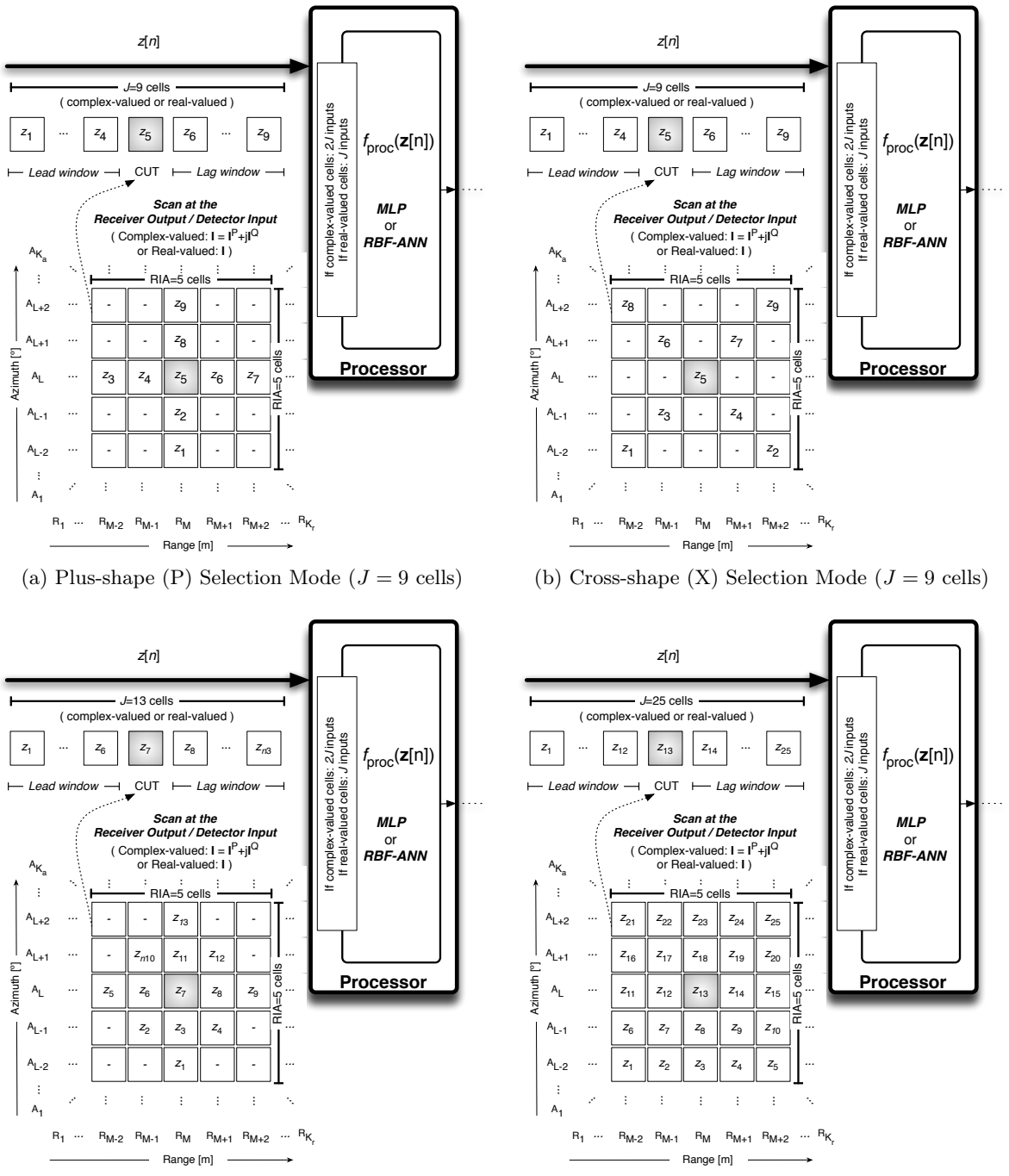

(a) Plus-shape (P) Selection Mode ($J = 9$ cells)

(b) Cross-shape (X) Selection Mode ($J = 9$ cells)

(c) Rombus (R) Selection Mode ($J = 13$ cells)

(d) Square (S) Selection Mode ($J = 25$ cells)

Figure 4.5: Delayed 2-D selection modes considering RIA = 5 cells in the general proposed detection scheme

1. For the plus-shape (P) selection mode, the detector must wait for $\frac{\text{RIA}-1}{2}$ cells to receive the cell with the same azimuthal direction as the CUT but from the last range sweep inside

the squared zone of selection. Its delay time is:

$$t_{\mathrm{d}}^{\mathrm{P}} = \frac{\mathrm{RIA}-1}{2} \cdot t_{\mathrm{d}}^{\mathrm{Az}} = \frac{\mathrm{RIA}-1}{2} \cdot \frac{1}{\mathrm{PRF}} \,. \tag{4.16}$$

For instance, considering the example given in Fig. 4.5a for RIA = 5 cells, the delay time to apply in this case is $t_{\mathrm{d}}^{\mathrm{P}} = 2 \cdot \frac{1}{\mathrm{PRF}}$. This delay corresponds to the time elapsed between the reception of the CUT (x_5) and the last cell that compose the observation vector (x_9).

2. For the cross-shape (X) selection mode, the detector must wait for $\frac{\mathrm{RIA}-1}{2}$ cells to receive the last cell with the same azimuthal direction as the CUT from the last range sweep and $\frac{\mathrm{RIA}-1}{2}$ cells to receive the cell of the last range bin of this range sweep Its delay time is:

$$t_{\mathrm{d}}^{\mathrm{X}} = \frac{\mathrm{RIA}-1}{2} \cdot t_{\mathrm{d}}^{\mathrm{Az}} + \frac{\mathrm{RIA}-1}{2} \cdot t_{\mathrm{d}}^{\mathrm{Ran}} = \frac{\mathrm{RIA}-1}{2} \cdot \left(\frac{1}{\mathrm{PRF}} + \tau\right) \,. \tag{4.17}$$

For instance, considering the example given in Fig. 4.5b for RIA = 5 cells, the delay time to apply in this case is $t_{\mathrm{d}}^{\mathrm{X}} = 2 \cdot \left(\frac{1}{\mathrm{PRF}} + \tau\right)$. This delay corresponds to the time elapsed between the reception of the CUT (x_5) and the last cell that compose the observation vector (x_9).

3. For the rhombus (R) selection mode, because the last cell to receive is the same as in the P selection mode, the delay times are equal in both modes, being:

$$t_{\mathrm{d}}^{\mathrm{R}} = \frac{\mathrm{RIA}-1}{2} \cdot t_{\mathrm{d}}^{\mathrm{Az}} = \frac{\mathrm{RIA}-1}{2} \cdot \frac{1}{\mathrm{PRF}} \,. \tag{4.18}$$

For instance, considering the example given in Fig. 4.5c for RIA = 5 cells, the delay time to apply in this case is $t_{\mathrm{d}}^{\mathrm{R}} = 2 \cdot \frac{1}{\mathrm{PRF}}$, being the same as in the P mode example.

4. For the square (S) selection mode, because the last cell to receive in this mode is the same as the one in the X selection mode, the delay times are equal in both modes, being:

$$t_{\mathrm{d}}^{\mathrm{S}} = \frac{\mathrm{RIA}-1}{2} \cdot t_{\mathrm{d}}^{\mathrm{Az}} + \frac{\mathrm{RIA}-1}{2} \cdot t_{\mathrm{d}}^{\mathrm{Ran}} = \frac{\mathrm{RIA}-1}{2} \cdot \left(\frac{1}{\mathrm{PRF}} + \tau\right) \,. \tag{4.19}$$

For instance, considering the example given in Fig. 4.5d for RIA = 5 cells, the delay time to apply in this case is $t_{\mathrm{d}}^{\mathrm{S}} = 2 \cdot \left(\frac{1}{\mathrm{PRF}} + \tau\right)$, being the same as in the X mode example.

4.3 Detection threshold setting

The value of the detection threshold, THR, in the proposed detection scheme is adjusted in the design stage of the detectors for a given P_{fa} [Neyman1933]. Since the core (processor) of the proposed detection scheme is based on different AI techniques and considers different selection modes, the output of each processor achieved for a given observation vector is usually different. It involves that different detection thresholds must be set in each detector for approximating the same P_{fa}. To analytically determine the desired threshold for a given P_{fa}, the pdf of the system output under H_0 must be known. In the case of study of the thesis, it is not possible to determine this pdf. So, numerical techniques, as the Monte Carlo simulation [Coates1988], are used to estimate the P_{fa} and P_{d} for a given threshold, as discussed in Sect. 4.4.2. For these estimations, a set of pre-classified scans is required, where the desired detector output scans are needed.

Among others, two methods can be applied to find the detection threshold that approximates the desired P_{fa} in the design stage:

1. In the first method, several hundreds of thresholds are used and their corresponding P_{fa}'s are estimated by Monte Carlo simulation. In this case, the value of P_{fa} that best approximates the desired one is selected, and consequently its corresponding threshold. This method presents two problems:

   - the desired P_{fa} is sometimes not exactly achieved; and
   - the time to compute all the P_{fa}'s for all the thresholds is huge.

2. In the second method, an iterative algorithm is applied to find the desired threshold. In this algorithm, if the P_{fa} achieved for the current threshold is greater than the desired P_{fa}, the threshold is increased to reduce the P_{fa}, and vice versa. The threshold is increased or decreased according to a step that is decreasing when the achieved P_{fa} is closed to the desired P_{fa}. The threshold is initialized in the half of the dynamic range of the processor output. The threshold increase/decrease step is initialized to the 10% of the dynamic range of the processor output. This threshold setting method presents two advantages with respect to the previous one:

   - it is faster finding the desired threshold; and
   - it finds the threshold associated to the desired P_{fa} with more accuracy.

Because of the accuracy and time saving achieved by the second method, this iterative method is used in the experiments developed in the thesis.

4.4 Objective evaluation of the detector performance

By now, the general concepts for designing the proposed detection scheme have been discussed. In this section, the way of evaluating the performance of the proposed and reference detectors is discussed. The quality of the results can be evaluated by visual comparison of the input and output radar scans. Nevertheless, this visual analysis involves a subjective interpretation of the results. In this sense, an objective evaluation of the detector performance is needed to avoid any type of subjective interpretation. This objective evaluation is made in the thesis by the estimation of two main parameters: the improvement of the SCR achieved by the processor embedded in the detector; and the performance of the detector in terms of P_{fa} and P_{d} for different detection thresholds, obtaining an estimation of the receiver operating characteristics (ROC) curve.

4.4.1 Average Signal-to-clutter ratio (SCR) improvement

The objective measurements of the performance concerning to the processor of the detectors are described below for a given radar scan and for a set of them.

The objective estimations of the processor performance for a given radar scan are:

- Consider the target and clutter powers at the processor input, P_{t}^{in} (dBm) and P_{c}^{in} (dBm), and output, $P_{\text{t}}^{\text{out}}$ (dBm) and $P_{\text{c}}^{\text{out}}$ (dBm). The estimations of the target and clutter powers are done considering the CUTs where target is present and absent, respectively. Then, the

target and clutter power improvements (dB) achieved by the processor for the l-th radar scan are

$$\mathrm{P}_{\mathrm{t},l}^{\mathrm{imp.}} = P_{\mathrm{t},l}^{\mathrm{out}} - P_{\mathrm{t},l}^{\mathrm{in}}\,, \tag{4.20}$$

$$\mathrm{P}_{\mathrm{c},l}^{\mathrm{imp.}} = P_{\mathrm{c},l}^{\mathrm{out}} - P_{\mathrm{c},l}^{\mathrm{in}}\,. \tag{4.21}$$

- The Signal-to-Clutter Ratio improvement (dB) for the l-th radar scan is obtained as:

$$\begin{aligned}\mathrm{SCR}_{l}^{\mathrm{imp.}} &= \mathrm{SCR}_{l}^{\mathrm{out}} - \mathrm{SCR}_{l}^{\mathrm{in}} \\ &= \left[P_{\mathrm{t},l}^{\mathrm{out}} - P_{\mathrm{c},l}^{\mathrm{out}}\right] - \left[P_{\mathrm{t},l}^{\mathrm{in}} - P_{\mathrm{c},l}^{\mathrm{in}}\right]\,.\end{aligned} \tag{4.22}$$

Applying Eq. (4.20) and (4.21) in Eq. (4.22), it is obtained:

$$\mathrm{SCR}_{l}^{\mathrm{imp.}} = \mathrm{P}_{\mathrm{t},l}^{\mathrm{imp.}} - \mathrm{P}_{\mathrm{c},l}^{\mathrm{imp.}}\,. \tag{4.23}$$

The objective estimations of the processor performance for a given set of M radar scans are:

- The average P_{t} (dB) and P_{c} (dB) improvements:

$$P_{\mathrm{t}}^{\mathrm{av.imp.}} = \frac{1}{M}\sum_{l=1}^{M}\mathrm{P}_{\mathrm{t},l}^{\mathrm{imp.}}\,, \tag{4.24}$$

$$P_{\mathrm{c}}^{\mathrm{av.imp.}} = \frac{1}{M}\sum_{l=1}^{M}\mathrm{P}_{\mathrm{c},l}^{\mathrm{imp.}}\,. \tag{4.25}$$

- The average SCR improvement (dB):

$$\mathrm{SCR}^{\mathrm{av.imp.}} = \frac{1}{M}\sum_{l=1}^{M}\mathrm{SCR}_{l}^{\mathrm{imp.}}\,. \tag{4.26}$$

4.4.2 Receiver operating characteristics (ROC) curves: P_{fa} and P_{d} estimations

A ROC curve gives information of the performance of a detector in terms of P_{fa} and P_{d}. In this sense, a ROC curve is composed of pairs of points P_{fa}-P_{d}, being each one obtained for different detection thresholds, THRs. The ROC curve is the element used to compare different detectors.

The design of a detector requires setting the threshold, THR, for a desired P_{fa} [Neyman1933]. This threshold can be set following the procedure presented in Sect. 4.3. Thereafter, the P_{d} is evaluated for this threshold. To analytically determine the desired threshold for a given P_{fa}, the pdf of the system output under H_0 must be known. To analytically determine the P_{d} for this threshold, the pdf of the system output under H_1 must be known. Both pdf's are usually difficult to determine, especially if some parameters of the clutter change in time, as occurred in the case of study of this thesis. Moreover, the discriminant function achieved for the detector (division of the pdf's under H_1 and H_0) should be known. When the pdf's or the discriminant function are unknown, numerical techniques, such as the Monte Carlo simulation [Coates1988],

are used to estimate the P_{fa} and P_{d} for a given threshold. To make these estimations, a set of pre-classified scans is required. Since these probabilities are estimated in both the design and test stages, M_{train} and M_{val} scans for designing and M_{test} scans for testing, and their corresponding desired output scans ($\mathbf{D}$) are used. To be as general as possible, suppose that these estimations are done for M input scans ($\mathbf{I}(l)$, $l = 1, 2 \dots M$) and their corresponding M desired output scans ($\mathbf{D}(l)$, $l = 1, 2 \dots M$). Once the M scans at the output of a processor of Fig. 4.1-4.5 ($\mathbf{O}^{\text{Proc}}(l)$, $l = 1, 2 \dots M$) are obtained, the estimations of the P_{fa} and P_{d} for a given threshold THR are obtained as:

$$P_{\text{fa}} = \sum_{l=1}^{M} \sum_{r=1}^{K_{\text{a}}} \sum_{c=1}^{K_{\text{r}}} \frac{(O_{r,c}^{\text{Proc}}(l) > \text{THR}) \& (D_{r,c}(l) == 0)}{\text{Num. Observations Under } H_0}, \tag{4.27}$$

$$P_{\text{d}} = \sum_{l=1}^{M} \sum_{r=1}^{K_{\text{a}}} \sum_{c=1}^{K_{\text{r}}} \frac{(O_{r,c}^{\text{Proc}}(l) > \text{THR}) \& (D_{r,c}(l) == 1)}{\text{Num. Observations Under } H_1}, \tag{4.28}$$

where r and c are the row and column indexes, respectively, of each CUT in $\mathbf{O}^{\text{Proc}}$ and $\mathbf{D}$.

The number of observation vectors, and consequently the number of radar scans, used to estimate the P_{fa} and P_{d} conditions the accuracy of these estimations. In this way, the dimensioning of the synthetic databases of radar scans used in the experiments of the thesis are conditioned to this constraint (estimation accuracy). This dimensioning is described in more detail in Chap. 7, exactly in Sect. 7.1.1 (page 107). On the other hand, if a set of radar scans is given, such as the case of study of having real-live sea clutter measurements, the number of radar scans, and consequently the number of observation vectors, limits the accuracy of the estimates. This accuracy is also studied in Chap. 7, exactly in Sect. 7.2 (page 117). With this analysis, we can realize where the limits of the estimations are.

In this thesis, standard Monte Carlo techniques are used to get the estimations of the probabilities. But other ways of evaluating the P_{fa} and P_{d} of a detector can also be used. As an example, the use of modified Monte Carlo techniques, such as importance sampling techniques, could be considered for this purpose [Srinivasan2002]. These techniques allow estimating these probabilities with much less radar scans than the standard Monte Carlo method maintaining the same accuracy for the estimations.

4.5 Selection of radar data for designing (training) AI-based detectors

An important issue during the design of the learning machines is related to how many and what kind of data are used in the training of this machines. Four important aspects must be taken into account for that purpose:

1. Since supervised learning methods are used, a learning machine needs sufficient training data to produce high and accurate performances.

2. Since the best number of machine inputs (J) is not known for each selection mode, a lot of information is needed during the training of the machine to consider the situation where a large number of inputs are used. A limitation of J can be set if operational parameters

are established for a given radar. In our case of study, no limitation is considered a priori for J.

3. Since the number of cells where target is absent (null hypothesis: H_0) is sometimes much greater than the number of cells where target is present (true hypothesis: H_1) in a radar scan (see Fig. 1.3 in page 5 as an example), the learning machine will tend to give outputs close to 0 (desired output for H_0 cells). So, this aspect should be reduced as much as possible.

4. The learning process is too low when a lot of information is used during training.

Since the quantity of data when working with synthetic radar scans can be controlled, let's focus the problem presented above on situations where real-live radar scans are processed, as the one depicted in Fig. 1.3 (page 5). The quantity of data available ($\approx 38 \cdot 10^6$ cells) in the 128 radar scans contained in each of the training and validation data sets (see Sect. 7.2) is a priori enough to fulfill the first two aspects. But, the last two aspects are converted into problems. To solve these two problems, a selection of the most relevant zones of each scan is carried out to balance the number of cells belonging to H_0 and H_1 hypotheses and increase the training speed. The criteria taken for this selection are based on choosing:

- All the cells that contain information of a ship and some cells surrounding the ship; and
- Several sets of cells near and far the radar site.

In the application of these criteria, and exactly due to the third aspect, an additional constraint is applied to balance the ratio between cells belonging to H_0 and H_1. This constraint establishes that the 10% of the selected cells belongs to H_1 and the remaining 90% of the selected cells to H_0. These rates are selected to find a detection threshold with low estimation error sensibility and to obtain a high performance MLP or RBFN after training. These rates will be discussed in more detail when dimensioning the database of synthetic radar scans used in the thesis (see Sect. 7.1.1). As an example, consider that the radar scan of Fig. 1.3 (page 5) is used for training the learning machines. Fig. 4.6 shows the result of applying these selection criteria. In this case, 714 cells of the radar scan belong to H_1, being all selected. These cells corresponds to the 10% of all the selected cells. The remaining 90% of selected cells, corresponding to 6426 cells in this case, are selected from cells belonging to H_0 in the radar scan. Note that only $714 + 6426 = 7140$ cells of the $1060 \times 256 = 271360$ valid cells of this radar scan ($\approx 2.6\%$ of the total) would be selected for training the learning machine. Since other ship sizes and shapes are also considered in the database of marine radar scans, ≈ 6600 cells/scan are approximately selected in average. In consequence, a total of $128\,\text{scans} \times 6600\,\text{cells/scan} \approx 850000$ cells of the training and validation data sets are used to train MLPs and RBFNs. The quantity of data obtained after this data selection keeps fulfilling the first two aspects, while solving the problems generated in the last two aspects.

Other techniques could be used to reduce the number of observation vectors to be used in the training of ANNs, such as the importance sampling techniques. Some examples of their use in ANN training can be found in [Sanz2001, Sanz2002a, Sanz2002b, Vicen2010d]. Even when these techniques reduce the number of observation vectors to be used in the training and can

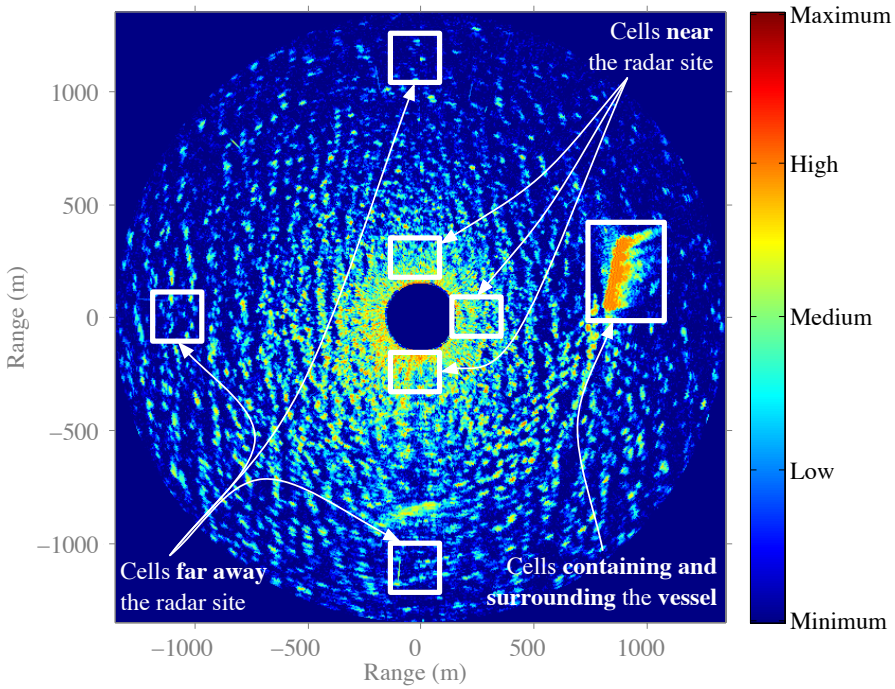

(a) Cartesian plot of range data

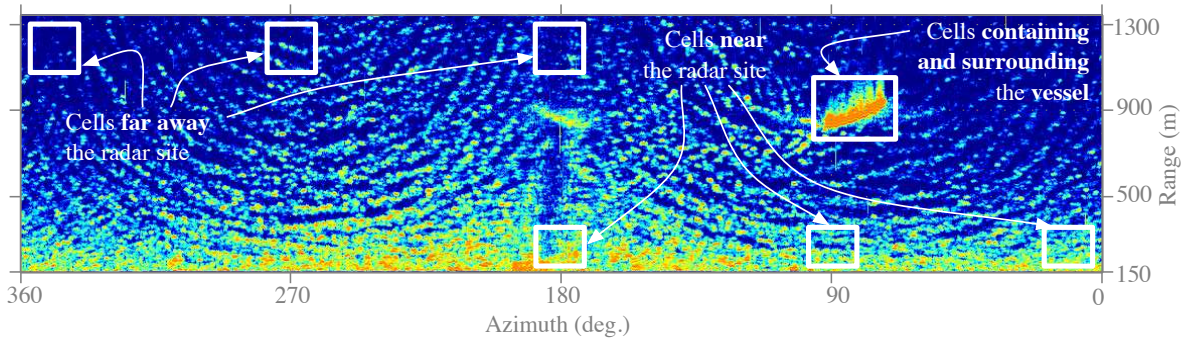

(b) Cartesian plot of polar data

Figure 4.6: Example of selected cells form a radar scan obtained by using the high resolution marine radar configuration of Table 2.8 (scan size: [1060 azimuth cells × 256 range cells]).

improve the performance of the obtained ANN-based detector due to the high accuracy of the estimation of the cost function used for training, they are not considered in the thesis. They are not used because for applying these techniques, the pdf of the clutter must be known, including its statistical parameters (skewness and scale parameters in the case of Weibull-distributed clutter), and in our case of study these parameters vary in time, as will be discussed in Chap. 10 (page 201). These parameters could be estimated to solve this problem, but it will introduce an error in the performance estimation. Therefore inaccurate trainings would be expected.

CHAPTER 5

Detection based on AI: Feed-Forward ANNs (MLPs)

Sect. 4.1 describes how an observation vector extracted from a radar scan is processed by a general processor-based detector, independently whether coherent or incoherent data are considered. Several AI techniques could be used to implement the scheme proposed to detect desired signals in Weibull-distributed clutter and white Gaussian noise. In the current chapter, the detectors presented as example in Fig. 4.1 and 4.2 are considered, where the processor of each scheme is implemented by a feed-forward ANN. In this case, MLPs, a kind of feed-forward ANN, are selected because of their capabilities of learning from a set of pre-classified data and their easy implementation once designed. MLPs are trained in a supervised way, because in this way they are able to approximate to the Neyman-Pearson detector [Jarabo2009]. Moreover, they are trained in a batch mode and with an off-line actualization of their weights [Haykin2009]. The way to obtain the outputs of these MLP-based processors and detectors is described in depth below. The processing of the data presented below can be extrapolated to the other selection modes considered in the thesis, as depicted in Fig. 4.3-4.5.

Consider $\mathbf{z}[n]$ is the observation vector at the n-th instant, being extracted from a radar scan following one of the selection modes presented in Sect. 4.2. In this case, the MLP-based processor output is computed as

$$x[n] = f_{\text{MLP}}(\mathbf{z}[n])\,, \tag{5.1}$$

where $f_{\text{MLP}}(\cdot)$ denotes the non-linear transformation carried out by the MLP.

Once $x[n]$ is obtained, the output of the MLP-based detector is computed by

$$y[n] = \begin{cases} 1 & \text{, if } x[n] \geq \text{THR}_{\text{MLP}}, \\ 0 & \text{, if } x[n] < \text{THR}_{\text{MLP}}, \end{cases} \tag{5.2}$$

where the detection threshold of this detector, THR_{MLP}, is selected to obtain a desired P_{fa} following the procedure presented in Sect. 4.3. This threshold setting is made in the design stage of the MLP-based processor, but once the MLP is trained.

The following sections focus on the application of MLPs in the proposed detection scheme. These sections present:

- What is the selected MLP architecture.

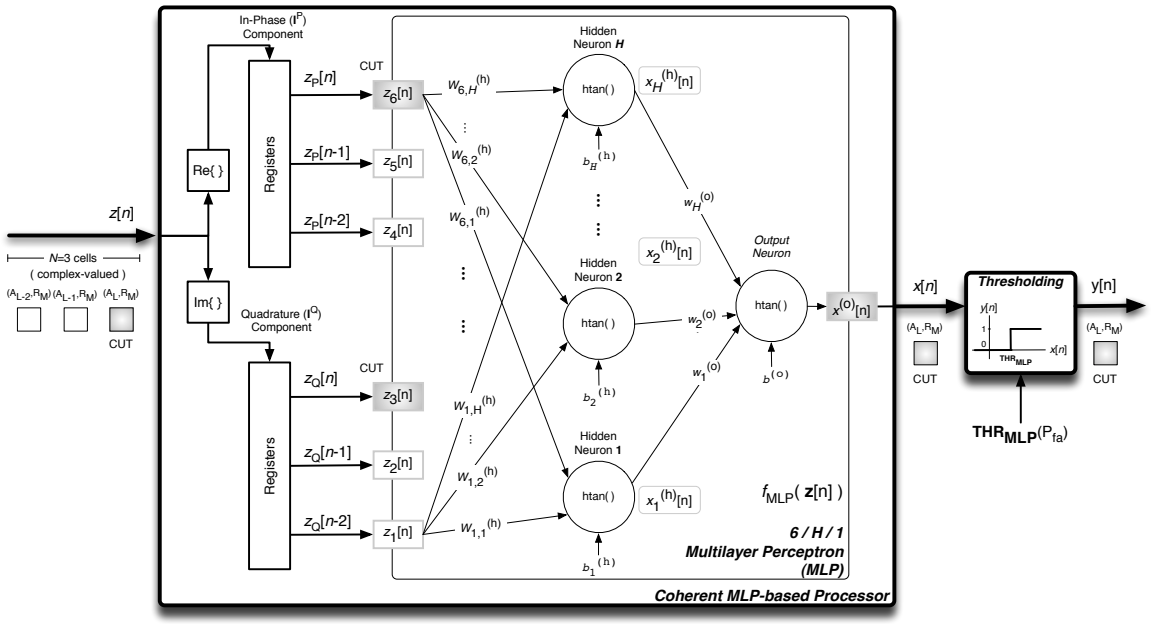

Figure 5.1: MLP-based coherent detector working with a non-delayed (azimuthal) selection mode. In this case, a $2N/H/1$ MLP structure is used, being $N = 3$

- How MLPs are applied in the proposed detection scheme when both coherent and incoherent radar scans are used.
- How MLPs are trained to learn from the data of the radar environment.
- What is the MLP computational cost once trained.

5.1 Coherent MLP-based detection schemes

First, taking the detection scheme of Fig. 4.1 as reference, the proposed detector based on MLPs is presented when non-delayed selection modes and coherent radar scans are used. And second, taking as reference the detection scheme of Fig. 4.2, the implementation of the proposed detector based on MLPs is studied when delayed selection modes are considered with coherent data.

The proposed coherent detector based on MLPs working with a non-delayed selection mode is depicted in Fig. 5.1, where $N = 3$ cells selected by an azimuthal mode are processed. Since coherent data are used and the MLP works with real-arithmetic, the complex-valued observation vector given in Eq. (4.1) is converted into a real-valued one by

$$\begin{aligned}\mathbf{z}[n] &= [z_{\mathrm{Q}}[n-2]\ z_{\mathrm{Q}}[n-1]\ z_{\mathrm{Q}}[n]\ z_{\mathrm{P}}[n-2]\ z_{\mathrm{P}}[n-1]\ z_{\mathrm{P}}[n]]^{\mathrm{T}} \\ &= [z_1[n] \quad z_2[n] \quad z_3[n] \quad z_4[n] \quad z_5[n] \quad z_6[n]\,]^{\mathrm{T}}\ ,\end{aligned} \tag{5.3}$$

splitting the coherent data in its in-phase (z_{P}) and quadrature (z_{Q}) components.

Once the observation vector is composed, the output of the MLP-based processor is obtained. An MLP structure with two layers (an input layer, not computed, a hidden layer and an output layer) are implemented. In [Bishop1995, Haykin2009] it is demonstrated that an MLP with this

number of layers is enough to solve a wide variety of problems. The size of the MLP is defined as $K/H/1$, where K inputs, H hidden neurons in its hidden layer and 1 neuron in its output layer are considered. Since coherent data are processed and real-arithmetic is used in the MLP, the number of MLP inputs is $K = 2N$ in this case. Both K and H are studied in the thesis to determine the best dimensioning of the MLP-based processor that composes the proposed detector. The internal neurons of the MLP can use different kinds of activation functions, such as linear, hard limit ($\psi_{\text{hard}}(\cdot)$), hyperbolic-tangent ($\psi_{\text{htan}}(\cdot)$), log-sigmoid ($\psi_{\text{log-sig}}(\cdot)$), etc. The hyperbolic-tangent and log-sigmoid transfers functions are commonly used in the literature because they are able to improve the performance achieved by the MLP with respect to the other functions in a wide variety of problems [Bishop1995, Haykin2009]. Both transfer functions also allow to improve the learning process because of its non-linear wide output margins [Jarabo2004], $[-1, 1]$ for the hyperbolic-tangent and $[0, 1]$ for the log-sigmoid. Moreover, Jarabo demonstrated in [Jarabo2004] that the use of wider output margins allows to achieve better robustness in the training. Because of that, the hyperbolic-tangent is selected as transfer function in the MLPs used in this thesis.

Once the MLP architecture is selected, the computation of the output of the MLP is described, being computed in two steps. First, the computation of the outputs of the hidden neurons is made. After that, the computation of the output of the output neuron is made. The computation of these steps is presented by using a matrix notation.

The computation of the outputs of the hidden neurons depends on the activation (input) of each hidden neuron. In this case, the activation of the i-th hidden neuron ($v_i^{(\text{h})}[n]\,, i = 1, 2, \ldots H$) is computed as

$$\mathbf{v}^{(\text{h})}[n] = \left[v_1^{(\text{h})}[n] \ \ldots \ v_H^{(\text{h})}[n]\right]^{\text{T}} = \mathbf{W}^{(\text{h})} \cdot \mathbf{z}[n] + \mathbf{b}^{(\text{h})}\,. \tag{5.4}$$

Next, the output of each hidden neuron ($x_i^{(\text{h})}[n]\,, i = 1, 2, \ldots H$) is computed as

$$\mathbf{x}^{(\text{h})}[n] = \psi_{\text{htan}}\left(\mathbf{v}^{(\text{h})}[n]\right)\,, \tag{5.5}$$

$$\mathbf{x}^{(\text{h})}[n] = \left[x_1^{(\text{h})}[n] \ \ldots \ x_H^{(\text{h})}[n]\right]^{\text{T}} = \left[\frac{e^{v_1^{(\text{h})}[n]} - e^{-v_1^{(\text{h})}[n]}}{e^{v_1^{(\text{h})}[n]} + e^{-v_1^{(\text{h})}[n]}} \ \cdots \ \frac{e^{v_H^{(\text{h})}[n]} - e^{-v_H^{(\text{h})}[n]}}{e^{v_H^{(\text{h})}[n]} + e^{-v_H^{(\text{h})}[n]}}\right]^{\text{T}}.$$

After that, the activation of the output neuron is achieved by

$$v^{(\text{o})}[n] = \mathbf{w}^{(\text{o})} \cdot \mathbf{x}^{(\text{h})}[n] + b^{(\text{o})}\,, \tag{5.6}$$

and the output of the MLP is

$$x^{(\text{o})}[n] = \psi_{\text{htan}}\left(v^{(\text{o})}[n]\right)\,, \tag{5.7}$$

$$x[n] = x^{(\text{o})}[n] = \frac{e^{v^{(\text{o})}[n]} - e^{-v^{(\text{o})}[n]}}{e^{v^{(\text{o})}[n]} + e^{-v^{(\text{o})}[n]}}\,.$$

According to the selected MLP structure and size ($K/H/1$), the free parameters (synaptic weights and biases) of the MLP are stored in:

- $\mathbf{W}^{(\text{h})}$: matrix containing the synaptic weights that connect the K inputs with the H neurons of the hidden layer. The j-th row of $\mathbf{W}^{(\text{h})}$ contains the synaptic weights that connect each of the K MLP inputs with the j-th hidden neuron. The size of this matrix is $[H \times K]$.

- $\mathbf{b}^{(\mathrm{h})}$: column vector containing the bias weights of the H hidden neurons. The size of this vector is $[H \times 1]$.

- $\mathbf{w}^{(\mathrm{o})}$: row vector containing the synaptic weights that connect the H hidden neurons with the output neuron. The size of this vector is $[1 \times H]$.

- $b^{(\mathrm{o})}$: variable containing the output bias weight.

Once the output of the MLP-based processor is computed, the output of the detector is achieved by Eq. (5.2). This output is stored in the corresponding cell of the output detector scan, as shown in Fig. 4.1. Finally, the procedure exposed above is repeated for each CUT of the input radar scans.

The coherent detection scheme based on MLPs presented above considered a non-delayed selection mode as example. Next, another coherent detection scheme based on MLPs is presented. In this case, a delayed selection mode is considered. The general detection scheme presented in Fig. 4.2 is taken as reference to create the proposed MLP-based detector. The same selection mode as in this general scheme is selected, i.e. an horizontal selection mode is used. The proposed detection scheme based on MLPs is shown in Fig. 5.2. Thus, considering that J cells are selected to make the final decision (target is present or not), and remembering that the MLP works with real-arithmetic, the following observation vector is achieved at the n-th instant for a given CUT:

$$\begin{aligned}\mathbf{z}[n] &= \left[z_{\mathrm{Q}}[n-\tfrac{J-1}{2}] \ldots z_{\mathrm{Q}}[n] \ \ldots \ z_{\mathrm{Q}}[n+\tfrac{J-1}{2}]\ z_{\mathrm{P}}[n-\tfrac{J-1}{2}] \ldots z_{\mathrm{P}}[n] \ \ \ldots \ \ z_{\mathrm{P}}[n+\tfrac{J-1}{2}]\right]^{\mathrm{T}} \\ &= \left[z_1[n] \quad \ldots \quad z_{\frac{J+1}{2}}[n] \ldots z_J[n] \qquad z_{J+1}[n] \quad \ldots \quad z_{\frac{3J+1}{2}} \ \ldots \ z_{2J}[n] \right]^{\mathrm{T}}.\end{aligned} \tag{5.8}$$

The processing made by the MLP of this vector is the same as the one given in Eq. (5.4)-(5.7). But, in this case, the number of MLP inputs in its structure $(K/H/1)$ is $K = 2J$. The final decision is made by Eq. (5.2), where the detection threshold has a different value of the one achieved in Fig. 5.1 for the same P_{fa}. The decision for the CUT is stored in the corresponding coordinates of the output detector scan. Finally, this procedure is repeated for each CUT of the input radar scans.

5.2 Incoherent MLP-based detection schemes

In this section, two detection approaches based on MLPs working with incoherent radar scans are presented. In the first one, non-delayed selection modes are used. In the second one, delayed selection modes are used.

Taking the general detection scheme given in Fig. 4.1 as reference, where a non-delayed selection mode is used, the incoherent detection scheme based on MLPs is presented in Fig. 5.3. As an example, $N = 3$ cells are selected by using an azimuthal mode in this figure. Since the received data are real-arithmetic and the MLP works with the same kind of arithmetic, a $K/H/1$ MLP structure is used, where $K = N$. These selected real-valued cells compose the observation

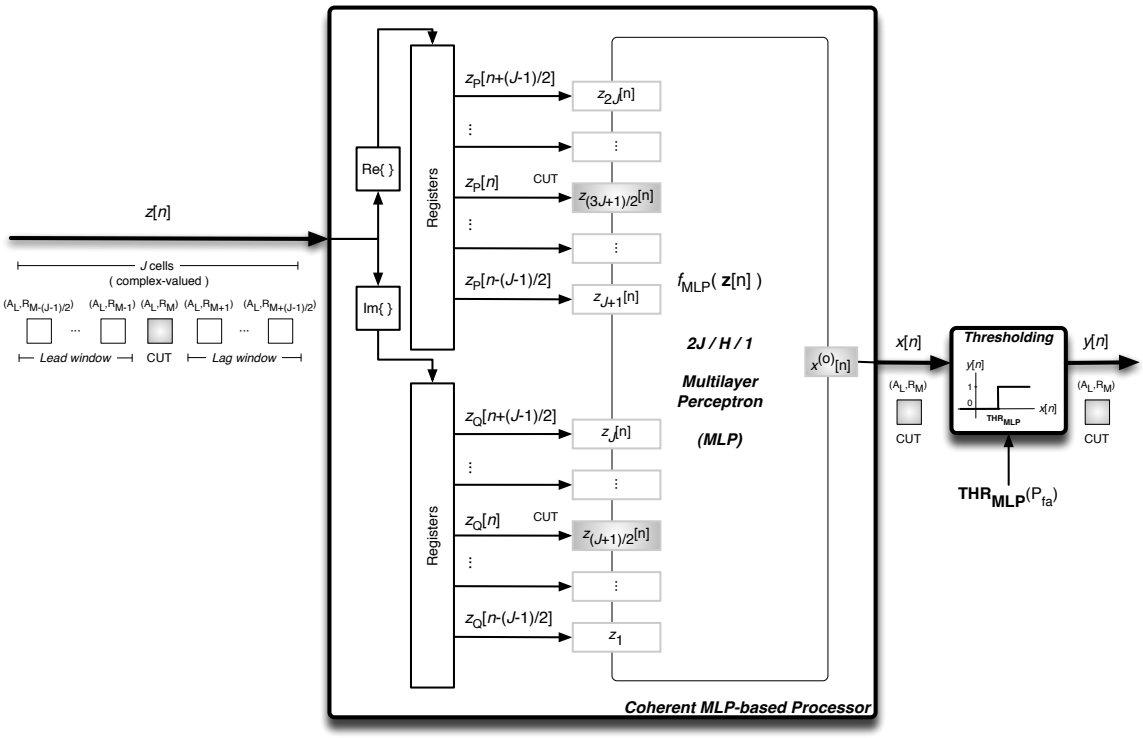

Figure 5.2: MLP-based coherent detector working with a delayed (horizontal/range) selection mode. In this case, a $2J/H/1$ MLP structure is used

vector at the n-th instant:

$$\begin{aligned}\mathbf{z}[n] &= [z[n-2]\ z[n-1]\ z[n]\ ]^{\mathrm{T}} \\ &= [z_1[n] \quad z_2[n] \quad z_3[n]\,]^{\mathrm{T}}\ .\end{aligned} \tag{5.9}$$

The processing of this observation vector made by the MLP is the same as the one given in Eq. (5.4)-(5.7), but having $K = N$ inputs. The final decision is made according to Eq. (5.2), where the detection threshold has a different value of the one achieved in Fig. 5.1 and 5.2 for the same P_{fa}. The decision for the CUT is stored in the corresponding coordinates of the output detector scan. Finally, this process is repeated for each CUT of the input scans.

Taking as reference the general detection scheme given in Fig. 4.2, where an horizontal delayed selection mode is used, the proposed incoherent detection scheme based on MLPs is presented in Fig. 5.4. Since the received data are real-arithmetic and the MLP works with the same kind of arithmetic, a $K/H/1$ MLP structure is used, being $K = J$ cells in this case. These selected real-valued cells compose the observation vector at the n-th instant as:

$$\begin{aligned}\mathbf{z}[n] &= \left[z[n-\tfrac{J-1}{2}]\ \ldots\ z[n] \quad \ldots \quad z[n+\tfrac{J-1}{2}]\ \right]^{\mathrm{T}} \\ &= \left[z_1[n] \quad \ldots \quad z_{\frac{J+1}{2}}[n]\ \ldots\ z_J[n] \quad\right]^{\mathrm{T}}\ .\end{aligned} \tag{5.10}$$

The signal processing made by the MLP for this vector is the same as the one given in Eq. (5.4)-(5.7). But, in this case, the number of MLP inputs is $K = J$. The final decision

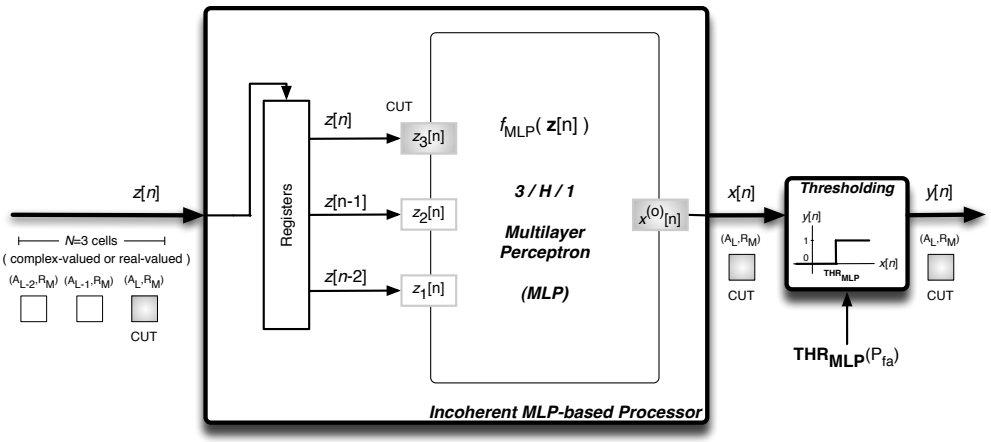

Figure 5.3: MLP-based incoherent detector working with a non-delayed (azimuthal) selection mode. In this case, an $N/H/1$ MLP structure is used, being $N = 3$

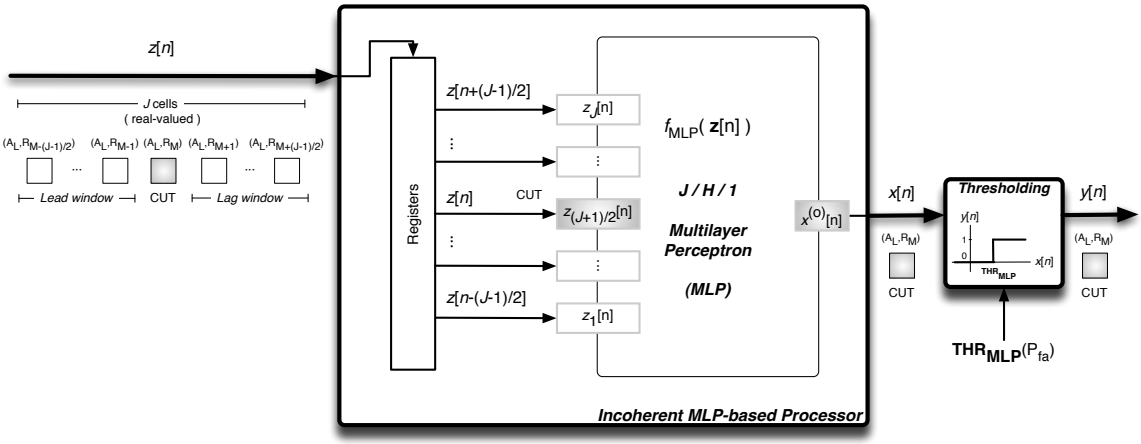

Figure 5.4: MLP-based incoherent detector working with a delayed (horizontal/range) selection mode. In this case, a $J/H/1$ MLP structure is used

is made according to Eq. (5.2), where the detection threshold has a different value of the one achieved in Fig. 5.1-5.3 for the same P_{fa}. The decision for the CUT is stored in the corresponding coordinates of the output detector scan. Finally, this process is repeated for each CUT of the input scans.

5.3 MLP-based detector design: MLP training algorithms

Since supervised learning is used to train the MLP that composes the proposed detection scheme of Fig. 5.1-5.4, a cost function to be minimized must be set. In this case, the *mean squared error* (MSE) is selected as cost function (E_{MS}) [Jarabo2004, Haykin2009]. Other cost functions, such as the sum-of-squares error (SSE) [Bishop1995], are also commonly used in the literature. This cost function (E_{SS}) is very similar to E_{MS}, being related as $E_{\text{MS}} = \frac{1}{P} E_{\text{SS}}$, where P is the number of observation vectors used to estimate these error functions. Due to the only difference

is a multiplication by a constant of $\frac{1}{P}$, minimizing one of these functions, the other is also minimized. Since the MSE cost function has been successfully used to train ANNs approximating the Neyman-Pearson detector for any pair of likelihood functions [Jarabo2009], this cost function is selected in the thesis.

The MSE can be estimated for a training data set composed of $M^{(\mathrm{d})}$ scans and their corresponding desired output scans ($\mathbf{D}$) as the averaged and squared difference between the desired and processed ($\mathbf{O}^{\text{MLP-Proc}}$) output scans, i.e:

$$E_{\mathrm{MS}} = \frac{1}{M^{(\mathrm{d})} K_{\mathrm{a}} K_{\mathrm{r}}} \sum_{l=1}^{M^{(\mathrm{d})}} \sum_{r=1}^{K_{\mathrm{a}}} \sum_{c=1}^{K_{\mathrm{r}}} \frac{\left(o_{r,c}^{\text{MLP-Proc}}(l) - d_{r,c}(l)\right)^2}{2} = \frac{1}{M^{(\mathrm{d})} K_{\mathrm{a}} K_{\mathrm{r}}} E_{\mathrm{SS}} \,. \tag{5.11}$$

From this training data set, a total of $P = M^{(\mathrm{d})}(K_{\mathrm{a}} K_{\mathrm{r}})$ CUTs can be extracted. So, a total of P observation vectors can be used: $\mathbf{z}[n]$, where $n = 1, 2, \ldots, P$. Since the output of the MLP ($x[n]$) can be achieved for each observation vector by Eq. (5.1), Eq. (5.11) can be rewritten as

$$E_{\mathrm{MS}} = \frac{1}{P} \sum_{n=1}^{P} \frac{(x[n] - d[n])^2}{2} = \frac{1}{P} E_{\mathrm{SS}} \,, \tag{5.12}$$

where the desired output is $d[n] = d_{r,c}(l)$, $n = c + (r-1)K_{\mathrm{r}} + (l-1)K_{\mathrm{r}}K_{\mathrm{a}}$. Note that since the output of the MLP is in the range $[-1, 1]$ due to the used hyperbolic-tangent function, and the desired radar scans ($\mathbf{D}$) contain values of 0 (target is absent) or 1 (target is present), the desired output (d) is obtained from the conversion of ranges from $[0, 1]$ to $[-1, 1]$.

The MSE is a way of measuring the performance of the processor. This measurement is constant when the weights and biases of the MLP and the input observation vectors do not change in time. Nevertheless, since the weights and biases of the MLP vary in time, the MSE also varies in time from one iteration ($E_{\mathrm{MS},k}$) to the next one ($E_{\mathrm{MS},k+1}$) during the training of the MLP.

Several training algorithms could be considered to iteratively adjust the MLP weights to minimize the MSE. The commonly used algorithms are based on the conjugate gradient descent [Haykin2009]. This learning algorithm presents low convergence speed. Faster learning algorithms can be applied, such as the Newton, Gauss-Newton or Levenberg-Marquardt algorithms. These algorithms are based on second order optimization techniques [Bishop1995]. Nevertheless, they require more computational cost than gradient descent algorithms, as discussed below. In the Newton algorithm, the Hessian matrix is estimated by the approximation of second order derivatives. Gauss-Newton algorithms use recursive expressions that iteratively approximate the inverse of the Hessian matrix. The Levenberg-Marquardt algorithm is a special case of Gauss-Newton algorithms. This algorithm is only applicable to cost functions of the type MSE or SSE, from which the Hessian matrix can be approximated by Jacobian matrixes, where first order derivatives are computed. These last two algorithms reduce the computational cost and increase the speed of convergence with respect to the Newton algorithm [Bishop1995].

The second order optimization techniques presented above also allow to obtain high success rates finding the global minima, especially for low MLP sizes. Nevertheless, they need a huge number of observation vectors to estimate the Hessian or Jacobian matrixes with a minimum accuracy [Bishop1995]. Moreover, it is important to note that this training is effective in terms of computational cost if low-size MLPs are used. Considering that the MLP is formed of $F =$

$KH + H + H + 1$ weights, the sizes of the estimated Hessian and Jacobian matrixes are $[F \times F]$ and $[P \times F]$, respectively. Therefore, if F increases linearly, the computational cost needed in each algorithm iteration increases exponentially. Since the best MLP size is not known a priori, and according to the limitations and advantages of the above analyzed training algorithms:

- MLPs of huge and medium sizes ($F \geq 200$ weights) are trained by a gradient descent algorithm, such as the error *back-propagation* algorithm with variable learning rate and momentum [Haykin2009, Vicen2009a]. The application of this algorithm to train MLPs is presented in Sect. 5.3.1 following a similar nomenclature as previously.

- MLPs of low size ($F < 200$ weights) are trained by the Levenberg-Marquardt algorithm. The application of this algorithm to train MLPs is presented in Sect. 5.3.2 following a similar nomenclature as previously.

Note that the value of 200 weights is an empirically value found during the experiments done in this thesis.

Apart of the MLP structure (size) and the correct dimensioning of the training data set, the training of the MLP rises as another important topic in the design stage of an MLP-based processor. This process usually presents two problems: the training is sometimes not correctly done; and the trained MLP does not always allow to achieve the best solution when other data set is processed. To solve the first problem, the training process is repeated 10 times, where the MLP weights are initialized each trial by using the Nguyen-Widrow algorithm [Nguyen1990]. Whereas to solve the second problem, a new data set of $M^{(v)}$ radar scans is used in an external validation process done during the training. This validation process allows to stop the training process before the MLP is specializing in (memorizing) the training data set, improving the generalization capabilities of the MLP once trained to work with other radar scans different of the training ones. Moreover, considering the overall behavior of the MLP working as detector (the detection threshold, THR, is calculated for a given P_{fa}), once the 10 MLPs are trained, the THR is calculated for each MLP-based detector to obtain a given P_{fa}. Once the 10 MLP-based detectors are obtained (10 MLPs are trained and 10 THRs are calculated), the best one is selected. This selection is made according to the best P_{d} for a given P_{fa} (e.g. $P_{\text{fa}} = 10^{-4}$) achieved by each MLP-based detector.

But, why 10 trials of MLP training and threshold setting are used? Why not using more or less trials? The reasons can be extracted from the results plotted in Fig. 5.5. This figure plots the performance obtained by MLP-based detectors when working in synthetic coherent sea clutter conditions (as done in Sect. 8.2), using 50/10/1 MLPs and a square selection mode, when different number of trials are used. These performances (P_{d} for $P_{\text{fa}} = 10^{-4}$) are obtained in the design stage, using the radar scans of the validation data set. From these plots, it is observed that if less than 10 trials are made (see Fig. 5.5a), the maximum performance is not guaranteed. On the other hand, if more than 10 trials are made (see Fig. 5.5c and 5.5d), not only low performance improvement is achieved, but also the computational cost to make all these trials increases, being 2 and 5 times greater than when making 10 trials, respectively. Therefore, 10 trials of MLP training and threshold setting are selected.

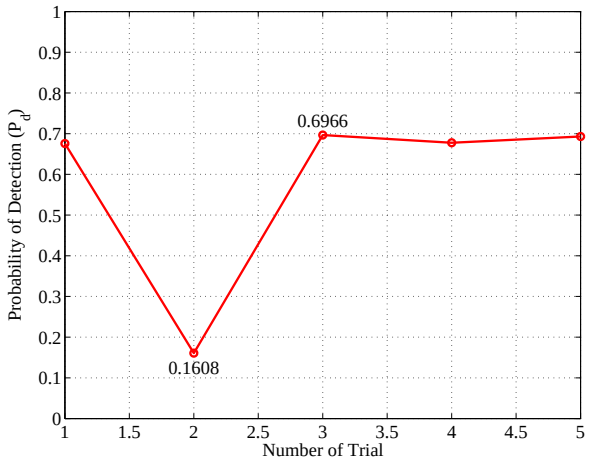

(a) 5 "MLP training - threshold setting" trials

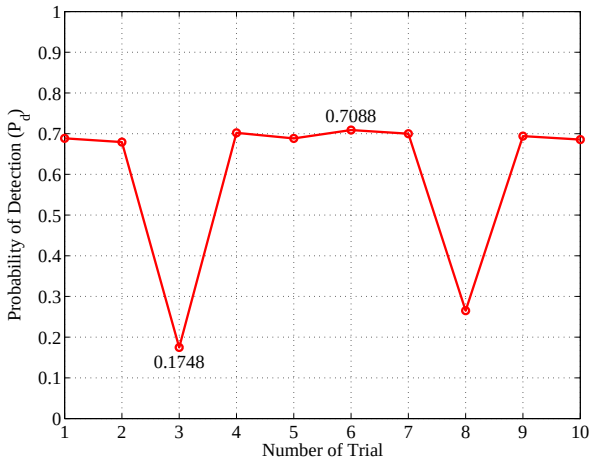

(b) 10 "MLP training - threshold setting" trials

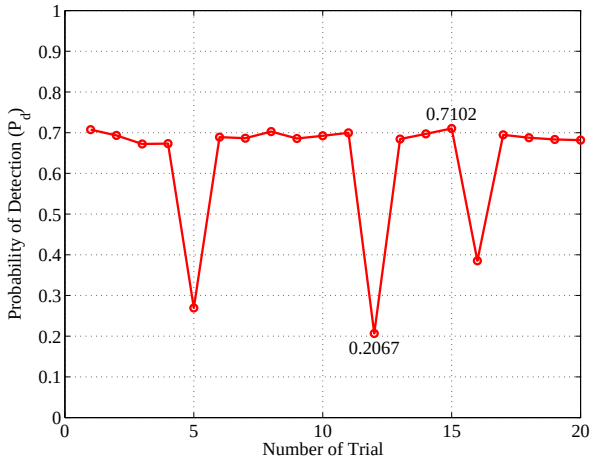

(c) 20 "MLP training - threshold setting" trials

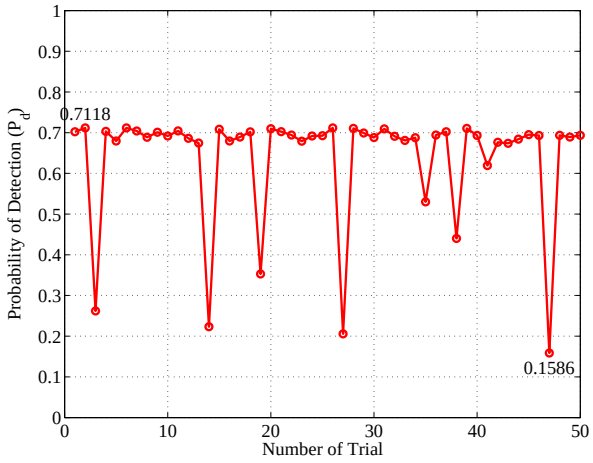

(d) 50 "MLP training - threshold setting" trials

Figure 5.5: Influence of the number of "MLP training - threshold setting" trials in the achieved MLP-based detector performance (P_{d} for $P_{\mathrm{fa}} = 10^{-4}$).

5.3.1 Training algorithm for huge and medium-size MLPs: Error backpropagation with adaptive learning rate and momentum

The error *back-propagation* algorithm [Haykin2009] with variable learning rate (α_k) and momentum (μ) updates for the next iteration, $k+1$, the MLP synaptic weights that connect the inputs with the hidden neurons ($\mathbf{W}_k^{(\mathrm{h})}$) and those that connect the hidden neurons with the output neuron ($\mathbf{w}_k^{(\mathrm{o})}$) in the current iteration, k. The weights update is made considering all the observation vectors ($\mathbf{z}[n], n = 1, 2 \ldots P$) and following Eq. (5.13) and (5.14), respectively.

$$w_{i,j,k+1}^{(\mathrm{h})} = w_{i,j,k}^{(\mathrm{h})} - \alpha_k \cdot \frac{1}{P} \cdot \sum_{n=1}^{P} \left(\delta_{i,k}^{(\mathrm{h})}[n] \cdot z_j[n] \right) + \mu \cdot w_{i,j,k-1}^{(\mathrm{h})}, \begin{cases} i = 1, 2, \ldots, H \\ j = 1, 2, \ldots, K \end{cases} \tag{5.13}$$

$$w_{i,k+1}^{(\mathrm{o})} = w_{i,k}^{(\mathrm{o})} - \alpha_k \cdot \frac{1}{P} \cdot \sum_{n=1}^{P} \left(\delta_k^{(\mathrm{o})}[n] \cdot x_{i,k}^{(\mathrm{h})}[n] \right) + \mu \cdot w_{i,k-1}^{(\mathrm{o})} \,, \; i = 1, 2, \ldots, H \tag{5.14}$$

On the other hand, the biases of the hidden ($\mathbf{b}_k^{(\mathrm{h})}$) and output ($b_k^{(\mathrm{o})}$) neurons are updated to the next iteration, $k+1$, by Eq. (5.15) and (5.16), respectively. Note that these expressions are very similar to the ones given in Eq. (5.13) and (5.14) for updating the synaptic weights, but considering that the virtual input of the neuron connected by the bias is unity, i.e. $z_0[n] = 1$ and $x_{0,k}^{(\mathrm{h})}[n] = 1$.

$$b_{i,k+1}^{(\mathrm{h})} = b_{i,k}^{(\mathrm{h})} - \alpha_k \cdot \frac{1}{P} \cdot \sum_{n=1}^{P} \left(\delta_{i,k}^{(\mathrm{h})}[n] \cdot 1 \right) + \mu \cdot b_{i,k-1}^{(\mathrm{h})} \,, \; i = 1, 2, \ldots, H \tag{5.15}$$

$$b_{k+1}^{(\mathrm{o})} = b_k^{(\mathrm{o})} - \alpha_k \cdot \frac{1}{P} \cdot \sum_{n=1}^{P} \left(\delta_k^{(\mathrm{o})}[n] \cdot 1 \right) + \mu \cdot b_{k-1}^{(\mathrm{o})} \,. \tag{5.16}$$

As observed in these expressions, all the training parameters and inner signals of the MLP depend on k, except the momentum constant (μ) and the observation vectors containing the CUT at the n-th instants ($\mathbf{z}[n], n = 1, 2 \ldots P$). Since the MLP is trained in a batch mode, the weights and biases are not updated until the error of the P CUTs of the training dat set are obtained. On the other hand, the matrix $\delta_k^{(\mathrm{h})}[n]$ and the vector $\delta_k^{(\mathrm{o})}[n]$ are the local derivatives of the MSE function at the k-th iteration of the algorithm with respect to the output of each neuron for the observation vector $\mathbf{z}[n]$. These partial derivatives estimate the sensibility of the synaptic weights with respect to the error and are obtained by Eq. (5.17) and (5.18), respectively [Haykin2009].

$$\delta_{i,k}^{(\mathrm{h})}[n] = \psi'_{\mathrm{htan}} \left(v_{i,k}^{(\mathrm{h})}[n] \right) \cdot \left[\left(\sum_{j=1}^{H} \delta_k^{(\mathrm{o})}[n] \cdot w_{j,k}^{(\mathrm{o})} \right) + \delta_k^{(\mathrm{o})}[n] \cdot b_k^{(\mathrm{o})} \right] \,, \; \begin{cases} i = 1, 2, \ldots, H \\ n = 1, 2, \ldots, P \end{cases} \tag{5.17}$$

$$\delta_k^{(\mathrm{o})}[n] = \psi'_{\mathrm{htan}} \left(v_k^{(\mathrm{o})}[n] \right) \cdot e_{\mathrm{MS},k}[n] \,, \; n = 1, 2, \ldots, P \tag{5.18}$$

being $e_{\mathrm{MS},k}[n]$ the error achieved for the n-th observation vector, $\mathbf{z}[n]$.

The functions $\psi'_{\mathrm{htan}}(v_{i,k}^{(\mathrm{h})}[n])$ and $\psi'_{\mathrm{htan}}(v_k^{(\mathrm{o})}[n])$ denote the partial derivatives of the activation function $\psi_{\mathrm{htan}}(\cdot)$ with respect to the neuron activations $v_{i,k}^{(\mathrm{h})}[n]$ and $v_k^{(\mathrm{o})}[n]$, respectively. These partial derivatives are given in Eq. (5.19) and (5.20), respectively.

$$\psi'_{\mathrm{htan}} \left(v_{i,k}^{(\mathrm{h})}[n] \right) = \left[1 - x_{i,k}^{(\mathrm{h})}[n] \right] \cdot \left[1 + x_{i,k}^{(\mathrm{h})}[n] \right] \,, \; \begin{cases} i = 1, 2 \ldots H \\ n = 1, 2, \ldots, P \end{cases} \tag{5.19}$$

$$\psi'_{\mathrm{htan}} \left(v_k^{(\mathrm{o})}[n] \right) = \left[1 - x_k^{(\mathrm{o})}[n] \right] \cdot \left[1 + x_n^{(\mathrm{o})}[n] \right] \,, \; n = 1, 2, \ldots, P \tag{5.20}$$

Once the partial derivatives have been computed, and the weights are updated according to the current parameters of the algorithm (α_k and μ), the learning rate is automatically adapted for the following algorithm iteration (α_{k+1}) by

$$\alpha_{k+1} = \begin{cases} \alpha_k * (1 + \alpha_{\mathrm{inc}}) & \text{if } e_{\mathrm{MS},k} < e_{\mathrm{MS},k-1} \\ \alpha_k * (1 - \alpha_{\mathrm{dec}}) & \text{if } e_{\mathrm{MS},k} \geq e_{\mathrm{MS},k-1} * (1 + p_{\max}) \\ \alpha_k & \text{otherwise} \end{cases} \tag{5.21}$$

where the parameters α_{inc} and α_{dec} are the increasing and decreasing rates of the learning rate (α). Moreover, in order to guarantee the stability of the learning algorithm, a learning rate constraint is set. This constraint controls the maximum error increase for not surpassing a certain limit. In this way, this constraint is controlled by the parameter $p_{\max}$. In the cases of study of the thesis, these parameters are set to: $\alpha_{\text{inc}} = 0.05$, $\alpha_{\text{dec}} = 0.30$ and $p_{\max} = 0.04$. Moreover, the initial value of the learning rate is set to $\alpha_{k=0} = 0.01$. These parameter values guarantee convergence and stability in the learning algorithm. It has been empirically proven in the cases of study of the thesis.

5.3.2 Training algorithm for low-size MLPs: Levenberg-Marquardt

The gradient descent is one of the simplest and most commonly used MLP training algorithms [Bishop1995]. This algorithm starts initializing the MLP weights with random values, as made by the applied Nguyen-Widrow initialization algorithm [Nguyen1990]. After that, these weights are updated iteratively, moving a short distance in the direction of the greatest rate of decrease of the error. To compare the gradient descent algorithm with the Levenberg-Marquardt algorithm, consider that all the MLP weights to be adapted in the k-th iteration are stored in the following vector of length F:

$$\mathbf{w}_k = [w_{1,k} \ \dots \ w_{F,k}] = \left[w^{(\text{h})}_{1,1,k} \ \dots \ w^{(\text{h})}_{H,K,k} \, , \, b^{(\text{h})}_{1,k} \ \dots \ b^{(\text{h})}_{H,k} \, , \, w^{(\text{o})}_{1,k} \ \dots \ w^{(\text{o})}_{H,k} \, , \, b^{(\text{o})}_{k} \right] , \tag{5.22}$$

being F the number of MLP weights ($F = KH + H + H + 1$). Therefore, the update of the weights by the gradient descent algorithm (neither learning rate adaptation nor momentum are considered) from the k-th to the $(k+1)$-th iteration is made by

$$\mathbf{w}_{k+1} = \mathbf{w}_k - \alpha \nabla E_{\text{MS}}(\mathbf{w}_k) = \mathbf{w}_k - \alpha \mathbf{J}_k \, . \tag{5.23}$$

Note that the cost function for a given weight vector, $\mathbf{w}_k$, is denoted by $E_{\text{MS}}(\mathbf{w}_k)$, and $\mathbf{J}_k$ represents the Jacobian matrix of the cost function evaluated in $\mathbf{w}_k$. This Jacobian matrix ($P \times F$ elements) is given by:

$$\mathbf{J}_k = \begin{pmatrix} \frac{\partial e_{\text{MS}}(\mathbf{w}_k, \mathbf{z}[1])}{\partial w_{1,k}} & \cdots & \frac{\partial e_{\text{MS}}(\mathbf{w}_k, \mathbf{z}[1])}{\partial w_{F,k}} \\ \vdots & \ddots & \vdots \\ \frac{\partial e_{\text{MS}}(\mathbf{w}_k, \mathbf{z}[P])}{\partial w_{1,k}} & \cdots & \frac{\partial e_{\text{MS}}(\mathbf{w}_k, \mathbf{z}[P])}{\partial w_{F,k}} \end{pmatrix} . \tag{5.24}$$

where $e_{\text{MS}}(\mathbf{w}_k, \mathbf{z}[i])$ is the error produced at the output of the MLP working with a set of weights and biases, $\mathbf{w}_k$, for a given observation vector, $\mathbf{z}[i]$.

Since the gradient is re-evaluated at each algorithm iteration, the learning rate is of great importance for the convergence of the algorithm. On the one hand, if α is low, the learning process will be slow, and it may take long time. On the other hand, if α is high, the learning process will be much faster, but the algorithm may not converge, and the system could become unstable. Therefore, α must be between these limits.

The Newton method can be seen as an evolution of the gradient descent, where information from the second derivative is considered. The expression for the weight update is given by:

$$\mathbf{w}_{k+1} = \mathbf{w}_k - \mathbf{H}_k^{-1} \nabla E_{\text{MS}}(\mathbf{w}_k) \, , \tag{5.25}$$

where $\mathbf{H}_k$ represents the Hessian matrix of the cost function $E_{\mathrm{MS}}(\mathbf{w}_k)$ evaluated in $\mathbf{w}_k$ for the whole training data set, which is given by:

$$\mathbf{H}_k = \begin{pmatrix} \frac{\partial^2 E_{\mathrm{MS}}(\mathbf{w}_k)}{\partial w_{1,k}^2} & \cdots & \frac{\partial^2 E_{\mathrm{MS}}(\mathbf{w}_k)}{\partial w_{1,k} \partial w_{F,k}} \\ \vdots & \ddots & \vdots \\ \frac{\partial^2 E_{\mathrm{MS}}(\mathbf{w}_k)}{\partial w_{F,k} \partial w_{1,k}} & \cdots & \frac{\partial^2 E_{\mathrm{MS}}(\mathbf{w}_k)}{\partial w_{F,k}^2} \end{pmatrix} . \tag{5.26}$$

This method converges in only one iteration when the error surface is quadratic, and it is, in general, much more efficient than the gradient descent method for two reasons: first, there is no need to adapt any constants; and second, the direction in which the weights vary is more efficient than for the gradient descent.

The main problem of the Newton method is the calculation of the Hessian matrix and its inverse. The Gauss-Newton method simplifies this method for the case when the cost function is a sum-of-squares error, as in the problem presented in the thesis. In this case, the Hessian matrix can be approximated by a function of the Jacobian ($\mathbf{J}_k^T \mathbf{J}_k$), and the gradient of the cost function can be approximated by a function of the Jacobian and the cost function ($\mathbf{J}_k^T E_{\mathrm{MS},k}$). The expression for the adaptation of the MLP weights is thus given by:

$$\mathbf{w}_{k+1} = \mathbf{w}_k - \left(\mathbf{J}_k^T \mathbf{J}_k + \lambda \mathbf{I} \right)^{-1} \mathbf{J}_k^T E_{\mathrm{MS},k} \, , \tag{5.27}$$

where the parameter λ is chosen to ensure that the matrix $\mathbf{J}_k^T \mathbf{J}_k + \lambda \mathbf{I}$ is positive-defined. That is, the parameter λ compensates the most negative eigenvalue in case the matrix is not positive-defined. Note that, if $\lambda = 0$, Eq. (5.27) leads to the Newton method. While, if λ is very high, the method behaves like the gradient descent with a small learning rate. In the Levenberg-Marquardt algorithm [Hagan1994], this parameter varies depending on the value of the cost function, being smaller when the cost function decreases and higher when it increases.

Finally, it is important to note that because of the inaccurate estimation of the Hessian matrix when MLPs with a lot of weights is used, only low-size MLPs are trained using the Levenberg-Marquardt algorithm.

5.4 MLP-based detector computational cost

Not only the performance evaluation of the proposed detector in terms of MSE (see Eq. (5.11)) and P_{fa}-P_{d} (see Sect. 4.4) is important, but also its computational cost. The computational cost of its core, i.e. the MLP-based processor, is analyzed here because this is the only block in the MLP-based detector which size varies in the studies of the thesis.

The computational cost of a $K/H/1$ MLP is presented in terms of:

- Number of memory registers needed to store:
  - the weights and bias of the hidden layer: KH and H registers, respectively; and
  - the weights and bias of the output layer: H and 1 registers, respectively.
- Number of products of two elements to compute:
  - all outputs of the hidden neurons: KH products from Eq. (5.4); and

  - the MLP output: H products from Eq. (5.6).

- Number of sums of two elements to compute:
  - all outputs of the hidden neurons: KH sums from Eq. (5.4); and
  - the MLP output: H sums from Eq. (5.6).

- Number of evaluations of the activation function of each (hidden or output) neuron: $H+1$.

The computational cost presented above is given for each CUT.

The memory requirements and number of operations for a $K/H/1$ MLP and for each CUT are summarized in the following equations:

$$\text{MLP memory registers}: \quad (K+1)H + (H+1) \tag{5.28}$$

$$\text{MLP products}: \quad KH + H \tag{5.29}$$

$$\text{MLP sums}: \quad KH + H \tag{5.30}$$

$$\text{Activation function evaluations}: \quad H + 1 \tag{5.31}$$

CHAPTER 6

Detection based on AI: Radial Basis Function (RBF) ANNs

The general detection scheme based on the AI-based processor described in Sect. 4.1 explains how an observation vector extracted from a radar scan is processed, independently whether coherent or incoherent data are considered. Several AI techniques could be considered to solve the problem of detecting desired signals in Weibull-distributed clutter and white Gaussian noise. In the previous chapter (Chap. 6), MLPs were considered to solve this problem. In the current chapter, the way to implement the processor of the proposed detector, such as in Fig. 4.1-4.2, is described in depth when using a different kind of real-arithmetic feed-forward ANNs. The ANNs used in this case are the radial basis function artificial neural networks (RBF-ANNs). The acronyms RBF-ANN or RBFN (radial basis function network) are commonly used in the literature to refer to this kind of ANNs. In the thesis, the acronym RBFN is used. RBFNs are selected to form the proposed AI-based detector because it has been demonstrated in [Jarabo2004, Jarabo2009] that being trained in a semi-supervised way, they are able to approximate to the Neyman-Pearson detector. Moreover, RBFNs are selected because of their capabilities of learning from a set of pre-classified data and their easy implementation once designed. The selected RBFNs are trained in two stages: one unsupervised and the other supervised, in a batch mode and with an external validation of the training process [Bishop1995].

Before continuing with the presentation of the signal processing made by the RBFNs, some differences between MLPs and RBFNs are analyzed. It is known that MLPs create a decision boundary combining hyper-planes transformed by the activation functions. If this activation functions are linear, the transformed hyper-planes are linear. Otherwise, they are non-linear, as done in the architecture selected for the MLP, where non-linear activation functions were used in the selected architecture. In [Bishop1995, Haykin2009], the use of non-linear activation functions in MLPs is demonstrated to be better than the use of linear activation functions for solving of a wide variety of problems. On the other hand, RBFNs can use different kinds of activation functions. Among others, the commonly used activation functions depend on the squared distance between the observation vectors and the centroids of the functions. These activation functions present radial symmetry. Moreover, the activation functions used in RBFNs, e.g. Gaussian functions, are usually non-linear. It implies that a non-linear decision boundary is implemented by RBFNs.

According to the above mentioned differences between MLPs and RBFNs, the performance of the detectors based on them is expected to be different. But, which of these ANNs works better when trying to detect desired signals in Weibull-distributed and white Gaussian noise? It will be investigated in the experimental results chapters (see Chap. 8-11).

Once discussed the differences between MLPs and RBFNs, let's focus on the way a decision "target present/target absent" is made for a given observation vector. For this purpose, consider $\mathbf{z}[n]$ being the observation vector at the n-th instant extracted from a radar scan following one of the selection modes presented in Sect. 4.2. In this case, the RBFN-based processor output is computed as

$$x[n] = f_{\text{RBFN}}(\mathbf{z}[n]) \,, \tag{6.1}$$

where $f_{\text{RBFN}}(\cdot)$ denotes the transfer function mapped by the RBFN.

Once $x[n]$ is obtained, the output of the RBFN-based detector is computed by

$$y[n] = \begin{cases} 1 & \text{, if } x[n] \geq \text{THR}_{\text{RBFN}}, \\ 0 & \text{, if } x[n] < \text{THR}_{\text{RBFN}}, \end{cases} \tag{6.2}$$

where the detection threshold of this detector, THR_{RBFN}, is adapted to achieve a desired P_{fa} following the procedure presented in Sect. 4.3.

The following sections focus on the application of RBFNs in the proposed detection scheme of Fig. 4.1-4.2. These sections present:

- Which is the selected RBFN architecture;
- How RBFNs are applied in the proposed detection scheme when both coherent and incoherent radar scans are used;
- How RBFNs are trained to learn from the data collected by the radar from the environment; and
- Which is the RBFN computational cost once trained.

6.1 Coherent RBFN-based detection schemes

First, taking as reference the detection scheme of Fig. 4.1, the proposed detector based on RBFNs is presented considering non-delayed selection modes and coherent radar scans. And second, taking as reference the detection scheme of Fig. 4.2, the implementation of the proposed detector based on RBFNs is studied when delayed selection modes are considered with coherent data.

The proposed coherent detector based on RBFNs working with non-delayed selection modes is depicted in Fig. 6.1, where $N = 3$ cells in an azimuthal selection mode are processed. Since coherent data are used and the RBFN works with real-arithmetic, the complex-valued observation vector at the n-th instant given in Eq. (4.1) is converted into a real-valued one by

$$\begin{aligned} \mathbf{z}[n] &= [z_{\text{Q}}[n-2] \;\; z_{\text{Q}}[n-1] \;\; z_{\text{Q}}[n] \;\; z_{\text{P}}[n-2] \;\; z_{\text{P}}[n-1] \;\; z_{\text{P}}[n]]^{\text{T}} \\ &= [z_1[n] \qquad z_2[n] \qquad z_3[n] \;\; z_4[n] \qquad z_5[n] \qquad z_6[n]]^{\text{T}} \,, \end{aligned} \tag{6.3}$$

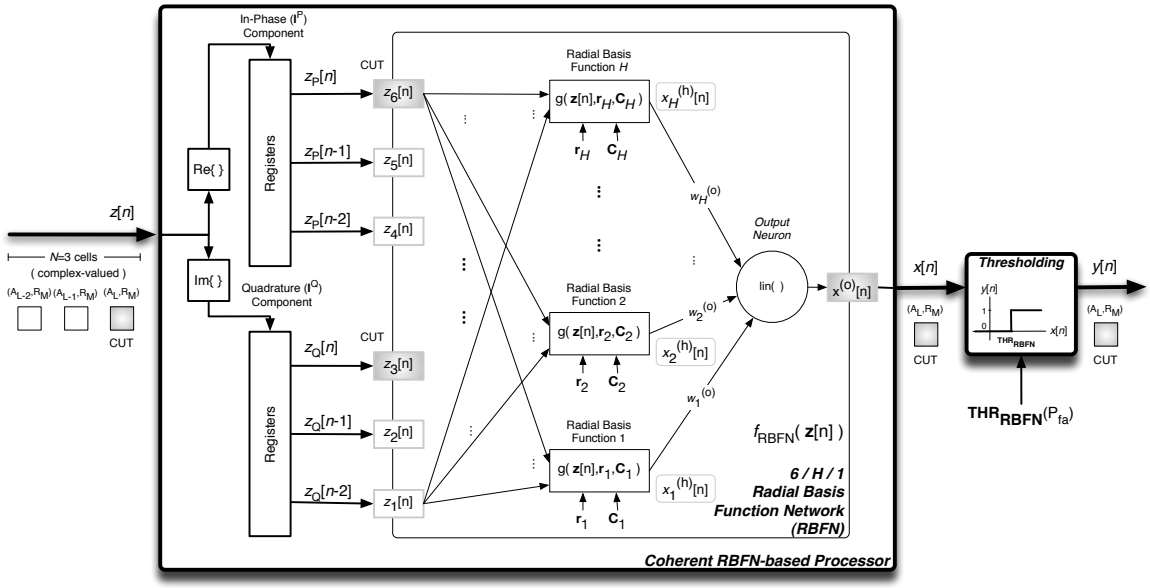

Figure 6.1: RBFN-based coherent detector working with a non-delayed (azimuthal) selection mode. In this case, a $2N/H/1$ RBFN structure is used, being $N = 3$

splitting the coherent data in its in-phase (z_{P}) and quadrature (z_{Q}) components. As observed, this vector is the same as the one used in Eq. (5.3) for the case of working with MLPs. It is reproduced here for convenience purposes.

Once the observation vector is obtained, the RBFN-based processor output is achieved. RBFN structures are composed of two layers. Its size is $K/H/1$, where K inputs (dimension of the observation vector), H radial basis functions (RBFs) and 1 output neuron are considered. Since coherent data are processed and real-arithmetic is used in the RBFN, $K = 2N$ in this case. Both K and H are studied in the thesis to determine the best dimensioning of the RBFN-based processor that composes the proposed detector. The RBFN can use different kinds of radial basis functions, such as Gaussian/exponential, multiquadratic, polyharmonic spline, etc. The most commonly used radial basis function is the Gaussian one, which has been successfully applied to solve different kind of problems [Bishop1995, Haykin2009, Jarabo2004]. Moreover, in the design of RBF-ANNs, it is convenient to use activation functions with local behavior. In this way, Gaussian/exponential RBFs present this behavior, apart of several useful analytical properties. For those reasons, Gaussian/exponential RBFs are considered in the studies made in the thesis.

The non-linear function implemented by the RBFN given in Eq. (6.1) is presented below using matrix notation. The activation of the i-th RBF at the n-th instant ($v_i^{(\mathrm{h})}$) is a function of the observation vector at this instant, $\mathbf{z}[n]$, the reference vector containing the centers of this RBF, $\mathbf{r}_i$, and the matrix $\mathbf{C}_i$: $v_i^{(\mathrm{h})}[n] = f_{\mathrm{RBF}}(\mathbf{z}[n], \mathbf{r}_i, \mathbf{C}_i)$. This function is:

$$v_i^{(\mathrm{h})}[n] = |\mathbf{z}[n] - \mathbf{r}_i|^2_{\mathbf{C}_i} = (\mathbf{z}[n] - \mathbf{r}_i)^{\mathrm{T}} \, \mathbf{C}_i^{-1} \, (\mathbf{z}[n] - \mathbf{r}_i) \quad , i = 1 \cdots H, \tag{6.4}$$

where the square of the Mahalanobis distance [Mahalanobis1936] between $\mathbf{z}[n]$ and $\mathbf{r}_i$ is considered. Note that both vectors has the same dimension, i.e. $\mathbf{z}[n]$ and $\mathbf{r}_i$ are of size $[K \times 1]$, and the dimension of $\mathbf{C}_i$ is $[K \times K]$.

By using an exponential function in each RBF, the output of the i-th RBF at the n-th instant is

$$x_i^{(\mathrm{h})}[n] = g\left(v_i^{(\mathrm{h})}[n]\right) = \exp\left(-\frac{v_i^{(\mathrm{h})}}{2}[n]\right), \tag{6.5}$$

which also depends on $\mathbf{r}_i$ and $\mathbf{C}_i$ for a given observation vector, $\mathbf{z}[n]$, i.e. $x_i^{(\mathrm{h})}[n] = g(\mathbf{z}[n], \mathbf{r}_i, \mathbf{C}_i)$. Apart of a scale factor, the expression given in Eq. (6.4)-(6.5) is a generalized Gaussian function in a K-dimensional space, where $\mathbf{r}_i$ contains the means and $\mathbf{C}_i$ is the covariance matrix. The output of the H RBFs are stored in the column vector

$$\mathbf{x}^{(\mathrm{h})}[n] = \left[x_1^{(\mathrm{h})}[n] \ \ldots \ x_H^{(\mathrm{h})}[n]\right]^{\mathrm{T}}. \tag{6.6}$$

Finally, a linear function is considered in the output neuron. It involves that the activation ($v^{(\mathrm{o})}[n]$) and output ($x^{(\mathrm{o})}[n]$) of this neuron are equal each other and equal to the RBFN output ($x[n]$), i.e.

$$x[n] = x^{(\mathrm{o})}[n] = \psi_{\mathrm{lin}}\left(v^{(\mathrm{o})}[n]\right) = v^{(\mathrm{o})}[n] = \mathbf{w}^{(\mathrm{o})} \cdot \mathbf{x}^{(\mathrm{h})}[n] + b^{(\mathrm{o})}, \tag{6.7}$$

where $\mathbf{w}^{(\mathrm{o})}$ is a row vector of size $[1 \times H]$ containing the synaptic weights that connect the H RBFs with the output neuron, and $b^{(\mathrm{o})}$ is a variable containing the output bias weight. Therefore, the output of the RBFN depends on the observation vector ($\mathbf{z}[n]$), the reference matrix containing the centroids of the Gaussian RBFs ($\mathbf{R} = [\mathbf{r}_1\, \mathbf{r}_2 \ldots \mathbf{r}_H]$), the covariance matrix of each RBF ($\mathbf{C} = [\mathbf{C}_1\, \mathbf{C}_2 \ldots \mathbf{C}_H]$), and the weights ($\mathbf{w}^{(\mathrm{o})}$) and bias ($b^{\mathrm{o}}$) of the output layer, i.e. $x[n] = f_{\mathrm{RBF}}(\mathbf{z}[n], \mathbf{R}, \mathbf{C}, \mathbf{w}^{(\mathrm{o})}, b^{\mathrm{o}})$.

Once the output of the RBFN-based processor is computed, the output of the detector is obtained with Eq. (6.2). This output is stored in the corresponding cell of the output detector scan, as shown in Fig. 4.1. Finally, the procedure presented above is repeated for each CUT of the input radar scans.

The coherent detection scheme based on RBFNs presented above works with non-delayed selection modes. Next, the same detection scheme but considering delayed selection modes, as the ones presented in Sect. 4.2.2 and 4.2.3, is analyzed. In this case, the general detection scheme presented in Fig. 4.2 is taken as reference to create the proposed one based on RBFNs. This detection scheme is shown in Fig. 6.2. Considering that J cells are selected to make the final decision (target is present or not), and remembering that the RBFN works with real-arithmetic, the following observation vector is considered at the n-th instant for a given CUT:

$$\begin{aligned}\mathbf{z}[n] &= \left[z_{\mathrm{Q}}[n - \tfrac{J-1}{2}] \ldots z_{\mathrm{Q}}[n] \ \ldots \ z_{\mathrm{Q}}[n + \tfrac{J-1}{2}]\ z_{\mathrm{P}}[n - \tfrac{J-1}{2}] \ldots z_{\mathrm{P}}[n] \ \ \ldots \ \ z_{\mathrm{P}}[n + \tfrac{J-1}{2}]\right]^{\mathrm{T}} \\ &= \left[z_1[n] \quad \ldots \quad z_{\frac{J+1}{2}}[n] \ldots z_J[n] \qquad z_{J+1}[n] \quad \ldots \quad z_{\frac{3J+1}{2}}[n] \ldots z_{2J}[n]\right]^{\mathrm{T}}.\end{aligned} \tag{6.8}$$

The processing made by the RBFN to this vector is the same as the one given in Eq. (6.4)-(6.7). But, in this case, the number of RBFN inputs (structure $K/H/1$) is $K = 2J$. The final decision is made by Eq. (6.2), where the detection threshold has a different value of the one used in Fig. 6.1 for the same P_{fa}. The decision for the CUT is stored in the corresponding coordinates of the output detector scan. Finally, this procedure is repeated for each CUT of the input radar scans.

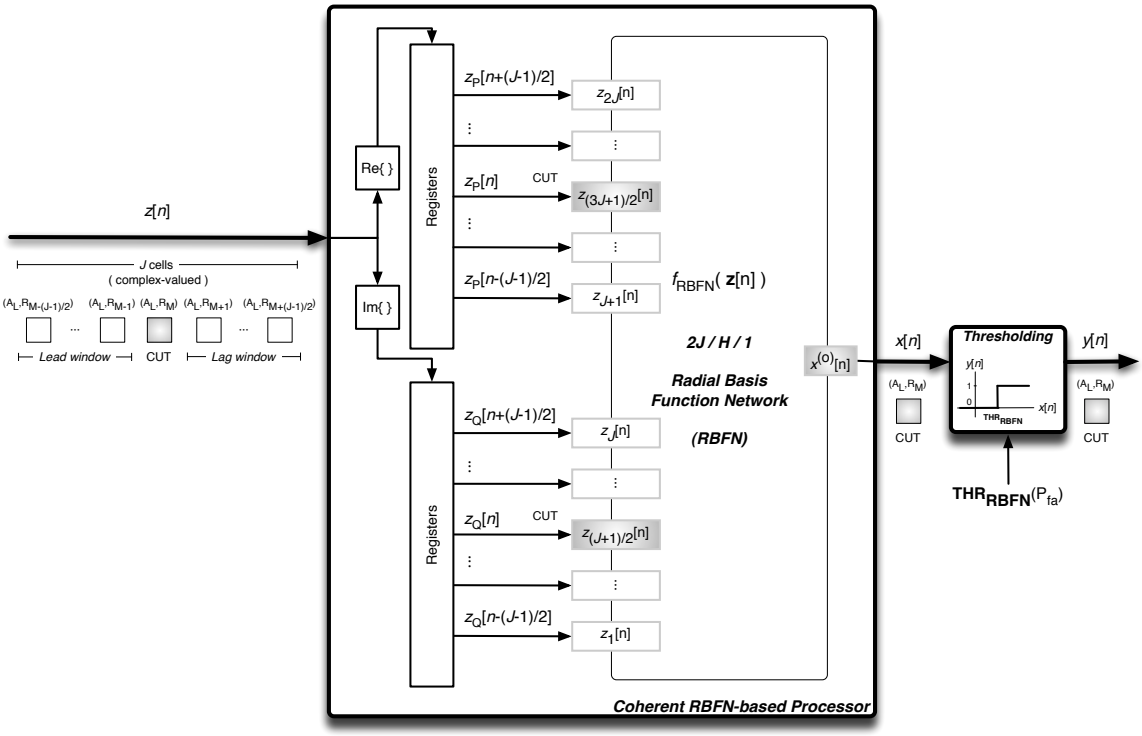

Figure 6.2: RBFN-based coherent detector working with a delayed (horizontal/range) selection mode. In this case, a $2J/H/1$ RBFN structure is used

6.2 Incoherent RBFN-based detection schemes

In this section, two detection approaches based on RBFNs working with incoherent radar scans are presented. In the first one, non-delayed selection modes are used. In the second one, delayed selection modes are used.

Taking as reference the general detection scheme given in Fig. 4.1, where non-delayed selection modes are used, the incoherent detection scheme based on RBFNs is presented in Fig. 6.3. As an example, $N = 3$ cells are selected in this figure. Since the received data are real-arithmetic and the RBFN works with the same kind of arithmetic, a $K/H/1$ RBFN structure is used, considering $K = N$. These selected real-valued cells compose the observation vector at the n-th instant:

$$\begin{aligned}\mathbf{z}[n] &= [z[n-2]\ z[n-1]\ z[n]\ ]^{\mathrm{T}} \\ &= [z_1[n] \quad z_2[n] \quad z_3[n]\ ]^{\mathrm{T}}\ .\end{aligned} \tag{6.9}$$

The processing made by the RBFN of this vector is the same as the one given in Eq. (6.4)-(6.7). But, in this case, the number of RBFN inputs is $K = N$. The final decision is made according to Eq. (6.2), where the detection threshold has a different value of the one achieved in Fig. 6.1 and 6.2 for the same P_{fa}. The decision for the CUT is stored in the corresponding coordinates of the output detector scan. Finally, this process is repeated for each CUT of the input scans.

Taking as reference the general detection scheme given in Fig. 4.2, where delayed selection modes are used, the incoherent detection scheme based on RBFNs is presented in Fig. 6.4. Since

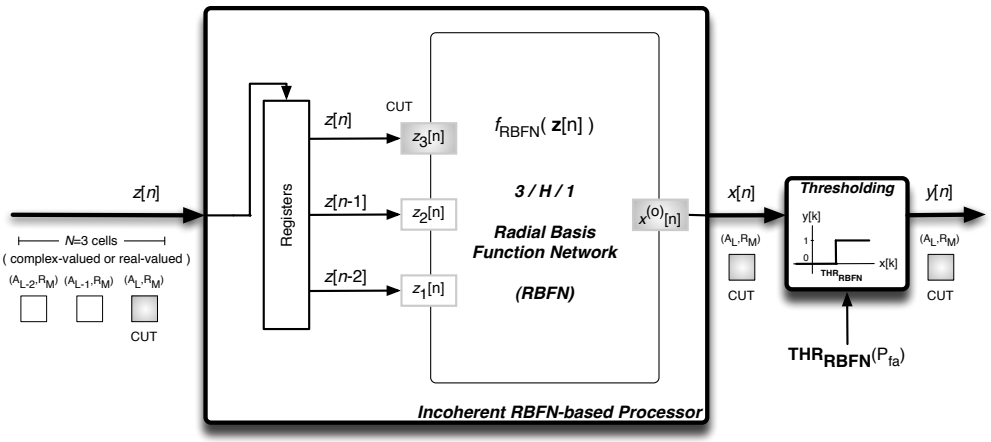

Figure 6.3: RBFN-based incoherent detector working with a non-delayed (azimuthal) selection mode. In this case, an $N/H/1$ RBFN structure is used, being $N = 3$

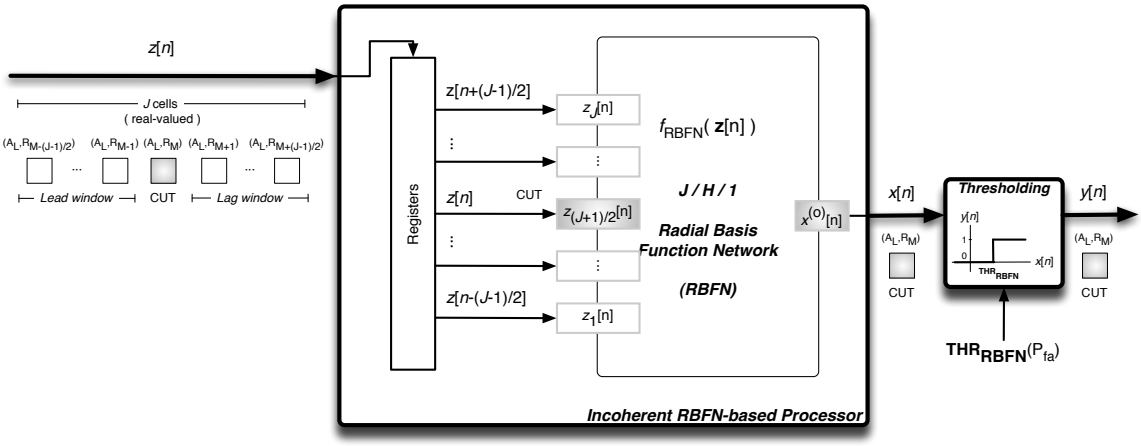

Figure 6.4: RBFN-based incoherent detector working with a delayed (horizontal/range) selection mode. In this case, a $J/H/1$ RBFN structure is used

the received data are real-arithmetic and the RBFN works with the same kind of arithmetic, a $K/H/1$ RBFN structure is used, considering $K = J$ cells in this case. These selected real-valued cells compose the observation vector at the n-th instant:

$$\begin{aligned}\mathbf{z}[n] &= \left[z[n-\tfrac{J-1}{2}] \ldots z[n] \quad \ldots \quad z[n+\tfrac{J-1}{2}]\right]^{\mathrm{T}} \\ &= \left[z_1[n] \quad \ldots \quad z_{\frac{J+1}{2}}[n] \ldots z_J[n]\right]^{\mathrm{T}}.\end{aligned} \tag{6.10}$$

The processing made by the RBFN to this vector is the same as the one given in Eq. (6.4)-(6.7). But, in this case, the number of RBFN inputs is $K = J$. The final decision is made according to Eq. (6.2), where the detection threshold has a different value of the one achieved in Fig. 6.1-6.3 for the same P_{fa}. The decision for the CUT is stored in the corresponding coordinates of the output detector scan. Finally, this process is repeated for each CUT of the input scans.

6.3 RBFN-based detector design: RBFNs training algorithm

Since the learning algorithm selected to train the RBFNs that compose the proposed detector is semi-supervised, a cost function must be set. As mentioned at the beginning of this chapter, this semi-supervised algorithm is divided in two stages: the first stage is unsupervised, while the second stage is supervised. In the unsupervised stage, the input space (observation vectors) is transformed to a non-linear space by the radial basis functions of the hidden neurons. This transformation is critical because, in the supervised stage, a linear output neuron is used. This output neuron linearly relates the output of the RBFN with the outputs of the hidden neurons by using so many synaptic weights as the number of hidden neurons. It is critical because the hidden layer must be able to transform the observation vectors to a space where these transformed vectors are linearly separable.

The cost function to be minimized during the supervised stage is the same as the one used to train MLPs, i.e. the MSE. In [Jarabo2004], it has been proven that RBFNs trained in a semi-supervised way to minimize this cost function approximate the Neyman-Pearson detector for any pair of likelihood functions. For a training set composed of $M^{(\mathrm{d})}$ scans and their corresponding desired output scans ($\mathbf{D}$), the MSE is estimated as the averaged and squared difference between the desired and processed ($\mathbf{O}^{\text{RBFN-Proc}}$) output scans as:

$$E_{\mathrm{MS}} = \frac{1}{M^{(\mathrm{d})} K_{\mathrm{a}} K_{\mathrm{r}}} \sum_{l=1}^{M^{(\mathrm{d})}} \sum_{r=1}^{K_{\mathrm{a}}} \sum_{c=1}^{K_{\mathrm{r}}} \frac{\left(o_{r,c}^{\text{RBFN-Proc}}(l) - d_{r,c}(l)\right)^2}{2} . \tag{6.11}$$

From this training data set, $P = M^{(\mathrm{d})} K_{\mathrm{a}} K_{\mathrm{r}}$ CUTs can be extracted. So, a total of P observation vectors can be used: $\mathbf{z}[n]$, $n = 1, 2 \ldots P$. Since the output of the RBFN ($x[n]$) can be achieved for each observation vector by Eq. (6.1), Eq. (6.11) can be rewritten as

$$E_{\mathrm{MS}} = \frac{1}{P} \sum_{n=1}^{P} \frac{(x[n] - d[n])^2}{2} , \tag{6.12}$$

where the desired output is $d[n] = d_{r,c}(l)$, being $n = c + (r-1)K_{\mathrm{r}} + (l-1)K_{\mathrm{r}}K_{\mathrm{a}}$, where K_{r} and K_{a} are the number of range sweeps and azimuth bins of each radar scan. Finally, since $x[n] = f_{\mathrm{RBF}}(\mathbf{z}[n], \mathbf{R}, \mathbf{C}, \mathbf{w}^{(\mathrm{o})}, b^{\mathrm{o}})$, the MSE is also a function of the RBFN parameters for a given set of observation vectors, i.e. $E_{\mathrm{MS}} = g(\mathbf{R}, \mathbf{C}, \mathbf{w}^{(\mathrm{o})}, b^{\mathrm{o}})$

The MSE is a way of measuring the performance of the processor. This measurement is constant when the RBFN weights are fixed. Nevertheless, during the training of the RBFN that forms the processor, this MSE varies because $\mathbf{R}$, $\mathbf{C}$, $\mathbf{w}^{(\mathrm{o})}$, b^{o} are iteratively adjusted to minimize this cost function. The update of the RBFN parameters during training is discussed below.

The theoretical foundations of the design of ANNs based on RBFs are given in the "*theorem of the universal approximation*" proposed by Hartman et al. in [Hartman1990]. They proposed the use of Gaussian RBFs to approximate functions, where the covariance matrix of each RBF ($\mathbf{C}_i$, $i = 1, 2 \ldots H$) are the parameters to be adjusted. Park and Sandberg demonstrated in [Park1991] that this property could be extended to ANNs with integral, bounded and continuous activation functions for which $\int_{\mathbb{R}^K} g(\mathbf{z}[n]) d\mathbf{z}[n] \neq 0$, considering the same variance for each RBF, i.e. $\sigma_i^2 = \sigma_j^2 = \sigma^2, i \neq j$. They demonstrated that the function approximated by the

RBFN is close to the desired function for any norm, i.e. for any dimension K of the observation vector $\mathbf{z}[n]$.

In the general case, the parameters of the RBFs, centroids ($\mathbf{r}_i$, $i = 1, 2 \dots H$) and covariance matrixes ($\mathbf{C}_i$, $i = 1, 2 \dots H$), can be different for each RBF. To minimize Eq. (6.12), the adaptation of these parameters and the parameters concerning to the output layer (synaptic weights and bias) can be divided in two stages [Bishop1995]:

- First, the selection of the RBF centroids ($\mathbf{r}_i$, $i = 1, 2 \dots H$) is done by an unsupervised stage. In this stage, these centroids are initialized by a clustering algorithm. After this stage, H reference vectors minimizing the distance between them and the observation vectors of the training data set are selected. The algorithm used in this stage, the k-means clustering algorithm, is discussed in Sect. 6.3.1.

- And second, the covariance matrixes ($\mathbf{C}_i$, $i = 1, 2 \dots H$) of the RBFs are fixed manually, whereas the parameters of the output layer are set by using a supervised learning algorithm. The algorithm used in this stage is discussed in Sect. 6.3.2.

Other adaptation methods can be used to find the RBFN parameters that minimize a given cost function. As an example, a commonly used method in the literature for this purpose is the expectation-maximization (EM) method [Dempster1977]. The EM method is an iterative method which alternates between performing an expectation step, which computes the expectation of the log-likelihood evaluated using the current estimate for the parameters, and a maximization step, which computes parameters maximizing the expected log-likelihood found on the expectation step. These parameter-estimates are then used to determine the distribution of the input variables in the next expectation step.

As occurred in the designing of MLPs, apart from the RBFN structure (size) and the correct dimensioning of the training data set, the training of the RBFN is an important topic in the designing stage of an RBFN-based processor. This training also presents the same two problems as in MLP training: the training is sometimes not correctly done; and the trained RBFN does not always allow to achieve the best solution when other data set is processed. These two problems are mainly due to the supervised stage of the training process. The first problem can be solved by repeating the training process 10 times, randomly initializing the synaptic weights of the output layer in each trial. The second problem can be solved by using an external validation of the learning process. This validation process is made by using a new data set of $M^{(\mathrm{v})}$ radar scans to estimate the MSE and to decide when the learning process must be stopped to mitigate the specialization in (memorizing) the training data set and to improve the generalization capabilities to work with other radar scans. Moreover, considering the overall behavior of the RBFN working as detector, once the 10 RBFNs are trained, their corresponding 10 detection thresholds (THRs) are calculated for a given P_{fa}. After that, the P_{d}'s achieved by each of these 10 RBFN-based detectors (10 "trained RBFNs-calculated THRs" trials) are estimated. The RBFN selection is made according to the one that gives the best P_{d} for a given P_{fa} (e.g. $P_{\mathrm{fa}} = 10^{-4}$).

As done for the training of MLPs (see Sect. 5.3), the number of trials "RBFN training - threshold setting" is studied. The performances given below are obtained by RBFN-based detectors when working in synthetic coherent sea clutter conditions (as done in Sect. 8.2), using 50/20/1 RBFNs and a square selection mode, when different number of trials are used. These

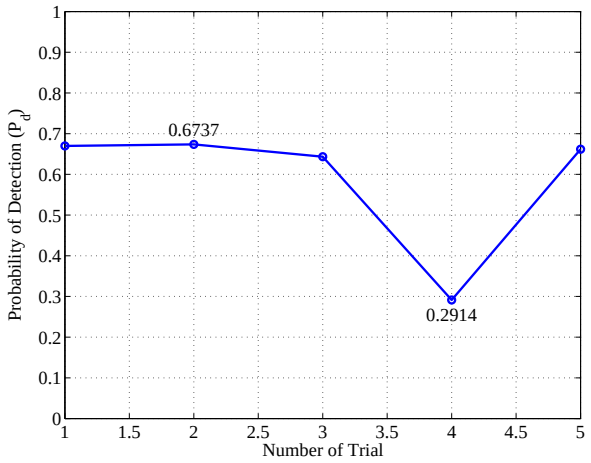

(a) 5 "RBFN training - threshold setting" trials

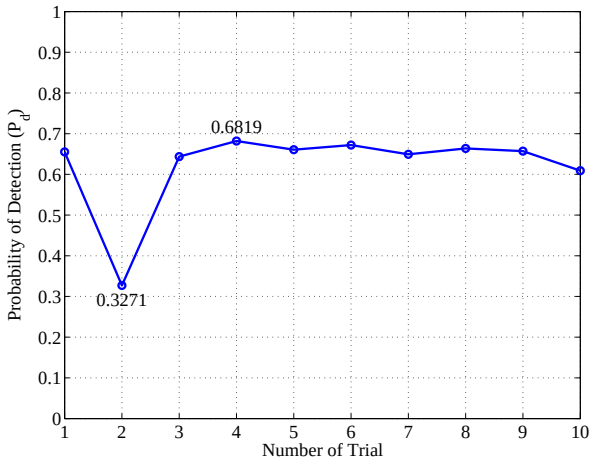

(b) 10 "RBFN training - threshold setting" trials

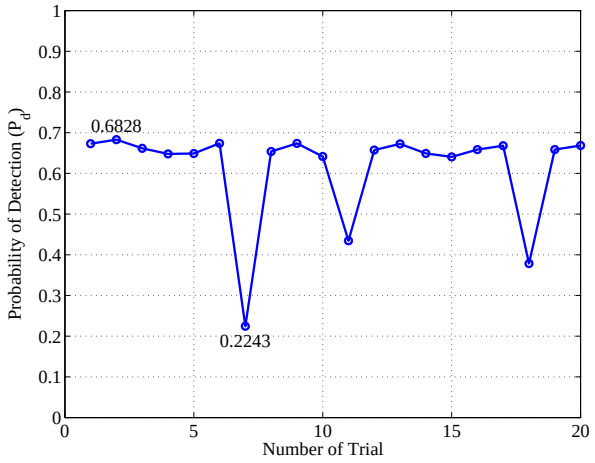

(c) 20 "RBFN training - threshold setting" trials

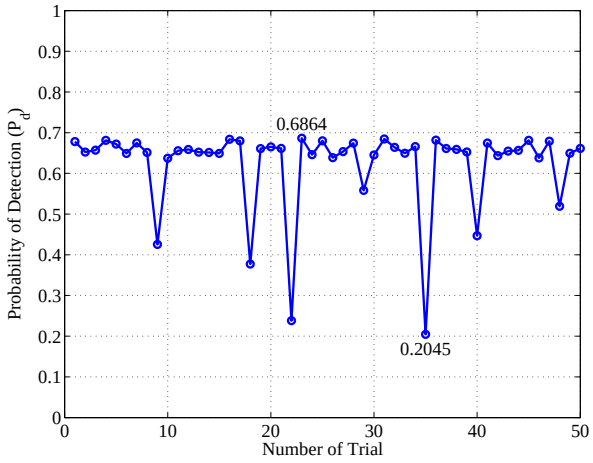

(d) 50 "RBFN training - threshold setting" trials

Figure 6.5: Influence of the number of "RBFN training - threshold setting" trials in the achieved RBFN-based detector performance (P_{d} for $P_{\mathrm{fa}} = 10^{-4}$).

performances (P_{d} for $P_{\mathrm{fa}} = 10^{-4}$) are obtained in the designing stage, using the radar scans of the validation data set. The achieved performances for different number of trials is plotted in Fig. 6.5. From these plots, it is observed that if less than 10 trials are made (see Fig. 6.5a), the maximum performance is not guaranteed. On the other hand, if more than 10 trials are made (see Fig. 6.5c and 6.5d), not only low performance improvement is achieved, but also the computational cost to make all these trials increases, being 2 and 5 times greater than when making 10 trials, respectively. Therefore, 10 trials of RBFN training and threshold setting are selected.

6.3.1 Unsupervised stage of the RBFN training algorithm

As mentioned above, the adaptation of the centroids of each RBF, i.e. the mean of each Gaussian function, is done by using an unsupervised learning algorithm. Among the unsupervised algorithms that can be used for that purpose, the following ones are commonly used in the literature: methods based on unsupervised clustering [Moody1989]; methods based on vectorial quantification [Schwenker1994]; and the expectation maximization method [Dempster1977], where an estimate of the maximum likelihood of the RBF parameters is made. In this thesis, a method based on unsupervised clustering is selected to find the centroids of the RBFs ($\mathbf{r}_i$, $i = 1, 2 \dots H$). The selected method is the k-means clustering algorithm. The application of this algorithm to the RBFNs used in Fig. 6.1-6.4 is briefly presented below.

Let's consider a given set of observation vectors $\mathbf{Z} = [\mathbf{z}[1], \mathbf{z}[2], \dots \mathbf{z}[P]]$, where each observation vector is a K-dimensional real-valued vector. Then, the k-means clustering algorithm aims to partition the P observations into H sets ($H < P$), such as $\mathbf{S} : \{S_1, S_2, \dots S_H\}$, to minimize the within-cluster sum of squares:

$$\arg\min_{\mathbf{S}} \sum_{i=1}^{H} \sum_{\mathbf{z}[n] \in S_i} ||\mathbf{z}[n] - \mathbf{r}_i||^2 \tag{6.13}$$

where $\mathbf{r}_i$ is the mean of the vectors in the cluster S_i, i.e. the centroid of the i-th RBF.

To minimize this cost function, the k-means algorithm follows these steps:

1. Choose the number of clusters, H.

2. Randomly generate H clusters and determine the cluster centers in the first iteration of the algorithm: $\mathbf{r}_i[1]$, $i = 1, 2 \dots H$.

3. For the k-th iteration of the algorithm, assign each observation vector, $\mathbf{z}[n]$, to the nearest cluster center, i.e.

$$S_{i,k} = \{\mathbf{z}[n] : ||\mathbf{z}[n] - \mathbf{r}_{i,k}|| \leq ||\mathbf{z}[n] - \mathbf{r}_{j,k}||, i \neq j \text{ and } j = 1, 2 \dots H\} \ , \ n = 1, 2 \dots P \, . \tag{6.14}$$

4. Recompose the new cluster centers for the following iteration:

$$\mathbf{r}_{i,k+1} = \frac{1}{N_i} \sum_{\mathbf{z}[n] \in S_i} \mathbf{z}[n] \, , \quad i = 1, 2 \dots H \, , \tag{6.15}$$

   where N_i is the number of vectors in the cluster S_i.

5. Repeat steps 3 and 4 until the centroids $\mathbf{r}_i$ remain constant (algorithm stopping criteria).

Finally, after some empirical studies made in the thesis, it was observed that when the number of RBFs, H, is lower than the number of observation vectors, P, the centroids of the RBFs ($\mathbf{r}_i$, $i = 1, 2 \dots H$) determined in the unsupervised stage are usually not equal to any of the observation vectors.

6.3.2 Supervised stage of the RBFN training algorithm

In a general situation, the parameters of each RBF (centroids, $\mathbf{r}_i$, and covariance matrixes, $\mathbf{C}_i$) can be different each other. This is the case of the generalized RBFs. But, due to the learning algorithm selected in the thesis for training RBFNs and since the centroids are determined in its unsupervised stage, the covariance matrixes of the RBFs ($\mathbf{C}_i$, $i = 1, 2 \dots H$) must be adjusted in the supervised stage. In the case of generalized RBFs, a total of HKK elements are different in these matrixes. Therefore, as the best value of K (RBFN inputs) is a priori unknown in the thesis, the computational cost to solve this problem can be very large. In this case, diagonal matrixes could be used to solve this problem, where the elements of the main diagonal can be equal or not. In the practice, a trade-off between the number of RBFs and the number of parameters that define these RBFs exists. This relationship sets that less RBFs with more parameters or more RBFs with less parameters can be used [Bishop1995]. In this thesis, the second situation is selected. In this way, the covariance matrix of each RBF is given by a diagonal matrix with the same elements in its main diagonal, i.e.

$$\mathbf{C}_i = \sigma^2 \mathbf{I} = \begin{pmatrix} \sigma^2 & 0 & \cdots & 0 \\ 0 & \sigma^2 & \cdots & 0 \\ \vdots & \vdots & \ddots & \vdots \\ 0 & 0 & \cdots & \sigma^2 \end{pmatrix} . \tag{6.16}$$

where $\mathbf{I}$ is the unity matrix in this case. The sizes of $\mathbf{I}$ and $\mathbf{C}_i$ are $[K \times K]$. In the supervised stage, a set of V variances (σ_i^2, $i = 1, 2, \dots V$) is taken. For each variance of this set (σ_i^2), the weights ($\mathbf{w}^{(o)}$) and bias (b^o) of the RBFN output layer are updated to minimize the MSE considering the training data set. Once the V RBFNs and their corresponding MSEs are obtained, the best one is selected. For this selection, V MSEs are computed considering the validation data set and the parameters ($\mathbf{R}$, $\mathbf{w}^{(o)}$, b^o) found for each of the V variances. Finally, the best variance is chosen according the variance for which the minimum of these MSEs is obtained.

Next, the way to obtain $\mathbf{w}^{(o)}$ and b^o for a given variance is discussed. For this purpose, let's consider the RBFN output of Eq. (6.7), which is rewritten as

$$x^{(o)}[n] = \sum_{i=1}^{H} w_i^{(o)} g\left(|\mathbf{z}[n] - \mathbf{r}_i|^2_{\mathbf{C}_i}\right) + b^{(o)} . \tag{6.17}$$

Consider also that both the bias and weights of the RBFN output layer are stored in the row vector $\widetilde{\mathbf{w}}^{(o)} = [b^{(o)}\, w_1^{(o)} \dots w_H^{(o)}]$. Moreover, consider that the output of the i-th RBF for the n-th observation vector is denoted as

$$g_i[n] = g\left(|\mathbf{z}[n] - \mathbf{r}_i|^2_{\mathbf{C}_i}\right) . \tag{6.18}$$

Thus, a new column vector can be composed considering all the RBF outputs (output neuron inputs) for the n-th instant, being $\mathbf{g}[n] = [1\, g_1[n] \dots g_H[n]]^{\mathrm{T}}$. Note that a unit input is considered for the bias because $b^{(o)}$ and $\mathbf{w}^{(o)}$ are adapted at the same time. Considering a matrix notation by using $\widetilde{\mathbf{w}}^{(o)}$ and $\mathbf{g}[n]$ in Eq. (6.17), we obtain

$$\widetilde{\mathbf{w}}^{(o)} \mathbf{g}[n] = x^{(o)}[n] , \tag{6.19}$$

where a system of $H+1$ equations is set to find the $H+1$ parameters (bias and weights) that compose the output layer of the RBFN ($\widetilde{\mathbf{w}}^{(\mathrm{o})}$).

As set at the beginning of this section, the objective during the RBFN training is minimizing the MSE of Eq. (6.12) for a given training data set. In this case, a set of P pre-classified observation vectors ($\mathbf{Z} = [\mathbf{z}[1]\,\mathbf{z}[2]\ldots\mathbf{z}[P]]$), with their corresponding desired outputs ($\mathbf{d} = [d[1]\,d[2]\ldots d[P]]$), is available. This set is processed obtaining the corresponding P RBFN outputs ($\mathbf{x}^{(\mathrm{o})} = [x^{(\mathrm{o})}[1]\,x^{(\mathrm{o})}[2]\ldots x^{(\mathrm{o})}[P]]$), considering that the centroids and covariance matrixes of the RBFN are fixed. Thus, according to $\mathbf{x}^{(\mathrm{o})}$ and $\mathbf{d}$, the MSE can be rewritten in matrix notation as [Bishop1995]

$$E_{\mathrm{MS}} = \frac{1}{2P}(\mathbf{x}^{(\mathrm{o})} - \mathbf{d})(\mathbf{x}^{(\mathrm{o})} - \mathbf{d})^{\mathrm{T}}\,, \tag{6.20}$$

Since the objective is minimizing the MSE for a given data set in a batch mode, the system of equations given in Eq. (6.19) is rewritten taking into account the RBF outputs for all the observation vectors and all the RBFN outputs as

$$\widetilde{\mathbf{w}}^{(\mathrm{o})}\mathbf{G} = \mathbf{x}^{(\mathrm{o})}\,, \tag{6.21}$$

where $\mathbf{G}$ is a matrix of size $[H \times P]$ containing all the outputs of the RBFs for all the observation vectors ($\mathbf{G} = [\mathbf{g}[1]\,\mathbf{g}[2]\ldots\mathbf{g}[P]]$).

Finally, the unknown parameters that minimize the MSE, i.e. $\widetilde{\mathbf{w}}^{(\mathrm{o})}_{\mathrm{min}}$, can be achieved from the following system of equations:

$$\frac{\partial E_{\mathrm{MS}}}{\partial \widetilde{w}_u^{(\mathrm{o})}} = 0\,,\ u = 0, 1, 2\ldots H\ \rightarrow\ \widetilde{\mathbf{w}}^{(\mathrm{o})}_{\mathrm{min}}\,. \tag{6.22}$$

Applying the least squares linear discriminant analysis [Hastie2001], these parameters can found by

$$\widetilde{\mathbf{w}}^{(\mathrm{o})}_{\mathrm{min}} = \mathbf{d}\mathbf{G}^{T}\left(\mathbf{G}\mathbf{G}^{T}\right)^{-1}\,. \tag{6.23}$$

Other non-linear activation functions could be used in the output neuron. But, in this case, the search of the output layer parameters is not a linear problem, requiring non-linear optimization techniques, with the associated computational cost increase.

6.4 RBFN-based detector computational cost

Not only the performance evaluations of the RBFN-based processor in terms of MSE (see Eq. (6.11)) and RBFN-based detector in terms of P_{fa}-P_{d} (see Sect. 4.4) are important, but also its computational cost. The computational cost of its core, i.e. the RBFN-based processor, is analyzed here because this is the only block in the RBFN-based detector which size varies in the studies of the thesis.

The computational cost of a $K/H/1$ RBFN is presented in terms of:

- Number of memory registers needed to store:
  - the centroids: HK registers;
  - the covariance matrixes: KK registers, considering that the covariance matrix of each RBF is equal to the matrix given in Eq. (6.16); and

  - the weights and bias of the output layer: H and 1 registers, respectively.

- Number of products of two elements to compute:
  - all the RBF outputs: $H(KK+K)$ products from Eq. (6.4) and H products from the factor $1/2$ of Eq. (6.5); and
  - the RBFN output: H products from Eq. (6.7).

- Number of sums of two elements to compute:
  - all the RBF outputs: $H((K-1)K+(K-1))$ sums from Eq. (6.4); and
  - the RBFN output: H sums from Eq. (6.7).

- Number of evaluations of the activation function of each (hidden or output) neuron: $H+1$. Note that, in a general case, the evaluation of the linear activation function of the output neuron is also considered.

The computational cost presented above is given for each CUT.

The computational cost of the RBFN-based processor per CUT is summarized in Eq. (6.24)-(6.27).

$$\text{RBFN memory registers}: \quad H(K+1)+KK+1 \tag{6.24}$$

$$\text{RBFN products}: \quad H(KK+K+2) \tag{6.25}$$

$$\text{RBFN sums}: \quad H(KK+1) \tag{6.26}$$

$$\text{Activation function evaluations}: \quad H+1 \tag{6.27}$$

Part III

Research and Results

CHAPTER 7

Dimension and Composition of the Synthetic and Real-live Databases

This chapter is focused on two aims. The first one focuses on the dimension of the databases used in the experiments of the thesis, i.e. the number of radar scans that composes each database. The database dimension study is made because a minimum accuracy in the estimations of the MSE and ROC curves (P_{fa} and P_{d}) is needed. The second one is focused on the composition of the database, i.e. the radar environmental conditions used in the experiments. These two aims are studied for synthetic and real-live radar databases.

7.1 Dimension and composition of synthetic databases

Due to synthetic databases can be created as needed, their dimensions and compositions are studied in this section. These studies are done regardless of the arithmetic of the received radar data (coherent or incoherent). We consider radar scans of size $[K_{\text{a}} \times K_{\text{r}}]$ in the next studies, where K_{a} azimuth bins and K_{r} range sweeps are available in each one. In this case, a total of $K_{\text{a}}K_{\text{r}}$ observation vectors can be obtained. According to the number of available observation vectors from each radar scan, we study the minimum number of observation vectors needed in the database in order to have accurate estimations of certain parameters during the design and test stages of the reference and proposed detectors.

7.1.1 Dimension of synthetic databases: Sizes of train, validation and test data sets

In this section, the number of synthetic radar scans that composes the synthetic databases used in the thesis is studied. The sizes of the databases are the same for all the radar environments (clutter conditions), regardless of the arithmetic of the received radar data (coherent or incoherent radar systems). Due to the use of supervised learning algorithms to design AI-based detectors (see Sect. 5.3 in page 82 and Sect. 6.3 in page 97), the database of synthetic radar scans must be divided into three data sets: one for training purposes (design stage), other for validation purposes (design stage) and the remaining one for testing purposes (test stage). Since different kind of detectors must be designed and tested (TSKAP, CFAR and AI-based detectors), each

data set contains a certain number of radar scans and is used for different purposes:

- The *train data set* is used in the design stage of the TSKAP, CFAR and AI-based detectors. It is used for two main purposes. The first purpose is to design the non-linear prediction filters of the TSKAP coherent detector and to train the MLPs and RBFNs of the AI-based detectors. The second purpose is to estimate the threshold of each detector for each desired P_{fa}. This data set contains a total of $M^{(\text{d})}$ radar scans. This number of radar scans is mainly conditioned by the second purpose. Exactly, it is conditioned by the minimum P_{fa} to be estimated for which the threshold must be set. It is worth mentioning that for design the non-linear filters or processors of the different detectors, not all the radar scans are used. In this case, during the MLP or RBFN training, the minimum MSE to be estimated determines the number of used radar scans. And since this minimum MSE is not so low as the minimum P_{fa}, not so many radar scans are needed for this purpose. These aspects will be discussed with more detail when the exact number of radar scans that compose this data set is obtained.

- The *validation data set* is also used in the design stage of the TSKAP, CFAR and AI-based detectors. It is used for three main purposes. The first purpose is to validate the design of the non-linear prediction filters of the TSKAP detector, as well as in the external validation of the MLP or RBFN learning processes. The second purpose is to select which is the best MLP-based detector of the 10 trained MLPs, mitigating the dependency of the MLP training with respect to their initial conditions. The same is done for the RBFN-based detector design. And the third purpose is to validate the TSKAP, CFAR and AI-based detectors once designed as a whole, i.e. once the filters or processors are designed and the thresholds are set. This data set is composed of $M^{(\text{v})}$ radar scans. This number is determined by the minimum P_{fa} to be estimated. Again, just only a few of these $M^{(\text{v})}$ radar scans are used during the external validation process of the learning algorithm. Finally, the radar scans of the validation data set are different of the ones used in the train data set, although its statistical properties can be the same.

- The *test data set* is only used in the test stage of the TSKAP, CFAR and AI-based detectors. It is used for testing the performance of these designed detectors in environmental conditions equal or different of the ones used in the design stage. With this test we want to know whether the performance of the detectors in the design stage are maintained or not in the test stage. This data set is composed of $M^{(\text{t})}$ radar scans. In this case, this number is only limited by the accuracy of the ROC curve estimations. These radar scans are always different to the ones used in the train and validation data sets, although its statistical properties can be the same.

The MSE goal during the MLP or RBFN train is set to 10^{-4} and the maximum relative error in its estimation by Monte Carlo simulations is set to 10%. Under these constraints, a minimum of $m = \frac{1}{0.1^2 \text{MSE}} = \frac{100}{10^{-4}} = 10^6$ cells under H_1 and H_0 hypotheses (in total) are approximately needed [Gentle2003]. The designer of the detectors could use more data to reduce the relative error of the MSE, but the train of MLPs and RBFNs will take long time. Nevertheless, this MSE goal can be considered good enough to achieve high performance AI-based detectors, as the results presented in the thesis support.

Table 7.1: Sizes of the different targets considered in the studies of the thesis.

	Physical sizes of targets		Target sizes in resolution	
	Length	Width	Range dir.	Azimuthal dir.
		Sea clutter conditions		
Maximum:	54 m	9 m	12 cells	12 cells
Minimum:	18 m	3 m	4 cells	4 cells
		Sea-ice clutter conditions		
Maximum:	60 m	23 m	10 cells	10 cells
Minimum:	12 m	9 m	2 cells	2 cells
		Ground clutter conditions		
Maximum:	248 m	120 m	4 cells	4 cells
Minimum:	67 m	25 m	1 cell	1 cell

The accuracy for estimating ROC curves by Monte Carlo simulations during the design and test stages is set to a maximum of 10% of the relative error of the estimated probabilities. Note that for a given data set, the lower the probabilities to estimate, the higher the relative error. Since the minimum P_{fa} to be estimated in both stages is 10^{-5}, where P_{d}'s in the range $[0.1-1]$ are usually achieved, the limitation of the relative error is set by the estimation of this P_{fa} because the relative error of the P_{d}'s is lower than for the P_{fa}. Therefore, a minimum of $m = \frac{1}{0.1^2 P} = \frac{100}{P}$ cells are needed for estimating the probability P with the required accuracy [Ravid1992]. Considering the minimum P_{fa}, i.e. $P_{\text{fa}} = 10^{-5}$, $m_{H_0} = 10^7$ cells under H_0 are needed in each data set. On the other hand, considering the minimum P_{d}, i.e. $P_{\text{d}} = 10^{-1}$, a minimum of $m_{H_1} = \frac{1}{0.1^2 P_{\text{d}}} = 10^3$ cells under H_1 are need for P_{d} estimations.

The synthetic scans considered in each data set contain a variable number of Swerling 0 targets in movement, where different positions, shapes and sizes are considered. Table 7.1 presents the different sizes used in the experiments. For creating this table, the cell resolutions of the different radar models under study are considered, being given in Table 2.2 for sea clutter, in Table 2.4 for sea-ice clutter and in Table 2.6 for ground clutter.

Jarabo et al. demonstrated in [Jarabo2009] that AI techniques, such as MLPs and RBFNs, allow to create a detector that approximates the Neyman-Pearson detector. Moreover, they also presented a relationship between the thresholds needed in the likelihood ratio detector, THR_{LR}, and in the AI-based detectors, THR. This relationship was found to be related to: the prior probabilities of the hypothesis H_0 and H_1 ($P(H_0)$ and $P(H_1)$, respectively); and the desired output of the AI technique for observation vectors under hypothesis H_0 and H_1 (t_{H_0} and t_{H_1}, respectively). This relationship is [Jarabo2009]:

$$\text{THR} = \frac{\text{THR}_{\text{LR}} P(H_1) t_{H_1} + P(H_0) t_{H_0}}{\text{THR}_{\text{LR}} P(H_1) + P(H_0)} \,. \tag{7.1}$$

Since THR_{LR} is fixed by the statistical distributions of the processes under H_0 and H_1 in the Neyman-Pearson detector (see Eq. (3.8)) and t_{H_0} and t_{H_1} are fixed once the architecture

of the AI techniques is set, we study the influence of $P(H_0)$ and $P(H_1)$ in THR. For doing so, let's suppose the following example taken from the experiments made in the thesis: for a given pair of likelihood functions, $f(\mathbf{z}|H_0)$ and $f(\mathbf{z}|H_1)$, we need a threshold of $\text{THR}_{\text{LR}} = 9.0$ in the Neyman-Pearson detector for obtaining $P_{\text{fa}} = 10^{-4}$. Let's also consider that an MLP is used to create the AI-based detector, where hyperbolic tangent functions are used as activation functions in its neurons (see Eq. (5.7)), for which the desired outputs are $t_{H_0} = -1$ and $t_{H_1} = +1$.

Next, the study of the dependence of THR with respect to $P(H_0)$ and $P(H_1)$ is presented. First, this study is presented from a general point of view, and second, it is particularized for the case of study presented above. To make this study, we use the work of Jarabo et al. presented in [Jarabo2005b], where the sensitivity of the P_{fa} and P_{d} ($P_i, i = 0, 1$) with respect to THR was set. Considering the nomenclature used in the thesis, this sensitivity is given by:

$$\frac{\partial P_i}{\partial \text{THR}} = \frac{\partial P_i}{\partial \text{THR}_{\text{LR}}} \frac{\partial \text{THR}_{\text{LR}}}{\partial \text{THR}}, \quad i = 0, 1. \tag{7.2}$$

The first partial derivative of the right side of Eq. (7.2) depends on the likelihood ratio detector and cannot be modified for given likelihood functions, being a constant $K = \frac{\partial P_i}{\partial \text{THR}_{\text{LR}}}$ in our case of study. The second partial derivative of the right side of Eq. (7.2) is given in Eq. (7.3) [Jarabo2005b]. It is observed that it depends on the prior probabilities and the desired outputs selected for training, factors that can be controlled by the designer, and THR.

$$\frac{\partial \text{THR}_{\text{LR}}}{\partial \text{THR}} = \frac{P(H_0)}{P(H_1)} \frac{(t_{H_1} - t_{H_0})}{(t_{H_1} - \text{THR})^2}. \tag{7.3}$$

According to Eq. (7.3), this sensitivity can be decreased by: increasing $P(H_1)$ (decreasing $P(H_0)$), and/or decreasing THR (increasing $(t_{H_1} - \text{THR})^2$). From Eq. (7.1) we obtain that the rate between the prior probabilities is related to THR as follows:

$$\frac{P(H_0)}{P(H_1)} = \frac{t_{H_1} - \text{THR}}{\text{THR} - t_{H_0}} \text{THR}_{\text{LR}}. \tag{7.4}$$

Introducing Eq. (7.4) into Eq. (7.3), we get that

$$\frac{\partial \text{THR}_{\text{LR}}}{\partial \text{THR}} = (t_{H_1} - t_{H_0}) \text{THR}_{\text{LR}} \frac{1}{(\text{THR} - t_{H_0})(t_{H_1} - \text{THR})}, \tag{7.5}$$

where $(t_{H_1} - t_{H_0})\text{THR}_{\text{LR}}$ is equal to a constant C once selected the activation functions of the MLP and for a given pair of likelihood functions. Concluding, it is observed that the sensitivity of the probabilities with respect to the threshold in the MLP-based detector depends directly on two constants K and C, which depend on the problem and MLP configuration, and inversely on THR as:

$$\frac{\partial P_i}{\partial \text{THR}} = KC \frac{1}{(\text{THR} - t_{H_0})(t_{H_1} - \text{THR})}, \quad i = 0, 1. \tag{7.6}$$

Considering the case of study taken as example, where $\text{THR}_{\text{LR}} = 9.0$, and $t_{H_0} = -1$ and $t_{H_1} = +1$, we get that the constant $C = 18.0$. Moreover, for simplicity, we suppose that $K = \frac{\partial P_i}{\partial \text{THR}_{\text{LR}}} = 1.0$ in this case of study. Therefore, evaluating Eq. (7.6) for different values of THR, we get the plot of Fig. 7.1. As can be observed from this plot, the minimum sensitivity can be obtained for $\text{THR} = 0$. But once known the best value of THR to minimize this sensitivity,

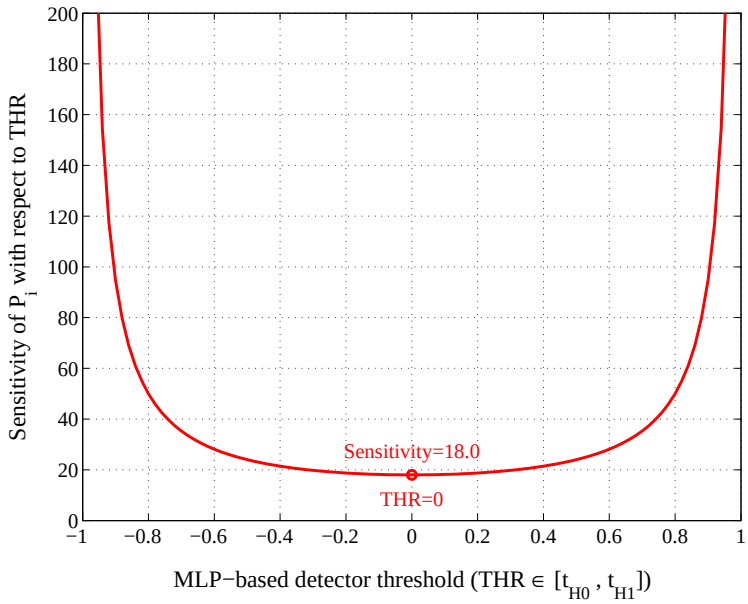

Figure 7.1: Sensitivity of the probabilities to be estimated ($P_{\rm d} = P_1$ and $P_{\rm fa} = P_0$) with respect to the threshold used in the MLP-based detector.

we have to set the prior probabilities for dimensioning the databases. Particularizing Eq. (7.1) for $t_{H_0} = -1$, $t_{H_1} = +1$ and THR $= 0$, we obtain:

$$0 = \frac{\mathrm{THR}_{\rm LR} P(H_1) - P(H_0)}{\mathrm{THR}_{\rm LR} P(H_1) + P(H_0)} \quad \rightarrow \quad P(H_0) = \mathrm{THR}_{\rm LR} P(H_1)\,. \tag{7.7}$$

Moreover, knowing that $P(H_1) = 1 - P(H_0)$, we have that $P(H_0)$ is related to $\mathrm{THR}_{\rm LR}$ as:

$$P(H_0) = \frac{\mathrm{THR}_{\rm LR}}{1 + \mathrm{THR}_{\rm LR}}\,. \tag{7.8}$$

Considering the value set for the selected example ($\mathrm{THR}_{\rm LR} = 9.0$ for $P_{\rm fa} = 10^{-4}$), the prior probabilities under H_0 and H_1 for working with a threshold that allows to achieve the lowest sensitivity are: $P(H_0) = 0.90$ and $P(H_1) = 0.10$. Even when this values are obtained for a given example, it is observed that similar prior probabilities were used by Sekine et al. in [Sekine1990] to design TSKAP detectors. Therefore these prior probabilities are taken for dimensioning the synthetic databases used in the thesis.

The dimensioning of the synthetic databases is established by the values of m_{H_0} and m_{H_1}, values that must be selected for fulfilling the selected prior probabilities. Taking into account that the strongest restriction in selecting the values of m_{H_0} and m_{H_1} belongs to the estimation of $P_{\rm fa}$, the number of CUTs under H_0 is set to $m_{H_0} = 10^7$. Therefore, the total number of CUTs is $\frac{m_{H_0}}{P(H_0)} = \frac{10^7}{0.9}$. It involves that we approximately need $m_{H_1} = \frac{10^7}{0.9} - 10^7 \sim 0.11 \cdot 10^7$ CUTs under H_1. On the other hand, and since each radar scan is of size $[K_{\rm a} \times K_{\rm r}]$, a total of $K_{\rm a} K_{\rm r}$ cells can be extracted. Taking into account the total number of CUTs needed, the minimum number of

Table 7.2: Number of radar scans in each data set depending on the radar configuration used in the different synthetic clutter conditions under study

	Sea clutter	Sea-ice clutter	Ground clutter
	Size of Radar Scans		
	(from Table 2.2)	(from Table 2.4)	(from Table 2.6)
(azimuth bins) K_{a}	256	250	228
(range bins) K_{r}	427	256	45
(train) $M^{(\mathrm{d})}$	10 scans	16 scans	98 scans
(threshold setting) $M^{(\mathrm{d})}$	102 scans	174 scans	1,083 scans
(ext. validation during training) $M^{(\mathrm{v})}$	10 scans	16 scans	98 scans
(validating designed detector) $M^{(\mathrm{v})}$	102 scans	174 scans	1,083 scans
(test) $M^{(\mathrm{t})}$	102 scans	174 scans	1,083 scans

radar scans of each data set is:

$$M^{(\mathrm{d})} = M^{(\mathrm{v})} = M^{(\mathrm{t})} = \left\lceil \frac{\frac{10^7}{0.9}}{K_{\mathrm{a}} K_{\mathrm{r}}} \right\rceil , \tag{7.9}$$

where $\lceil \cdot \rceil$ denotes the nearest integer greater than or equal to the value of this division.

Note that the number of radar scans given in Eq. (7.9) is determined by the accuracy of the lowest P_{fa} estimation for which the threshold must be set. Nevertheless, not all the radar scans of the train and validation data sets must be used in the train stage (MSE goal is 10^{-4}). In this case, only

$$M^{(\mathrm{d})} = M^{(\mathrm{v})} = \left\lceil \frac{10^6}{K_{\mathrm{a}} K_{\mathrm{r}}} \right\rceil \tag{7.10}$$

radar scans are needed. Thus, from the radar scans used in the design stage and given in Eq. (7.9), just only the number of radar scans given in Eq. (7.10) are needed for training MLPs and RBFNs. They are randomly selected when the statistical properties are equal scan-to-scan. On the other hand, they are strategically selected when they are different scan-to-scan. This strategic selection is made taking into account that radar scans with different clutter parameters must be considered in the train and validation data sets.

Depending on the configuration of the radar used to measure each kind of clutter (see tables 2.2, 2.4 and 2.6), different numbers of azimuth (K_{a}) and range (K_{r}) bins per scan are used. These values are summarized in Table 7.2. Taking into account Eq. (7.9)-(7.10), this table also presents the number of radar scans needed in each data set for each kind of clutter.

7.1.2 Composition of the synthetic databases: Statistical properties of the train, validation and test data sets

As established in the previous section, the synthetic database is divided in three different data sets, independently of the kind of radar (coherent or incoherent) and clutter (sea, sea-ice or

Table 7.3: Statistical properties of the data sets for different experimental conditions (i denotes the statistical properties of the i-th radar scan and varies from 1 to $M^{(\mathrm{d})}$, $M^{(\mathrm{v})}$ or $M^{(\mathrm{t})}$, depending on the data set). When the skewness is randomly distributed, it varies in the range $a_i \in [a_{\min}\,,\, a_{\max}]$.

	Design Conditions		Test Conditions
Experimental conditions	Train Data Set	Validation Data Set	Test Data Set
Minimum conditions	$a_i^{(\mathrm{d})} = a_{\min}$	$a_i^{(\mathrm{v})} \sim \mathrm{N}(\mu_a, \sigma_a^2)$	$a_i^{(\mathrm{t})} \sim \mathrm{N}(\mu_a, \sigma_a^2)$
Typical conditions	$a_i^{(\mathrm{d})} = a_{\mathrm{typ}}$	$a_i^{(\mathrm{v})} \sim \mathrm{N}(\mu_a, \sigma_a^2)$	$a_i^{(\mathrm{t})} \sim \mathrm{N}(\mu_a, \sigma_a^2)$
Maximum conditions	$a_i^{(\mathrm{d})} = a_{\max}$	$a_i^{(\mathrm{v})} \sim \mathrm{N}(\mu_a, \sigma_a^2)$	$a_i^{(\mathrm{t})} \sim \mathrm{N}(\mu_a, \sigma_a^2)$
Practical conditions	$a_i^{(\mathrm{d})} \sim \mathrm{N}(\mu_a, \sigma_a^2)$	$a_i^{(\mathrm{v})} \sim \mathrm{N}(\mu_a, \sigma_a^2)$	$a_i^{(\mathrm{t})} \sim \mathrm{N}(\mu_a, \sigma_a^2)$

ground). In the current section, the statistical properties considered in each data set are studied. As observed from the environmental conditions of sea (see Table 2.3), sea-ice (see Table 2.5) and ground (see Table 2.7) clutters, the only parameter that varies in the clutter model is the skewness parameter (a) of the Weibull distribution. The scale parameter (b) of the Weibull clutter also varies with a for obtaining a desired clutter power. The other parameters of the clutter (CNR, f_{c}, ρ_{c}) remain constant in the studies of the thesis. Let's denote as $a^{(\mathrm{d})}$, $a^{(\mathrm{v})}$ and $a^{(\mathrm{t})}$ the skewness parameters that model the clutter in the radar scans of the train, validation and test data sets, respectively. Let's apply the same nomenclature for the scale parameter, being $b^{(\mathrm{d})}$, $b^{(\mathrm{v})}$ and $b^{(\mathrm{t})}$ for these sets, respectively.

In order to find which are the best design conditions related to the clutter properties, let's define four experimental conditions: minimum, typical, maximum and practical conditions. Each experimental condition is defined by different clutter conditions. Because temporal fluctuation is assumed for the radar scans of a given data set, the statistical properties of the clutter in the i-th radar scan of a set of M scans vary. The variation of the skewness parameter follows a normal distribution with mean μ_a and variance σ_a^2 ($\mathrm{N}(\mu_a, \sigma_a^2)$) and take values in the range $a_i \in [a_{\min}\,,\, a_{\max}]$. And since the scale parameter is related to the skewness parameter, this parameter also follows a normal distribution of mean μ_b and variance σ_b^2 ($\mathrm{N}(\mu_b, \sigma_b^2)$) and take values in the range $b_i \in [b_{\min}\,,\, b_{\max}]$, $i = 1, 2 \ldots M$. Table 7.3 presents the values of a used for each experimental condition. To simplify the formulation of the problem, the values of b are not presented in the table because they are given in tables 2.2, 2.4 and 2.6 for each kind of clutter.

It is important to note that the first three design (train) conditions of Table 7.3 can be used for designing TSKAP, CFAR and AI-based detectors because the value of $a^{(\mathrm{d})}$ is the same for all the radar scans of this data set. But, the last design conditions (practical conditions) can only be used for design CFAR and AI-based detectors. It is due to the necessity of knowing a priori the value of the skewness parameter of the Weibull clutter to design the TSKAP detector. Therefore, since this value is varied in the practical conditions and not known a priori for each radar scan, this detector cannot be designed correctly.

Finally, note that since the first objective of the thesis is focused on studying the properties

Table 7.4: Properties of the targets considered in the train, validation and test data sets

Target Type		Swerling 0
Target Doppler Frequency	f_t	$0.2 \times$ PRF
One-lag Target Corr. Coef.	ρ_t	1.0
Signal-to-Noise Ratio	SNR	40.0 dB
Signal-to-Clutter Ratio	SCR	10.0 dB

of the designed detectors against changes in clutter conditions, the target conditions are fixed to generate the three data sets. Moreover, when the TSKAP detector is designed, these conditions must be fixed because the TSKAP detector needs to know the target sequence, as depicted in Fig. 3.3. The target conditions considered in the data sets are given in Table 7.4 and discussed below. Since the target model considered in the thesis is the Swerling 0, the one-lag correlation coefficient of the target sequence is the unity, i.e. all the consecutive cells concerning to a target are completely correlated, having all of them the same amplitude. Since targets in movement are considered in the thesis, a non-null Doppler frequency is selected. A Doppler frequency of $0.2 \times$ PRF is selected because poorer TSKAP detector performances are achieved for lower Doppler frequencies, and vice versa [Farina1986a, Farina1987b, Farina1987b]. The SCR is fixed to have a signal power 10 dB greater than clutter power. If higher SCR values are used, better performances are expected, and vice versa. With this value of SCR, critical results are achieved for the TSKAP detector [Farina1987a]. In this way, we can realize whether the proposed AI-based detectors outperform the reference detectors or not. Finally, a high value of SNR (40 dB) is selected because the clutter power must be much higher than the noise power in order to make the TSKAP works properly, as discussed in [Farina1987a].

7.1.3 Dimension and composition of the data sets when sea, sea-ice and ground clutter conditions are present

The dimension and composition of the synthetic databases used in the experiments of the thesis are presented in this section for the three different kinds of clutter under study. Table 7.2 summarizes the number of radar scans needed in each data set of each database, and Table 7.3 presents the statistical properties needed for each radar scan of the data sets when different experimental conditions are considered, independently of the kind of clutter. Taking into consideration both tables, Table 7.5 summarizes the number of radar scans and the statistical properties of the radars scans of the three data sets used in the different experimental conditions considered in the sea clutter studies. The same information is given in tables 7.6 and 7.7 for the sea-ice and ground clutter studies, respectively.

Table 7.5: Statistical properties and number of scans in the data sets used for the different experimental conditions considered in the thesis when synthetic sea clutter is used. When the skewness is randomly distributed, it varies in the range $a_i \in [4.11\,,\,5.17]$.

	Design Conditions		Test Conditions
Experimental conditions	Train Data Set	Validation Data Set	Test Data Set
	($M^{(\mathrm{d})} = 10$ Scans)	($M^{(\mathrm{v})} = 10$ Scans)	($M^{(\mathrm{t})} = 102$ Scans)
Minimum conditions	$a_i^{(\mathrm{d})} = 4.11$	$a_i^{(\mathrm{v})} \sim \mathrm{N}(4.46, 0.12)$	$a_i^{(\mathrm{t})} \sim \mathrm{N}(4.46, 0.12)$
Typical conditions	$a_i^{(\mathrm{d})} = 4.46$	$a_i^{(\mathrm{v})} \sim \mathrm{N}(4.46, 0.12)$	$a_i^{(\mathrm{t})} \sim \mathrm{N}(4.46, 0.12)$
Maximum conditions	$a_i^{(\mathrm{d})} = 5.17$	$a_i^{(\mathrm{v})} \sim \mathrm{N}(4.46, 0.12)$	$a_i^{(\mathrm{t})} \sim \mathrm{N}(4.46, 0.12)$
Practical conditions	$a_i^{(\mathrm{d})} \sim \mathrm{N}(4.46, 0.12)$	$a_i^{(\mathrm{v})} \sim \mathrm{N}(4.46, 0.12)$	$a_i^{(\mathrm{t})} \sim \mathrm{N}(4.46, 0.12)$

Table 7.6: Statistical properties and number of scans in the data sets used for the different experimental conditions considered in the thesis when synthetic sea-ice clutter is used. When the skewness is randomly distributed, it varies in the range $a_i \in [0.50\,,\,1.65]$.

	Design Conditions		Test Conditions
Experimental conditions	Train Data Set	Validation Data Set	Test Data Set
	($M^{(\mathrm{d})} = 16$ Scans)	($M^{(\mathrm{v})} = 16$ Scans)	($M^{(\mathrm{t})} = 174$ Scans)
Minimum conditions	$a_i^{(\mathrm{d})} = 0.50$	$a_i^{(\mathrm{v})} \sim \mathrm{N}(1.20, 0.14)$	$a_i^{(\mathrm{t})} \sim \mathrm{N}(1.20, 0.14)$
Typical conditions	$a_i^{(\mathrm{d})} = 1.20$	$a_i^{(\mathrm{v})} \sim \mathrm{N}(1.20, 0.14)$	$a_i^{(\mathrm{t})} \sim \mathrm{N}(1.20, 0.14)$
Maximum conditions	$a_i^{(\mathrm{d})} = 1.65$	$a_i^{(\mathrm{v})} \sim \mathrm{N}(1.20, 0.14)$	$a_i^{(\mathrm{t})} \sim \mathrm{N}(1.20, 0.14)$
Practical conditions	$a_i^{(\mathrm{d})} \sim \mathrm{N}(1.20, 0.14)$	$a_i^{(\mathrm{v})} \sim \mathrm{N}(1.20, 0.14)$	$a_i^{(\mathrm{t})} \sim \mathrm{N}(1.20, 0.14)$

Table 7.7: Statistical properties and number of scans in the data sets used for the different experimental conditions considered in the thesis when synthetic ground clutter is used. When the skewness is randomly distributed, it varies in the range $a_i \in [1.50\,,\,2.00]$.

	Design Conditions		Test Conditions
Experimental conditions	Train Data Set	Validation Data Set	Test Data Set
	($M^{(\mathrm{d})} = 98$ Scans)	($M^{(\mathrm{v})} = 98$ Scans)	($M^{(\mathrm{t})} = 1,083$ Scans)
Minimum conditions	$a_i^{(\mathrm{d})} = 1.50$	$a_i^{(\mathrm{v})} \sim \mathrm{N}(1.76, 0.03)$	$a_i^{(\mathrm{t})} \sim \mathrm{N}(1.76, 0.03)$
Typical conditions	$a_i^{(\mathrm{d})} = 1.76$	$a_i^{(\mathrm{v})} \sim \mathrm{N}(1.76, 0.03)$	$a_i^{(\mathrm{t})} \sim \mathrm{N}(1.76, 0.03)$
Maximum conditions	$a_i^{(\mathrm{d})} = 2.00$	$a_i^{(\mathrm{v})} \sim \mathrm{N}(1.76, 0.03)$	$a_i^{(\mathrm{t})} \sim \mathrm{N}(1.76, 0.03)$
Practical conditions	$a_i^{(\mathrm{d})} \sim \mathrm{N}(1.76, 0.03)$	$a_i^{(\mathrm{v})} \sim \mathrm{N}(1.76, 0.03)$	$a_i^{(\mathrm{t})} \sim \mathrm{N}(1.76, 0.03)$

7.2 Dimension and composition of the real-live database

The database of real-live radar scans used in the thesis is composed of 12 different radar scan sequences. These sequences are acquired by the incoherent marine radar system presented in Sect. 2.4. All these sequences are different each other, including different types of ships and sea states (height, period, and character of waves on the surface of a large body of water). Different kind of ships are available in the database (see Sect. 2.5.1): general cargo ships, ferries, container ships and cruise ships, with widths in the range $[18, 35]$ m and lengths in the range $[120, 350]$ m. Sea states 1-5 of the World Meteorological Organization [WMO] are present in the sequences (see Sect. 2.5.2). Thus, this variability of sequences tries to cover the different conditions where the system usually works.

The way the synthetic databases are divided into three data sets to design, validate and test the detectors is also used to divide the real-live database. Thus, 8 of the original 12 sequences are used in the design stage: 4 to compose the train data set and 4 to compose the validation data set. The remaining 4 sequences are dedicated to compose the test data set. In each data set, two sequences are obtained when the marine radar is configured in low-resolution mode and the other two sequences are obtained when the radar is configured in high-resolution mode (see Table 2.8). The division of the database is summarized in Fig. 7.2.

On the one hand, according to the range resolution and azimuthal sampling period of the marine radar when it is configured in low-resolution mode, radar scans of size [1287 azimuth cells $\times$ 256 range cells] are obtained. Thus, a total of 2 seq. $\times$ 32 scans/seq. $\times$ (1287×256) cells/scans $\approx$ $21 \cdot 10^6$ cells are available from the two sequences of radar scans of this type in each data set. On the other hand, according to the range resolution and azimuthal sampling period of the marine radar when it is configured in high-resolution mode, radar scans of size [1060 azimuth cells $\times$ 256 range cells] are obtained. Thus, a total of 2 seq. $\times$ 32 scans/seq. $\times$ (1060×256) cells/scans $\approx$ $17 \cdot 10^6$ cells are available from the two sequences of radar scans of this type in each data set. Therefore, a total of $\approx 38 \cdot 10^6$ cells are available in each data set.

According to the composition of the different data sets, two important aspects are emphasized. First, the dimension of the data sets (number of cells) is suitable to achieve high estimation accuracies. The following accuracies are achieved in the different stages:

- In the design stage: a minimum MSE estimation of $\approx 1.2 \cdot 10^{-4}$ with a maximum relative error of 10% can be achieved by using the $\approx$ 850000 cells obtained after applying the selection of cells presented in Sect. 4.5 for training MLPs and RBFNs. On the other hand, using all the cells of the validation data set ($\approx 38 \cdot 10^6$), P_{fa}'s up to $\approx \frac{100}{38 \cdot 10^6} \approx 2.6 \cdot 10^{-6}$ can be estimated with a maximum relative error of 10%.

- In the test stage: $\approx 38 \cdot 10^6$ cells are used for estimating the P_{fa} and P_{d} during the test of the CFAR and AI-based detectors. In this case, P_{fa}'s up to $\approx 2.6 \cdot 10^{-6}$ can be estimated with a maximum relative error of 10%.

And second, since the test data set is composed of target (ship) and clutter (sea states) conditions different of the ones used for designing, the robustness of the detector against changes in the environmental conditions can be estimated.

Finally, due to the supervised training of the detectors and the estimation of their objective performances in both the design and test stages, the desired (ideal) output radar scans are needed.

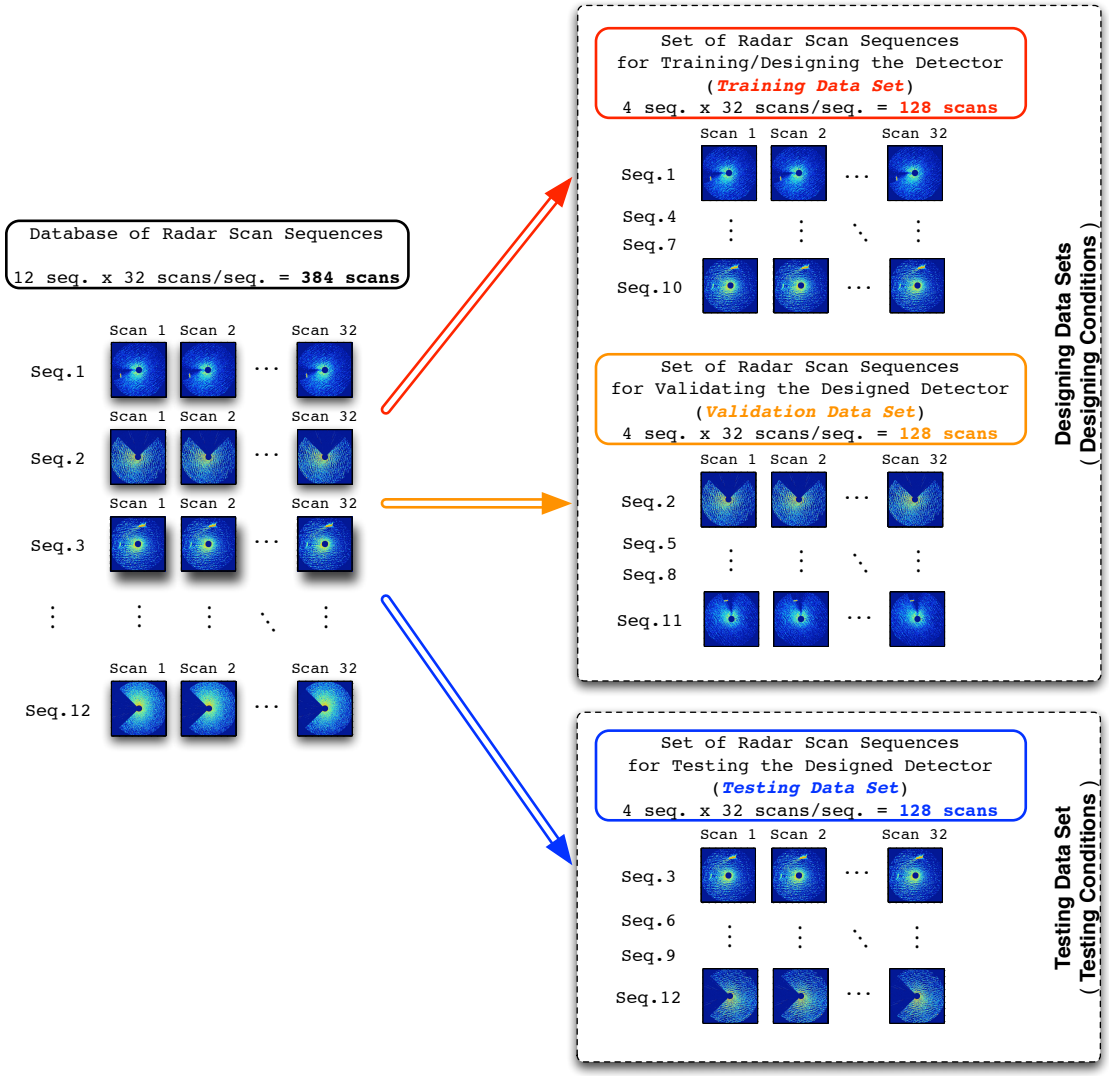

Figure 7.2: Database of real-live data achieved by the incoherent radar system

These ideal scans are obtained following the procedure explained in [Vicen2009a], consisting basically on three steps:

1. Statistical study of the length and width of the ship present on a given sequence.
2. Model the ship according to its average length and width. In this model, the edges are rounding to approximate to the real shape of the ship.
3. Manual superposition of the ship model obtained for this sequence in each radar scan until the model is correctly placed over the ship in radar scan.

The desired output radar scans are binary, indicating in each cell the existence of ship information by a unity value or the non-existence of ship information by a null value. An example of these desired output radar scans for a given input radar scan will be given in the section concerning to the results of processing real-live radar scans (see Sect. 11.1.4 in page 219).

CHAPTER 8

Coherent Detectors in Synthetic Clutter: Design and Test

This chapter presents the main aspects concerning to the design and test stages of the coherent detectors under study when processing synthetic radar scans. The chapter starts in Sect. 8.1 with an analysis of the performance decrease obtained in real-live situations with respect to theoretical/ideal situations. The chapter continues with an analysis of the performance of the detectors in design and test stages when three different environments are considered: sea clutter in Sect. 8.2, sea-ice clutter in Sect. 8.3, and ground clutter in Sect. 8.4. A study of the effect of the different parameters to be tuned in the detectors during the design stage is made first for each environment. Moreover, a study of the robustness of these detectors with respect to clutter condition changes is made in each case. Once the detector parameters are tuned, a test stage is used, where the performance with new radar scans is compared to the ones obtained in the design stage. After these studies, several conclusions are drawn for each environment. From these particular conclusions, it is observed that most of them are similar for the different environments, being summarized in Sect. 8.5. From these common conclusions, the advantages of the proposed AI-based coherent detectors are clearly observed.

8.1 From theoretical to practical situations

Several studies have approximated the performance of the detectors under study by analytical methods, but these approximations are only valid when all the cells of each observation vector belongs to either H_0 (absence of target) or H_1 (presence of target). As an example, in [Farina1987b, Sekine1990], the theoretical approximation to the performance of TSKAP detectors is given for different cases of study when coherent Weibull clutter is present. In [Vicen2006a, Vicen2007a, Vicen2007b, Vicen2007c], an empirical study of the performance of MLP-based detectors was presented under different coherent Weibull-distributed clutter conditions. But, these approximations are only valid if the observation vectors contain only information from the null hypothesis (all the cells contain only clutter and noise) or from the alternative hypothesis (all the cells contain information of target, clutter and noise). This situation is called in the thesis theoretical situation. But, what does it happen if the observation vectors contain cells belonging to both hypotheses? This is what happens in practical situations, as depicted in Fig. 8.1. This

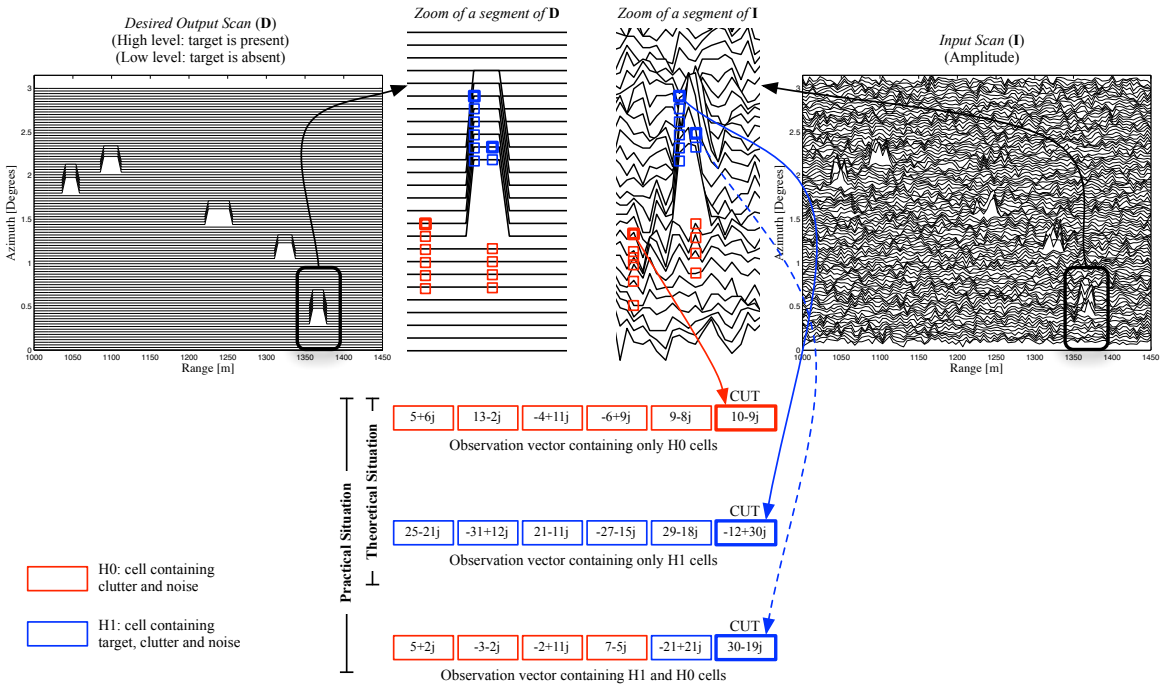

Figure 8.1: Observation vectors under theoretical and practical situations.

figure shows three examples of the different possibilities we can find: all the cells belong to H_0 (low level in the desired output scan of Fig. 8.1), all the cells belong to H_1 (low level in the desired output scan of Fig. 8.1) and a mixture of cells belonging to H_0 and H_1. Moreover, note that only the amplitude of the complex-valued radar scans is plotted for simplicity, although the coherent data are given in the observation vectors.

In order to realize the importance of these data combinations in practical situations and its effect in the performance of the detectors under study, let's consider the situation where sea clutter measurements are obtained by a coherent radar. For this purpose, let's consider the target conditions presented in Table 7.4 and the typical clutter conditions presented in Table 7.5 for sea clutter. Moreover, let's consider the detectors are designed for a non-delayed azimuthal selection mode, where $N = 6$ cells are integrated. Taking into account that MLPs and RBFNs work with real arithmetic and considering they have 20 hidden neurons for this study, the used MLPs and RBFNs have a structure 12/20/1. The performance achieved by these detectors for theoretical and practical situations are presented in Fig. 8.2. As observed in this figure, a performance decrease is achieved. It is due to the combination of data of both hypotheses in some observation vectors extracted from the radar scans. These observation vectors are extracted from the target-clutter boundaries.

8.2 Coherent Detectors in Synthetic Sea Clutter

This section is dedicated to study the design of coherent detectors when synthetic sea clutter conditions are considered. During the design of the coherent detectors under study, i.e. TSKAP

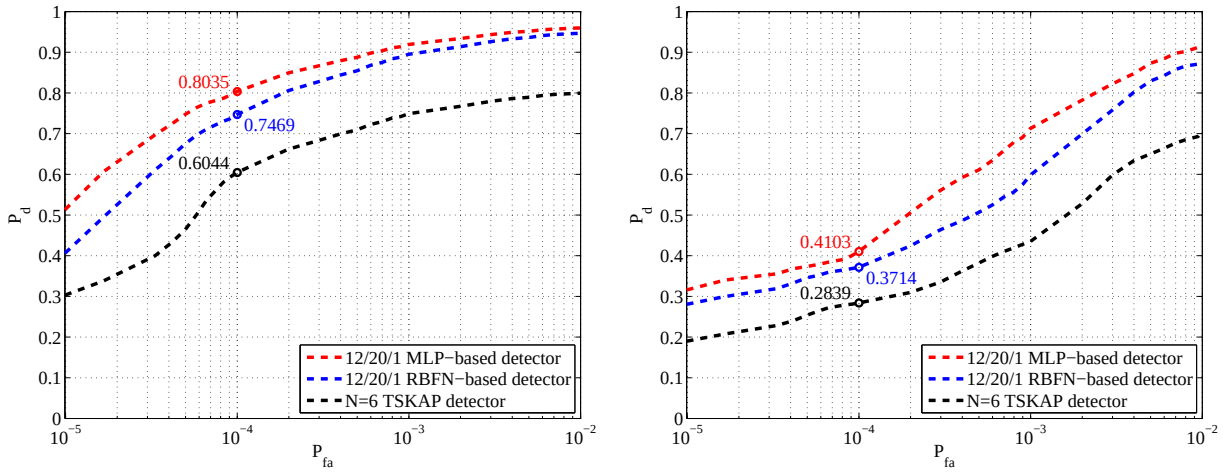

(a) Theoretical situations (b) Practical situations

Figure 8.2: Performance of TSKAP, MLP and RBFN-based detectors selecting $N = 6$ cells by a non-delayed azimuthal selection mode when typical sea clutter conditions are used. The ROC curves are achieved in the test stage. Theoretical situations (all the cells belong to H_0 or H_1 in a given observation vector) and practical situations (for some observation vectors, some cells belong to H_0 and others to H_1) are considered and compared.

and AI-based coherent detectors, some parameters must be tuned to find the values that maximize the performance of the detectors. Thus, the detectors are designed considering:

- Different environmental (clutter) conditions, as set in Table 7.5.
- Constant target conditions (see Table 7.4) because the aim of the thesis is to study the performance of the detectors against changes in clutter conditions.
- Different selection modes, as presented in Sect. 4.2.
- Different number of selected cells for each selection mode.
- And different number of hidden neurons in the MLPs and RBFNs that form the proposed AI-based coherent detectors.

The selection of the best value of these parameters is made during the design stage, for which the training and validation data sets of Table 7.5 are used. These data sets are generated once for all the experiments made during the design of TSKAP and AI-based coherent detectors in synthetic sea clutter. The performance of the processors and detectors presented in this section and its subsections are given for the validation data set. This performance is given in terms of average SCR improvement ($\text{SCR}^{\text{av.imp.}}$) for the processors and P_{d} for a $P_{\text{fa}} = 10^{-4}$ for the detectors, as discussed in Sect. 4.4. Performance for radar scans different of the ones used to design are given in a different section (see Sect. 8.2.4).

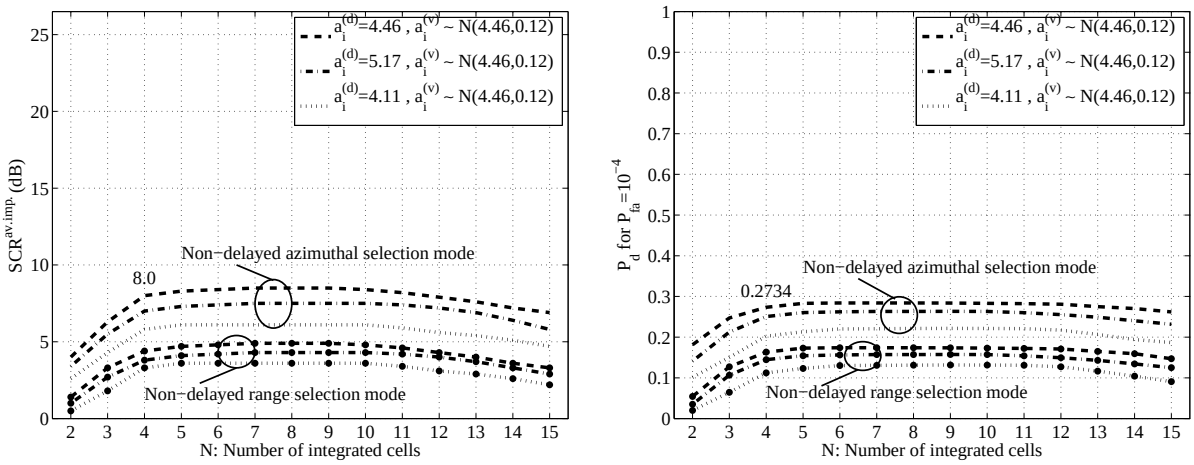

(a) TSKAP processors (b) TSKAP detectors

Figure 8.3: Performance of TSKAP processors and detectors using non-delayed selection modes and varying N when sea clutter conditions are used. Minimum ($a_i^{(\mathrm{d})} = 4.11$), typical ($a_i^{(\mathrm{d})} = 4.46$) and maximum ($a_i^{(\mathrm{d})} = 5.17$) design conditions are considered. Performance is given for the validation data set.

8.2.1 Design of TSKAP Detectors in Synthetic Sea Clutter

During the design of TSKAP detectors in synthetic sea clutter, the following parameters are studied:

- The environmental (clutter) conditions that maximizes the performance in the design stage. Note that for this study, only the cases concerning to the minimum ($a_i^{(\mathrm{d})} = 4.11$), typical ($a_i^{(\mathrm{d})} = 4.46$) and maximum ($a_i^{(\mathrm{d})} = 5.17$) conditions of Table 7.5 are considered. It is because for designing the TSKAP detector, the skewness parameter of the Weibull distribution must be known a priori. This parameter is the same scan-to-scan in the considered conditions (no temporal fluctuation is supposed for the clutter scan-to-scan).

- The non-delayed selection mode that works better in the TSKAP detector. Note that from all the selection modes presented in Sect. 4.2, only non-delayed modes are applicable in this detector because the non-linear prediction filters that form this detector are causal (non-anticipative).

- The number of selected cells (N) in each selection mode that allows to achieve the highest performance.

These three parameters are studied at the same time. The performance obtained for the TSKAP processor ($\mathrm{SCR}^{\mathrm{av.imp.}}$) and detector ($P_\mathrm{d}$ for a $P_\mathrm{fa} = 10^{-4}$) is depicted in Fig. 8.3 considering the validation data set. Some important aspects can be observed in this figure:

- The tendency of the performance with respect to N is practically the same for the processor and detector, each given by its own objective measurement.

- The clutter conditions that allow to achieve the best performance are always the typical ones ($a_i^{(\mathrm{d})} = 4.46$), regardless of the non-delayed selection mode and N. It is important to note that better performance would be achieved if the validation conditions are the same as the design ones ($a_i^{(\mathrm{v})} = a_i^{(\mathrm{d})}$). But, since these experiments are not suitable for practical situations, where the skewness parameter vary scan-to-scan, they are not reported.

- The selection mode that allows to achieve better performance in the TSKAP detector is the one based on azimuthal integration. But, why does it happen? Because the filters that compose the TSKAP detector work better when the data are correlated [Farina1987b, Sekine1990], and since to the way the radar scans are synthetically generated (see Sect. 2.3.1 for more details), this correlation is present for consecutive cells in azimuth.

- The best number of selected cells is practically in the same margin for each design condition ($a_i^{(\mathrm{d})}$) and selection mode, being $N \in [4, 12]$ cells. More than 12 or less than 4 selected cells involve lower performance. Paying attention to Table 7.1, where the sizes of the targets considered in the thesis are set, it is observed that this margin corresponds to the sizes of these targets, which vary from 4 to 12 cells.

After this study, the use of typical conditions ($a_i^{(\mathrm{d})} = 4.46$) and an integration of $N = 4$ cells using a non-delayed azimuthal selection mode is proposed to design TSKAP coherent detectors to detect moving Swerling 0 targets in the synthetic sea clutter conditions considered in the thesis.

8.2.2 Design of MLP-based Coherent Detectors in Synthetic Sea Clutter

As done for the TSKAP coherent detectors, the following parameters are studied to design MLP-based coherent detectors in synthetic sea clutter:

- The environmental (clutter) conditions that maximize the performance in the design stage. Note that for this study, all the conditions of Table 7.5 are considered, what did not happen in the case of study of the TSKAP detector.

- The selection modes that work better in the MLP-based detector. On the contrary to the TSKAP detector, all the selection modes (delayed and non-delayed) presented in Sect. 4.2 are used in MLP-based detectors.

- The number of selected cells (J) that allows to achieve the highest performance, which depends on the selection mode and RIA, as discussed in Sect. 4.2.2 and 4.2.3.

- The number of hidden neurons (H) in the MLP that forms the processor and detector.

At the beginning, the first three parameters are studied at the same time, considering non-delayed selection modes. It is done in this way to be able to compare its performance with the one achieved by the TSKAP coherent detector. After this study, these parameters are also studied for the other (delayed) selection modes.

The performance obtained for the MLP-based processor ($\mathrm{SCR}^{\mathrm{av.imp.}}$) and detector ($P_\mathrm{d}$ for a $P_\mathrm{fa} = 10^{-4}$) when using non-delayed selection modes are depicted in Fig. 8.4. Some important aspects can be observed in this figure:

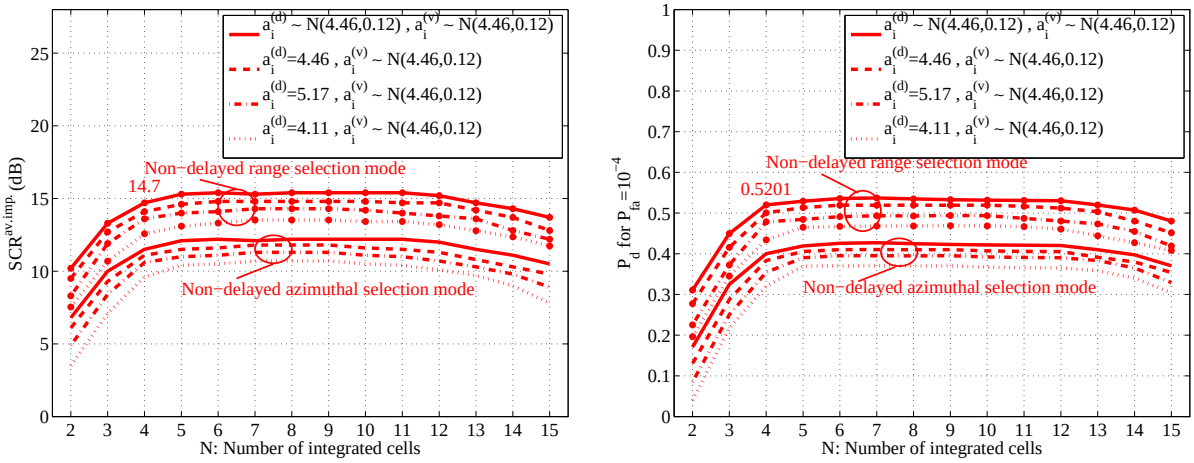

(a) MLP-based processors (b) MLP-based detectors

Figure 8.4: Performance of $2N/10/1$ MLP-based processors and detectors using non-delayed selection modes and varying N when sea clutter conditions are used. Minimum ($a_i^{(\mathrm{d})} = 4.11$), typical ($a_i^{(\mathrm{d})} = 4.46$), maximum ($a_i^{(\mathrm{d})} = 5.17$) and practical ($a_i^{(\mathrm{d})} \sim \mathrm{N}(4.46, 0.12)$) design conditions are considered. Performance is given for the validation data set.

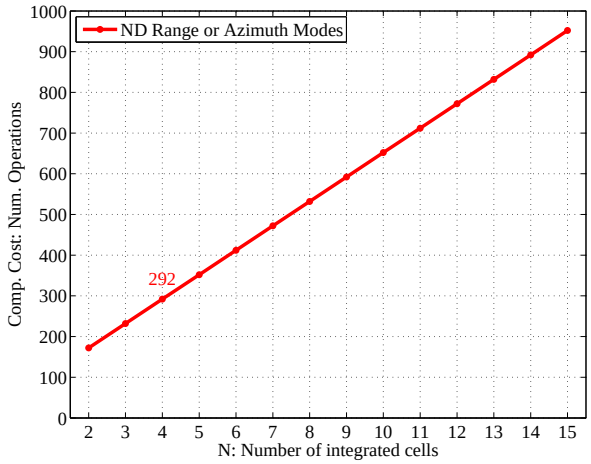

Figure 8.5: Computational cost of $2N/10/1$ MLP-based detectors using non-delayed (azimuthal or range) selection modes and varying N when sea clutter conditions are used.

- The tendency of the performance with respect to N is practically the same for the processor and detector, each given by its own objective measurement of the performance.
- The clutter conditions that allow to achieve the highest performance are always the practical ones ($a_i^{(\mathrm{d})} \sim \mathrm{N}(4.46, 0.12)$), regardless of the non-delayed selection mode and N.
- The selection mode that allows to achieve the highest performance in the MLP-based detector is the one based on range integration. As observed, it presents the opposite behavior of the one observed for the TSKAP detector. But, why does it happen? Because

the non-linear filter implemented by the MLP in the processor works better when no-correlation exists in the data. According to the way the radar scans are synthetically generated (see Sect. 2.3.1 on page 29 for more details), this correlation is not present for consecutive cells in range.

- The best number of selected cells is practically in the same margin for each design condition ($a_i^{(\mathrm{d})}$) and selection mode, being $N \in [4, 12]$ cells. More than 12 or less than 4 selected cells involve lower performance. Analyzing the sizes of the targets considered for the sea clutter environment and given in Table 7.1, it is observed that this margin is related to the sizes of these targets, which vary from 4 to 12 cells. But, what value of N could we select for using in the proposed MLP-based configuration? The answer to this question can be found in the computational cost required for each value of N. Fig. 8.5 plots the computational cost of this MLP-based configuration, being calculated by using Eq. (5.28)-(5.31). From this figure, we can conclude that the configuration using $N = 4$ cells presents the lowest computational cost.

After this study, and considering only non-delayed selection modes, the use of practical conditions ($a_i^{(\mathrm{d})} \sim \mathrm{N}(4.46, 0.12)$) and a selection of $N = 4$ cells in the range direction is proposed to design MLP-based coherent detectors to detect moving Swerling 0 targets in the synthetic sea clutter conditions considered in the thesis. As observed, similar conclusions for this and the TSKAP detector are obtained, but with a main difference: the proposed MLP-based processor and detector outperforms the TSKAP processor and detector approximately in $\Delta\mathrm{SCR}^{\mathrm{av.imp.}} \simeq 6.5\,\mathrm{dB}$ and $\Delta P_{\mathrm{d}} \simeq 0.25$, respectively, considering the best detectors in each case (compare Fig. 8.3 and 8.4).

Nevertheless, this thesis goes one step ahead and investigates how the performance of MLP-based detectors could be improved. For that purpose, improved selection modes are used, both in 1-D and 2-D. Fig. 8.6 and 8.7 plot the performance achieved by MLP-based processors and detectors when: synthetic sea clutter conditions are considered, MLPs are formed of 10 hidden neurons, 1-D and 2-D selection modes are used and RIA is varied. A study of the influence of the number of hidden neurons in the detector is given at the end of this subsection.

Similar conclusions as obtained for the case of using non-delayed selection modes in MLP-based detectors are achieved from the analysis of Fig. 8.6 and 8.7, but with three main differences:

1. The most important difference concerns to the performance improvement achieved in the processor and detector. The performance improvement achieved when using delayed selection modes instead of non-delayed selection modes is up to $\Delta\mathrm{SCR}^{\mathrm{av.imp.}} \simeq 7\,\mathrm{dB}$ and $\Delta P_{\mathrm{d}} \simeq 0.18$ (S mode, RIA $= 5$ cells and practical conditions of Fig. 8.7 with respect to the selected case of Fig. 8.4). Note that the worst results are obtained for the V mode (azimuthal integration with delay), as occur with the non-delayed azimuthal selection mode in Fig. 8.4. Moreover, the use of the V mode does not allow to surpass the performance achieved when a non-delayed range selection mode is used in the MLP-based detector (compare Fig. 8.4 and 8.7).

2. The value of RIA (even values are only valid) that maximizes the performance of the detector is in the range $[5, 13]$ cells. This range is in consonance with the size of the targets considered in the study (from 4 to 12 cells). But, from this range of RIA, which value

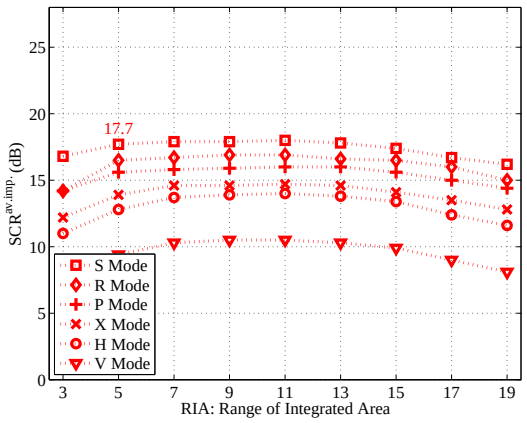

(a) MLP-based processors ($a_i^{(\mathrm{d})} = 4.11$)

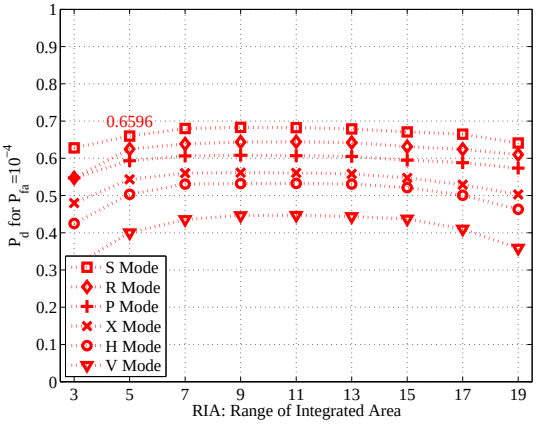

(b) MLP-based detectors ($a_i^{(\mathrm{d})} = 4.11$)

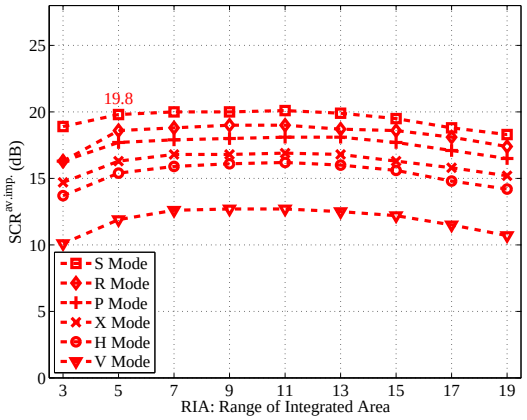

(c) MLP-based processors ($a_i^{(\mathrm{d})} = 4.46$)

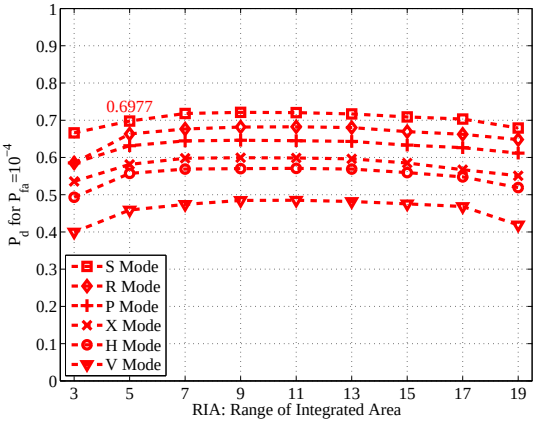

(d) MLP-based detectors ($a_i^{(\mathrm{d})} = 4.46$)

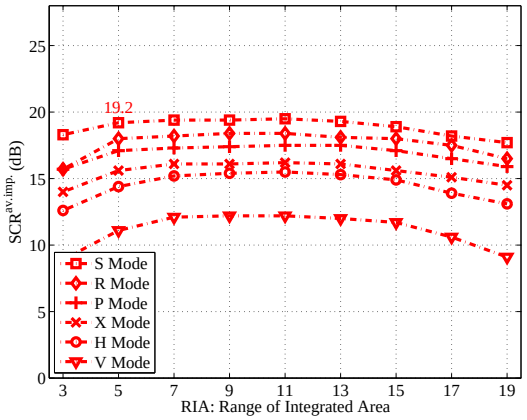

(e) MLP-based processors ($a_i^{(\mathrm{d})} = 5.17$)

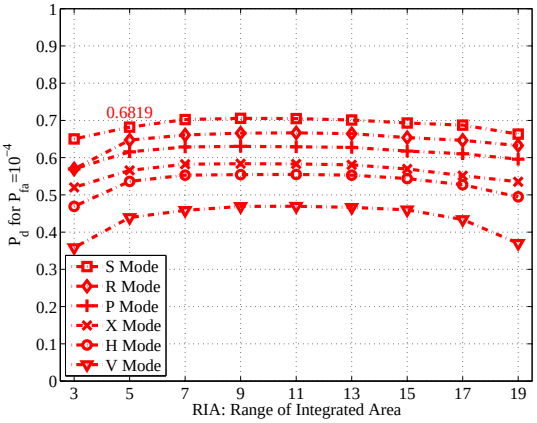

(f) MLP-based detectors ($a_i^{(\mathrm{d})} = 5.17$)

Figure 8.6: Performance of processors and detectors based on $2J/10/1$ MLPs varying the RIA in 1D and 2D selection modes and considering three different design conditions for sea clutter: $a_i^{(\mathrm{d})} = 4.11$, $a_i^{(\mathrm{d})} = 4.46$ and $a_i^{(\mathrm{d})} = 5.17$. Performance is given for the validation data set.

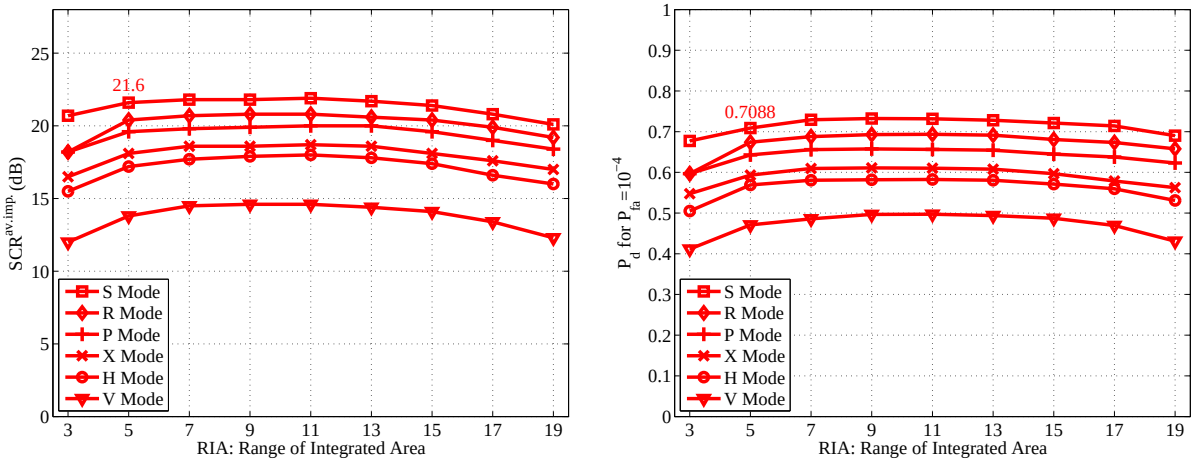

(a) MLP-based processors

(b) MLP-based detectors

Figure 8.7: Performance of processors and detectors based on $2J/10/1$ MLPs varying the RIA in 1D and 2D selection modes and considering the practical design conditions for sea clutter ($a_i^{(\mathrm{d})} \sim \mathrm{N}(4.46, 0.12)$). Performance is given for the validation data set.

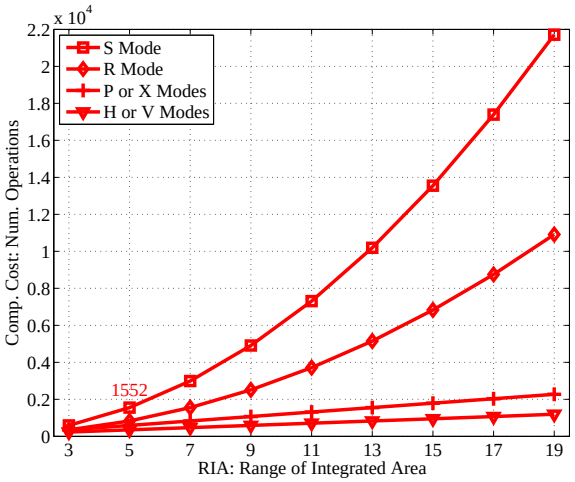

Figure 8.8: Computational cost of detectors based on $2J/10/1$ MLPs varying the RIA in 1D and 2D selection modes for synthetic sea clutter conditions.

should we select? Observing the computational cost of the different configurations of the proposed MLP-based detector under study ($2J/10/1$) depicted in Fig. 8.8, we realize that the lowest computational cost is achieved for the minimum value of RIA in this range, i.e. RIA $= 5$ cells.

3. The selection mode for which the highest performance is achieved is the S mode (a 2-D mode). Nevertheless, the improved selection modes under study, and exactly this one, present a cost: a time delay (see Sect. 4.2) and higher computational cost than the other selection modes (see Fig. 8.8). Exactly, for the proposed selection mode and considering

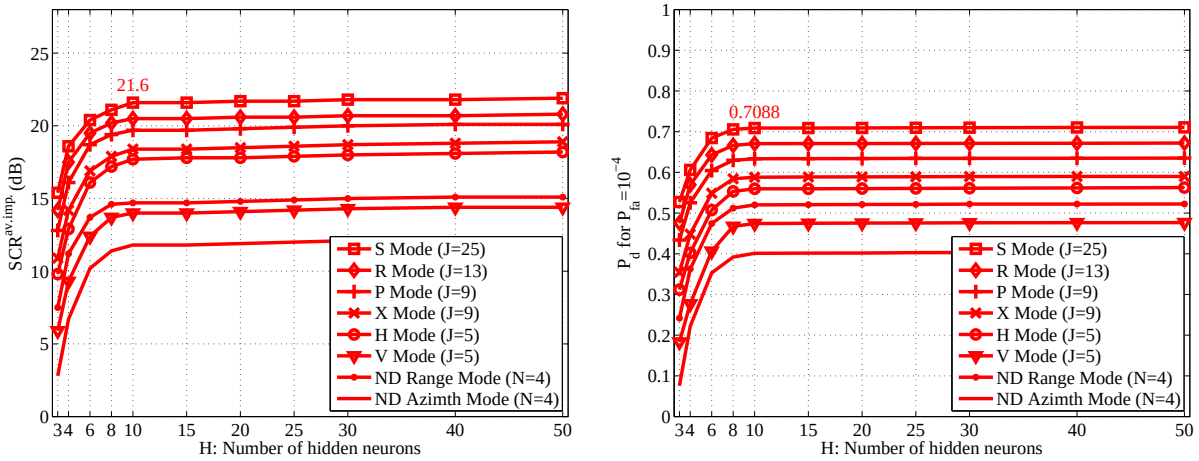

(a) MLP-based processors (b) MLP-based detectors

Figure 8.9: Performance of processors and detectors based on $2J/H/1$ MLPs varying the number of hidden neurons. Non-delayed and delayed (1-D and 2-D) selection modes and the best training strategy ($a_i^{(\mathrm{d})} \in [4.11, 5.17]$) are considered for the case of study of sea clutter. Performance is given for the validation data set.

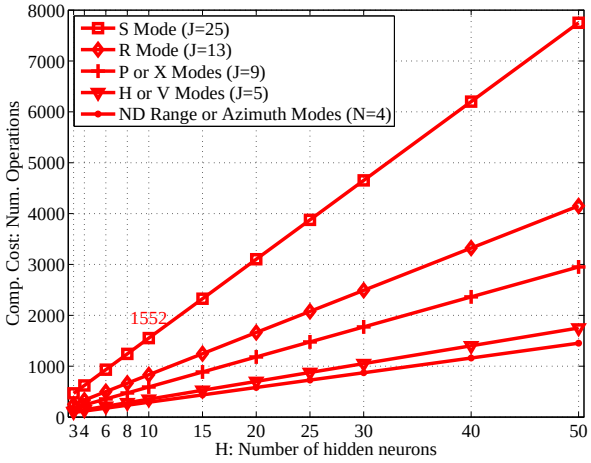

Figure 8.10: Computational cost of detectors based on $2J/H/1$ MLPs varying the number of hidden neurons. Non-delayed and delayed (1-D and 2-D) selection modes are considered for the case of study of sea clutter.

the minimum RIA, this delay is 0.5 ms, as set the parameters of the radar for sea clutter measurements given in Table 2.2 and Eq. (4.19).

Apart of these conclusions, the following question could be formulated: Why 2-D selection modes allow to achieve better performance than 1-D selection modes? The answer is related to: the improved capability of the MLP to learn from the environment regardless of the target orientation by using 2-D modes; and the increase of available information to make the decision.

As previously mentioned, a last study is done. This study is related to the number of hidden neurons (H) the MLP should have to maximize the performance in the processor and detector. If too many free weights are used, the capability of the MLP to generalize will be poor. On the contrary, if too few parameters are considered, the training data cannot be learned satisfactorily. Therefore, since the best size is not known a priori, H is varied from 3 to 50. The performance achieved for the different selection modes under study considering the validation data set are plotted in Fig. 8.9. Moreover, the computational cost of each MLP-based detector configuration for the different values of H under study are plotted in Fig. 8.10. As observed, regardless of the selection mode, low performance improvement is achieved from $H = 10$ hidden neurons (it is observed by making a zoom of Fig. 8.10), whereas a linear computational cost increase with H is observed. Therefore, $H = 10$ is selected.

After these studies, an MLP-based detector designed by using practical conditions ($a_i^{(\mathrm{d})} \sim \mathrm{N}(4.46, 0.12)$), RIA= 5 cells selected by an S mode and $H = 10$ hidden neurons is proposed to detect moving Swerling 0 targets in the synthetic sea clutter conditions considered in the thesis. The proposed MLP-based detector configuration requires a total of 1552 operations to process the output concerning to each CUT. The proposed MLP-based processor and detector outperforms the best configuration of the TSKAP processor and detector up to $\Delta\mathrm{SCR}^{\mathrm{av.imp.}} \simeq 13.5$ dB and $\Delta P_{\mathrm{d}} \simeq 0.43$, respectively (compare the selected cases of Fig. 8.3 and 8.7).

8.2.3 Design of RBFN-based Coherent Detectors in Synthetic Sea Clutter

As done for the TSKAP and MLP-based coherent detectors, the following parameters are studied to design RBFN-based coherent detectors in synthetic sea clutter:

- The environmental (clutter) conditions that maximize the performance in the design stage. All the environmental conditions of Table 7.5 are considered, as done for MLP-based detectors.

- The selection modes that work better in RBFN-based detectors. All the selection modes (delayed and non-delayed) presented in Sect. 4.2 are used, as occurred for MLP-based detectors.

- The number of selected cells (J), which depends on the selection mode and RIA (see Sect. 4.2.2 and 4.2.3), that allows to achieve high detector performance while maintaining low computational cost.

- The number of hidden neurons (H) in the RBFN that maximizes the processor and detector performance, while maintaining low computational cost.

At the beginning, the first three parameters are studied at the same time. In this case, non-delayed selection modes are only considered to be able to compare the RBFN-based detector performance with the one achieved by the detector taken as reference (TSKAP detector). After this study, these parameters are also studied for the other (delayed) selection modes.

Considering non-delayed selection modes, the performance obtained for the RBFN-based processor ($\mathrm{SCR}^{\mathrm{av.imp.}}$) and detector ($P_{\mathrm{d}}$ for a $P_{\mathrm{fa}} = 10^{-4}$) are depicted in Fig. 8.11. The computational cost needed in each configuration to obtain the detector output for each CUT (see

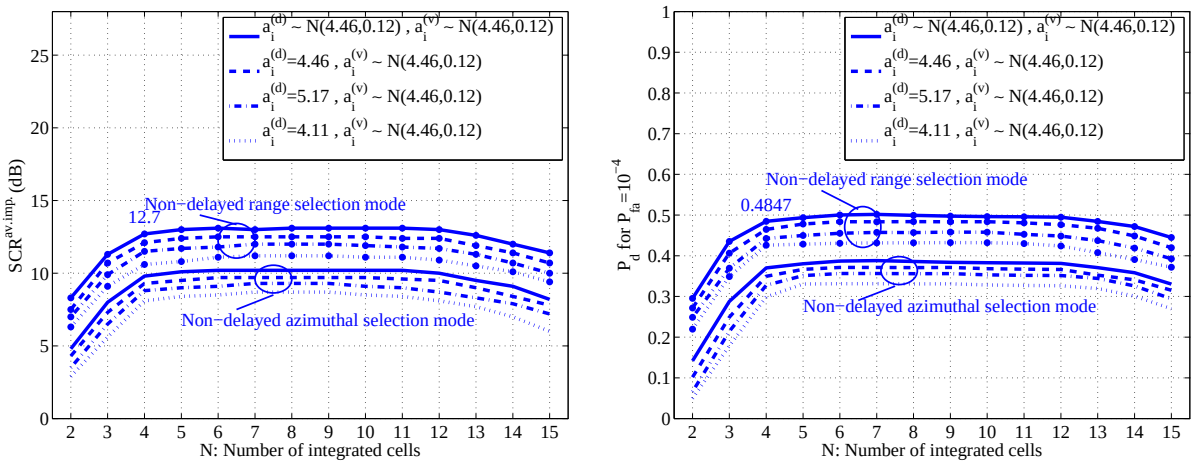

(a) RBFN-based processors (b) RBFN-based detectors

Figure 8.11: Performance of $2N/20/1$ RBFN-based processors and detectors using non-delayed selection modes and varying N when sea clutter conditions are used considering minimum ($a_i^{(\mathrm{d})} = 4.11$), typical ($a_i^{(\mathrm{d})} = 4.46$), maximum ($a_i^{(\mathrm{d})} = 5.17$) and practical ($a_i^{(\mathrm{d})} \sim \mathrm{N}(4.46, 0.12)$) design conditions. Performance is given for the validation data set.

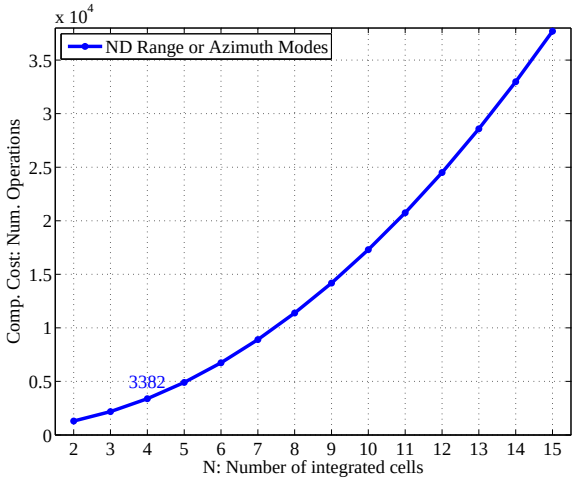

Figure 8.12: Computational cost of $2N/20/1$ RBFN-based detectors using non-delayed (azimuthal or range) selection modes and varying N when synthetic sea clutter conditions are used.

Eq. (6.24)-(6.27)) is depicted in Fig. 8.12. As observed, the computational cost of the RBFN-based detector exponentially increases with N. Therefore, N must be as lower as possible in the detector. From these figures, some important aspects are observed, concerning to: the tendency of N in terms of performance, the clutter conditions that maximize the RBFN-based detector performance, the selection modes for which the highest performance is achieved, the relationship between RIA and the target sizes, and the computational cost of the detector. No more details are given about these aspects because they are very similar to the ones obtained for MLP-based detectors, which were discussed in pages 123 - 125. But, there is a difference. The performance

of the RBFN-based detector (see Fig. 8.11) is slightly lower than the one achieved by the MLP-based detector (see Fig. 8.4) but greater than the one achieved by the TSKAP detector (see Fig. 8.3).

After this study, the use of practical conditions ($a_i^{(\mathrm{d})} \sim \mathrm{N}(4.46, 0.12)$) and a selection of $N = 4$ cells by the range mode is proposed to design RBFN-based coherent detectors that solves the detection problem this thesis deals with. The proposed RBFN-based processor and detector is able to outperform the TSKAP processor and detector up to $\Delta\mathrm{SCR}^{\mathrm{av.imp.}} \simeq 4.5$ dB and $\Delta P_{\mathrm{d}} \simeq 0.21$, respectively (compare the selected cases of Fig. 8.3 and 8.11).

As done for MLP-based detectors, this thesis goes one step ahead and investigates how the performance of the RBFN-based detector could be improved. For that purpose, improved selection modes are used, both in 1-D and 2-D. Fig. 8.13 and 8.14 plot the performance achieved in RBFN-based processors and detectors when: synthetic sea clutter conditions are considered, RBFNs are formed of 20 hidden neurons, 1-D and 2-D selection modes are used and RIA is varied. A study of the influence of the number of hidden neurons in the detector is made at the end of this subsection.

Analyzing the performance presented in Fig. 8.13 and 8.14 for the case of using delayed selection modes in RBFN-based detectors, the same conclusions as presented for the case of using non-delayed selection modes are obtained. But taken as reference the best results achieved for the non-delayed range selection mode (see Fig. 8.11), three main differences are observed:

1. The most important difference concerns to the performance improvement achieved by the processor and detector. The performance improvement achieved when using delayed selection modes is up to $\Delta\mathrm{SCR}^{\mathrm{av.imp.}} \simeq 7$ dB and $\Delta P_{\mathrm{d}} \simeq 0.20$ better (S mode, RIA = 5 cells and practical conditions of Fig. 8.14). Note that the worst results are obtained for the V mode (azimuthal integration with delay), as occurred for the non-delayed azimuthal selection mode in Fig. 8.11. Moreover, the use of the V mode does not allow to surpass the performance achieved when a non-delayed range selection mode is used in RBFN-based detectors (compare Fig. 8.11 and 8.14).

2. The range of RIAs for which the highest performance are achieved is in $[5, 13]$ cells. This range is in consonance with the size of the targets considered in the study (between 4 and 12 cells). But, as occurred with MLP-based coherent detectors, we wonder which is the value of RIA that should be selected for obtaining high detector performance with low computational cost. Observing the performance given in Fig. 8.14 and the computational cost required for each of these RBFN-based detector configurations given in Fig. 8.15, we observe that the lowest computational cost is achieved for the lowest value of RIA in this range, i.e. RIA = 5 cells.

3. The selection mode for which the highest detector performance is achieved is a 2-D mode, the S mode. Nevertheless, the improved selection modes under study, and exactly this one, present again a cost: a time delay (see Sect. 4.2) and an exponential computational cost increase with respect to the other modes (see Fig. 8.15). Exactly, considering the minimum RIA (5 cells) in the proposed selection mode, this delay is 0.5 ms, as set the parameters of the radar for sea clutter measurements given in Table 2.2 and Eq. (4.19).

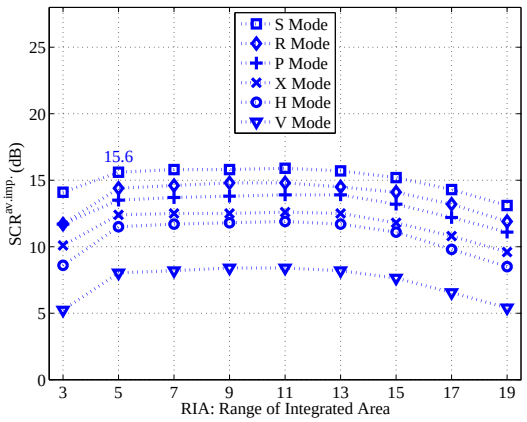

(a) RBFN-based processors ($a_i^{(\mathrm{d})} = 4.11$)

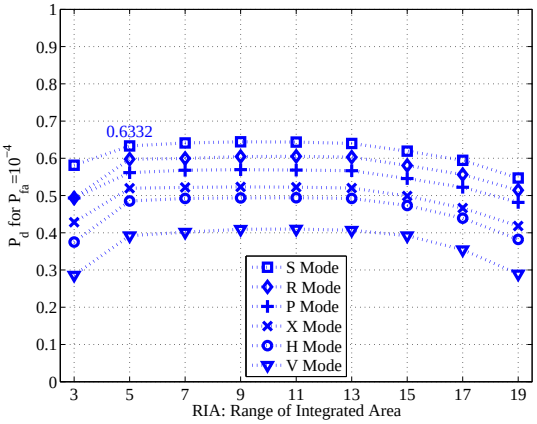

(b) RBFN-based detectors ($a_i^{(\mathrm{d})} = 4.11$)

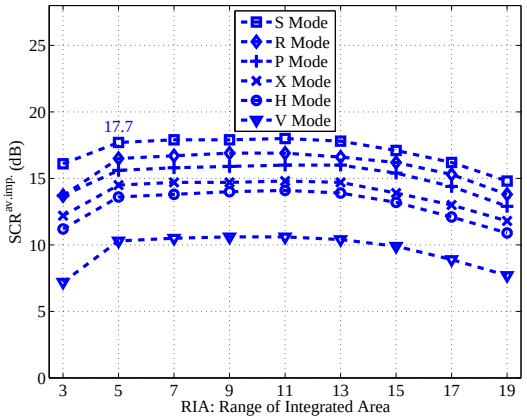

(c) RBFN-based processors ($a_i^{(\mathrm{d})} = 4.46$)

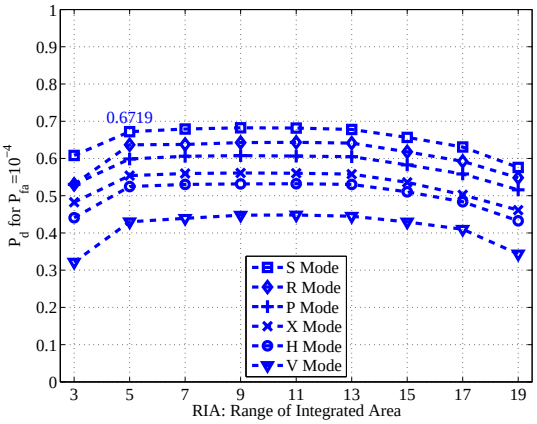

(d) RBFN-based detectors ($a_i^{(\mathrm{d})} = 4.46$)

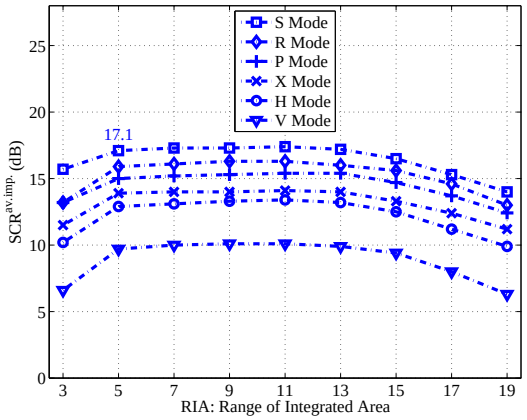

(e) RBFN-based processors ($a_i^{(\mathrm{d})} = 5.17$)

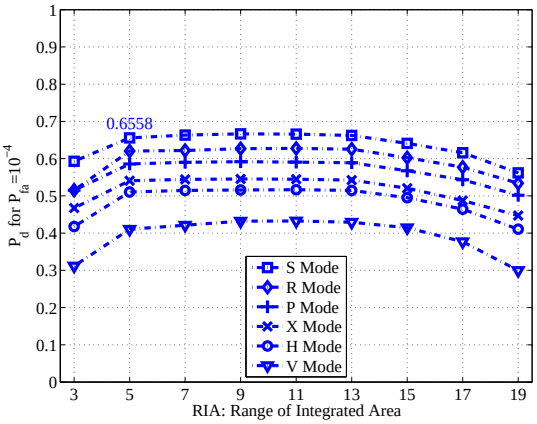

(f) RBFN-based detectors ($a_i^{(\mathrm{d})} = 5.17$)

Figure 8.13: Performance of processors and detectors based on $2J/20/1$ RBFNs varying the RIA in 1D and 2D selection modes and considering three different design conditions for sea clutter: $a_i^{(\mathrm{d})} = 4.11$, $a_i^{(\mathrm{d})} = 4.46$ and $a_i^{(\mathrm{d})} = 5.17$. Performance is given for the validation data set.

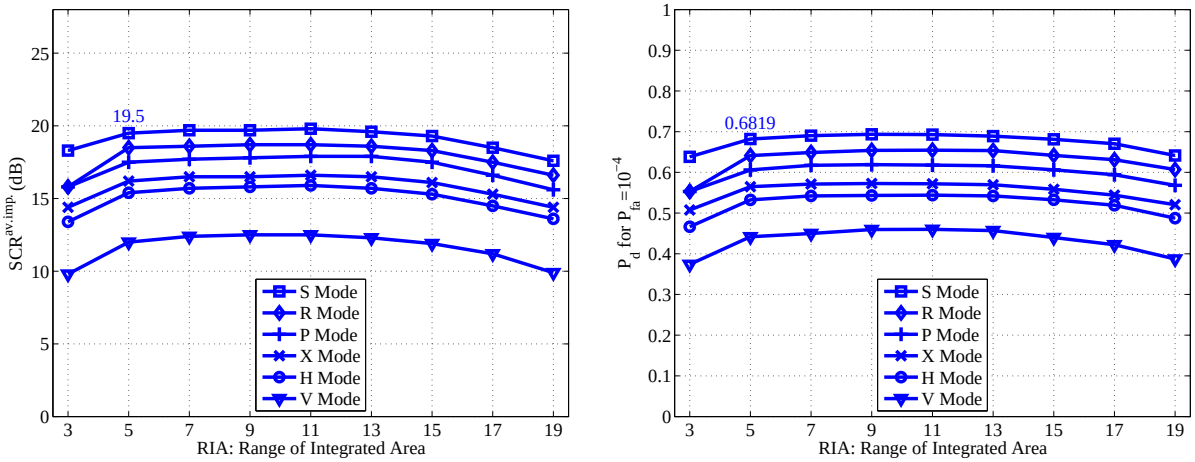

(a) RBFN-based processors (b) RBFN-based detectors

Figure 8.14: Performance of processors and detectors based on $2J/20/1$ RBFNs varying the RIA in 1D and 2D selection modes and considering the best design conditions for sea clutter ($a_i^{(\mathrm{d})} \sim \mathrm{N}(4.46, 0.12)$). Performance is given for the validation data set.

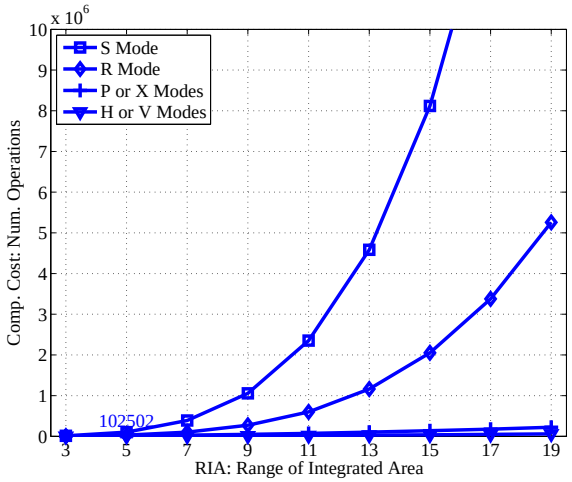

Figure 8.15: Computational cost of detectors based on $2J/20/1$ RBFNs varying the RIA in 1D and 2D selection modes for synthetic sea clutter conditions.

As observed from the RBFN-based detector performance, detectors using 2-D selection modes outperform detectors using 1-D modes, as occurred in MLP-based detectors. The reasons are the same as given for the MLP-based detector analysis, i.e. improved capability to learn form the environment regardless of the target orientation and increase of available information to make the decision.

As previously mentioned, a study of the influence of the number of hidden neurons (H) in RBFN-based processor and detector performance is done. For this study, H is varied from 3 to 50, and the performance achieved for the different selection modes under study are plotted in Fig. 8.16. The computational cost required for each RBFN-based detector configuration under

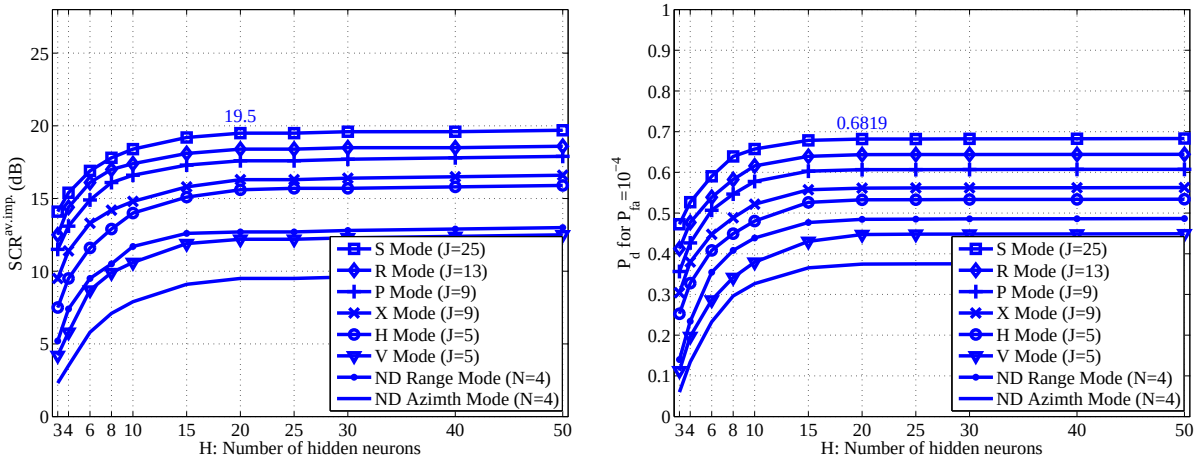

(a) RBFN-based processors

(b) RBFN-based detectors

Figure 8.16: Performance of processors and detectors based on $2J/H/1$ RBFNs varying the number of hidden neurons considering Non-delayed, 1-D and 2-D selection modes for the best training strategy ($a_i^{(\mathrm{d})} \in [4.11\text{-}5.17]$). Performance is given for the validation data set.

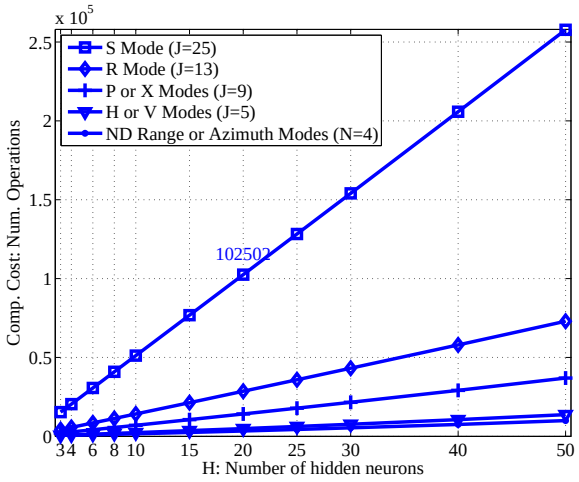

Figure 8.17: Computational cost of detectors based on $2J/H/1$ RBFNs varying the number of hidden neurons considering Non-delayed, 1-D and 2-D selection modes for synthetic sea clutter conditions.

study when varying H is plotted in Fig. 8.17. As observed from these figures, for all the modes under study, low performance improvement (observed by making a zoom in Fig. 8.16) and high computational cost increase are achieved from $H = 20$ hidden neurons. Therefore, $H = 20$ is selected in this case.

After these studies, an RBFN-based detector designed by using practical conditions ($a_i^{(\mathrm{d})} \sim \mathrm{N}(4.46, 0.12)$), RIA= 5 cells selected by an S mode and $H = 20$ hidden neurons is proposed to detect moving Swerling 0 targets in the synthetic sea clutter conditions considered in the thesis. The proposed RBFN-based detector configuration requires a total of 102502 operations to process

the output concerning to each CUT. The proposed RBFN-based processor and detector is able to outperform the best achieved TSKAP processor and detector up to 11.5 dB and 0.41, respectively (compare Fig. 8.3 and 8.14).

8.2.4 Comparison of Coherent Detectors in Design and Test Stages under Synthetic Sea Clutter Conditions

During the last subsections, attention has been paid to some important aspects of the design of TSKAP and AI-based coherent detectors, such as the clutter conditions, the selection modes and the dimensionality of the detectors. In this section, special attention is paid to the following question: What does it happen when other (different) radar scans are processed? This is what happens in real-live situations, where the incoming radar scans are different of the ones used for design, although their statistical properties could be equal or similar. In this way, this thesis investigates if the performance achieved in the designed stage is maintained or not for these new radar scans. And, in case of change, what kind of changes are observed and their magnitudes.

For this study, the sea clutter conditions presented in Sect. 7.1.3 for testing, exactly in Table 7.5, are considered. This study is divided in two parts. At the beginning, the performance of the detectors in the design and test stages is compared by ROC curves. At the end, two radar scans of the test data set are selected and processed to analyze what is really happening and trying to find an answer to the performance achieved in each case.

The configurations used for each detector are extracted from the design stage, being:

- MLP-based coherent detector: designed considering practical conditions ($a_i^{(\mathrm{v})} \sim \mathrm{N}(4.46, 0.12)$) and selecting $J = 25$ (RIA= 5 cells) complex-valued cells by an S selection mode. The number of hidden neurons is set to $H = 10$. Since real-arithmetic is used in the MLP, a total of 50 inputs are needed, having an MLP structure of 50/10/1.

- RBFN-based coherent detector: designed considering practical conditions ($a_i^{(\mathrm{v})} \sim \mathrm{N}(4.46, 0.12)$) and selecting $J = 25$ (RIA= 5 cells) complex-valued cells by an S selection mode. The number of hidden neurons is set to $H = 20$. Since real-arithmetic is used in the RBFN, a total of 50 inputs are needed, having an RBFN structure of 50/20/1.

- TSKAP coherent detector: designed considering typical conditions ($a_i^{(\mathrm{d})} = 4.46$) and selecting $N = 4$ complex-valued cells by a non-delayed azimuthal selection mode.

The ROC curves achieved in the design stage of these three detectors are depicted in Fig. 8.18a. These ROC curves are obtained for the validation data set. The ROC curves obtained in the test stage, considering the test data set, i.e. a set of radar scans never processed by these detectors, are given in Fig. 8.18b. From the results presented in both figures, several conclusions can be extracted:

- The tendency of the ROC curves is maintained, involving that the best detector continues being the one based on MLPs, followed by the RBF-based detector, and surpassing the performance achieved by the reference one, the TSKAP detector.

- The performance of the detectors decrease both in terms of $\mathrm{SCR}^{\mathrm{av.imp.}}$ (see the values given in the legends) and P_{d}. Focusing on the TSKAP detector, the performance loss

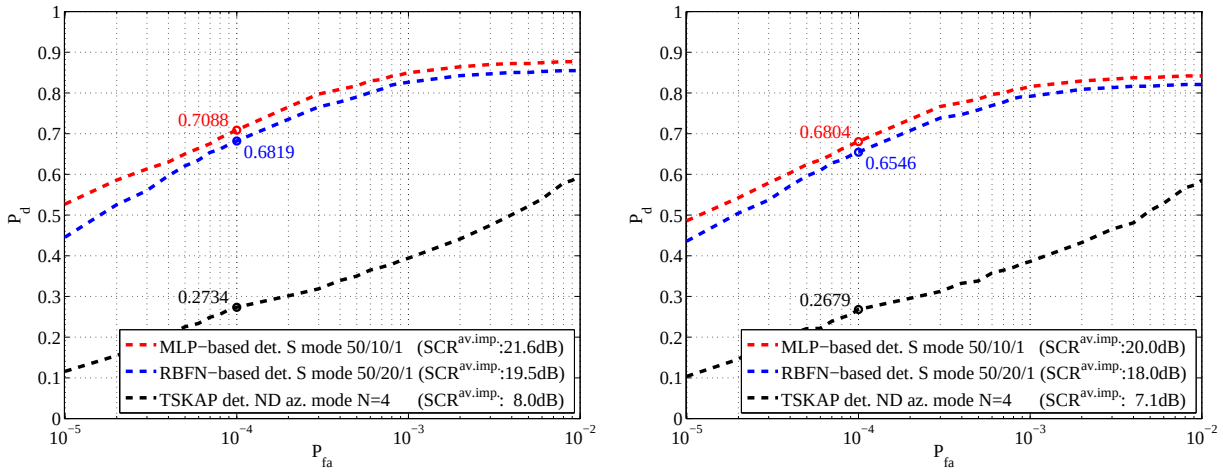

(a) Validation data set (b) Test data set

Figure 8.18: Performances of the selected configurations of TSKAP, MLP and RBFN-based coherent detectors using the validation ($a_i^{(\mathrm{v})} \sim \mathrm{N}(4.46, 0.12)$) and test ($a_i^{(\mathrm{t})} \sim \mathrm{N}(4.46, 0.12)$) data sets when synthetic sea clutter measurements are considered.

of the processor and detector is $\Delta\mathrm{SCR}^{\mathrm{av.imp.}} \simeq -1\,\mathrm{dB}$ and $\Delta P_{\mathrm{d}} \simeq -0.01$, respectively. On the other hand, the performance loss observed in AI-based processors and detectors is $\Delta\mathrm{SCR}^{\mathrm{av.imp.}} \simeq -1.5\,\mathrm{dB}$ and $\Delta P_{\mathrm{d}} \simeq -0.02$, respectively. Although the magnitude of the performance losses is greater for AI-based detectors than for the TSKAP detector, the relative performance loss is lower ($\simeq \frac{-0.02}{0.65} \cdot 100 \simeq -3\%$ for AI-based detectors versus $\simeq \frac{-0.01}{0.26} \cdot 100 \simeq -4\%$ for the TSKAP detector).

After the analysis of these results, we can conclude that good robustness is achieved in the detectors under study when different (new) radar scans are processed. This is an important issue because it gives us an approximation of how their performance will be when the detectors autonomously work processing never-processed radar scans.

Next, subjective and objective analyses of the performance of the detectors for radar scans with different clutter conditions are presented. For that purpose, two radar scans of the test data set are selected. As observed from the figures of the studies done during the design stage of Sect. 8.4.1-8.4.3, the clutter conditions for obtaining the best and worst performances, when $a_i^{(\mathrm{d})}$ is a constant, are $a_i^{(\mathrm{d})} = 4.46$ and $a_i^{(\mathrm{d})} = 4.11$, respectively. It can be better-understood by the plot of the pdf of the clutter amplitude for different skewness parameters, as depicted in Fig. 8.19, and the analysis of the probability of having each skewness parameter in the data set. In Fig. 8.19, it is observed that the lower the skewness parameter, the higher the probability of having a clutter cell with high amplitude. It involves that to achieve a desired P_{fa}, the detection threshold for $a = 4.11$ must be grater than for $a = 5.17$, being lower the P_{d} for $a = 4.11$ than for $a = 5.17$. According to this relationship, the P_{d} for $a = 4.46$ should be lower than for $a = 5.17$, but the achieved results go on the opposite direction. But, why this behavior? This behavior is given because of the probability that a radar scan in the data set has $a = 4.46$ is greater than for $a = 5.17$, what involves that the threshold in the design stage is mainly conditioned by the

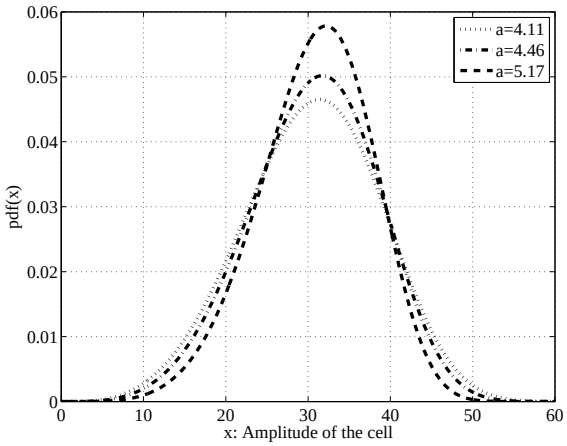

Figure 8.19: Probability density functions (pdf's) of the clutter amplitude when minimum ($a = 4.11$), typical ($a = 4.46$) and maximum ($a = 5.17$) sea clutter conditions are considered.

most probable skewness parameter value ($a = 4.46$).

Since the radar scans having $a_i^{(t)} = 4.46$ are the most probable in the environment conditions selected for synthetic sea clutter, and the radar scans having $a_i^{(t)} = 4.11$ are the ones for which the worst performance is achieved, two radar scans of the test data set having these skewness parameters are selected, being called $\mathbf{I}^{(4.46)}$ and $\mathbf{I}^{(4.11)}$, respectively. The real and imaginary parts of these scans are plotted in Fig. 8.20 and 8.21, respectively. Note that not all the azimuthal and range coverage of the radar scan (see Table 2.2) is plotted because details will be lost in presentation. Only a segment of the full-coverage, between 0° and 3° in azimuth and 1000 m and 1450 m in range, is selected for plotting and making a subjective analysis of the performance. Nevertheless, it is important to note that the objective performances given for each processed radar scan are given for the whole scan and not for the selected segment.

In order to facilitate the subjective analysis made for the processed radar scans, the positions, sizes and shapes of the targets in the radar scans of Fig. 8.20 and 8.21 are the same, being depicted in Fig. 8.22. Note that this plot denote in the different cells that compose the radar scan: the physical positions where the targets are present by a high level, and the physical positions where no target is present by a low level. Moreover, the physical size of the targets are also depicted in terms of cells.

The radar scans at the output of the TSKAP and AI-based coherent processors and detectors for $\mathbf{I}^{(4.11)}$ and $\mathbf{I}^{(4.46)}$ are depicted in Fig. 8.23 and 8.24. According to these results: first, a subjective analysis of the images is made; second, the performance of each detector for each radar scan is analyzed; and third, some conclusions are drawn.

From a subjective point of view, in Fig. 8.23 and 8.24, it is observed that the clutter reduction and the detection of cells belonging to target (H_1) is better for MLP and RBFN-based detectors than for the TSKAP detector. Taken as example the results for $\mathbf{I}^{4.46}$ (Fig. 8.24), it is observed that there are a lot of cells of most of the targets that are not detected when using the TSKAP detector. It converts into a problem when, for instance, a next step, such as the estimate of the target size and shape, is implemented. This effect is even stronger when processing $\mathbf{I}^{4.11}$ by the TSKAP detector (see Fig. 8.23), where more cells belonging to target are not detected. On the

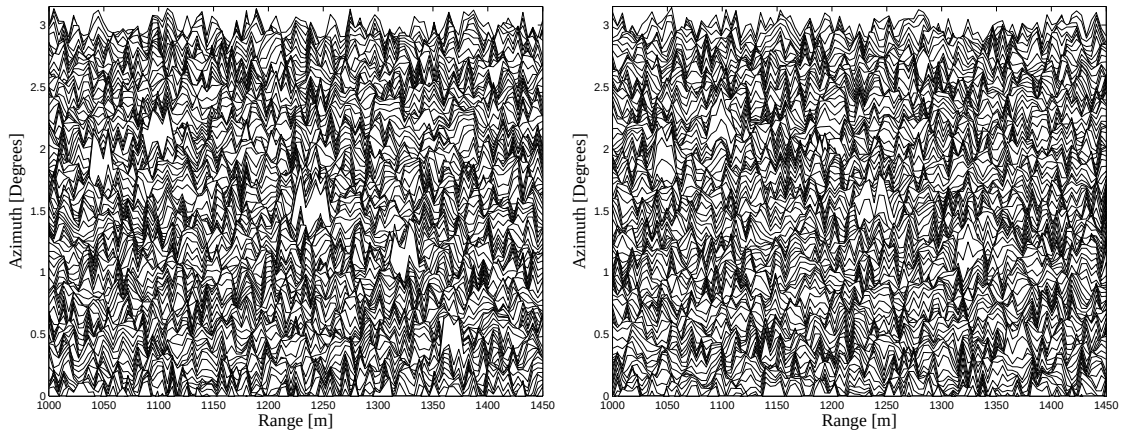

(a) $\mathrm{Re}\{\mathbf{I}^{(4.11)}\}$ (b) $\mathrm{Im}\{\mathbf{I}^{(4.11)}\}$

Figure 8.20: Real (Re{}) and imaginary (Im{}) parts of a radar scan ($\mathbf{I}$) taken from test data set with $a_i^{(\mathrm{t})} = 4.11$ ($\mathbf{I}^{(4.11)}$) when synthetic sea clutter is considered.

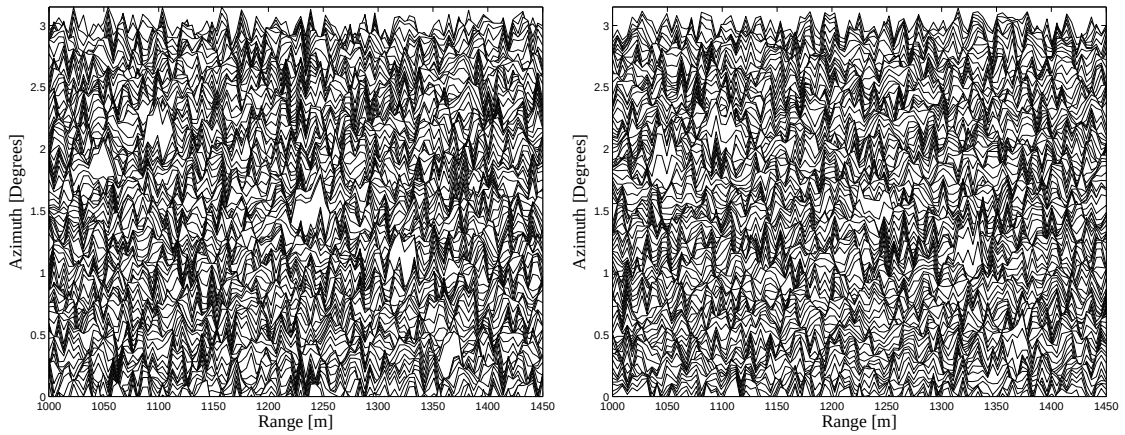

(a) $\mathrm{Im}\{\mathbf{I}^{(4.46)}\}$ (b) $\mathrm{Im}\{\mathbf{I}^{(4.46)}\}$

Figure 8.21: Real (Re{}) and imaginary (Im{}) parts of a radar scan ($\mathbf{I}$) taken from test data set with $a_i^{(\mathrm{t})} = 4.46$ ($\mathbf{I}^{(4.46)}$) when synthetic sea clutter is considered.

other hand, and observing the results obtained when using the proposed MLP and RBFN-based detector (see Fig. 8.24, as an example), it is observed that the number of cells belonging to target increases. In this way, better estimations of target size and shape could be done in next steps. Regardless of the detector and processed radar scan, it is observed that some false alarm exist in the examples given in Fig. 8.23 and 8.24.

Taken as reference the values achieved for the validation and test data sets reported in Fig. 8.18, the performance of each detector for the selected radar scans are analyzed. From the performance achieved by each detector for these radar scans, we can observe that:

- The performance of each detector for the radar scan $\mathbf{I}^{(4.11)}$ is always lower than the one achieved when processing all the test data set (see Fig. 8.18b) or all the validation data

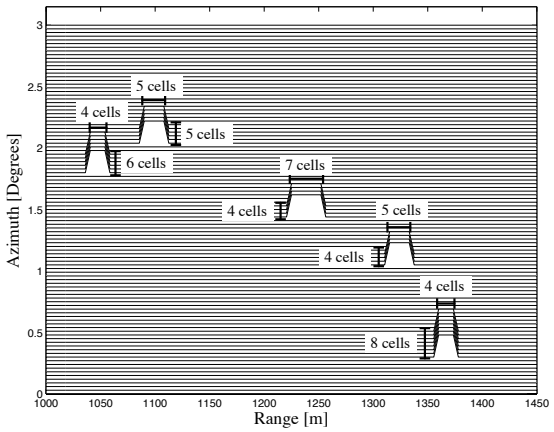

Figure 8.22: Desired (ideal) output radar scan ($\mathbf{D}$) when synthetic sea clutter is considered.

set (see Fig. 8.18a). It happens because the detection in these clutter conditions is more difficult than in the above considered clutter conditions.

- The performance of each detector for the radar scan $\mathbf{I}^{(4.46)}$ is higher than the one achieved when processing all the test data set (see Fig. 8.18b) and lower than the one achieved when processing all the validation data set (see Fig. 8.18a). It happens because the detection in these clutter conditions is easier than in the other clutter conditions.

- The P_{fa} remains constant (10^{-4}) for the threshold set during the design stage, as observed in Fig. 8.23 and 8.24. It happens due to the similarity of the statistical distributions of the sea clutter conditions under study, as observed in Fig. 8.19.

Analyzing the radar scans presented in Fig. 8.23 and 8.24, we can find two reasons why AI-based detectors outperform the reference detector. First, because the proposed processors are able to reduce better and in a high rate the level of clutter. And second, because they are even able to enhance the level of signal where target is present. Both reasons can be extracted from the radar scans at the output of the processors, which lead to improve the detection rate.

8.2.5 Conclusions about Coherent Detectors in Synthetic Sea Clutter

From the studies made in the design and test stages of coherent detectors in synthetic sea clutter (see Sect. 8.2.1-8.2.4), the following conclusions are drawn:

- The best clutter conditions for designing AI-based detectors are the practical ones, where the skewness parameter of the Weibull-distributed clutter vary scan-to-scan following a normal distribution with parameters $a_i^{(\text{d})} \sim \text{N}(4.46, 0.12)$ in this case of study. In the case where these situations are not applicable, as for the reference detector (TSKAP), the best design conditions are the typical ones ($a_i^{(\text{d})} = 4.46$ in this case).

- Selection modes using 2-D templates work better than 1-D modes in AI-based detectors, although they require more computational cost. From the 2-D selection modes under study,

the best one is found to be the square mode (S). The computational cost required to implement the selected MLP and RBFN-based coherent detectors is 1552 and 102502 operations per CUT, respectively. Other selection modes proposed in the thesis, as the rhombus (R) and plus-shape (P) modes allow to achieve lower but comparable performances, reducing considerably the computational cost of the AI-based detector. If 1-D selection modes are used in AI-based detectors, the highest performance is achieved when cells are integrated in range. This effect is opposite to the one achieved for the TSKAP detector, where the highest performance was obtained when selecting cells in azimuthal direction.

- The range of integrated area (RIA) that maximizes the detector performance (RIA $\in [5, 13]$ in this case) is found to be related to the size of the targets considered in the study ($\in [4, 12]$ cells in azimuth and range in these experiments). This effect is observed regardless of the coherent detector under study. The value of RIA conditions the number of AI-based detector inputs according to the selection mode the detector is using. Moreover, selecting the lowest range of integrated area (RIA = 5 in this case) is recommended because the lowest computational cost is needed when implementing the detector.

- A suitable number of hidden neurons (H) in AI-based detectors is found, being different for detectors based on MLPs ($H = 10$) and RBFNs ($H = 20$). As occurred for the selection of RIA, this number of hidden neurons is selected considering a trade-off between the detector performance and the computational cost needed to implement it.

- It is observed that the dimensionality and design of the detector can be done by using two kind of metrics: $\mathrm{SCR}^{\mathrm{av.imp.}}$ in the processor; and P_{d} for a given P_{fa} in the detector. Both metrics present a similar behavior with the parameters of the detectors under study.

- A high robustness of the detector performance is observed when new radar scans (different of the ones used in the design stage) are processed. A performance loss lower than $\Delta\mathrm{SCR}^{\mathrm{av.imp.}} \simeq -1.5\,\mathrm{dB}$ and $\Delta P_{\mathrm{d}} \simeq -0.02$ for $P_{\mathrm{fa}} = 10^{-4}$ is achieved regardless of the coherent detector under study. It gives us an idea of the performance that the detector could achieve when processing new radars scans with these clutter conditions in the future.

- The performance achieved by the coherent detectors when processing radar scans having a skewness value equal to its typical value ($a_i^{(\mathrm{t})} = 4.46$ in this case) is higher than the ones achieved for radar scans having a skewness parameter close to the limits of variation the skewness parameter in a given data set. In our case of study, these limits are set in $a_i^{(\mathrm{t})} = 4.11$, for which the results of a radar scan are given, and in $a_i^{(\mathrm{t})} = 5.17$), obtaining similar performances to the ones obtained for the other limit. It is also observed that the P_{fa} remains constant for radar scans having different skewness parameter values. This effect happens because the threshold setting is mainly conditioned by radar scans having skewness parameter values close to the typical value. Even when different performances are achieved, these differences are always lower than $\Delta\mathrm{SCR}^{\mathrm{av.imp.}} \simeq -2\,\mathrm{dB}$ and $\Delta P_{\mathrm{d}} \simeq -0.03$ for $P_{\mathrm{fa}} = 10^{-4}$ (compare Fig. 8.23 and 8.24), regardless of the detector.

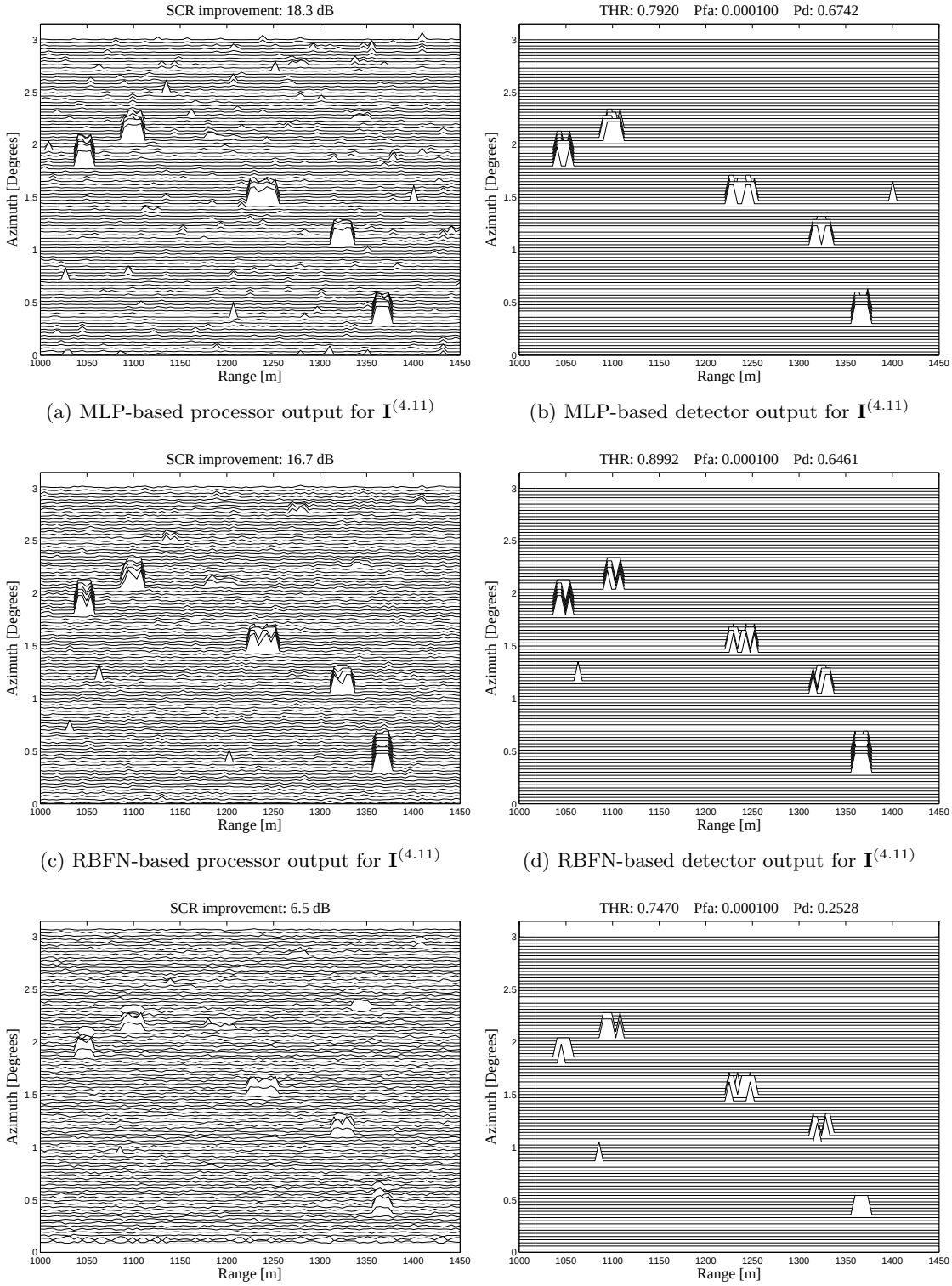

(a) MLP-based processor output for $\mathbf{I}^{(4.11)}$

(b) MLP-based detector output for $\mathbf{I}^{(4.11)}$

(c) RBFN-based processor output for $\mathbf{I}^{(4.11)}$

(d) RBFN-based detector output for $\mathbf{I}^{(4.11)}$

(e) TSKAP processor output for $\mathbf{I}^{(4.11)}$

(f) TSKAP detector output for $\mathbf{I}^{(4.11)}$

Figure 8.23: Radar scans at the output of the MLP-based, RBFN-based and TSKAP processors and detectors when the input radar scan $\mathbf{I}^{(4.11)}$ from the test data set of sea clutter conditions is processed.

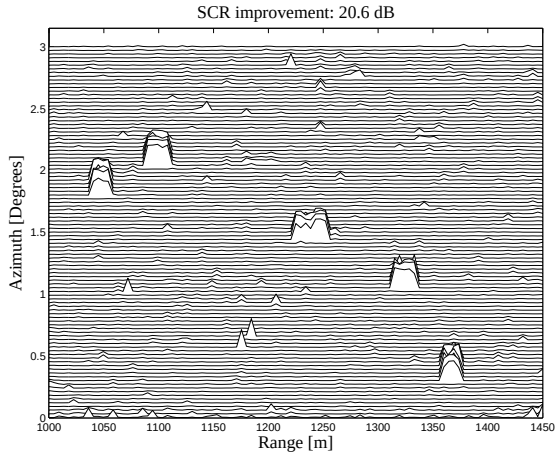

(a) MLP-based processor output for $\mathbf{I}^{(4.46)}$

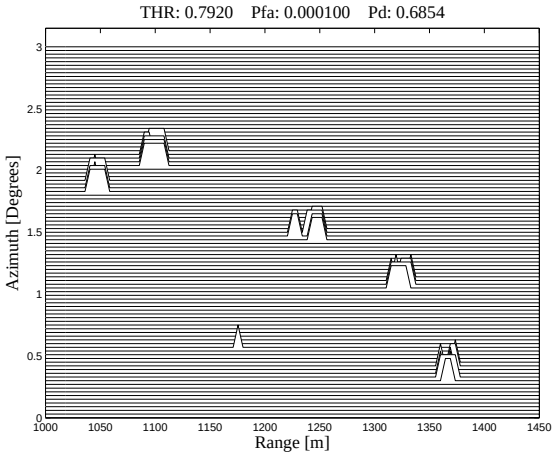

(b) MLP-based detector output for $\mathbf{I}^{(4.46)}$

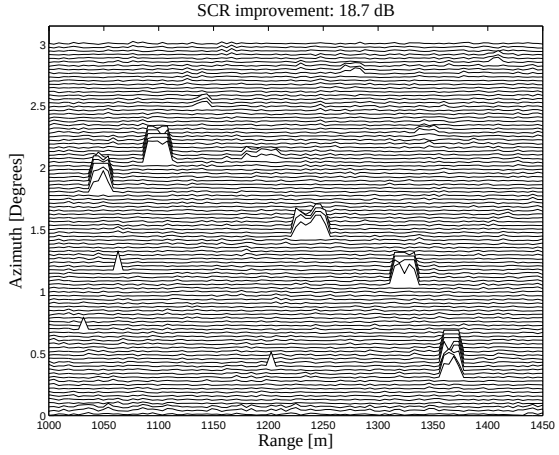

(c) RBFN-based processor output for $\mathbf{I}^{(4.46)}$

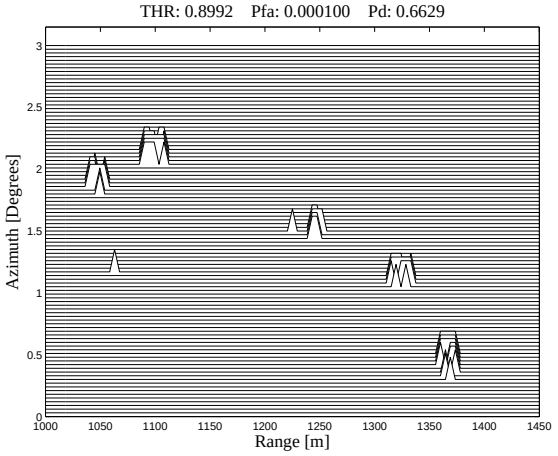

(d) RBFN-based detector output for $\mathbf{I}^{(4.46)}$

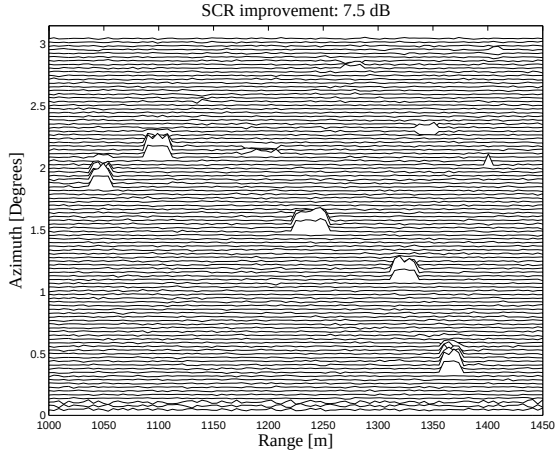

(e) TSKAP processor output for $\mathbf{I}^{(4.46)}$

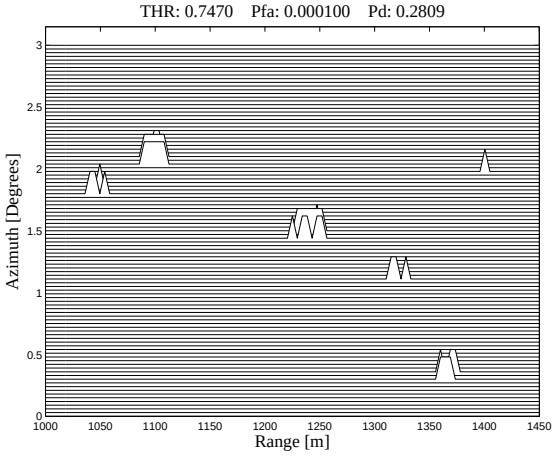

(f) TSKAP detector output for $\mathbf{I}^{(4.46)}$

Figure 8.24: Radar scans at the output of the MLP-based, RBFN-based and TSKAP processors and detectors when the input radar scan $\mathbf{I}^{(4.46)}$ from the test data set of sea clutter conditions is processed.

8.3 Coherent Detectors in Synthetic Sea-Ice Clutter

This section deals with the design and test of coherent detectors when synthetic sea-ice clutter conditions are considered. During the design of the coherent detectors under study, i.e. TSKAP and AI-based coherent detectors, some parameters must be tuned to find the values that maximize their performance. These parameters are:

- The environmental (clutter) conditions used in the design stage, as set in Table 7.6.
- The selection mode to be used, as presented in Sect. 4.2.
- The number of integrated/selected cells in each selection mode.
- And the number of hidden neurons in the MLPs and RBFNs that form the AI-based coherent detectors.

Since the aim of the thesis is to study the performance of the detectors against changes in clutter conditions, constant amplitude (Swerling 0) targets are considered. Moreover, since high performance is achieved for the detectors under study when considering the parameters given in Table 7.4, as observed in the paper [Vicen2010c] derived from the thesis (see Sect. 14), the target and clutter conditions considered in the current study are modified to become more complicated. In this way, we can realize the improvement achieved by the proposed detectors against the reference detector. Thus, SNR is reduced from 40 dB to 30 dB. Consequently, and since CNR is constant in the studies, SCR is reduced from 10 dB to 0 dB.

The selection of the best value of the above-mentioned parameters is made during the design stage, for which the training and validation data sets of Table 7.6 are used. Following the philosophy used in the study considering synthetic sea clutter, the data sets are generated once for all the experiments done when considering synthetic sea-ice clutter. The performance of the processors and detectors presented in subsections 8.3.1-8.3.3 are given for the validation data set and in terms of average SCR improvement ($\mathrm{SCR}^{\mathrm{av.imp.}}$) and P_{d} for $P_{\mathrm{fa}} = 10^{-4}$, respectively. Finally, performance for a new data set is given in Sect. 8.3.4. These results will let us realize which is the performance that can be expected when processing new radar scans in the future, having the clutter conditions considered here.

8.3.1 Design of TSKAP Detectors in Synthetic Sea-Ice Clutter

Following the same steps of Sect. 8.2.1 for synthetic sea clutter, during the design of TSKAP detectors in synthetic sea-ice clutter, the following parameters are tuned:

- The environmental (clutter) conditions that maximize the performance in the design stage. Note that for this study, only the minimum, typical and maximum conditions of Table 7.6 are considered because the skewness parameter of the Weibull distribution must be known a priori for designing TSKAP detectors. This parameter is the same scan-to-scan ($a_i^{(\mathrm{d})} = a_{i+1}^{(\mathrm{d})}$).
- The non-delayed selection mode that makes TSKAP detectors work better. Note that from all the selection modes presented in Sect. 4.2, only non-delayed modes are applicable in this detector because the non-linear prediction filters that form this detector are causal.

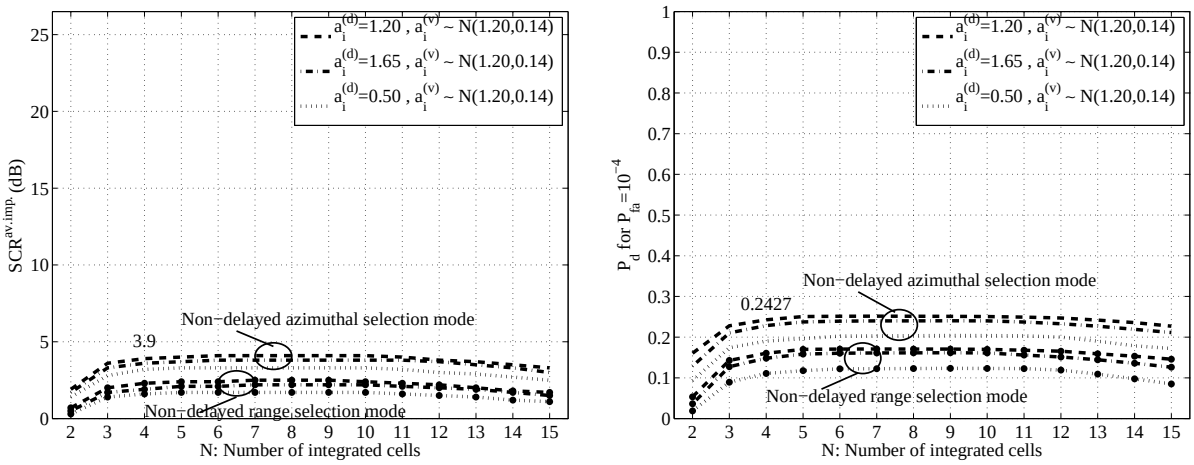

(a) TSKAP processors

(b) TSKAP detectors

Figure 8.25: Performances of TSKAP processors and detectors using non-delayed selection modes and varying N when sea-ice clutter conditions are used. Minimum ($a_i^{(\mathrm{d})} = 0.50$), typical ($a_i^{(\mathrm{d})} = 1.20$) and maximum ($a_i^{(\mathrm{d})} = 1.65$) design conditions are considered. Performance is given for the validation data set.

- The best number of integrated/selected cells (N) in each selection mode that allow to achieve the highest performance.

These three parameters are simultaneously studied. The performance obtained for both the TSKAP processor ($\mathrm{SCR}^{\mathrm{av.imp.}}$) and detector ($P_{\mathrm{d}}$ for $P_{\mathrm{fa}} = 10^{-4}$) are depicted in Fig. 8.25. Some important aspects can be observed from these results:

- The tendency of the performance with respect to N is practically the same for the processor and detector, each given by its own objective measurement of the performance.
- The clutter conditions that allow to achieve the best performance are always the typical ones ($a_i^{(\mathrm{d})} = 1.20$), regardless of the non-delayed selection mode and N.
- The selection mode that allows to achieve better performance in the TSKAP detector is the one based on azimuthal integration/selection. It happens because the filters that form the TSKAP detector work better when the data are correlated [Farina1987b, Sekine1990] and the correlation of the data of the synthetic radar scans is given in the azimuthal direction (see Sect. 2.3.1).
- The best number of integrated cells is practically in the same margin for each design condition ($a_i^{(\mathrm{d})}$) and selection mode, being $N \in [4, 10]$ cells. Since the performance achieved by the detector is very similar in this range, $N = 4$ cell is selected because it presents the lowest computational cost. Paying attention to Table 7.1, where the sizes of the targets considered in the thesis are set for sea-ice clutter conditions (from 2 to 10 cells both in range and azimuth), a direct relationship between the obtained margin and the sizes is observed.

After this study, the use of typical conditions ($a_i^{(\mathrm{d})} = 1.20$) and an integration of $N = 4$ cells using a non-delayed azimuthal selection mode is proposed to design TSKAP coherent detectors to detect moving Swerling 0 targets in the synthetic sea-ice clutter conditions considered in the thesis.

8.3.2 Design of MLP-based Coherent Detectors in Synthetic Sea-Ice Clutter

A similar procedure as for the case of study of synthetic sea clutter conditions presented in Sect. 8.2.2, and as done above for the TSKAP coherent detectors in synthetic sea-ice clutter, is followed next. In this way, the following parameters are studied for designing MLP-based coherent detectors in synthetic sea-ice clutter:

- The environmental (clutter) conditions that maximize the performance in the design stage. Note that for this study, all the conditions of Table 7.6 are considered.
- The selection modes that work better in the MLP-based detector. In this case, all the selection modes presented in Sect. 4.2 (delayed and non-delayed) are used.
- The number of integrated/selected cells that allow to achieve high performance while maintaining low computational cost. This number depends on the selection mode and the range of integrated area (RIA), as discussed in Sect. 4.2.2 and 4.2.3.
- The number of hidden neurons (H) in the MLP that maximizes the processor and detector performance while maintaining low computational cost.

At the beginning of these experiments, the first three parameters (clutter conditions, selection modes and RIA) are simultaneously studied, but only considering non-delayed selection modes. In this way, we can compare its performance with the one achieved by the TSKAP coherent detector. After this study, these parameters are also studied for the other (delayed) selection modes.

Considering only non-delayed selection modes, the performance obtained for both the MLP-based processor ($\mathrm{SCR}^{\mathrm{av.imp.}}$) and detector ($P_{\mathrm{d}}$ for $P_{\mathrm{fa}} = 10^{-4}$) is depicted in Fig. 8.26. Some important aspects can be extracted from this figure:

- The tendency of the performance with respect to N is practically the same for the processor and detector, each given by its own objective measurement of the performance, as occurred for the TSKAP detector.
- The clutter conditions that allow to achieve the best performance are always the practical ones ($a_i^{(\mathrm{d})} \sim \mathrm{N}(1.20, 0.14)$), regardless of the non-delayed selection mode and N.
- The selection mode that allows to achieve the best performance in MLP-based detectors is the one based on range selection. It presents the opposite behavior as the TSKAP detector because the non-linear filter implemented by the MLP in the processor, and consequently in the detector, work better when the data are uncorrelated. According to the way the radar scans are synthetically generated (see Sect. 2.3.1 for more details), this correlation is not present for consecutive cells in range.

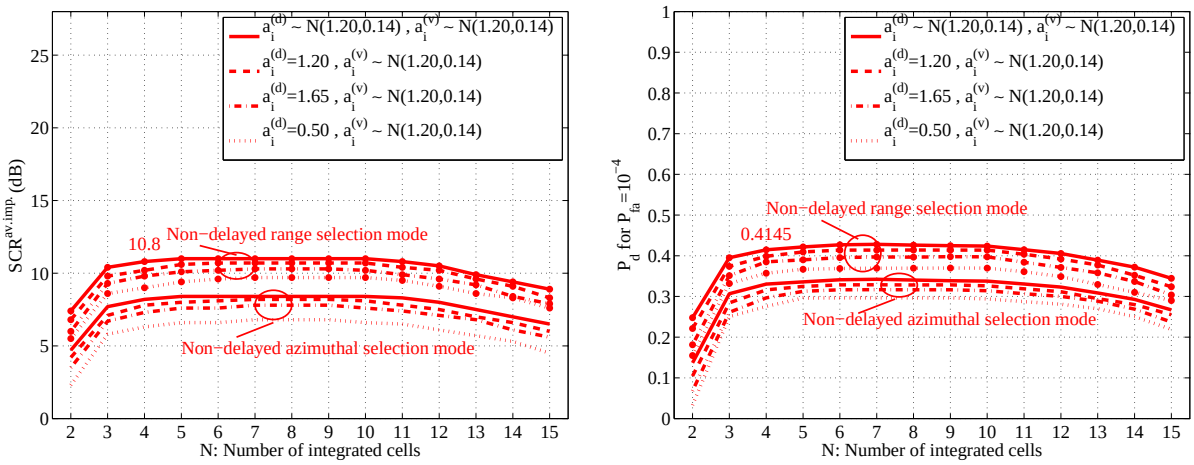

(a) MLP-based processors (b) MLP-based detectors

Figure 8.26: Performances of $2N/10/1$ MLP-based processors and detectors using non-delayed selection modes and varying N when sea-ice clutter conditions are used. Minimum ($a_i^{(\mathrm{d})} = 0.50$), typical ($a_i^{(\mathrm{d})} = 1.20$), maximum ($a_i^{(\mathrm{d})} = 1.65$) and practical ($a_i^{(\mathrm{d})} \sim \mathrm{N}(1.20, 0.14)$) design conditions are considered. Performance is given for the validation data set.

- The best number of integrated cells is practically in the same margin for each design condition ($a_i^{(\mathrm{d})}$) and selection mode, being $N \in [4, 10]$ cells. This margin is directly related to the sizes of the targets considered in the thesis (see Table 7.1), which vary from 2 to 10 cells both in range and azimuth. The behavior observed in this case is the same as the one for the TSKAP detector. Since the number of hidden neurons ($H = 10$) used here is the same as the one used for the same study but for synthetic sea clutter (see Sect. 8.2.2), the variation of the computational cost with N is the same as in Fig. 8.5. In consequence, the proposed value of N is $N = 4$ cells because it allows to achieve high detector performance while maintaining low computational cost (292 operations in total).

After this study, it is observed that the use of practical conditions ($a_i^{(\mathrm{d})} \sim \mathrm{N}(1.20, 0.14)$) and an integration of $N = 4$ cells by using a range selection mode to design MLP-based coherent detectors to detect moving Swerling 0 targets in the synthetic sea-ice clutter conditions considered in the thesis is a good solution. This MLP-based approach outperforms the TSKAP processor and detector in approximately $\Delta\mathrm{SCR}^{\mathrm{av.imp.}} \simeq 7\,\mathrm{dB}$ and $\Delta P_{\mathrm{d}} \simeq 0.17$, respectively, considering the best detectors in each case.

Nevertheless, this thesis goes one step ahead and investigates how the performance of the MLP-based detector could be improved. For that purpose, improved selection modes are used, both in 1-D and 2-D. The performance obtained for both the MLP-based processor and detector is depicted in Fig. 8.27 when RIA is varied (even values are not possible for RIA), the practical clutter conditions $a_i^{(\mathrm{d})} \sim \mathrm{N}(1.20, 0.14)$ are considered and $H = 10$ hidden neurons are used. A deep study of the number of hidden neurons in the detector is given at the end of this subsection.

From the results presented in Fig. 8.27 for the study of the influence of RIA in the MLP-based processor and detector, the following conclusions can be drawn:

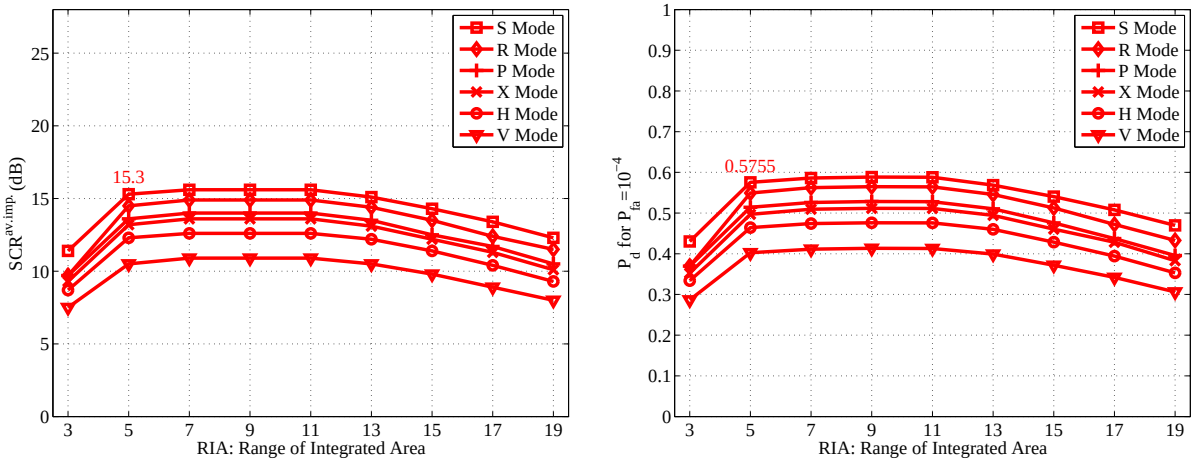

(a) MLP-based processors

(b) MLP-based detectors

Figure 8.27: Performances of processors and detectors based on $2J/10/1$ MLPs varying the RIA in 1D and 2D selection modes and considering the practical design conditions for sea-ice clutter ($a_i^{(\mathrm{d})} \sim \mathrm{N}(1.20, 0.14)$). Performance is given for the validation data set.

- The tendency of the performance with respect to the RIA is practically the same for the processor and for the detector, as occurred in the previous study.

- The RIA, and consequently the number of integrated cells, that maximize the performance of the detector is practically in the same margin for each selection mode, being RIA $\in [5, 11]$ cells. Once again, it is observed that this margin is related to the size of the targets considered for sea-ice clutter conditions (see Table 7.1), which vary from 2 to 10 cells both in range and azimuth. The computational cost of each configuration with respect to RIA is the same as the one depicted in Fig. 8.8 for the case of study of MLPs in synthetic sea clutter conditions ($H = 10$ is the same in both cases). From this plot, it is observed that the lowest computational cost is achieved for the lowest value of RIA in this range, i.e. RIA $= 5$ cells (1552 operations).

- The best selection mode is the S mode (a 2-D mode). Nevertheless, the improved selection modes under study, and exactly this one, present two costs: a temporal delay (see Sect. 4.2) and a computational cost increase (see Fig. 8.8). Exactly, for the proposed selection mode and considering the minimum RIA of the proposed range (RIA $= 5$ cells), this delay is of 1.2 ms, as set the parameters of the radar for sea-ice clutter measurements given in Table 2.4 and Eq. (4.19).

- The performance of the proposed MLP-based detector is always better than the TSKAP detector performance (compare Fig. 8.27 and 8.25), even for the worst selection mode chosen in the MLP-based approach. Taking as reference the performance of the TSKAP detector using a non-delayed azimuthal selection mode, the processor and detector performance improvements approximately vary from a minimum of $\Delta\mathrm{SCR}^{\mathrm{av.imp.}} \simeq 6\,\mathrm{dB}$ and $\Delta P_{\mathrm{d}} \simeq 0.16$ (V selection mode) to a maximum of $\Delta\mathrm{SCR}^{\mathrm{av.imp.}} \simeq 11\,\mathrm{dB}$ and $\Delta P_{\mathrm{d}} \simeq 0.33$

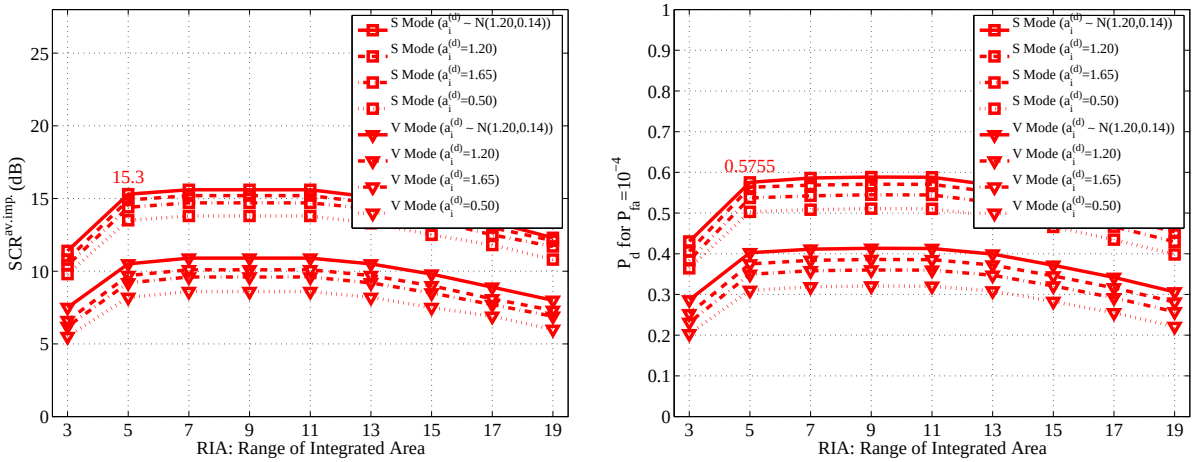

(a) MLP-based processor

(b) MLP-based detector

Figure 8.28: Performances of MLP-based processors and detectors for sea-ice clutter conditions and during the design stage. During this stage, the best (S) and worst (V) selection modes are used and RIA and the design conditions are varied. Performance is given for the validation data set.

(S selection mode).

As occurred in the case of study of MLPs in synthetic sea clutter, 2-D selection modes work better than 1-D selection modes. It happens because the decision target present/target absent is made regardless of the target orientation in the scan by using 2-D selection modes. Moreover, the performance increase is also achieved because the quantity of available information to make this decision is greater for 2-D selection modes than for 1-D modes.

Let's focus now on an empirical study made to analyze the influence of the clutter conditions during the design of the MLP-based detector. The same experiments as made for the case of study of synthetic sea clutter (see Sect. 8.2.2) have been made here for synthetic sea-ice clutter. But, on the contrary to the long presentation of results extracted from the study made when considering synthetic sea clutter, a shorter presentation of the main results is done for synthetic sea-ice clutter. The results are summarized in Fig. 8.28, where the results for the best (S) and worst (V) selection modes are only depicted considering all the clutter conditions. In the non-incorporated results, it is observed that the performance of the selection modes continues being sorted as presented in Fig. 8.27 for the case of study of the practical conditions. From Fig. 8.27 and 8.28, it can be observed that the best clutter conditions for designing MLP-based detectors are the practical ones. Moreover, it is observed that the best range of values of RIA continues being in $[5, 11]$ cells.

As previously mentioned, a last study is done. This study is related to the number of hidden neurons (H) the MLP should incorporate to achieve high processor and detector performance. Since the best size is not known a priori, H is varied from 3 to 50 in this study. The performance achieved for the different selection modes under study is plotted in Fig. 8.29, considering the validation data set and RIA = 5 cells in 1-D and 2-D selection modes and $N = 4$ cell for non-

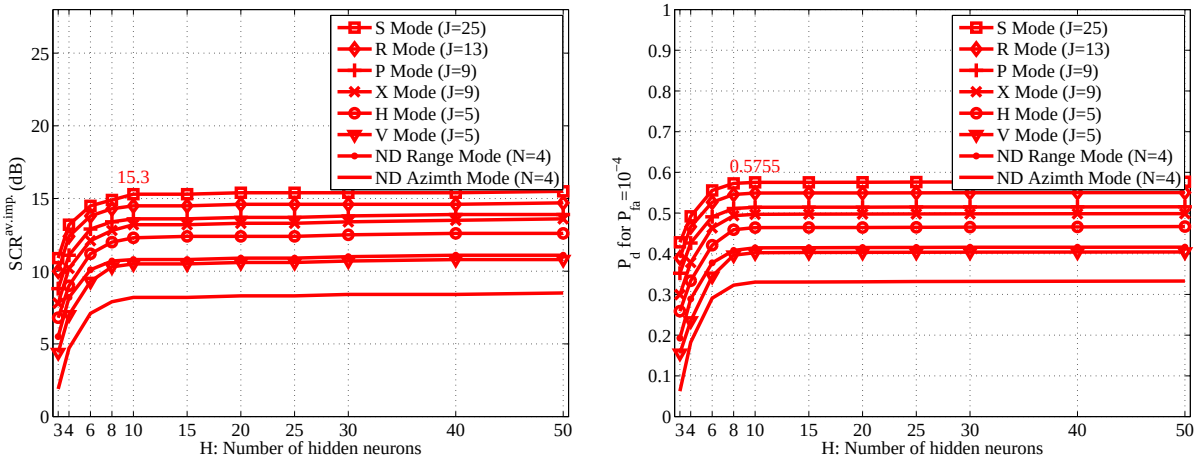

(a) MLP-based processors

(b) MLP-based detectors

Figure 8.29: Performances of processors and detectors based on $2J/H/1$ MLPs varying the number of hidden neurons. Non-delayed and delayed (1-D and 2-D) selection modes and the best training strategy ($a^{(\mathrm{d})} \in [0.50, 1.65]$) are considered for the case of study of sea-ice clutter. Performance is given for the validation data set.

delayed selection modes. Since the value of RIA selected for each mode is the same as for the case of study of MLPs in synthetic sea clutter (see Sect. 8.2.2), the variation of the computational cost of the MLP-based detector with respect to H given in Fig. 8.10 is also valid here. As observed in Fig. 8.29 and 8.10, for all the modes under study, low performance improvement (observed by making a zoom of Fig. 8.29) and high computational cost increase are achieved from $H = 10$ hidden neurons. Thus, this value can be used as the best one taking into account a trade-off between detector performance and computational cost.

After these studies, an MLP-based detector using a structure 50/10/1 with an S selection mode and trained using the practical conditions data set ($a_i^{(\mathrm{d})} \sim \mathrm{N}(1.20, 0.14)$) is proposed to detect moving Swerling 0 targets in the synthetic sea-ice clutter conditions considered in the thesis.

8.3.3 Design of RBFN-based Coherent Detectors in Synthetic Sea-Ice Clutter

The same parameters as for the MLP-based coherent detectors (clutter conditions, selection modes, J|RIA and H) are studied for designing RBFN-based coherent detectors in synthetic sea-ice clutter.

At the beginning, the first three parameters (clutter conditions, selection modes and RIA) are simultaneously studied, but considering only non-delayed selection modes to be able to compare its performance with the one achieved by the detector taken as reference (TSKAP detector). After this study, these parameters are also studied for the other (delayed) selection modes.

The performance obtained for the RBFN-based processor and detector is depicted in Fig. 8.30 when non-delayed selection modes are used. Since the number of hidden neurons ($H = 20$) used in this study and for the case of study of RBFNs in synthetic sea clutter is the same, the plot of

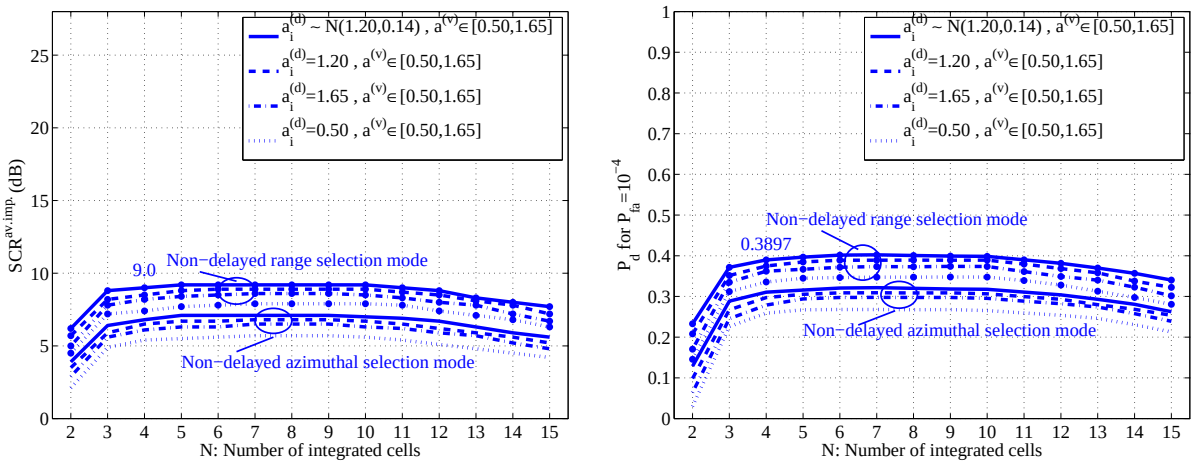

(a) RBFN-based processors

(b) RBFN-based detectors

Figure 8.30: Performances of $2N/20/1$ RBFN-based processors and detectors using non-delayed selection modes and varying N when sea-ice clutter conditions are used. Minimum ($a_i^{(\mathrm{d})} = 0.50$), typical ($a_i^{(\mathrm{d})} = 1.20$), maximum ($a_i^{(\mathrm{d})} = 1.65$) and practical ($a_i^{(\mathrm{d})} \sim \mathrm{N}(1.20, 0.14)$) design conditions are considered. Performance is given for the validation data set.

the computational cost versus N given in Fig. 8.12 is applicable here. From Fig. 8.30 and 8.12, aspects similar to the ones observed for MLP-based detectors (see Sect. 8.3.2) can be observed. These aspects are focused on:

- The similar tendency observed for the processor and detector performance with N.
- The selection mode that allows to achieve the highest performance (range integration).
- The number of selected cells that allow to achieve the highest performance ($N \in [4, 10]$), which is related to the sizes of these targets (from 2 to 10 cells). According to the variation of the computational cost of the RBFN-based detector with N (see Fig. 8.12), $N = 4$ is selected because it allows the detector to achieve high performance with low computational cost.

The main differences between MLP and RBFN-based approaches are related to the reduction of the performance and to the increment of the computational cost observed in the RBFN-based approach. The performance of the RBFN-based detector is lower than the one achieved by the MLP-based detector in $\Delta P_{\mathrm{d}} \simeq -0.03$ (see Fig. 8.26) but greater than the one achieved by the TSKAP detector in $\Delta P_{\mathrm{d}} \simeq 0.14$ (see Fig. 8.25). The computational cost of this approach is increased from 1552 operations for the MLP-based detector to 102502 operations for the RBFN-based detector.

After this study, and considering only non-delayed selection modes, the use of practical conditions ($a_i^{(\mathrm{d})} \sim \mathrm{N}(1.20, 0.14)$) and an integration of $N = 4$ cells in a range selection mode is proposed as a partial solution to design RBFN-based coherent detectors to detect moving Swerling 0 targets in the synthetic sea-ice clutter conditions considered in the thesis. The proposed RBFN-based processor and detector is able to outperform the TSKAP processor and detector

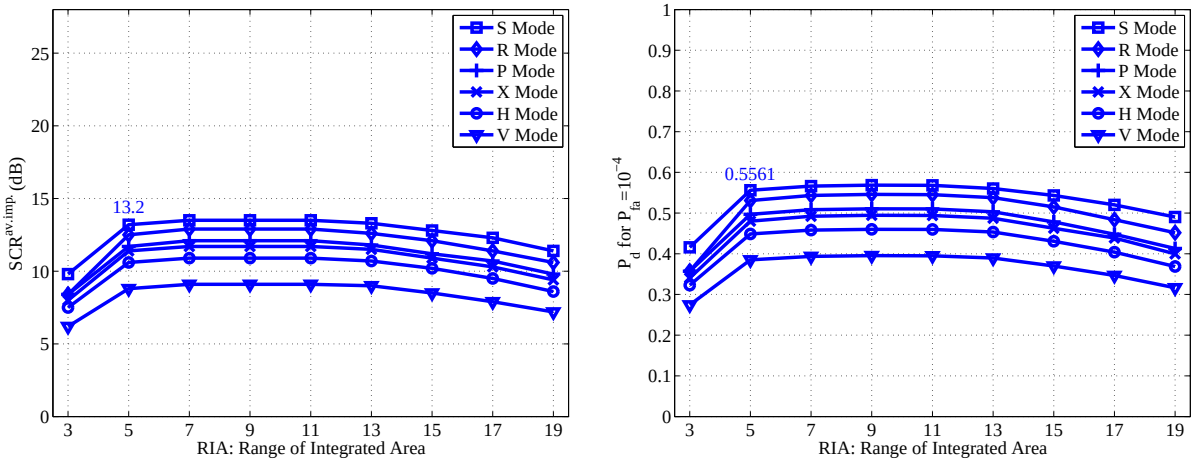

(a) RBFN-based processors

(b) RBFN-based detectors

Figure 8.31: Performances of processors and detectors based on $J/20/1$ RBFNs varying the RIA in 1D and 2D selection modes and considering the practical design conditions for sea-ice clutter ($a_i^{(\mathrm{d})} \sim \mathrm{N}(1.20, 0.14)$). Performance is given for the validation data set.

in $\Delta\mathrm{SCR}^{\mathrm{av.imp}} \simeq 5$ dB and $\Delta P_{\mathrm{d}} \simeq 0.14$, respectively, considering the selected configurations in each case (see Fig. 8.30 and 8.25).

As done for the MLP-based detector, this thesis goes one step ahead and investigates how the performance of the RBFN-based detector could be improved. For that purpose, improved selection modes are used, both in 1-D and 2-D. The performance obtained for the RBFN-based processor and detector is depicted in Fig. 8.31 when RIA is varied and the practical conditions ($a_i^{(\mathrm{d})} \sim \mathrm{N}(1.20, 0.14)$) are considered. The computational cost of the RBFN-based detector with respect to RIA is depicted in Fig. 8.15. These plots belong to the performance and computational cost achieved in RBFN-based processors and detectors formed of 20 hidden neurons. A study of the influence of the number of hidden neurons in RBFN-based detectors is given at the end of this subsection.

From the results presented in Fig. 8.31 and 8.15, similar conclusions as the ones obtained for the MLP-based detector (see Sect. 8.3.2) can be drawn in terms of:

- The similar tendency of the processor and detector performance with RIA.
- The RIA that maximizes the RBFN-based detector performance is in the range $[5, 11]$ cells, which is again related to the size of the targets considered in the thesis (from 2 to 10 cells). Moreover, and according to the computational cost of the detector, the value for which high performance and low computational cost are achieved is RIA $= 5$ cells.
- The best selection mode: the S mode, having the drawback of a temporal delay of 1.2 ms and presenting higher computational cost than the other modes.
- The performance achieved by the proposed RBFN-based detector is always better than the TSKAP detector one (using an azimuthal selection mode). The processor and detector

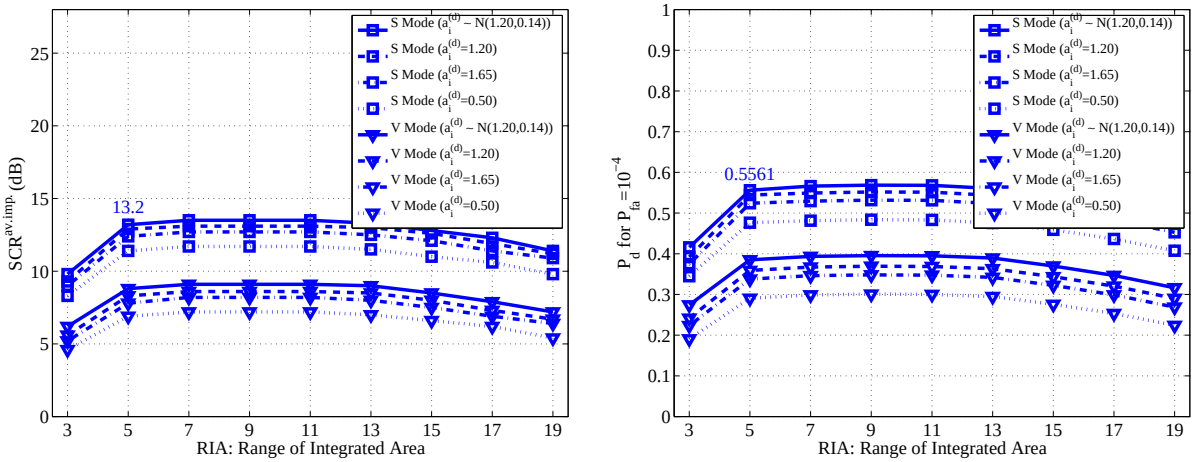

(a) RBFN-based processor

(b) RBFN-based detector

Figure 8.32: Performances of RBFN-based processors and detectors for sea-ice clutter conditions and during the design stage. During this stage, the best (S) and worst (V) selection modes are used and RIA and the design conditions are varied. Performance is given for the validation data set.

performance improvements (compare Fig. 8.31 and 8.25) approximately vary from a minimum of $\Delta\text{SCR}^{\text{av.imp.}} \simeq 5\,\text{dB}$ and $\Delta P_{\text{d}} \simeq 0.15$ (best case for V mode) to a maximum of $\Delta\text{SCR}^{\text{av.imp.}} \simeq 9\,\text{dB}$ and $\Delta P_{\text{d}} \simeq 0.31$ (best case for S mode).

Once again, 2-D selection modes allow to achieve better performance than 1-D modes because of the independency of the target orientation in the radar scan and the increase of the amount of information to make the decision.

As done for the case of study of the MLP-based detector, a summary of the results obtained for the study of the influence of the design clutter conditions is given. These results are depicted in Fig. 8.32 for the best (S) and worst (V) selection modes. From this figure, it is observed that the best clutter conditions for designing RBFN-based detectors are the practical ones. Moreover, it is observed that the best range of values of RIA continues being $[5, 11]$ cells.

Finally, a study of the number of hidden neurons (H) for which the RBFN achieves the best processor and detector performance is made. RBFNs of size $2J/H/1$ are used, where the best RIA, and consequently the best J, for each delayed selection mode and $N = 4$ cells for the non-delayed selection modes are selected. Since the best number of hidden neurons is not known a priori, H is varied from 3 to 50. The performance achieved for the different selection modes under study are plotted in Fig. 8.33. The computational cost of each RBFN-based detector configuration is given in Fig. 8.17 when H is varied. As observed, for all the modes under study, low performance improvements are achieved from $H = 20$ hidden neurons. Therefore, $H = 20$ hidden neurons can be used as the best one taking into account a trade-off between performance ($\text{SCR}^{\text{av.imp.}} = 13.2\,\text{dB}$ and $P_{\text{d}} = 0.5561$ for $P_{\text{fa}} = 10^{-4}$) and computational cost (102502 operations).

After these studies, an RBFN-based detector using a structure 50/20/1 with an S selection

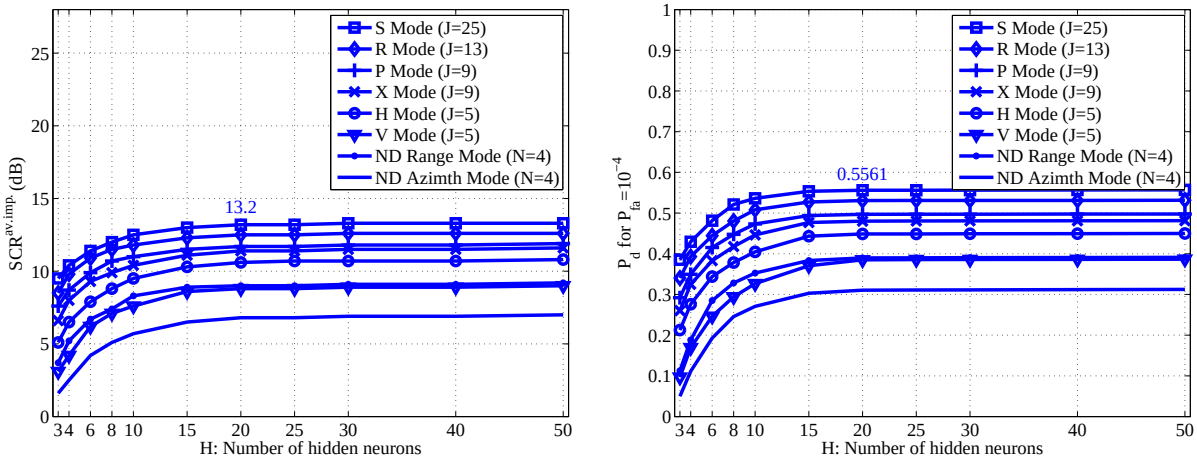

(a) RBFN-based processors

(b) RBFN-based detectors

Figure 8.33: Performances of processors and detectors based on $2J/H/1$ RBFNs varying the number of hidden neurons. Non-delayed and delayed (1-D and 2-D) selection modes and the best training strategy ($a^{(\mathrm{d})} \in [0.50, 1.65]$) are considered for the case of study of sea-ice clutter. Performance is given for the validation data set.

mode and trained using the practical conditions data set ($a_i^{(\mathrm{d})} \sim \mathrm{N}(1.20, 0.14)$) is proposed to detect moving Swerling 0 targets in the synthetic sea-ice clutter conditions considered in the thesis.

8.3.4 Comparison of Coherent Detectors in Design and Test Stages under Synthetic Sea-Ice Clutter Conditions

As done for the test stage of the coherent detectors under study when synthetic sea clutter was considered (see Sect. 8.2.4), this section pays special attention to the following question: Is there any change in the performance of the detector when processing new radar scans? This is what happens in real-live situations, where the processed data are different of the ones used for designing, although their statistical properties could be similar or not. Therefore, this thesis investigates if the performance achieved for these new radar scans is maintained or not with respect to the one obtained in the design stage, and, in case of change, which are the magnitudes of the changes.

For studying the variations of performance, the sea-ice clutter conditions used for test and presented in Table 7.6 of Sect. 7.1.3 are considered. This study is divided in two parts. At the beginning, the performance of the detectors in the design and test stages is compared by ROC curves. At the end, two radar scans of the test data set are selected and processed to analyze what is really happening and trying to find an answer to the performance achieved in each case.

The configurations used for each detector are extracted from the design stage, being:

- MLP-based coherent detector: designed considering the practical conditions of Table 7.6 ($a_i^{(\mathrm{d})} \sim \mathrm{N}(1.20, 0.14)$) and selecting $J = 25$ (RIA= 5 cells) complex-valued cells by an S

selection mode. The number of hidden neurons is set to $H = 10$. Because real-arithmetic is used in the MLP, a total of 50 inputs are needed, having an MLP structure of 50/10/1.

- RBFN-based coherent detector: designed considering the practical conditions of Table 7.6 ($a_i^{(\mathrm{d})} \sim \mathrm{N}(1.20, 0.14)$) and selecting $J = 25$ (RIA= 5 cells) complex-valued cells by an S selection mode. The number of hidden neurons is set to $H = 20$. Because real-arithmetic is used in the RBFN, a total of 50 inputs are needed, having an RBFN structure of 50/20/1.

- TSKAP coherent detector: designed considering the typical conditions ($a_i^{(\mathrm{d})} = 1.20$) and selecting $N = 4$ complex-valued cells in a non-delayed azimuthal selection mode.

The ROC curves obtained in the design stage by using the validation data set are depicted in Fig. 8.34a. On the other hand, the ROC curves obtained in the test stage (test data set), i.e. for a set of radar images never processed by the designed detectors, are given in Fig. 8.34b. Note that the performance of the processors are also given in the legends of the figures for reference purposes. Similar conclusions as the ones obtained for the case of study of synthetic sea clutter can be drawn from the results presented in Fig.8.34, but with some differences:

- The tendency of the ROC curves is maintained from design to test conditions. The best detector continues being the one based on MLPs, followed by the one based on RBFNs. Both approaches surpass the performance achieved by the TSKAP detector. This conclusion is the same as the one obtained for the case of study of synthetic sea clutter.

- The performance of the processors and detectors are decreased in terms of $\mathrm{SCR}^{\mathrm{av.imp.}}$ and P_{d}, respectively. Focusing on the TSKAP detector, the performance loss of the processor and detector is approximately $\Delta\mathrm{SCR}^{\mathrm{av.imp.}} \simeq -0.5$ dB and $\Delta P_{\mathrm{d}} \simeq -0.02$, respectively. On the other hand, the performance loss observed in AI-based processors and detectors is approximately $\Delta\mathrm{SCR}^{\mathrm{av.imp.}} \simeq -0.5$ dB and $\Delta P_{\mathrm{d}} \simeq -0.01$, respectively. From these results, it is observed that the proposed detectors are more robust than the one taken as reference. This performance improvements are slightly different to the ones obtained for the case of study of synthetic sea clutter.

From these conclusions, we can conclude that high robustness is achieved in all the detectors when new radar scans are processed. This is an important issue in a detector because it gives us an approximation of how its performance will be when working autonomously and in steady state.

Apart of the performance loss and robustness studies presented above for the detectors, a subjective and objective analysis of the performance of the detectors for radar scans with different clutter conditions is made. For that purpose, two radar scans of the test data set under synthetic sea-ice clutter conditions are selected. For selecting these radars scans, the same criteria as when considering sea clutter conditions is used, i.e. we select the radar scans for which the best and worst performance is achieved, being in this case $\mathbf{I}^{(1.20)}$ and $\mathbf{I}^{(0.50)}$, respectively. The plot of the pdf of each clutter condition is depicted in Fig. 8.35. In this plot, it is observed that for low values of a, such as $a = 0.50$, higher probability of finding very low and very high values of clutter is observed. Thus, for a low value of a (clutter being spiky) two effects can be expected: high thresholds are needed to maintain a constant false alarm rate, decreasing the detection rate; or an increase of the false alarm rate for a constant threshold is obtained.

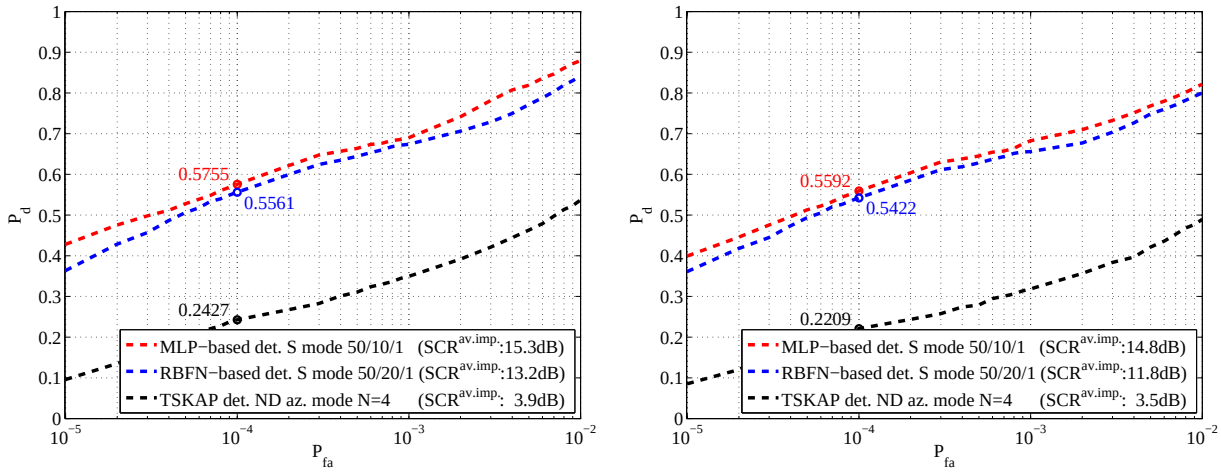

(a) Validation data set (b) Test data set

Figure 8.34: Performances of the selected configurations of TSKAP, MLP and RBFN-based coherent detectors using the validation ($a_i^{(\mathrm{v})} \sim \mathrm{N}(1.20, 0.14)$) and test ($a_i^{(\mathrm{t})} \sim \mathrm{N}(1.20, 0.14)$) data sets when synthetic sea-ice clutter measurements are considered.

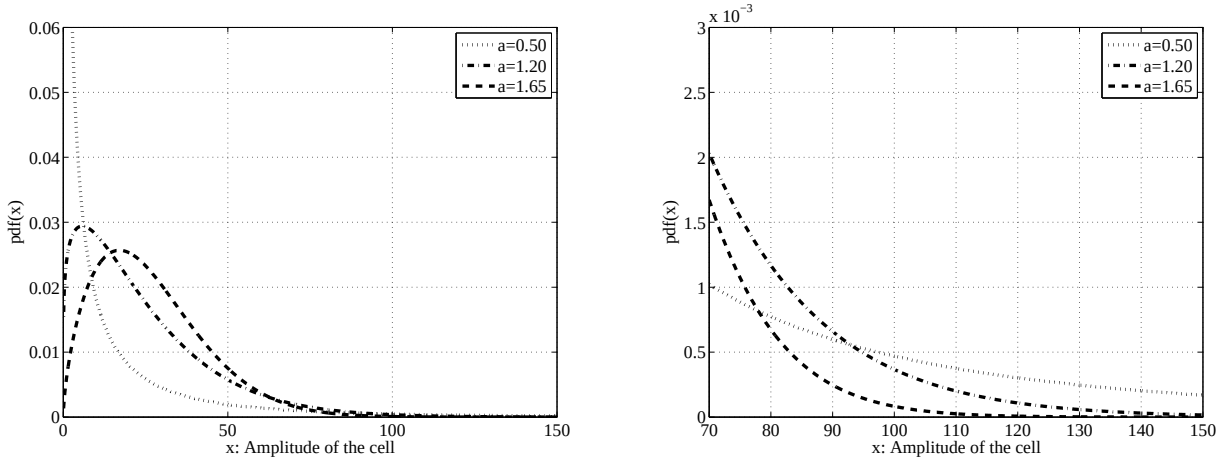

(a) Whole range (b) Zoom of Fig. 8.35b

Figure 8.35: Probability density functions (pdf's) of the clutter signal amplitude for minimum ($a = 0.50$), typical ($a = 1.20$) and maximum ($a = 1.65$) sea-ice clutter conditions.

The real and imaginary parts of the selected radar scans are plotted in Fig. 8.36 and 8.37. Note that not all the coverage of the radar scans (see Table 2.4) is plotted because details will be lost in presentation. Only a zone of the full-coverage, between 30 and 38 degrees in azimuth and between 1500 m and 2100 m in range, is selected for plotting and making the subjective analysis of the performance. It is important to note that the objective performance given for each processed radar scan is given for the whole scan and not for the selected zone. On the other hand, the physical positions of the targets (cell-by-cell) in the radar scenes of $\mathbf{I}^{(1.20)}$ and $\mathbf{I}^{(0.50)}$ are depicted in Fig. 8.38 by using a high level. A low level in a cell indicates that no target

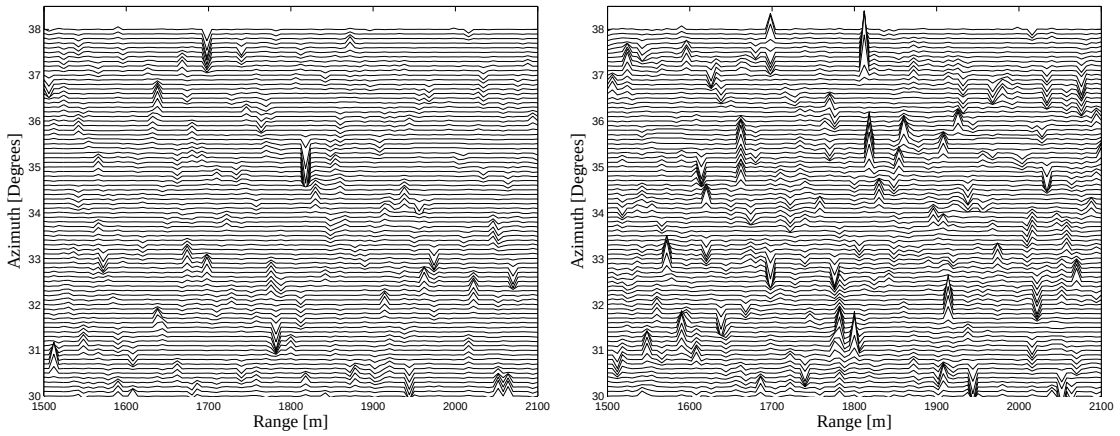

(a) $\mathrm{Re}\{\mathbf{I}^{(0.50)}\}$ (b) $\mathrm{Im}\{\mathbf{I}^{(0.50)}\}$

Figure 8.36: Real (Re{}) and imaginary (Im{}) parts of a radar scan ($\mathbf{I}$) taken from test data set with $a^{(\mathrm{t})} = 0.50$ ($\mathbf{I}^{(0.50)}$) when synthetic sea-ice clutter is considered.

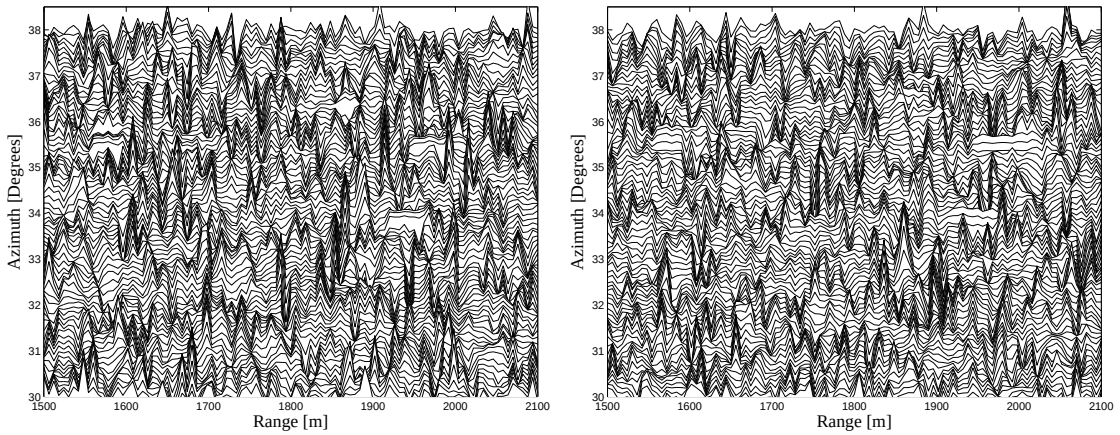

(a) $\mathrm{Im}\{\mathbf{I}^{(1.20)}\}$ (b) $\mathrm{Im}\{\mathbf{I}^{(1.20)}\}$

Figure 8.37: Real (Re{}) and imaginary (Im{}) parts of a radar scan ($\mathbf{I}$) taken from test data set with $a^{(\mathrm{t})} = 1.20$ ($\mathbf{I}^{(1.20)}$) when synthetic sea-ice clutter is considered.

information is present in it. The physical size of the targets are also depicted in terms of cells in this ideal scan.

The radar scans at the output of the TSKAP and AI-based coherent processors and detectors for $\mathbf{I}^{(0.50)}$ and $\mathbf{I}^{(1.20)}$ are depicted in Fig. 8.39 and 8.40, respectively. According to these results, a subjective analysis of the images is made, an analysis of detector performance loss is given, and some conclusions are drawn.

The same subjective analysis made in Sect. 8.2.4 when considering synthetic sea clutter is made here for the results given in Fig. 8.39 and 8.40. From this analysis, similar aspects are observed. First, there are more cells belonging to target that are detected when using AI-based detectors than when using the TSKAP detector, regardless of the radar scan. Second, more cells

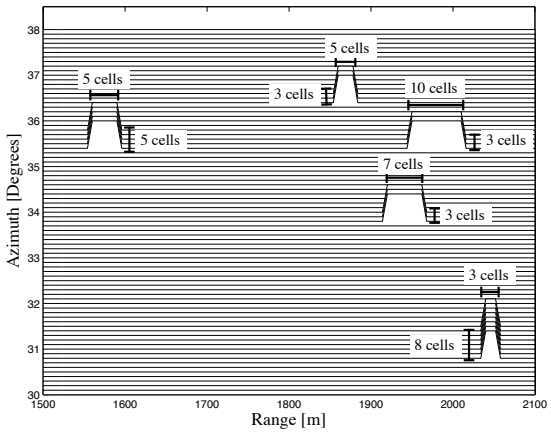

Figure 8.38: Desired (ideal) output radar scan ($\mathbf{D}$) when synthetic sea-ice clutter is considered.

belonging to target are detected for the case of having $a = 1.20$ than for $a = 0.50$ because the second case is a more complicated clutter case (spiky clutter). And third, more false alarms are detected for the case of $a = 0.50$ than for $a = 1.20$ and for the TSKAP detector than the AI-based detectors.

For analyzing the performance loss of each detector, we take as reference the $\mathrm{SCR}^{\mathrm{av.imp.}}$ and P_{d}'s for $P_{\mathrm{fa}} = 10^{-4}$ achieved when the validation and test data sets are used (see Fig. 8.34). From the performance achieved by each detector, we can observe that:

- The performance achieved for $\mathbf{I}^{(0.50)}$ is always lower than the ones achieved for the validation and test data sets. It happens because the detection of targets in these clutter conditions (spiky clutter) is more difficult than in the other ones, as expected.

- The performance achieved for $\mathbf{I}^{(1.20)}$ is always greater than the ones achieved for the validation and test data sets. It happens because the detection of targets in these clutter conditions is easier than in the other ones.

- The P_{fa} remains constant with the threshold set during the design stage for the case of $a^{(\mathrm{t})} = 1.20$. Whereas for the case of $a^{(\mathrm{t})} = 0.50$, the P_{fa} is slightly higher due to the statistical properties of the clutter for this skewness parameter value (spiky clutter).

As concluded for the synthetic sea clutter case, analyzing the radar scans presented in Fig. 8.39 and 8.40, we can find two reasons why AI-based detectors outperform the reference detector. First, because they are able to reduce better and in a high rate the level of clutter. And second, because they are able to emphasize the level of signal where target is present. Both reasons can be extracted from the radar scans at the output of the processors, which lead to improve the detection rate.

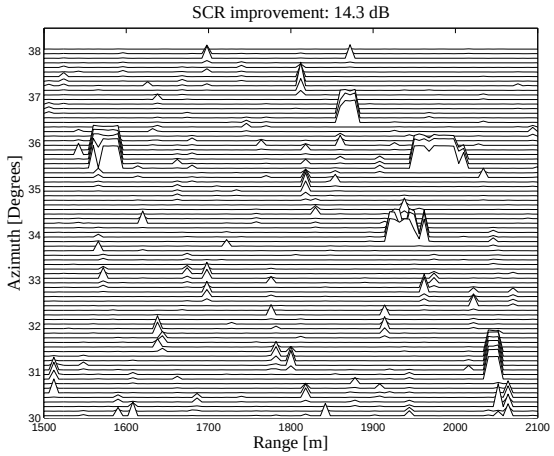

(a) MLP-based processor output for $\mathbf{I}^{(0.50)}$

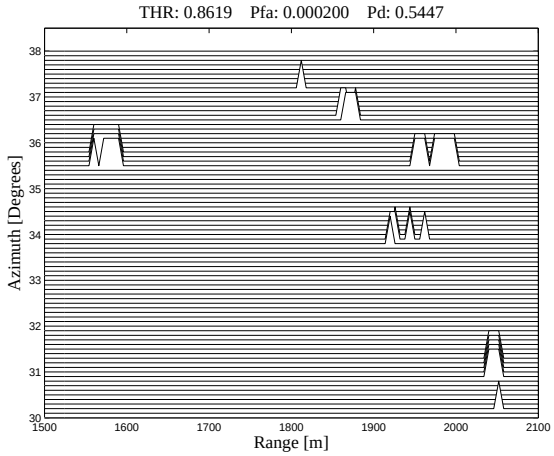

(b) MLP-based detector output for $\mathbf{I}^{(0.50)}$

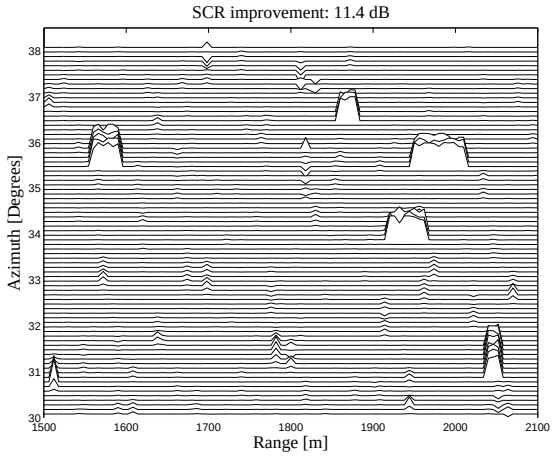

(c) RBFN-based processor output for $\mathbf{I}^{(0.50)}$

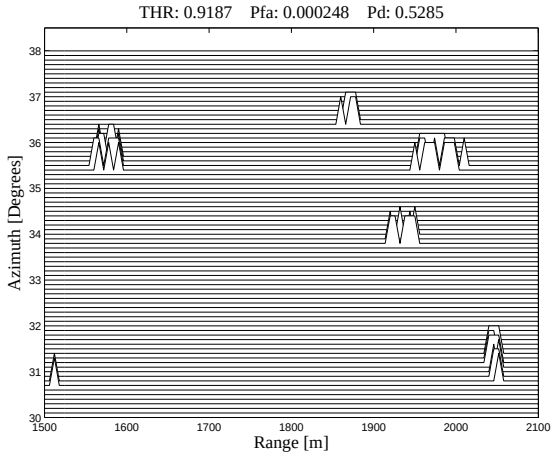

(d) RBFN-based detector output for $\mathbf{I}^{(0.50)}$

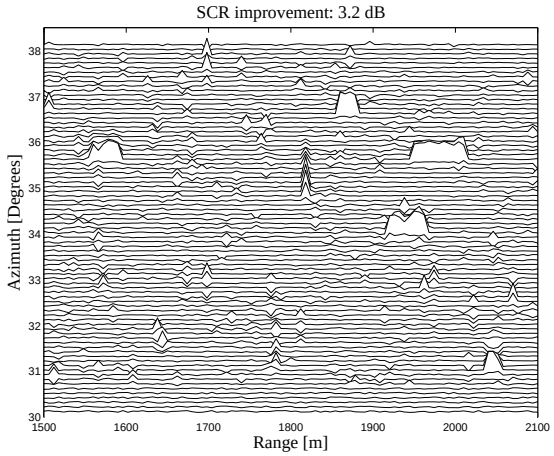

(e) TSKAP processor output for $\mathbf{I}^{(0.50)}$

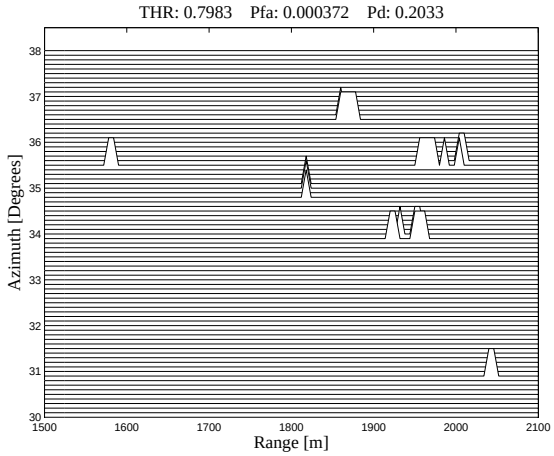

(f) TSKAP detector output for $\mathbf{I}^{(0.50)}$

Figure 8.39: Radar scans at the output of the MLP-based, RBFN-based and TSKAP processors and detectors when the input radar scan $\mathbf{I}^{(0.50)}$ from the test data set of sea-ice clutter conditions is processed.

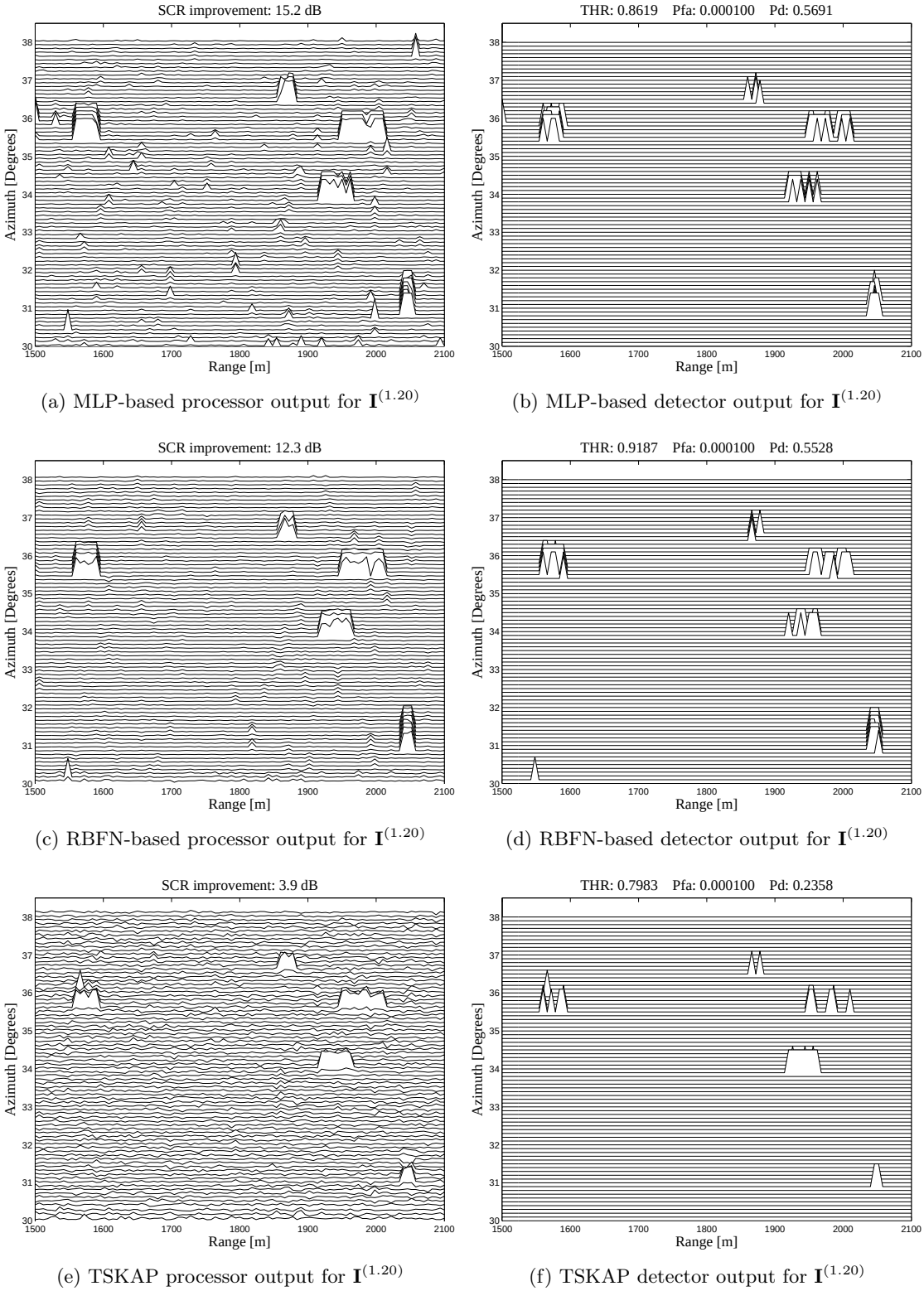

(a) MLP-based processor output for $\mathbf{I}^{(1.20)}$

(b) MLP-based detector output for $\mathbf{I}^{(1.20)}$

(c) RBFN-based processor output for $\mathbf{I}^{(1.20)}$

(d) RBFN-based detector output for $\mathbf{I}^{(1.20)}$

(e) TSKAP processor output for $\mathbf{I}^{(1.20)}$

(f) TSKAP detector output for $\mathbf{I}^{(1.20)}$

Figure 8.40: Radar scans at the output of the MLP-based, RBFN-based and TSKAP processors and detectors when the input radar scan $\mathbf{I}^{(1.20)}$ from the test data set of sea-ice clutter conditions is processed.

8.3.5 Conclusions about Coherent Detectors in Synthetic Sea-Ice Clutter

In general, similar conclusions to the ones achieved when using coherent detectors in synthetic sea clutter (see Sect. 8.2.5) are drawn here when using coherent detectors in synthetic sea-ice clutter. But, some differences are found because different clutter and target (sizes) conditions are used. These conclusions and differences are:

- The clutter conditions that maximize the performance of AI-based detectors in the design stage are the practical ones (skewness parameter varying scan-to-scan and following a normal distribution with parameters $a_i^{(\mathrm{d})} \in \mathrm{N}(1.20, 0.14)$ in this case). When these situations are not applicable, as for the reference detector (TSKAP), the best design conditions are the typical ones ($a_i^{(\mathrm{d})} = 1.20$ in this case).

- The selection modes for obtaining the highest performance in AI-based coherent detectors are based on 2-D templates. From these templates, the best one is the square (S) integration mode. But, detectors using this mode present high computational cost (1552 and 102502 operations per CUT in the selected MLP and RBFN-based coherent detector configurations). To reduce it, while solving the problem of detecting moving Swerling 0 targets in sea-ice clutter with slightly lower performance, the rhombus (R) and plus-shape (P) selection modes become a solution. On the other hand, if 1-D selection modes are used in AI-based detectors, the best ones are based on selecting the cells in the range direction, which effect is opposite to the one achieved for the TSKAP detector.

- The range of RIA for which the highest performance is achieved ($\in [5, 11]$ cells in this case) is highly related to the target sizes considered in the study ($\in [2, 10]$ cells in azimuth and range in this case), regardless of the coherent detector. Moreover, according to the computational cost required to implement the detector, it is proposed that the value selected for RIA is the lowest one (RIA = 5 cells in this case of study).

- A suitable number of hidden neurons in AI-based detectors is found, being different for detectors based on MLPs ($H = 10$) and RBFNs ($H = 20$). This number is selected considering a trade-off between detector performance and computational cost.

- It is observed that the dimensionality of the detector can be done using two kind of performance measurements: $\mathrm{SCR}^{\mathrm{av.imp.}}$ in the processor; and P_{d} for a given P_{fa} in the detector. Both performance measurements present similar tendencies with the parameters of the detectors under study.

- High robustness is observed when processing radar scans different of the ones used in the design stage of coherent detectors. No performance loss greater than $\Delta\mathrm{SCR}^{\mathrm{av.imp.}} \simeq -0.5$ dB and $\Delta P_{\mathrm{d}} \simeq -0.02$ for $P_{\mathrm{fa}} = 10^{-4}$ is expected in average.

- Slightly higher performance is observed for radar scans having a skewness parameter of its typical value ($a_i^{(\mathrm{t})} = 1.20$ in this case) than for radar scans having a skewness parameter far from its typical value ($a_i^{(\mathrm{t})} = 0.50$, as an example). Moreover, low P_{fa} increase is observed in the test stage for radar scans having low skewness values ($a_i^{(\mathrm{t})} = 0.50$ in this case) with respect to radar scans having a typical value of skewness ($a_i^{(\mathrm{t})} = 1.20$ in this case) because a more spiky clutter is observed for this skewness parameter.

8.4 Coherent Detectors in Synthetic Ground Clutter

As done for the case of study of designing detectors in synthetic sea and sea-ice clutters (see Sect. 8.2 and 8.3), the current section is dedicated to design and test coherent detectors but when synthetic ground clutter conditions are considered. During the design of the coherent detectors under study, i.e. TSKAP and AI-based coherent detectors, some parameters must be tuned to find which are the ones that maximize the performance of the detectors. These parameters are the same as the ones considered in the studies of the cases of synthetic sea and sea-ice clutters, being: the clutter conditions used to design the detectors; the selection modes incorporated in them; the number of cells integrated in the detector; and number of hidden neurons that compose the AI-based processor of the detector. On the other hand, and as done for the case of study of sea-ice clutter, the SNR is reduced from 40 dB to 30 dB (SCR is reduced from 10 dB to 0 dB) because for SNR = 40 dB no performance improvement would be appreciated.

As occurred for the previous cases of study, the selection of the best value of the above-mentioned parameters is done during the design stage, for which the training and validation data sets of Table 7.7 are used. As done for the previous studies considering sea and sea-ice clutters, these data sets are generated once for all the experiments done during the design and test of TSKAP and AI-based coherent detectors in synthetic ground clutter. The performance of the processors and detectors presented in subsections 8.4.1-8.4.3 are given for the validation data set and in terms of $\mathrm{SCR}^{\mathrm{av.imp.}}$ and P_{d} for $P_{\mathrm{fa}} = 10^{-4}$, respectively. Finally, performance for radar scans never used during the detector design are given in Sect. 8.4.4), in which the robustness of the detectors when processing new radar scans is presented.

8.4.1 Design of TSKAP Detectors in Synthetic Ground Clutter

The same steps followed in Sect. 8.2.1 for synthetic sea clutter or in and Sect. 8.3.1 for synthetic sea-ice clutter are considered below during the design of TSKAP detectors in synthetic ground clutter. In this way, the influence of the clutter conditions, the non-delayed selection modes and the number of integrated/selected cells is simultaneously studied. The performance of the different configurations of the TSKAP detector attending to the variation of these parameters is depicted in Fig. 8.41. From these results, the same important aspects as observed, for instance, in Sect. 8.4.1 are obtained in terms of: the tendency of the processor and detector performance with N; the best clutter conditions used for designing (the typical ones: $a_i^{(\mathrm{d})} = 1.76$); the best selection mode (non-delayed azimuthal mode); and the range of N in which the best performance is achieved ($N \in [3, 5]$ cells), which is related to the target sizes (from 1 to 4 cells both in range and azimuth from Table 7.1).

After this study, the use of typical conditions ($a^{(\mathrm{d})} = 1.76$) and an integration of $N = 4$ cells using a non-delayed azimuthal selection mode is proposed to design TSKAP coherent detectors to detect moving Swerling 0 targets in the synthetic ground clutter conditions considered in the thesis.

8.4.2 Design of MLP-based Coherent Detectors in Synthetic Ground Clutter

The same procedure followed for designing MLP-based detectors in synthetic sea-ice clutter (see Sect. 8.3.2) is followed here but for designing MLP-based detectors in synthetic ground clutter.

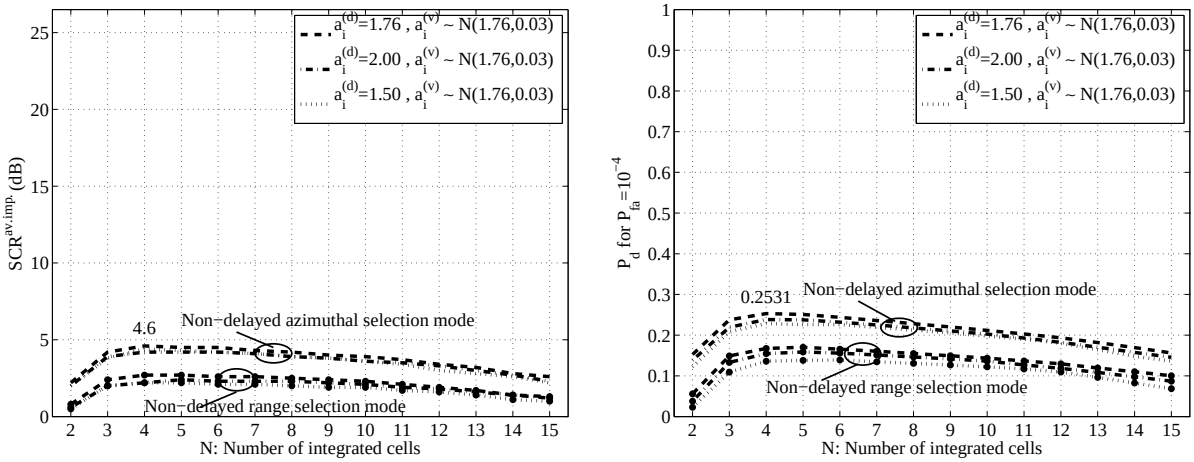

(a) TSKAP processors (b) TSKAP detectors

Figure 8.41: Performance of TSKAP processors and detectors using non-delayed selection modes and varying N when ground clutter conditions are used. Minimum ($a^{(\mathrm{d})} = 1.50$), typical ($a^{(\mathrm{d})} = 1.76$) and maximum ($a^{(\mathrm{d})} = 2.00$) design conditions are considered. Performance is given for the validation data set.

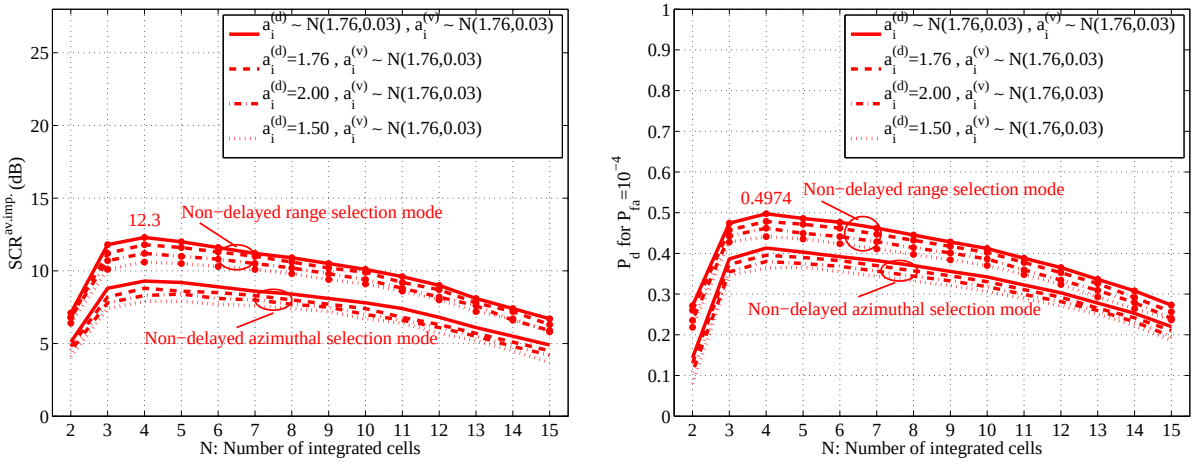

(a) MLP-based processors (b) MLP-based detectors

Figure 8.42: Performance of $2N/10/1$ MLP-based processors and detectors using non-delayed selection modes and varying N when ground clutter conditions are used. Minimum ($a^{(\mathrm{d})} = 1.50$), typical ($a^{(\mathrm{d})} = 1.76$), maximum ($a^{(\mathrm{d})} = 2.00$) and practical ($a_i^{(\mathrm{d})} \sim \mathrm{N}(1.76, 0.03)$) design conditions are considered. Performance is given for the validation data set.

As done in Sect. 8.3.2, the influence of the clutter conditions, the selection mode, the number of integrated cells (RIA and J) and the number of hidden neurons is studied during the design of MLP-based detectors.

In the first experiments, only the influence of the clutter conditions, the selection mode and

RIA are simultaneously studied considering non-delayed selection modes. In this way, we can compare the achieved performance with the one achieved by the TSKAP coherent detector. The performance obtained for the different configurations of MLP-based processor ($\mathrm{SCR}^{\mathrm{av.imp.}}$) and detector ($P_{\mathrm{d}}$ for $P_{\mathrm{fa}} = 10^{-4}$) are depicted in Fig. 8.42. From these results, the same conclusions reported in Sect. 8.3.2 are drawn here but particularized for the Weibull-distributed ground clutter: the observed tendency of the processor and detector with N is similar; the best clutter conditions used for designing are the practical ones ($a_i^{(\mathrm{d})} \sim \mathrm{N}(1.76, 0.03)$); the best selection mode is the non-delayed range mode; and the range of N in which the best performance is achieved is $N \in [3, 5]$ cells, which is related to the target sizes (from 1 to 4 cells both in range and azimuth from Table 7.1).

After this study, it is observed that the use of practical conditions ($a_i^{(\mathrm{d})} \sim \mathrm{N}(1.76, 0.03)$) and an integration of $N = 4$ cells in a range selection mode to design MLP-based coherent detectors to detect moving Swerling 0 targets in the synthetic ground clutter conditions considered in the thesis is a good solution. This MLP-based configuration requires a computational cost of 292 operations per CUT (extracted from Fig. 8.5). In this case, the selected solution outperforms the TSKAP processor and detector in $\Delta\mathrm{SCR}^{\mathrm{av.imp.}} \simeq 7.5$ dB and $\Delta P_{\mathrm{d}} \simeq 0.24$, respectively, considering the selected detector configurations in each case (compare Fig. 8.42 and 8.41).

As done for the previous kind of clutters, the use of 1-D and 2-D delayed selection modes is investigated. The performance obtained for both the MLP-based processor and detector is depicted in Fig. 8.43 when RIA is varied, where the practical clutter conditions ($a_i^{(\mathrm{d})} \sim \mathrm{N}(1.76, 0.03)$) are used for training and 10 hidden neurons are considered. From this results, the same conclusions as obtained for the case of study of sea-ice clutter (see Sect. 8.3.2) are obtained: similar tendency of the processor and detector with RIA; the values of RIA for which the best performance is achieved ($\in [3, 5]$ cells), being related to the size of the targets (from 1 to 4 cells both in range and azimuth); the selection mode for which the best performance is achieved (S mode), presenting computational cost of 1552 operations per CUT (extracted from Table 8.8); and presenting a minimum improvement of $\Delta\mathrm{SCR}^{\mathrm{av.imp.}} \simeq 7\,\mathrm{dB}$ and $\Delta P_{\mathrm{d}} \simeq 0.23$ (V selection mode) and a maximum improvement of $\Delta\mathrm{SCR}^{\mathrm{av.imp.}} \simeq 12.5\,\mathrm{dB}$ and $\Delta P_{\mathrm{d}} \simeq 0.42$ (S selection mode) comparing to the selected TSKAP detector configuration (see Fig. 8.41). As observed, the performance obtained when using 2-D selection modes is better than when using 1-D selection modes. The reasons, the same as for the other kind of clutters, i.e. the decision is made regardless of the target orientation and improved because more information is available.

The same experiments as in Fig. 8.43 where done considering the minimum ($a_i^{(\mathrm{d})} = 1.50$), typical ($a_i^{(\mathrm{d})} = 1.76$) and maximum ($a_i^{(\mathrm{d})} = 2.00$) clutter conditions for designing MLP-based detectors. But, only the most relevant ones are depicted below. In this way, Fig. 8.44 presents only the results for the best (S) and worst (V) selection modes, considering all the clutter conditions used in the design stage. In the non-incorporated results, it is observed that the performance for the different selection modes continue being sorted as presented for the case of study of the practical conditions (see Fig. 8.43). From Fig. 8.43 and 8.44, it can be observed that the best clutter conditions for designing MLP-based detectors are the practical ones ($a_i^{(\mathrm{d})} \sim \mathrm{N}(1.76, 0.03)$), regardless of the selection mode. Moreover, it is observed that the best range of values of RIA continues being in $[3, 5]$ cells.

A last study concerning to the number of hidden neurons (H) in the MLP is made. As done for

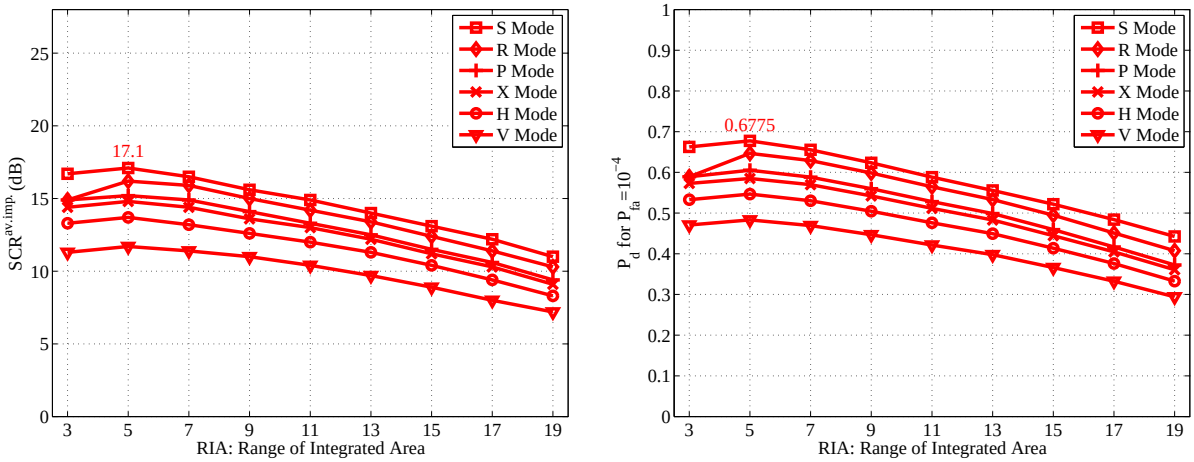

(a) MLP-based processors (b) MLP-based detectors

Figure 8.43: Performance of processors and detectors based on $J/10/1$ MLPs varying the RIA in 1D and 2D selection modes and considering the practical design conditions for ground clutter ($a_i^{(\mathrm{d})} \sim \mathrm{N}(1.76, 0.03)$). Performance is given for the validation data set.

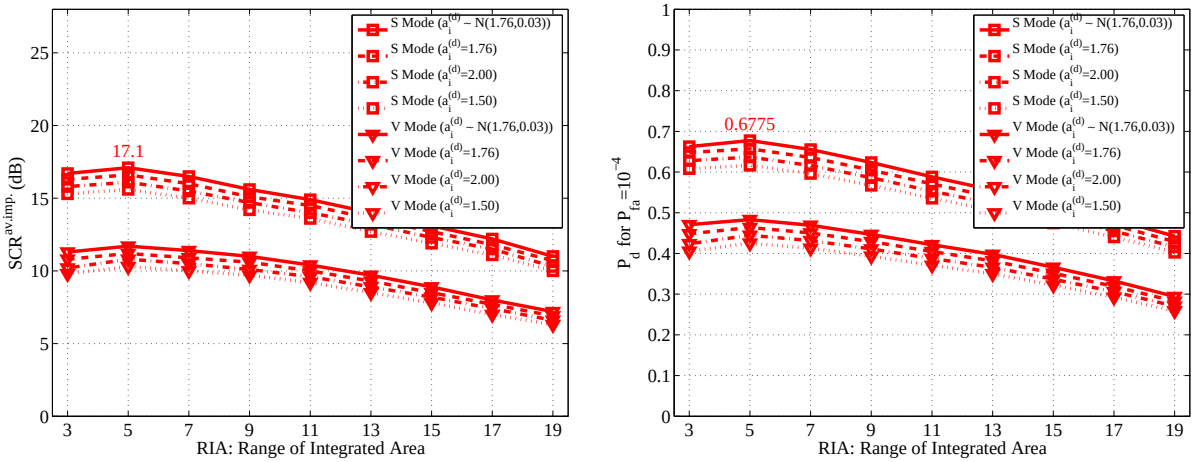

(a) MLP-based processor (b) MLP-based detector

Figure 8.44: Performance of MLP-based processors and detectors for ground clutter conditions and during the design stage. During this stage, the best (S) and worst (V) selection modes are used and RIA and the design conditions are varied. Performance is given for the validation data set.

the cases of study of synthetic sea and sea-ice clutter, H is varied from 3 to 50. The performance achieved for the different selection modes under study is plotted in Fig. 8.45, considering the validation data set and RIA $= 5$ cells for 1-D and 2-D selection modes and $N = 4$ cells for non-delayed selection modes. Since the RIA selected for each mode is the same as for the case of study of MLPs in synthetic sea and sea-ice clutters (see Sect. 8.2.2 and 8.3.2), the variation

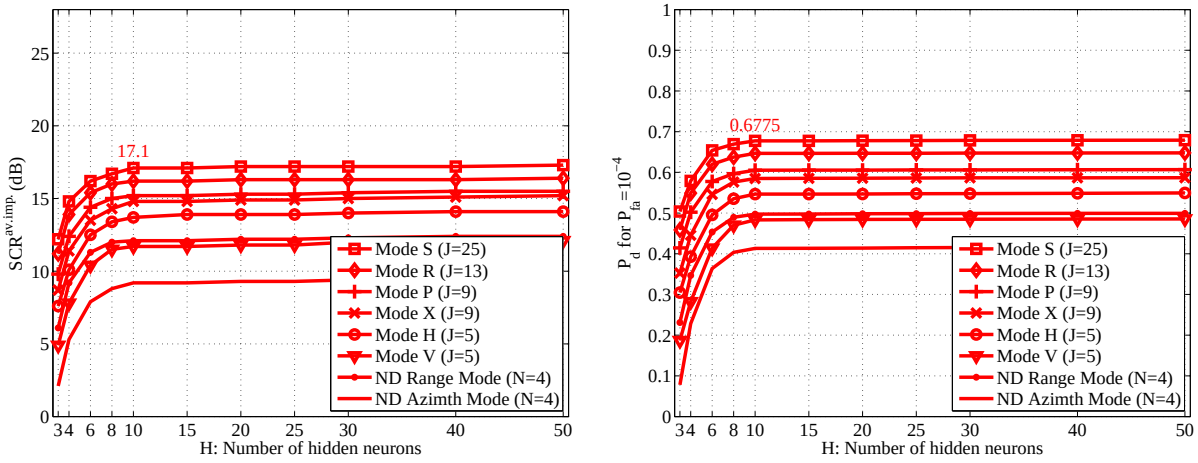

(a) MLP-based processors

(b) MLP-based detectors

Figure 8.45: Performance of processors and detectors based on $2J/H/1$ MLPs varying the number of hidden neurons. Non-delayed and delayed (1-D and 2-D) selection modes and the best training strategy ($a^{(\mathrm{d})} \in [1.50, 2.00]$) are considered for the case of study of ground clutter. Performance is given for the validation data set.

of the computational cost of the MLP-based detector with H given in Fig. 8.10 is observed. As observed in Fig. 8.45 and 8.10, for all the modes under study, low performance improvement and high computational cost increase are achieved from $H = 10$ hidden neurons. Thus, $H = 10$ is selected.

After these studies, an MLP-based detector using a structure 50/10/1 with an S selection mode and trained using the practical conditions data set ($a_i^{(\mathrm{d})} \sim \mathrm{N}(1.76, 0.03)$) is proposed to detect moving Swerling 0 targets in the synthetic ground clutter conditions considered in the thesis. This MLP-based approach outperforms the TSKAP detector in $\Delta\mathrm{SCR}^{\mathrm{av.imp.}} \simeq 12.5\,\mathrm{dB}$ and $\Delta P_{\mathrm{d}} \simeq 0.42$, requiring a total of 1552 operations per CUT.

8.4.3 Design of RBFN-based Coherent Detectors in Synthetic Ground Clutter

As done for MLP-based coherent detectors, the clutter conditions, the selection modes, $J|\mathrm{RIA}$ and H are studied when designing RBFN-based coherent detectors in synthetic ground clutter.

At the beginning, the first three parameters (clutter conditions, selection modes and RIA) are simultaneously studied, considering only non-delayed selection modes to compare the RBFN-based approach to the TSKAP detector. The performance obtained by RBFN-based processors and detectors are depicted in Fig. 8.46 when non-delayed selection modes are used. Since the number of hidden neurons ($H = 20$) used in this study is the same as for the cases of synthetic sea and sea-ice clutter when designing RBFN-based detectors, the variation of the computational cost with N given in Fig. 8.12 is used. From Fig. 8.46, some important aspects are observed. These aspects are similar to the ones observed for the case of designing MLP-based detectors in synthetic ground clutter (see Sect. 8.4.2) in terms of: the tendency of the processor and

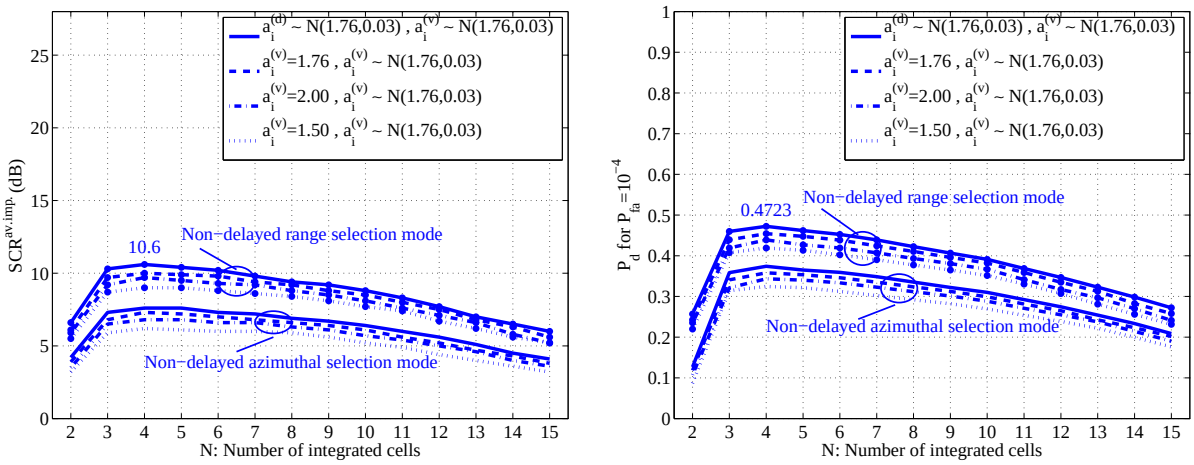

(a) RBFN-based processors (b) RBFN-based detectors

Figure 8.46: Performance of $2N/20/1$ RBFN-based processors and detectors using non-delayed selection modes and varying N when ground clutter conditions are used. Minimum ($a^{(\mathrm{d})} = 1.50$), typical ($a^{(\mathrm{d})} = 1.76$), maximum ($a^{(\mathrm{d})} = 2.00$) and practical ($a_i^{(\mathrm{d})} \sim \mathrm{N}(1.76, 0.03)$) design conditions are considered. Performance is given for the validation data set.

detector performance with N; the selection mode that allows achieving the highest performance (range integration); the number of selected cells that allow achieving the highest performance ($N \in [3, 5]$), being again related to the target sizes (from 1 to 4 cells). But, two differences are observed between RBFN and MLP-based approaches. First, the performance achieved by the RBFN-based detector is lower than the one achieved by the MLP-based detector in $\Delta P_{\mathrm{d}} \simeq -0.02$ (see Fig. 8.42), but it is still greater than the one achieved by the TSKAP detector in $\Delta P_{\mathrm{d}} \simeq 0.22$ (see Fig. 8.41). And second, the computational cost of the proposed detector is increased from 1552 operations (MLP-based approach) to 102502 operations (RBFN-based approach) per CUT.

After this study, and considering only non-delayed selection modes, the use of practical conditions ($a_i^{(\mathrm{d})} \sim \mathrm{N}(1.76, 0.03)$) and an integration of $N = 4$ cells in a range selection mode is proposed as a partial solution to design RBFN-based coherent detectors to detect moving Swerling 0 targets in the synthetic ground clutter conditions considered in the thesis. The proposed RBFN-based processor and detector outperforms the TSKAP processor and detector in $\Delta P_{\mathrm{d}} \simeq 6\,\mathrm{dB}$ and $\Delta P_{\mathrm{d}} \simeq 0.22$, respectively, considering the selected detectors in each case.

Next, the way to improve the performance RBFN-based detectors by using 1-D and 2-D delayed selection modes is studied. The performance obtained for the RBFN-based processor and detector are depicted in Fig. 8.47 when RIA is varied and the practical conditions ($a_i^{(\mathrm{d})} \sim \mathrm{N}(1.76, 0.03)$) are considered. The computational cost of the RBFN-based detector ($H = 20$ is considered) when varying RIA was depicted in Fig. 8.15. From the results presented in Fig. 8.47 and 8.15, similar conclusions as the ones obtained when designing MLP-based detectors can be drawn. These conclusions are similar in the case of MLP and RBFN-based approaches in terms of: the tendency of the processor and detector performance with RIA; the range of RIA for which the best performance is achieved ($\in [3, 5]$ cells), being related to the target sizes (from 1 to 4 cells); the best selection mode: the S mode. For the case of using an S selection mode with RIA $= 5$ cells,

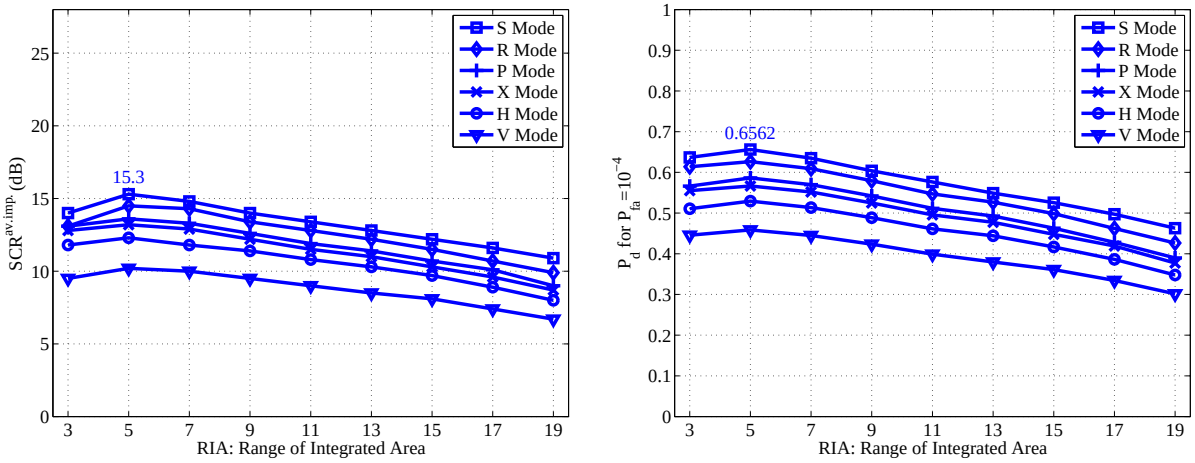

(a) RBFN-based processors

(b) RBFN-based detectors

Figure 8.47: Performance of processors and detectors based on $J/20/1$ RBFNs varying the RIA in 1D and 2D selection modes and considering the practical design conditions for ground clutter ($a_i^{(\mathrm{d})} \sim \mathrm{N}(1.76, 0.03)$). Performance is given for the validation data set.

this detector presents two drawbacks: a temporal delay of 4 ms (according to the radar parameters for ground clutter measurements given in Table 2.6 and Eq. (4.19)); and a computational cost increase with the other selection modes. The performance improvement achieved by the proposed RBFN-based detector compared to the TSKAP detector (using an azimuthal selection mode in Fig. 8.41) vary from a minimum of $\Delta\mathrm{SCR}^{\mathrm{av.imp.}} \simeq 5\,\mathrm{dB}$ and $\Delta P_{\mathrm{d}} \simeq 0.21$ (V selection mode) to a maximum of $\Delta\mathrm{SCR}^{\mathrm{av.imp.}} 10\,\mathrm{dB}$ and $\Delta P_{\mathrm{d}} \simeq 0.40$ (S selection mode).

As done for the case of study of MLP-based detectors, a summary of the results obtained for the study of the influence of the design clutter conditions is given. These results are depicted in Fig. 8.48 for the best (S) and worst (V) selection modes. From this figure, it is observed that the best clutter conditions for designing RBFN-based detectors are the practical ones ($a_i^{(\mathrm{d})} \sim \mathrm{N}(1.76, 0.03)$). Moreover, it is observed that the best range of values of RIA continues being in the range $[3, 5]$ cells, regardless of the clutter conditions used for designing.

Finally, a study of the number of hidden neurons (H) for which the RBFN achieves the best processor and detector performance is done. RBFNs of size $J/H/1$ are used, where the best RIA, and consequently the best J, is selected for each delayed selection mode and $N = 4$ cells are selected for each non-delayed selection mode. In this study, H is varied from 3 to 50. The performance achieved for the different selection modes under study is plotted in Fig. 8.49. As observed, for all the modes under study, low performance improvements are achieved from $H = 20$, although greater computational cost is required (see Fig. 8.17). Therefore, $H = 20$ hidden neurons is used taking into account a trade-off between performance ($\mathrm{SCR}^{\mathrm{av.imp.}} 15.3\,\mathrm{dB}$ and $P_{\mathrm{d}} = 0.6562$ for $P_{\mathrm{fa}} = 10^{-4}$) and computational cost (102502 operations per CUT).

After these studies, an RBFN-based detector using a structure $50/20/1$ by using an S selection mode and trained using the practical conditions data set ($a_i^{(\mathrm{d})} \sim \mathrm{N}(1.76, 0.03)$) is proposed to detect moving Swerling 0 targets in the synthetic ground clutter conditions considered in the thesis. This RBFN-based approach outperforms the TSKAP detector in $\Delta\mathrm{SCR}^{\mathrm{av.imp.}} \simeq 11.5\,\mathrm{dB}$

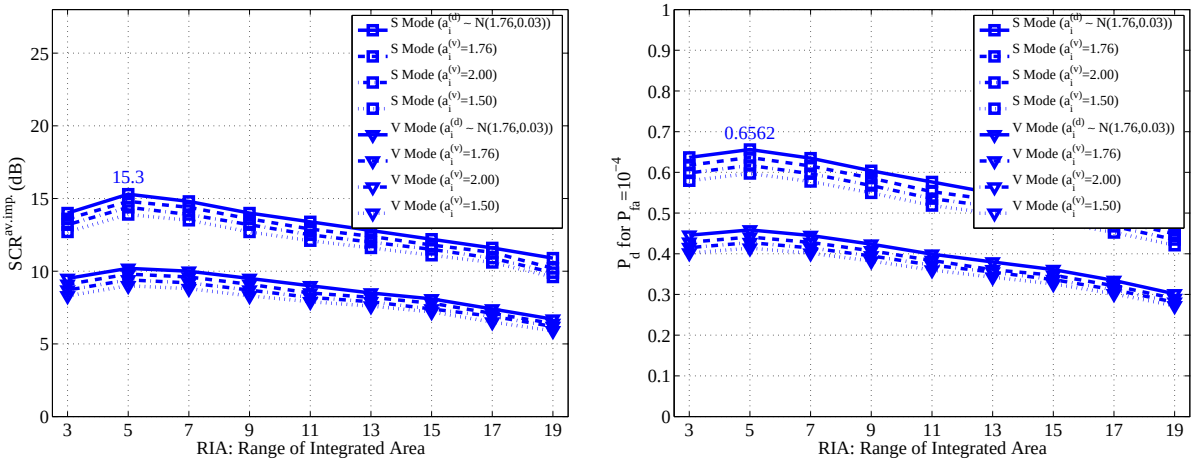

(a) RBFN-based processor (b) RBFN-based detector

Figure 8.48: Performance of RBFN-based processors and detectors for ground clutter conditions and during the design stage. During this stage, the best (S) and worst (V) selection modes are used and RIA and the design conditions are varied. Performance is given for the validation data set.

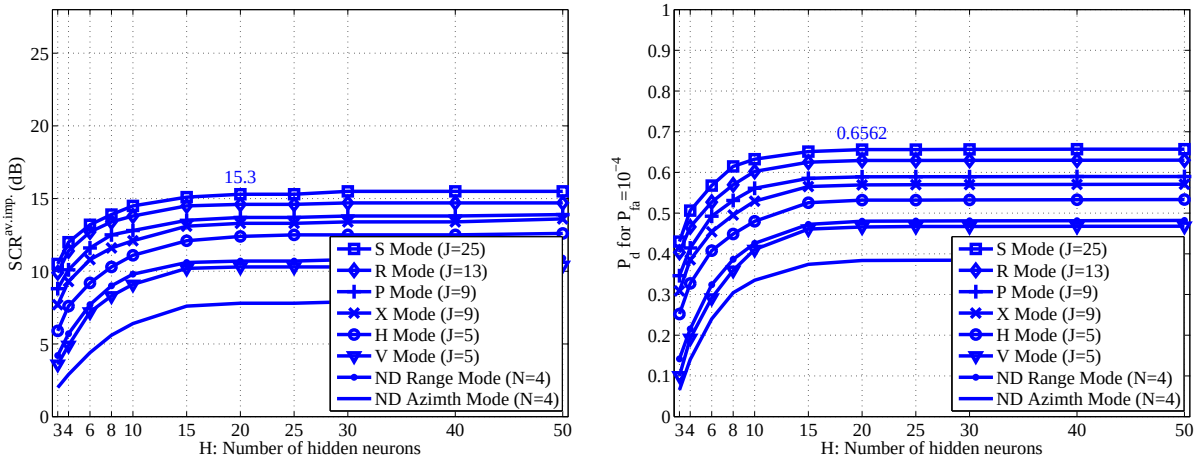

(a) RBFN-based processors (b) RBFN-based detectors

Figure 8.49: Performance of processors and detectors based on $2J/H/1$ RBFNs varying the number of hidden neurons. Non-delayed and delayed (1-D and 2-D) selection modes and the best training strategy ($a^{(\mathrm{d})} \in [1.50, 2.00]$) are considered for the case of study of ground clutter. Performance is given for the validation data set.

and $\Delta P_{\mathrm{d}} \simeq 0.40$, requiring a total of 102502 operations per CUT.

8.4.4 Comparison of Coherent Detectors in Design and Test Stages under Synthetic Ground Clutter Conditions

In the previous sections, attention has been paid to the main aspects concerning to the design of TSKAP and AI-based coherent detectors in synthetic ground clutter. In this section, and as done for the cases of study of synthetic sea and sea-ice clutters, we wonder what happens when radar scans never used before are processed by the designed detectors. This is what happens in real-live situations, where the processed data are different of the ones used for designing, where their statistical properties can be similar or not. Therefore, this section investigates if the performance achieved for these new radar scans changes or not, and, in case of change, which is its magnitude.

As done for the case of synthetic sea (Sect. 8.2.4) and sea-ice (Sect. 8.3.4) clutters, the current study is divided in two parts. At the beginning, the performance of the detectors in the design and test stages is compared by ROC curves. At the end, two radar scans of the test data set are selected and processed to analyze what is really happening and trying to find an answer to the performance achieved in each case. In these studies, the ground clutter conditions presented in Sect. 7.1.3 (see Table 7.7) are considered.

The configurations used in each detector are extracted from the design stage, being:

- MLP-based coherent detector: designed considering the practical conditions ($a^{(\mathrm{d})} \in [1.50, 2.00]$) and selecting $J = 25$ complex-valued cells (RIA= 5 cells) by an S selection mode. The number of hidden neurons is set to $H = 10$. Since real-arithmetic is used in the MLP, a total of 50 inputs are needed, having an MLP structure of 50/10/1.

- RBFN-based coherent detector: designed considering the practical conditions ($a^{(\mathrm{d})} \in [1.50, 2.00]$) and selecting $J = 25$ complex-valued cells (RIA= 5 cells) by an S selection mode. The number of hidden neurons is set to $H = 20$. Since real-arithmetic is used in the RBFN, a total of 50 inputs are needed, having an RBFN structure of 50/20/1.

- TSKAP coherent detector: designed considering the typical conditions ($a^{(\mathrm{d})} = 1.76$) and selecting $N = 4$ complex-valued cells by a non-delayed azimuthal selection mode.

The ROC curves achieved in the design stage (with the validation data set) and in the test stage (with the test data set, i.e. with radar scans never processed before) are depicted in Fig. 8.50. For reference purposes, the performance of the processors are also given in the legend of the figure. From the results presented in this figure, conclusions similar to the ones obtained in the case of synthetic sea-ice clutter can be drawn. These conclusions are:

- The tendency of the ROC curves is maintained from design to test conditions. The best detector continues being the one based on MLPs, followed by the RBF-based detector, and surpassing both the performance achieved by the reference one, the TSKAP detector.

- The performance of the processors ($\mathrm{SCR}^{\mathrm{av.imp.}}$) and detectors ($P_{\mathrm{d}}$) is decreased from the design to the test stages. Focusing on the TSKAP detector, the performance loss of the processor and detector is approximately $\Delta\mathrm{SCR}^{\mathrm{av.imp.}} \simeq -0.3\,\mathrm{dB}$ and $\Delta P_{\mathrm{d}} \simeq -0.01$, respectively. On the other hand, the performance loss observed in AI-based processors and

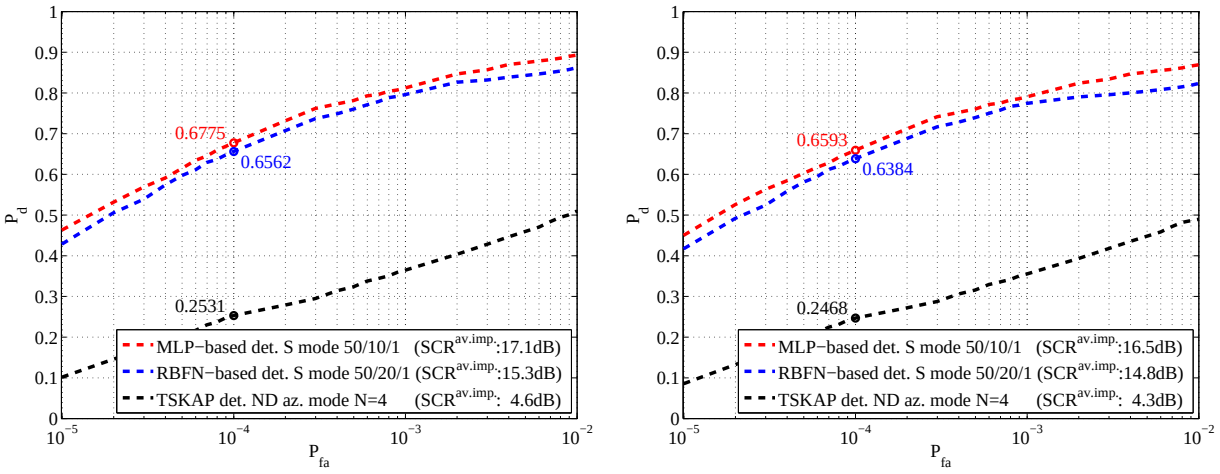

(a) Validation data set (b) Test data set

Figure 8.50: Performances of the selected configurations of TSKAP, MLP and RBFN-based coherent detectors using the validation ($a_i^{(\mathrm{v})} \sim \mathrm{N}(1.76, 0.03)$) and test ($a_i^{(\mathrm{t})} \sim \mathrm{N}(1.76, 0.03)$) data sets when synthetic ground clutter measurements are considered.

detectors is approximately $\Delta\mathrm{SCR}^{\mathrm{av.imp.}} \simeq -0.5\,\mathrm{dB}$ and $\Delta P_\mathrm{d} \simeq -0.02$, respectively. Analyzing the relative performance loss ($\Delta P_\mathrm{d} \simeq \frac{-0.01}{0.25} \simeq -4\%$ for the TSKAP detector and $\Delta P_\mathrm{d} \simeq \frac{-0.02}{0.65} \simeq -3\%$ for the AI-based detectors), better robustness against changes is observed for AI-based detectors than for the reference detector.

After analyzing these results, we can conclude that high detector robustness is achieved when processing new radar scans, regardless of the detector under study. This is an important issue for evaluating detectors because it gives us an approximation of how their performance will be when working autonomously and in steady state.

As done for the cases of study when considering sea (Sect. 8.2.4) and sea-ice (Sect. 8.3.4) clutters, subjective and objective analyses of the detector performance for radar scans with different clutter conditions is made. For that purpose, two radar scans of the test data set are selected. Following the same criteria as presented in the case of processing synthetic sea-ice clutter, the radar scans for $a^{(\mathrm{d})} = 1.76$ ($\mathbf{I}^{(1.76)}$) and $a^{(\mathrm{d})} = 1.50$ ($\mathbf{I}^{(1.50)}$) are selected. These scans correspond to the radar scans for which the best and worst performance is obtained from the test data set, respectively. A plot of the pdf for the minimum ($a = 1.50$), typical ($a = 1.76$) and maximum ($a = 2.00$) skewness parameter of the test data set is given in Fig. 8.51. In this plot, it is observed that for low values of a, such as $a = 1.50$, higher probability of finding low and high values of clutter is observed. Thus, for a low value of a (a more spiky clutter) two effects are expected: high thresholds for maintaining a constant false alarm rate, decreasing the detection rate in consequence; or an increase of the false alarm rate for a constant threshold.

The real and imaginary parts of $\mathbf{I}^{(1.50)}$ and $\mathbf{I}^{(1.76)}$ are plotted in Fig. 8.52 and 8.53, respectively. Not all the coverage of the radar scans (see Table 2.6) is plotted because details will be lost in presentation. Only the zone between 95° and 105° in azimuth and between 1400 m and 1700 m in range is selected for plotting and making the subjective analysis of the performance. It is

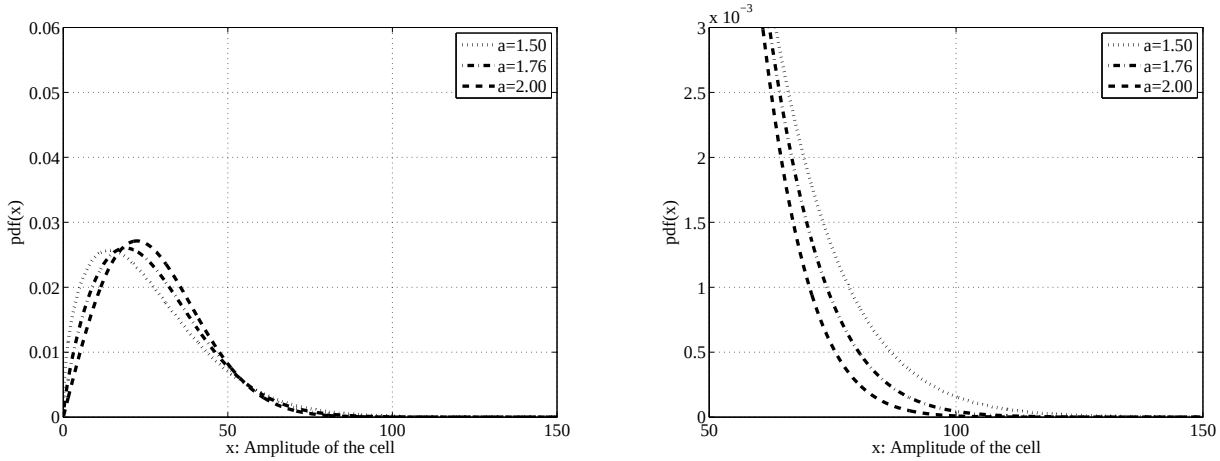

(a) Whole range (b) Zoom of Fig. 8.51b

Figure 8.51: Probability density functions (pdf's) of the clutter signal amplitude for minimum ($a = 1.50$), typical ($a = 1.76$) and maximum ($a = 2.00$) ground clutter conditions.

important to note that the objective performance given for each processed radar scan is given for the whole scan and not for the selected zone. As done in previous studies, the physical positions, sizes and shapes of the targets in the radar scans of Fig. 8.52 and 8.53 are the same, being depicted in Fig. 8.54 (high level: target is present; low level: target is absent).

The radar scans at the output of the TSKAP and AI-based coherent processors and detectors for $\mathbf{I}^{(1.50)}$ and $\mathbf{I}^{(1.76)}$ are depicted in Fig. 8.55 and 8.56, respectively. Reproducing the same procedure followed for analyzing radar scans with synthetic sea and sea-ice clutters: first, a subjective analysis of both radar scans is made; second, an analysis of detector performance loss is given; and third, some conclusions are drawn.

The same subjective analysis made in Sect. 8.2.4 and Sect. 8.3.4 for sea and sea-ice clutters, respectively, is made here for the results given in Fig. 8.55 and 8.56. From this analysis, three similar aspects are observed. First, more cells belonging to target are detected when using AI-based detectors than when using the TSKAP detector, regardless of the radar scan. Second, more cells belonging to target are detected when the clutter is distributed with its typical value ($a^{(\mathrm{t})} = 1.76$) than when it is distributed with its minimum value ($a^{(\mathrm{t})} = 1.50$). It happens because the case of $a^{(\mathrm{t})} = 1.50$ corresponds to a more spiky clutter than the case of $a^{(\mathrm{t})} = 1.76$. And third, more false alarms are detected for the case of $a^{(\mathrm{t})} = 1.50$ than for $a^{(\mathrm{t})} = 1.76$, and for the TSKAP detector than for the AI-based detectors. Finally, observing the radar scans at the output of each detector, it is observed that next tasks, such as the estimation of the target size and shape, become more difficult when using the TSKAP detector than when using AI-based detectors.

For analyzing the performance loss of each detector, we take as reference the values of $\mathrm{SCR}^{\mathrm{av.imp.}}$ and P_{d} for $P_{\mathrm{fa}} = 10^{-4}$ achieved with the validation and test data sets (see Fig. 8.50). From the performance achieved by each detector when processing the selected radar scans, we can observe that:

- The performance achieved for $\mathbf{I}^{(1.50)}$ (see titles of Fig. 8.55) is always lower than the ones

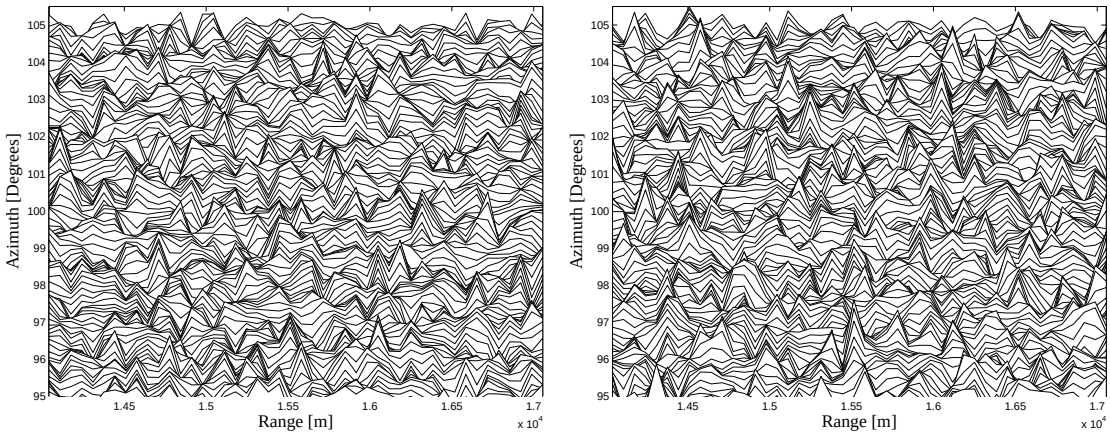

(a) $\mathrm{Re}\{\mathbf{I}^{(1.50)}\}$ (b) $\mathrm{Im}\{\mathbf{I}^{(1.50)}\}$

Figure 8.52: Real (Re{}) and imaginary (Im{}) parts of a radar scan ($\mathbf{I}$) taken from test data set with $a^{(\mathrm{t})} = 1.50$ ($\mathbf{I}^{(1.50)}$) when synthetic ground clutter is considered.

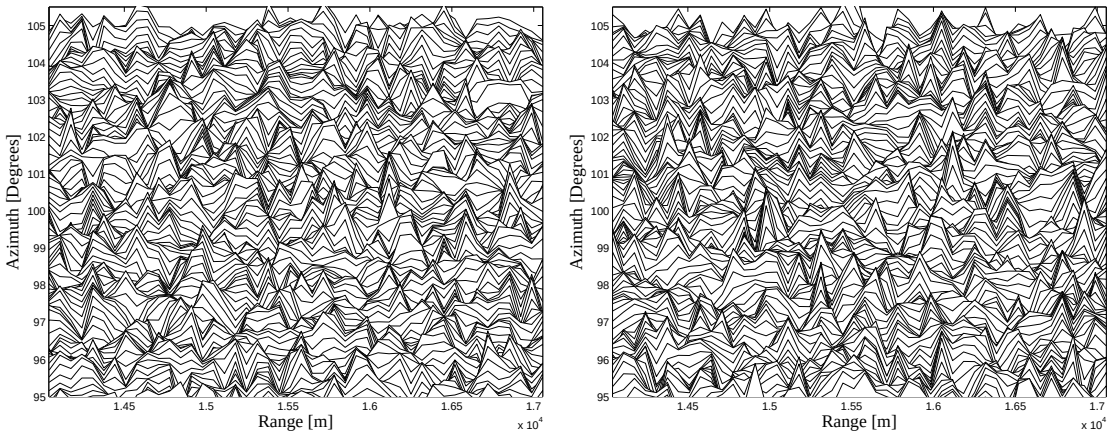

(a) $\mathrm{Im}\{\mathbf{I}^{(1.76)}\}$ (b) $\mathrm{Im}\{\mathbf{I}^{(1.76)}\}$

Figure 8.53: Real (Re{}) and imaginary (Im{}) parts of a radar scan ($\mathbf{I}$) taken from test data set with $a^{(\mathrm{t})} = 1.76$ ($\mathbf{I}^{(1.76)}$) when synthetic ground clutter is considered.

achieved for the validation and test data sets (see Fig. 8.50). It happens because the detection of targets in these clutter conditions is more difficult than in the other clutter conditions (clutter is more spiky than the others).

- The performance achieved for $\mathbf{I}^{(1.76)}$ (see titles of Fig. 8.56) is always greater than the one achieved for the validation data set, but lower than the one for the test data set (see Fig. 8.50). It happens because the detection of targets in these clutter conditions is easier than in the other ones. Moreover, since the threshold is set to obtain a overall P_{fa} for the whole data set, and $a^{(\mathrm{t})} = 1.76$ is the most likely skewness, the threshold is conditioned by the clutter synthesized for this value of skewness.

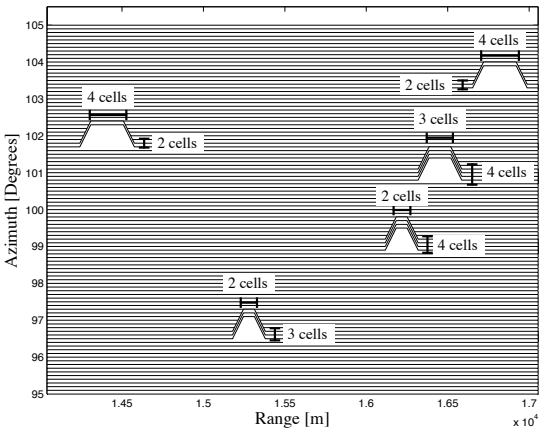

Figure 8.54: Desired (ideal) output radar scan ($\mathbf{D}$) when synthetic ground clutter is considered.

- The P_{fa} remains constant with the threshold set during the design stage when processing $\mathbf{I}^{(1.76)}$. Whereas for the case of processing $\mathbf{I}^{(1.50)}$, the P_{fa} is slightly higher than the one set in the design stage because of the statistical properties of the clutter for this skewness parameter value (this clutter is more spiky than the others).

As concluded for the studies made using synthetic sea and se-ice clutters, and after analyzing the radar scans presented in Fig. 8.55 and 8.56, we can find two reasons why AI-based detectors outperform the reference detector. First, because they highly reduce the level of clutter and with a rate higher than for the TSKAP detector. And second, because they are able to emphasize the level of signal where target is present. Both reasons can be extracted from the radar scans at the output of the processors, which lead to improve the detection rate.

8.4.5 Conclusions about Coherent Detectors in Synthetic Ground Clutter

Similar conclusions to the ones obtained for the case of study of synthetic sea and sea-ice clutters (see Sect. 8.2.5 and 8.3.5, respectively) can be drawn in general for the case of study of synthetic ground clutter conditions. But, since the clutter properties are different to the ones used in the other two cases of study, especially when synthetic sea clutter is concern, some differences are observed. These conclusions and differences are:

- The clutter conditions for obtaining the highest performance when designing AI-based coherent detectors in synthetic ground clutter are the practical ones (skewness parameter varying scan-to-scan following a normal distribution $a_i^{(\text{d})} \sim \text{N}(1.76, 0.03)$). When these situations are not applicable, as for the reference detector (TSKAP), the design conditions for maximizing the detector performance are the typical ones ($a_i^{(\text{d})} = 1.76$ in this case).

- The selection modes that maximize the performance of AI-based coherent detectors are based on 2-D templates, being the square (S) mode the best one. When computational cost is concerned, and since the square mode requires high computational cost (1552 and

102502 operations per CUT in the selected MLP and RBFN-based coherent detector configurations), the rhombus (R) and plus-shape (P) selection modes become an alternative. These two modes allow to achieve slightly lower performances, while reducing considerably the computational cost of the detector. On the other hand, if 1-D selection modes are used in AI-based detectors, the best ones are achieved when cells are integrated in range, which effect is opposite to the effect observed for the TSKAP detector.

- The range of integrated area for which the performance is maximize (RIA $\in [3, 5]$ cells in this case) is related to the size of the targets considered in the study ($\in [1, 4]$ cells in azimuth and range). This effect is observed regardless of the coherent detector under study.

- A suitable number of hidden neurons (H) in AI-based detectors is found taking into account a trade-off between performance and computational cost. This number is different for detectors based on MLPs ($H = 10$) and RBFNs ($H = 20$).

- The tuning of the parameters considered in the design of the detectors can be done using two kind of performance measurement: $\mathrm{SCR}^{\mathrm{av.imp.}}$ in the processor; and P_{d} for a given P_{fa} in the detector. Both performance measurements present a similar behavior with the variation of the parameters (clutter conditions in the design stage, RIA and H) of the detectors under study.

- High robustness is observed when the detectors process radar scans different of the ones used in the design stage. This robustness is observed both for the processors and detectors under study, presenting low performance losses (no more than $\Delta\mathrm{SCR}^{\mathrm{av.imp.}} \simeq -0.5\,\mathrm{dB}$ and $\Delta P_{\mathrm{d}} \simeq -0.02$ for $P_{\mathrm{fa}} = 10^{-4}$ in average).

- Low variations of performance ($\mathrm{SCR}^{\mathrm{av.imp.}}$ and P_{d} for $P_{\mathrm{fa}} = 10^{-4}$) is observed when processing different radar scans in the test stage, regardless of the skewness parameter of the radar scan. These variations are limited to a maximum of $\Delta\mathrm{SCR}^{\mathrm{av.imp.}} \simeq -0.5\,\mathrm{dB}$ and $\Delta P_{\mathrm{d}} \simeq -0.03$ for $P_{\mathrm{fa}} = 10^{-4}$ (compare Fig. 8.55 and 8.56). Low P_{fa} increase is observed in the test stage for radar scans having low skewness values ($a_i^{(\mathrm{t})} = 1.50$, for example). It is due to the clutter is more spiky than for the other radar scans, which have higher skewness values ($a_i^{(\mathrm{t})} = 1.76$, for example). Nevertheless, this P_{fa} increase is lower than for the case of study of synthetic sea-ice clutter, where even lower skewness values were considered ($a_i \sim \mathrm{N}(1.20, 0.14)$). This decrease of the skewness involved a much more spiky clutter, presenting in consequence higher probability of finding false alarms.

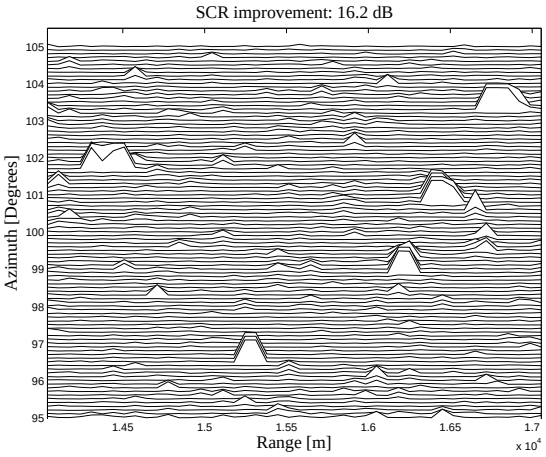

(a) MLP-based processor output for $\mathbf{I}^{(1.50)}$

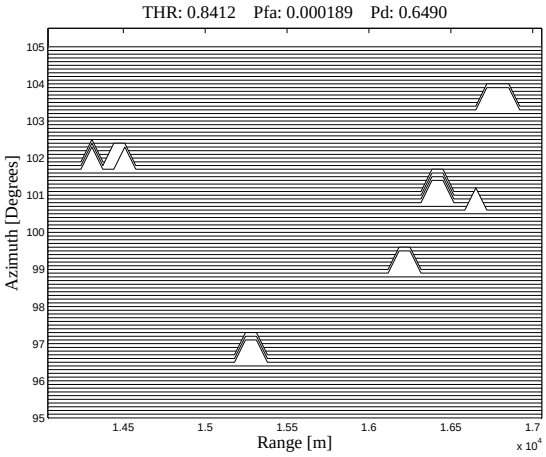

(b) MLP-based detector output for $\mathbf{I}^{(1.50)}$

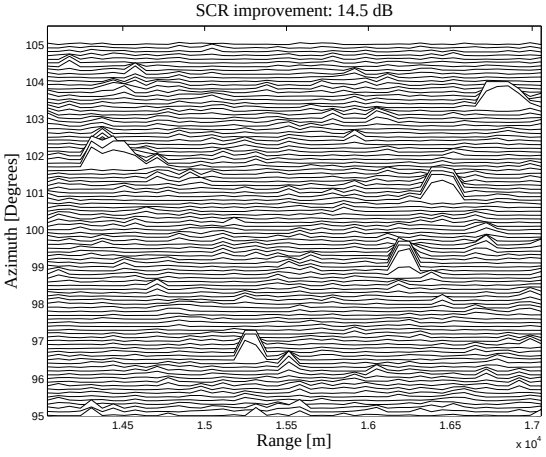

(c) RBFN-based processor output for $\mathbf{I}^{(1.50)}$

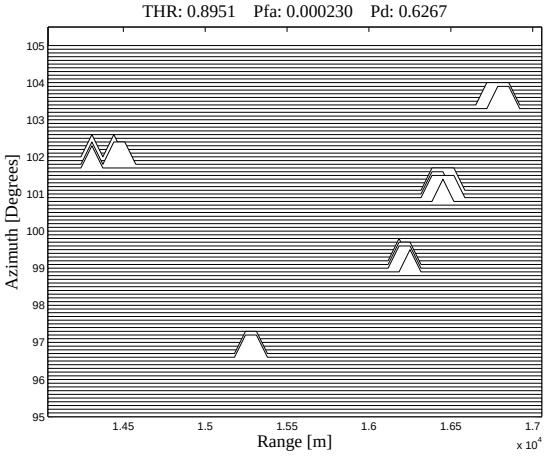

(d) RBFN-based detector output for $\mathbf{I}^{(1.50)}$

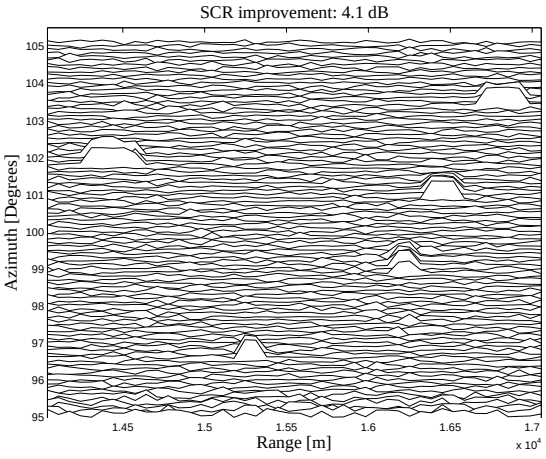

(e) TSKAP processor output for $\mathbf{I}^{(1.50)}$

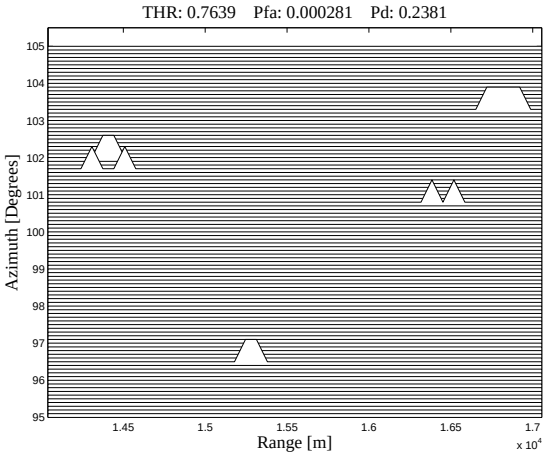

(f) TSKAP detector output for $\mathbf{I}^{(1.50)}$

Figure 8.55: Radar scans at the output of the MLP-based, RBFN-based and TSKAP processors and detectors when the input radar scan $\mathbf{I}^{(1.50)}$ from the test data set of ground clutter conditions is processed.

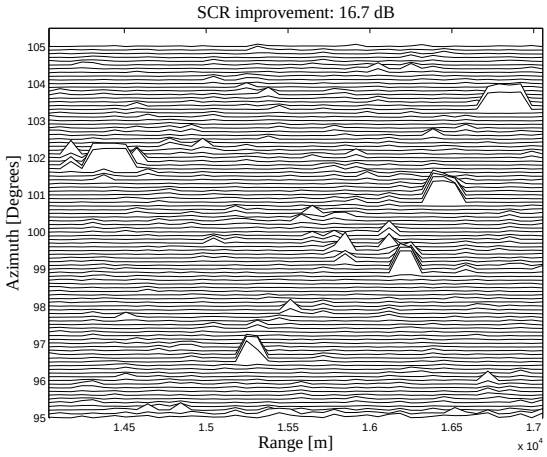

(a) MLP-based processor output for $\mathbf{I}^{(1.76)}$

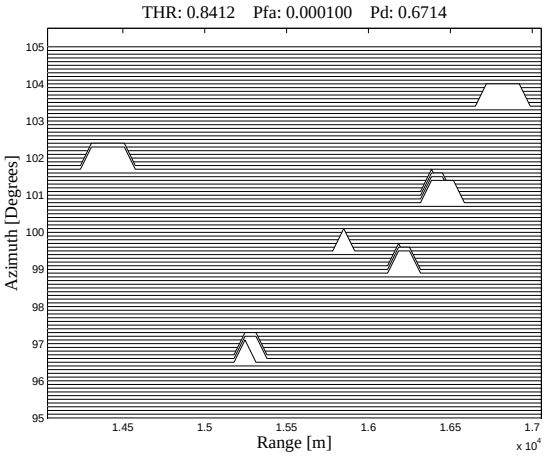

(b) MLP-based detector output for $\mathbf{I}^{(1.76)}$

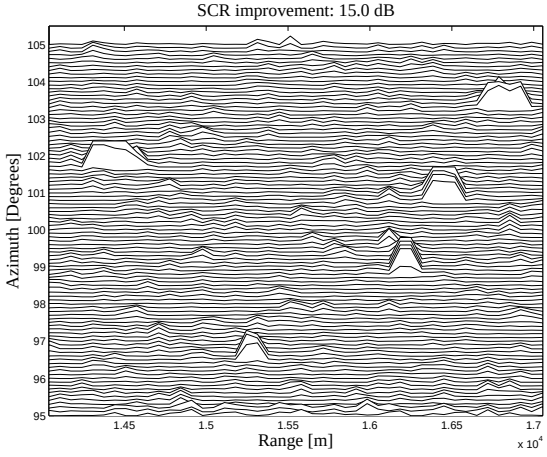

(c) RBFN-based processor output for $\mathbf{I}^{(1.76)}$

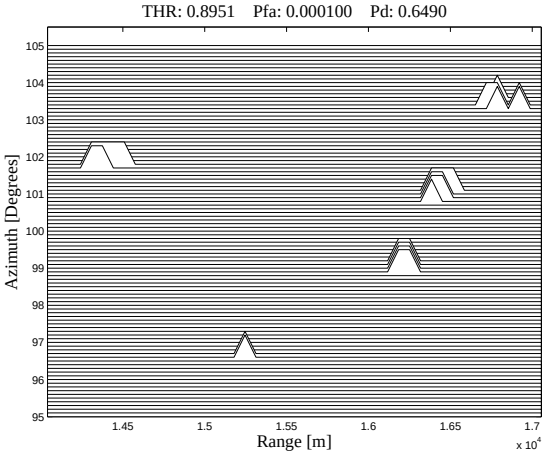

(d) RBFN-based detector output for $\mathbf{I}^{(1.76)}$

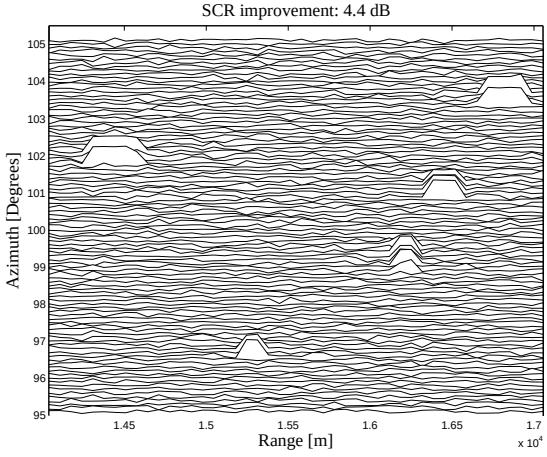

(e) TSKAP processor output for $\mathbf{I}^{(1.76)}$

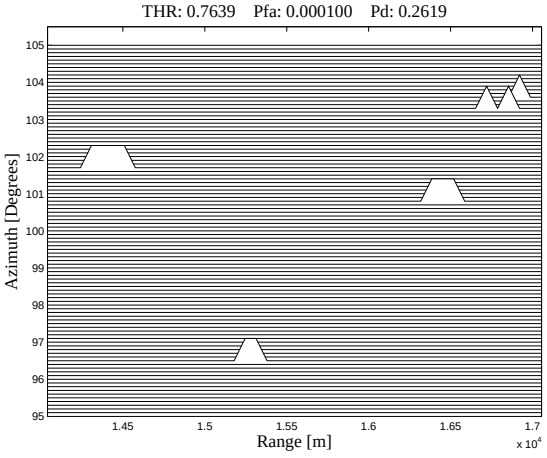

(f) TSKAP detector output for $\mathbf{I}^{(1.76)}$

Figure 8.56: Radar scans at the output of the MLP-based, RBFN-based and TSKAP processors and detectors when the input radar scan $\mathbf{I}^{(1.76)}$ from the test data set of ground clutter conditions is processed.

8.5 General Conclusions about Coherent Detection in Synthetic Clutter

The first and main conclusion we can draw from the studies made for detecting moving Swerling 0 targets in sea, sea-ice and ground Weibull-distributed clutter is: the proposed AI-based coherent detectors outperform the coherent detector taken as reference (the commonly used TSKAP detector) in all the cases of study. Other important conclusions can be drawn from the studies made when designing and testing coherent detectors in the clutter conditions considered in the thesis. At the beginning, some conclusions are drawn by comparing the performance obtained when the detectors work in different clutter conditions. These conclusions are focused on the observed variations of the performance when tuning the parameters to be set in the design of the proposed detectors, as well as the variations observed once they are designed. At the end, general conclusions about the use of the proposed coherent detectors are obtained, regardless of the clutter conditions. These conclusions are obtained when comparing the particular conclusions obtained for each case of study (sea, sea-ice and ground clutters).

On the one hand, comparing the performance obtained when designing coherent detectors in synthetic sea clutter (see Sect. 8.2) with the ones obtained in synthetic sea-ice clutter (see Sect. 8.3), an important conclusion can be drawn. This conclusion is related to the dependency of the detector performance (P_{d} for a given P_{fa}) with: the one-lag correlation coefficient of the clutter (ρ_{c}); the skewness parameter of the Weibull distribution (a); and the signal-to-noise ratio (SNR). Farina et al. set in [Farina1987b], when proposing the TSKAP detector, that the P_{d} decreases with a decrease of each of these parameters. The values of these parameters under synthetic sea (see Table 2.3) and sea-ice (see Table 2.5) clutter conditions were varied:

- From $a_i \sim \mathrm{N}(4.46, 0.12)$ in sea clutter to $a_i \sim \mathrm{N}(1.20, 0.14)$ in sea-ice clutter.
- From $\rho_{\mathrm{c}} = 0.99$ in sea clutter to $\rho_{\mathrm{c}} = 0.95$ in sea-ice clutter.
- From $\mathrm{SNR} = 40\,\mathrm{dB}$ in sea clutter to $\mathrm{SNR} = 30\,\mathrm{dB}$ in sea-ice clutter.

Therefore, a performance decrease is expected in the coherent detectors (TSKAP and AI-based approaches) because all these parameters decrease. This is what happens in the performance obtained in the experiments (compare the ROC curves of Fig. 8.18 and 8.34).

The same conclusions can be drawn when comparing the performance obtained for the reference and proposed coherent detectors when working in sea (see Fig. 8.18) and ground (see Fig. 8.50) clutter conditions. In this comparison, the clutter parameters were reduced to: $a_i \sim \mathrm{N}(1.76, 0.03)$; $\rho_{\mathrm{c}} = 0.90$; and $\mathrm{SNR} = 30\,\mathrm{dB}$.

Comparing the performance of the reference and proposed coherent detectors in synthetic sea-ice (see Fig. 8.34) and ground (see Fig. 8.50) clutters, a performance increase is observed, even when the ρ_{c} decreases from 0.95 in sea-ice clutter to 0.90 in ground clutter ($\mathrm{SNR} = 30\,\mathrm{dB}$ in both cases). This effect is opposite to the one observed above. It happens because the skewness parameter increases from $a_i \sim \mathrm{N}(1.20, 0.14)$ in sea-ice clutter to $a_i \sim \mathrm{N}(1.76, 0.03)$ in ground clutter (close to the Gaussian case: $a_i = 2.00$). After that, we can infer that the skewness parameter effect is stronger than the one-lag correlation coefficient effect in the overall performance of the coherent detectors.

On the other hand, from the particular conclusions obtained in sea, sea-ice and ground clutters (see Sect. 8.2.5, 8.3.5 and 8.4.5), we can draw the following general conclusions when using the reference and proposed coherent detectors in synthetic Weibull-distributed clutter:

- The best clutter conditions for designing AI-based detectors are the practical ones, where the skewness parameter of the Weibull-distributed clutter ($a_i^{(\mathrm{d})}$) vary scan-to-scan ($i = 1, 2 \cdots M^{(\mathrm{d})}$). When these situations are not applicable, as for the TSKAP detector (the knowledge of $a_i^{(\mathrm{d})}$ scan-to-scan is mandatory), the best design conditions are the typical ones ($a_i^{(\mathrm{d})}$ is equal to its typical value scan-to-scan).

- Selection modes using 2-D templates work better than 1-D modes in AI-based detectors, although they require more computational cost. From the 2-D selection modes under study, the best one is found to be the square mode (S). Other selection modes proposed in the thesis, such as the rhombus (R) and plus-shape (P) modes, allow to achieve lower but comparable performances, reducing considerably the computational cost of the AI-based detector. If 1-D selection modes are used in AI-based detectors, the highest performance will be achieved when cells are integrated in range. This effect is opposite to the one achieved for the TSKAP detector, where the highest performance was obtained when selecting cells in azimuthal direction. It is due to their different working philosophies.

- The range of integrated area (RIA) that maximizes the detector performance is related to the size of the targets considered in the experiments, varying both in similar ranges. This effect is observed regardless of the coherent detector under study. The value of RIA conditions the number of AI-based detector inputs (J) according to the selection mode the detector uses, conditioning the computational cost of the detector. The lowest RIA of the found range is recommended for reducing the computational cost of the detectors.

- A suitable number of hidden neurons (H) in AI-based detectors is found, being different for detectors based on MLPs and RBFNs. This value is always lower in MLP-based detectors than in RBFN-based detectors. As occurred for the selection of RIA, H is selected considering a trade-off between the detector performance and computational cost.

- The dimensionality and design of the detector can be done by using two kind of performance measurements: $\mathrm{SCR}^{\mathrm{av.imp.}}$ in the processor; and P_{d} for a given P_{fa} in the detector. It was observed that both performance measurements present similar behaviors when varying the parameters of the coherent detectors.

- High robustness of the detector performance is observed when new radar scans (different of the ones used in the design stage) are processed. It gives us an idea of the performance of the detectors when processing in the future new radar scans having similar clutter conditions.

- The performance achieved by the coherent detectors when processing radar scans having a skewness value equal to its typical value is slightly higher than when processing radar scans having a skewness parameter close to the limits of variation the skewness parameter in a given data set. This effect happens because the threshold setting is mainly conditioned by radar scans having skewness parameter values close to the typical value.

CHAPTER 9

Incoherent Detectors in Synthetic Clutter: Design and Test

This chapter is focused on the main aspects concerning to the design and test of incoherent detectors (CFAR and AI-based incoherent detectors) when processing radar scans containing synthetic sea clutter measurements. Sect. 8.1 presented an analysis of the performance loss when coherent data are selected in practical and theoretical/ideal situations. This analysis is not repeated here because similar behaviors (performance losses) are obtained when processing incoherent data. In Sect. 9.1.1-9.1.3, a study of the influence of the different parameters to be tuned during the design of incoherent detectors is presented. Once these parameters are tuned, the performance achieved when processing new radar scans is compared in Sect. 9.1.4 to the one obtained in the design stage. This performance comparison allows to have an idea of the performance loss of the detectors when processing other (new) radar scans in the future. After the studies made in the design and test stages, general conclusions are drawn in Sect. 9.2, being compared with those obtained when coherent detectors in synthetic sea clutter were used.

9.1 Incoherent Detectors in Synthetic Sea Clutter

This section deals with the design of incoherent detectors when synthetic sea clutter conditions are considered. During the design of the incoherent detectors under study, i.e. CFAR and AI-based incoherent detectors, some parameters must be tuned to find which ones maximize the performance of the detectors. Following a similar procedure to the one used in the case of study of coherent detectors in synthetic sea clutter (see Sect. 8.2), the detectors are designed considering:

- Different environmental (clutter) conditions, as set in Sect. 7.1.3 (Table 7.5).
- The target conditions presented in Sect. 7.1.2 (Table 7.4). These target conditions are the same in all the experiments made under incoherent clutter measurements.
- Different selection modes, as presented in Sect. 4.2. It is important to note that even when non-delayed and delayed (1-D and 2-D) selection modes can be used in CFAR detectors, only delayed selection modes are usually considered in the literature. For this reason, only delayed selection modes are used in the studies presented below concerning to CFAR and AI-based detectors.

- Different number of integrated/selected cells in the considered selection modes.
- And different number of hidden neurons in the MLPs and RBFNs that form the AI-based incoherent detectors.

The selection of the values of these parameters is done in the design stage, where the training and validation data sets of Table 7.5 are used. These data sets are generated once for all the experiments made in the design of CFAR and AI-based incoherent detectors in synthetic sea clutter. Moreover, they are the same as the ones used in Sect. 8.2 for the case of study of coherent sea clutter measurements, but considering only the amplitude of the complex-valued radar scans. The performance of the processors and detectors presented in Sect. 9.1.1-9.1.3 are obtained with the validation data set. This performance is given in terms of average SCR improvement ($\text{SCR}^{\text{av.imp.}}$) for the processors and P_{d} for $P_{\text{fa}} = 10^{-4}$ for the detectors, as discussed in Sect. 4.4. Performance for data (radar scans) different of the ones used in the design stage is given in Sect. 9.1.4.

9.1.1 Design of CFAR Detectors in Synthetic Sea Clutter

During the design of CFAR detectors in synthetic sea clutter, the influence of the following parameters is studied:

- The design conditions in the performance of CFAR detectors. Since the skewness parameter of the clutter ($a^{(\text{d})}$) must be known a priori in ML and OS-CFAR detectors to set the detection threshold (see Eq. (3.77) and (3.74) in Sect. 3.3.2), not all the clutter conditions presented in Table 7.5 are used in the design stage. Only the minimum, typical and maximum clutter conditions are used because the value of $a^{(\text{d})}$ is constant scan-to-scan.
- The way of processing the CUT adjacent cells to estimate the scale parameter (clutter power) and to adjust the detection threshold. In this way, three different approaches are studied by using the CA, ML and OS-CFAR detectors.
- The delayed selection mode that works better in each CFAR detector (see Sect. 4.2).
- The RIA, and consequently the number of integrated/selected cells (J), in each selection mode that allow to achieve the highest performance in each CFAR detector.

The last two parameters (selection mode and RIA) are simultaneously studied below for each CFAR detector. The second parameter (way of processing the CUT adjacent cells) is independently studied by the performance obtained for each CFAR detector (P_{d} for $P_{\text{fa}} = 10^{-4}$). In this way, the performance of CA, ML and OS-CFAR approaches are independently depicted in Fig. 9.1-9.3. The threshold of each detector is adjusted using the design data set, whereas the performance presented for each detector is achieved with the validation data set. The number guard cells (G) considered in the CFAR detectors under study are set in three different ways, depending on the value of RIA considered to obtain the number of available cells (J). When RIA is lower than the maximum size of the targets considered in the study (12 cells), G is obtained considering $\text{RIA} - 2$ cells in the expressions given in Eq. (4.7) and (4.12)-(4.15) for each selection mode. But, when RIA = 3 cells, no guard cells are selected because there would be a unique

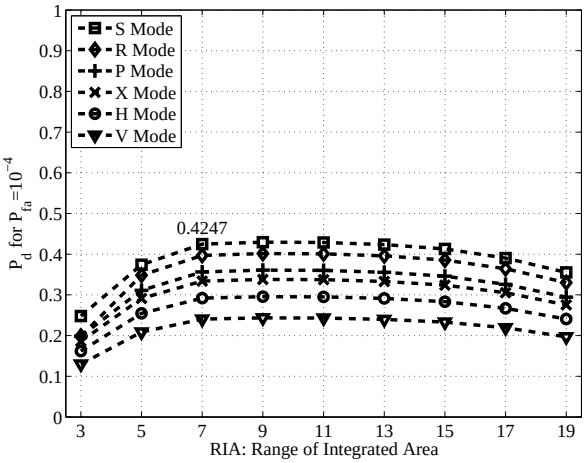

Figure 9.1: Performance of CA-CFAR detectors using 1-D and 2-D delayed selection modes and varying RIA. Performance is given for the validation data set.

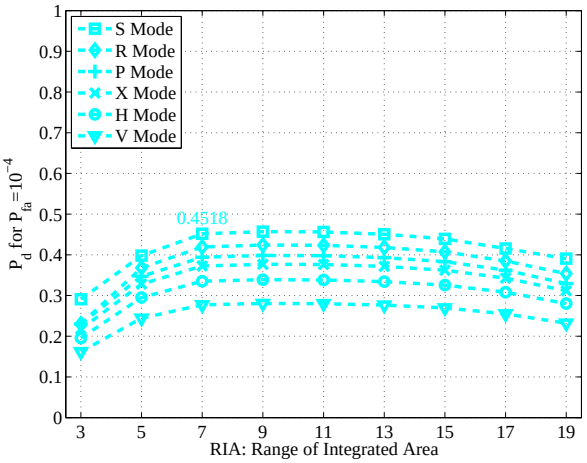

Figure 9.2: Performance of ML-CFAR detectors using 1-D and 2-D delayed selection modes and varying RIA. In these detectors, $a^{(\mathrm{d})} = 4.46$ (typical value) is used. Performance is given for the validation data set.

guard cell, which would be the CUT. Finally, when RIA is greater than the maximum size of these targets (12 cells), G is obtained considering 11 cells in the expressions given in Eq. (4.7) and (4.12)-(4.15) for each selection mode. Therefore, the value of RIA that sets the limit of variation of G is conditioned to the size of the targets we are expecting in the radar scans. From the results presented in Fig. 9.1-9.3, the following important aspects can be observed:

- In general, the selection mode that allows to achieve the highest performance is the S mode, regardless of the CFAR detector. The R selection mode can achieve a performance slightly lower, while considerably reducing the computational cost of the detectors because the number of selected cells in the integrated area is lower. Moreover, it is observed that the use of 2-D (S, R, P and X) selection modes allow to achieve better performance than

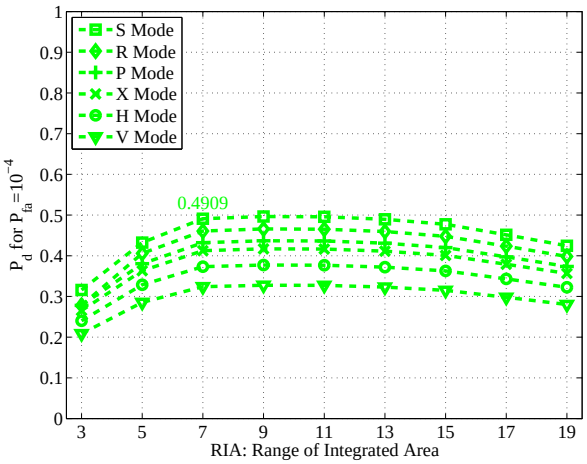

(a) Influence of RIA in OS-CFAR detectors for $k = \lceil 0.5(J-G) \rceil$, being J the number of extracted cells for a given RIA and G the number of guard cells.

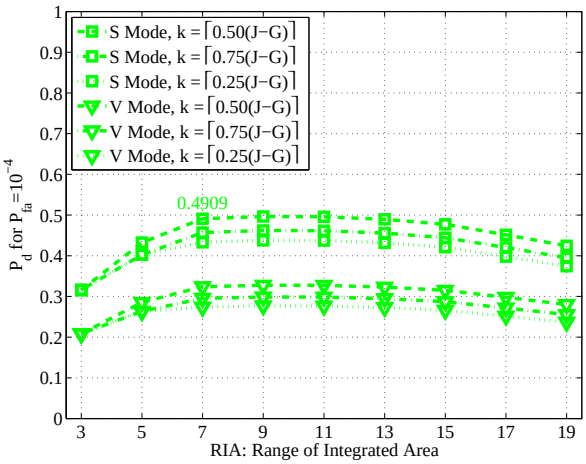

(b) Influence of k in OS-CFAR detectors using square (best) and vertical (worst) selection modes for different values of RIA.

Figure 9.3: Performance of OS-CFAR detectors using 1-D and 2-D delayed selection modes and varying RIA and k (order for selection). In these detectors, $a^{(\mathrm{d})} = 4.46$ (typical value). Performance is given for the validation data set.

1-D (H and V) selection modes.

- In general, the RIA for achieving the highest performance is found to be in the range $[7, 13]$ cells, regardless of the selection mode and CFAR detector. This result is not exactly in consonance with the size of the targets considered in the study (from 4 to 12 cells, as set in Table 7.1). It is because the quantity of available information used to estimate the clutter power is not enough for low values of RIA (3 and 5 cells). In this way, the threshold is not properly adapted, having a poorer detection. As occurred for the case of study of coherent detectors in synthetic sea clutter, lower performances are obtained for values of RIA greater than 13 cells because of the existence of other (close) targets in the radar scene that confuse the detector when setting the threshold.

- In particular, the performance achieved by ML-CFAR detectors is better than the ones achieved by CA-CFAR detectors. It is due to the philosophy of working of this detector (see Eq. (3.73)-(3.74) of Sect. 3.3.2), which allows to improve the detector performance in multi-target environments. But due to this philosophy, the knowledge of the skewness parameter ($a^{(\mathrm{d})}$) is needed a priori, what can be a problem in real-live situations. In this case, the value selected for this parameter is the typical value of the radar scans of the design data set, i.e. $a^{(\mathrm{d})} = 4.46$ (see Table 7.5).

- In particular, OS-CFAR detectors achieve the highest performance. Moreover, for this detector, a study of the influence of the order of selection (k) is done, as presented in Fig. 9.3b. In this study, it is observed that the best performance is achieved when the selection of the order is approximately in the middle of the number of useful cells (J available cells minus G guard cells).

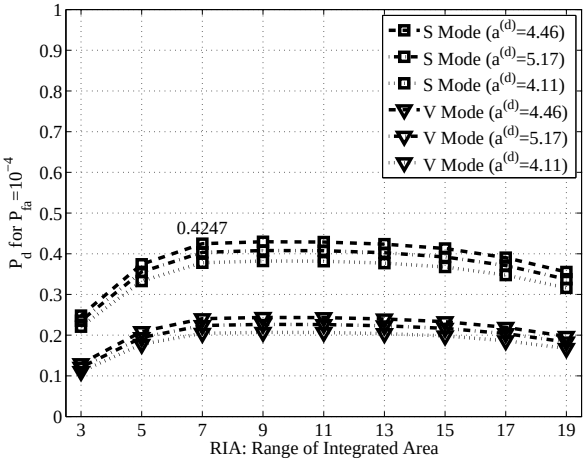

(a) CA-CFAR detector

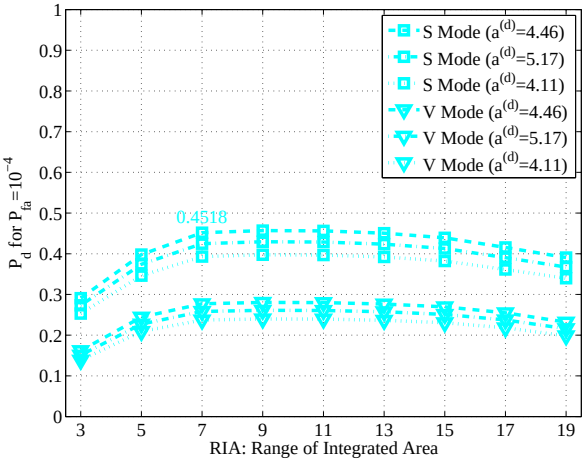

(b) ML-CFAR detector using different values of $a^{(\mathrm{d})}$

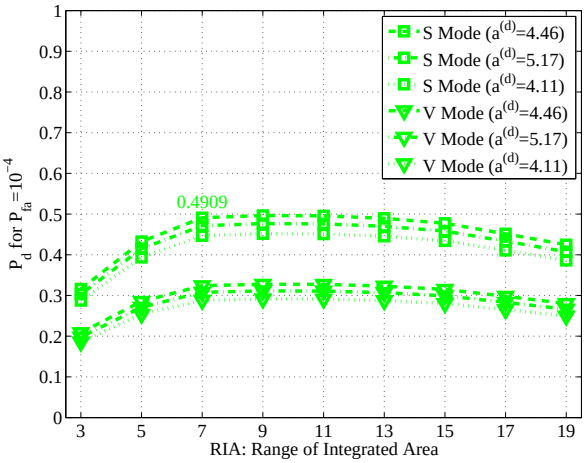

(c) OS-CFAR detector using $k = 0.5\lceil (J-1) - G \rceil$ and different values of $a^{(\mathrm{d})}$

Figure 9.4: Performance of CA, ML and OS-CFAR detectors considering the best (S mode) and worst (V mode) selection modes and varying RIA and the design conditions (minimum: $a_i^{(\mathrm{d})} = 4.11$; typical: $a_i^{(\mathrm{d})} = 4.46$; and maximum: $a_i^{(\mathrm{d})} = 5.17$). Performance is given for the validation data set.

Once the influence of the RIA is studied for each selection mode and CFAR detector using the typical clutter conditions, the influence of the clutter conditions in the design of CFAR detectors is studied below. Even when a complete study has been made for all the CFAR detectors and selection modes, only a summary of the most important ones is presented here. In this way, the results obtained for the best (S) and worst (V) selection modes are plotted in Fig. 9.4. From these plots, it is observed that the best clutter conditions for designing CFAR detectors are the typical ones, regardless of the CFAR detector. Moreover, it is observed that the range of values of RIA for which the highest performance is achieved continues being in $[7, 13]$ cells, also regardless of the CFAR detector.

After these studies, the use of OS-CFAR detectors designed for typical conditions ($a^{(\mathrm{d})} = 4.46$) and using the S selection mode with RIA = 7 cells is proposed to work with this database of synthetic sea clutter scans. The minimum value of RIA in the range $[7, 13]$ is proposed because it involves the lowest computational cost in the detectors. Under this configuration, the processor has $J = \mathrm{RIA} \times \mathrm{RIA} = 49$ cells (1 CUT and 48 surrounding cells) to make the decision. From the 48 surrounding cells, $G = (\mathrm{RIA}\text{-}2) \times (\mathrm{RIA}\text{-}2) - 1 = 24$ cells are guard cells. In consequence, $(J-1)-(G-1) = J-G = 24$ cells are used to estimate the clutter parameters and to adapt the detection threshold, where the cell with order $k = \lceil 0.50 \cdot 24 \rceil = 12$ is used to make the estimate of the clutter parameter in the OS-CFAR detector.

9.1.2 Design of MLP-based Incoherent Detectors in Synthetic Sea Clutter

The influence of the four main parameters when designing MLP-based coherent detectors in synthetic sea clutter was studied in Sect. 8.2.2. In the current section, the influence of the same parameters (with small differences) is studied but when designing MLP-based incoherent detectors. These parameters are:

- The environmental (clutter) condition that maximizes the performance in the design stage. Since the proposed detector does not depend on having a constant value of $a^{(\mathrm{d})}$ scan-to-scan in the design data set, all the experimental/design conditions of Table 7.5 are considered in this study.

- The selection mode that works better in the MLP-based detector. Since delayed selection modes were chosen for selecting the data surrounding the CUT when CFAR detectors are used, these modes are also selected to design MLP-based incoherent detectors. Non-delayed selection modes could also be used. Nevertheless, since the performance achieved with them in the case of coherent detectors in sea clutter is always lower than the ones obtained when using delayed selection modes, the same behavior is expected when using incoherent detectors. Therefore, non-delayed selection modes are not considered in the results presented in this section.

- The number of integrated/selected cells (J) that allows to achieve the highest performance while maintaining low computational cost. This number depends on the delayed selection mode and the range of integrated area (RIA), as discussed in Sect. 4.2.2 and 4.2.3.

- The number of hidden neurons (H) in the MLP of the incoherent processor and detector that maximizes the performance and maintains low computational cost.

At the beginning, the second (selection mode) and third (RIA and J) parameters are simultaneously studied, considering the practical design conditions of Table 7.5. The performance obtained for the MLP-based processor ($\mathrm{SCR}^{\mathrm{av.imp.}}$) and detector ($P_{\mathrm{d}}$ for $P_{\mathrm{fa}} = 10^{-4}$) is depicted in Fig. 9.5 when RIA is varied. The computational cost of the detector (number of operations in total per CUT) when varying RIA is plotted in Fig. 9.6, considering an MLP formed of $H = 15$ hidden neurons. A deep study of the number of hidden neurons in the detector will be made after studying the influence of the clutter conditions in the design stage.

Analyzing the results given in Fig. 9.5 and 9.6 when varying RIA for the different delayed selection modes under study, the following conclusions can be drawn:

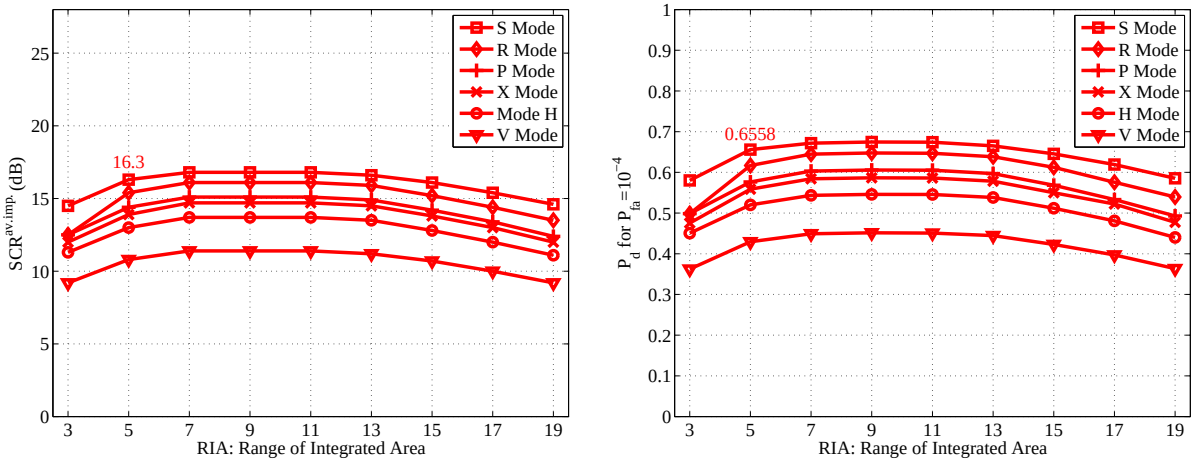

(a) MLP-based processors

(b) MLP-based detectors

Figure 9.5: Performance of incoherent processors and detectors when being formed of $J/15/1$ MLPs, using 1-D and 2-D selection modes, considering the practical design conditions ($a_i^{(\mathrm{d})} \sim \mathrm{N}(4.46, 0.12)$) and varying RIA. Performance is given for the validation data set.

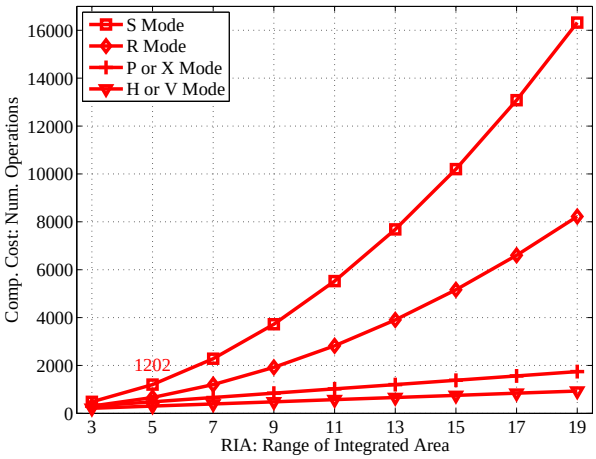

Figure 9.6: Computational cost of incoherent detectors in synthetic sea clutter when being formed of $J/15/1$ MLPs, using 1-D and 2-D selection modes and varying RIA.

- The tendency of the performance with respect to RIA is practically the same for the processor and detector, each given by its own objective measurement of the performance.
- The number of integrated cells for which the highest performance is achieved is practically in the same range for each selection mode (RIA $\in [5, 13]$ cells). It is observed that this range is related to the size of the targets considered in the study, which vary from 4 to 12 cells in range and azimuth (see Table 7.1).
- Selection modes using 2-D templates allow to achieve higher performance than 1-D templates. As occurred for coherent detectors in synthetic sea clutter, it happens because:

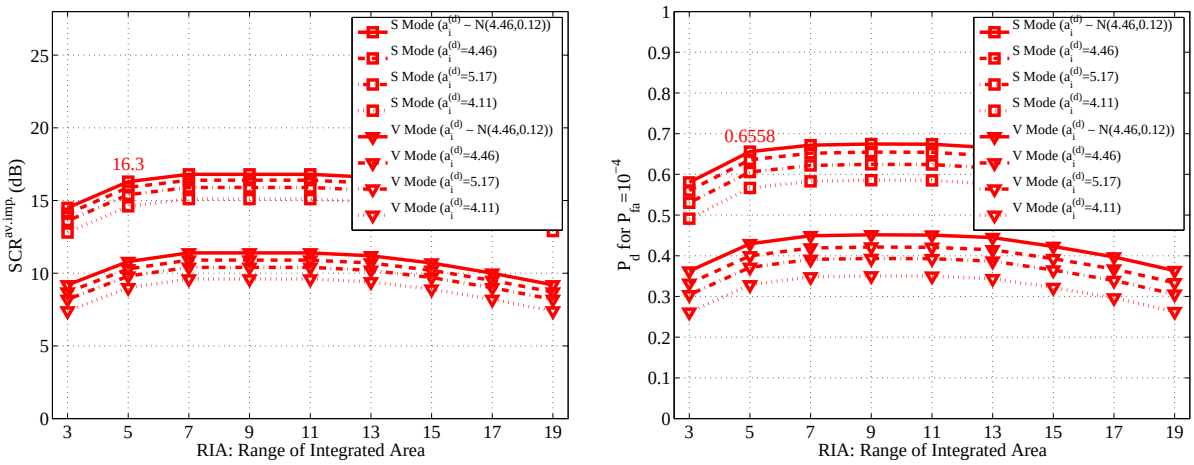

(a) MLP-based processor

(b) MLP-based detector

Figure 9.7: Performance of MLP-based incoherent processors and detectors when using the best (S mode) and worst (V mode) selection modes and varying RIA and the design conditions ($a_i^{(\mathrm{d})}$). Performance is given for the validation data set.

more information is available to make the decision target present/absent for each CUT; and the decision is made regardless of the orientation of the target in the radar scan. The selection mode for obtaining the highest performance is the S mode (2-D template). Nevertheless, delayed selection modes present two limitations: a temporal delay linearly increasing with RIA (see Sect. 4.2); and a computational cost exponentially increasing with RIA (see Fig. 9.6). For the selection mode for which the highest performance is achieved (S mode), and considering the minimum RIA of the proposed range (RIA = 5 cells), the obtained delay is 0.5 ms, as set the parameters of the radar for sea clutter measurements given in Table 2.2 and Eq. (4.19). This approach (S mode with RIA = 5 cells) needs a total of 1202 operations per CUT to be implemented.

- The proposed MLP-based detector always outperforms the best CFAR detector (OS-CFAR in Fig. 9.3a). The achieved performance improvement varies from a minimum of $\Delta P_{\mathrm{d}} \simeq 0.10$ (V selection mode) to a maximum of $\Delta P_{\mathrm{d}} \simeq 0.16$ (S selection mode).

Once the influence of the selection mode and RIA have been studied, and as done for the case of study of CFAR detectors and MLP-based coherent detectors, the influence of the design conditions is also studied in MLP-based incoherent detectors. The performance of MLP-based incoherent processors and detectors is depicted in Fig. 9.7 when using different design conditions and varying RIA. In this case, only the best (S) and worst (V) selection modes are used. From this study, it can be observed that the best clutter conditions for designing MLP-based detectors are the practical ones. Moreover, it is observed that the best range of values of RIA continues being $\in [5, 13]$ cells.

After studying the influence of the selection modes, RIA and the design clutter conditions, a last study is done. This study is related to the number of hidden neurons (H) the MLP should have to give the highest performance in the processor and detector while maintaining low

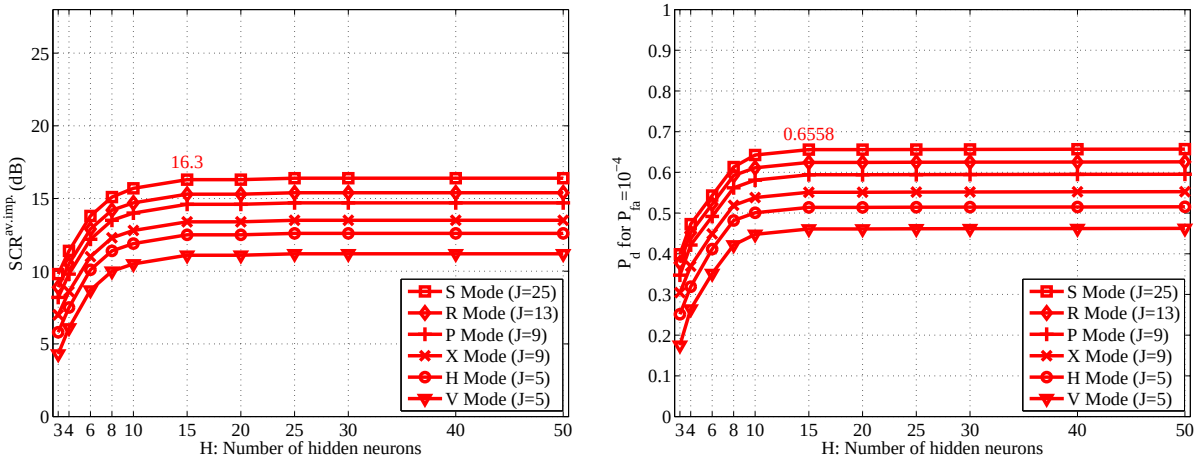

(a) MLP-based processors

(b) MLP-based detectors

Figure 9.8: Performance of incoherent processors and detectors being formed of $J/H/1$ MLPs, using 1-D and 2-D selection modes, considering the practical design conditions ($a_i^{(\mathrm{d})} \sim \mathrm{N}(4.46, 0.12)$) and varying the number of hidden neurons (H). Performance is given for the validation data set.

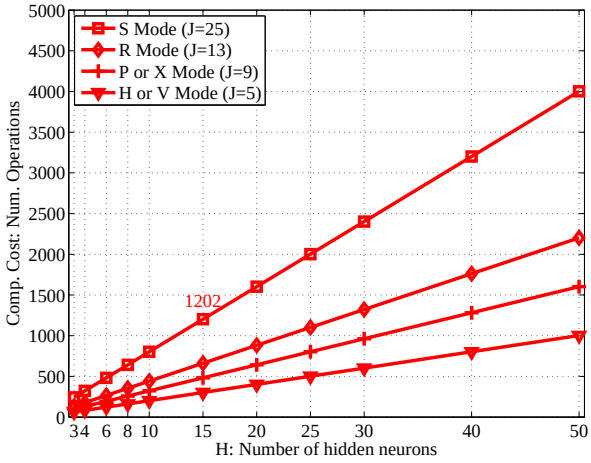

Figure 9.9: Computational cost of incoherent detectors in synthetic sea clutter when being formed of $J/H/1$ MLPs, using 1-D and 2-D selection modes and varying the number of hidden neurons (H).

computational cost. As done when designing MLP-based coherent detectors, H is varied from 3 to 50 hidden neurons. The performance achieved for the different selection modes under study, considering the validation data set, is plotted in Fig. 9.8. The variation of the computational cost of the detector with H is plotted in Fig. 9.9. As observed, for all the modes under study, from $H = 15$ hidden neurons low performance improvement (observed by making a zoom of Fig. 9.8) and high computational cost increase are achieved. Thus, this value can be used as the best one considering a trade-off between performance ($\mathrm{SCR}^{\mathrm{av.imp.}} = 16.3\,\mathrm{dB}$ and $P_{\mathrm{d}} = 0.6558$)

and computational cost (1202 operations per CUT).

After these studies, an MLP-based incoherent detector designed with practical conditions ($a_i^{(\mathrm{d})} \sim \mathrm{N}(4.46, 0.12)$), using $H = 15$ hidden neurons and RIA= 5 cells from an S selection mode is proposed. The proposed MLP-based detector is able to outperform the best configuration of the CFAR detectors under study (OS-CFAR) detector in $\Delta P_{\mathrm{d}} \simeq 0.16$.

9.1.3 Design of RBFN-based Incoherent Detectors in Synthetic Sea Clutter

As previously done for MLP-based incoherent detectors, the influence of the following parameters is studied in the design of RBFN-based incoherent detectors in synthetic sea clutter: the environmental (clutter) conditions; the selection mode; the RIA and number of selected cells (J); and the number of hidden neurons (H).

At the beginning, the second (selection mode) and third (RIA) parameters are simultaneously studied considering the practical conditions of Table 7.5 ($a_i^{(\mathrm{d})} \sim \mathrm{N}(4.46, 0.12)$). The performance obtained by the different configurations of RBFN-based processors ($\mathrm{SCR}^{\mathrm{av.imp.}}$) and detectors ($P_{\mathrm{d}}$ for $P_{\mathrm{fa}} = 10^{-4}$) is depicted in Fig. 9.10 when RIA is varied. The computational cost of RBFN-based incoherent detectors when varying RIA is plotted in Fig. 9.11. Both figures are achieved considering RBFNs of $H = 20$ hidden neurons. From the results presented in Fig. 9.10 and 9.11, several conclusions can be drawn. These conclusions are similar to the ones achieved for MLP-based incoherent detectors (given in page 184-186) in terms of: tendency of the processor and detector performance with RIA (very similar); range of RIA for which the performance is better (RIA $\in [5, 13]$ cells); and selection mode for which the performance is better (S mode followed by R, P and X modes). The performance achieved by the proposed RBFN-based incoherent detector compared to the best CFAR detector (OS-CFAR in Fig. 9.3a) is always better. The achieved performance improvement varies from a minimum of $\Delta P_{\mathrm{d}} \simeq 0.08$ (V selection mode) to a maximum of $\Delta P_{\mathrm{d}} \simeq 0.14$ (S selection mode). Comparing these results with the ones achieved by the MLP-based incoherent detectors, a performance loss of $\Delta P_{\mathrm{d}} \simeq -0.02$ is observed. Apart of this difference between the proposed MLP and RBFN-based approaches, there is one more important: the required computational cost. Using the same configuration as for the MLP-based approach in the RBFN-based approach (S mode and RIA = 5 cells), a computational cost increase form 1202 (see Fig. 9.11) to 26502 (see Fig. 9.6) operations per CUT is observed.

As occurred for MLP-based detectors, the achieved performance improvement compared to CFAR detectors is due to the ability of the RBFNs to learn form the environment. Moreover, if data are selected by using 2-D modes instead of 1-D modes, the RBFN can: detect targets regardless of their orientations in the radar scan; and obtain better performance because more information is available to make the decision target present/absent.

After studying the influence of the RIA and the selection mode in RBFN-based incoherent detectors, and as done for the case of study of CFAR and MLP-based incoherent detectors, the influence of the clutter conditions is also studied when designing RBFN-based incoherent detectors. Even when the influence of the design conditions in RBFN-based incoherent detectors has been studied for all the selection modes under study, only the results when using the selection modes for which the best (S) and worst (V) performances are obtained are depicted in Fig. 9.12. From this study, it can be observed that the best clutter conditions for designing RBFN-based incoherent detectors are the practical ones, as occur for the MLP-based incoherent detectors.

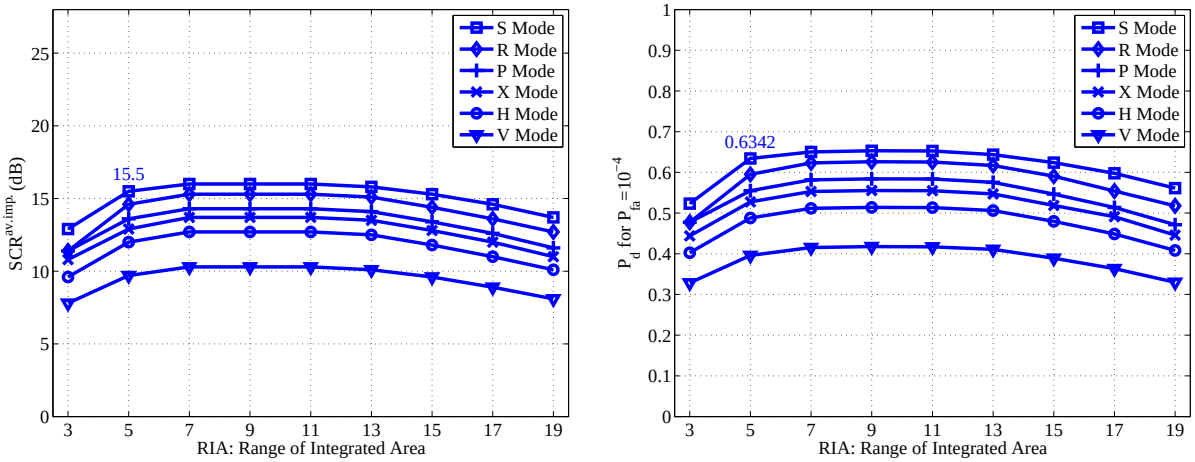

(a) RBFN-based processors (b) RBFN-based detectors

Figure 9.10: Performance of incoherent processors and detectors being formed of $J/20/1$ RBFNs, using 1-D and 2-D selection modes, considering the practical design conditions ($a_i^{(\mathrm{d})} \sim \mathrm{N}(4.46, 0.12)$) and varying RIA. Performance is given for the validation data set.

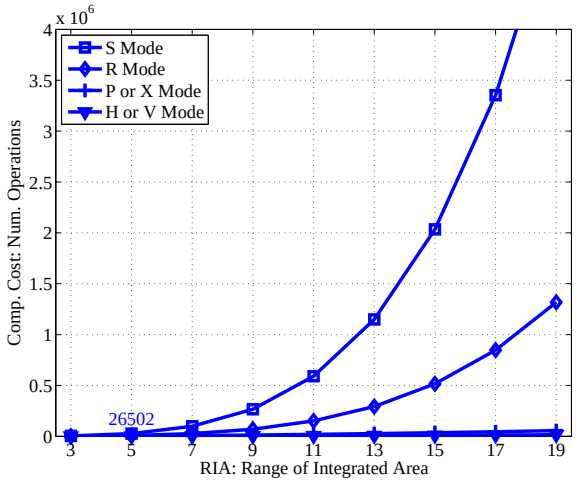

Figure 9.11: Computational cost of incoherent detectors in synthetic sea clutter when being formed of $J/20/1$ RBFNs, using 1-D and 2-D selection modes and varying RIA.

Moreover, it is observed that the range of values of RIA for which the highest performance is achieved continues being in the range $[5, 13]$ cells. Similar conclusions where extracted when designing MLP-based coherent detectors in synthetic sea clutter.

Finally, after studying the influence of the clutter conditions, RIA and selection mode in the design of RBFN-based incoherent detectors, the influence of the number of hidden neurons (H) in these detectors is studied. The computational cost of the detector is also taken into account in the selection of H. As done in previous cases of study, H is varied from 3 to 50. The performance achieved for the different selection modes under study is plotted in Fig. 9.13. The computational cost of each RBFN-based detector configuration is plotted in Fig. 9.14 when varying H. As

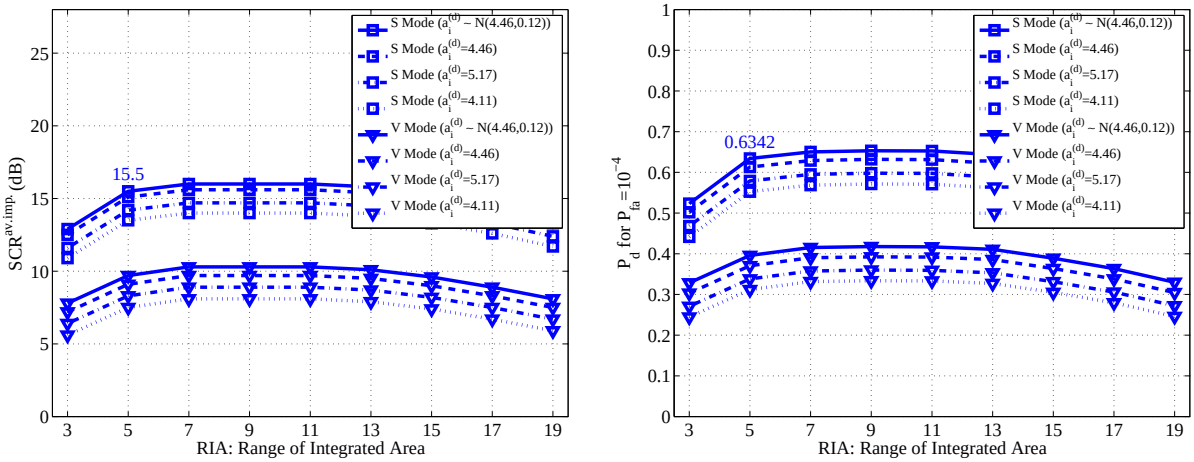

(a) RBFN-based processor (b) RBFN-based detector

Figure 9.12: Performance of RBFN-based incoherent processors and detectors when using the best (S mode) and worst (V mode) selection modes and varying RIA and the design conditions ($a_i^{(\mathrm{d})}$). Performance is given for the validation data set.

observed, regardless of the selection mode, low performance improvement (viewed by using a zoom of Fig. 9.13) is achieved while higher computational cost is required from $H = 20$ hidden neurons. Thus, this value is selected as the best one considering a trade-off between performance ($\mathrm{SCR}^{\mathrm{av.imp.}} = 15.5\,\mathrm{dB}$ and $P_{\mathrm{d}} = 0.6342$) and computational cost (26502 operations per CUT).

After these studies, an RBFN-based incoherent detector designed with practical conditions ($a_i^{(\mathrm{d})} \sim \mathrm{N}(4.46, 0.12)$), using $H = 20$ hidden neurons and selecting RIA= 5 cells by an S mode is proposed. The proposed RBFN-based incoherent detector is able to outperform the best configuration of the CFAR detectors taken as reference in $\Delta P_{\mathrm{d}} \simeq 0.14$.

9.1.4 Comparison of Incoherent Detectors in Design and Test Stages under Synthetic Sea Clutter

In the last subsections, the design of CFAR and AI-based incoherent detectors in synthetic sea clutter conditions has been studied, paying special attention to their dimensionality. In this section, the Thesis tries to solve the following question: What does it happen when other (different) radar scans are processed? This is what happens in real-live situations, where the processed data are different of the ones used for designing, although their statistical properties could be equal or similar. Thus, this Thesis investigates if the performance achieved for these new radar scans is maintained or varied. And, in case of change, it is also investigated which are the changes and their magnitudes.

The test data sets presented in Sect. 7.1, exactly in Table 7.5 for sea clutter conditions, are considered. The following study is divided in two parts. At the beginning, the performance of the detectors in the design and test stages is compared by ROC curves. At the end, two radar scans of the test data set are selected and processed to analyze what is really happening and trying to find an answer to the performance that is being achieved in each case.

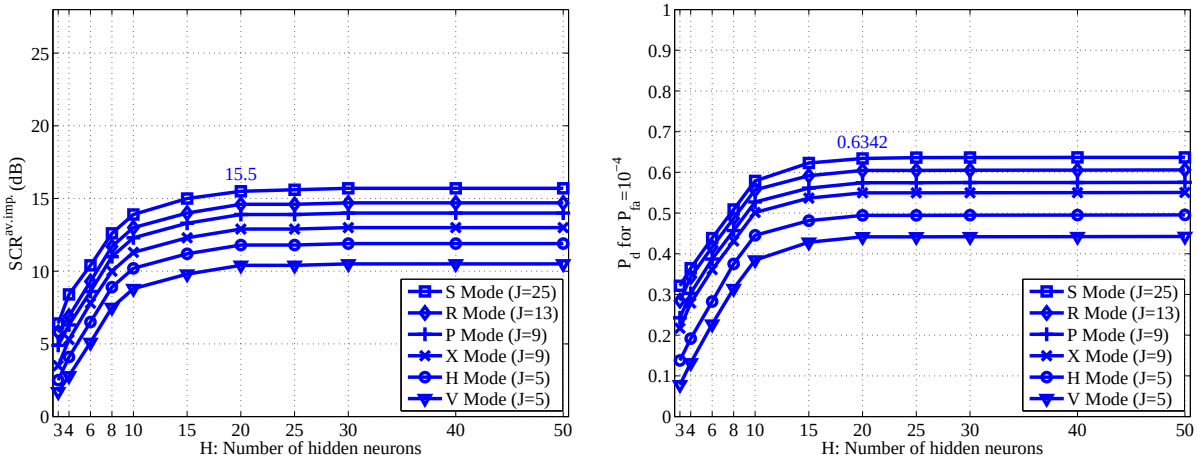

(a) RBFN-based processors

(b) RBFN-based detectors

Figure 9.13: Performance of incoherent processors and detectors being formed of $J/H/1$ RBFNs, using 1-D and 2-D selection modes, considering the practical design conditions ($a_i^{(\mathrm{d})} \sim \mathrm{N}(4.46, 0.12)$) and varying the number of hidden neurons (H). Performance is given for the validation data set.

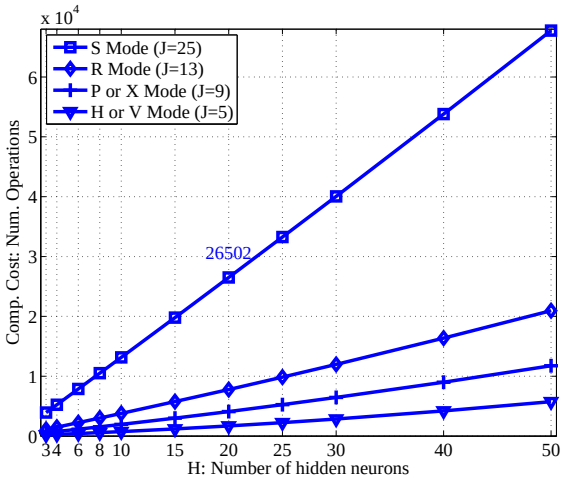

Figure 9.14: Computational cost of incoherent detectors in synthetic sea clutter when being formed of $J/H/1$ RBFNs, using 1-D and 2-D selection modes and varying the number of hidden neurons (H).

The configurations used for each detector are extracted from the design stage, being:

- MLP-based incoherent detector: designed selecting $J = 25$ (RIA= 5 cells) cells in an S selection mode and using $H = 15$ hidden neurons. So, an MLP structure of 25/15/1 is used.

- RBFN-based incoherent detector: designed selecting $J = 25$ (RIA= 5 cells) cells in an S selection mode and using $H = 20$ hidden neurons. So, an RBFN structure of 25/20/1 is

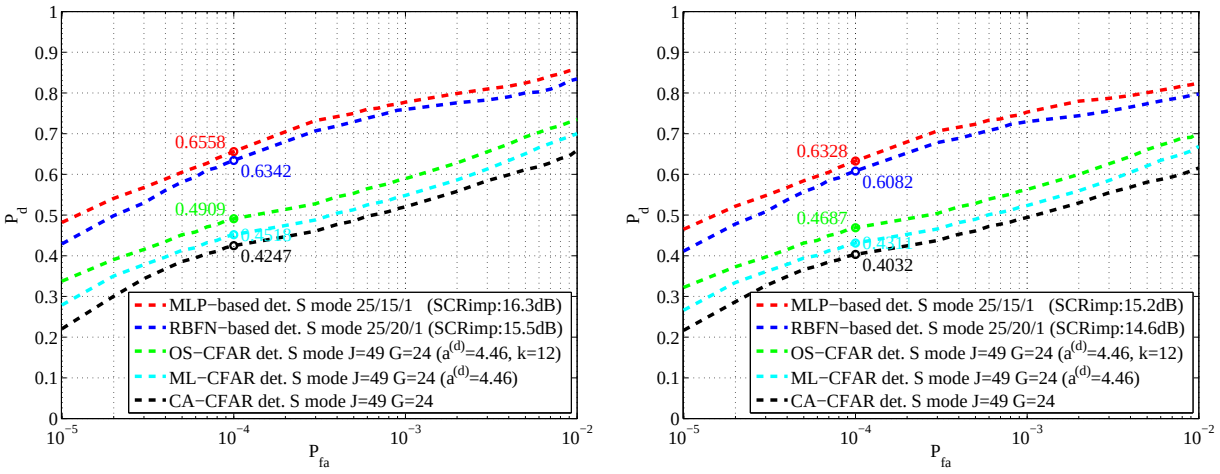

(a) Validation data set (b) Test data set

Figure 9.15: Performances of the selected configurations of CFAR, MLP and RBFN-based incoherent detectors using the validation and test data sets when synthetic sea clutter measurements are considered.

used.

- CFAR incoherent detectors: designed selecting $J = 49$ (RIA= 7 cells) cells in an S selection mode. For the ML-CFAR detector, the value of skewness for the CFAR processor is set to the typical value of the clutter in the design data set, i.e. $a^{(\mathrm{d})} = 4.46$. For the OS-CFAR detector, the order of cell selection is set in $k = 12$.

The results achieved in the design stage, i.e. considering the validation data set, are depicted in Fig. 9.15a. While the results obtained in the test stage, i.e. considering the test data set, which contains radar images never processed by the designed detectors, are given in Fig. 9.15b. From the results achieved for the design and test conditions, several conclusions can be drawn:

- The tendency of the ROC curves is maintained, involving that the best detector continues being the one based on MLPs, followed by the RBF-based detector, and surpassing the performance achieved by the reference ones, the CFAR detectors.

- The performance of the detectors decrease in the test stage both in terms of SCR improvement (see the values given in the legend of each figure) and P_{d}. Focusing on the CFAR detectors, the performance losses of these detectors are close to 0.02. On the other hand, the performance losses observed in AI-based processors and detectors is close to 1 dB in $\mathrm{SCR}^{\mathrm{av,imp}}$ and 0.02 in P_{d}, respectively.

After the analysis of these results, we can conclude that great robustness against changes in clutter conditions is achieved in all the detectors when different radar scans are present, specially for the proposed ones. It is an important question because it gives us an approximation of how their performance will be when working in steady state.

After the study of the performance loss and robustness of the incoherent detectors, subjective and objective studies of their performances for specific radar scans with different clutter

conditions are done. For that purpose, two radar scans of the test data set are selected. As observed from the figures of the studies done during the design stage of Sect. 9.1, the clutter conditions for which the best ($a^{(\mathrm{d})} = 4.46$) and worst ($a^{(\mathrm{d})} = 4.11$) performances are achieved are selected. It can be better understood by the plot of the PDF of each clutter condition done in Fig. 8.19. As discussed for the coherent detection case (see Sect. 8.2.4), it is observed in this plot that the probability of achieving a clutter cell with high amplitude is greater for low values of the skewness parameter ($a = 4.11$) than for high values ($a = 5.17$). It involves that to achieve a desired P_{fa} the thresholding level applied for $a = 4.11$ must be grater than for $a = 5.17$, being consequently reduced the P_{d} for $a = 4.11$ in comparison with the one achieved for $a = 5.17$. According to this law, the P_{d} for $a = 4.46$ should be lower than for $a = 5.17$, but the achieved results go on the opposite direction. Thus, why this behavior? This behavior is given because the probability that a radar scan in the data set has $a = 4.46$ is greater than for $a = 5.17$, what involves that the threshold in the design stage is mainly conditioned by the data belonging to $a = 4.46$ rather than for $a = 5.17$.

According to the reasons given in the previous paragraph, two radar scans are selected from the test data set having $a^{(\mathrm{t})} = 4.46$ and $a^{(\mathrm{t})} = 4.11$. These radar scans ($\mathbf{I}^{(4.11)}$ and $\mathbf{I}^{(4.46)}$) are plotted in Fig. 9.16 by their magnitude (no phase information is available). Note that not all the coverage of the radar scan (see Table 2.2) is plotted. It is due to details will be lost in presentation. Only a zone of the full-coverage, between 0 and 3 degrees in azimuth and between 1000 m and 1450 m in range, is selected for plotting and making the subjective analysis of the performance. Nevertheless, it is important to note that the objective performances given for each processed radar scan are given for the whole scan and not for the selected zone.

In order to make easier the subjective analysis done for the processed radar scans, the positions, sizes and shapes of the targets in the radar scenes of Fig. 9.16 are the same, being depicted in Fig. 9.17 (high level means that target is present in this cell, otherwise target is absent and only clutter is present).

The radar scans at the output of the CFAR and AI-based incoherent processors and detectors for $\mathbf{I}^{(4.11)}$ are depicted in Fig. 9.18 and 9.19, while for $\mathbf{I}^{(4.46)}$ are depicted in Fig. 9.20 and 9.21, respectively. According to these results, first the performance of each detector is analyzed, and thereafter some conclusions are drawn.

For analyzing the performance loss of each detector, we take as reference the values achieved when the validation and test data set are used, which are summarized in Fig. 9.15. Thus, from the performance achieved by each detector, we can observe that:

- The performances achieved for the radar scan $\mathbf{I}^{(4.11)}$ are always lower than the ones achieved for the test data set presented in Fig. 9.15b and for the validation data set presented in Fig. 9.15a. It happens because the detection in these clutter conditions is more difficult than in the other clutter conditions, as discussed in Sect. 8.2.4.

- The performances achieved for the radar scan $\mathbf{I}^{(4.46)}$ are always higher than the ones achieved for the test data set presented in Fig. 9.15b and lower than the ones achieved for the validation data set presented in Fig. 9.15a. It happens because the detection in these clutter conditions is easier than in the other clutter conditions, as discussed in Sect. 8.2.4.

- The P_{fa} remains constant with the threshold set during the design stage, as observed for

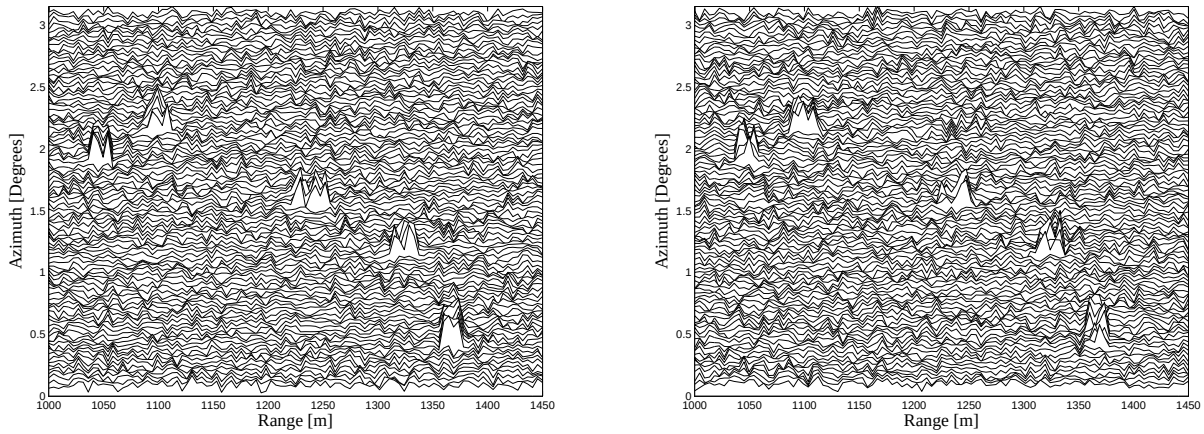

(a) $\mathbf{I}^{(4.11)}$ (b) $\mathbf{I}^{(4.46)}$

Figure 9.16: Magnitude of two radar scans ($\mathbf{I}$) with $a^{(\mathrm{t})} = 4.11$ ($\mathbf{I}^{(4.11)}$) and $a^{(\mathrm{t})} = 4.46$ ($\mathbf{I}^{(4.46)}$) taken from test data set.

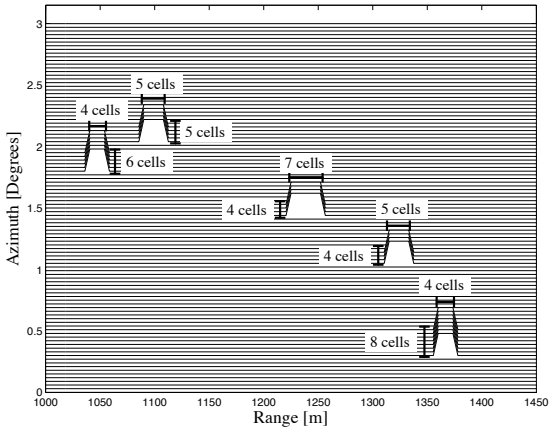

Figure 9.17: Desired (ideal) output radar scan ($\mathbf{D}$).

this case of study of $P_{\mathrm{fa}} = 10^{-4}$.

Analyzing the radar scans presented in Fig. 9.18-9.19 and 9.20-9.21, we can find two reasons why AI-based detectors outperform the reference detector. First, because they are able to reduce in a high rate the level of clutter. And second, because they are able to emphasize the level of signal where target is present. Both reasons can be extracted from the radar scans at the output of the processors, which lead to improve the detection rate, as observed in the radar scans at the output of the detectors. Note that the output of the processors for CFAR detectors are not given because it doesn't make any contribution due to the applied threshold is not a fixed value and is adapted by the output of the CFAR processor.

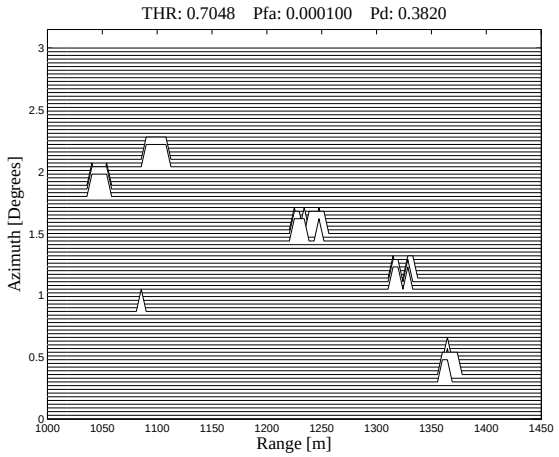

(a) CA-CFAR detector output for $\mathbf{I}^{(4.11)}$

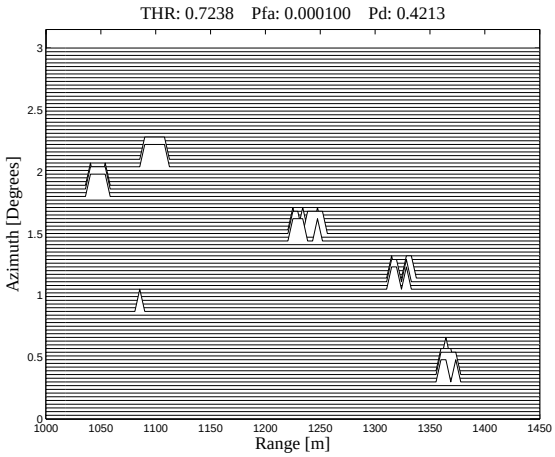

(b) ML-CFAR detector output for $\mathbf{I}^{(4.11)}$

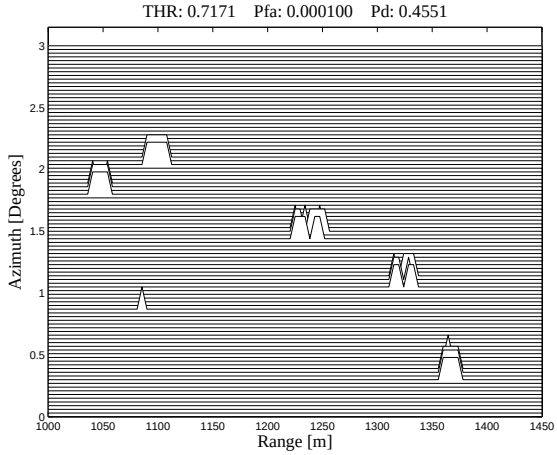

(c) OS-CFAR detector output for $\mathbf{I}^{(4.11)}$

Figure 9.18: Radar scans at the output of the CA, ML and OS-CFAR detectors when the input radar scan $\mathbf{I}^{(4.11)}$ is processed.

9.2 General Conclusions about Incoherent Detection in Synthetic Sea Clutter

Before starting with the presentation of the main conclusions drawn from the analysis of the results obtained when designing and testing incoherent detectors in synthetic sea clutter, it is important to note a relevant issue. Experiments using incoherent detectors in sea-ice and ground clutters have been also made in the experimental stage of the thesis, as made for incoherent detectors in synthetic sea clutter. But, no performance has been reported in the thesis for these cases of study because of the following reasons:

- First, because the performance losses observed for incoherent detectors with respect to the ones for coherent detectors in synthetic sea-ice and ground clutters are very similar to the losses observed when using coherent and incoherent detectors in synthetic sea clutter (losses discussed below).

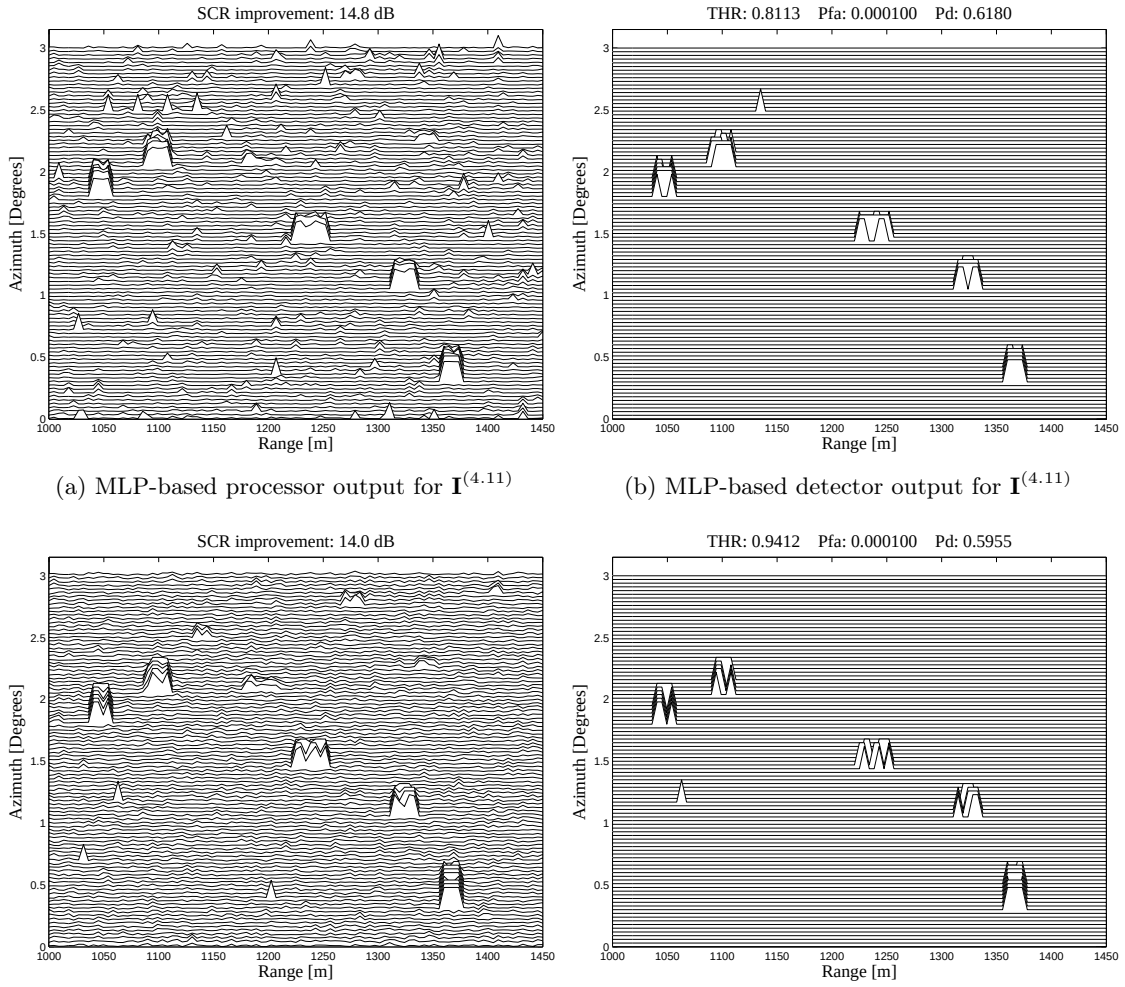

(a) MLP-based processor output for $\mathbf{I}^{(4.11)}$

(b) MLP-based detector output for $\mathbf{I}^{(4.11)}$

(c) RBFN-based processor output for $\mathbf{I}^{(4.11)}$

(d) RBFN-based detector output for $\mathbf{I}^{(4.11)}$

Figure 9.19: Radar scans at the output of the MLP and RBFN-based processors and detectors when the input radar scan $\mathbf{I}^{(4.11)}$ is processed.

- Second, because the dimensionality and design clutter conditions of coherent and incoherent detectors in synthetic sea-ice and ground clutters follow a similar behavior as observed for coherent and incoherent detectors in synthetic sea clutter.
- And third, because real-live data were not available for sea-ice and ground clutter measurements.

Therefore, the general conclusions drawn below when using incoherent detectors in synthetic sea clutter can be extrapolated to the cases of study of incoherent detectors in synthetic sea-ice and ground clutters.

Comparing the performance of coherent and incoherent detectors in synthetic sea clutter, several conclusions are obtained:

- Comparing the performance of the coherent detector taken as reference, the TSKAP detector (see Sect. 8.2.1), to the ones obtained for the incoherent detectors taken as reference, the

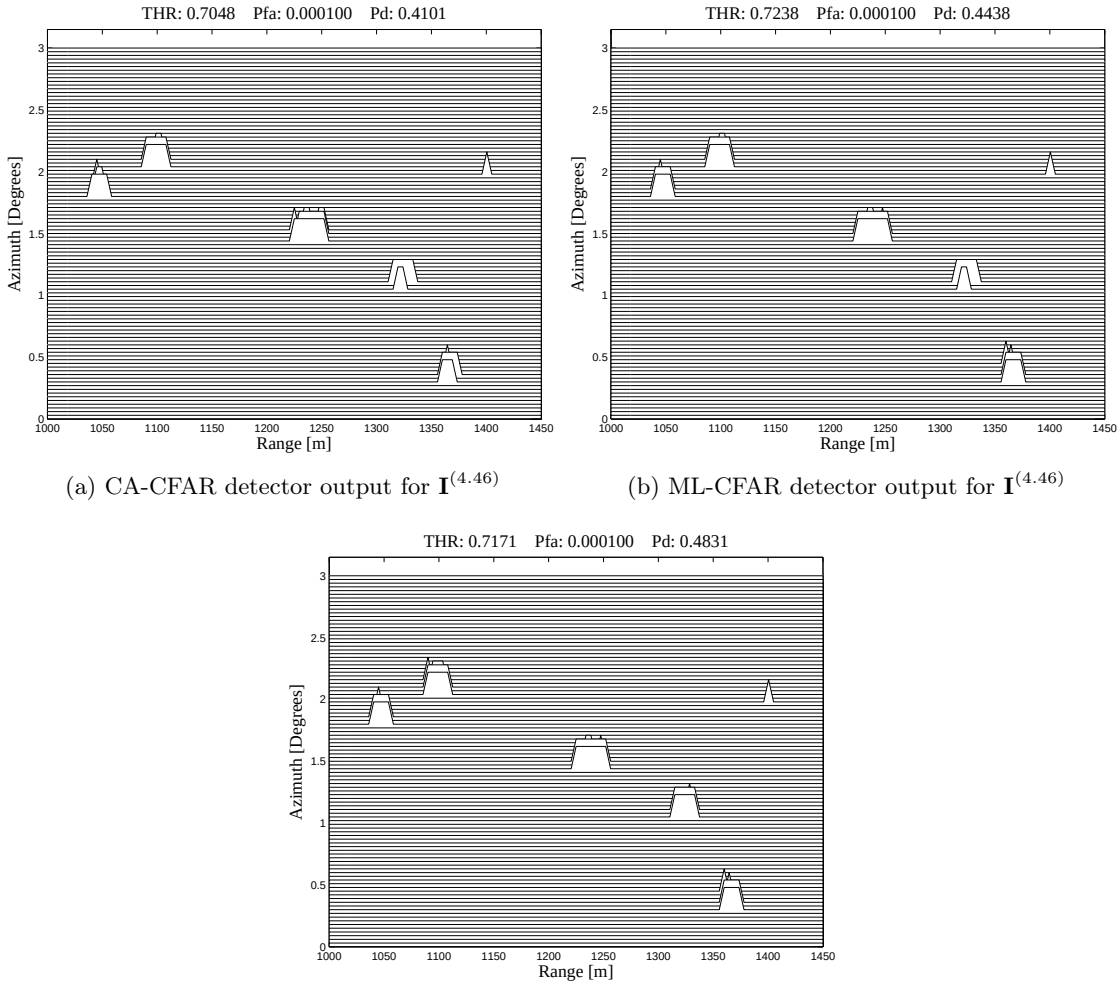

(a) CA-CFAR detector output for $\mathbf{I}^{(4.46)}$

(b) ML-CFAR detector output for $\mathbf{I}^{(4.46)}$

(c) OS-CFAR detector output for $\mathbf{I}^{(4.46)}$

Figure 9.20: Radar scans at the output of the CA, ML and OS-CFAR detectors when the input radar scan $\mathbf{I}^{(4.46)}$ is processed.

CFAR detectors (see Sect. 9.1.1), some differences are observed. Considering the selected configuration of the TSKAP detector (selecting $N = 4$ cells by a non-delayed azimuthal selection mode), $P_{\mathrm{d}} = 0.2734$ for $P_{\mathrm{fa}} = 10^{-4}$ is achieved (see Fig. 8.3). Whereas, considering the best selected configuration of the CFAR detectors under study (OS-CFAR detector using an S selection mode with RIA = 7 cells), $P_{\mathrm{d}} = 0.4909$ for $P_{\mathrm{fa}} = 10^{-4}$ is achieved (see Fig. 9.3). As observed, the selected incoherent approach outperforms the selected coherent approach in $\Delta P_{\mathrm{d}} = 0.22$. This behavior is not what could be expected, because the detection using coherent data should be better than when using incoherent data (more information (phase information) is available to make the decision). This effect is due to the different philosophies of working of the coherent and incoherent detectors taken as reference. In this sense, while the TSKAP detectors are designed for: filtering the signals (reducing the level of clutter), working with a fixed threshold and using non-delayed selection modes; the CFAR detectors estimate the statistical parameters of the clutter to

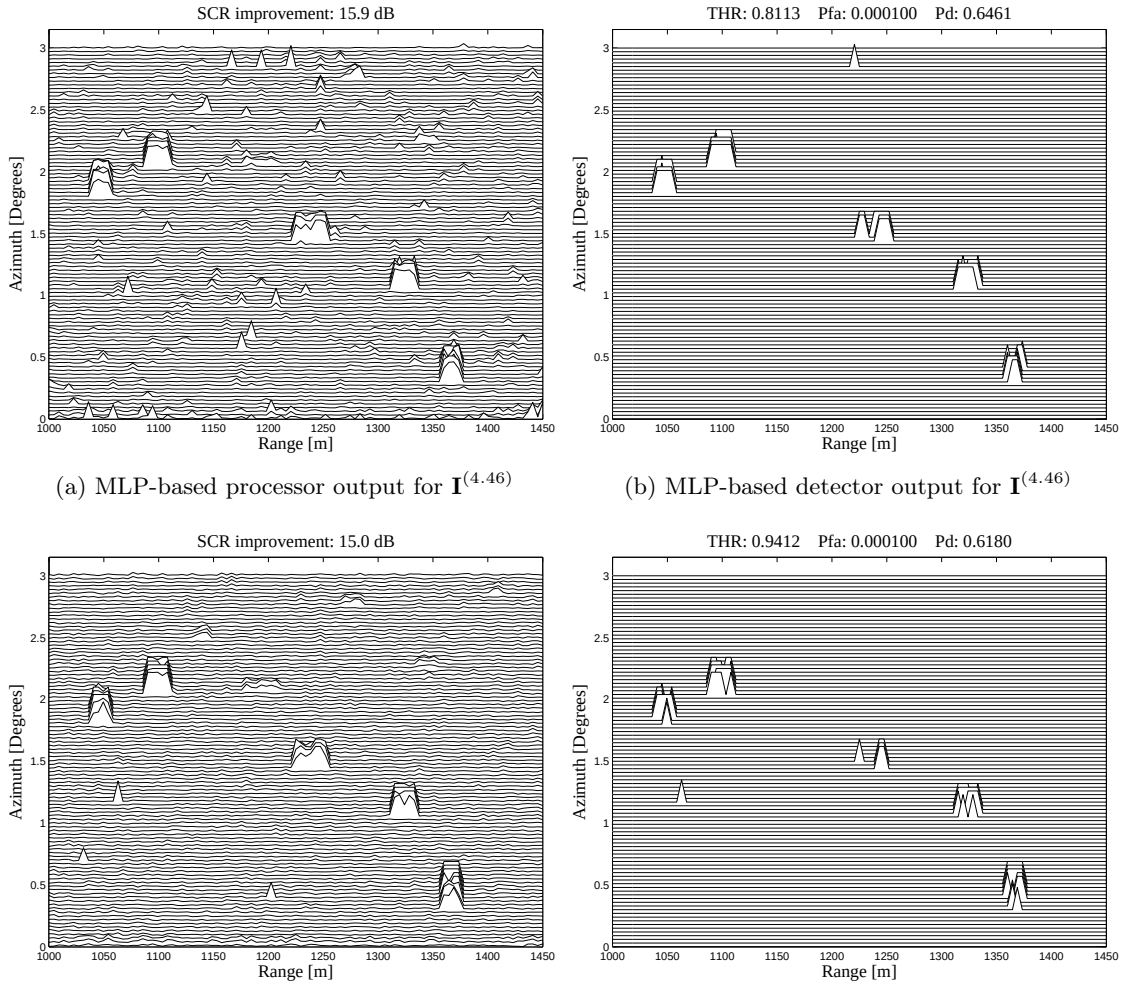

(a) MLP-based processor output for $\mathbf{I}^{(4.46)}$

(b) MLP-based detector output for $\mathbf{I}^{(4.46)}$

(c) RBFN-based processor output for $\mathbf{I}^{(4.46)}$

(d) RBFN-based detector output for $\mathbf{I}^{(4.46)}$

Figure 9.21: Radar scans at the output of the MLP and RBFN-based processors and detectors when the input radar scan $\mathbf{I}^{(4.46)}$ is processed.

adapt the detection threshold by using delayed (1-D and 2-D) selection modes.

- Comparing the performance of MLP-based coherent detectors (see Sect. 8.2.2) to the one obtained when using MLP-based incoherent detectors (see Sect. 9.1.2) in synthetic sea clutter, a performance loss is observed. On the one hand, a performance of $\text{SCR}^{\text{av.imp.}} = 21.6\,\text{dB}$ and $P_\text{d} = 0.7088$ for $P_\text{fa} = 10^{-4}$ is achieved using the selected configuration for the MLP-based coherent detector (see Fig. 8.7). On the other hand, a performance of $\text{SCR}^{\text{av.imp.}} = 16.3\,\text{dB}$ and $P_\text{d} = 0.6558$ for $P_\text{fa} = 10^{-4}$ is achieved using the selected configuration for the MLP-based incoherent detector (see Fig. 9.5). This performance loss ($\Delta\text{SCR}^{\text{av.imp.}} \simeq -5\,\text{dB}$ and $\Delta P_\text{d} \simeq -0.05$) is expected because the coherent approach incorporates more information (amplitude and phase) than the incoherent approach (only amplitude) to make the final decision. But, a computational cost decrease of $\simeq -19\%$ is obtained from coherent to incoherent approaches: from 1552 operations per CUT when

using the proposed coherent approach configuration (see Fig. 8.8) to 1202 operations per CUT when using the proposed incoherent approach configuration (see Fig. 9.6). It is important to note that, regardless of using coherent or incoherent detectors, the same range of RIA and the best selection mode (S mode) are achieved.

- Making the same comparison as done above for MLP-based detectors, but for the case of RBFN-based coherent (see Sect. 8.2.3) and incoherent (see Sect. 9.1.3) detectors in synthetic sea clutter, similar differences are observed. On the one hand, a maximum performance of $\mathrm{SCR}^{\mathrm{av.imp.}} = 19.5\,\mathrm{dB}$ and $P_{\mathrm{d}} = 0.6819$ for $P_{\mathrm{fa}} = 10^{-4}$ is achieved using the selected configuration for the RBFN-based coherent detector (see Fig. 8.14). On the other hand, a maximum performance of $\mathrm{SCR}^{\mathrm{av.imp.}} = 15.5\,\mathrm{dB}$ and $P_{\mathrm{d}} = 0.6342$ for $P_{\mathrm{fa}} = 10^{-4}$ is achieved using the selected configuration for RBFN-based incoherent detector (see Fig. 9.10). After this comparison, a performance loss of $\Delta\mathrm{SCR}^{\mathrm{av.imp.}} \simeq -4\,\mathrm{dB}$ and $\Delta P_{\mathrm{d}} \simeq -0.05$ is obtained. As occurred for MLP-based detectors, this performance loss can be expected because incoherent detectors use less information (only amplitude) than the coherent detectors (amplitude ad phase). But, a computational cost decrease of $\simeq -74\%$ is obtained from coherent to incoherent approaches: from 102502 operations per CUT when using the proposed coherent approach configuration (see Fig. 8.15) to 26502 operations per CUT when using the proposed incoherent approach configuration (see Fig. 9.11). Moreover, the same range of values of RIA is achieved and the best selection mode continues being the S mode, regardless of the type of detector (coherent or incoherent).

Apart of these changes in performance (loss) and computational cost (decrease) when using incoherent approaches instead of coherent approaches, the following general conclusions are drawn from the analysis of the results of incoherent detectors in synthetic sea clutter:

- The clutter conditions (used to design incoherent detectors) that maximize the detector performance are the practical ones, where the skewness parameter of the Weibull-distributed clutter vary scan-to-scan ($a_i^{(\mathrm{d})} \sim \mathrm{N}(4.46, 0.12)$ in this case). When these situations are not applicable, as for the reference detectors (CA, ML and OS-CFAR detectors), the best design conditions are the typical ones ($a_i^{(\mathrm{d})} = 4.46$ scan-to-scan in this case).

- Selection modes with 2-D templates allow to achieve greater performance than 1-D selection modes, regardless of the used incoherent detector (CFAR or AI-based detector). Nevertheless, these modes provoke that the detector requires more computational cost. From the 2-D selection modes under study, the best one is the square (S) mode. But, other selection modes, such as the rhombus (R) and plus-shape (P) selection modes allow to achieve a performance slightly lower, while considerably reducing the computational cost of AI-based detectors.

- The range of integrated area (RIA) for obtaining the highest performance (RIA $\in [5, 13]$ cells in this case) is related to the size of the targets considered in the study ($\in [4, 12]$ cells in this case). This effect is observed in the reference (CFAR) and proposed (AI-based) detectors. From this interval of RIA, we propose to use of the minimum value (RIA = 5 cells in this case) because the performance is very close to the highest one and the computational cost of the detector is considerably reduced (exponential relationship with RIA, as observed in Fig. 9.6 and 9.11).

- A suitable value of hidden neurons (H) in AI-based detectors is found, being smaller for MLP-based incoherent detectors ($H = 15$) than for RBFN-based incoherent detectors ($H = 20$). This value is selected considering a trade-off between the performance achieved by the detector and its computational cost, as done when selecting the RIA.

- It is observed that the setup of the detector parameters in the design stage can be done by using two different ways of measuring the detector performance: $\mathrm{SCR}^{\mathrm{av.imp.}}$ achieved in the processor; and P_{d} for a given P_{fa} in the detector. Both performance measurements vary similarly with the parameters of the detectors (clutter conditions in the design stage, selection mode and RIA).

- High robustness is observed in the detector performance when processing radar scans different of the ones used for designing. It gives us an idea of the performance that can be expected when the designed detector processes in the future new radar scans under the same or similar statistical properties. it is very important because this is what happens in real-live situations.

- Finally, it is observed that the performance of the detector processing radar scans with different clutter parameters (skewness parameters) is very similar. It involves high robustness of the detector against changes in the clutter conditions.

The above-presented conclusions are in consonance with the ones obtained for the case of using coherent detectors in synthetic sea clutter (see Sect. 8.2.5), but with small differences corresponding to the achieved performances.

CHAPTER 10

Statistical Relation between Synthetic and Real-Live Sea Clutter

This chapter is dedicated to study if the sea clutter returns measured by a real-live marine radar follow a Weibull distribution. Once found that this real-live sea clutter fits the Weibull distribution, their statistical properties are studied, extracting the Weibull parameters that model the clutter from the real-live radar returns.

10.1 Statistical Analysis of Real-Live Sea Clutter

In this section, the study of the statistical properties of a set of real-live radar scans is done. First, the study focuses on the extraction of the statistical properties of three given sectors of three different radar scans. Second, the statistical properties for all the sectors of these radar scans are extracted. And third, the statistical properties of the whole data set are achieved and summarized in Sect. 10.2.

Three real-live radar scans are randomly selected from the sequences of radar images that compose each data set (training, validation and test of Sect. 7.2). These radar scans are depicted in Fig. 10.1 using a Cartesian plot of the polar (range-azimuth) information.

For the statistical analysis of the distribution that follows the clutter and its statistical parameters, the radar scans are divided into several sectors, as depicted in Fig. 10.1. Note that the range coverage of the three radar scans is not the same, being smaller (short range radar configuration) for the radar scan selected from the testing data set. With this difference, the thesis tries to demonstrate that the proposed detectors can properly work with different radar configurations.

Let's focus on the analysis of a certain sector of each radar scan. This sector is in $[720, 1200]$ m and $[45, 90]^\circ$ for the radar scans of the training and validation data sets and in $[450, 750]$ m and $[45, 90]^\circ$ for the radar scan of the testing data set. For these three sectors, first it is studied if the data of each sector fit a Weibull distribution. For that purpose, a Weibull probability plot is done for each sector, being depicted in Fig. 10.2. Note that since the marine radar used in the experiment incorporates a logarithmic amplifier, this logarithmic transformation is inverted in order to get the measured values. This logarithmic inversion is done because in the literature, such as in [Sekine1990], it has been demonstrated that the sea clutter return measurements follow

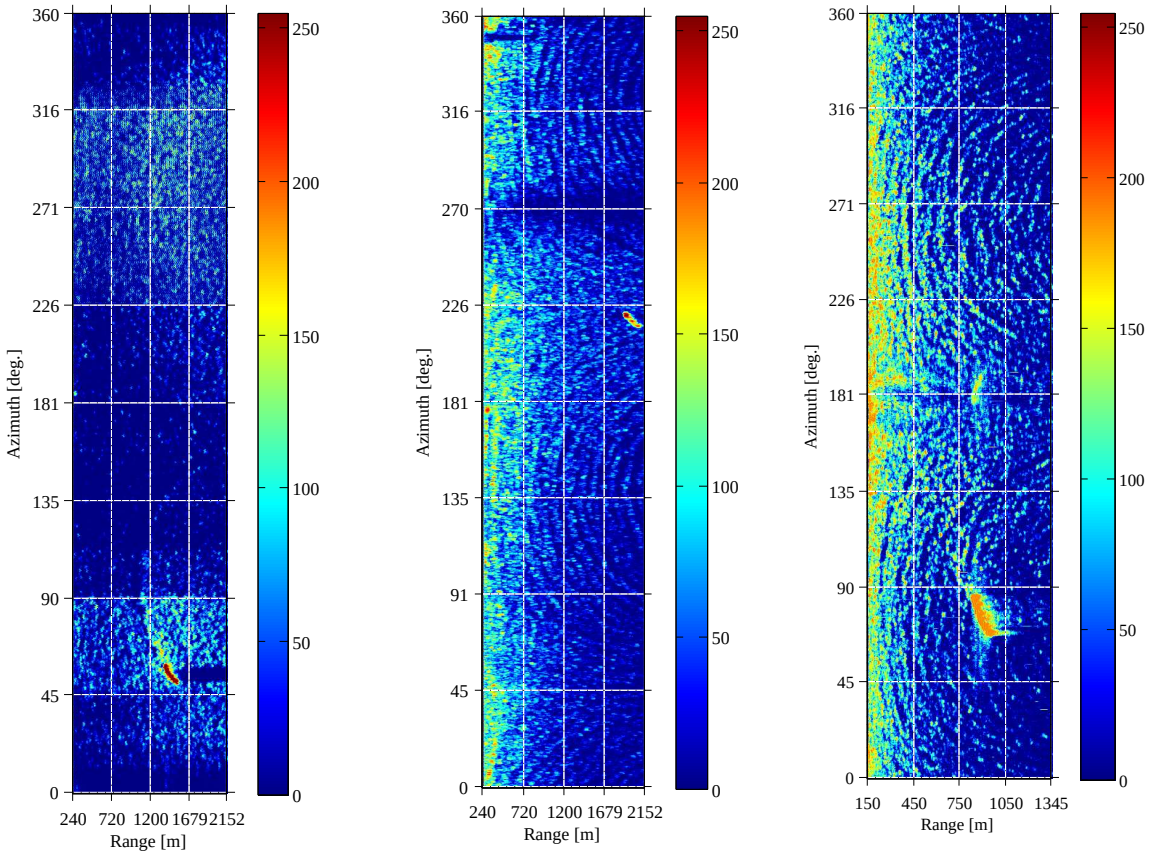

(a) Scan of the training data set. (b) Scan of the validation data set. (c) Scan of the testing data set.

Figure 10.1: Division in sectors of three scans extracted from the designing (training and validation) and testing data sets to be statistically analyzed.

a Weibull distribution when they are measured directly, and not by using a logarithmic amplifier. As can be observed in Fig. 10.2, the data of each selected sector fit a Weibull distribution with low error. Different statistical parameters (skewness and scale parameters) are needed for each fit because different sea states are observed in each radar scan. Therefore, the first objective is fulfilled: the sea clutter measurements fit the Weibull distribution.

Let's study now which are the parameters of the Weibull distribution that approximate these data. For that purpose, the estimates of the skewness (a) and scale (b) parameters are done following a maximum likelihood estimate. Moreover, to realize the accuracy of the estimates, the confidence intervals for the estimated parameters are given for a confidence of 95%. The estimated parameters and their confidence intervals for each sector are given in Table 10.1.

Following the procedure followed for the above-processed sectors but for the other sectors in which the radar scans are divided, the estimates of the parameters and their confidence intervals are achieved. Therefore, for the radar scan selected from the training data set, the estimates and confidence intervals of the skewness and scale parameters for each sector are depicted in Fig. 10.3. The parameter estimates and confidence intervals for the radar scans of the validation and testing data sets are depicted in Fig. 10.4 and 10.5, respectively. Analyzing these results,

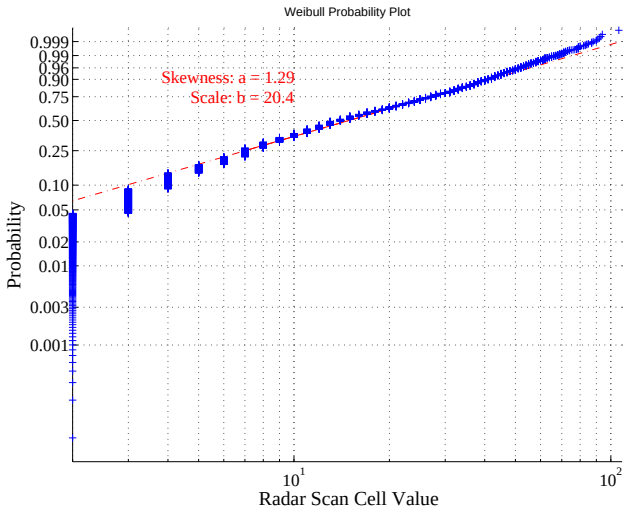

(a) Training radar scan: Sector from 720 m to 1200 m and from 45° to 90°.

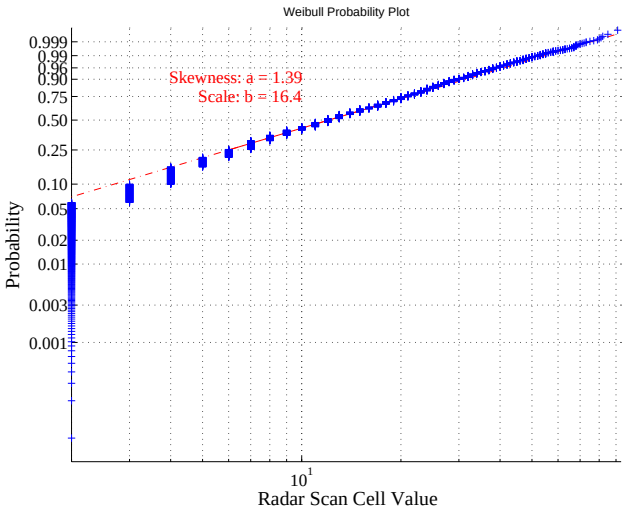

(b) Validation radar scan: Sector from 720 m to 1200 m and from 45° to 90°.

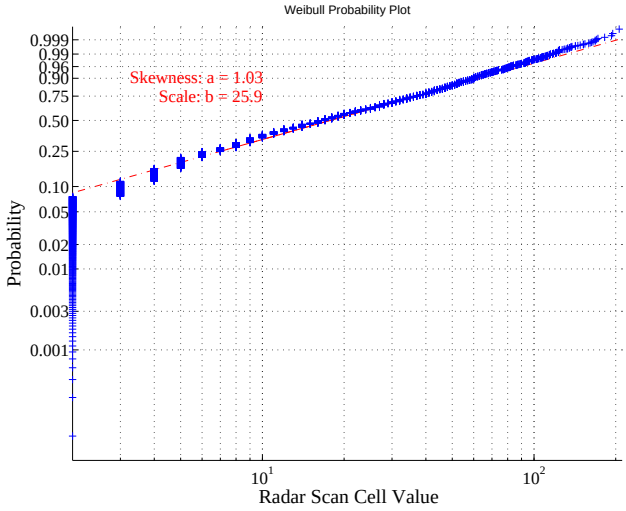

(c) Testing radar scan: Sector from 450 m to 750 m and from 45° to 90°.

Figure 10.2: Statistical analysis of a given sector: Weibull plot of the data contained in this sector.

several conclusions can be drawn:

- The skewness parameter is greater for sectors from which the sea waves are coming to the radar site and lower for the sectors for which the sea waves travel from the radar site. To clarify this conclusion, as an example, let's pay attention to the estimated skewness parameter given in Fig. 10.3. In this plot, the sea waves travel to the radar site in the sectors between 45° and 90°, where the skewness is found to be the greatest one in average

Table 10.1: Weibull statistical parameters and confidence intervals (95%) of the sector in $[720, 1200]$ m and $[45, 90]^\circ$ for radar scans of Fig. 10.1a and 10.1b, and the sector in $[450, 750]$ m and $[45, 90]^\circ$ for the radar scan of Fig. 10.1c.

Statistical Parameter		Sector in scan of Fig. 10.1a	Sector in scan of Fig. 10.1b	Sector in scan of Fig. 10.1c
Skewness value	a	1.29	1.39	1.03
Skewness conf. interval	$[a_{\min}, a_{\max}]$	[1.26 , 1.31]	[1.37 , 1.42]	[1.01 , 1.05]
Scale value	b	20.4	16.4	25.9
Scale conf. interval	$[b_{\min}, b_{\max}]$	[20.1 , 20.8]	[16.2 , 16.7]	[25.2 , 26.6]

for the different ranges, and travel from the radar site in sectors between 225° and 270°, where the averaged skewness is the lowest.

- Note that the scale parameter is greater for the sectors near the radar site than for sectors far away from it. This effect can be clearly observed in Fig. 10.4 and 10.5. It happens because this parameter is directly related to the power of the data, being this power greater for the returns in cells near the radar site. Note that it doesn't happen in the analysis of the radar scan from the training data set (Fig. 10.3) because the sea state that exists in it is the lowest one of the ones considered in the studies of the thesis (Sea state 1: Calm sea, as discussed in Sect. 2.5.2).

- And finally, the data is approximated by the Weibull distribution with high accuracy because of the confidence intervals for the estimated skewness and scale parameters are very small.

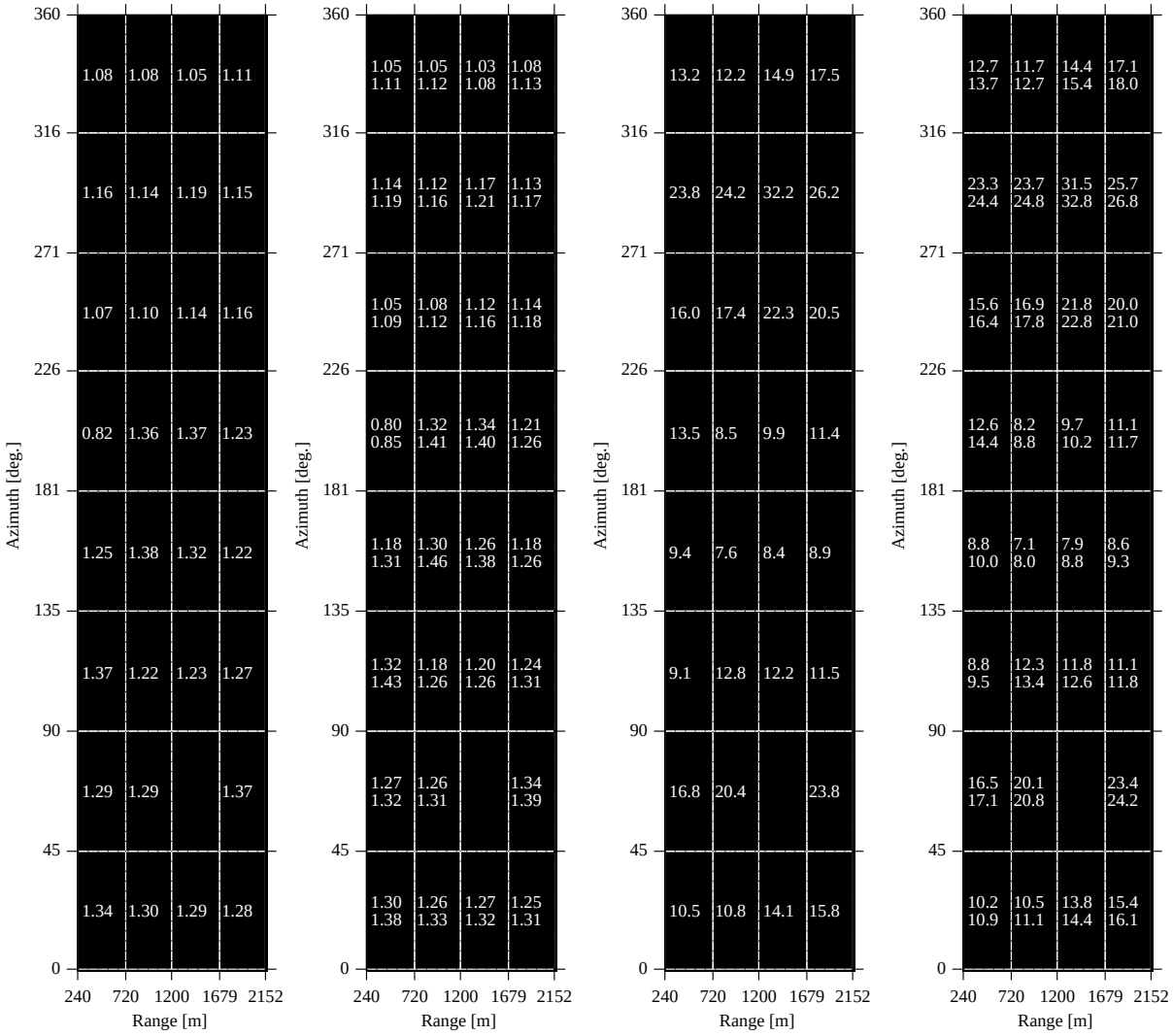

(a) Estimation of skewness for each sector.

(b) Confidence interval of the skewness estimate.

(c) Estimation of scale for each sector.

(d) Confidence interval of the scale estimate.

Figure 10.3: Estimates of the skewness and scale parameters of the Weibull distribution and their intervals of confidence at 95% for each sector of the radar scan extracted from the training data set.

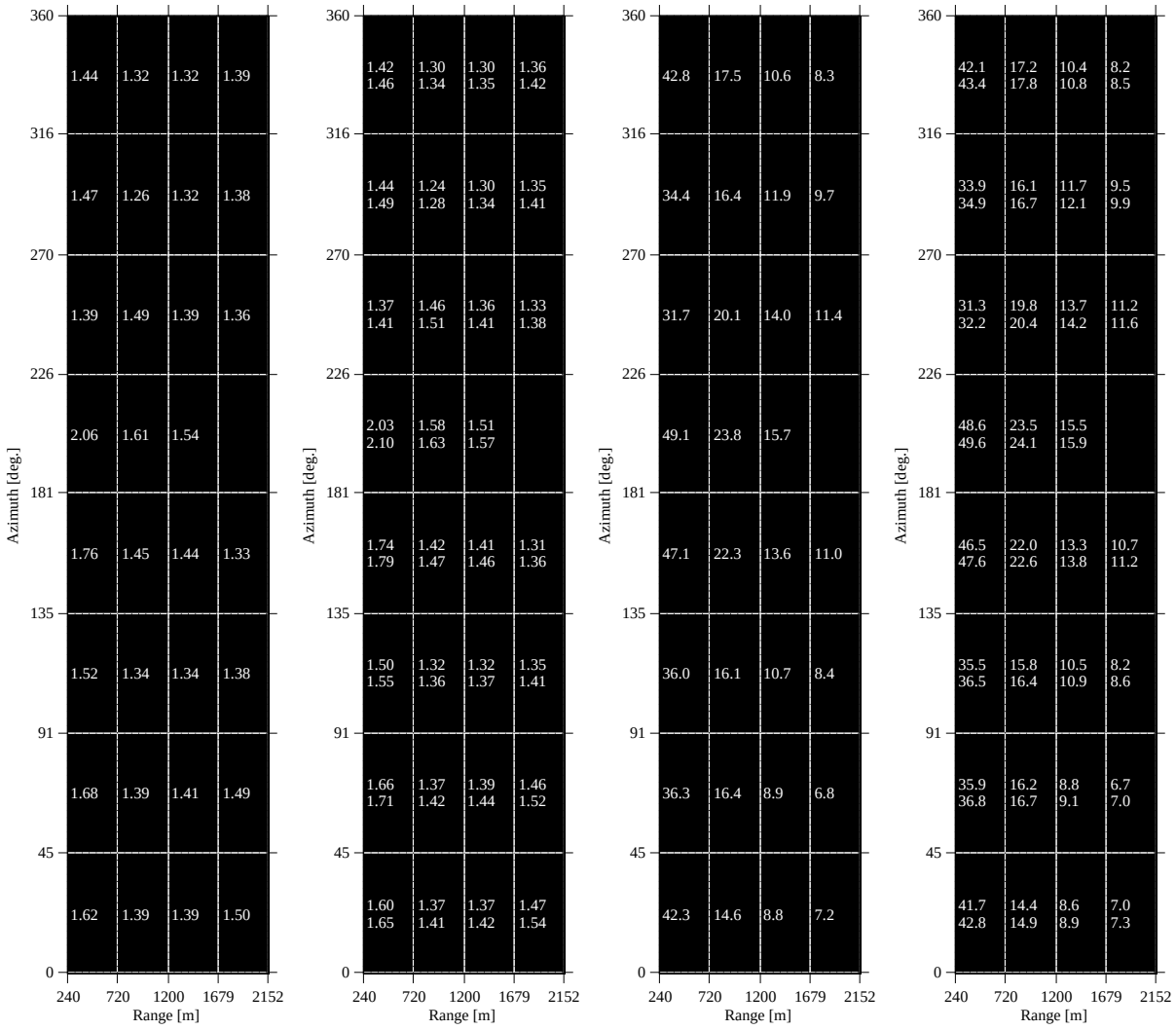

(a) Estimation of skewness for each sector.

(b) Confidence interval of the skewness estimate.

(c) Estimation of scale for each sector.

(d) Confidence interval of the scale estimate.

Figure 10.4: Estimates of the skewness and scale parameters of the Weibull distribution and their intervals of confidence at 95% for each sector of the radar scan extracted from the validation data set.

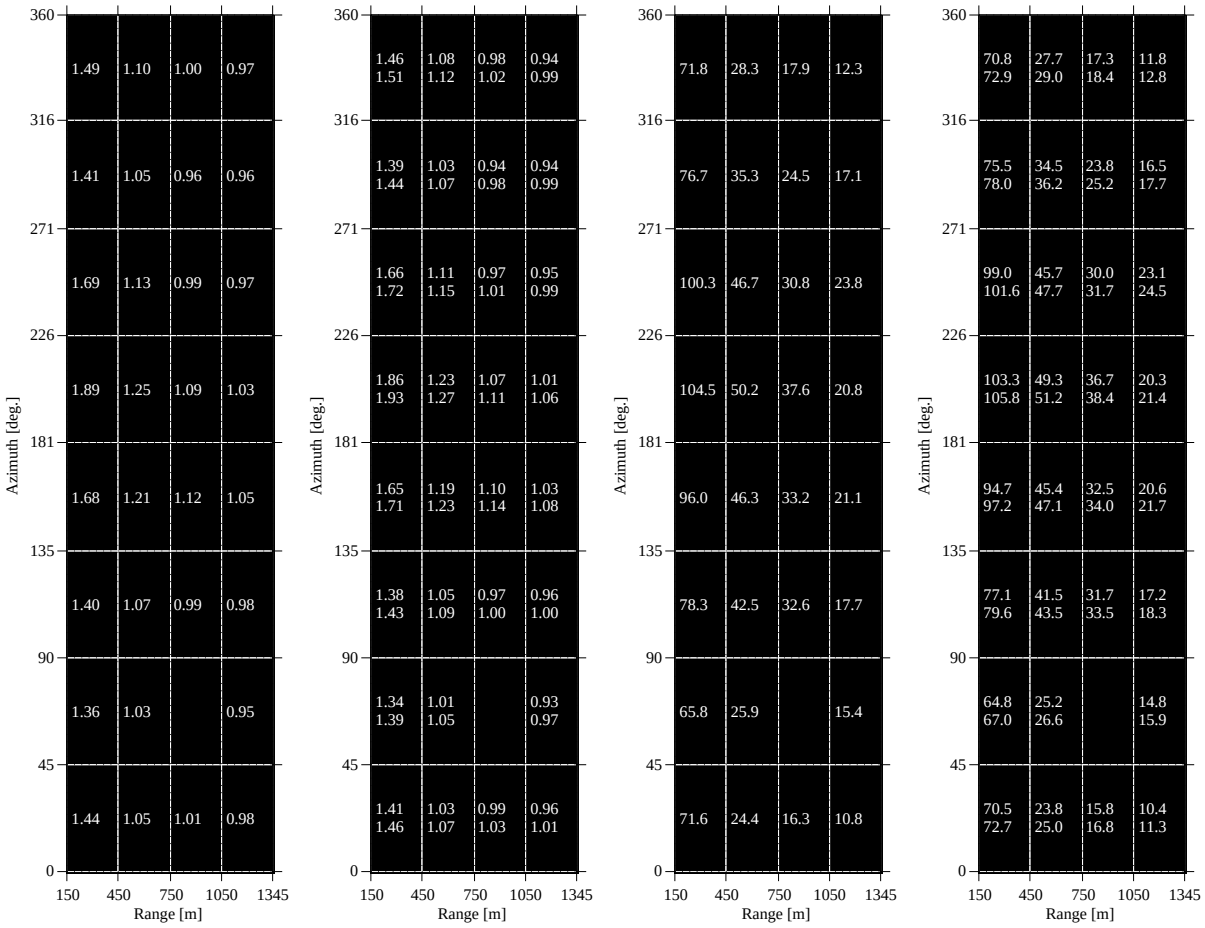

(a) Estimation of skewness for each sector.

(b) Confidence interval of the skewness estimate.

(c) Estimation of scale for each sector.

(d) Confidence interval of the scale estimate.

Figure 10.5: Estimates of the skewness and scale parameters of the Weibull distribution and their intervals of confidence at 95% for each sector of the radar scan extracted from the testing data set.

Table 10.2: Statistical properties and number of scans in the data sets used in the experiments made with real-live sea clutter data.

	Designing Conditions		Testing Conditions
	Training Data Set	Validation Data Set	Testing Data Set
Statistical Parameter	($M^{(\mathrm{d})} = 128$ Scans)	($M^{(\mathrm{v})} = 128$ Scans)	($M^{(\mathrm{t})} = 128$ Scans)
Skewness	$a_i^{(\mathrm{d})} \sim \mathrm{N}(1.38\,,\,0.19)$	$a_i^{(\mathrm{v})} \sim \mathrm{N}(1.59\,,\,0.18)$	$a_i^{(\mathrm{t})} \sim \mathrm{N}(1.42\,,\,0.13)$
	$a_i^{(\mathrm{d})} \in [0.80\,,\,2.75]$	$a_i^{(\mathrm{v})} \in [1.05\,,\,3.12]$	$a_i^{(\mathrm{t})} \in [0.96\,,\,2.97]$
Scale	$b_i^{(\mathrm{d})} \sim \mathrm{N}(38.2\,,\,11.0)$	$b_i^{(\mathrm{v})} \sim \mathrm{N}(36.3\,,\,9.9)$	$b_i^{(\mathrm{t})} \sim \mathrm{N}(35.7\,,\,9.6)$
	$b_i^{(\mathrm{d})} \in [5.2\,,\,115.9]$	$b_i^{(\mathrm{v})} \in [6.3\,,\,121.2]$	$b_i^{(\mathrm{t})} \in [6.9\,,\,132.6]$

10.2 Statistical Properties of Training, Validation and Testing Data Sets from Real-Live Sea Clutter

In the previous section, it was empirically demonstrated that the sea clutter data contained in the real-live radar scans this thesis considers fit the Weibull distribution. Moreover, the values of the statistical parameters of the Weibull distribution that approximate these data for three different radar scans were reported.

In this section, the statistical parameters for the whole training, validation and data sets are given. Applying a similar procedure as the one followed for a given radar scan, but for all the radar scans of a data set, the typical and variance of the skewness and scale parameters are given, as well as their intervals of variation. From the obtained results, it is observed that the statistics of the skewness and scale parameters follow a normal distribution with the reported typical and variance values ($\mathrm{N}(\mu_a, \sigma_a^2)$ for the skewness and $\mathrm{N}(\mu_b, \sigma_b^2)$ for the scale). These distributions and intervals of variation are summarized in Table 10.2 for each data set.

CHAPTER 11

Incoherent Detectors in Real-Live Sea Clutter: Design and Test

In this chapter, the design and test of incoherent radar detectors is studied in real-live sea clutter measurements. First, the design of CFAR and AI-based incoherent detectors is presented, where parameters such as their dimensionality and the clutter conditions used in the design stage are studied. Thereafter, the detectors are tested with different radar scans to analyze which is the performance of the detectors once designed. Finally, some conclusions are drawn from theses studies.

11.1 Incoherent Detectors in Real-Live Sea Clutter

In chapters 8 and 9, several studies about the design of coherent and incoherent detectors (reference and AI-based detectors) in different kinds of synthetic clutter conditions were made. Among other synthetic clutter models, coherent and incoherent synthetic sea clutter models were considered in those studies. In this section, a study of the design of incoherent detectors in real-live sea clutter conditions is presented. With this new study, this thesis tries to demonstrate the validity of the proposed detectors to work in real-live clutter conditions. As made for the cases of study of coherent and incoherent detectors in synthetic sea clutter (see Sect. 8.2 and 9.1), during the design of incoherent detectors (CFAR and AI-based detectors) in real-live clutter conditions, some parameters must be tuned to find which are the ones that maximize the performance of the detectors. In this way, the detectors are designed considering:

- Different environmental (clutter) and target conditions, as presented in the database of real-live marine radar scans used in the experiments (see Sect. 7.2).
- Different selection modes, as presented in Sect. 4.2. Note that only delayed selection modes are considered because these ones were the modes used when designing CFAR detectors in synthetic sea clutter. Non-delayed selection modes are not commonly in the literature related to CFAR detection.
- Different range of integrated area (number of integrated/selected cells) in each selection mode.

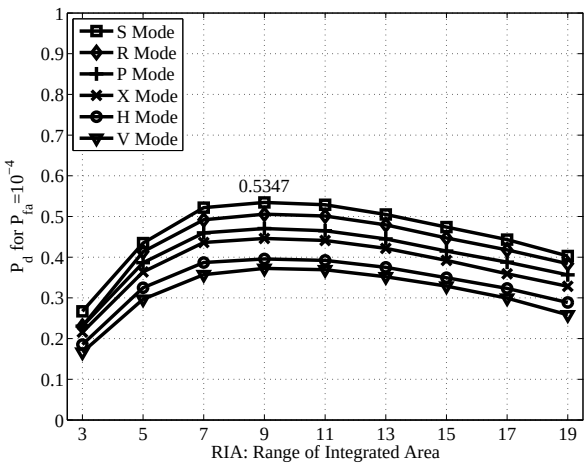

Figure 11.1: Performance of CA-CFAR detectors in real-live sea clutter when using 1-D and 2-D delayed selection modes and varying RIA. Performance is given for the validation data set.

- And different number of hidden neurons in the MLPs and RBFNs that form the AI-based incoherent processors and detectors.

The selection of the values of these parameters that maximize the performance of the proposed detector is made in the design stage, for which the training and validation data sets of Fig. 7.2 are used. The performance of the processors and detectors presented in Sect. 11.1.1-11.1.3 are obtained with the validation data set. This performance is given in terms of average SCR improvement ($\text{SCR}^{\text{av.imp.}}$) and P_{d} for $P_{\text{fa}} = 10^{-4}$, respectively, as discussed in Sect. 4.4. Processor and detector performance for data different of the ones used for designing is given in a different section (see Sect. 11.1.4).

11.1.1 Design of CFAR Detectors in Real-Live Sea Clutter

As done for the case of designing CFAR detectors in synthetic sea clutter in Sect. 9.1.1, the influence of the following parameters are studied in the design stage of CFAR detectors in real-live sea clutter:

- Different ways of processing the CUT adjacent cells, i.e. CA, ML and OS-CFAR detectors are studied.
- Different selection modes (see Sect. 4.2) to maximize the performance of CFAR detectors.
- The RIA, and consequently the number of integrated/selected cells (J), in each selection mode that allows to achieve the highest performance in CFAR detectors.

The last two parameters are studied at the same time for each CFAR detector. The performance obtained for each CFAR detector (P_{d} for $P_{\text{fa}} = 10^{-4}$), considering the validation data set, is depicted in Fig. 11.1-11.3. The threshold of each detector is adjusted in the design stage by using the design data set. The number guard cells (G) considered in the CFAR detectors under study are set in three different ways, depending on the value of RIA considered to obtain the

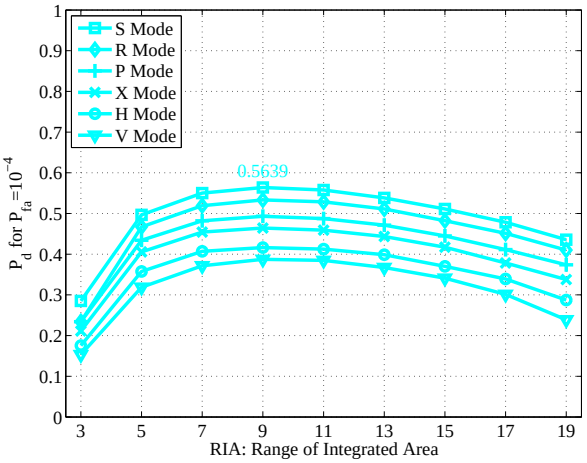

Figure 11.2: Performance of ML-CFAR detectors in real-live sea clutter when using 1-D and 2-D delayed selection modes and varying RIA. This detector uses $a^{(\mathrm{d})} = 1.38$. Performance is given for the validation data set.

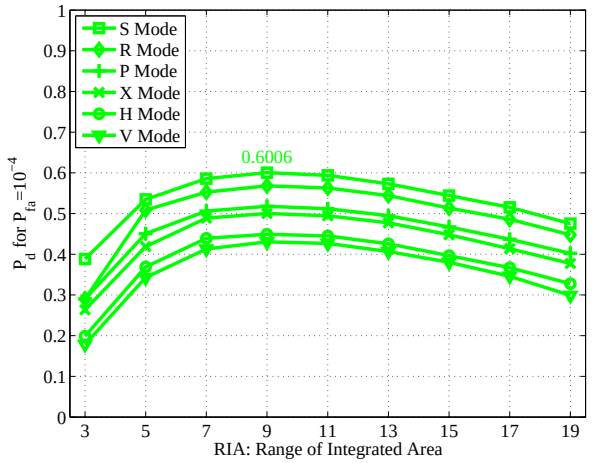

(a) Influence of RIA in OS-CFAR detectors for $k = \lceil 0.50(J-G-2)\rceil$, being J the number of selected cells for given RIA and G the number of guard cells.

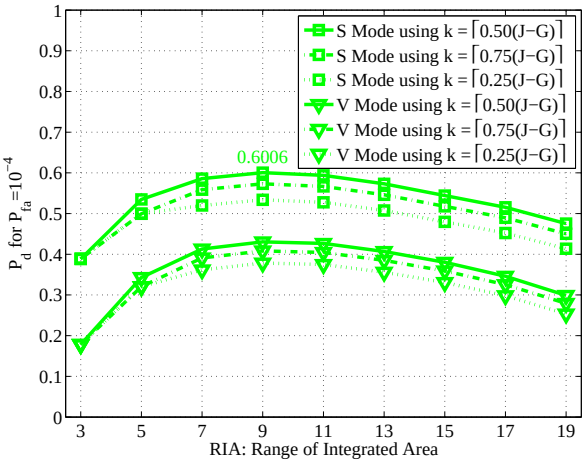

(b) Influence of k in OS-CFAR detectors using a square (best) and vertical (worst) selection modes for different values of RIA.

Figure 11.3: Performance of OS-CFAR detectors under real-live sea clutter conditions in the design stage (results for the validation data set) when using 1-D and 2-D delayed selection modes and varying RIA and k (order for selection). $a^{(\mathrm{d})} = 1.38$ is used in this detector. Performance is given for the validation data set.

number of available cells (J). When RIA $= 3$ cells, no guard cells are selected because there would be a unique guard cell, the CUT. When RIA $= [5, 7]$ cells (limited to the maximum width of the available targets in the real-live database, as set in Sect. 2.5.1), G is obtained considering RIA $- 2$ cells ($[3, 5]$ cells) in the expressions given in Eq. (4.7) and (4.12)-(4.15) for each selection mode. Finally, when RIA is greater than the maximum target widths (RIA $\in [9, 19]$ cells), G is

obtained considering a fixed value of 7 cells in the expressions given in Eq. (4.7) and (4.12)-(4.15) for each selection mode. Therefore, the value of RIA that sets the limit of variation of G is conditioned by the width of the targets we are expecting in the radar scans. Experiments considering the adaptation of the number of guard cells (G) according the maximum target sizes (47 cells, as set in Sect. 2.5.1) have been made, but poorer results than the ones reported here have been obtained. Note that the limitation of G is different in this case than in the case of synthetic sea clutter. In that case, G was limited by the maximum target size, but since the width and length of the targets were equal in that case of study, we did not realize which parameter of the target (width or length) was conditioning G. In the current case of study, we realize that the value of G is mainly conditioned by the lowest dimension, i.e. the target width, instead of by the greatest dimension, i.e. the target length. Some important aspects can be observed from these results:

- In general, the selection mode that allows to achieve the highest performance is the S mode, regardless of the CFAR detector. The R selection mode can achieve performance slightly lower, but this mode is able to reduce considerably the computational cost of the detectors because the number of selected cells in the integration area is lower. Moreover, it is observed that the use of 2-D selection modes always allow to achieve better performance than when using 1-D selection modes.

- In general, the RIA for achieving the highest performance is 9 cells, regardless of the selection mode and CFAR detector. Similar performance can be achieved using 7 and 11 cells, but they are slightly lower. In these cases, if low computational cost detectors are desired, the use of RIA = 7 cells is recommended.

- In particular, the performance achieved by ML-CFAR detectors are better than the ones achieved by CA-CFAR detectors. It is due to the philosophy of working of this detector (see Table 3.1 of Sect. 3.3.2), which allow to improve the detector performance in multi-target environments (case of study of the thesis) by making a more accurate estimate of the clutter parameters. But due to this philosophy, the knowledge of the skewness parameter ($a^{(\mathrm{d})}$) is needed a priori, what is a problem in real-live situations. In this case, the value selected for this parameter is the typical value of the radar scans of the design data set, i.e. $a^{(\mathrm{d})} = 1.38$ (see Table 10.2 of Sect. 10.2).

- In particular, OS-CFAR detectors achieve the highest performance. Moreover, for this detector, a study of the influence of the order of selection is made, being presented in Fig. 11.3b. For this study, it is observed that the best performance is achieved when the selection of the order is approximately the half of difference between the number of selected cells (J) and the number of guard cells (G).

After this study, the use of OS-CFAR detectors using the S selection mode with a RIA of 9 cells is proposed to detect targets (vessels) in real-live sea clutter radar scans. The skewness parameter to be used in the detector is set by the typical value of the skewness of the design data set ($a^{(\mathrm{d})} = 1.38$). According to the proposed selection mode and the value of RIA, $J = 81$ cells are selected/available (CUT and 80 surrounding cells). Since RIA $- 2 = 7$ cells are used to set the number of guard cells, $G - 1 = 48$ cells (CUT and $G - 1$ surrounding cells) from the 80 available cells are guard cells. Thus, only $(J - 1) - (G - 1) = J - G = 32$ cells are useful

to estimate the clutter parameters. The order of selection in the OS-CFAR detector is set to $k = \lceil 0.5(J - G) \rceil = 16$ cells.

11.1.2 Design of MLP-based Incoherent Detectors in Real-Live Sea Clutter

Following with the way the CFAR detectors were designed, MLP-based incoherent detectors in real-live sea clutter are designed. A new parameter is included in the study. Therefore, the influence of the following parameters is studied:

- The selection mode that works better in MLP-based detectors (see Sect. 4.2). Only 1-D and 2-D selection modes are considered in the design of MLP-based detectors, as done for the CFAR detectors.
- The number of integrated/selected cells (J) that allows to achieve the highest performance. This number depends on the selection mode and the range of integrated area (RIA), as discussed in Sect. 4.2.2 and 4.2.3. RIA and J are selected taking also into account the computational cost of the detector.
- The number of MLP hidden neurons (H) that allows to achieve the highest performance in the MLP-based processor and detector, while maintaining low computational cost.

At the beginning, the first two parameters are simultaneously studied. The performance obtained in the MLP-based processor ($\text{SCR}^{\text{av.imp.}}$) and detector ($P_{\text{d}}$ for $P_{\text{fa}} = 10^{-4}$) is depicted in Fig. 11.4. For these studies, $H = 15$ hidden neurons are considered in the MLPs. The computational cost of each MLP-based detector configuration is given in Fig. 11.7 considering MLP structures of size $J/15/1$, where J depends on RIA and the selection mode. Some important aspects can be observed from the results achieved in the study of the selection mode and RIA:

- The tendency of the processor and detector performance with RIA is similar, each given by its own objective performance measurement.
- The most important difference between the proposed detector and the best one of the incoherent reference detectors (OS-CFAR detector using an S selection mode and RIA= 9 cells) concerns to the performance improvement. Thus, comparing the results presented in Fig. 11.4 and 11.3a, this performance improvement varies approximately from a minimum of $\Delta P_{\text{d}} \simeq 0.09$ (V mode) to a maximum of $\Delta P_{\text{d}} \simeq 0.16$ (S mode) for $P_{\text{fa}} = 10^{-4}$.
- The value of RIA for achieving the highest performance is 9 cells, which is in consonance with the size found for the CFAR detectors and being related to the maximum size of the width of the targets.
- The selection mode for obtaining the highest performance is based on a 2-D mode, the S mode. This mode allows to achieve a performance improvement of $\Delta\text{SCR}^{\text{av.imp.}} \simeq 6\,dB$ and $\Delta P_{\text{d}} \simeq 0.24$ for $P_{\text{fa}} = 10^{-4}$ in the processor and detector with respect to the performance achieved for the worst delayed selection mode under study (V mode). Nevertheless, the improved selection modes under study, and exactly this one, present two costs: a temporal delay (see Sect. 4.2) and a high computational cost (7367 operations from Fig. 11.7). Exactly, for RIA= 9 cells, and as set Eq. (4.19), this delay is 5.4 ms when considering the

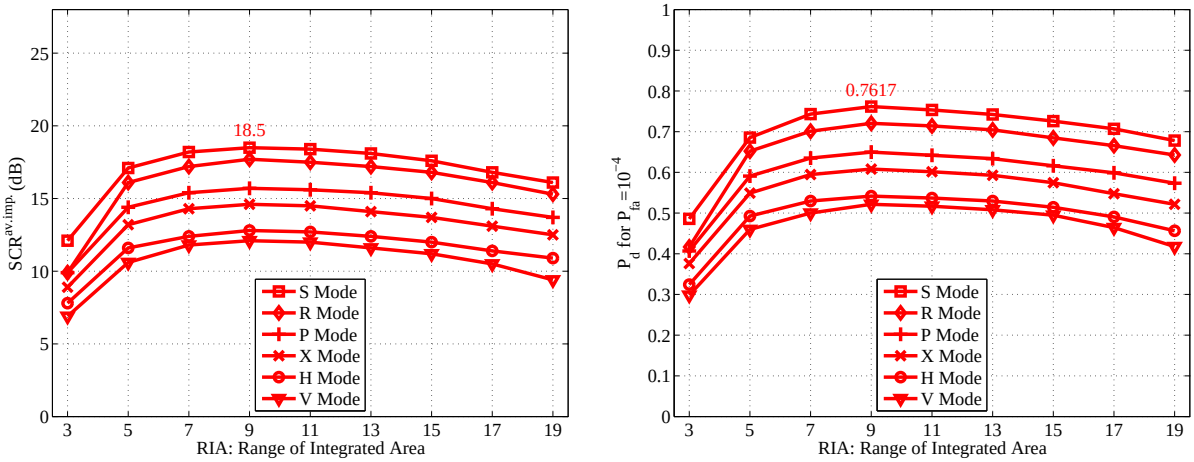

(a) MLP-based processors (b) MLP-based detectors

Figure 11.4: Performance of incoherent processors and detectors based on $J/15/1$ MLPs in real-live sea clutter when varying RIA in 1-D and 2-D selection modes. Performance is given for the validation data set.

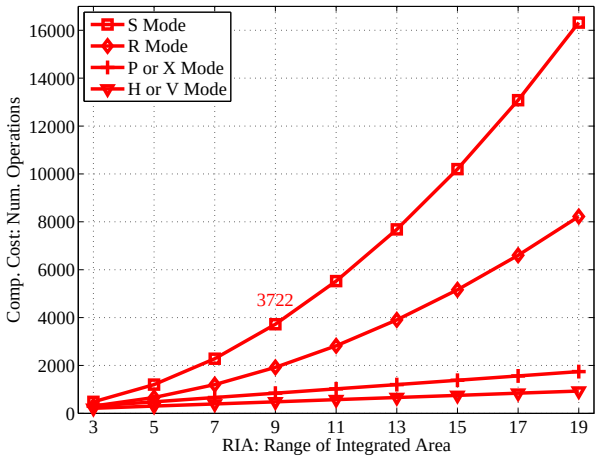

Figure 11.5: Computational cost of incoherent detectors based on $J/15/1$ MLPs in real-live sea clutter when varying RIA in 1-D and 2-D selection modes.

low-resolution configuration of the radar and 8.8 ms when considering the high-resolution configuration of the radar (see Sect. 2.4).

As occurred for the case of study of coherent and incoherent detectors in synthetic clutter, 2-D selection modes work better than 1-D selection modes in MLP-based detectors. The reasons, the same as observed in previous studies, i.e. the detectors have more information to make a decision "target present/target absent" when using 2-D selection modes, and the detection is independent of the orientation of the ship in the radar scan.

The study of the last parameter (H) is made below. As usually done, H is varied from 3 to 50. The performance achieved for the different selection modes under study is plotted in Fig. 11.6.

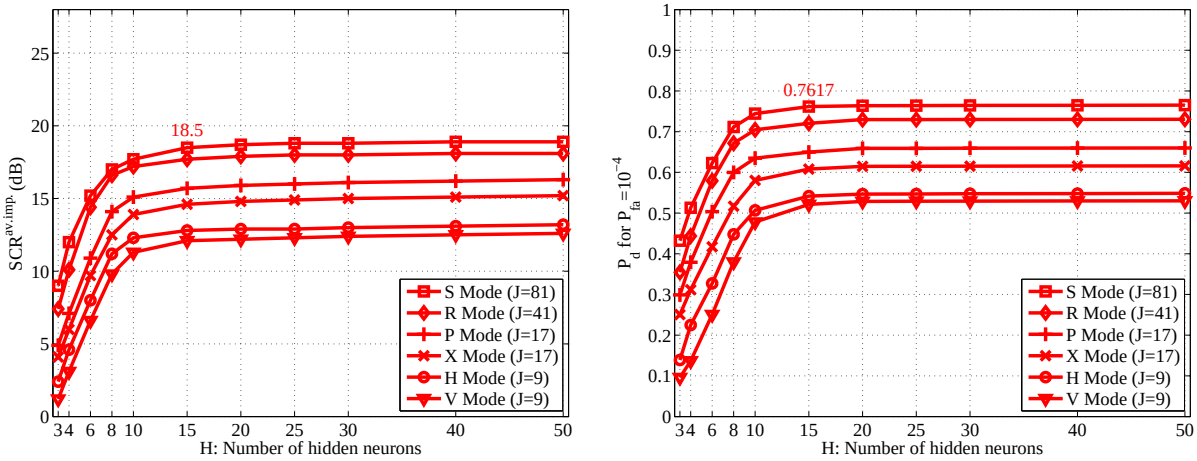

(a) MLP-based processors

(b) MLP-based detectors

Figure 11.6: Performance of incoherent processors and detectors based on $J/H/1$ MLPs in real-live sea clutter when varying the number of hidden neurons (H) and considering 1-D and 2-D selection modes. Performance is given for the validation data set.

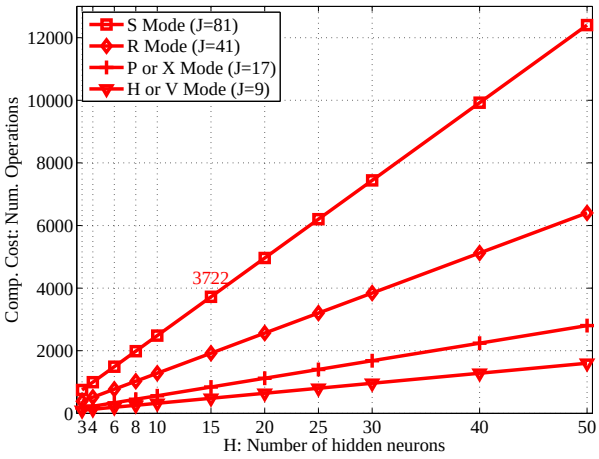

Figure 11.7: Computational cost of incoherent detectors based on $J/H/1$ MLPs in real-live sea clutter when varying the number of hidden neurons (H) and considering 1-D and 2-D selection modes.

The computational cost of each MLP-based detector configuration is plotted in Fig. 11.7. As observed, from $H = 15$ hidden neurons low performance improvement and high computational cost are achieved. Thus, $H = 15$ is selected in our case of study considering a trade-off between performance ($\text{SCR}^{\text{av.imp.}} = 18.5$ dB and $P_{\text{d}} = 0.7617$ for $P_{\text{fa}} = 10^{-4}$) and computational cost (3722 operation per CUT).

After these studies, an MLP-based detector using RIA = 9 cells in an S selection mode with $H = 15$ hidden neurons is proposed. The proposed MLP-based processor and detector is able to outperform the best configuration of the CFAR detectors (OS-CFAR) up to $\Delta P_{\text{d}} \simeq 0.16$ for

$P_{fa} = 10^{-4}$.

11.1.3 Design of RBFN-based Incoherent Detectors in Real-Live Sea Clutter

As done for MLP-based incoherent detectors, the same parameters are studied for designing RBFN-based incoherent detectors in real-live sea clutter measurements (selection modes, RIA and J, and H).

At the beginning, we study the influence of RIA and selection mode. The performance obtained for the RBFN-based processor ($SCR^{av.imp.}$) and detector (P_d for $P_{fa} = 10^{-4}$) is depicted in Fig. 11.8. For this study, $H = 20$ hidden neurons are considered. The computational cost of RBFN-based detectors formed of $J/20/1$ neurons are depicted in Fig. 11.9 for the selection modes under study. Important aspects can be observed from these figures, some of them being similar to the ones obtained for the case of MLP-based incoherent detectors in real-live sea clutter, but with some differences:

- The tendency of the processor and detector performance with RIA is similar, as occurred for the case of study of using MLPs.
- A important difference between the proposed detector and the selected CFAR detector (OS-CFAR detector using an S selection mode and RIA= 9 cells) is observed on the achieved performance improvement. Comparing the results presented in Fig. 11.8 and 11.3a, this improvement varies from a minimum of $\Delta P_d \simeq 0.06$ (V mode) to a maximum of $\Delta P_d \simeq 0.13$ (S mode) for $P_{fa} = 10^{-4}$. These values are slightly lower than the ones achieved with MLPs.
- The RIA for obtaining the highest performance is 9 cells, which is in consonance with the size found for the CFAR and MLP-based detectors.
- The best selection modes are based on 2-D templates, being the S mode the best one. This mode allows to outperform the one obtained for the worst mode (the V mode) in $\Delta SCR^{av.imp.} \simeq 6\,dB$ and $\Delta P_d \simeq 0.23$ for $P_{fa} = 10^{-4}$. Nevertheless, the improved selection modes under study, and exactly the S mode, present two costs: a temporal delay between 5.4 ms and 8.8 ms for RIA = 9 cells (as set in Sect. 11.1.2 when studying MLP-based incoherent detectors) and a high computational cost (266182 operations per CUT from Fig. 11.9).
- Another difference is observed when comparing the performance obtained with RBFN-based detectors (see Fig. 11.8) and with MLP-based detectors (see Fig. 11.4). A performance loss of about $\Delta SCR^{av.imp.} \simeq -1\,dB$ and $P_d \simeq -0.03$ for $P_{fa} = 10^{-4}$ is observed with respect to the performance obtained by the proposed MLP-based detector configuration.

Once again, the use of 2-D selection modes in RBFN-based detectors allows to outperform their performance with respect to 1-D modes. The reasons why it happens are the same as the ones given for the CFAR and MLP-based detectors studied before (more available information and independency of the ship orientation).

A last study concerning to the number of RBFN hidden neurons (H) is reported below. For this study, H is varied from 3 to 50, and the performance achieved for the different selection modes under study are depicted in Fig. 11.10. The computational cost of each detector configuration is

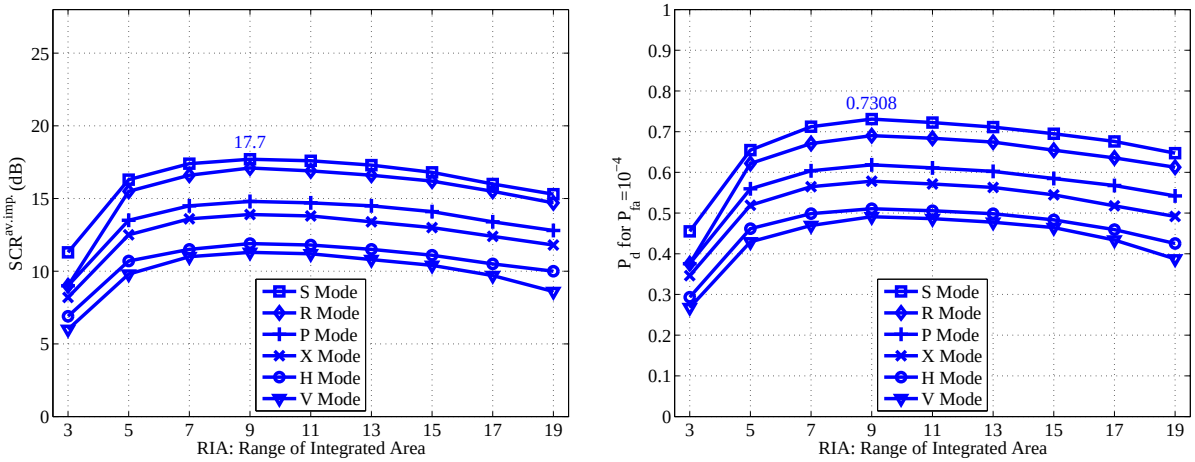

(a) RBFN-based processors (b) RBFN-based detectors

Figure 11.8: Performance of incoherent processors and detectors based on $J/20/1$ RBFNs in real-live sea clutter when varying RIA in 1-D and 2-D selection modes. Performance is given for the validation data set.

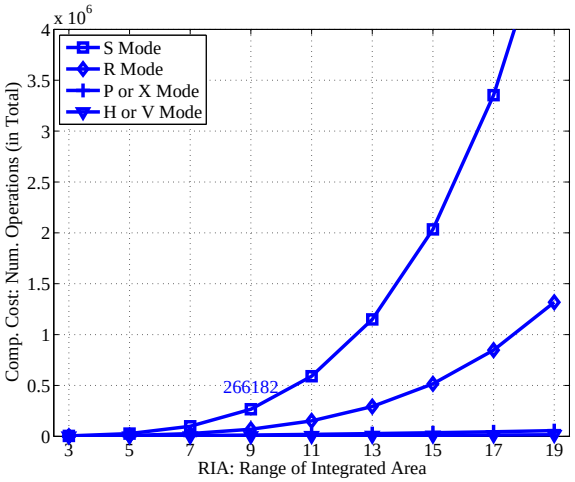

Figure 11.9: Computational cost of incoherent detectors based on $J/20/1$ RBFNs in real-live sea clutter when varying RIA in 1-D and 2-D selection modes.

plotted in Fig. 11.11. As observed, for all the modes under study, from $H = 20$ hidden neurons low performance improvements and high computation cost increase are achieved. Therefore, $H = 20$ is selected considering a trade-off between detector performance ($P_{\mathrm{d}} = 17.7\,\mathrm{dB}$ and $P_{\mathrm{d}} = 0.7308$ for $P_{\mathrm{fa}} = 10^{-4}$) and computational cost (266182 operations per CUT).

After these studies, the use of an S selection mode with a RIA of 9 cells and $H = 20$ hidden neurons is proposed to design RBFN-based incoherent detectors to detect moving ships in the real-live sea clutter conditions considered in the thesis. Using this configuration, the proposed RBFN-based incoherent detector is able to outperform the best configuration of the reference detectors (SO-CFAR) in up to $\Delta P_{\mathrm{d}} \simeq 0.13$ for $P_{\mathrm{fa}} = 10^{-4}$.

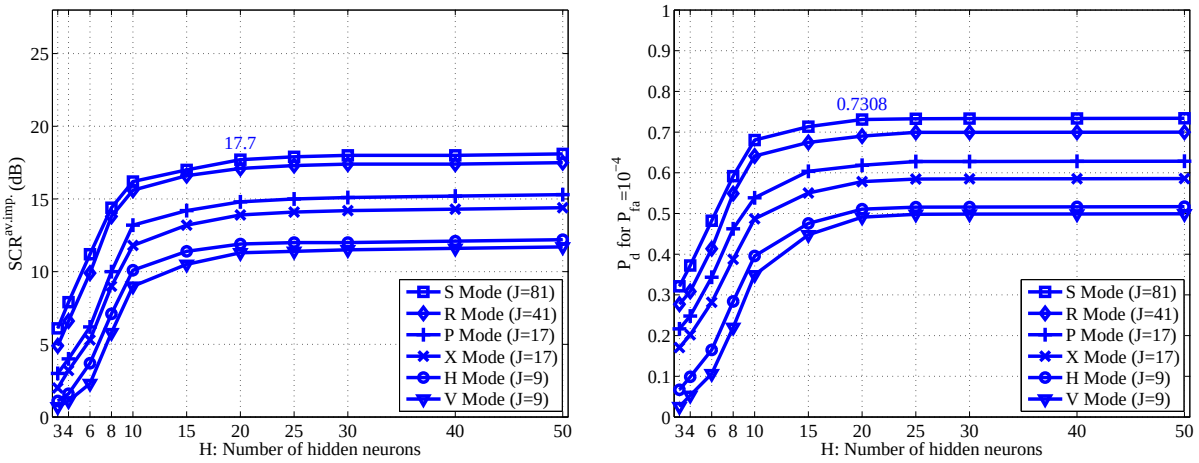

(a) RBFN-based processors

(b) RBFN-based detectors

Figure 11.10: Performance of incoherent processors and detectors based on $J/H/1$ RBFNs in real-live sea clutter when varying the number of hidden neurons (H) and considering 1-D and 2-D selection modes. Performance is given for the validation data set.

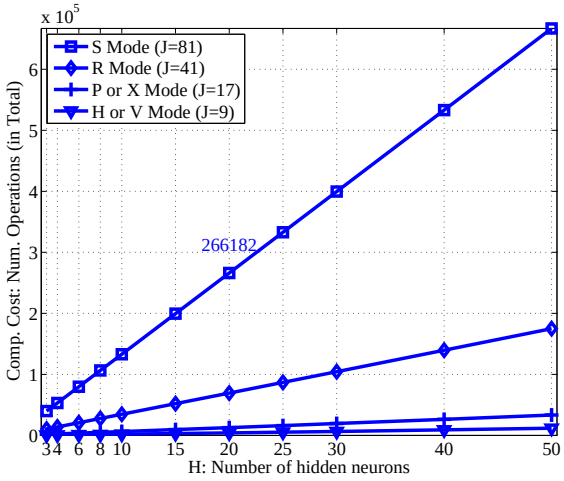

Figure 11.11: Computational cost of incoherent detectors based on $J/H/1$ RBFNs in real-live sea clutter when varying the number of hidden neurons (H) and considering 1-D and 2-D selection modes.

11.1.4 Comparison of Incoherent Detectors in Design and Test Stages under Real-live Sea Clutter

In the previous subsections, the design of CFAR and AI-based incoherent detectors in real-live sea clutter conditions has been studied, paying special attention to their dimensionality. In the current section, the thesis tries to solve the following question: Is the performance of the designed incoherent detectors maintained when processing other (new) radar scans? For doing so, the test data set presented in Sect. 7.2 (see Fig. 7.2) is considered. The current study is divided in two parts. At the beginning, the performance of the detectors in the design and test stages is compared by ROC curves (objective measurements of its performance). At the end, a radar scan of the test data set is selected, for which subjective and objective analyses are made. This scan is processed by CFAR and AI-based incoherent detectors. The processed radar scans are analyzed to find an answer of what is really happing in each detector.

The configurations used in each detector are extracted from the design stage (see Sect. 11.1.1-11.1.3), being:

- MLP-based incoherent detector (structure 81/15/1): designed selecting $J = 81$ (RIA= 9 cells) cells by an S selection mode and using $H = 15$ hidden neurons.
- RBFN-based incoherent detector (structure 81/20/1): designed selecting $J = 81$ (RIA= 9 cells) cells by an S selection mode and using $H = 20$ hidden neurons.
- CFAR incoherent detectors: designed selecting $J = 81$ (RIA= 9 cells) cells by an S selection mode. In the ML and OS-CFAR detectors, the skewness parameter needed in the CFAR processor is set to its typical value in the design data set, i.e. $a^{(\mathrm{d})} = 1.38$. In the OS-CFAR detector, the order for selection is set to $k = 16$ ($G = 49$ guard cells).

The ROC curves achieved in the design stage, considering the validation data set, are depicted in Fig. 11.12a. The ROC curves obtained in the test stage, considering the test data set, i.e. a set of radar images never processed by the designed detectors, are given in Fig. 11.12b. From the results presented in both figures, several conclusions can be drawn:

- The tendency of the ROC curves is maintained in both stages, involving that the best detector continues being the one based on MLPs, followed by the RBFN-based detector, and surpassing the performance achieved by the reference ones, the CFAR detectors.
- The detector performance decrease in the test stage in terms of $\mathrm{SCR}^{\mathrm{av.imp.}}$ (see legends) and P_{d}. Focusing on CFAR detectors, the performance loss of the detector from design to test conditions is between $\Delta P_{\mathrm{d}} \simeq -0.03$ for the OS-CFAR detector and $\Delta P_{\mathrm{d}} \simeq -0.05$ for the CA-CFAR detector (considering the P_{d} for $P_{\mathrm{fa}} = 10^{-4}$). On the other hand, the performance loss observed in AI-based processors and detectors is of $\Delta\mathrm{SCR}^{\mathrm{av.imp.}} \simeq -1$ dB and $\Delta P_{\mathrm{d}} \simeq -0.03$ (for $P_{\mathrm{fa}} = 10^{-4}$), respectively.

After the analysis of these results, high performance robustness when processing new radar scans is observed, regardless of the detector. This is an important question because it gives us an approximation of how their performance will be when these detectors work in steady-state (once designed) processing new radar scans in the future.

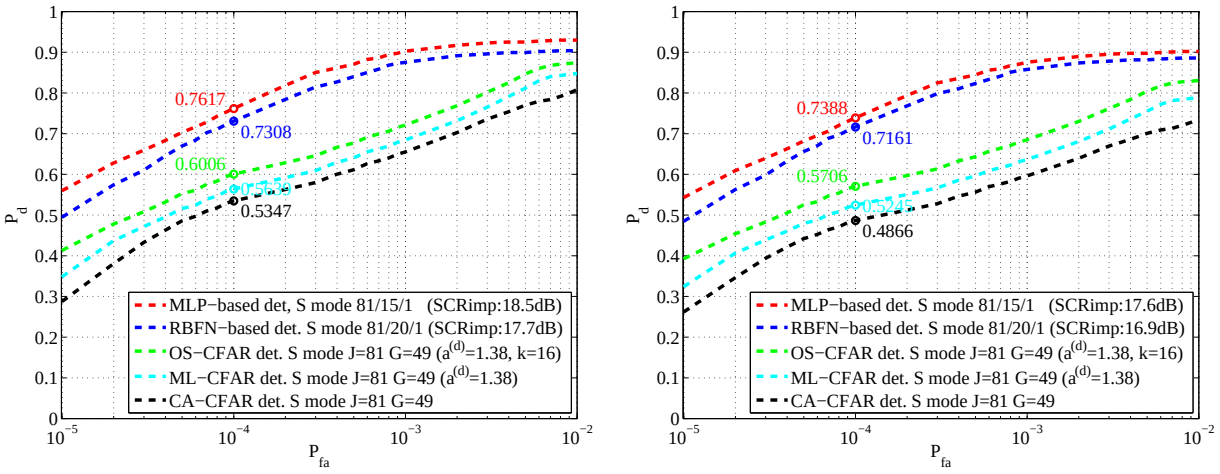

(a) Validation data set (b) Test data set

Figure 11.12: Performance of the selected configurations of CFAR, MLP and RBFN-based detectors in real-live sea clutter when processing the validation and test data sets.

Next, subjective and objective analyses of the performance of the detectors for a specific radar scan are made. For that purpose, a radar scan of the test data set is selected, being depicted in Fig. 11.13a. This radar scan is selected because the worst performance is achieved for it, i.e. because it is the most difficult radar scan of the test data set. The desired output scan for this radar scan is depicted in Fig. 11.13b. To realize what is happening in the zone where the ship is located, a sector of this radar scan is selected covering the full range coverage and the half azimuthal coverage (see Fig. 11.14). The objective measurements of the performance given below for each processed radar scan are obtained for the whole scan (not for the selected zone).

The radar scans at the output of the CFAR incoherent detectors are depicted in Fig. 11.15. The radar scans at the output of the AI-based incoherent processors and detectors are depicted in Fig. 11.16. According to these results, first, a subjective analysis of the processed radar scans is made, to continue with an objective analysis of the performance of each detector.

Focusing on the processed radar scans obtained at the output of each CFAR detector under study (see Fig. 11.15), we observe that the number of false alarms (detections outside the ship cells) is very low, regardless of the detector. Moreover, we observe that the density of detected ship cells is greater for the case of using the OS-CFAR detector. The same effect is observed when visually analyzing the radar scans obtained at the output of the AI-based detectors (see Fig. 11.16). But, in this case, the density of detected ship cells is greater than in the case of CFAR detectors. This improvement is achieved because of the high level of clutter reduction and the enhancement of the target signal the detector is applying. Ending with this subjective analysis of the processed radar scans, we observe a difference between the results obtained by the MLP and RBFN-based incoherent detectors. This difference is focused on the way the clutter reduction is made. Observing Fig. 11.16a and 11.16c, we realize that even when the level of clutter is highly reduced in both cases (the levels of clutter are close to the minimum), the MLP-based processor reduces more the level of clutter in cells near the radar site than in the far range, and vice versa for the RBFN-based processor.

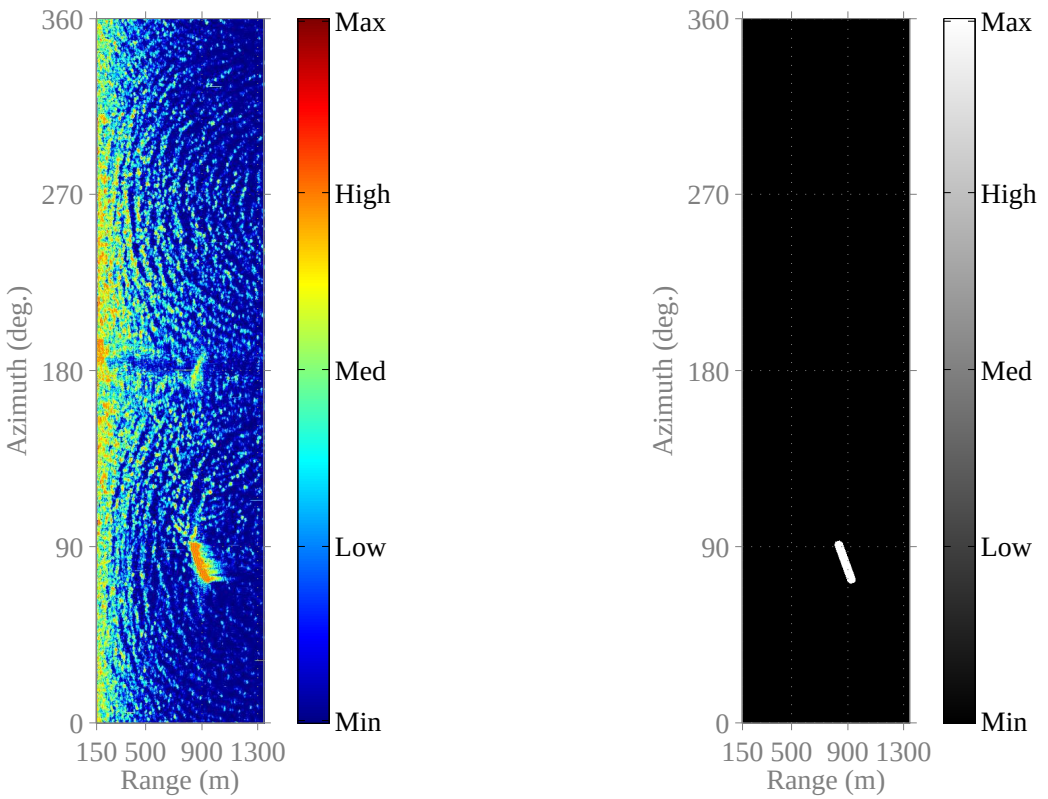

(a) Input radar scan

(b) Output desired radar scan

Figure 11.13: Input radar scan selected from the test data set and its corresponding desired output (plot of polar data).

After the subjective analysis developed above for the processed radars scans, we focus now on an objective analysis of the performance achieved for each detector. For doing so, we take as reference the performance achieved when the validation and test data sets are used (see Fig. 11.12). Thus, from the performance achieved by each detector for the radar scan under study (see the titles of Fig. 11.15 and 11.16), it is observed that:

- The P_{fa} approximately remains constant for the threshold set during the design stage of each detector (THR for $P_{\text{fa}} = 10^{-4}$).
- A performance loss of $\Delta P_{\text{d}} \simeq -0.01$ for $P_{\text{fa}} = 10^{-4}$ is observed for this radar scan with respect to the average performance achieved for the whole test data set when using CFAR detectors.
- A performance loss of $\Delta\text{SCR}^{\text{av.imp.}} \simeq -1.0\,\text{dB}$ and $\Delta P_{\text{d}} \simeq -0.02$ for $P_{\text{fa}} = 10^{-4}$ is observed for this radar scan with respect to the average performance achieved for the whole test data set when using AI-based detectors.

From this objective analysis, and according to the performance loss obtained for this radar scan with respect to the mean performance of the whole test data set, we infer an important property: the performance achieved for most of the radar scans of the test data set are close to

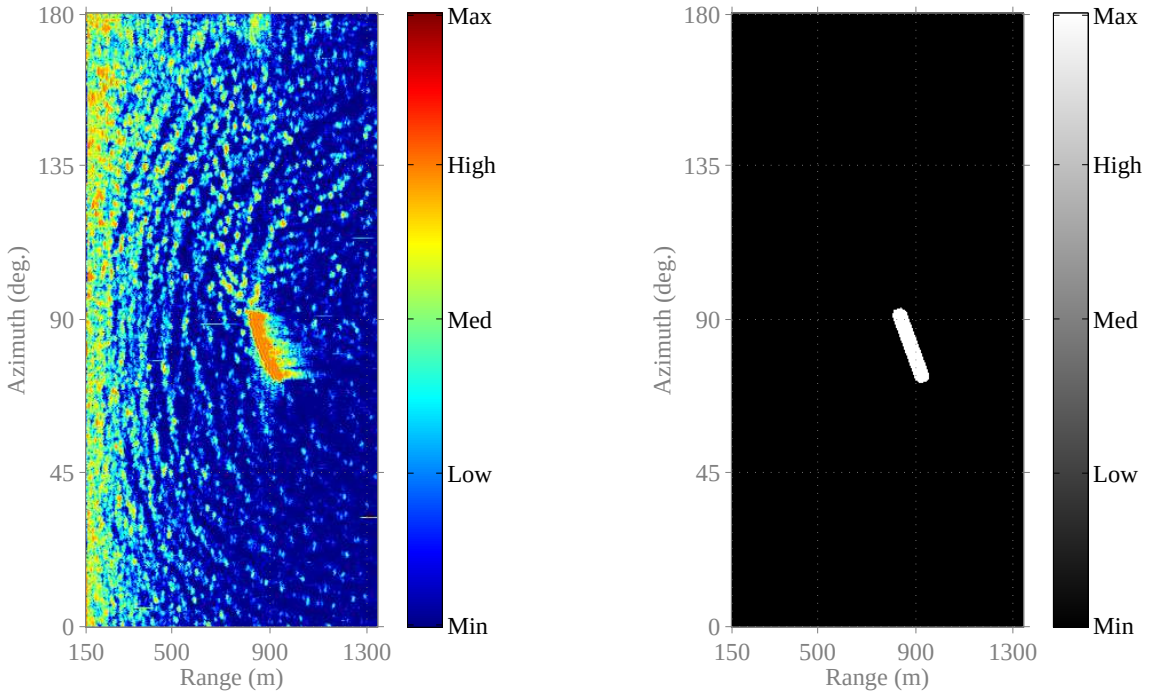

(a) Zoom of the input radar scan

(b) Zoom of the output desired radar scan

Figure 11.14: Zoom of the input radar scan selected from the test data set and its corresponding desired output (plot of polar data).

its mean value. In other words, low variations of performance are obtained, regardless of the clutter conditions and target type present in a radar scan.

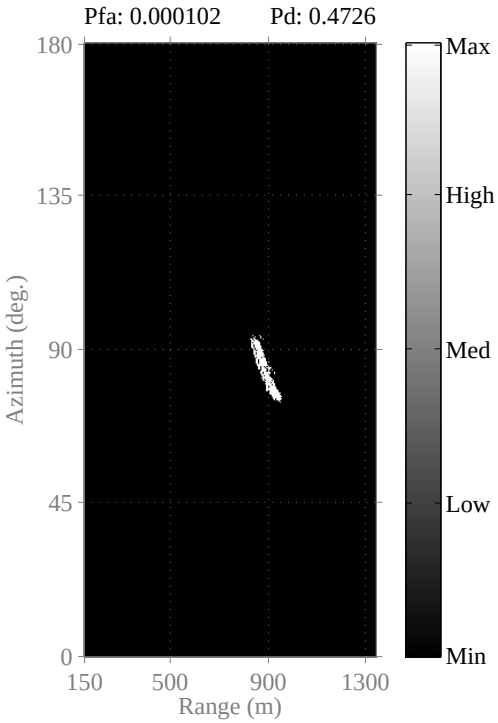

(a) CA-CFAR detector output

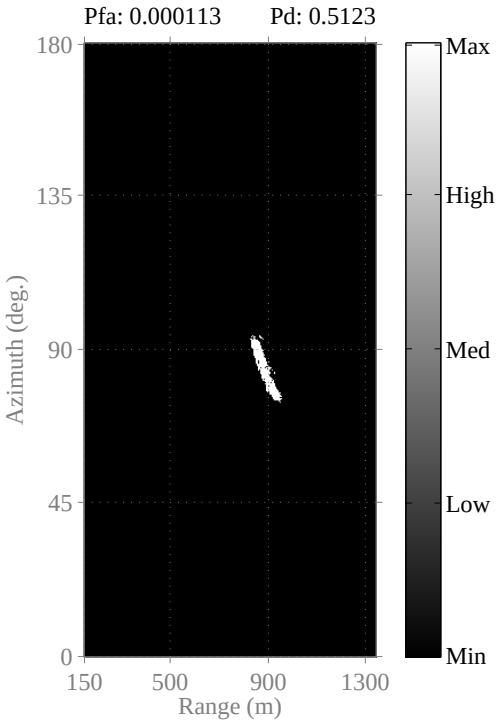

(b) ML-CFAR detector output

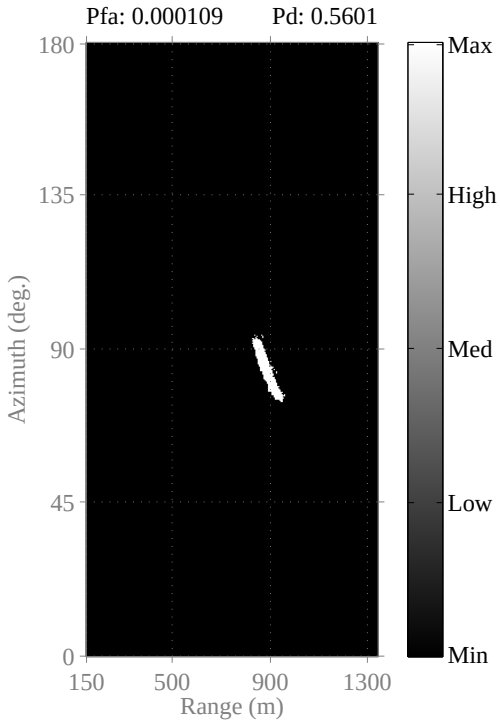

(c) OS-CFAR detector output

Figure 11.15: Radar scans at the output of the CFAR detectors.

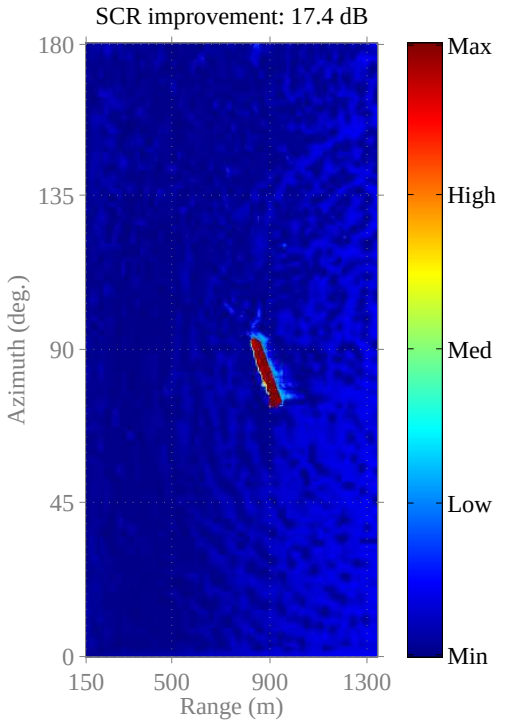

(a) MLP-based processor output

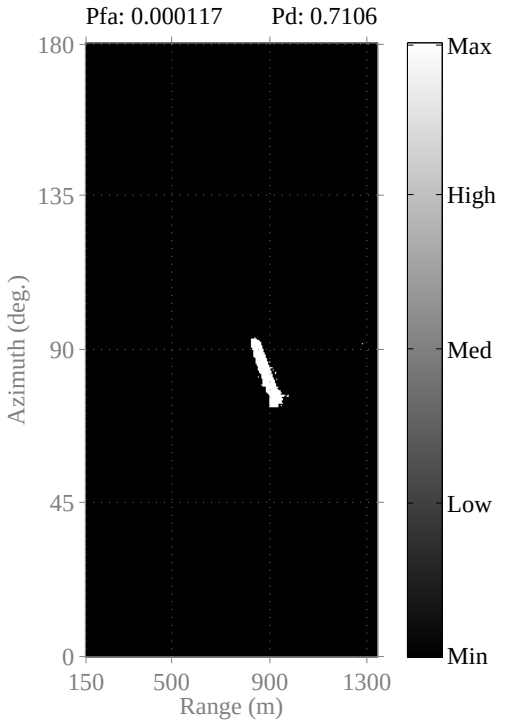

(b) MLP-based detector output

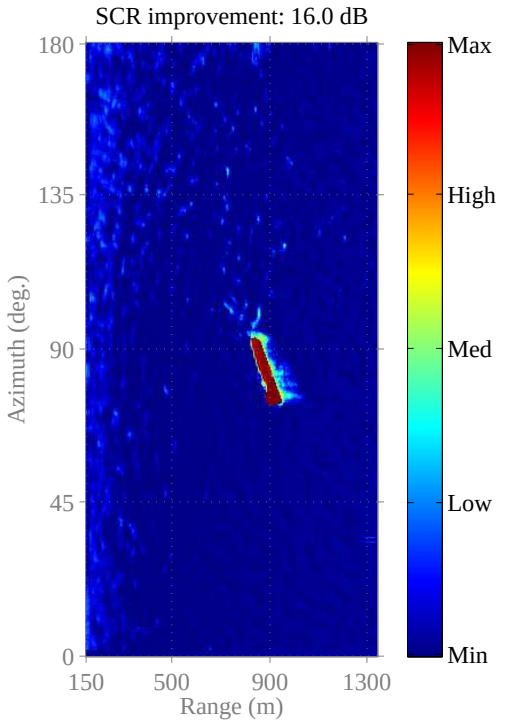

(c) RBFN-based processor output

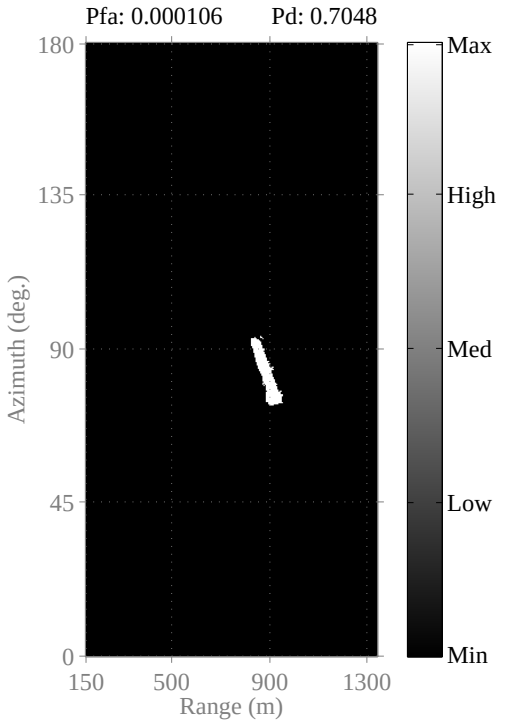

(d) RBFN-based detector output

Figure 11.16: Radar scans at the output of the AI-based incoherent processors and detectors.

11.2 General Conclusions about Incoherent Detection in Real-live Sea Clutter

From the studies made about the design and test of CFAR and AI-based incoherent detectors in real-live sea clutter conditions (see Sect. 11.1), the following conclusions are drawn:

- The most important one is that the proposed detectors based on AI techniques (MLPs and RBFNs) outperform the commonly used CFAR detectors (CA, ML and OS-CFAR detectors) in up to $\Delta P_{\mathrm{d}} \simeq 0.16$ for $P_{\mathrm{fa}} = 10^{-4}$ (see Fig. 11.12).

- It is observed that detectors using 2-D selection modes achieve higher performances than detectors using 1-D modes, regardless of the used incoherent approach (CFAR or AI-based detectors). Comparing the performance (P_{d} for $P_{\mathrm{fa}} = 10^{-4}$) achieved by using the S (best case) and V (worst case) selection modes: an improvement of up to $\Delta P_{\mathrm{d}} \simeq 0.17$ is achieved in CFAR detectors (compare Fig. 11.1-11.3); while an improvement of up to $\Delta P_{\mathrm{d}} \simeq 0.24$ is obtained in AI-based detectors (see Fig. 11.4). Moreover, it is observed that the R selection mode allow to achieve a performance slightly lower than the one achieved for the S mode, but considerably reducing the computational cost of the detector.

- It is also observed a suitable value of RIA in CFAR and AI-based detectors. This value is RIA= 9 cells, regardless of the selection mode and detector.

- Considering a trade-off between detector performance and computational cost, a suitable number of hidden neurons is found in detectors based on MLPs ($H = 15$ hidden neurons) and RBFNs ($H = 20$ hidden neurons), regardless of the selection mode.

- Comparing the performance achieved in the design and test stages (P_{d} for $P_{\mathrm{fa}} = 10^{-4}$ in Fig. 11.12), it is observed that low performance losses of $\Delta P_{\mathrm{d}} \simeq -0.03$ are achieved in AI-based detectors. The performance losses in CFAR detectors are between $\Delta P_{\mathrm{d}} \simeq -0.03$ for OS-CFAR detectors and $\Delta P_{\mathrm{d}} \simeq -0.05$ for CA-CFAR detectors. Since these performance losses are very low, high robustness of the detector is observed when working in different clutter conditions (the real-live database is composed of radar scan sequences having different clutter and target conditions). It involves that similar performance to the ones observed here are expected in the future when processing new radar scans having different environmental conditions.

- The difference of performance mentioned in the previous points can also be visually observed when analyzing the processed radar scans at the output of the detectors. This difference is observed by the density of detected target cells. This subjective analysis is very useful in cases where an objective measurement of the performance cannot be estimated. But, considering that an objective measurement of the detector performance can be estimated (P_{d}), we compare the P_{d} obtained by each detector when processing a radar scan of the test data set (see Fig. 11.15 and 11.16) with the mean P_{d} obtained for the whole test data set (see Fig. 11.12b). Since the radar scan selected in this case corresponds to the one for which the worst performance of the radar scans of the test data set was obtained, low variations of the performance for each radar scan of a given data set are observed. In

other words, the performance obtained for the radar scans of a given data set are very similar each other, even when different sea clutter conditions are present.

- The computational cost of the selected AI-based incoherent detector configurations (S selection mode with RIA = 9 cells, and $H = 15$ and $H = 20$ hidden neurons in MLP and RBFN-based approaches, respectively) is 3722 operations/CUT for the MLP-based detector and 266182 operations/CUT for the RBFN-based detector. Since different marine radar configurations are used in the experiments (see Table 2.8), different sizes of radar scans are obtained, needing different number of operations to process them. In this way:
  - Considering the marine radar working in low-resolution mode, radar scans of size [1287 azimuth cells $\times$ 256 range cells] are obtained. Therefore, $\simeq 1.2 \cdot 10^9$ operations in the selected MLP-based detector and $\simeq 87.6 \cdot 10^9$ operations in the selected RBFN-based detector are needed to process a low-resolution radar scan. Knowing that the antenna rotation period for the low-resolution mode is $T_a \simeq 2.6\,s$, processing units running at $\simeq \frac{1.2 \cdot 10^9\ op.}{2.6\,s} \simeq 0.5$ GIPS (Giga Instructions Per Second) and $\simeq \frac{87.6 \cdot 10^9\ op.}{2.6\,s} \simeq 33.7$ GIPS are needed to work in real-time with the selected MLP and RBFN-based detectors, respectively.
  - Considering the marine radar working in high-resolution mode, radar scans of size [1060 azimuth cells $\times$ 256 range cells] are obtained. Therefore, $\simeq 1.0 \cdot 10^9$ and $\simeq 72.2 \cdot 10^9$ operations in the selected MLP and RBFN-based incoherent detectors are needed to process a high-resolution radar scan, respectively. Since the antenna rotation period is $T_a \simeq 1.4\,s$ in this case, processing units running at $\simeq \frac{1.0 \cdot 10^9\ op.}{1.4\,s} \simeq 0.7$ GIPS and $\simeq \frac{72.2 \cdot 10^9\ op.}{1.4\,s} \simeq 50.5$ GIPS are needed to work in real-time with the selected MLP and RBFN-based detectors, respectively.

  Even when the required number of operations per second is elevated (up to $\simeq 50.5$ GIPS), the proposed approaches can work in real-time by using commercial GPU (Graphical Process Unit) devices. As an example, the Nvidia Tesla C2050 GPU can process a total of 515 double-precision GFLOPS (Giga FLoating-point Operations Per Second) [Nvidia]. Therefore, considering that 1 instruction is approximately equal to 1 floating-point operation, real-time is fulfilled.

Summarizing, in this chapter it has been demonstrated that the proposed AI-based incoherent detectors outperform the classical and commonly used CFAR detectors when processing marine radar scans obtained in different sea states (clutter conditions). Therefore, the performance of posterior radar tasks, such as, the tracking of ships, the ship size estimation or the prediction of target position and speed, will be improved.

Part IV

Conclusions, Contributions and Future Research Lines

CHAPTER 12

Conclusions

This thesis started assuming that learning machines, such as MLPs and RBFNs (artificial intelligence (AI) techniques), trained to minimize the mean-square error in a supervised way approximate the Neyman-Pearson detector [Jarabo2009] . That work demonstrated that the final error obtained depends on the selected structure (kind of AI technique), the number of free parameters and the training strategy. The experiments were made considering the detection of simple target models in additive white Gaussian interference. Moreover, in the design and test stages of the AI-based approaches, the experiments were made considering observation vectors with cells belonging only to H_0 or H_1. But, that work did not consider the existence of combined H_0-H_1 observation vectors, as the ones obtained from the target-interference boundaries in real systems. From the limitations of that work, this thesis presents the design of AI-based detectors for detecting targets in conditions closer to a real environment. Thus, the principal elements introduced in this thesis are:

- Real-live radar environments have been simulated, which statistical characterization is available in the specialized literature. This statistical characterization was made from real-live measurements by using different kind of radars, working at different frequencies and with different resolutions. Sea, sea-ice and ground environments have been simulated in the thesis following a correlated Weibull-distributed clutter.

- Taking into account the fact that most of the radars do not have an accurate characterization of the targets to detect, and that this characterization is not affordable when the system is running, a simple target model (Swerling 0) has been used. Targets in movement have been considered, for which a Doppler frequency of the 20% of the radar PRF is assumed, being more conservative that the commonly used (25% of the radar PRF).

- The data sets synthesized in the thesis neither are composed of independent observation vectors nor all the elements of an observation vector contain cells belonging to H_0 or H_1. Thus, sequences of radar scans have been generated for the clutter models mentioned above and in a multi-target environment with different target sizes. The observation vectors have been extracted from these synthetic sequences by using a sliding window process (selection mode), strategy commonly used in practical systems. Working in this way, the use of

different selection modes is proposed in this thesis. In this way, more accurate estimations of what is happening in the proximity of the cell under test (CUT) in azimuth and range directions can be made.

- In a first approach, AI-based detectors have been designed considering static clutter parameters, being tested in environments with variable clutter parameters with the objective of evaluating the sensitivity of the detector with the clutter parameters. But, variable Weibull-distributed clutter parameters have also been considered in the design of AI-based detectors in the thesis.

Considering the wide application of coherent and incoherent measurement systems, coherent and incoherent detectors commonly used in the literature have been taken as reference in the thesis. Starting from the formulation of the optimum detector in each case, we realize that its application in Weibull-distributed clutter environments is not possible. For this reason, commonly used suboptimum coherent and incoherent approaches have been selected from the literature. Both detection approaches have been analyzed considering the problem formulated in thesis: automatic detection of moving Swerling 0 targets in Weibull-distributed interference. Their performances have been set as reference for making comparisons with the ones obtained by the proposed AI-based coherent and incoherent approaches.

Apart of the experiments developed in synthetic environments, the thesis is extended with the design and test of AI-based detectors processing radar scans obtained by an incoherent marine radar. Previous to this step, we tested that the characterization of the sea clutter measurements follows the clutter model set for synthetic clutter measurements, i.e. we tested that measurements fulfill the Weibull distribution and found their statistical parameters.

Following the extended experimentation presented above, and from the results obtained for each environmental condition, we find an important conclusion of the thesis: the proposed AI-based detectors outperform the reference detectors in all the cases of study presented in the thesis. More specifically, and considering the particular conclusions obtained for the different simulated and real-live radar scenarios used in the thesis, the main conclusions drawn from the thesis are summarized from different points of view:

1. *According to the kind of radar used in the measurements: coherent or incoherent radars.* It has been observed that the performance of the incoherent detectors taken as reference (CFAR detectors) achieved higher performance than the coherent detector taken as reference (TSKAP detector). It happens because of the different philosophies they use to process the data and to make the final decision "target present/absent" in each CUT of the radar scans. But, focusing on the proposed AI-based detectors, it has been observed that the performance of incoherent AI-based detectors is slightly lower than the one obtained when using coherent AI-based detectors. This performance loss is produced because less information is used in the decision (only amplitude in incoherent detectors). On the other hand, the computational cost required to implement AI-based incoherent detectors is much lower than the one needed to implement AI-based coherent detectors.

2. *According to the used AI technique.* From the two AI techniques considered in the thesis, the performance achieved by detectors based on MLPs and RBFNs are very close each other. But, the performance achieved by MLP-based detectors is always greater than the

one achieved by RBFN-based detectors. In addition, the computational cost required to implement MLP-based detectors is much lower than the one required for RBFN-based detectors. Therefore, the use of MLPs to implement coherent and incoherent AI-based detectors is proposed.

3. *According to the design of the detectors.* The dimensionality and design of the reference and AI-based detectors can be made by using two kinds of performance measurement: the average SCR improvement in the processor; and the P_{d} for a given P_{fa} in the detector. It was observed that both performance measurements present similar behaviors when varying the parameters of the detectors. The tuning of these parameters in the design stage of reference and AI-based detectors allow to improve their performance. The influence of these parameters was studied in the thesis, and the main effects observed are summarized below according to:

   (a) *The properties of the data set used in the design stage of the detectors.* The clutter conditions used in the design stage have an important effect in the performance of reference and AI-based detectors. In this way, it is observed that the performance of AI-based detectors improves when the design data set is composed of radar scans having different clutter parameters (skewness parameter in the case of the Weibull distribution). When this clutter properties cannot be varied for any reason, as occurred for the coherent (TSKAP) and incoherent (CFAR) reference detectors (the clutter parameters are the same scan-to-scan), the highest detector performance is obtained when the clutter parameter is equal to its typical value.

   (b) *The selection modes used in the detectors.* Non-delayed (depending on past cells) and delayed (depending on past and future cells) selection modes have been studied in the thesis. It has been empirically demonstrated that the detectors that use delayed selection modes (V: vertical; H: horizontal; X: X-shape; P: P-shape; R: rhombus; and, S: square) outperform the detectors that use non-delayed modes (azimuthal and range modes). But, detectors using delayed selection modes present two drawbacks: a time delay because they must be converted into causal systems; and more computational cost because the number of cells selected by them is usually higher than the one selected by non-delayed modes. From the delayed selection modes under study, it has been observed that detectors using 2-D selection modes (X, P, R and S) present higher performance than the ones using 1-D modes (V and H). Again, time delays and computational cost increases are assumed when using 2-D selection modes. Finally, from the 2-D selection modes under study, it has been observed that the highest performance is achieved when using an S mode. Detectors working with this mode present the highest time delay and computational cost, but it allows to achieve the highest performance, while maintaining real-time properties.

   (c) *The value of range of integrated area (RIA) that indicates the dimension of the selection modes used in the detectors.* A range of variation of RIA for having the highest detector performance has been found in the different cases of study of the thesis. It has been observed that this range is related to the size of the targets present in the radar environment, specially to the maximum width of the targets considered in the

studies. Taking into account that the greater the RIA, the higher the computational cost of the detector, the use of the minimum RIA of this range is proposed. Since the value of RIA depends on the target sizes, if targets with different sizes want to be detected with high performance, this number should be retuned. But, if this value would not be retuned, a performance loss will be achieved, as observed in the plots given in the thesis for studying the influence of the RIA.

(d) *The number of hidden neurons (H) used in AI-based detectors.* From the studies made according to this parameter, it has been observed a typical range of variation between 10 and 20 hidden neurons. In this way, using MLPs or RBFNs with $H \in [10, 20]$, it is very likely that high performance is achieved in the designed AI-based detector, while maintaining a reasonable computational cost that allow the detector to work in real-time.

(e) *The differences between the ways of working of reference and AI-based detectors.* Considering the coherent detector taken as reference, the *target sequence known a priori* (TSKAP) detector, it is observed that this detector depends on the knowledge of two parameters: the instantaneous target signal; and the skewness parameter of the Weibull-distributed clutter present in each radar scan. These parameters could be estimated, reducing in consequence the performance of the TSKAP detector. But, since the proposed AI-based detectors outperform the TSKAP detector in all the cases of study, these parameters are not estimated. Something similar occurs with the incoherent detectors taken as reference (CFAR detectors). But, in some of the selected CFAR strategies, they only require the knowledge of the skewness parameter (clutter parameter) and not the knowledge of the target parameters. The most important difference obtained from this study is that the designed AI-based detector does not depend on the target and clutter parameters.

4. *According to the achieved performance of the reference and AI-based detectors.* From the experiments made in the thesis, it has been empirically demonstrated that the proposed AI-based detectors outperform the detectors taken as reference from the literature, regardless of the selection mode (non-delayed or delayed) and kind of radar (coherent or incoherent). Apart of this performance improvement, other important aspects are observed in the performance of the detectors, being analyzed below according to:

   (a) *The capability of generalization of the detectors.* High generalization capability has been observed in the AI-based detectors. This capability is justified because low performance decrease has been observed when processing radar scans never processed before (test stage). This low performance decrease invites us to think that when processing (in the future) new radar scans with similar statistical properties, as the ones used in the experiments, similar performances to the ones reported here will be obtained. Similar generalization capabilities have been observed when studying the reference (TSKAP and CFAR) detectors.

   (b) *The sensitivity of the detectors to the variation of the clutter parameters.* Different radar scans have been selected to analyze the performance of the detectors considered in each case of study. These radar scans have clutter parameters that are inside the

limits of the statistical parameters reported in the literature and for which the best and worst performances were obtained. From the results obtained for these specific radar scans, low performance variations were observed in terms of P_{fa} and P_{d}. These low performance variations with the clutter parameters indicate us that both the reference and proposed AI-based detectors are very robust against changes in the clutter statistics.

5. *According to the capability of working in real-time.* The computational cost required to implement incoherent detectors for processing radar scans obtained by a commercial marine radar has been reported in the thesis. Even when the computational cost of the proposed AI-based detectors is high, specially for the detector based on RBFNs, it has been demonstrated in the thesis that the proposed detectors can work in real-time. For doing so, the use of commercial GPUs is proposed.

To summarize this chapter, and from the general conclusions of the thesis reported above, we can conclude that:

> "*The objectives of the thesis (see Sect. 1.3) have been fulfilled by the proposed AI-based detectors, being implemented by two different kind of AI techniques: the MLPs and the RBFNs. First, because the proposed detection schemes (coherent and incoherent) present high performance working in different environments (sea, sea-ice and ground clutters). Second, because these detectors outperform the reference coherent (TSKAP) and incoherent (CFAR) detectors commonly used in the literature. Third, because the performance of the proposed detectors is slightly reduced when processing new radar scans and when processing radar scans with a wide range of clutter properties. And fourth, because the proposed detectors have been optimized to reduce their computational cost as much as possible, while maintaining high performance, in order to implement them in commercial devices to work in real-time.*"

CHAPTER 13

Future Research Lines

This thesis presents a novel scheme for detecting targets in clutter by using coherent and incoherent measurements of the environment. Nevertheless, the scheme proposed here cannot be considered closed. For instance, this scheme could be improved in performance and optimized in computational cost. In this way, this thesis tries to open new research lines. Among others, these new research lines could be focused on:

- Investigate different cost functions used to train MLPs and RBFNs during the design stage of AI-based detectors in order to improve the performance of the designed detector.

- Apply other kind of ANNs, such as, probabilistic ANNs, recursive ANNs, etc. Moreover, the use of support vector machines (SVMs) could be also considered. Since SVMs and RBFNs have similar principals of design, similar performances and computational cost could be expected. Following with this research line, an investigation on how to reduce the number of selected support vectors could be done.

- Investigate the use of ensembles of ANNs to improve the overall detection performance. Working in this way, some ANNs of the ensemble could be specialized in some detection cases (e.g. strong clutter conditions), others specialized in other cases (e.g. weak clutter conditions), etc.

- Study different selection modes to improve the performance of reference and AI-based detectors. Moreover, the design of these selection modes could also be focused on reducing the computational cost of the proposed detector.

- Since the sea clutter measurements made by the marine radar used in the experiments of the thesis fits a Weibull distribution, the use of synthetic data to design AI-based incoherent detectors is proposed. In this way, the designed detectors would work in real-live conditions/environments. The proposed research line is very interesting because during an experimental campaign of measurements, it is likely that not all the sea states are present. Thus, following the procedure used in the thesis for generating synthetic radar scans, radar scans for these sea states could be modeled, completing the database used in the design

stage of the detectors. Moreover, rare events could be also modeled, giving more potential to the proposed detectors to work with high performance in case they happen in the future.

- Apply the proposed detection scheme and philosophy to other research areas or topics. For instance, for detecting intrusions in telematic networks, for detecting flaws in materials by using ultrasonic signals, etc.
- Apply pre-processing techniques to reduce the level of clutter and noise of the radar scans at the input of the proposed AI-based detectors. Post-processing techniques could also be applied to reduce the rate of false alarms and/or to improve the rate of target detections.
- Use the proposed AI-based detectors to improve the performance of next radar tasks, such as, the estimate of the size of the targets, the estimate of the position of the targets, the estimate of the speed of the targets, etc. Moreover, they could be used to improve the accuracy of the target position prediction, to improve the estimation of the direction of arrival, the velocity, etc.
- Investigate new techniques to improve the accuracy of the cost function estimation during training, especially when very few training data are available

As a conclusion, novel or experimented researches looking for new research lines can find here some challenging ideas.

CHAPTER 14

Contributions

This chapter presents a resume of the main contributions of the thesis, relating them to the publications obtained from the thesis. A list of the publications derived from the thesis is given at the end of the chapter. This list uses the nomenclature **Vicen20XXx**.

The first contributions of the thesis were obtained from 2006 to 2008, where the proposed detection scheme based on MLPs working with non-delayed selection modes was presented. In the first work derived from the thesis (**Vicen2006a**), the proposed MLP-based detector working with constant clutter conditions in the design and test stages was studied. Later, two studies of the robustness of the proposed MLP-based detector against changes in target and clutter conditions were published in **Vicen2007b** and **Vicen2007c**. A new study of the influence of the training algorithm and MLP size in the MLP-based detector performance was published in **Vicen2007a**. Deeper analyses of the robustness of the proposed MLP-based detector against changes in target and clutter parameters were published in **Vicen2008b** and **Vicen2008a**, respectively. A study of the simultaneous influence of target and clutter parameters in the design and test stages of the detectors was published in **Vicen2009d**.

From 2009, two of the main contributions of the thesis were published. The first one was based on the use of efficient and effective selection modes to improve the performance of the proposed MLP-based detector (delayed selection modes in 1 and 2 dimensions (1-D and 2-D)). The second one was based on the use of MLPs as non-linear filters to reduce the power of clutter and to emphasize the power of target. Moreover, from this year, instead of using ideal observation vectors containing only samples from H_1 (target and interference) or H_0 (only interference), synthetic radar scans were used. A study of the proposed MLP-based clutter reduction system when processing time-correlated radar scans synthesized for coherent radars was published in **Vicen2009c**. In this work, only non-delayed selection modes were considered. On the other hand, the first works using 1-D selection modes were presented in **Vicen2009a** and **Vicen2009b**, where radar scans obtained from a marine radar (real-live data) were used. In these three works, the MLP was presented as a clutter reduction system (main function of the processor of Fig. 4.1), being a previous stage of the proposed MLP-based detector scheme.

From 2010, some research works about the use of MLPs to detect targets in synthetic and real-live radar environments were accepted by the scientific community. In these publications,

the proposed MLP-based approach was used to automatically detect ships (**Vicen2011a, Vicen2011b**) and to automatically estimate their sizes (**Vicen2010c**) in real-live marine environments. These works also presented another contribution of the thesis: the use of 2-D selection modes in the proposed detectors, where the performance improvement achieved by each mode was reported. On the other hand, two additional works were accepted for publication in 2010. In these works, it was demonstrated the applicability of the proposed detection scheme based on MLPs to detect targets in synthetic ground (**Vicen2010a**) and sea-ice (**Vicen2010c**) environments. In these two works, non-delayed selection modes were only considered when the proposed MLP-based detector processes synthetic measurements from coherent radars.

The use of new strategies for training MLPs was also studied in the experimental stage of the thesis. But, since these experiments were made considering Gaussian interference, they were not reported in the thesis memory. high performance was achieved when detecting targets in Gaussian-distributed interference, as presented in **Vicen2010d**. In this work, different cost functions were considered in the design (train) stage of MLP-based detectors to improve their performance. For making accurate estimations of the error achieved for these cost functions, importance sampling techniques were used, as well as a novel way of training MLPs based on genetic algorithms.

Apart of the publication of the above-mentioned contributions, other important contributions of the thesis are still pending to be published. For instance, the application of 1-D and 2-D selection modes in MLP-based detectors working with measurements obtained by coherent systems is pending to be published. Moreover, no publications have been made yet concerning to the use of RBFN-based detectors. For these detectors, a lot of contributions are still pending to be published: use of non-delayed selection modes in the detector; use of 1-D and 2-D delayed selection modes in the detector; application in sea, se-ice and ground clutter environments; application when processing coherent and incoherent measurements; etc.

The list of research works published in peer-review journals and conference proceedings that support the main contributions of the thesis are given below chronologically sorted from the newest to the oldest one:

- **Vicen2011a** - R. Vicen-Bueno, R. Carrasco-Álvarez, M.P. Jarabo-Amores, J.C. Nieto-Borge and E. Alexandre-Cortizo. Detection of ships in marine environments by square integration mode and Multilayer Perceptrons. *IEEE Trans. Instrum. Meas.*, Vol. 60, n. 3, (2011), 712–724.

- **Vicen2011b** - R. Vicen-Bueno, R. Carrasco-Álvarez, M.P. Jarabo-Amores, J.C. Nieto-Borge, and M. Rosa-Zurera. Ship Detection by different data selection templates and multilayer perceptrons from incoherent maritime radar data. *IET Radar Son. Nav.*, Vol. 5, n. 2, (2011), 144–155.

- **Vicen2010a** - R. Vicen-Bueno, M. Rosa-Zurera, M.P. Jarabo-Amores and R. Gil-Pita. Automatic target detection in simulated ground clutter (Weibull distributed) by multilayer perceptrons in a low-resolution coherent radar. *IET Radar Son. Nav.*, Vol. 4, n. 2, (2010), 315–328.

- **Vicen2010b** - R. Vicen-Bueno, R. Carrasco-Álvarez, M. Rosa-Zurera, J.C. Nieto-Borge, and M.P. Jarabo-Amores. Artificial Neural Network-based Clutter Reduction Systems for Ship Size Estimation in Maritime Radars. *EURASIP J. Adv. Signal Process.*, Vol. 2010, (2010), 1–15.

- **Vicen2010c** - R. Vicen-Bueno, M. Rosa-Zurera, P. Jarabo-Amores, and D. Mata-Moya. Coherent detection of Swerling 0 targets in sea-ice Weibull-distributed clutter using Neural Networks. *IEEE Trans. Instrum. Meas.*, Vol. 59, n. 12, (2010), 3139–3151.

- **Vicen2010d** - R. Vicen-Bueno, M.P. Jarabo-Amores, M. Rosa-Zurera, J.L. Sanz-González and S. Maldonado-Bascón. Importance Sampling for Objective Function Estimations in Neural Detector Training Driven by Genetic Algorithms. *Neural Process. Lett.*, Vol. 32, n. 3, (2010), 249–268.

- **Vicen2009a** - R. Vicen-Bueno, R. Carrasco-Álvarez, M. Rosa-Zurera and J. C. Nieto-Borge. Sea Clutter Reduction and Target Enhancement by Neural Networks in a Marine Radar System. *Sensors*, Vol. 9, n. 3, (2009), 1913–1936.

- **Vicen2009b** - R. Vicen-Bueno, R. Carrasco-Álvarez, M. Rosa-Zurera and J. C. Nieto-Borge. Sea Clutter Power Reduction in Radar Measurement Systems by Feedforward Multilayer Perceptrons with Medium Input Data Integration Rate. In *IEEE Int. Instrum. Meas. Tech. Conf. - I2MTC 2009*. 2009, 1069–1074.

- **Vicen2009c** - R. Vicen-Bueno, M Rosa-Zurera, M. P. Jarabo-Amores and D. Mata-Moya. Medium-High Correlated Weibull-distributed Clutter Reduction by Neural Networks in Coherent Radar Systems. In *IEEE Int. Instrum. Meas. Tech. Conf. - I2MTC 2009*. 2009, 846–851.

- **Vicen2009d** - R. Vicen-Bueno, M. Rosa-Zurera, M.P. Jarabo-Amores, R. Gil-Pita and D. Mata-Moya. Intelligent Radar Detectors. In *Encyclopedia of Artificial Intelligence*. 2009, 933–939.

- **Vicen2008a** - R. Vicen-Bueno, E. Galán-Fernández, M. Rosa-Zurera and M.P. Jarabo-Amores. MLP-Based Detection of Targets in Clutter: Robustness with Respect to the Shape Parameter of Weibull-Disitributed Clutter. In *Artificial Neural Networks - ICANN 2008*. 2008, 121–130.

- **Vicen2008b** - R. Vicen-Bueno, M.P. Jarabo-Amores, M. Rosa-Zurera, R. Gil-Pita and D. Mata-Moya. Detection of known targets in Weibull clutter based on Neural Networks. Robustness study against target parameters changes. In *IEEE Radar Conf. 2008* - RADAR'08. 2008, 1–6.

- **Vicen2007a** - R. Vicen-Bueno, M.P. Jarabo-Amores, D. Mata-Moya, M. Rosa-Zurera and R. Gil-Pita. Low Complexity MLP-Based Radar Detector: Influence of the Training Algorithm and the MLP Size. In *Computational and Ambient Intelligence*. 2007, 630–637.

- **Vicen2007b** - R. Vicen-Bueno, M.P. Jarabo-Amores, M. Rosa-Zurera, R. Gil-Pita and D. Mata-Moya. Performance Analysis of MLP-Based Radar Detectors in Weibull-Distributed Clutter with Respect to Target Doppler Frequency. In *Artificial Neural Networks - ICANN 2007*. 2007, 690–698.

- **Vicen2007c** - R. Vicen-Bueno, M.P. Jarabo-Amores, M. Rosa-Zurera, D. Mata-Moya and R. Gil-Pita. Robustness with Respect to the Signal-to-Noise Ratio of MLP-based Detectors in Weibull Clutter. In *Proc. of the 15^{t}h European Signal Proc. Conf.* - EUSIPCO 2007. 2007, vol. 1, 1736–1740.

- **Vicen2006a** - R. Vicen-Bueno, M. Rosa-Zurera, M.P. Jarabo-Amores and R. Gil-Pita. NN-Based Detector for Known Targets in Coherent Weibull Clutter. In *Intelligent Data Engineering and Automated Learning - IDEAL 2006*. 2006, 522–529.

Part V

Bibliography

BIBLIOGRAPHY

[Almarshad2008] Almarshad, M.N., M. Barkat, and S.A. Alshebeili. «A Monte Carlo simulation for two novel automatic censoring techniques of radar interfering targets in log-normal clutter.» *Signal Process.*, 88, n. 3, (2008), 719–732.

[Aloisio1994] Aloisio, V., A. Di Vito, and G. Galati. «Optimum Detection of Moderately Fluctuating Radar Targets.» *IEE Proc.-Radar Sonar Navig.*, 141, (1994), 164–170.

[Aluffi1992] Aluffi Pentini, F., A. Farina, and F. Zirilli. «Radar detection of targets located in a coherent K distributed clutter background.» *IEE Proc. F Radar and Signal Proc.*, 139, n. 3, (1992), 239–245.

[Anastassopoulos1995] Anastassopoulos, V., and G.A. Lampropoulos. «Optimal CFAR detection in Weibull clutter.» *IEEE Trans. Aerosp. Electron. Syst.*, 31, n. 1, (1995), 52–64.

[Andina1995a] Andina, D. *Optimización de detectores neuronales. Aplicación a radar y sonar.* Ph.d. thesis, E.T.S.I. Telecomunicación, U.P.M., 1995. Supervised by J. L. Sanz González.

[Andina1995b] Andina, D., J. Sanz-González, and J. Jiménez-Pajares. «A comparison of criterion functions for a neural network applied to binary detection.» In *Proc. IEEE Int. Conf. Neural Netw.* 1995, vol. 1, 492–495.

[Andina1995c] Andina, D., J. Sanz-González, and O. Rodríguez-Martín. «Performance improvements for a neural network detector.» In *Proc. IEEE Int. Conf. Neural Netw.* 1995, vol. 1, 492–495.

[Andina1996] Andina, D., and J.L. Sanz-Gonzalez. «Comparison of a neural network detector vs Neyman-Pearson optimal detector.» *IEEE Int. Conf. Acoustics, Speech, and Signal Proc.*, 6, (1996), 3573–3576.

[Armstrong1991] Armstrong, B. C., and H. D. Griffiths. «CFAR detection of fluctuating targets in spatially correlated K-distributed clutter.» *IEE Proc. F Radar Signal Proc.*, (1991), –.

[Bailey1935] Bailey, W. N. *Generalised Hypergeometric Series.* Cambridge, 1935.

[Baker1985] Baker, C.J. «K-distributed coherent sea clutter.» *IEE Proc.-Radar Signal Proces.*, 138, n. 2, (1985), 89–92.

[Barni2003] Barni, M., F. Bartolini, A. De Rosa, and A. Piva. «Optimum decoding and detection of multiplicative watermarks.» *IEEE Trans. Signal Process.*, 51, n. 4, (2003), 1118–1123.

[Barton1985] Barton, D.K. «Land clutter models for radar design and analysis.» *Proc. IEEE*, 73, n. 2, (1985), 198–204.

[Battacharya1992] Bhattacharya, T.K., and S. Haykin. «Neural network-based adaptive radar detection scheme for small ice targets in sea clutter.» *Electron. Lett.*, 28, n. 16, (1992), 1528–1529.

[Billingsley2002] Billingsley, J.B. *Low-Angle Radar Land Clutter.* William Andrew, 2002.

[Billingsley1999] Billingsley, J.B., A. Farina, F. Gini, M.V. Greco, and L. Verrazzani. «Statistical Analyses of Measured Radar Ground Clutter Data.» *IEEE Trans. Aerosp. Electron. Syst.*, 35, (1999), 579–593.

[Bishop1995] Bishop, C.M. *Neural networks for pattern recognition.* Oxford University Press Inc., 1995.

[Burian1999] Burian, A., P. Kuosmanen, and J. Saarinen. «Neural detectors with variable threshold.» In *Proc. ISCAS.* 1999, vol. 5, 599–602.

[Caroni2004] Caroni, C., and A. Kimber. «Detection of frailty in weibull lifetime data using outlier tests.» *Journal of Statistical Computation and Simulation*, 74, n. 1, (2004), 15–23.

[Casasent2003a] Casasent, D., and X. Chen. «New training strategies for RBF neural networks for X-ray agricultural product inspection.» *Pattern Recognition*, 36, n. 2, (2003), 535 – 547.

[Casasent2003b] —. «Radial basis function neural networks for nonlinear Fisher discrimination and Neyman-Pearson classification.» *Neural Networks*, 16, n. 5-6, (2003), 529 – 535.

[Cheikh2004] Cheikh, K., and S. Faozi. «Application of neural networks to radar signal detection in K-distributed clutter.» In *First Int. Symp. on Control, Comm. and Signal Proc.* 2004, 295–298.

[Cheikh2006] Cheikh, K., and F. Soltani. «Application of neural networks to radar signal detection in K-distributed clutter.» *IEE Proc.-Radar Sonar Navig.*, 153, n. 5, (2006), 460–466.

[Cheng2003] Cheng, Q., and T.S. Huang. «Robust optimum detection of transform domain multiplicative watermarks.» *IEEE Trans. Signal Process.*, 51, n. 4, (2003), 906–924.

[Coates1988] Coates, R.F.W., G.J. Janacek, and K.V. Lever. «Monte Carlo simulation and random number generation.» *IEEE J. Sel. Areas Commun.*, 6, n. 1, (1988), 58–66.

[Conte2005] Conte, E., A. De Maio, and A. Farina. «Statistical Tests for Higher Order Analysis of Radar Clutter: Their Application to L-band Measured Data.» *IEEE Trans. Aerosp. Electron. Syst.*, 41, (2005), 205–218.

[Conte1991] Conte, E., M. Longo, M. Lops, and S.L. Ullo. «Radar detection of signals with unknown parameters in K-distributed clutter.» *IEE Proc.-Radar Sonar Navig.*, 138, n. 2, (1991), 131–138.

[Conte1994] Conte, E., M. Lops, and G. Ricci. «Radar detection in K-distributed clutter.» *IEE Proc.-Radar Sonar Navig.*, 141, n. 2, (1994), 116–118.

[Conte1999] —. «Incoherent radar detection in compound-Gaussian clutter.» *IEEE Trans. Aerosp. Electron. Syst.*, 35, n. 3, (1999), 790–800.

[Conte2004] Conte, E., A. de Maio, and C. Galdi. «Statistical analysis of real clutter al different range resolutions.» *IEEE Trans. Aerosp. Electron. Syst.*, 40, n. 3, (2004), 903–918.

[Davidson2004] Davidson, G., H.D. Griffiths, and S. Ablett. «Analysis of high-resolution land clutter.» *IEE Proc.-Vision, Image and Signal Process.*, 151, n. 1, (2004), 86–91.

[DeMiguel1998] De Miguel, G., J.A. Besada, and J.R. Casar. «Probability of false alarm of CA-CFAR detector in Weibull clutter.» *Electronics Letters*, 34, n. 8, (1998), 806–807.

[Dempster1977] Dempster, A.P., N. Laird, and D.B. Rubin. «Maximum likelihood from incomplete data via the EM algorithm.» *J. Royal Statistic Society B*, 39, (1977), 1–38.

[Diani1996] Diani, M., G. Corsini, F. Berizzi, and D. Calugi. «Ground clutter model for airborne MPRF radars in look-down search mode.» *IEE Proc.-Radar Sonar Navig.*, 143, n. 2, (1996), 113–120.

[Dimitrijevic2001] Dimitrijevic, D.D., M.M. Petrovic, M.G. Hrasovec, and B.V. Damnjanovic. «Implementation of radar CFAR-based target detection algorithm in a real-time multiprocessor environment.» In *5th Int.*

Conf. Telecommunications in Modern Satellite, Cable and Broadcasting Service. TELSIKS 2001. 2001, vol. 2, 749–752.

[Eaves1987] Eaves, J., and E. Reedy. *Principles of Moder Radar.* Van Nostrand Reinhold, 1987.

[Erfanian2008] Erfanian, S., and V. T. Vakili. «Introducing excision switching-CFAR in K distributed sea clutter.» *Signal Process.*, 89, n. 6, (2009), 1023–1031.

[Farina1997] Farina, A. «Linear and non-linear filters for clutter cancellation in radar systems.» *Signal Process.*, 59, n. 1, (1997), 101–112.

[Farina1995] Farina, A., F. Gini, M.V. Greco, and P. Lombardo. «Coherent radar detection of targets against a combination of K-distributed and Gaussian clutter.» In *IEEE 1995 Int. Radar Conf.* 1995, 83–88.

[Farina1998] Farina, A., F. Gini, M.V. Greco, and L. Verrazzani. «High resolution sea clutter data: statistical analysis of recorded live data.» *IEE Proc.-Radar Sonar Navig.*, 144, n. 3, (1997), 121–130.

[Farina1986a] Farina, A., and A. Russo. «Radar Detection of Correlated Targets in Clutter.» *IEEE Trans. Aerosp. Electron. Syst.*, AES-22, n. 5, (1986), 513–532.

[Farina1987a] Farina, A., A. Russo, and F. Scannapieco. «Radar detection in coherent Weibull clutter.» *IEEE Trans. Acous. Speech Signal Proc.*, 35, n. 6, (1987), 893–895.

[Farina1987b] Farina, A., A. Russo, F. Scannapieco, and S. Barbarossa. «Theory of radar detection in coherent Weibull clutter.» *IEE Proc. F Comm. Radar Signal Proc.*, 134, n. 2, (1987), 174–190.

[Farina1986b] Farina, A., A. Russo, and F.A. Studer. «Coherent radar detection in log-normal clutter.» *IEE Proc. F Comm. Radar Signal Proc.*, 133, n. 1, (1986), 39–53.

[Farrouki2007] Farrouki, A., and M. Barkat. «Automatic censored mean level detector using a variability-based censoring with non-coherent integration.» *Signal Process.*, 87, n. 6, (2007), 1462–1473.

[Friedberg1999] Friedberg, S.H., A.J. Insel, and L.E. Spence. *Linear Algebra (3rd. Edition).* Prentice Hall, 1999.

[Fung1985] Fung, K. Y., and S.R. Paul. «Comparisons of outlier detection procedures in weibull or extreme-value distribution.» *Communications in Partial Differential Equations*, 14, n. 4, (1985), 895–917.

[Gandhi1997] Gandhi, P., and V. Ramamurti. «Neural networks for signal detection in non-Gaussian noise.» *IEEE Trans. Signal Process.*, 45, n. 11, (1997), 2846–2851.

[Gandhi1995] Gandhi, P.P., E. Cardona, and L. Baker. «CFAR signal detection in nonhomogeneous Weibull clutter and interference.» In *Proc. 1995 IEEE Radar Conf.* 1995, 583–588.

[Gandhi1988] Gandhi, P.P., and S.A. Kassam. «Analysis of CFAR processors in nonhomogeneous background.» *IEEE Trans. Aerosp. Electron. Syst.*, 24, n. 4, (1988), 427–445.

[Gentle2003] Gentle, James E. *Random number generation and Monte Carlo methods (Second ed.)*. Springer, 2003.

[Gini1997a] Gini, F. «A cumulant-based adaptive technique for coherent radar detection in a mixture of K-distributed clutter and Gaussian disturbance.» *IEEE Trans. Signal Process.*, 45, n. 6, (1997), 1507–1519.

[Gini1997b] —. «Sub-optimum coherent radar detection in a mixture of K-distributed and Gaussian clutter.» *IEE Proc.-Radar Sonar Navig.*, 144, n. 1, (1997), 39–48.

[Gini2002] Gini, F., and M. Greco. «Covariance matrix estimation for CFAR detection in correlated heavy tailed clutter.» *Signal Process.*, 82, n. 12, (2002), 1847–1859.

[Gini2000] Gini, F., M.V. Greco, M. Diani, and L. Verrazzani. «Performance analysis of two adaptive radar detectors against non-Gaussian real sea clutter data.» *IEEE Trans. Aerosp. Electron. Syst.*, 36, n. 4, (2000), 1429–1439.

[Gini1995] Gini, F., and F. Lombardini. «A novel linear-quadratic technique for coherent radar detection in mixed clutter environment.» In *European Microwave Conference, 1995. 25th.* 1995, vol. 1, 360–364.

[Golden1998] Golden, K.M., and et. al. «Forward electromagnetic scattering models for sea ice.» *IEEE Trans. Geosci. Remote Sensing*, 36, n. 5, (1998), 1655–1674.

[Gray2003] Gray, L. «A Mathematician Looks at Wolfram's New Kind of Science.» *Not. Amer. Math. Soc.*, 50, (2003), 200–211.

[Greco2004] Greco, M., F. Bordoni, and F. Gini. «X-band sea-clutter nonstationarity: influence of long waves.» *IEEE J. Ocean. Eng.*, 29, n. 2, (2004), 269–283.

[Hagan1994] Hagan, M., and M. Menhaj. «Training feedforward networks with the Marquardt algorithm.» *IEEE Trans. Neural Netw.*, 5, n. 6, (1994), 989–993.

[Hamadouche2000] Hamadouche, M., M. Barakat, and M. Khodja. «Analysis of the clutter map CFAR in Weibull clutter.» *Signal Process.*, 80, n. 1, (2000), 117–123.

[Hammoudi2004] Hammoudi, Z., and F. Soltani. «Distributed IVI-CFAR detection in non-homogeneous environments.» *Signal Processing*, 84, n. 7, (2004), 1231–1237.

[Hartman1990] Hartman, E. J., Keeler J.D., and J. M. Kowalski. «Layered Neural Networks with gaussian hidden units as universal approximations.» *Neural Computation*, 2, n. 2, (1990), 210–215.

[Hastie2001] Hastie, T., R. Tibshirani, and J. Friedman. *The elements of statistical learning: Data mining, inference, and prediction.* Springer Verlag, 2001.

[Hayes1996] Hayes, M.H. *Statistical Digital Signal Processing and Modelling.* Wiley, 1996.

[Haykin2009] Haykin, S. *Neural networks and learning machines, (Third edition).* Prentice-Hall, 2009.

[Haykin2002] Haykin, S., R. Bakker, and B.W. Currie. «Uncovering nonlinear dynamics-the case study of sea clutter.» *Proc. IEEE*, 90, n. 5, (2002), 860–881.

[Haykin1994] Haykin, S., and T. Bhattacharya. «Wigner-Ville distribution: an important functional block for radar target detection in clutter.» In *Twenty-Eighth Asilomar Conf. on Signals, Systems and Computers.* 1994, vol. 1, 68–72.

[Haykin1997] Haykin, S., and S. Puthusserypady. «Chaotic dynamics of sea clutter.» *Chaos: An Interdisciplinary Journal of Nonlinear Science*, 7, n. 4, (1997), 777–802.

[Jakeman1976] Jakeman, E., and P. N. Pusey. «A model for non-Rayleigh sea echo.» *IEEE Trans. Antennas Propagat.*, 24, n. 6, (1976), 806–814.

[Jandhyala1999] Jandhyala, V.K., S.B. Fotopoulos, and N. Evaggelopoulos. «Change-point methods for Weibull models with applications to detection of trends in extreme temperatures.» *Environmetrics*, 10, n. 5, (1999), 547–564.

[Jarabo2009] Jarabo-Amores, M.-P., M. Rosa-Zurera, R. Gil-Pita, and F. López-Ferreras. «Study of two error functions to approximate the Neyman-Pearson detector using supervised learning machines.» *IEEE Trans. Signal Process.*, 57, n. 11, (2009), 4175–4181.

[Jarabo2004] Jarabo-Amores, M.P. *Desarrollo y optimización de un detector neuronal de blancos radar en presencia de interferencia aditiva.* Ph.d. thesis, Escuela Politécnica Superior, 2004. Supervised by F. López Ferreras.

[Jarabo2003] Jarabo-Amores, P., R. Gil-Pita, M. Rosa-Zurera, and F. López-Ferreras. «MLP and RBFN for detecting white gaussian signals in white gaussian interference.» In *Artificial Neural Nets Problem Solving Methods*. 2003, vol. 2687, 790–797.

[Jarabo2005b] —. «Sensitivity of Neural Networks which approximate the Neyman-Pearson detector to threshold variations.» In *Proc. of the 13th European Signal Proc. Conf. - EUSIPCO 2005*. 2005, vol. 1, 4 pages.

[Jarabo2005] Jarabo-Amores, P., M. Rosa-Zurera, R. Gil-Pita, and F. López-Ferreras. «Sufficient condition for an adaptive system to approximate the Neyman-Pearson detector.» In *Proc. IEEE Workshop Stat. Signal Process.* 2005, 295–300.

[Kay1988] Kay, S.M. *Modern Spectral Estimation*. Prentice Hall, 1988.

[Levanon1990] Levanon, N., and M. Shor. «Order statistics CFAR for Weibull background.» *IEE Proc.-Radar Signal Proces.*, 137, n. 3, (1990), 157–162.

[Lewinski1983] Lewinski, D. «Nonstationary probabilistic target and clutter scattering models.» *IEEE Trans. Antennas Propagat.*, 31, n. 3, (1983), 490–498.

[Li1989] Li, G., and K.B. Yu. «Modelling and Simulation of Coherent Weibull Clutter.» *IEE Proc.-Radar Signal Proces.*, 136, (1989), 2–12.

[Liu1982] Liu, B., and D. Jr. Munson. «Generation of a random sequence having a jointly specified marginal distribution and autocovariance.» *IEEE Trans. Acous. Speech Signal Proc.*, 30, n. 6, (1982), 973–983.

[Liu2003] Liu, W., and X. Liu. «And-CFAR and Or-CFAR detectors design in Weibull background.» In *Proc. IEEE 37th Annual Int. Carnahan Conf. on Security Tech.* 2003, 83–86.

[Lombardo1999a] Lombardo, P., and J.B. Billingsley. «A new model for the Doppler spectrum of windblown radar ground clutter.» In *Proc. 1999 IEEE Radar Conf.* 1999, 142–147.

[Lombardo1996] Lombardo, P., and A. Farina. «Coherent radar detection against K-distributed clutter with partially correlated texture.» *Signal Process.*, 48, n. 1, (1996), 1–15.

[Lombardo1999b] Lombardo, P., and D. Pastina. «Multiband coherent radar detection against compound-Gaussian clutter.» *IEEE Trans. Aerosp. Electron. Syst.*, 35, n. 4, (1999), 1266–1282.

[Lombardo1998] Lombardo, P., D. Pastina, and T. Bucciarelli. «CFAR coherent radar detection against K-distributed clutter plus thermal noise.» In *Proc. 1998 IEEE Radar Conf.. RADARCON 98*. 1998, 129–134.

[Magaz2008] Magaz, B., and M.L. Bencheikh. «DSP implementation of a Range Azimuth CFAR processor.» In *2008 Int. Radar Symp.* 2008, 1–4.

[Mahalanobis1936] Mahalanobis, P.C. «On the generalised distance in statistics.» *Proc. National Institute of Sciences of India*, 2, n. 1, (1936), 49–55.

[Makhoul1975] Makhoul, J. «Linear Prediction: A Tutorial Review.» *Proc. IEEE*, 63, (1975), 561–580.

[Marier1995] Marier, L.J. «Correlated k-distributed Clutter Generation for Radar Detection and Track.» *IEEE Trans. Aerosp. Electron. Syst.*, 31, (1995), 568–580.

[Mashade1997] Mashade, M.B. El. «Performance analysis of the excision CFAR detection techniques with contaminated reference channels.» *Signal Process.*, 60, n. 2, (1997), 213–234.

[Mashade1998b] —. «Analysis of adaptive radar systems processing M-sweeps in target multiplicity and clutter boundary environments.» *Signal Process.*, 67, n. 3, (1998), 307–329.

[Mashade1998a] —. «Detection analysis of linearly combined order statistic CFAR algorithms in nonhomogeneous background environments.» *Signal Process.*, 68, n. 1, (1998), 59–71.

[Mashade2000] —. «Detection analysis of CA family of adaptive radar schemes processing M-correlated sweeps in homogeneous and multiple-target environments.» *Signal Process.*, 80, n. 5, (2000), 787–801.

[Mashade2001] —. «Postdetection integration analysis of the excision CFAR radar target detection technique in homogeneous and nonhomogeneous environments.» *Signal Process.*, 81, n. 11, (2001), 2267–2284.

[Mashade2002b] —. «M-correlated sweeps performance analysis of mean-level CFAR processors in multiple target environments.» *IEEE Trans. Aerosp. Electron. Syst.*, 38, n. 2, (2002), 354–366.

[Mashade2002] —. «Target Multiplicity Performance Analysis of Radar CFAR Detection Techniques for Partially Correlated Chi-Square Targets.» *AEU-Int. J. Electron. Commun.*, 56, n. 2, (2002), 84–98.

[Mashade2008] —. «Analysis of CFAR Detection of Fluctuating Targets.» *Progress In Electromagnetics Research B*, 2, (2008), 65–94.

[McDonald2005] McDonald, M., and S. Lycett. «Fast versus slow scan radar operation for coherent small target detection in sea clutter.» *IEE Proc.-Radar Sonar Navig.*, 152, n. 6, (2005), 429–435.

[Mezache2007] Mezache, A., and F. Soltani. «A novel threshold optimization of ML-CFAR detector in Weibull clutter using fuzzy-neural networks.» *Signal Process.*, 87, n. 9, (2007), 2100–2110.

[Mezache2008] —. «Threshold optimization of decentralized CFAR detection in weibull clutter using genetic algorithms.» *Signal, Image and Video Processing*, 2, n. 1, (2008), 1–7.

[Moody1989] Moody, J., and C.J. Darken. «Fast learning in networks of locally-tunes processing units.» *Neural Computation*, 1, n. 3, (1989), 284–294.

[Munro1996] Munro, D., O. Ersoy, M. Bell, and J. Sadowsky. «Neural network learning of low-probability events.» *IEEE Trans. Aerosp. Electron. Syst.*, 32, (1996), 898–910.

[Nathanson1999] Nathanson, F. E., J. P. Reilly, and M. N. Cohen. *Radar Design Principles: Signal Processing and the Environment (2nd Edition)*. SciTech Publishing, 1999.

[Neyman1933] Neyman, J., and K. Pearson. «On the problem of the most efficient test of statistical hypotheses.» *Philosph. Trans. Roy. Soc. London A, Math. Phys. Sci.*, 231, (1933), 492–510.

[Nguyen1990] Nguyen, D., and B. Widrow. «Improving the Learning Speed of 2-layer Neural Networks by Choosing Initial Values of the Adaptive Weights.» In *Int. Joint Conf. on Neural Netw., IJCNN 1990.* 1990, 21–26.

[Nieto2005] Nieto-Borge, J.C., and K. Hessner. «Comparison of WaMoS II with in situ measurements.» In *Hauser, D., Kahma, K., Krogstad, H.E., Lehner, S., Monbaliu, J.A.J., and Wyatt, L.R. (Eds.): Measuring and analysing the directional spectra of ocean waves EU COST Action 714.* 2005, 465.

[Nohara1994] Nohara, T.J., and S. Haykin. «Growler detection in sea clutter with coherent radars.» *IEEE Trans. Aerosp. Electron. Syst.*, 30, n. 3, (1994), 836–847.

[Nvidia] Nvidia, official Web site. «*http://www.nvidia.com/.*», 2011.

[OceanWaves] Ocean Waves, official Web site. «*http://www.oceanwaves.org/start.html.*»

[Ogawa1987] Ogawa, H., M. Sekine, T. Musha, M. Aota, and M. Ohi. «Weibull-distributed radar clutter reflected from sea ice.» *Trans. IEICE*, E70, (1987), 116–120.

[Oliver1985] Oliver, C.J. «Correlated K-distributed Clutter Models.» *Journal of Modern Optics*, 32, n. 12, (1985), 1515–1547.

[Oostveen2000] Oostveen, J., T. Kalker, and J.P. Linnartz. «Optimal detection of multiplicative watermarks.» In *Proc. 10th Eur. Signal Process. Conf.* 2000, 1–4.

[Papoulis1984] Papoulis, A. *Probability, Random Variables and Stochastic Processes.* McGraw-Hill, 1984.

[Park1991] Park, J., and I.W. Sandberg. «Universal approximation using RadialbBasis-Function Networks.» *Neural Computation*, 3, (1991), 246–257.

[Rajesh1999] Rajesh, K., and K.M.M. Prabhu. «Radar target detection in Weibull clutter by adaptive filtering with embedded CFAR.» *Electron. Lett.*, 35, n. 7, (1999), 597–599.

[Ramamurti1993] Ramamurti, V., S.S. Rao, and P.P. Gandhi. «Neural detectors for signals in non-Gaussian noise.» In *Proc. Int. Conf. Acoustics, Speech, Signal Processing (ICASSP)*. 1993, vol. 1, 481–484.

[Ravid1992] Ravid, R., and N. Levanon. «Maximum-likelihood CFAR for Weibull background.» *IEE Proc.-Radar Signal Proces.*, 139, n. 3, (1992), 256–264.

[Rholing1987] Rholing, H. «Robust algorithms for point target detection in different background situations.» In *Onzieme Colloque*. 1987, 123–126.

[Richards2005] Richards, M. A. *Fundamentals of Radar Signal Processing.* McGraw-Hill, 2005.

[Ruck1990] Ruck, D., S. Rogers, M. Kabrisky, M. Oxley, and B. Suter. «The multilayer perceptron as an approximation to a Bayes optimal discriminant function.» *IEEE Trans. Neural Netw.*, 1, (1990), 296–298.

[Sanz2002b] Sanz-González, J., and F. Alvarez-Vaquero. «Adaptive Importance Sampling Technique for Neural Detector Training.» In *Artificial Neural Networks - ICANN 2002* (J. Dorronsoro, ed.), Springer Berlin / Heidelberg, 2002, vol. 2415 of *Lecture Notes in Computer Science*. 141–141.

[Sanz2001] Sanz-González, J., and D. Andina. «Importance Sampling Techniques in Neural Detector Training.» In *Machine Learning: ECML 2001* (Luc De Raedt, and Peter Flach, eds.), Springer Berlin / Heidelberg, 2001, vol. 2167 of *Lecture Notes in Computer Science*. 431–441.

[Sanz2002a] Sanz-González, J. L., D. Andina, and J. Seijas. «Importance Sampling and Mean-Square Error in Neural Detector Training.» *Neural Process. Lett.*, 16, (2002), 259–276.

[Sayama2001] Sayama, S., and H. Sekine. «Weibull, log-Weibull and K-distributed ground clutter modeling analyzed by AIC.» *IEEE Trans. Aerosp. Electron. Syst.*, 37, n. 3, (2001), 1108–1113.

[Sayama2002] Sayama, S., and M. Sekine. «Amplitude Statistics of Sea-Ice Clutter Using a Millimeter Wave Radar.» *Int. J. Infrared Millimeter Waves*, 23, n. 11, (2002), 1583–1593.

[Sayama2004] —. «Suppression of Sea-Ice Clutter Observed by a Millimeter Wave Radar Using a New Log-Weibull/CFAR System.» *Int. J. Infrared Millimeter Waves*, 25, n. 10, (2004), 1481–1494.

[Sayama2005] —. «Amplitude Statistics of Sea Clutter Observed by a Millimeter Wave Radar Analyzed by Minimum Description Length (MDL) Principle.» *Int. J. Infrared Millimeter Waves*, 26, n. 11, (2005), 1639–1649.

[Schleher1976] Schleher, D.C. «Radar Detection in Weibull Clutter.» *IEEE Trans. Aerosp. Electron. Syst.*, AES-12, n. 6, (1976), 736–743.

[Schleher1980] —. *Automatic Detection and Radar Data Processing.* Artech House, 1980.

[Schwenker1994] Schwenker, F., H.A. Kestler, G. Palm, and M. Hoher. «Similarities of LVQ and RBF learning.» In *Proc IEEE Int. Conf. SMC*. 1994, 646–651.

[Schweppe1965] Schweppe, F. «Evaluation of likelihood functions for Gaussian signals.» *IEEE Trans. Inf. Theory*, 11, n. 1, (1965), 61–70.

[Sciotti2001] Sciotti, M., and P. Lombardo. «Performance evaluation of radar detection schemes based on CA-CFAR against K-distributed clutter.» In *Proc. 2001 CIE Int. Conf. Radar*. 2001, 345–349.

[Sekine1990] Sekine, M., and Y. Mao. *Weibull Radar Clutter.* Peter Pregrinus Ltd., 1990.

[Sen2009] Sen, S., and A. Nehorai. «Target Detection in Clutter Using Adaptive OFDM Radar.» *IEEE Signal Process. Lett.*, 16, n. 7, (2009), 592–595.

[Sheikhi2006] Sheikhi, A., and A. Zamani. «Adaptive Target Detection in Clutter Using MIMO Radar.» In *Int. Radar Symp., 2006. IRS 2006.* 2006, 1–4.

[Sheikhi2008] —. «Temporal coherent adaptive target detection for multi-input multi-output radars in clutter.» *IET Radar Son. Nav.*, 2, n. 2, (2008), 86–96.

[Skolnik2001] Skolnik, M. *Introduction to Radar Systems.* McGraw-Hill, 2001.

[Skolnik2008] —. *Radar Handbook, 3rd Ed.* McGraw-Hill, 2008.

[Srinivasan2002] Srinivasan, R. *Importance Sampling: Applications in Communications and Detection.* Speinger-Verlag, 2002.

[Sujuan1996] Sujuan, F., L. Wugao, and Z. Dejun. «Modeling and simulation of non-Gaussian correlated clutter.» In *Proc. CIE Int. Conf. Radar, 1996.* 1996, 195–199.

[Swerling1997] Swerling, P. «Radar probability of detection for some additional fluctuating target cases.» *IEEE Trans. Aerosp. Electron. Syst.*, 33, n. 2, (1997), 698–709.

[Szajnowski1977] Szajnowski, W.J. «The Generation of Correlated Weibull Clutter for Signal Detection Problems.» *IEEE Trans. Aerosp. Electron. Syst.*, AES-13, n. 5, (1977), 536–540.

[WMO] World Meteorological Organization, official Web site. «*http://www.wmo.int/pages/index_en.html*.», 2011.

[VanTrees1997] Trees, H.L. Van. *Detection, Estimation and Modulation Theory. Part I.* John Wiley and Sons, 1997.

[Trunk1972] Trunk, G.V. «Radar Properties of Non-Rayleigh Sea Clutter.» *Aerospace and Electronic Systems, IEEE Transactions on*, AES-8, n. 2, (1972), 196–204.

[Trunk1970] Trunk, G.V., and S.F. George. «Detection of targets in non-Gaussian sea clutter.» *IEEE Trans. Aerosp. Electron. Syst.*, AES-6, n. 5, (1970), 620–628.

[Vicen2009a] Vicen-Bueno, R., R. Carrasco-Álvarez, M. Rosa-Zurera, and J. C. Nieto-Borge. «Sea Clutter Reduction and Target Enhancement by Neural Networks in a Marine Radar System.» *Sensors*, 9, n. 3, (2009), 1913–1936.

[Vicen2007a] Vicen-Bueno, R., M.P. Jarabo-Amores, D. Mata-Moya, M. Rosa-Zurera, and R. Gil-Pita. «Low Complexity MLP-Based Radar Detector: Influence of the Training Algorithm and the MLP Size.» In *Computational and Ambient Intelligence*. 2007, 630–637.

[Vicen2007b] Vicen-Bueno, R., M.P. Jarabo-Amores, M. Rosa-Zurera, R. Gil-Pita, and D. Mata-Moya. «Performance Analysis of MLP-Based Radar Detectors in Weibull-Distributed Clutter with Respect to Target Doppler Frequency.» In *Artificial Neural Networks - ICANN 2007*. 2007, 690–698.

[Vicen2007c] Vicen-Bueno, R., M.P. Jarabo-Amores, M. Rosa-Zurera, D. Mata-Moya, and R. Gil-Pita. «Robustness with Respect to the Signal-to-Noise Ratio of MLP-based Detectors in Weibull Clutter.» In *Proc. of the 15^{t}h European Signal Proc. Conf. - EUSIPCO 2007*. 2007, vol. 1, 1736–1740.

[Vicen2010d] Vicen-Bueno, R., M.P. Jarabo-Amores, M. Rosa-Zurera, J. Sanz-González, and S. Maldonado-Bascón. «Importance Sampling for Objective Function Estimations in Neural Detector Training Driven by Genetic Algorithms.» *Neural Process. Lett.*, 32, (2010), 249–268.

[Vicen2006a] Vicen-Bueno, R., M. Rosa-Zurera, M.P. Jarabo-Amores, and R. Gil-Pita. «NN-Based Detector for Known Targets in Coherent Weibull Clutter.» In *Intelligent Data Engineering and Automated Learning - IDEAL 2006*. 2006, 522–529.

[Ward2006] Ward, K.D., R.J.A. Tough, and S. Watts. *Sea Clutter: Scattering the K-Distribution and Radar Performance*. IET Radar Son. Nav. Series, 2006.

[Watts1985] Watts, S. «Radar detection prediction in sea clutter using the compound K-distribution model.» *IEE Proc. F Comm. Radar Signal Proc.*, 132, n. 7, (1985), 613–620.

[Watts1987a] —. «Radar Detection Prediction in K-Distributed Sea Clutter and Thermal Noise.» *IEEE Trans. Aerosp. Electron. Syst.*, AES-23, n. 1, (1987), 40–45.

[Watts1990] Watts, S., C.J. Baker, and K.D. Ward. «Maritime surveillance radar. II. Detection performance prediction in sea clutter.» *IEE Proc. F Radar and Signal Proc.*, 137, n. 2, (1990), 63–72.

[Watts1987b] Watts, S., and K.D. Ward. «Spatial correlation in K-distributed sea clutter.» *IEE Proc. F Comm. Radar Signal Proc.*, 134, n. 6, (1987), 526–532.

[Xie2003] Xie, N., H. Leung, and H. Chan. «A multiple-model prediction approach for sea clutter modeling.» *IEEE Trans. Geosci. Remote Sensing*, 41, n. 6, (2003), 1491–1502.

[Zaimbashi2008] Zaimbashi, A., M. Reza Taban, M. Mehdi Nayebi, and Y. Norouzi. «Weighted order statistic and fuzzy rules CFAR detector for Weibull clutter.» *Signal Process.*, 88, n. 3, (2008), 558–570.

[Zaimbashi2006] Zaimbashi, A., M.R. Taban, and M.M. Nayebi. «Order Statistic and Algebraic Product CFAR Detector for Weibull Clutter.» In *Int. Conf. Radar, 2006 (CIE '06)*. 2006, 1–4.

Part VI

Appendixes

APPENDIX A

Symbols and Acronyms

A.1 Symbols with Latin Letters

1-D	1-dimension (selection mode).
2-D	2-dimension (selection mode).
$[A_1$ - $A_{K_\mathrm{a}}]$	Azimuthal coverage (A_1: Minimum azimuth; and A_{K_a}: Maximum azimuth).
$[R_1$ - $R_{K_r}]$	Range coverage (R_1: Minimum range; and R_{K_r}: Maximum range).
A	Amplitude of the target sequence.
A_i	i-th azimuthal bin of a radar scan.
$\mathbf{C}$	Matrix containing the covariance matrixes of the H radial basis functions of an RBFN.
$\mathbf{C}_i$	Covariance matrix of the i-th radial basis function of an RBFN.
$\mathbf{D}$	Desired output scan.
$E\{\cdot\}$	Mathematical expectation of a random variable or sequence.
E_{MS}	Mean squared error.
E_{SS}	Sum-of-squares error.
$F(\cdot)$	Function implemented or approximated by a given processor (MLP-based, RBFN-based, etc.).
F	Number of free parameters in an MLP.
G	Number of guard cells in selection modes used in CFAR detectors.
J	Number of MLP and RBFN inputs, and CFAR cells.
$J/H/1$	MLPs or RBFNs formed of J inputs, H hidden neurons and 1 output.
$\mathbf{J}_k$	Jacobian matrix at the k-th iteration of the Levenberg-Marquadt learning algorithm.
$\mathbf{H}_k$	Hessian matrix at the k-th iteration of the Levenberg-Marquadt learning algorithm.
H_0	Alternative hypothesis in the detection problem (target is absent).
H_1	True hypothesis in the detection problem (target is present).
$\mathbf{I}$	Radar scan.

$\mathbf{I}^{(a)}$	Radar scan considering that the clutter properties in it follows a Weibull distribution with a skewness value of a.
K	Number of MLP and RBFN inputs.
K_{a}	Number of azimuth bins in a radar scan.
K_{r}	Number of range bins in a radar scan.
$\mathbf{L}$	Matrix with the eigenvalues of the linear prediction filter.
$\mathbf{M}_{\mathrm{c}}$	Covariance matrix of the clutter sequence.
$\hat{\mathbf{M}}_{\mathrm{c}}$	Estimate of the covariance matrix of the clutter sequence.
$\mathbf{M}_{\mathrm{cG}}$	Covariance matrix of a coherent Gaussian sequence/process.
$\mathbf{M}_{\mathrm{cW}}$	Covariance matrix of a coherent Weibull sequence/process.
$\mathbf{M}_{\mathrm{i}}$	Covariance matrix of the interference sequence.
$\hat{\mathbf{M}}_{\mathrm{i}}$	Estimate of the covariance matrix of the interference sequence.
$M^{(\mathrm{t})}$	Number of radars scans in the test data set.
$M^{(\mathrm{d})}$	Number of radars scans in the train data set.
$M^{(\mathrm{v})}$	Number of radars scans in the validation data set.
$\mathrm{N}(\mu, \sigma^2)$	Normal distribution with mean μ and variance σ^2.
N	Number of selected cells when using non-delayed modes.
$\mathbf{O}^{\mathrm{Det}}$	Output scan at the output of the detector.
$\mathbf{O}^{\mathrm{Proc}}$	Output scan at the output of the processor.
P	Number of observation vectors extracted from a data set of radar scans.
P_{fa}	Probability of false alarm.
P_{d}	Probability of detection.
P_{c}	Clutter power.
$P_{\mathrm{c}}^{\mathrm{imp.}}$	Clutter power improvement.
P_{cG}	Power of a Gaussian sequence.
P_{cW}	Power of a Weibull sequence.
$P_i[n\|n-1]$	Estimate of the variance (power) of the received signal under H_i hypothesis.
P_{t}	Target power.
$P_{\mathrm{t}}^{\mathrm{imp.}}$	Target power improvement.
$P(H_i)$	A priori probability of the hypothesis H_i.
$\mathbf{R}$	Matrix containing the centroids of the H radial basis functions of an RBFN.
$R_{uu}[k]$	Autocorrelation sequence of a given sequence $u[n]$.
$R_{uv}[k]$	Autocorrelation sequence of two given sequences $u[n]$ and $v[n]$.
$R_{\mathrm{cW}}[k]$	Autocorrelation sequence of a Weibull sequence.
$R_{\xi}[n]$	Autocorrelation sequence of a Gaussian sequence.
R_i	i-th range bin of a radar scan.
$\mathrm{SCR}^{\mathrm{av.imp.}}$	Average signal-to-clutter improvement.
T	Threshold of the envelope detector.
$\mathbf{U}$	Matrix with the eigenvectors of the linear prediction filter.
$\mathbf{W}$	Vector that contains the LPF coefficients in the TSKAP detector working in batch mode.
$\mathbf{W}^{(\mathrm{h})}$	Matrix of size $[H \times K]$ that contains the synaptic weights of the hidden layer of an MLP.
$\mathbf{Z}$	Matrix containing a set of P observation vectors.

a	Skewness parameter of the Weibull distribution.
$a^{(\mathrm{d})}$	Skewness parameter of the Weibull distribution in the design stage.
$a_i^{(\mathrm{d})}$	Skewness parameter of the Weibull-distributed clutter of the i-th radar scan of the design data set.
b	Scale parameter of the Weibull distribution.
$\hat{b}$	Estimate of the scale parameter of the Weibull distribution.
$\mathbf{b}^{(\mathrm{h})}$	Vector of size $[H \times 1]$ that contains the bias of the hidden neurons of an MLP.
$b^{(\mathrm{o})}$	Bias of the output neuron of an MLP.
c	Propagation speed of the electromagnetic waves in the air.
$c[n]$	Received clutter sequence (coherent or incoherent).
$\hat{c}[n]$	Estimate of the received clutter sequence (coherent or incoherent).
$\tilde{c}[n]$	Residual of the estimated clutter sequence (coherent or incoherent).
$\mathbf{c}[n]$	Set of N samples of the clutter sequence.
$f(\cdot\|H_i)$	Probability density function of a given signal under hypothesis H_i.
f_{c}	Frequency at which the radar works.
$f_{\mathrm{cW}}[k]$	Doppler frequency of a Weibull sequence.
$f_{\mathrm{cG}}[k]$	Doppler frequency of a Gaussian sequence.
f_{dc}	Doppler frequency of the clutter.
f_{dt}	Doppler frequency of the target.
$f_{\mathrm{proc}}(\cdot)$	Function implemented by the processor of a certain detector.
$f_{\mathrm{MLP}}(\cdot)$	Function implemented by the processor of an MLP-based detector.
$f_{\mathrm{RBFN}}(\cdot)$	Function implemented by the processor of an RBFN-based detector.
f_{s}	Sampling frequency.
$g(\cdot)$	Activation function of a radial basis function.
$g[n]$	White Gaussian noise sequence (coherent or incoherent).
$g_{\mathrm{P}}[n]$	In-phase component (real-part) of a coherent white Gaussian noise sequence.
$g_{\mathrm{Q}}[n]$	Quadrature component (imaginary-part) of a coherent white Gaussian noise sequence.
$\mathbf{g}[n]$	Set of N samples of the white Gaussian noise sequence.
h_{a}	Antenna height.
k	Order of selection in OS-CFAR detectors.
m_{H_i}	Number of observation vectors extracted from a data set under hypothesis H_i.
$o[n]$	Sequence at the input of the NLPF and NLMLT^{-1}.
$p[n]$	Sequence at the output of the NLMLT^{-1} and at the input of the LPF.
$\mathbf{p}$	Input vector at the input of the LPF of the TSKAP detector in batch mode.
$q[n]$	Sequence at the output of the LPF and at the input of the NLMLT.
$\mathbf{q}$	Vector at the output of the LPF of the TSKAP detector in batch mode.
$r[n]$	Sequence at the output of the NLMLT and output of the NLPF.
$\mathbf{r}_i$	Vectors containing the centers of the i-th radial basis function of an RBFN.
$r_x[n]$	Autocorrelation sequence of the sequence $x[n]$.
$r_{uu}[n]$	Normalized autocorrelation sequence of a given sequence $u[n]$.
$r_{uv}[n]$	Normalized crosscorrelation sequence of two given sequences $u[n]$ and $v[n]$.
$r_w[n]$	Normalized autocorrelation sequence of a Weibull sequence.
$r_\xi[n]$	Normalized autocorrelation sequence of a Gaussian sequence.

$s[n]$	Received target sequence (coherent or incoherent).
$\mathbf{s}[n]$	Set of N samples of the target sequence.
t_{d}	Delay time produced in the different selection modes.
t_{H_i}	Desired MLP and RBFN output for an observation vector under hypothesis H_i.
u	Real-part of the coherent Weibull random variable.
$u_i[n\|n-1]$	Residues after the estimations done in the TSKAP detectors under hypothesis H_1 ($i=1$: target is present) and H_0 ($i=0$: target is absent).
v	Imaginary-part of the coherent Weibull random variable.
$v[n]$	Output of the TSKAP processor.
$v_i^{(\mathrm{h})}[n]$	Activation of the i-th hidden neuron of an MLP or RBFN.
$\mathbf{v}^{(\mathrm{h})}[n]$	Vector containing the activation of the H hidden neurons of an MLP or RBFN.
$v^{(\mathrm{o})}[n]$	Activation of the output neuron of an MLP or RBFN.
w	Coherent Weibull random variable.
$\mathbf{w}$	Vector that contains the LPF coefficients in the TSKAP detector.
$\mathbf{w}^{(\mathrm{o})}$	Vector of size $[1 \times H]$ that contains the synaptic weights of the output layer of an MLP.
$x[n]$	Real-part of a coherent correlated Gaussian sequence or output at the processor used in each detector under study.
$x_i^{(\mathrm{h})}[n]$	Output of the i-th hidden neuron of the MLP.
$\mathbf{x}^{(\mathrm{h})}[n]$	Vector containing the outputs of the H hidden neurons of an MLP.
$x^{(\mathrm{o})}[n]$	Output of the output neuron of the MLP.
$x'[n]$	Real-part of a coherent white Gaussian sequence.
$y[n]$	Imaginary-part of a coherent correlated Gaussian sequence or output the detectors under study.
$y'[n]$	Imaginary-part of a coherent white Gaussian sequence.
$z[n]$	Received radar echo (coherent or incoherent).
$\mathbf{z}[n]$	Set of N samples of the received radar echoes.
$\hat{z}_i[n\|n-1]$	Estimate of the mean value of the received signal under H_i hypothesis.
$z_{\mathrm{P}}[n]$	In-phase component (real-part) of a coherent received echo.
$z_{\mathrm{Q}}[n]$	Quadrature component (imaginary-part) of a coherent received echo.

A.2 Symbols with Greek Letters

ΔA	Azimuthal sampling period (angle between consecutive azimuths: $A_i - A_{i-1}$).
ΔR	Range resolution (range between consecutive range cells: $R_j - R_{j-1}$).
$\Gamma(\cdot)$	Gamma function.
$\Lambda[n]$	n-th sample of the log-likelihood ratio (LLR).
$\Lambda(\cdot)$	Log-likelihood ratio (LLR) for a given signal or vector.
$\Lambda_{c+g}[n]$	n-th sample of the LLR when only clutter and noise are present (hypothesis H_0).
$\Lambda_{s+c+g}[n]$	n-th sample of the LLR when target is present in clutter (hypothesis H_1).
α	Multiplication constant in CFAR detectors to adapt the threshold.
α_k	Adaptive learning rate of the error back-propagation algorithm.
$\xi[n]$	Coherent correlated Gaussian sequence.
$\xi'[n]$	Coherent white Gaussian sequence.
$\delta_k^{(\mathrm{h})}$	Local derivative of the MSE at the k-th hidden neuron in an MLP.
$\delta^{(\mathrm{o})}$	Local derivative of the MSE at the output neuron of an MLP.
ϵ	Mean square error of the LPF estimation.
μ	Mean of a random variable or momentum constant in the error back-propagation algorithm.
μ_a	Mean of the skewness parameter of a Weibull distribution.
μ_b	Mean of the scale parameter of a Weibull distribution.
ω_{a}	Antenna rotation speed.
ψ	Phase of the coherent Weibull random variable.
$\psi_{\mathrm{htan}}(\cdot)$	Hyperbolic tangent activation function (used in the neurons of an MLP).
$\psi_{\mathrm{htan}'}(\cdot)$	First derivative of the hyperbolic tangent activation function.
$\psi_{\mathrm{lin}}(\cdot)$	Linear activation function in a neuron of an MLP.
ρ_{c}	One-lag correlation coefficient of the clutter sequence.
ρ_{cW}	One-lag correlation coefficient of a Weibull sequence.
ρ_{cG}	One-lag correlation coefficient of a Gaussian sequence.
ρ_{t}	One-lag correlation coefficient of the target sequence.
σ	Standard deviation of a random variable.
σ^2	Variance of a random variable.
σ_g^2	Variance of the noise sequence.
σ_a^2	variance of the skewness parameter of a Weibull distribution.
σ_b^2	Variance of the scale parameter of a Weibull distribution.
τ	Radar pulse width.
θ	Instantaneous phase of the target signal.
θ_{h}	Antenna horizontal beamwidth.
θ_{v}	Antenna vertical beamwidth.
θ_{g}	Grazing incidence angle (measured from the horizontal).
θ_{e}	Antenna elevation angle.

A.3 Acronyms

ACF	Autocorrelation function.
AI	Artificial intelligence.
ANN	Artificial neural network.
AOD	Asymptotically optimum detector.
CA-CFAR	Cell averaging constant false alarm rate (processor or detector).
CCGS	Coherent correlated Gaussian sequence.
CCWS	Coherent correlated Weibull sequence.
CFAR	Constant false alarm rate (processor or detector).
CNR	Clutter-to-noise ratio.
CUT	Cell under test.
CWGS	Coherent white Gaussian sequence.
MSE	Mean squared error.
SSE	Sum-of-squares error.
FINO-1	Forschungsplattformen in Nord- und Ostsee 1.
FFT	Fast Fourier transform.
GLR	Generalized likelihood ratio.
H	Horizontal selection mode.
IF	Intermediate frequency.
LR	Likelihood ratio.
LLR	Log-likelihood ratio.
LPF	Linear prediction filter.
MIMO	Multiple-input multiple-output.
MLP	Multilayer perceptron.
MTD	Moving target detector.
MTI	Moving target indicator.
ML-CFAR	Maximum likelihood constant false alarm rate (processor or detector).
NLMLT	Non-linear memoryless transformation.
NLMLT^{-1}	Inverse of the non-linear memoryless transformation.
NLPF	Non-linear prediction filter.
OFDM	Orthogonal frequency division multiplexing.
OS-CFAR	Order statistics constant false alarm rate (processor or detector).
P	Plus-shape selection mode.
PRF	Pulse repetition frequency.
R	Rhombus-shape selection mode.
ROC	Receiver operating characteristics.
RCS	Radar cross section.

RBF	Radial basis function.
RBFN	Radial basis function network.
RBF-ANN	Radial basis function artificial neural network.
RIA	Range of integrated area (size of the side of a selection mode).
S	Square-shape selection mode.
SCR	Signal-to-clutter ratio.
SNR	Signal-to-noise ratio.
SVM	Support vector machine.
THR	Threshold of a detector.
TSKAP	Target sequence know a priori (detector).
V	Vertical selection mode.
WaMoS II	Wave Monitoring System II.
WVD	Wigner-Ville decomposition.
X	Cross-shape selection mode.
pdf	Probability density function.

APPENDIX B

Wiener Filtering

Consider the design of a Finite Impulse Response (FIR) Wiener filter [Hayes1996] that produces the minimum mean-square estimate of a given process $q[n]$ by filtering a set of observations of a statistically related process $p[n]$. It is assumed that $p[n]$ and $q[n]$ are jointly wide-sense stationary with known autocorrelations, $r_p[k]$ and $r_q[k]$, and known cross-correlation $r_{qp}[k]$. denoting the unite sample response of the Wiener filter by $w[n]$, and assuming a (m-1)st order filter, its impulse response is

$$\mathbf{w} = \begin{bmatrix} w[n] \\ w[n-1] \\ \vdots \\ w[n-m+1] \end{bmatrix} \tag{B.1}$$

Being $p[n]$ the input to the filter, the output, which we denote by $\hat{q}[n]$, is the linear convolution of $p[n]$ and $w[n]$, i.e.,

$$\hat{q}[n] = \sum_{l=0}^{m-1} w[l]p[n-l] \tag{B.2}$$

The Wiener filter design problem requires that we find the filter coefficients, $w[n]$, that minimize the mean-square error [1]

$$\epsilon = E\{|e[n]|^2\} = E\{|q[n] - \hat{q}[n]|^2\} \tag{B.3}$$

If we want that a set of filter coefficients minimize ϵ, it is necessary and sufficient that the derivative of ϵ with respect to $w^*[k]$ be equal to zero for $k = 0, 1, \ldots, m-1$,

$$\frac{d\epsilon}{dw^*[k]} = \frac{d}{dw^*[k]} E\{e[n]e^*[n]\} = E\{e[n]\frac{de^*[n]}{dw^*[k]}\} = 0 \tag{B.4}$$

where $e[n]$ is the error sequence, which is obtained as

$$e[n] = q[n] - \sum_{l=0}^{m-1} w[l]p[n-l]\,. \tag{B.5}$$

[1] Note that our wide-sense stationary assumption implies that the mean-square error does not depend upon n.

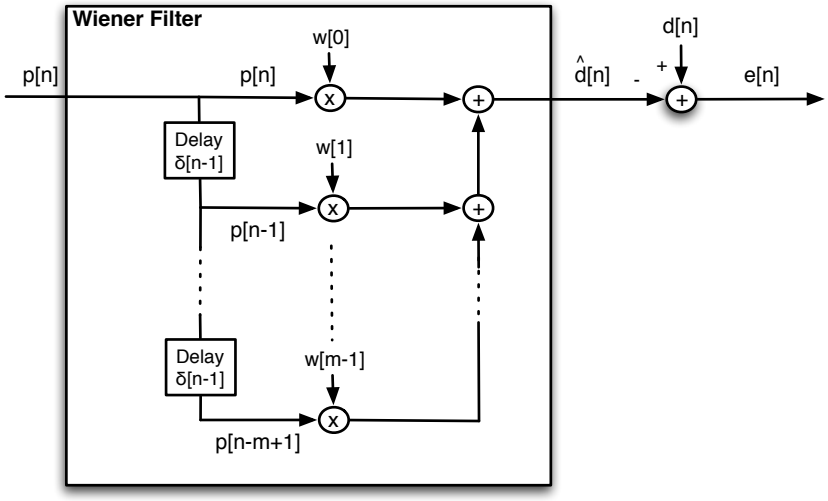

Figure B.1: Finite Impulse Response Wiener Filter.

So, applying

$$\frac{de^*[n]}{dw^*[k]} = -p^*[n-k] \tag{B.6}$$

in eq. (B.4) becomes

$$E\{e[n]p^*[n-k]\} = 0 \quad , \quad k = 0, 1, \cdots, m-1 \tag{B.7}$$

which is known as the orthogonality principle or the projection theorem. Substituting (B.5) into (B.7), we have

$$E\{q[n]p^*[n-k]\} - \sum_{l=0}^{m-1} w[l]E\{p[n-l]p^*[n-k]\} = 0\,. \tag{B.8}$$

Finally, since $p[n]$ and $q[n]$ are jointly wide-sense stationary, then $E\{p[n-l]p^*[n-k]\} = r_p[k-l]$ and $E\{q[n]p^*[n-k]\} = r_{qp}[k]$. So, eq. (B.8) becomes

$$\sum_{l=0}^{m-1} w[l]r_p[k-l] = r_{qp}[k] \tag{B.9}$$

which is a set of m linear equations in the m unknown $w[k]$, $k = 0, 1, \ldots, m-1$. If it is expressed in a matrix form, the following expression is achieved:

$$\begin{pmatrix} r_p[0] & r_p[-1] & \ldots & r_p[-m+1] \\ r_p[1] & r_p[0] & \ldots & r_p[-m+2] \\ r_p[2] & r_p[1] & \ldots & r_p[-m+3] \\ \vdots & \vdots & & \vdots \\ r_p[m-1] & r_p[m-2] & \ldots & r_p[0] \end{pmatrix} \begin{pmatrix} w[0] \\ w[1] \\ w[2] \\ \vdots \\ w[m-1] \end{pmatrix} = \begin{pmatrix} r_{qp}[0] \\ r_{qp}[1] \\ r_{qp}[2] \\ \vdots \\ r_{qp}[m-1] \end{pmatrix} \tag{B.10}$$

If the fact that the autocorrelation sequence is conjugate symmetric, i.e., $r_p[k] = r_p^*[-k]$, eq.

(B.10) becomes

$$\begin{pmatrix} r_p[0] & r_p^*[1] & \dots & r_p^*[m-1] \\ r_p[1] & r_p[0] & \dots & r_p^*[m-2] \\ r_p[2] & r_p[1] & \dots & r_p^*[m-3] \\ \vdots & \vdots & & \vdots \\ r_p[m-1] & r_p[m-2] & \dots & r_p[0] \end{pmatrix} \begin{pmatrix} w[0] \\ w[1] \\ w[2] \\ \vdots \\ w[m-1] \end{pmatrix} = \begin{pmatrix} r_{qp}[0] \\ r_{qp}[1] \\ r_{qp}[2] \\ \vdots \\ r_{qp}[m-1] \end{pmatrix} \tag{B.11}$$

which is the matrix form of the Wiener-Hopf equations. Equation (B.11) can be written more concisely as

$$\mathbf{R}_p \mathbf{w} = \mathbf{r}_{qp} \tag{B.12}$$

where $\mathbf{R}_p$ is an mxm Hermitian Toeplitz matrix of autocorrelations, $\mathbf{w}$ is the vector of the filter coefficients, and $\mathbf{r}_{qp}$ is the vector of cross-correlations between the desired signal $q[n]$ and the observed signal $p[n]$. So the coefficients of the LPF can be obtained with

$$\mathbf{w} = \mathbf{R}_p^{-1} \mathbf{r}_{qp} \,. \tag{B.13}$$

The minimum mean-square error in the estimate of $q[n]$ may be evaluated from eq. (B.3) as follows:

$$\epsilon = E\{|e[n]|^2\} = E\{e[n] \left[q[n] - \sum_{l=0}^{m-1} w[l] p[n-l] \right]^* \} \tag{B.14}$$

$$\epsilon = E\{e[n] q^*[n]\} - \sum_{l=0}^{m-1} w^*[l] E\{e[n] p^*[n-l]\}\} \tag{B.15}$$

recall that if $w[n]$ is the solution of the Wiener-Hopf equations, then, it follows from eq. (B.7) that $E\{e[n]p^*[n-k]\} = 0$. Therefore, the second term in (B.15) is equal to zero and

$$\epsilon_{min} = E\{e[n] q^*[n]\} = E\{ \left[q[n] - \sum_{l=0}^{m-1} w[l] p[n-l] \right] q^*[n] \} \,. \tag{B.16}$$

Finally, taking expected values, we have

$$\epsilon_{min} = r_q[0] - \sum_{l=0}^{m-1} w[l] r_{qp}^*[l] \tag{B.17}$$

or using vector notation,

$$\epsilon_{min} = r_q[0] - \mathbf{r}_{qp}^H \mathbf{w} \tag{B.18}$$

and applying eq. (B.13), the minimum mean-square error may also be written explicitly in terms of the autocorrelation matrix $\mathbf{R}_p$ and the cross-correlation vector $\mathbf{r}_{qp}$ as follows:

$$\epsilon_{min} = r_q[0] - \mathbf{r}_{qp}^H \mathbf{R}_p^{-1} \mathbf{r}_{qp} \,. \tag{B.19}$$